TRANSPORTATION RESEARCH

RECORD

No. 1393

*Bridges, Other Structures, and
Hydraulics and Hydrology*

Structures

A peer-reviewed publication of the Transportation Research Board

Transportation Research Record 1393

Contents

Foreword

This volume is composed of 20 papers that were presented in six sessions sponsored by four TRB Structures Section committees at the 1993 TRB Annual Meeting and 1 paper that was submitted for publication only.

The first seven papers were presented at a session sponsored by the Committee on General Structures. Burke discusses the attributes and limitations of integral bridges, which account for their general favor over jointed bridge counterparts. Van Lund describes bridge modular expansion joints and the steps taken by the Washington State Department of Transportation to improve their quality and durability. Fu et al. discuss an analysis method for design of base plates for span wire traffic signal poles. Sotiropoulos and GangaRao present a quantitative study of bridge deck deterioration factors and propose a method for mitigation. GangaRao et al. examine the effects of freeze-thaw cycles on various concrete structural components, especially on concrete-filled steel-grid bridge decks. Kuo et al. describe the use of a large-scale accelerated testing facility to simultaneously test five bridge rehabilitation joint systems. Hulsey and Powell present time-dependent empirical equations for various weather conditions at two bridge sites, describing how these exposure models were used to study thermal stresses and movements in the structures.

The Committees on General Structures and Sealants and Fillers for Joints and Cracks cosponsored a session on Development of Bridge Bearing Systems, at which the next two papers were presented. Mander et al. describe field tests on 30-year-old fixed and expansion steel bridge bearings along with an analytical study of the deck-substructure interaction. Atkinson discusses three types of modern high-load multirotational bridge bearings and how they act within the structural system.

The next three papers were presented at a session sponsored by the Committee on Steel Bridges. Menzemer and Fisher summarize a study to examine issues associated with the design of welded aluminum structures, including material characterization, residual stress measurements, fatigue testing, and detailed examination of fracture surfaces. Price discusses innovations in enhancement of the design, durability, constructability, and economics of composite steel box girder bridges. Wang et al. modeled multiple vehicles moving across rough bridge decks to study the vibration and impact in seven steel multigirder bridges.

Following these are five papers presented in a session sponsored by the Committee on Concrete Bridges. Cook et al. discuss a new type of short-span, precast, posttensioned, flat-slab bridge system for transversing wetlands and shallow waters to replace the traditional trestle-type bridge. Khaleel and Itani present a study of fatigue life of partially prestressed concrete girder bridges via modeling loadings due to a variety of alternative truck configurations and weights. Dusseau and Dubaisi analyze ambient vibration on 50 concrete bridges along two Interstate highways in the state of Washington. Buckingham et al. present favorable results of an experimental study of concrete bridge columns with interlocking spiral reinforcement. Deatherage et al. discuss prestressed girders and their behavior under static loading.

The final five papers in this volume result from the work of the Committee on Dynamics and Field Testing of Bridges. Four were presented at two Annual Meeting sessions; the final one was submitted to the committee for publication only. Nowak et al. present an approach for evaluating fatigue performance and apply the proposed approach to an existing steel girder bridge. Hulsey and Delaney summarize tests conducted on a cable-stayed bridge in Alaska with statically positioned trucks. Aktan et al. describe a comprehensive structural identification process that incorporates dynamic and static tests for a 3-D finite element model of a three-span steel-stringer bridge. Verma and Priestley present a design algorithm for optimal design of single-column circular reinforced concrete bridge piers to resist seismic loadings. Bednar compiles results of continuing field inspections to update the limits of environmental conditions for aluminized steel Type 2 drainage pipe.

Integral Bridges: Attributes and Limitations

MARTIN P. BURKE, JR.

In some areas of the United States, integral bridges are now being used whenever application limits do not favor another type of structure. Integral bridges have numerous favorable attributes and few limitations. Because design provisions can be made for some of the limitations, only application limitations such as length, skew, and curvature should negate the use of integral bridges in favor of their jointed bridge counterparts. Design procedures and details used for the construction of single- and multiple-span integral bridges of continuous moderate length [91 m (300 ft)] are described, and the comparative attributes and limitations of integral and jointed bridges are elaborated on. The integral bridges discussed have shallow, stub-type abutments supported by embankments and piles. For integral bridges with multiple spans, piers are either flexible and attached to the superstructure or semirigid and self-supporting with movable bearings.

Integral structures, or structures without movable joints, are ages old. The most celebrated are the natural arches carved from bedrock by water and wind. The largest such structure is Rainbow Bridge National Monument in Utah near the Arizona border. It is composed of pink sandstone and has a span of 85 m (278 ft).

However, in considering integral bridges built by human beings, one cannot go much further back into recorded history than the first arch bridges containing unreinforced concrete constructed by the Romans. More recently, most are familiar with the construction of reinforced concrete arch bridges in the early decades of this century.

BACKGROUND AND OVERVIEW

Reinforced concrete began as a substitute for stone masonry in the construction of filled spandrel arch bridges. In these bridges, the pavement and spandrel fill are supported on one or more continuously reinforced arched slabs. Although many of the multiple-span spandrel-filled arches were constructed with movable joints in spandrel walls and railings, many of the one- or two-span bridges of this type can be classified as true integral bridges because they were constructed without movable joints. (In this paper, the designation "movable joint" replaces the misnomer "expansion joint.")

By the third and fourth decades of this century, arch bridge construction culminated in the construction of long-span closed- and open-spandrel arch bridges. Although the major supporting elements of these bridges (abutments, piers, and arch ribs) have no movable joints, they are not true integral bridges because the deck slabs and spandrel walls have movable joints

at each intermediate pier and occasionally in the deck slabs and spandrel walls within each span.

By midcentury, however, many transportation departments were building concrete rigid frame bridges. These bridges represented a standard type of construction for many transportation departments. Those built in Canada by the province of Ontario are good examples. Although vertical movable joints are used between the bridges and their lateral wingwalls, the bridges can be classified as integral because they have no movable joints in their decks or primary supporting elements.

The construction of rigid frame bridges was paralleled by the construction of bridges with multiple-span, continuous-slab beams or girders. Ultimately, the overall economy of continuous construction made practicable the use of multiple spans, embankments, and small stub-type abutments supported on a single row of flexible piles in lieu of a conventional single- or multiple-span bridge with wall-type abutments (Figure 1). Many of the shortest of these bridges—those shorter than 61 m (200 ft)—were constructed without movable deck joints. The economy, durability, and simplicity of these early integral designs led to the use of this type of construction for progressively longer spans.

Thus, although various types of integral bridges have been constructed for centuries, the term "integral bridge" is now generally used to refer to continuous jointless bridges with single and multiple spans and capped-pile stub-type abutments (Figure 2).

Piers for integral bridges can be of any type. If the inherent flexibility of a chosen type will accommodate structure movements, the piers may be built integrally with the superstructure or connected to it with anchor bolts. Otherwise, piers are designed as semirigid self-supporting substructures with movable bearings between them and the superstructure.

ATTRIBUTES AND LIMITATIONS

The popularity of integral bridges has grown with their number (1–3). It soon became evident that these bridges, which were originally built as a reaction to the destructive effects of leaking deck joints and massive pavement pressures, had many more attributes and fewer limitations than their jointed counterparts. Interestingly enough, these attributes not only reduced a bridge's first cost and life-cycle cost, they also reduced the cost of its own future modification (e.g., widening) and its eventual replacement. Integral bridges have been found to be an ideal structure for secondary road systems for states and counties, and with thoughtful crafting they are becoming popular for rural and urban primary and Interstate systems.

Burgess & Niple, Ltd., 5085 Reed Road, Columbus, Ohio 43220.
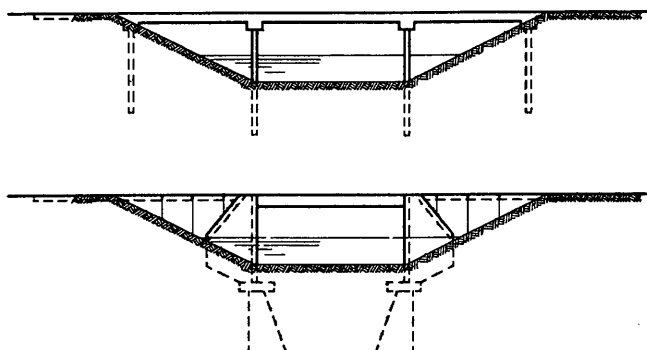
FIGURE 1 Different bridge types for the same site: (*top*)
multiple-span integral bridge with stub-type abutments; (*bottom*)
single span with movable bearings and wall-type abutments.

Although their jointless construction and resistance to
pavement pressure and consequent long-term durability ap-
pear to be the primary attributes that first motivated the con-
struction of longer and longer integral bridges, it also appears
that their simple design, rapid construction, and other attri-
butes have gained favor for them as these attributes become
more widely recognized.

For design engineers and engineer administrators who are
considering integral bridges for the first time, a review of the
discussion in this paper should help to explain why these
bridges are now being constructed with increasing frequency.

Attributes

Because discussions of attributes (and limitations) of integral
bridges would have little significance unless they were con-
sidered with respect to another bridge type with familiar char-
acteristics, the descriptions that follow and the comparisons
that are made all refer to similar single-span or multiple-span
continuous deck-type structures with movable deck joints at
abutments and with both fixed and movable bearings.

Simple Design

Where abutments and piers of a continuous bridge are each
supported by a single row of piles attached to the superstruc-
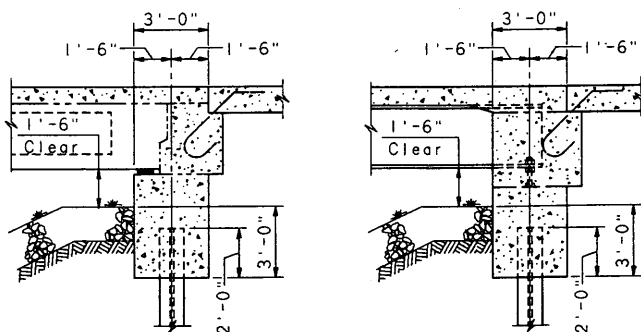
**FIGURE 2 Capped-pile stub-type abutments for integral
bridges:** (*left*) **for prestressed concrete box-beam stringers;**
(*right*) **for steel I-beam stringers.**

ture or where self-supporting piers are separated from the
superstructure by movable bearings, an integral bridge may,
for analysis and design purposes, be considered a continuous
frame with a single horizontal member and two or more ver-
tical members. When the stiffness and distribution factors are
calculated for such a frame, the vertical members are so flex-
ible when compared with the horizontal member that the
horizontal member may be assumed to have simple supports.
Consequently, except for the design of the continuity con-
nections at abutments, frame action in integral bridges can
be neglected in considering the effects of vertical loads applied
to superstructures.

The design of integral bridges is further simplified because
piers and abutments generally need not be designed to resist
either lateral or longitudinal loads. This is possible because
the laterally and longitudinally rigid concrete deck slab is
rigidly attached to both abutments, and the abutments are
rigidly restrained by the confining embankments. Conse-
quently, essentially all lateral and longitudinal loads applied
to the superstructures of integral bridges are distributed di-
rectly to abutment embankments. As a result, piers and abut-
ments need not be designed to resist horizontal loads applied
to superstructures.

The design of abutment-superstructure continuity connec-
tions and transverse wingwalls can be standardized for a wide
range of bridge applications. A nominal amount of reinforce-
ment will be suitable to resist the slight live and dead loads
typical of such applications plus a wide range of secondary
effects (shrinkage, creep, passive pressure, etc.). Also, a nom-
inal amount of reinforcement can be provided for transverse
wingwalls to resist the maximum anticipated passive pressure.
Once these standard details are established, each bridge
abutment can be configured and reinforced for the vertical
reactions associated with various roadway widths and span
lengths. In general, this consists of no more than the deter-
mination of an appropriate pile load and spacing and pile cap
reinforcement.

The design of piers is similarly accomplished. Essentially
all horizontal superstructure loads are distributed to approach
embankments, and moments resulting from pier-superstruc-
ture continuity are negligible. Therefore, piers of integral
bridges (capped-pile or free-standing types with movable
bearings) need be designed only for vertical superstructure
and pier loads and for lateral loads that may be applied di-
rectly to the piers (streamflow, stream debris, earth pressure,
wind). Where these lateral pier loads are small, and this is
usually the case, most piers, like abutments, can be designed
essentially for vertical loads alone.

For flexible piers that receive much of their lateral support
from their connection to the superstructure, construction pro-
cedures are necessary to ensure that these piers are not lat-
erally loaded until after they have been connected to the
superstructure and the continuity connections to the super-
structure abutment have been completed.

Because the superstructure and abutment embankments
resist primary lateral loads, piers (piles, columns, footings,
foundations) of integral bridges may be reduced to minimum
sizes and dimensions. Battered piles are not required. Fixed
piers are not required. In general, pier design can be simpli-
fied to the extent that standard designs can be developed for
a wide range of roadway widths and span lengths.

Jointless Construction

The primary attribute of integral bridges is their jointless construction. To fully appreciate this attribute, one must be familiar with the performance of bridges with movable joints.

Open-deck joints permit contaminated deck drainage to penetrate joints and cause extensive below-deck deterioration. Closed joints and sealed joints give a measure of protection from deck drainage deterioration. However, all movable deck joints (open, closed, or sealed) are vulnerable to the destructive effects of approach pavement growth and pressure. Bridges with movable deck joints constructed in conjunction with rigid, jointed approach pavement have inadvertently functioned as elaborate and expensive pavement pressure relief joints. As approach pavements grow and the moving deck joints accommodate this growth, bridges are progressively squeezed until the movable joints are closed. Thereafter, additional pavement growth and bridge elongation generate sufficient pavement pressure to crush joint seals and to fracture abutment backwalls and bridge seats. Consequently, the avoidance of such joints obviates the need for maintenance-prone joint seals and the extensive pressure-damage repair that has come to be associated with them.

As a secondary benefit, smooth jointless construction improves vehicular riding quality and diminishes vehicular impact stress levels.

Pressure Resistance

The solid, jointless construction of integral bridges distributes longitudinal pavement pressures over a total superstructure area substantially greater than that of the approach pavement cross section. Consequently, approach pavements are more likely to fail by progressive localized fracturing or instantaneous buckling than the more pressure-resistant bridge superstructure. Unless approaches to integral bridges are furnished with cycle control joints that are appropriately designed—joints that facilitate the thermal cycling of the bridge and attached approach slabs—they are more likely to experience early distress because restrained expansion of the bridge contributes to the generation of pavement pressure.

Because integral bridges are capable of sustaining significant longitudinal compression without distress, almost any pressure relief joint used by maintenance forces to relieve pavement pressure would be suitable for them. However, jointed bridges need highly efficient pressure relief joints if pavement pressures are to be reduced low enough to keep deck joints functioning. Few such pressure relief joints are being used by pavement design or maintenance engineers.

Rapid Construction

Numerous features of integral bridges facilitate their rapid construction, and these features are probably responsible for much of the outstanding economy that has been achieved by their construction. Dry construction, simple members, broad tolerances, few construction joints, few parts, few materials, elimination of labor-intensive practices, and many other features combine to make possible completion of such structures in a single, short construction season. The more rapid construction is possible even when the structures have to be built in stages to maintain traffic. Consider the following features in more detail.

Embankments   Embankments can be placed and constructed with large earth-moving and compaction equipment. Only limited use of hand-operated compaction equipment is needed.

Cofferdams   Integral bridges, especially those constructed with capped-pile or drilled-shaft piers, can be constructed with fewer delays due to inclement weather and stream flooding. Abutment excavations and pile driving near the top of approach embankments can be done without cofferdams and generally without the need for dewatering. Foundation construction can progress as fast as pier and abutment piling can be driven. Subsequently, pile cap and superstructure construction can proceed with little regard for streamwater levels.

Small Excavations   At abutment benches, excavations need be no more than 0.6 to 0.9 m (2 to 3 ft) deep.

Vertical Piles   At abutments, vertical piles are uniformly spaced and driven in a single horizontal row. In contrast, the typical abutment foundation of jointed bridges consists of two or more rows of both vertical and battered piles.

Pier piles also are uniformly spaced and driven vertically in a single horizontal row. This arrangement avoids the need for pile clusters with some battered piles for each column footing, the typical pier foundation for many cap and column piers of jointed bridges. For bridge sites with high water levels, driving piles for pier footings is more difficult because the piles must be driven inside deep cofferdams.

Simple Forms   Pier and abutment pile caps are formed quickly because they are usually composed of simple rectangular shapes.

Few Joints   Few construction joints are used for integral bridges. Consequently, few concrete placement and curing days are needed. For example, no more than four concrete placement days are needed for most integral bridges. Only one day each is required for placing pile caps, continuity connections, deck slab, and approach slabs. Single-span integral bridges in some states have been simplified to the extent that only two days are required; the second day is necessary only to place separately cast approach slabs. In contrast, constructing most jointed bridges requires five or more placement days and subsequent curing days.

Few Parts   Fixed and movable bearings, armor for deck joints, and deck joint seals are unnecessary. The normal de-

lays associated with deck joint installation, adjustment, and anchorage are avoided.

Broad Tolerances   The close construction tolerances usually associated with jointed bridges are not necessary for integral bridges. For example, the elevation, slope, and uniformity of bridge seats are not important because only rough-surfaced construction joints are required.

Reduced Removals   Using typical multiple-span integral bridges with embankments and stub abutments to replace shorter bridges with wall-type abutments permits new bridges to be constructed without requiring the complete removal of existing substructures. The new bridges can be configured to straddle existing foundations (Figure 3), and where existing abutments are located in the new embankments, most of the existing abutments need not be removed. At many sites, significant savings are possible. For example, where normal water levels are high, complete removal of existing substructures could require the building of large cofferdams for this purpose alone.

Simple Beam Seats   Some of the labor-intensive practices required for jointed bridge construction are either eliminated or substantially simplified in integral bridge construction. For example, consider the problem of providing appropriate loading surfaces for the elastomeric bearings of side-by-side and spread prestressed box-beam bridges.

Side-by-side prestressed box beams must be canted laterally to match the deck crown and tilted longitudinally to accommodate bridge grade. Also, because the ends of these beams are sloped owing to residual camber, adjustments usually need to be made in beam bottoms, bearings, or bridge seats to compensate for these geometric irregularities and provide parallel loading surfaces for elastomeric bearings. A number of options are available to the designer:

1. A longitudinally tapered recess can be cast in beam bottoms to match a longitudinally level and laterally crowned bridge seat surface,
2. Bridge seats can be sloped to match the orientation of beam bottoms, and
3. A tapered metal laminate can be molded within the bearings to compensate for differences in the longitudinal orientation of beam bottoms and seat surfaces, and bridge seats can be laterally crowned to match the canted beams.
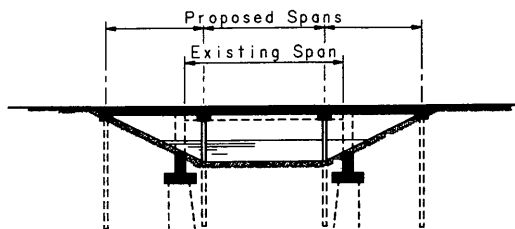
FIGURE 3   New bridge straddles old foundations.

If this is not complex enough, the specific provisions adopted to compensate for crown, grade, and camber may, in some bridges, have to be unique for each bridge seat because bearing geometry changes from one substructure to the next as a result of changes in grade and span lengths. In addition, poor estimates of residual camber, differences in residual camber from beam to beam, skew effects, errors in computing actual surface orientations, and errors in construction make the attainment of parallel loading surfaces uncertain. Consequently, even after all these considerations have been accounted for, occasionally it is necessary to use shims under elastomeric bearings to obtain solid seating of beams on bridge seats.

Integral bridge construction makes most of these considerations and procedures unnecessary. Because beams of integral bridges need only temporary support until continuity connections have been cast, a narrow temporary elastomeric erection strip can be used on a temporary bridge seat surface to support the beams. After continuity connections are cast and cured, all the beam reactions (dead, live, and impact loads) will be uniformly supported by cast-in-place continuity connections, connections that are far superior in supporting superstructure loads to the series of separate and uncertainly loaded elastomeric bearings characteristic of jointed box-beam bridges.

Because concrete or steel I-beams are placed vertically, crown effects need not be considered when appropriate bearings and bridge seats are provided. However, even for I-beam bridges, the use of integral construction (continuity connections) considerably simplifies bridge seat and bearing requirements and improves the distribution of superstructure reactions.

Elimination of Bearing Anchor Bars   For the typical jointed bridge, superstructures are usually fixed at one or more substructure elements, usually at an intermediate pier. For side-by-side prestressed box-beam bridges, this fixing often is done by placing anchor bars down through precast holes in the box beams and into field-drilled holes in bridge seats. Because of the uncertainties of beam fit-up, beam length, and substructure locations, holes in the bridge seat must be field drilled after all beams have been placed and compacted together. Considering the errors that are likely to occur in locating substructures accurately and the bridge-seat reinforcement in these substructures, it is reasonable to assume that some primary bridge-seat reinforcement is cut by field drilling anchor bar holes.

Because superstructures of integral bridges receive lateral and longitudinal support from abutment embankments, only flexible piers not integrally constructed with superstructures (the types of piers that depend upon the superstructure for lateral and longitudinal support) need to be provided with anchor bars and field-drilled holes. All other pier types (flexible integral piers and self-supporting piers with movable bearings) do not need bearing anchor dowels or field-drilled anchor dowel holes. For both pier types, because field-drilled anchors are not needed, the potential damage associated with drilling anchor-bar holes in the field is avoided.

Of particular significance is the saving per hour of work made possible by eliminating the labor-intensive procedures of drilling and cleaning the holes and placing anchor bars and

grout. This labor can be significant when such anchors are located in each beam and at every support.

Eliminating holes for field-drilled anchor bars is particularly important in projects for bridge modification. For example, in replacing the superstructure of an existing bridge (and this type of bridge modification occurs increasingly frequently), conversion of a jointed bridge to an integral bridge with continuity connections cast in place at abutments enables the designer, when working with self-supporting piers, to eliminate attachments between piers and superstructure. Fixed bearings and their anchor bars can be eliminated. Consequently, the designer of such a project can, by eliminating the need to field-drill anchor holes, avoid the probability of cutting existing primary pier cap reinforcement.

Broad-Span Ratios

The ratio of end span to center span of continuous spans (L_e/L_c) is generally set at or near 0.8 to achieve stable superstructures and a balanced beam design. This is the ratio most often used for stream crossings. Lesser ratios are often used for grade separation structures where short end spans are needed to achieve the shortest possible bridge length. However, for sites where a ratio of less than 0.6 is necessary for jointed bridges, provisions must be made to prevent beam uplift during deck placement and superstructure uplift because of movement of vehicular traffic. Such provisions can become complex and expensive when bearings must be provided that will allow horizontal movement of the superstructure but prevent uplift.

Integral bridges, on the other hand, are more resistant to uplift because the abutment weight resists it. Thus, a span ratio of 0.5 can be used without any change in the integral bridge design. For the smallest span ratios, a procedure for deck slab placement can be used to counteract uplift during construction.

Earthquake Resistance

Because decks of integral bridges are rigidly connected to both abutments and consequently to both embankments, these bridges are in fact part of the ground and will move with the ground during earthquakes. Consequently, when integral bridges are constructed on stable embankments and subsoils, they should have an adequate response to most earthquakes.

For an integral bridge located across a fault line—a highly unlikely situation—differential lateral movement of the ground at the fault line could seriously stress the bridge deck, but the integral construction of the structure should enable it to resist.

Simplified Widening and Replacement

Many of the bridges placed on the highway system in the past were designed for immediate needs with little consideration for future requirements. Through arches of concrete, through trusses of steel, and bridges with wall-type abutments with flared wingwalls are prime examples of such bridges. Most often, through structures have to be completely replaced when increased traffic and traffic speeds necessitate building wider roadways. Widening bridges with wall-type abutments and flared wingwalls is complex and expensive.

In contrast, integral bridges with straight capped-pile substructures are convenient to widen and easy to replace if future demands have not been accurately foreseen. Of particular significance is the fact that their substructures (the piling) can be recapped and reused or, if necessary, they can be withdrawn or left in place. They avoid the necessity of building extensive foundations that interfere with the placement of future foundations.

Many of the stream crossings in Ohio—and presumably the same is true for many states and provinces—have been spanned by at least three separate earlier bridges, with a fourth presently being planned. For many of these early bridges, the foundations have been left in place. Consequently, when planning today's replacement structure for small stream crossings, the engineer finds that parts of the streambed are filled with the old foundations. With the use of capped-pile substructures, the new substructure can be placed to clear existing foundations and avoid the expense of removing them. Also, the greater span ratio range gives the integral bridge great adaptability for the foundation-filled bridge sites.

Improvement in Live Load Distribution

Superstructures that are integrally constructed with capped-pile abutments and piers instead of separated from them by numbers of compressible elastomeric bearings give vehicular wheel loads broader distribution than would otherwise be possible. This arrangement reduces superstructure service load stresses.

Limitations

High Abutment-Pile Stresses

Except for abutment piling and wingwalls, the various members of integral bridges are subjected to essentially the same levels of primary stresses (dead load, live load, impact, etc.) and secondary stresses (shrinkage, creep, thermal gradients, etc.) as their jointed bridge counterparts. However, because the bending resistance of the vertical piling of integral bridge abutments will resist the lengthening and shortening of bridge superstructures responding to temperature changes, the piling of long integral bridges can be subjected to flexural stresses considerably greater than those of their jointed bridge counterparts. For longer integral bridges, research with abutments supported by steel piles has shown that abutment piling stresses of integral bridges can approach, equal, or even exceed the yield strength of pile material.

Such flexural piling stresses, if they are large enough, will result in the formation of plastic hinges that will limit the flexural resistance of the piles to additional superstructure elongation. At the same time, the laterally supported piles should retain their capacity to sustain vertical loads.

Because piles of integral bridges may be subjected to high bending stresses, only suitable pile types should be used for these applications. Such piles should retain sufficient axial load capacity while localized pile transformations occur that

will reduce the resistance to bending. For this reason, only steel H-piles or appropriately reinforced concrete or prestressed concrete piles should be used to support abutments of the longer [>91 m (>300 ft)] integral bridges.

For shorter integral bridges, pile flexural stresses should be well within normal allowable stress levels for the material under consideration.

In addition to the most appropriate piling, other provisions can be considered to reduce the resistance of piles to lateral abutment movement: Steel H-piles can be oriented to place the weak axis parallel to the abutment centerline, bridge skews can be limited (typically <30 degrees), piles can be placed in prebored holes filled with fine granular material, pile-footing connections can be altered to reduce the resistance of the piles to bending at this junction, appropriate reinforcement can be placed in concrete piles to facilitate the formation of hinges, and so forth.

For short- and medium-length bridges provided with the usual single row of cast-in-place concrete, precast concrete, or steel H-piles, pile flexural stresses should be well within the elastic range. No unusual provisions should need to be made in their design.

Limited Applications

The superior economy of integral bridges is due to their ability, within a limited application range, to satisfy all functional requirements with safety, durability, and optimal economy. They are not broadly adaptable to most bridge applications as are their jointed bridge counterparts.

Integral bridges with abutments supported on single rows of piling should be limited in a number of ways based on the primary design features that have been incorporated into standard designs. In general, their length should be limited for two reasons: to minimize passive pressure effects and to limit bridge movements to those that can be accommodated by the movement range of approach slab–approach pavement cycle control joints and standard approach guardrail connections. They should not be used where curved beams or beams with horizontal bends are used. They should not be used for extreme skews (>30 degrees). They should not be used where abutment piles cannot be driven through at least 3 to 4.5 m (10 to 15 ft) of overburden. They should not be used at sites where the stability of subsoils is uncertain or where vertical abutment settlement may be significant (where it cannot be effectively compensated for by added roadway overlays alone). Finally, they should not be used at sites where they can become submerged unless the superstructure is vented, vertically restrained to resist uplift due to superstructure buoyancy, or both.

Buoyancy

Because of their jointless construction, many types of integral bridges are subject to uplift when they become submerged. This is true for many I-beam bridges and some spread box-beam bridges.

The weight of diaphragms and abutments provides some resistance to uplift, but generally some positive design pro-

visions must be made to ensure that integral bridges have a reasonable factor of safety against flotation. I-beam webs can be pierced near top flanges by 76.2-mm (3-in.) diameter holes spaced uniformly throughout the beam length; the space between spread boxes can also be vented by placing 76.2-mm (3-in.) minimum diameter horizontal vent ducts near the top flange of all beams. These ducts should pass completely through the beams from one web to the other, and they should be placed in concrete diaphragms or be completely encased in concrete to prevent floodwaters from entering beam voids. Counterweights could be used, but their weight must be taken into account during beam design. Uplift restraints could be provided at pier bearings, or some piers can be integrally constructed with the superstructure to add sufficient uplift restraint to counteract buoyancy.

In lieu of vent holes, added weight, uplift restraints, or integral pier construction, most buoyant structures should be used only at those bridge sites where the highest floodwater levels are well below the superstructure.

Construction Procedures

Embankments   Abutments and piers of integral bridges composed primarily of a single row of piles have a very limited resistance to lateral loads. So they must be constructed in a way that either controls or eliminates lateral earth movements. In this respect, most major earthwork must be placed and compacted before piling is driven to ensure that lateral movement of subsoils both below and within embankments has been allowed to stabilize before piles are driven. A typical plan note used for this purpose can be phrased as follows:

> EMBANKMENTS shall be constructed up to the subgrade for a distance of 61 m (200 ft) (other) back of abutments before excavation is made for abutments, prebored holes placed, and pier and abutment piles driven.

The limitation given above for piers is important. Even though piers may be located beyond the toe of abutment embankments, they can be adversely affected by subsurface movement if they are placed before embankment construction has been completed. However, if they must be placed before embankment construction, they also must be of the type that can resist lateral earth pressure without depending upon their attachment to the superstructure for support.

Abutment and Approach Slab Concrete   Because concrete continuity connections at abutments and approach slabs must be cast integrally with superstructures and superstructures are continuously responding to changing ambient temperatures, such placement, especially for long bridges, should be controlled to minimize the effect of superstructure movement on fresh concrete.

It is generally not feasible to restrict concrete placement to those days of the year with the smallest temperature range and consequently to periods of the smallest potential for large superstructure movements. But it is practicable to limit concrete placement during daily periods when the superstructure movement is the smallest, generally shortly after the ambient temperature approaches, reaches, and departs from the day's peak temperature. A plan note to provide such control and

some protection for freshly placed concrete can be phrased somewhat as follows:

> CONCRETE for continuity connections at abutments shall be placed and completed at least four hours prior to the concrete placement day's peak ambient temperature.

Approach slab connections to abutments should be similarly protected from the effects of the superstructure's response to ambient temperature changes. A plan note somewhat as follows can be used:

> APPROACH SLAB concrete shall be placed towards the superstructure and be completed at least four hours prior to the concrete placement day's peak ambient temperature.

To avoid damaging freshly placed concrete continuity connections during sudden ambient temperature changes, especially for long superstructures, in some states superstructure beams are mechanically fastened to abutment pile caps before continuity connections are placed. Thus, after this attachment is completed, the continuity connection (abutment backwall) can be placed without concern for changes in the ambient temperature because concrete is being placed on a pile cap, a cap that is moving with the superstructure. However, even for these structures, control of approach slab concrete is still necessary.

Deck Slab Concrete   Deck slab placement on integral bridges with short end spans must be controlled to eliminate uplift of beams during concrete placement. This can occur when both deck slabs and continuity connections at abutments (integral backwalls) are placed simultaneously. To avoid uplift in these applications, continuity connections should be placed first and cured adequately before placement of deck slab concrete.

Approach Slabs

Full-width approach slabs should be provided for most integral bridges. They should be tied to the bridge to avoid having the slabs shoved off their seats by the constant horizontal cycling of the bridge as it responds to daily temperature changes. To facilitate the slab's movement, a sealed cycle-control joint should be provided between approach slabs and approach pavements to accommodate the cycling of the approach slabs. The sealed joint should also prevent roadway drainage from penetrating the joints and flooding the subbase. To protect the joints, approach slabs, and bridge from pavement pressure, an effective pavement pressure relief joint also should be provided in all jointed approach pavement.

Approach slabs have a number of beneficial effects. By spanning between abutments and approach embankment, approach slabs prevent vehicular traffic from consolidating the backfill adjacent to the abutment, thereby diminishing passive pressure effects. If the approach slabs are long enough, they eliminate live-load surcharge on abutment backfill. They help to control roadway drainage by conducting it across the abutment backfill to the bridge or pavement approaches and prevent erosion of abutment backfill or saturation and freezing of the backfill. Finally, they serve as a ramp from the rigidly supported abutments to approach pavements supported on consolidating embankments, and thereby help to retain a serviceable riding surface and minimize vehicular impact.

However, approach slabs tied to integral bridges become part of the bridges and respond to temperature and moisture changes. Consequently, they effectively increase the overall structure length and require cycle-control joints with greater movement ranges.

To minimize the amount of force necessary to move the slabs, they should be cast on smooth, low-friction (polyethylene, filter-fabric, etc.) surfaces.

Cycle-Control Joints

Integral bridges with attached approach slabs lengthen and shorten in respone to temperature and moisture changes. For such structures built adjacent to rigid approach pavement, the boundary between the approach slabs and approach pavement should be provided with cycle-control joints to facilitate such movement. Otherwise, the cycling of both structure and approach slabs can generate pressures sufficient to fracture the approach pavement either progressively or instantaneously (blow-up).

Over time, jointed approach pavement will lengthen progressively (grow). Where such progressive movement is restrained by an integral bridge, substantial longitudinal pressures will be generated in the pavements and adjacent bridge. To control such pressures, pressure relief joints should be used between rigid approach pavement and integral bridges.

Consequently, two types of joints are required adjacent to integral bridges. One should facilitate the cycling of the bridge and attached approach slabs, and the other should be capable of responding to the progressive growth of the approach pavement. Designs by four transportation departments are given elsewhere (*4*). All the designs in use have their limitations. To avoid the maintenance problems associated with complex or unusual cycle-control joints, maintenance engineers of the Ohio Department of Transportation (ODOT) prefer simple 0.3-m (12-in.) wide pressure-relief joints for longer integral bridges to facilitate both types of movement. The narrow joints will be progressively compressed by the growing approach pavement. When the bridge and attached approach slabs withdraw during periods of cold temperature, the joints will be open to water and debris. This is the primary fault of this design, but the fault is considered acceptable until a more suitable design becomes available. The joints can be filled by maintenance personnel during cold weather or they will be closed in warm weather by expanding pavement. Ultimately, the joints, approach pavement, and bridge will become compressed and joint movement will be limited. Eventually the joints will have to be restored through a process involving cutting away part of the approach pavement and replenishing filler extruded by prior joint compression.

No single-joint design is available to accommodate these movements suitably, so ODOT engineers say that they prefer to use the simple pressure relief joint because it is the only one that can be easily maintained by state maintenance personnel. Other, more complex designs now available do not function well and are difficult to repair and in many cases have to be replaced.

RESEARCH

Extensive research on passive pressure is needed to describe both the relationship between the amount of soil compression and the generation of passive pressure and the effect of alternating cycles of soil compression and expansion. Until such research has been accomplished, present integral bridge design procedures will depend on idealizations and simplifications that probably do not accurately predict passive pressure effects.

Shrinkage and creep studies are needed for both integral bridges and their jointed bridge counterparts. Although present research in this area has been illuminating, the numerical procedures presently recommended do not properly account for the composite behavior of various combinations of beam and slab sizes. Also, the results of recent computer studies have not been verified by comprehensive physical testing nor been presented in a form suitable for use by practicing design engineers.

The lack of comprehensive research on passive pressure is probably responsible for the lack of specifications to guide the development of suitable designs for integral bridges.

SUMMARY

As the above enumerations have shown, integral bridges have numerous attributes and few limitations. Because design provisions can be made to account for some of these limitations (cycle-control joints, pressure-relief joints, approach slabs, construction procedures, and structure buoyancy), only application limitations (structure length, curvature, skew, overburden depth, and unstable subsoils) should negate the use of integral bridges in favor of their jointed bridge counterparts. In many areas of the country, integral bridges are being used whenever application limitations do not prevent their use. The high abutment pile stresses and uncertain passive pressure effects are being accepted as the only negative aspects of such designs. However, these negative aspects are acceptable whenever they are weighed against all the attributes that integral bridges provide.

REFERENCES

1. J. H. Emanual et al. *Current Design Practice for Bridge Superstructures Connected to Flexible Substructures.* Civil Engineering Study 77-3. University of Missouri-Rolla, 1973.
2. A. M. Wolde-Tinsae and J. E. Klinger. *Integral Abutment Bridge Design and Construction.* Report FHWA/MD-87/04. University of Maryland, College Park, 1987.
3. M. P. Burke, Jr. *NCHRP Synthesis of Highway Practice 141: Bridge Deck Joints.* TRB, National Research Council, Washington, D.C., 1989, pp. 20–30.
4. M. P. Burke, Jr. Bridge Approach Pavements, Integral Bridges, and Cycle Control Joints. In *Transportation Research Record 1113,* TRB, National Research Council, Washington, D.C., 1987.

Improving the Quality and Durability of Modular Bridge Expansion Joints

JOHN A. VAN LUND

The Washington State Department of Transportation (WSDOT) has taken steps to improve the quality and durability of modular bridge expansion joints that have a movement rating greater than 150 mm. Expansion joints are subject to a greater number of load cycles than normal bridge components. As a result of premature fatigue failures of modular bridge expansion joints in Washington State and elsewhere, WSDOT requires that all modular joint components meet fatigue design and testing requirements. Components are designed for a fatigue life of 100 million cycles. Fatigue design and testing requirements are included in the contract specifications. Improved specifications and quality control during manufacture and construction are needed in order to eliminate possible loss of quality caused by competitive bidding and bid shopping. Preapproved expansion joint models and manufacturers should be identified in the contract plans and specifications. Contractors should identify which manufacturer is selected at the time of bid submission. It is recommended that modular bridge expansion joints have at least a 5-year guarantee on performance and durability.

The three functional areas concerning bridges are: design, construction, and maintenance. As shown in Figure 1, effective lines of communication between these three areas are critical to ensure that a bridge project is successfully constructed and that existing bridges are safe. The ultimate goal is an aesthetically pleasing bridge with a long service life.

Modular bridge expansion joints are lightweight steel structural systems that permit both translation and rotation between adjacent superstructure bridge elements. The joints are located in the plane of the bridge deck and are perpendicular to the direction of traffic. The movement ratings of modular bridge expansion joints range from 150 to 1280 mm. These watertight joints were developed in Europe in the 1960s and have been manufactured in the United States for more than 20 years.

Two design concepts are used for modular bridge expansion joints: the multiple support bar system and the single support bar system. The multiple support bar expansion joint shown in Figure 2 was first introduced in the United States in the early 1970s. Each steel center beam, which has a sealing element between parallel center beams, is rigidly connected to and supported below by a steel support bar. A horizontal force acting at the roadway surface produces an overturning moment that is resisted by the support bar's span. The horizontal force is transmitted to the bridge by horizontal control springs. The largest multiple support bar expansion joint in Washington State was installed on the Pasco-Kennewick In-

Bridge and Structures Branch, Washington State Department of Transportation, Transportation Building KF-01, Olympia, Wash. 98504.

tercity Bridge in 1978. The 10-seal joint has a total movement capability of 600 mm (*1*).

Figures 3 and 4 show the single support bar concept, which is more complicated than the multiple support bar system. The center beam has a steel yoke that accommodates the support bar. All center beams are supported by the same support bar. Precompressed springs and bearings trap the support bar between the bottom of the center beam and the yoke. The softer spring is below the support bar, and the stiffer bearing is between the center beam and the top of the support bar. The spring/bearing system must allow the center beams to translate along the length of the support bar to accommodate movement. The springs and bearings must also resist overturning while allowing sliding to occur. The two 1280-mm movement joints on the third Lake Washington floating bridge between Seattle and Mercer Island on Interstate 90 are the largest single support bar modular expansion joints in the United States (*2*).

In 1991, as a result of several premature fatigue failures of expansion joint components, the Washington State Department of Transportation (WSDOT) took steps to improve the quality and durability of modular bridge expansion joints. The steps involved fatigue design and testing, stricter quality-control requirements during manufacturing and construction, preapproval based on proven field experience, and a 5-year guarantee of satisfactory performance and durability.

This paper provides background information on fatigue design and testing of modular bridge expansion joints so that effective policy decisions can be made concerning improvements in the quality and durability of these systems.

FATIGUE DESIGN AND TESTING

Static Wheel Load Analysis

In the United States, expansion joints have been designed in accordance with the AASHTO *Standard Specifications for Highway Bridges* (*3*) using AASHTO HS20 wheel loads with an impact factor of 30 percent. Impact factors as high as 60 to 100 percent have been used, depending on local agency requirements. For a 30 percent impact factor, the wheel load is 92.5 kN, and for a 100 percent impact factor it is 142.3 kN. Until recently, the center beam has been analyzed for only static vertical loads either as a beam on rigid supports or as a beam supported by springs. For expansion joints on a 5 to 6 percent grade, an analysis based only on vertical loads may not reflect the actual loading if the effects of horizontal loads are not included. The wheel load distribution to each center
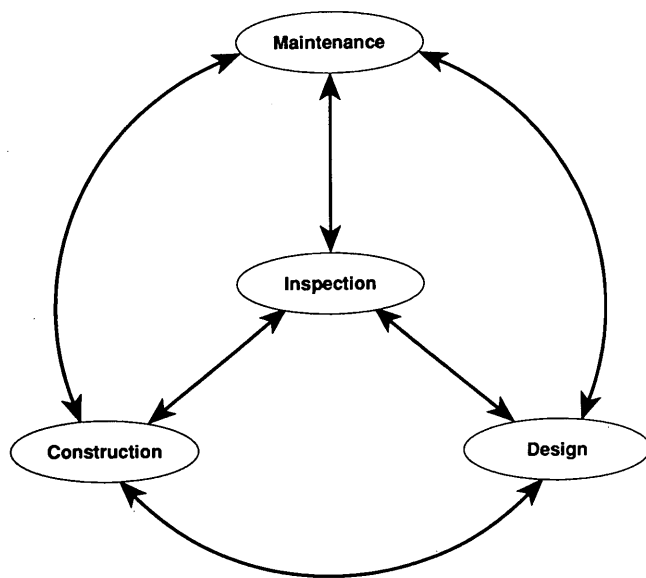
FIGURE 1 Lines of communication between functional areas.

beam depends on the gap between the center beams and the width of the center beam in contact with the tire (4).

Fatigue failures in Washington State and on the Burlington Bay Skyway on Queen Elizabeth Way, Ontario, Canada, have occurred after a very short service life: within the first 5 years (5). Three failures involved welded connection details. The stainless steel pin failure that occurred at the interface between a center beam and support bar may have been initiated by a crack caused by contact with a snowplow blade. However, "beach marks" on the fractured surface clearly indicate a progressive fatigue failure. It is apparent that a static analysis using allowable service load stresses is not adequate to ensure a long service life. The problem cannot be solved by arbitrarily specifying greater wheel loads or higher impact factors without considering the cumulative damage effects caused by fatigue.

Wheel Load Range for Fatigue Design

Wheel load ranges and allowable fatigue stress ranges for the design of expansion joint components subject to high cyclic loading are not available in the AASHTO *Standard Specifications for Highway Bridges* (3). Designers must either extrapolate existing data, which may not be based on adequate testing, or look elsewhere for guidance.

Research in Austria by Tschemmernegg indicates that the fatigue critical details, particularly connections, should be designed for a vertical limit states fatigue load range of 118.3 kN per wheel (+91.0 to −27.3 kN) and a horizontal load range of 36.4 kN/wheel (+18.2 to −18.2 kN) (4). These loads include a 40 percent impact factor and are shown in Figure 5; actual measured wheel loads are less than these loads. This vertical load range is very close to an HS25 wheel load plus 30 percent impact, which is 115.6 kN. An HS25 wheel load is 25 percent greater than an HS20 wheel load. The horizontal load range proposed by Tschemmernegg is approximately 30 percent of the vertical load range for an HS25 wheel load with a 30 percent impact factor (4).
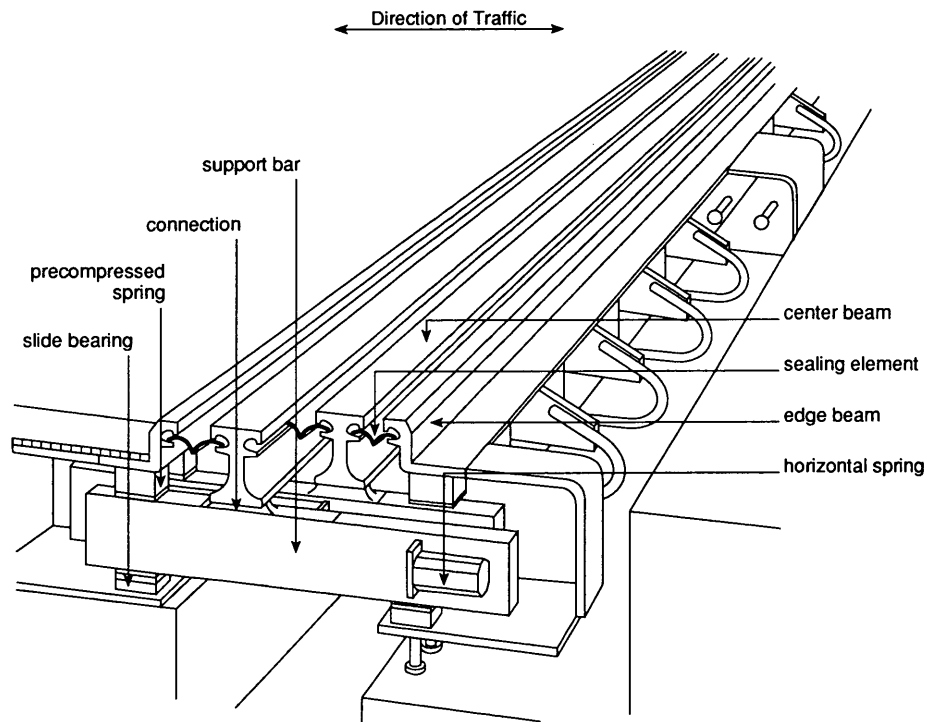
FIGURE 2 Multiple support bar expansion joint after Maurer-Söhne.
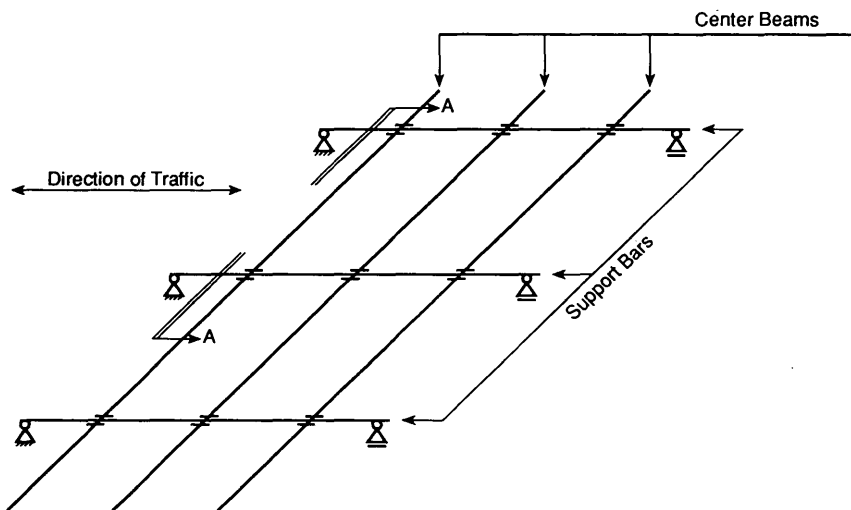
FIGURE 3 Plan, single support bar expansion joint.
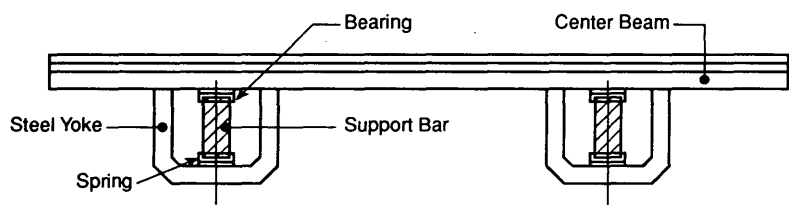
FIGURE 4 Section A-A showing center beam, support bar, springs, and bearings of single support bar system.

The effect of both vertical and horizontal loads on the expansion joint is a function of approach road surface roughness, vehicle speed, dynamic characteristics of both vehicle and expansion joint, and expansion joint vertical and horizontal stiffness. The horizontal loads are associated with the tire rolling resistance, air pressure acting on the vehicle, and tractive or braking forces.
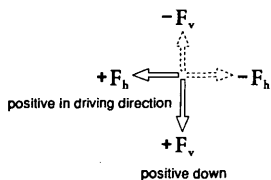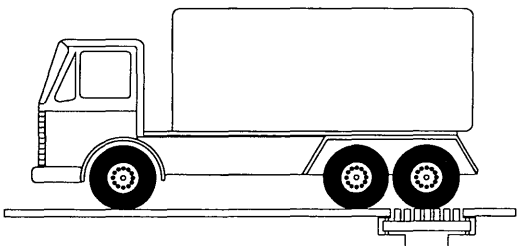
FIGURE 5 Limit states fatigue wheel loads proposed by Tschemmernegg (*4,9*).

Effect of Roadway Grade

The loads shown in Figure 5 are for an expansion joint on a flat or 0 percent grade. As the grade steepens, the horizontal loads parallel to the roadway surface increase by the component of the gravity acting wheel loads (Figure 6). This additional force component of the vertical wheel load is often overlooked by designers. It can be critical since horizontal forces produce a torque on the center beam and an increase in the stresses in the fatigue-sensitive connection between the center beam and support bar. The load ranges of fatigue limit states should be modified to account for the increased horizontal force caused by roadway grade.

Effect of Support Settlement

Settlement of the center beam is caused by deflection of the support bar, softening or creep of the support bar bearings, or potential foundation settlement in the anchorage area. In the more-complicated single support bar system, the potential for settlement is greater because there are additional springs and bearings at the intersection of the center beam and support bar. If these springs and bearings creep over time, the center beam can deflect under wheel impact loads.

Any support bar settlement caused by softening of the bearings or gaps caused by complete loss of precompression, including those at the ends of the support bar, will produce
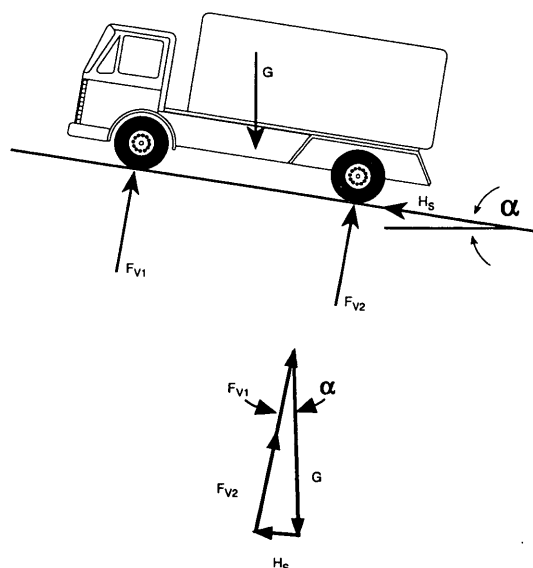
FIGURE 6   Effect of roadway grade (*top*) and horizontal force (H$_S$) on rear drive wheels due to grade (*bottom*).

additional stresses in the center beams. Settlement of supports may produce a greater fatigue stress range than initially assumed in the original design because the effective span has increased.

Fatigue Limit States Design

Limit states design has been widely used in Europe and Canada (*4,6*). In the 1980s, it gained acceptance in the United States for steel building design. Known as load and resistance factor design (LRFD) (*7*), this probabilistic design method was developed by Galambos and Ravindra at Washington University in St. Louis, Missouri (*8*).

For expansion joint design, no LRFD criteria, calibration, or evaluation studies have been done in the United States. However, as a result of long-range fatigue testing of expansion joint details, Tschemmernegg at the University of Innsbruck has developed a limit states fatigue procedure applicable to expansion joint design (*4*).

One of the design limit states is the serviceability of the expansion joint; specifically, the expansion joint components are to remain free of cracks after 100 million cycles, which is assumed by Tschemmernegg to be an infinite life. Since expansion joints are subject to a greater number of load cycles and higher impact than other bridge components, fatigue testing of critical components and connections is necessary to establish the theoretical limiting stress range at the endurance limit of 100 million cycles. The fatigue limit states equation proposed by Tschemmernegg (*4;9*,p.2) is

$$(0.5)f_{sr\ calc} \leq F_{sr\ test} \tag{1}$$

where $f_{sr\ calc}$ is calculated stress range based on fatigue wheel load range and $F_{sr\ test}$ is theoretical fatigue stress range at 100 million cycles determined from S-N tests.

Fatigue Testing and Development of S-N Diagrams for Critical Details

The phenomena of fatigue failure and fatigue cracking of steel bridge structures have been described by Fisher et al. (*10*,p.26;*11*,p.252). Plots of stress range versus number of cycles, or S-N diagrams, are developed from constant amplitude fatigue tests for critical details. Typical S-N diagrams for AASHTO Categories A to E' are shown plotted in Figure 7. For ferrous metals, these diagrams are generally straight lines with a slope of approximately 3 to 1 (horizontal to vertical) on a log-log plot.

Bridge structure components are subject to loads that produce variable amplitude stress ranges. However, research has shown that if a structure is to remain free of cracks, the maximum stress range it experiences due to live loads must be less than that obtained from a constant amplitude S-N diagram for a specific number of cycles. If any stress range cycles, including those produced by overloads, exceed the allowable fatigue stress ranges determined from a constant amplitude fatigue test, fatigue cracking is likely (*10*,p.26).

Each fatigue critical detail has a characteristic fatigue strength that is a function of loading range, number of cycles of loading, geometry, type of connection, inherent stress risers, and material properties. Figure 8 shows a welded center beam-to-support bar connection tested by Tschemmernegg (*4*). The proposed S-N diagram for this detail (Figure 9) shows that the slope from N = 100,000 cycles to N = 5 million cycles is 3 to 1 (*m* = 3). From N = 5 million to N = 100 million cycles, the slope is 5 to 1 (*m* = 5), and for more than 100 million cycles, the slope of the S-N curve is 0 (*m* = 0). The stress range at 100 million cycles is the theoretical endurance limit.

Figure 9 is constructed from constant amplitude fatigue testing of a number of test specimens at different stress ranges to determine the number of cycles to produce fatigue cracks. Generally, three specimens are tested and at least one specimen exceeds 2 million cycles without cracking. On the basis of a probability analysis, a stress range with a 95 percent confidence level is established at 2 million cycles (Point C, Figure 9). The proposed S-N diagram is drawn through the 95 percent confidence point. The theoretical endurance limit at 100 million cycles is established from the known slopes of the S-N diagram using the appropriate logarithmic relationships.

It is possible to satisfy the AASHTO fatigue design stress range for more than 2 million cycles while not satisfying the fatigue design stress range at 100 million cycles proposed by Tschemmernegg (*4*). Therefore, it is important that fatigue critical details be tested to establish S-N diagrams and to determine the theoretical endurance limit at 100 million cycles.

QUALITY AND DURABILITY

M. P. Burke recently noted the effects of the current competitive bidding practice on the quality and durability of bridge deck joints and bearings when specifications are incomplete:

As competition between products drives prices down, manufacturers are forced to reduce the prices of their products to remain
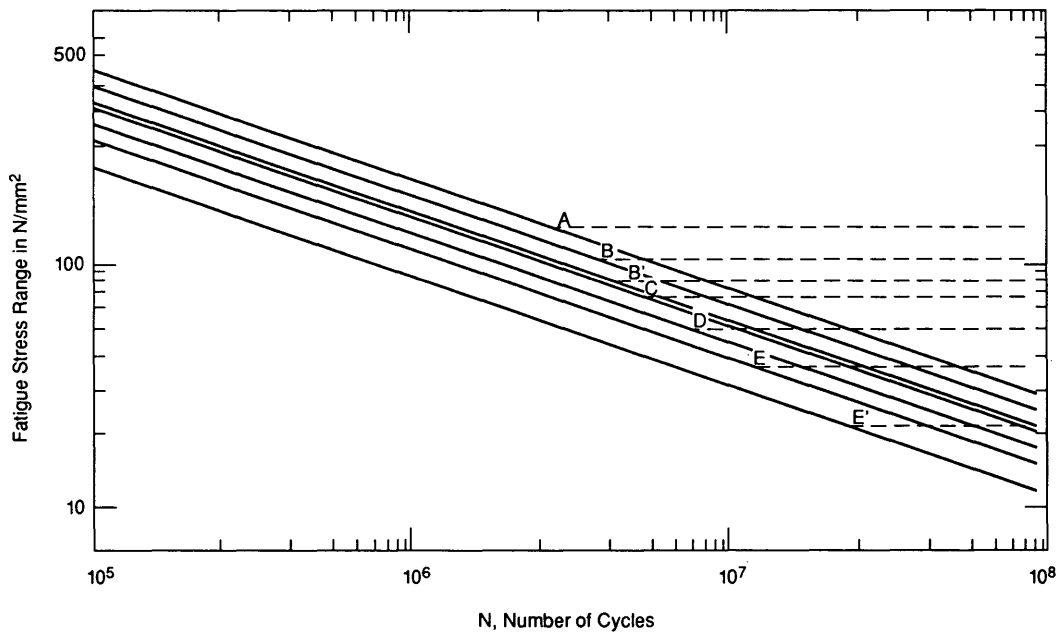
FIGURE 7 Design fatigue stress range curves for AASHTO Categories A to E′ (11).
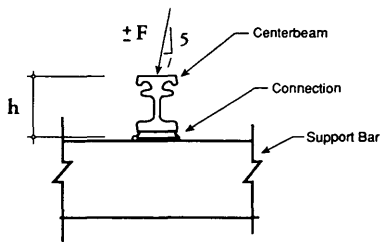
FIGURE 8 Fatigue testing of connection by Tschemmernegg (4,9).
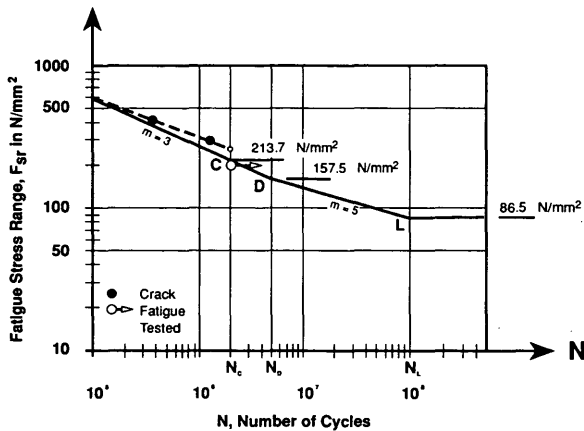
FIGURE 9 S-N diagram for connection proposed by Tschemmernegg (4,9).

competitive. And since the quality has not been described and quantified (measured), the design of products and their quality can be changed, lowered in most cases, to make them more competitive. Ultimately, the quality available in such devices will adversely affect their integrity and durability and consequently their suitability for particular applications. (12)

Competitive bidding, bid shopping (13), and value incentive clauses in contract specifications should not pose problems for owners if the contract specifications are complete. These documents should clearly specify the requirements and how compliance with these requirements is to be determined and enforced. Specifications should include acceptable manufacturers, design loads, design parameters, required testing, approved testing facilities, material specifications, testing requirements, quality-assurance requirements, guarantee, and certificates of compliance. Specifications should require that the manufacturer be identified at the time bids are submitted. In the contract bid documents, the pay item for expansion joints can be separated into two parts: supplying and installing the expansion joint.

The following topics describe criteria in WSDOT contract specifications to ensure that quality is addressed in expansion joint design, manufacture, and installation.

Quality Control During Design

Calculations for structural components are stamped by the engineer in responsible charge of the design. The engineer must be a full-time employee of the expansion joint manufacturer and a registered professional engineer. The design calculations shall include a fatigue analysis supported by test data. Fatigue testing is done at test sites approved by WSDOT,

not at the manufacturer's plant. Joints that have proven field experience are specified and are identified by model and manufacturer. Other design, specification, and shop plan review criteria for joints used by WSDOT have been described previously (*14*).

Required Certificates

Besides the submission of design calculations with the shop plans and welding procedures, certificates of compliance, test reports, and material samples are submitted for review, testing, and approval.

Some required certificates of compliance are

● Manufacturer's certificate of compliance with the American Institute of Steel Construction Quality Certification Program, Category III, Major Steel Bridges.
● Certification of welding inspectors under American Welding Society QC1, Standard for Qualification and Certification of Welding Inspectors.
● Certification of personnel as NDT Level II nondestructive testing inspectors under the American Society for Nondestructive Testing Recommended Practice SNT-TC-1a.
● Certified mill test reports for all steel and stainless steel in the expansion joints and other material certificates.
● Certified test reports confirming that the springs and bearings meet the design load requirements.

Inspection Requirements

Three levels of inspection must be satisfied before the expansion joints are accepted: quality-control inspection, quality-assurance inspection, and final inspection. The manufacturer provides for both quality-control and quality-assurance inspection. If the expansion joints fail any one of the three levels of inspection, they are replaced or repaired. Any proposed corrective procedure is submitted for WSDOT's approval before the corrective work is begun.

Quality-Control Inspection

During the fabrication process, the manufacturer provides full-time quality-control inspection to ensure that the materials and workmanship meet or exceed the minimum requirements of the contract. Quality-control inspection is the responsibility of the manufacturer's quality-control department.

Quality-Assurance Inspection

Quality-assurance inspection is performed by an independent inspection agency provided by the manufacturer and approved by WSDOT before fabrication is started. Quality-assurance inspection is not required to be full-time inspection but is done at all critical phases of the manufacturing process before and during assembly of the expansion joints.

Final Inspection

Upon arrival at the job site and before installation, the expansion joints are inspected by WSDOT personnel. A clean, dry, enclosed area is provided by the contractor for the final inspection.

Quality Assurance During Construction

Proper installation of the expansion joint during construction is critical to ensure a long service life. Expansion joints are one of the last items to be installed during bridge construction. WSDOT has taken the following steps to ensure adequate quality control during installation:

1. A qualified installation technician, who is employed full-time by the joint manufacturer, is on site to ensure that each expansion joint is installed properly.
2. The contractor shall adhere to recommendations made by the installation technician and approved by WSDOT's field engineer.
3. The contractor shall at all times protect the expansion joints from damage.
4. Before installation of the joint, the blockout and supporting system are protected from damage and construction traffic.
5. After installation, construction loads are not permitted on the joint. The contractor is required to bridge over the joint.
6. All forms and debris that tend to interfere with the free action of the joint are removed.
7. The expansion joint is water-tested after installation to ensure that it is watertight.
8. Upon completion of the water test, the joint manufacturer's installation technician certifies in writing that the contractor followed the proper installation procedure.

Partnering

In any undertaking, quality and durability are attainable only if all parties involved—contractor, owner, and joint manufacturer—are working as partners or team members with common goals. WSDOT uses partnering to enhance a cooperative climate with the contractor and to manage conflict on the construction project (*15*,p.14).

Guarantee

WSDOT has required a 5-year guarantee for two large-movement expansion joints to ensure satisfactory performance and durability. The following guarantee was used on a recent WSDOT contract for a large-movement expansion joint with a 900-mm movement range:

The Contractor shall provide a five-year written guarantee for the operation and durability of the expansion joints. Broken welds or bolts, cracks in steel members, fatigue, loss of precompression in springs or bearings, debonded TFE, breakdown of corrosion protection, and leakage shall constitute unsatisfac-

tory operation and durability of the joints. Replacement or repair of any joint parts within the first five years, commencing from the date of completion of the contract, shall be covered under the guarantee. The Contractor shall replace or repair any joint parts within the period of the guarantee at the Contractor's expense.

If problems occur with expansion joints, they will most likely occur within the first 5 years of service. Guarantees for manufactured items should be mandatory on all projects. Federal regulations that prohibit the use of federal funds from being used on a project if guarantees are specified should be revised. Guarantees for manufactured items provide a measure of security for owners.

ACCESSIBILITY AND MAINTAINABILITY

In 1990–1991, FHWA conducted a field evaluation on the performance of large-movement finger and modular expansion joints in six states: Florida, Kansas, Michigan, New York, Washington, and Wisconsin. Romack noted that limited-access space made inspection and repair of modular bridge expansion joints difficult for maintenance personnel (*16*). The complexity of these systems demands expertise and equipment that is beyond the capability of the average bridge maintenance crew. Training and technical assistance is required before undertaking repairs. Traffic control, lane closures, and the need to work at night make the repair of these systems expensive.

Bridge designers and expansion joint manufacturers must address the need for maintenance. Expansion joints are not maintenance-free. As with any mechanical system, replacement of parts subject to wear must be allowed for in the design (*17*). The manufacturer should make recommendations as to how often parts should be inspected. Wear tolerances and methods for determining wear should be made part of the maintenance and part replacement plan.

CONCLUSIONS

1. Background information on the fatigue design of modular expansion joints is given.

2. Design based on a static analysis and allowable service load stresses is inadequate to ensure a long service life for expansion joint components subjected to high cyclic loading.

3. Designers and joint manufacturers need to provide additional access space for inspection, maintenance, and repair of expansion joints.

4. Teamwork between contractor, owner, and joint manufacturer is essential to ensure a successful expansion joint installation.

5. Repair and replacement of failed expansion joint components is expensive and time-consuming.

RECOMMENDATIONS

1. Fatigue design and testing should be required for all modular bridge expansion joints. A minimum of 100 million cycles should be used to determine the theoretical endurance limit of fatigue critical details.

2. AASHTO specifications should include fatigue design and fatigue testing requirements and procedures for expansion joint components.

3. Specifications should include quality-control and inspection requirements during manufacture and installation to ensure durability and a long service life.

4. Specifications should be written in clear, specific language.

5. Preapproved expansion joint models and manufacturers should be identified in the contract plans and specifications. Contractors should identify at the time of bid submission which manufacturer is selected.

6. A written maintenance and part replacement plan should be included at the shop plan submission stage. A list of parts to be inspected, acceptable wear tolerances, and method of part replacement should be included.

7. A minimum 5-year guarantee on performance and durability should be required. Federal regulations prohibiting the use of guarantees should be revised.

ACKNOWLEDGMENTS

REFERENCES

1. A. P. Grant. Pasco-Kennewick Bridge—The Longest Cable-Stayed Bridge in North America. *Civil Engineering*, ASCE, Vol. 47, No. 8, Aug. 1977, pp. 62–66.
2. S. Brown and U. Haerle. Design of a Sealed Expansion Joint for the 3rd Lake Washington Bridge. In *ACI SP-94: Joint Sealing and Bearing Systems for Concrete Structures*, Vol. 2, American Concrete Institute, Detroit, Mich., 1986, pp. 967–974.
3. *Standard Specifications for Highway Bridges* (14th ed.). AASHTO, Washington, D.C., 1989.
4. F. Tschemmernegg. The Design of Modular Expansion Joints. Presented at the 3rd World Congress on Joint Sealing and Bearing Systems for Concrete Structures, American Concrete Institute, Toronto, Canada, Oct. 1991.
5. A. C. Agarwal. *Burlington Bay Skyway Expansion Joint Study, Queen Elizabeth Way Southbound (New Structure)*. Report SRR-91-02. Ministry of Transportation of Ontario, Canada, 1991.
6. *1983 Ontario Highway Bridge Code* (2nd ed.). Ministry of Transportation and Communications of Ontario, Canada, 1983.
7. *Manual of Steel Construction, Load and Resistance Factor Design for Steel* (1st ed.). American Institute of Steel Construction, Chicago, Ill., 1986.
8. M. K. Ravindra and T. V. Galambos. Load and Resistance Factor Design. *Journal of the Structural Division*, ASCE, Vol. 104, No. ST9, Sept. 1978, pp. 1337–1353.
9. Fatigue Design and Testing for Expansion Joints. *Technology Bulletin for Bridge Bearings, Expansion Joints and Components*, No. 1, D. S. Brown Co., North Baltimore, Ohio, Oct. 1991.
10. J. W. Fisher, D. R. Mertz, and A. Zhong. *NCHRP Report 267: Steel Bridge Members Under Variable Amplitude Long Life Fatigue Loading*. TRB, National Research Council, Washington, D.C., Dec. 1983.
11. J. W. Fisher, B. T. Yen, and D. Wang. *Fatigue Cracking of Steel Bridge Structures*, Vol. II. Report FHWA-RD-89-167. FHWA, U.S. Department of Transportation, March 1990.

12. M. P. Burke Jr. Flawed Assumptions and the Failure of Bridge Deck Joints and Bearings. Presented at the 3rd World Congress on Joint Sealing and Bearing Systems for Concrete Structures, American Concrete Institute, Toronto, Canada, Oct. 1991.
13. Shop Till They Drop. *Engineering News Record*, March 9, 1992, pp. 26–28.
14. J. A. Van Lund. Bridge Deck Joints in Washington State. Presented at the 3rd World Congress on Joint Sealing and Bearing Systems for Concrete Structures, American Concrete Institute, Toronto, Canada, Oct. 1991.
15. N. C. Anderson. *Managing Conflict on the Construction Project (Partnering)*. Washington State Department of Transportation, Olympia, April 1992.
16. G. P. Romack. Performance of Large Movement Joints. Presented at the 3rd World Congress on Joint Sealing and Bearing Systems for Concrete Structures, American Concrete Institute, Toronto, Canada, Oct. 1991.
17. W. Koster. Design, Performance and Maintenance of Bearings and Joints. *Maintenance, Repair and Rehabilitation of Bridges.* Reprint from the Introductory Report, International Association for Bridge and Structural Engineering Symposium, Washington, D.C., 1982.

Decomposed-Components Approach to Signal-Pole Base-Plate Design

Gongkang Fu, Sherif J. Boulos, Deniz Sandhu, and Sreenivas Alampalli

The AASHTO specification does not specify the analysis method for base-plate design of span-wire traffic signal poles. The study reported here consisted of full-scale testing and finite element analysis of a number of existing signal poles to examine their behavior and evaluate their structural adequacy. A simplified analysis method has been developed because present procedures were found to be unreliable. This method is consistent with the working stress design concept in the current code. It decomposes the base plate into three elementary components corresponding to three critical regions of maximum stress. The subsequent analyses become straightforward on the basis of these modelings, with the assistance of empirically determined coefficients to reach equivalent section capacities with respect to critical stresses. Hand calculation is adequate for applications of this method in routine design.

Traffic-signal poles that are span-wire mounted (referred to here simply as "signal poles") currently are designed according to the AASHTO specification (1). Provisions are given for analysis and design of the post and anchor bolts, but no method is specified for analysis of the base plate. This study examined structural adequacy of the base plates of signal poles supplied to New York State. As a result, a semiempirical method was developed for analyzing base plates because the current procedures were found to be unreliable. This method is intended to be consistent with the working stress design adopted by the current code and may be included in the specification for design applications.

In New York State, a typical signal pole consists of a round or polygonal steel post with changing diameter welded to a square steel base plate. The base plate is anchored to a concrete footing by four bolts. A reinforced hand hole is provided in the post. Typical pole details are shown in Figure 1. Dead, wind, and ice loads are required to be covered in pole design (1,2). Their combinations and corresponding strength requirements are provided by the code (1). In this paper signal poles are identified by the first letter of the manufacturer's name, design load in kips, and height in feet. For example, C530 is a pole manufactured by Carlan Manufacturing Company, with a design load of 22.2 kN (5 kips), that is 9.14 m (30 ft) tall. Two critical loadings are considered here: parallel loading, in which the wire runs parallel to a side of the square base plate, and diagonal loading, in which the wire runs along a diagonal of the base plate.

Full-scale load tests and material tests were performed to investigate signal pole behaviors under loading. Finite ele-

ment analysis (FEA) models were developed and verified by the test results. Typical areas of critical stress concentration in the base plate were identified. Simple models based on decomposed elementary components were developed for each critical case, with corresponding loads. Analysis of these critical cases can thus be simplified, with assistance of empirical coefficients to reach equivalent capacities with respect to critical stresses. These coefficients were determined by FEA for 23 representative signal poles and 5 inadequate ones that were redesigned.

TEST PROGRAM AND FEA

Three poles were instrumented with electrical resistance strain gauges and load tested. Two (C530 and C832) were from the manufacturer's standard stock. The third, C530(T), was specially built with a thinner base plate than the standard C530 pole, to examine the effect of this thickness on the behavior and strength of the base plate. Their dimensions are detailed in Table 1. They were selected to include various base plate thicknesses and clearances between the bolt circle diameter (BC) and the pole diameter at its bottom (DB). These were initially considered important factors affecting stress distribution in the base plate.

Test setup details are shown in Figure 2. All poles tested were individually anchored horizontally to a foundation. Figures 3, 4, and 5 show strain gauge identifications and locations on the post, base plate, and anchor bolts. Loads were applied laterally to each pole at 457 mm (18 in.) from its tip (where the span wire is mounted in service condition) by a hydraulic jack. Applied load levels were measured by a pressure gauge with a resolution of 0.995 kN (223.6 lb) [i.e., 690 kPa (100 psi) on a cylinder area of 0.00144 m² (2.236 in.²)]. The poles were subjected to either diagonal or parallel loading by rotating them about their central axes without changing the direction of load (Figure 2). No concrete packing was provided between the base plate and the steel test foundation (Figure 2) as would be the case in a critical—even if temporary—service condition.

After the load tests, samples were taken from each standard pole's post, base plate, and anchor bolts for material laboratory tests; the results are given in Table 2. A second sample from the C832 base plate was tested after the first showed an unexpectedly low strength, which was thus confirmed.

Load test results and FEA predictions will now be discussed. For simplicity of presentation, the structural response obtained in strain has been converted to stress according to
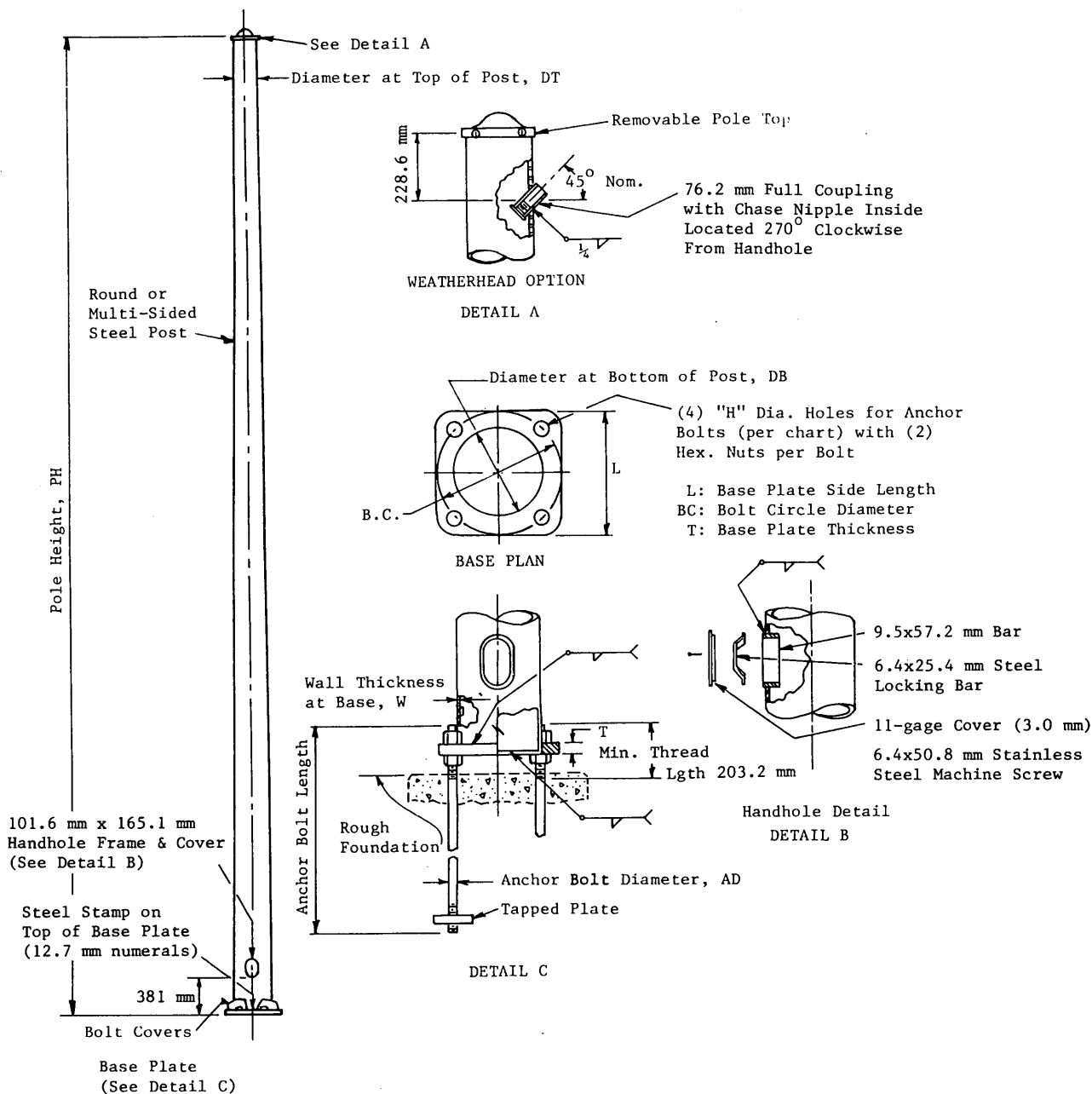
FIGURE 1 Typical traffic-signal pole in New York.

TABLE 1 Dimension Details of Tested Signal Poles

Pole ID	C530(T)	C530	C832
Pole Height (PH), m	9.14	9.14	9.75
Design Load, kN	22.2	22.2	22.2
Diameter at Top of Post (DT), mm	273	273	324
Diameter at Bottom of Post (DB), mm	324	324	406
Wall Thickness of Post at Base (W), mm	7.94	7.94	9.53
Base Plate Side Length (L), mm	584	584	559
Base Plate Thickness (T), mm	31.8	44.4	57.2
Bolt Circle Diameter (BC), mm	584	584	559
Anchor Bolt Diameter (AD), mm	38.1	38.1	50.8
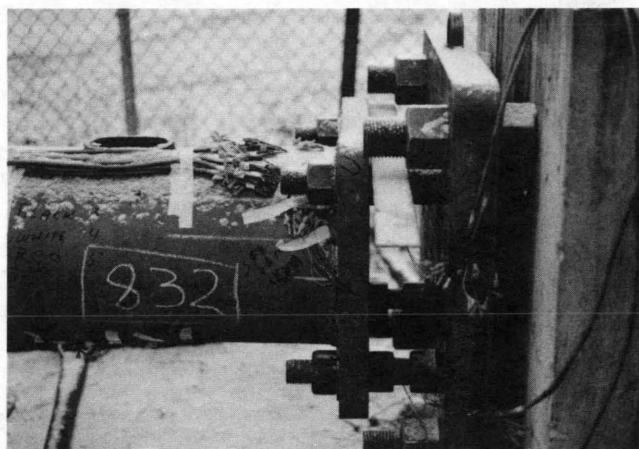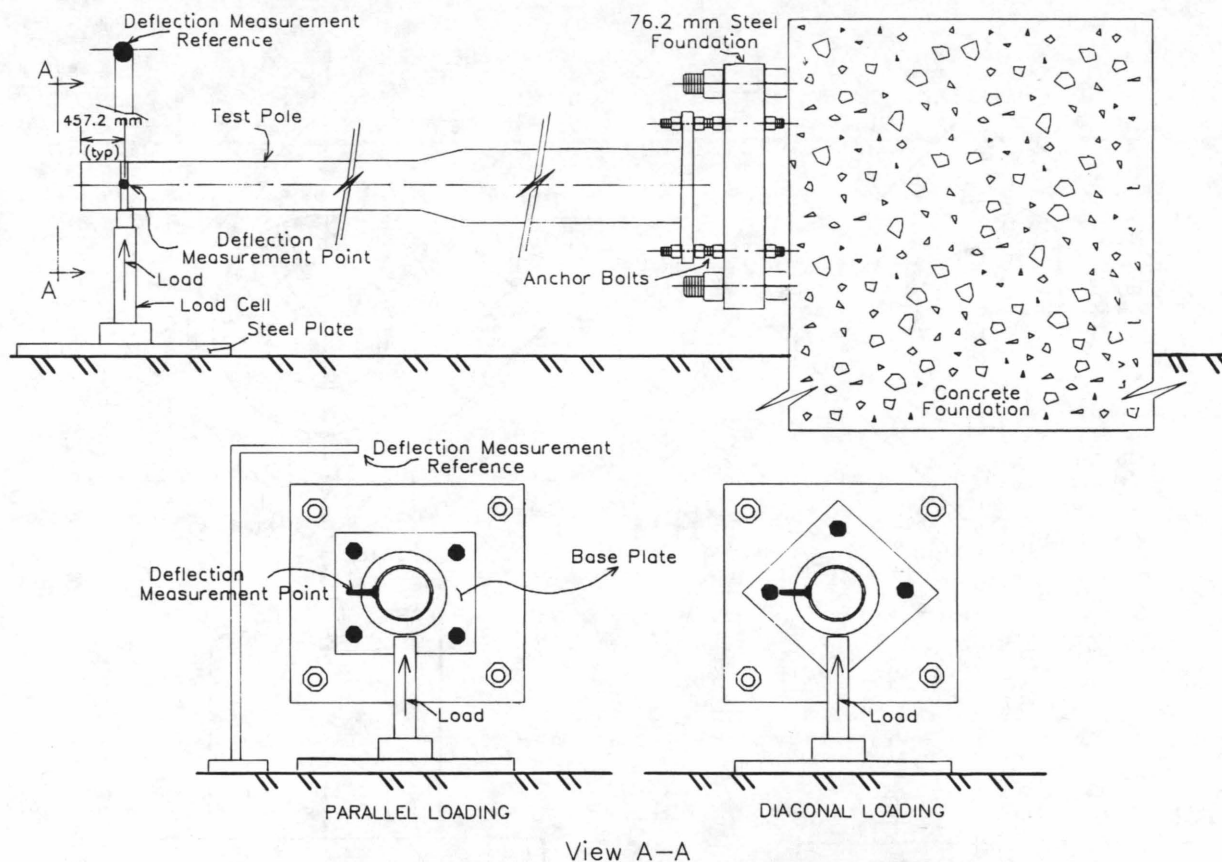
FIGURE 2 Load test setup (not to scale).

the elastic stress-strain constitutive relation, although it is obviously not valid in inelastic ranges. The FEA was performed using Graphics Interactive Finite Element Total System (GIFTS) software (3). This analysis was limited to the elastic range. Two quarter models were generated to analyze the poles under the diagonal and parallel loading, taking into account their symmetric and antisymmetric behaviors. The post was modeled by a combination of plate elements (for the top part) and solid elements (for the bottom part near the base). The base plate was modeled by multiple layers of solid elements. The anchor bolts were modeled by beam elements.

Load Test A

Pole C530(T) was loaded diagonally to failure, with the instrumentation shown in Figure 3. Two load cycles were applied up to loads of 17.9 kN (4,025 lb) and 20.5 kN (4,616 lb), respectively. Figure 6 shows the stress response of the base plate to the loads. Only the dominant component S_y (bending stress in the y direction) of Gauge R12 is included, showing the maximum response. The FEA predicted virtually the same stress shown by the strain gauge, within the elastic range. Note that the inelastic behavior under higher loads shown in Figure 6 was initiated in an anchor bolt (4). In
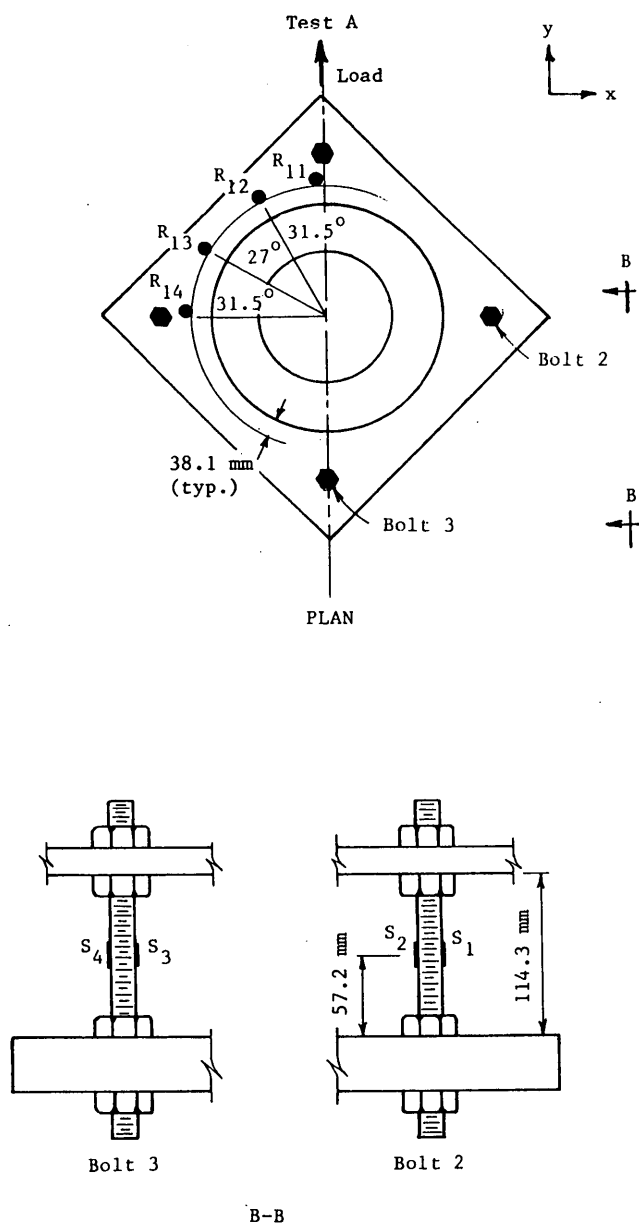
FIGURE 3 Instrumentation for Load Test A: C530(T).

FIGURE 4 Instrumentation for Load Test B: C530.

addition, by linear extrapolation of the first (elastic) part of the load-stress relation in Figure 6, the base plate was also a deficient component of the pole because of its reduced thickness. The base plate showed residual deformation in the area between Gauges R12 and R13 as well as its symmetric counterpart, which was apparently associated with the maximum stress discussed earlier.

Load Test B

Pole C530 was subjected to diagonal loading with strain gauges on the post observing tensile strains (Figure 4). It was loaded successively up to 10.9 and 12.9 kN (2,460 and 2,907 lb) in

two cycles. Among the strain gauges on the base plate, R4 showed the highest stress level. Its dominant component S_y is shown in Figure 7. The FEA result is in good agreement within the elastic range with that of the testing. Inelastic behavior of the pole was caused by partial yielding of an anchor bolt, a result similar to that in Load Test A (4). By linear extrapolation of the elastic part of its load-stress relation, the base plate also was found to be deficient. The same pole was load-tested again under a diagonal load after being turned
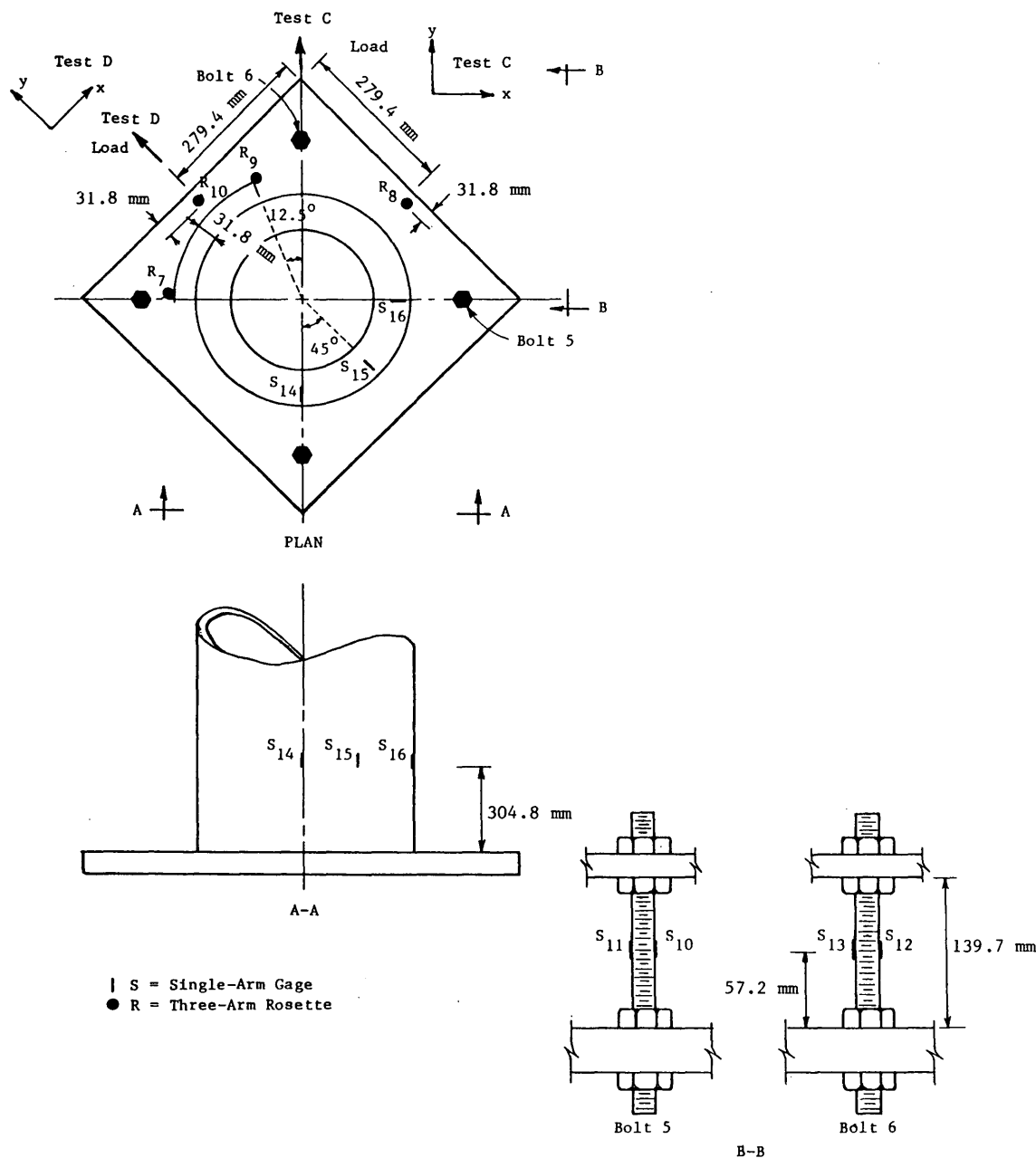
FIGURE 5   Instrumentation for Load Tests C and D: C832.

TABLE 2   Material Coupon Test Results

Sample	Steel Type	Nominal Yield, MPa	2% Yield Strength, MPa	Ultimate Strength, MPa
POLE C530				
Post	A 252	345	375	490
Plate	A 36	248	256	436
Bolt	A 366 M 55	379	417	611
POLE C832				
Post	A 53	345	326	489
Plate*	A 36	248	194	310
	A 36	248	200	304
Bolt	A 36 M 55	379	405	595

*Second sample tested for verification.

180 degrees about its central axis. Similar results were obtained, and the assumed symmetry was verified (*4*).

Load Test C

Pole C832 was first loaded diagonally, with the strain gauges on the post under tension (Figure 5). The pole was loaded up to 25.9 and 31.8 kN (5,814 and 7,155 lb) in two successive cycles. Among the base plate strain gauges, R8 and R10 showed the highest stress levels symmetrically. Figure 8 shows load-stress curves for R10; only the dominant (bending and shear) components are included. The validity of the FEA models for the elastic range is again demonstrated. Residual strains were observed at the ends of both cycles. Yielding was initiated at a load between 20.9 and 25.9 kN (4,696 and 5,814 lb) at an anchor bolt (*4*).
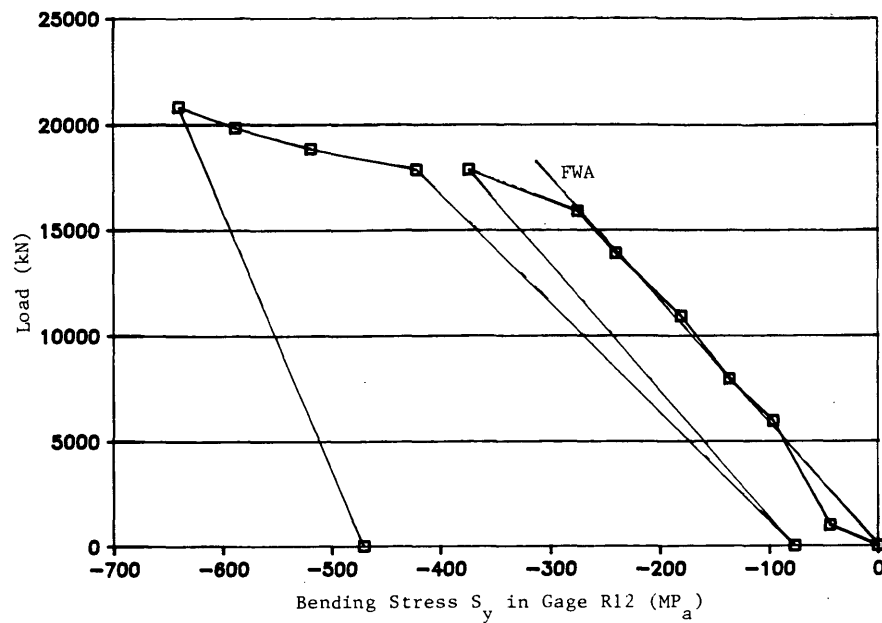
FIGURE 6   Load Test A: C530(T) under diagonal load.

Load Test D

Pole C832 was reset for parallel loading (Figure 5) and loaded through five cycles. Among the base-plate strain gauges, R8 and R10 showed the highest stress levels. Figure 9 shows load-stress curves of their respective dominant components. FEA again predicted these stresses fairly accurately. Inelastic behavior under higher loads shown in these figures was initiated in an anchor bolt, although the maximum stress level was much lower than that in Load Test C (*4*). This shows, as expected, that the diagonal load is the governing loading case

for the anchor bolts, which appears to have been ignored in the design of these poles.

Table 3 gives a numerical comparison of test and FEA results of C832 (Load Test C) as a typical case including nondominant components of stresses. These results are shown to be consistent with one another, especially for the pronounced stresses indicating critical response to the load. Relatively larger differences between FEA and test results (for example, in R7) are attributed to inevitable discrepancies between the location of a strain gauge and its corresponding element in FEA or higher noise-to-signal ratios in the acqui-
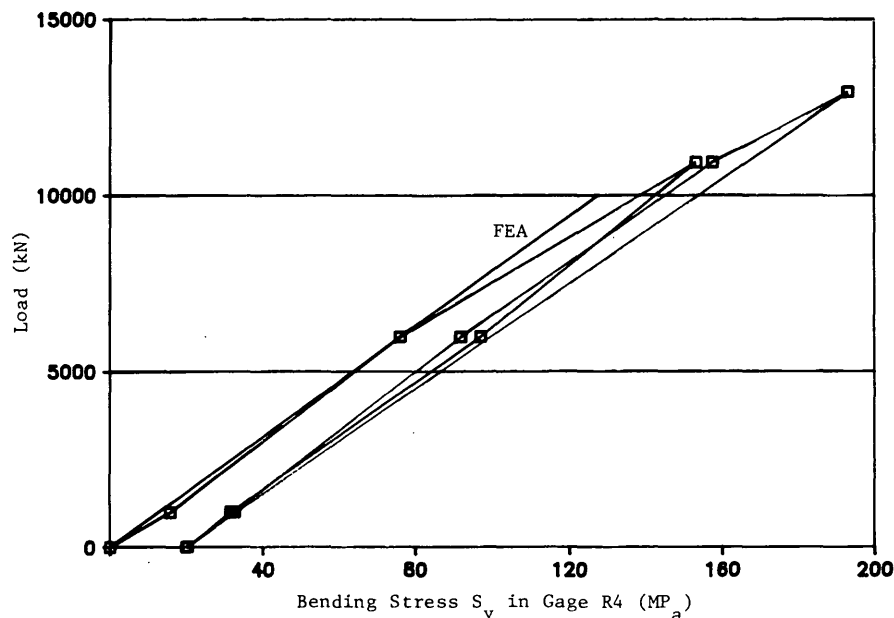
FIGURE 7   Load Test B: C530 under diagonal load.
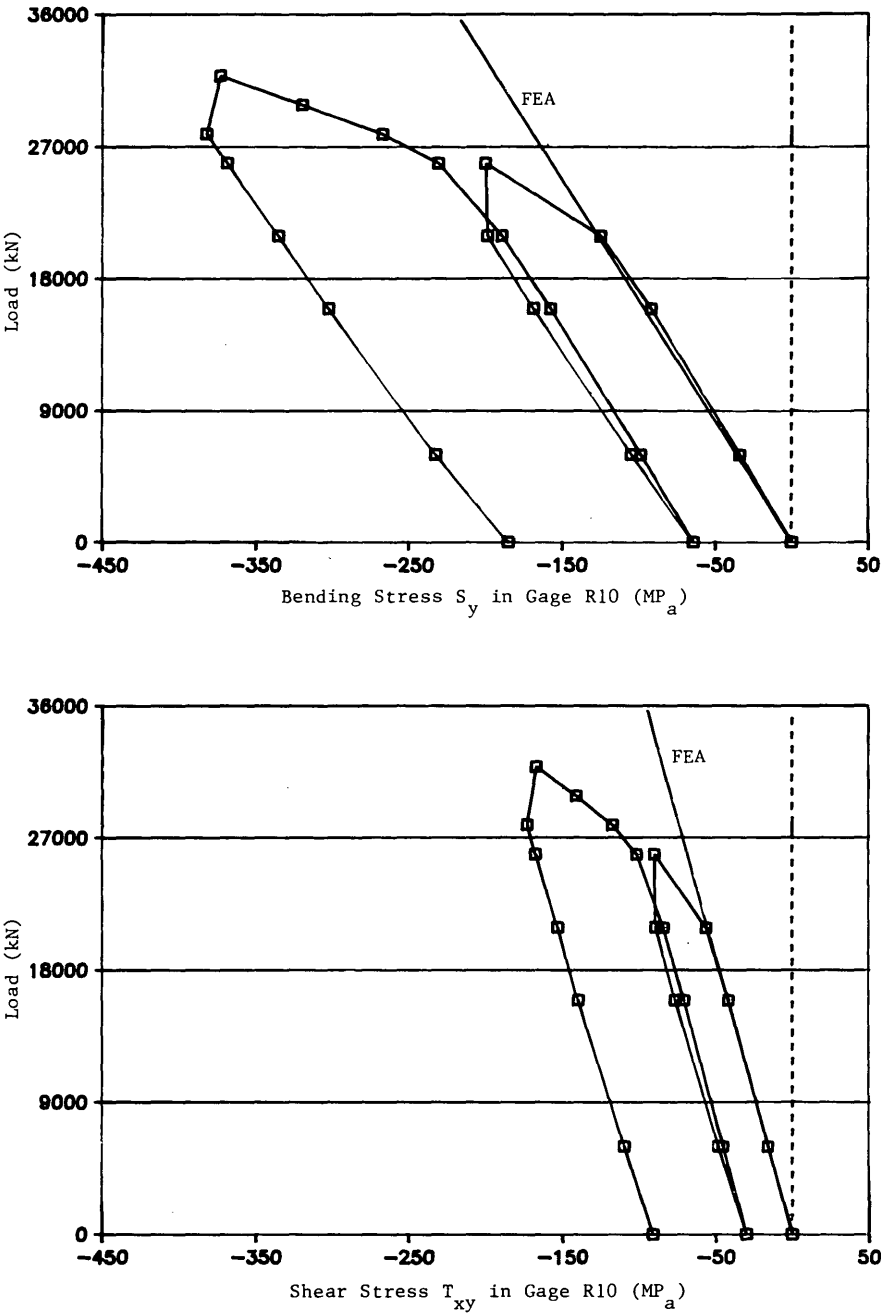
FIGURE 8 Load Test C: C832 under diagonal load: (*top*) bending stress, (*bottom*) shear stress.

sition of test data, or both, when the strain signal was low. Good agreement between FEA and test results was also observed for tip deflections and stresses on the post and in the anchor bolts (*4*). This agreement also verified the beam assumption adopted by the current AASHTO code.

BASE-PLATE BEHAVIOR AND DECOMPOSED-COMPONENTS METHOD FOR ANALYSIS

Figure 10 shows typical deflection distribution and stress contours of the top surface of a base plate under diagonal loading

as obtained by FEA for the design load. Stress is expressed as the percentage of overstress using the Von Mises criterion against the pole's nominal yield stress $F_y = 248$ MPa (36 ksi). The shaded area is a critical region (120 and 130 percent of F_y), obviously associated with the deflection described. Figure 11 shows another typical case of behavior under parallel loading. Stress contours again are expressed by overstress percentage using the same criterion as in Figure 10. Two shaded areas are identified as critical regions. It is interesting that they represent maximum stresses under the given load contributed by the dominant bending component (S_x in Region B) and shear component (T_{xy} in Region C). Figure 12 shows
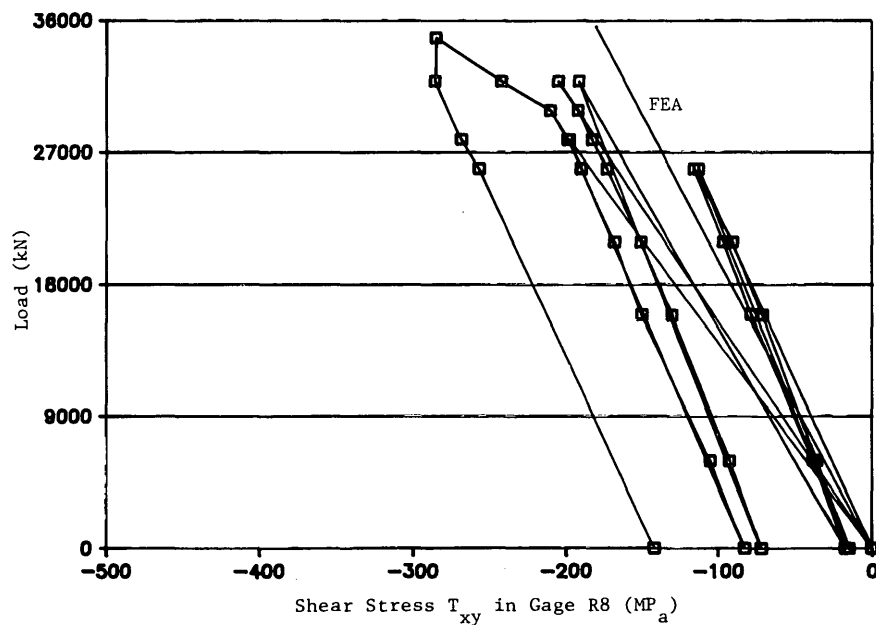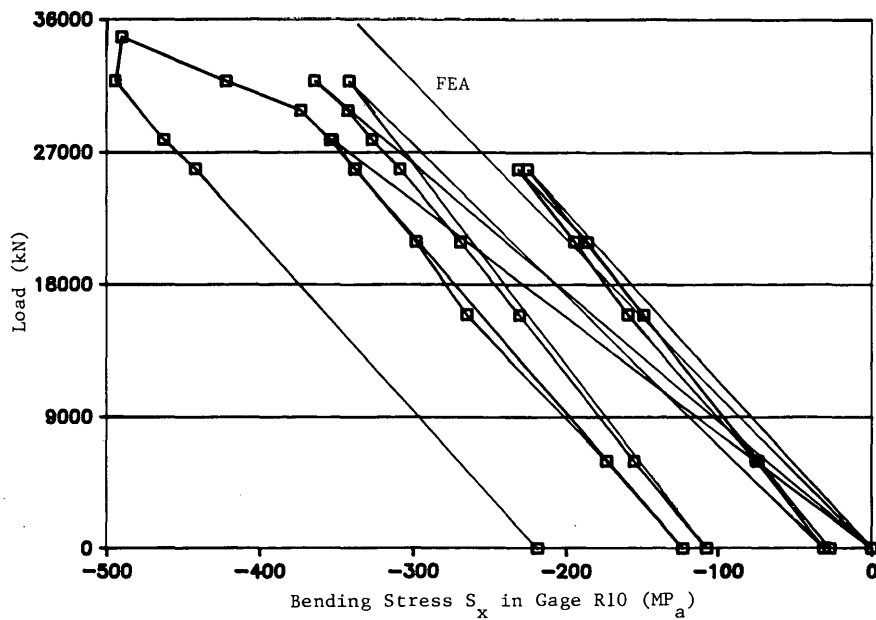
FIGURE 9   Load Test D: C832 under parallel load: (*top*) bending stress, (*bottom*)
shear stress.

TABLE 3   Numerical Comparison of Testing and FEA Results in Base Plate Stress (Pole C832 in
Load Test C Under Diagonal 15.9-kN Load)

Strain Gage ID	Stress Components, MPa						Dominant Stress Component	Difference In Dominant Stress Component, %
	Test			FEA				
	Sx	Sy	Txy	Sx	Sy	Txy		
R7	+3.65	-3.65	+27.7	+1.86	-9.31	+32.6	Txy	+17.7
R8	+1.79	-91.0	+41.4	+2.21	-90.9	+43.2	Sy	+0.1
R9	-13.7	-34.5	-54.1	-15.4	-53.6	-56.5	Txy	+4.5
R10	+1.59	-91.2	-41.4	+2.21	-90.9	-43.2	Sy	+0.2

NOTE: See Figure 5 for loading and gage locations.

	VON MISES CRITERIA	
A	0.000E+00	
B	1.000E+01	
C	2.000E+01	
D	3.000E+01	
E	4.000E+01	
F	5.000E+01	
G	6.000E+01	
H	7.000E+01	
I	8.000E+01	
J	9.000E+01	
K	1.000E+02	
L	1.100E+02	
M	1.200E+02	
N	1.300E+02	

LOAD

CRITICAL REGION A

MODEL
Y
Z—X
1.000E+00   DEFL. AND STRESSES (ENV.)

DEFLS.
Y
Z—X
1.000E+01

JOB: dd530
17-APR-92 13: 06
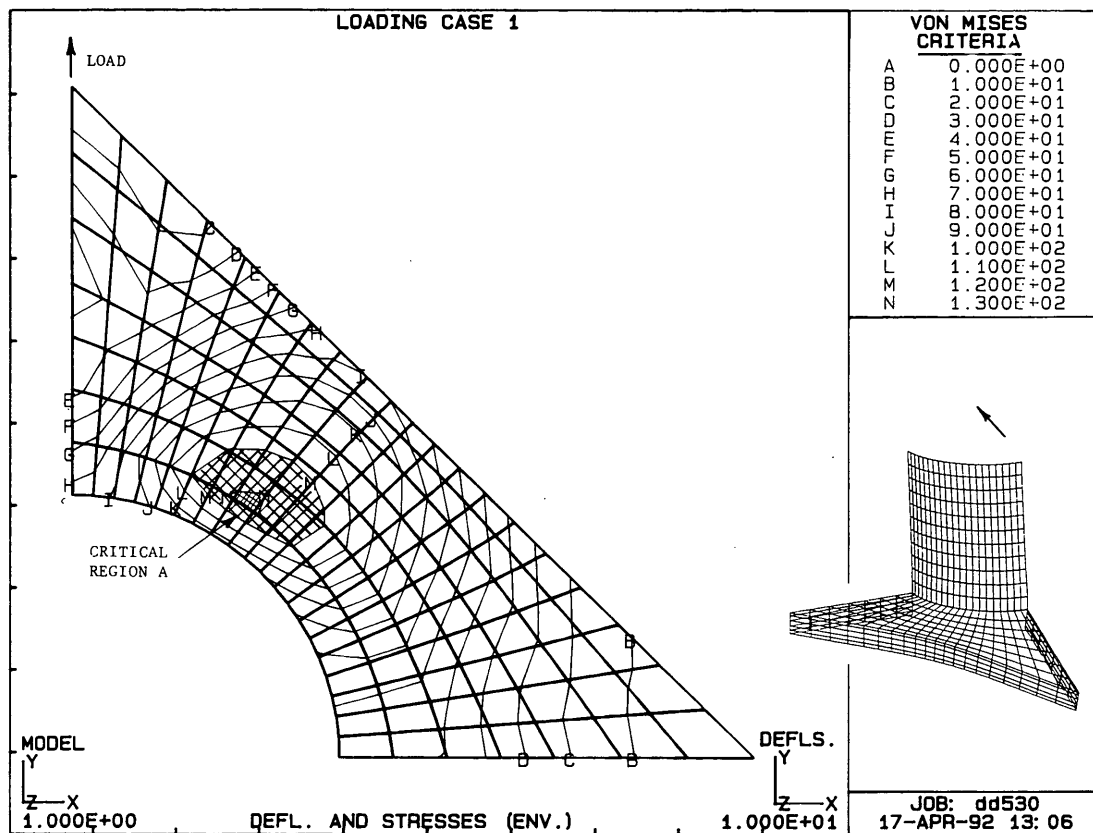
FIGURE 10   Typical deflection and stress distribution under diagonal load (C530, 22.2 kN).

	VON MISES CRITERIA	
A	0.000E+00	
B	1.000E+01	
C	2.000E+01	
D	3.000E+01	
E	4.000E+01	
F	5.000E+01	
G	6.000E+01	
H	7.000E+01	
I	8.000E+01	
J	9.000E+01	
K	1.000E+02	
L	1.100E+02	
M	1.200E+02	
N	1.300E+02	
O	1.400E+02	

LOAD

CRITICAL REGION B

CRITICAL REGION C

MODEL
Y
Z—X
1.000E+00   DEFL. AND STRESSES (ENV.)

DEFLS.
Y
Z—X
1.000E+01

JOB: car1530
22-APR-92 8: 41
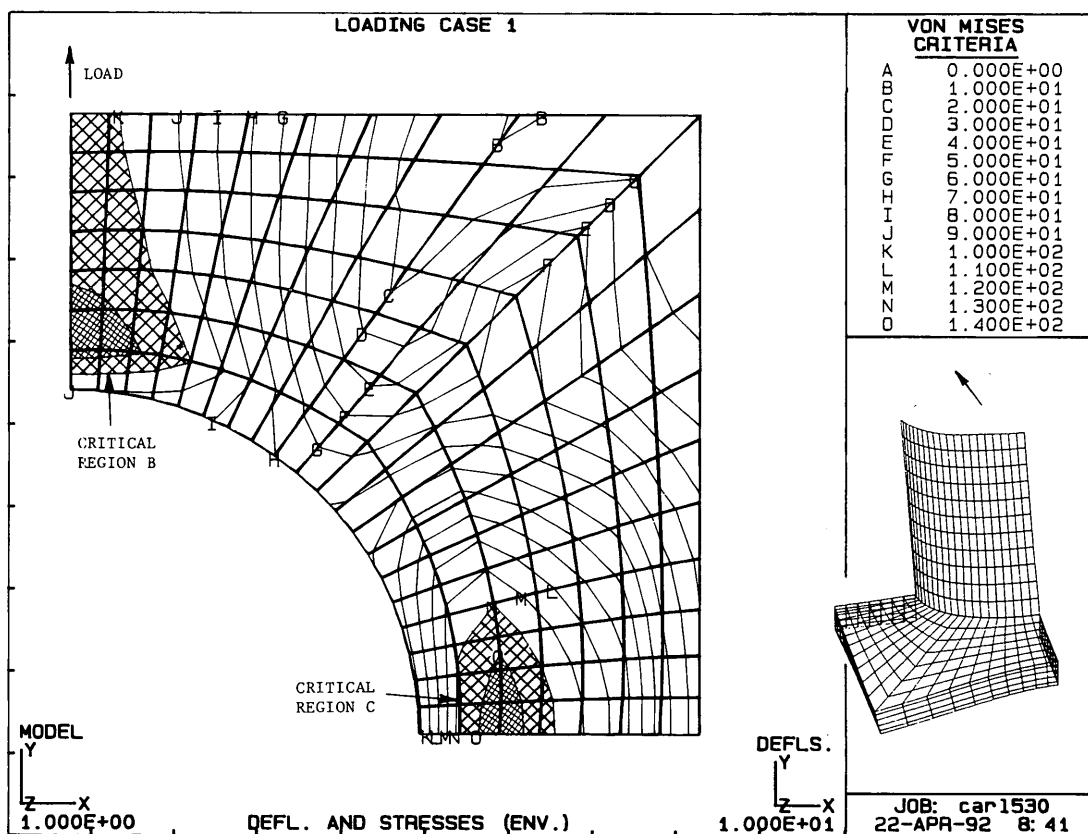
FIGURE 11   Typical deflection and stress distribution under parallel load (C530, 22.2 kN).

VIEW B

VIEW A

VIEW B
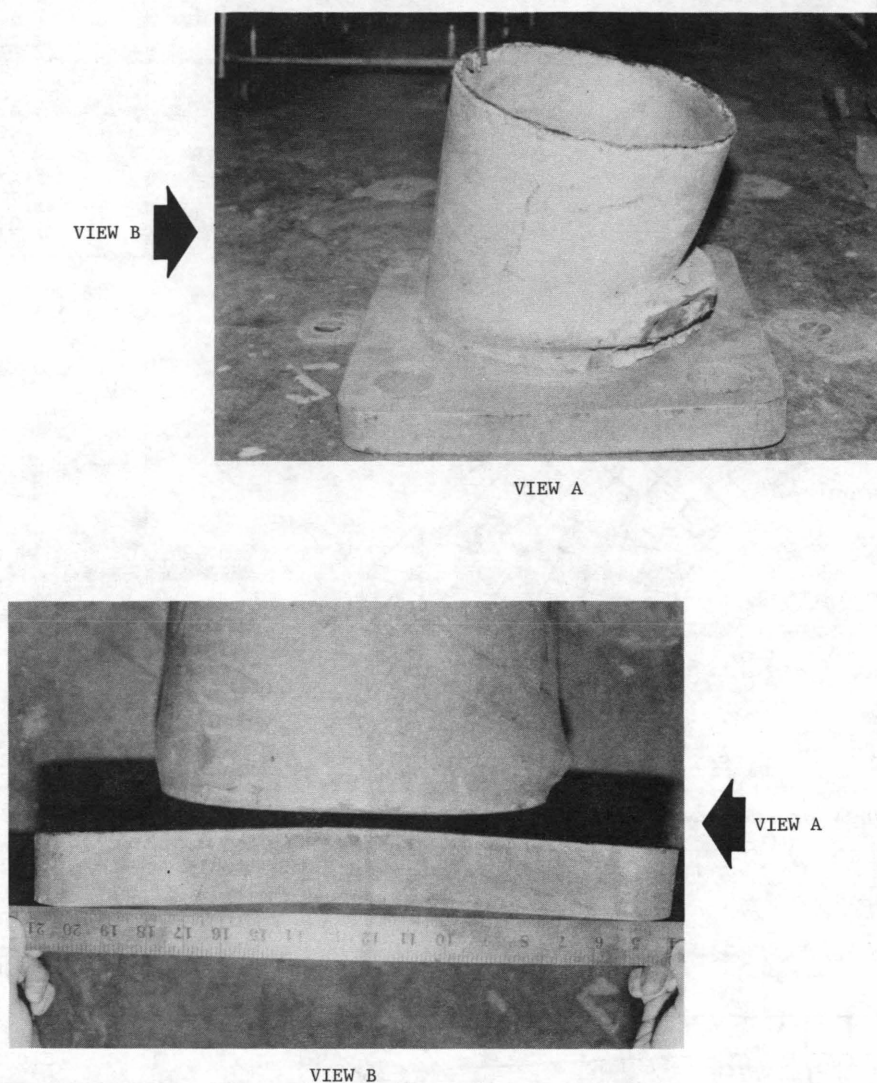
FIGURE 12   Actual residual deflection resulting from parallel loading in an accident.

the true deflection distribution of an accidental failure. This incident occurred under parallel loading when a truck snagged a span wire in service. The three critical regions indicated in Figures 10–12 are thus addressed in the suggested new analysis method for the base plate.

This method of analysis uses the concept of decomposed components for simplification. For each potential failure mode (or critical region), a part of the base plate is isolated and modeled by an elementary component (e.g., a beam or bar). Then a critical cross section and the corresponding load are identified. The subsequent analysis thus becomes straightforward, with the assistance of an empirical coefficient modifying the section's elastic capacity to reach an equivalent section modulus with respect to the maximum stress. These equivalent coefficients were determined empirically by considering 23 representative signal poles designed by three major New York State suppliers and 5 inadequate poles that were redesigned; the dimensions are given in Table 4.

This method is intended to be consistent with the current working stress design concept adopted by the AASHTO code with respect to strength requirements, to obtain critical stresses within the elastic range. The resulting stresses are to be used to meet the AASHTO strength requirements:

$$f_b \le kF_b \qquad f_v \le kF_v \tag{1}$$

where

k = value given by the current AASHTO code—for example, 1.4 for Group II load;
F = allowable stress;
f = computed stress; and
b and v = subscripts for bending and shear stresses, respectively.

All three critical stresses must be considered for proportioning.

TABLE 4 Dimension Details of Sample Poles

Pole ID	Post Dimensions, mm			Base Plate Dimensions, mm			Anchor Dimensions, mm
	DT	DB	w	L	T	BC	AD
EXISTING POLES							
C326	219	273	6.35	432	38.1	432	31.8
C328	219	273	6.35	457	38.1	457	31.8
C430	273	324	7.11	457	44.5	457	38.1
C530	273	324	7.94	584	44.5	584	38.1
C530'	273	324	7.94	457	50.8	457	44.5
C732	324	406	7.94	635	63.5	635	38.1
C832	324	406	9.53	559	57.2	559	50.8
S324	178	254	4.76	533	38.1	533	38.1
S328	191	279	4.76	533	38.1	533	38.1
S334	216	330	4.76	686	38.1	635	38.1
S434	241	356	4.76	686	44.5	635	44.5
S530	267	368	4.76	686	44.5	635	44.5
S632	305	419	4.76	686	50.8	737	50.8
S832	381	483	4.76	813	57.2	813	50.8
S934	419	533	4.76	838	57.2	851	57.2
S1036	445	572	4.76	889	57.2	851	57.2
U226	174	267	4.55	358	38.1	356	31.8
U530	249	356	6.35	521	50.8	508	44.5
U636	297	425	6.35	660	50.8	597	44.5
U832	305	419	7.94	622	63.5	597	50.8
U840	279	470	7.94	660	63.5	635	57.2
U1040	391	533	7.94	699	69.9	699	57.2
U1044	401	546	7.94	737	69.9	711	57.2
REDESIGN CASES							
632	305	419	4.76	686	57.2	737	50.8
934a	419	533	4.76	838	69.9	851	57.2
934b	419	533	4.76	838	76.2	851	57.2
226	174	267	4.55	358	44.5	356	31.8
1040	401	546	7.94	737	82.6	711	57.2

Dimensions (Fig. 1): DT = diameter at top of post, DB = diameter at bottom of post, w = wall thickness at its base, L = side length of square base plate, T = thickness of base plate, BC = bolt circle diameter, AD = anchor bolt diameter.

Bending stress due to diagonal load (for Critical Region A in Figure 10) is

f_b = anchor force * moment arm/equivalent flexural

elastic section modulus

$$= \frac{M}{BC} * \frac{BC - DB}{2} \Big/ \{\alpha(1.414L - DB)T^2/6\} \tag{2a}$$

where M is the moment at the post base due to the design load and α is an empirical coefficient for an equivalent section modulus in terms of the critical stress:

$$\alpha = \{4.304 - 0.02021BC/T - 4.304DB/L + 4.503(DB/L)^2$$

$$- 0.9750(L - 0.707BC)/(L - DB) - 1.686BC/L\}/C_\alpha \tag{2b}$$

$$C_\alpha = 1.097 \tag{2c}$$

Equations 2a, 2b, and 2c are obtained by simplifying the problem as a cantilever beam under a concentrated load at its free end applied by an anchor bolt, as shown in Figure 13. This assumes that the critical point being checked is in Section S_a.
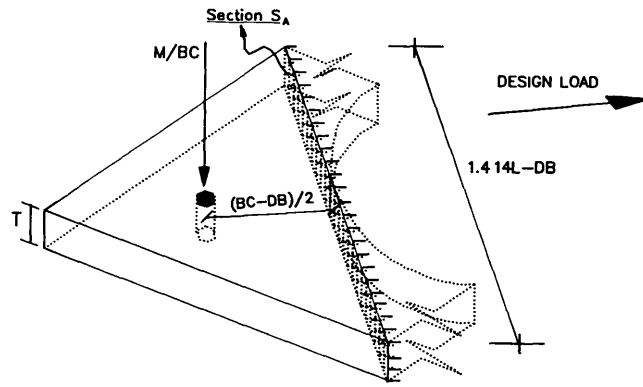
FIGURE 13 Simplified analysis model for maximum bending stress under diagonal load.

Bending stress due to parallel loading (for Critical Region B in Figure 11) is

f_b = midspan (maximum) moment/equivalent elastic flexural

section modulus

$$= \frac{M}{4(DB/L')^2}\{^1/_4 - (1 - DB/L')/3$$

$$+ (1 - DB/L')^4/12\}/\{\beta(L - DB)T^2/12\} \tag{3a}$$

where $L' = \max\{0.707BC, DB\}$ (max{ } means the maximum value of), and β is an empirically determined coefficient for an equivalent section modulus with respect to the critical stress:

$$\beta = \{157.6 - 21.85L/DB - 0.3300BC/T - 259.3DB/L$$

$$- 48.13(L * T/DB/(L - DB))^{1/2}$$

$$+ 194.6(DB/L)^2 + 127.4T/BC - 21.65DB/BC\}/C_\beta \tag{3b}$$

$$C_\beta = 1.080 \tag{3c}$$

This case is treated as a beam with both ends built in and a span of $0.707BC$ under a triangularly distributed load applied by the post, as shown in Figure 14. Equation 3a checks a critical point on Section S_b.

Shear stress due to parallel loading (for Critical Region C in Figure 11) is

f_v = torque by anchors/equivalent elastic

torsional section modulus

$$= \frac{M}{2} \Big/ \{\gamma C'bT^2\} \tag{4a}$$

where

$M/2$ = torque induced by anchor forces on the post base, which in turn is due to the design load;

b = min{0.707BC, DB} (min{ } means the minimum value of);
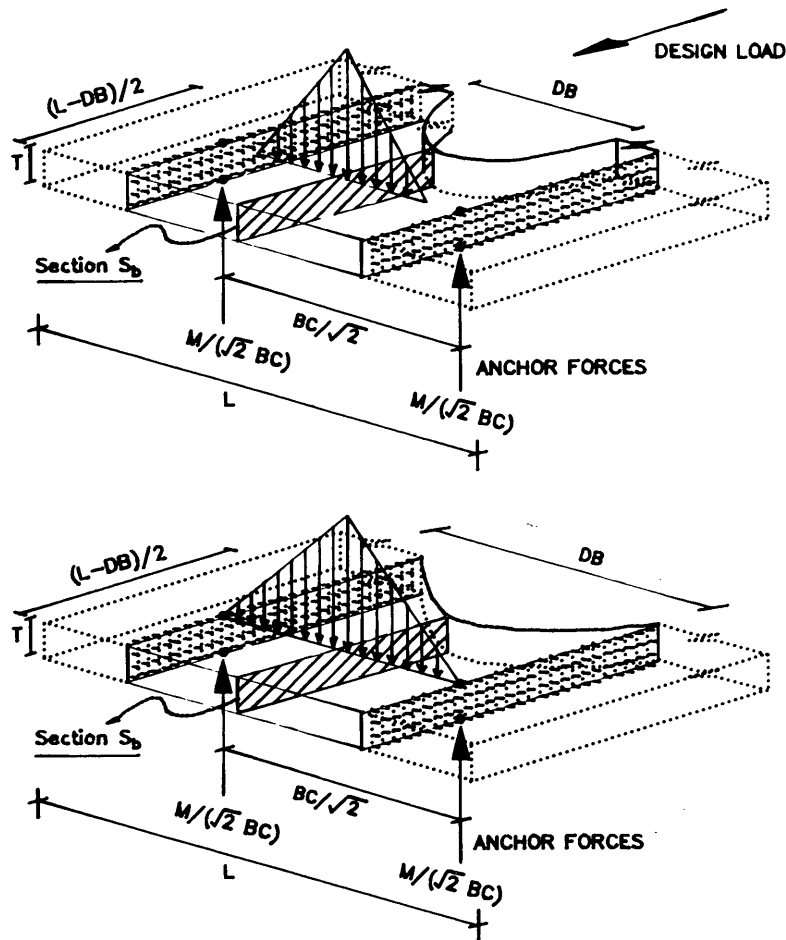
FIGURE 14 Simplified model for maximum bending stress under parallel load.

C' = coefficient given in Table 5 based on the elasticity solution, depending on the ratio b/T (5); and

γ = empirical coefficient to reach an equivalent cross section for prediction of critical stress:

$$\gamma = \{210.0 - 66.9BC/DB - 0.1719(BC - DB)/T$$

$$- 714.8DB/L + 358.3(DB/L)^2$$

$$- 48.16(L - 0.707BC)/(L - DB)$$

$$- 288.2(BC - DB)/(1.414L - DB)$$

$$+ 381.0BC/L\}/C_\gamma \qquad (4b)$$

$$C_\gamma = 1.094 \qquad (4c)$$

TABLE 5 Coefficient C' for Torsion (4)

b/T	C'	b/T	C'
1.0	0.208	3.0	0.267
1.2	0.219	4.0	0.282
1.5	0.231	5.0	0.291
2.0	0.246	10.0	0.312
2.5	0.258	∞	0.333

Equations 4a, 4b, and 4c are based on a simplification of the problem that considers a rectangular bar under torque $M/2$ applied by a pair of anchor bolts, as shown in Figure 15. The maximum shear stress occurs on Section S_c.

Figures 16–18 show the comparison of calculated stresses f by the suggested method and f_{FEA} by FEA for the three critical stress cases. The conservatism (overestimation) in f observed there is introduced by an amplification factor $C_i =$
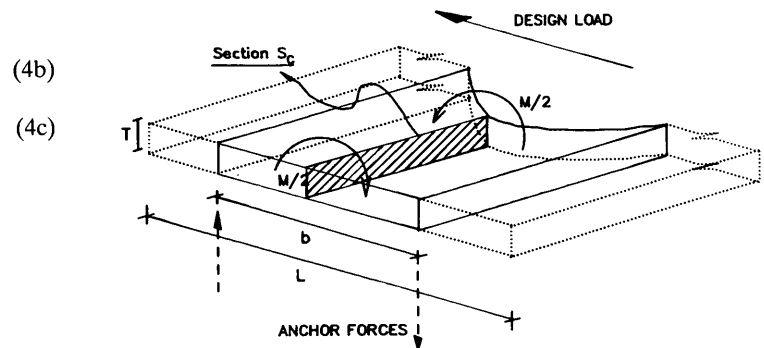
FIGURE 15 Simplified model for maximum shear stress under parallel load.
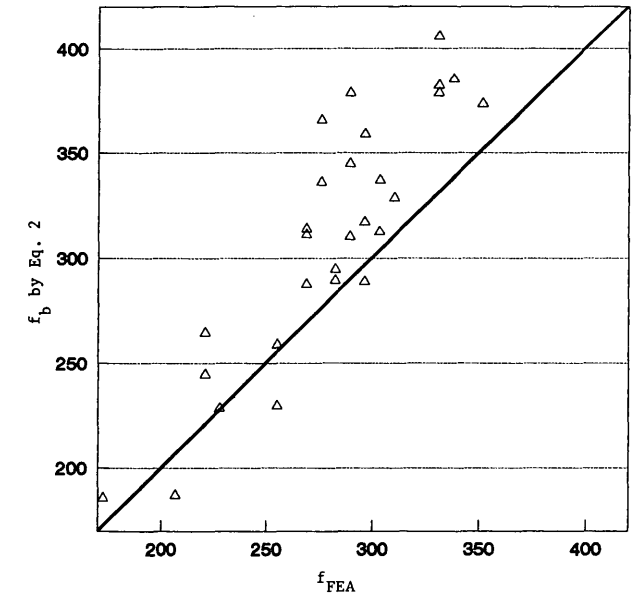
FIGURE 16 Comparison of critical stresses (MPa) by FEA and proposed method: bending under diagonal load.

$m_i + \sigma_i$ ($i = \alpha, \beta, \gamma$), where $m_i(m_i + \sigma_i)$ and $\sigma_i(m_i + \sigma_i)$ are, respectively, the mean and the standard deviation of f/f_{FEA} for respective cases of critical stresses. m_i is around 1.0 and σ_i is about 0.090 for each case.

ILLUSTRATIVE EXAMPLE

The suggested analysis method is applied here to Pole S632 for its evaluation and modification as an example. $F_y = 345$ MPa (50 ksi) is used for proportioning; $kF_b = 1.4 * 0.66 *$
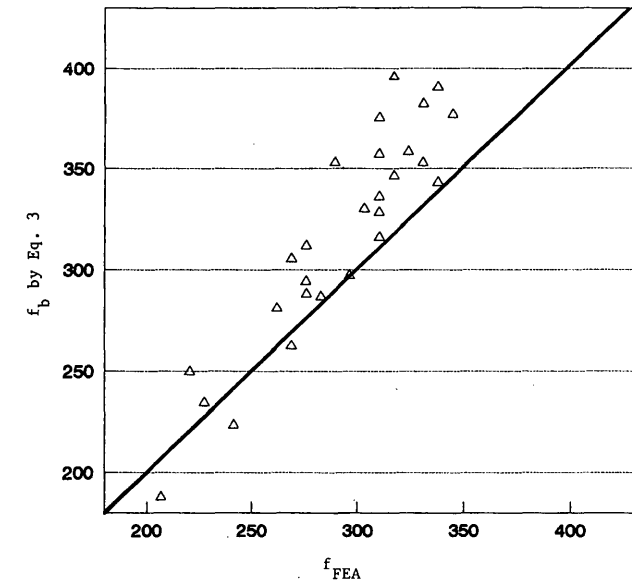
FIGURE 17 Comparison of critical stresses (MPa) by FEA and proposed method: bending under parallel load.
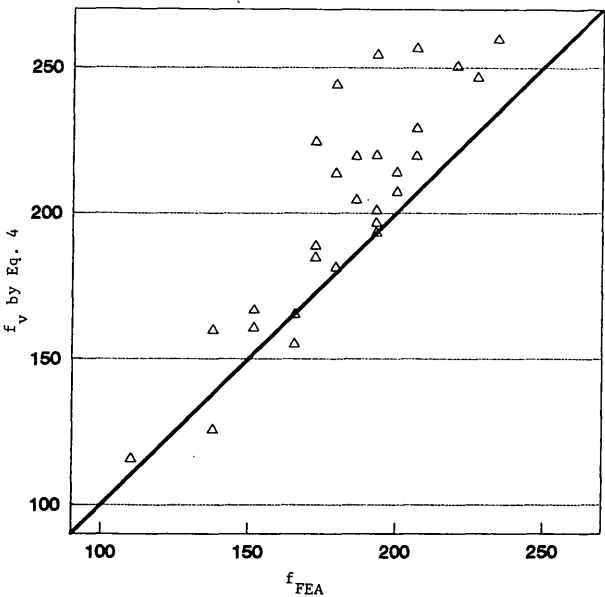
FIGURE 18 Comparison of critical stresses (MPa) by FEA and proposed method: shear under parallel load.

$345 = 0.924 * 345 = 319$ MPa (46.2 ksi) and $kF_v = 1.4 * 0.4 * 345 = 0.56 * 345 = 193$ MPa (28 ksi) are assumed for Load Groups II and III.

Step 1

From Table 4, $L = 686$ mm (27 in.), $T = 50.8$ mm (2 in.), $BC = 737$ mm (29 in.), and $DB = 419$ mm (16.50 in.). By definition, the pole is 9.75 m (32 ft) high and its design load is 26.7 kN (6 kips).

For maximum bending stress under diagonal loading,

Anchor force
$= 6 * (32 - 1.5) * 12/29(4.448) = 337$ kN (75.7 kips)
Moment arm $= 0.5 * (29 - 16.5)(25.4) = 159$ mm (6.25 in.)
Equivalent coefficient α
$= \{4.304 - 0.02021(29/2) - 4.304(16.5/27) + 4.503(16.5/27)^2 - 0.9750[27 - 0.707(29)]/(27 - 16.5) - 1.686(29/27)\}/1.097 = 0.5909$
Equivalent section modulus
$= 0.5909(1.414 * 27 - 16.5)2^2/6(25.4)^3 = 140 \times 10^3$ mm³ (8.541 in.³)
Maximum bending stress
$= 75.7 * 6.25/8.541(6.90) = 382$ MPa (55.4 ksi) > 319 MPa (46.2 ksi)   NG.

Step 2

Increase the thickness T by 6 mm (0.25 in.): $L = 686$ mm (27 in.), $T = 57$ mm (2.25 in.), $BC = 737$ mm (29 in.), and $DB = 419$ mm (16.50 in.).

For maximum bending stress under diagonal loading,

Anchor force = 337 kN (75.7 kips)
Moment arm = 159 mm (6.25 in.)
Equivalent coefficient α
  = {4.304 − 0.02021(29/2.25) − 4.304(16.5/27) + 4.503(16.5/27)^2 − 0.9750[27 − 0.707(29)]/(27 − 16.5) − 1.686(29/27)}/1.097 = 0.6206
Equivalent section modulus
  = 0.6206(1.414 * 27 − 16.5)2.25^2/6(25.4)^3 = 186 × 10^3 mm^3 (11.35 in.^{3}).
Maximum bending stress
  = 75.72(6.25)/11.35(6.90) = 288 MPa (41.7 ksi) < 319 MPa (46.2 ksi)   OK.

For maximum bending stress under parallel loading,

M = 6 * (32 − 1.5) * 12(4.45 * 25.4) = 248 × 10^3 mm^3 (2196 kip-in.)
L' = max{0.707 * 29, 16.5}(25.4) = 521 mm (20.50 in.)
DB/L' = 16.5/20.50 = 0.8049   1 − DB/L' = 0.1951
Midspan moment
  = 2,196/4/0.8049^2{0.25 − 0.1951/3 + 0.1951^4/12}(4.45 * 25.4) = 17.7 × 10^3 kN-mm (156.8 kip-in.)
β = {157.6 − 21.85(27/16.5) − 0.3300(29/2.25) − 259.3(16.5/27) − 48.13[(27) (2.25)/16.5/(27 − 16.5)]$^{1/2}$ + 194.6(16.5/27)^2 + 127.4(2.25/29) − 21.65(16.5/29)}/1.080 = 0.8070
Equivalent section modulus
  = 0.8070(29 − 16.5) * 2.25^2/12(25.4)^3 = 69.7 × 10^3 mm^3 (4.26 in.^{3})
Maximum bending stress
  = 156.8/4.256(6.9) = 254 MPa (36.84 ksi) < 319 MPa (46.2 ksi)   OK.

For maximum shear stress under parallel loading,

$M/2$ = 6 * (32 − 1.5) * 12/2(4.45 * 25.4) = 124 × 10^3 kN-mm (1,098 kip-in.)
b = min{0.707 * 29, 16.5}(25.4) = 419 mm (16.5 in.)
b/T = 7.333 C' = 0.301
γ = {210.0 − 66.9(29/16.5) − 0.1719(29 − 16.5)/2.25 − 714.8(16.5/27) + 358.3(16.5/27)^2 − 48.16[27 − 0.707(29)]/(27 − 16.5) − 288.2(29 − 16.5)/(1.414(27) − 16.5) + 381.0(29/27)}/1.094 = 1.545
Equivalent torsional section modulus = 1.545(0.301) 16.5(2.25^2)(25.4)^3 = 637 × 10^3 mm^3 (38.85 in.^{3})
Maximum shear stress = 1,098/38.85(6.90) = 195 MPa (28.28 ksi) ≈ 193 MPa (28 ksi)   OK.

The experience of several such redesigned examples for deficient existing poles shows that increasing the base-plate thickness is most effective in reducing the stress level in the base plate.

CONCLUSIONS

In general, both the diagonal and parallel loadings should be considered as critical loading cases in designing signal poles. Current AASHTO analysis methods for the post and the anchor bolts appear to be appropriate on the basis of the load test results. A semiempirical analysis method for the base plate is suggested that decomposes the base plate into three simple components for respective critical stresses under the two critical loadings. This method presents clear mechanical origins of the stress concentration simply and is based on FEA of 28 poles with modelings verified by five full-scale load tests. Hand calculation is sufficient for its design applications.

ACKNOWLEDGMENTS

REFERENCES

1. *Standard Specifications for Structural Supports for Highway Signs, Luminaires and Traffic Signals.* AASHTO, Washington, D.C., 1985.
2. *Method for Calculating the Loads Applied to Span Wire Traffic Signal Poles.* Engineering Instruction EI83-38. Facilities Design Division, New York State Department of Transportation, Albany, Sept. 14, 1983.
3. *CASA/GIFTS User's Reference Manual.* Software Package Version 6.4.3. CASA/GIFTS, Inc., Tucson, Ariz., Oct. 1989.
4. S. J. Boulos, G. Fu, and A. Alampalli. *Testing, Analysis, and Design of Steel Traffic Signal Poles.* Final Report. New York State Department of Transportation, Albany, Dec. 1992.
5. F. P. Beer and E. R. Johnston. *Mechanics of Materials.* McGraw-Hill, New York, 1981.

Design Anomalies in Concrete Deck–Steel Stringer Bridges

SOTIRIS N. SOTIROPOULOS AND HOTA V. S. GANGARAO

The deterioration of highway bridge decks has been recognized as the most important factor governing the serviceability of bridges. Because of limited information provided in American Association of State Highway and Transportation Officials (AASHTO) specifications for the design of highway composite bridges to account for deterioration with time, a quantitative study of bridge deterioration factors is provided here. A description of the most important factors influencing bridge deterioration is presented. A review of the mechanism of deterioration and the status of current practice for each of the deterioration factors is provided to demonstrate the need to incorporate them into the AASHTO specifications. Finally, a stress comparison between a typical design of a highway bridge deck based on AASHTO specifications and the proposed method that accounts for four deterioration factors is presented, with a list of research needs to establish a complete understanding of the effects of bridge deterioration via suitable design formulas.

The National Bridge Inventory (NBI) study found that 23.5 percent of the nation's highway bridges are structurally deficient. These deficient bridges have been restricted to light vehicles. The most common deficiency observed was deck deterioration (1).

Although American Association of State Highway and Transportation Officials (AASHTO) specifications (2) contain adequate information about the flexural or shear design of highway composite bridges subjected to dead or live loads, little information is given about the factors that need to be included in the bridge design to account for deterioration with time.

The objective of this paper is to review the factors that influence the deterioration of concrete deck–steel stringer bridges, which have not received adequate attention in the current AASHTO highway bridge design specifications, and to investigate the accuracy of current design procedures and suggest some modifications.

A brief literature review of the performance of composite bridges follows. The description of the mechanism for each deterioration is suggested to provide a better understanding of bridge system behavior. Such an assessment may help develop priorities for the incorporation of different time-dependent deterioration mechanisms in design. Although specific influences of different failure mechanisms are not computed, stress levels for some mechanisms of deterioration are provided for a typical bridge to enable the reader to appreciate the significance of these mechanisms.

FACTORS INFLUENCING DETERIORATION OF BRIDGE SUPERSTRUCTURES

Concrete deck–steel stringer bridges began to show an increasing degree of deterioration in the early 1960s. The main categories of deterioration are scaling, cracking, spalling, and delamination (3). The factors that seemed to play the most important role are

1. Corrosion of reinforcing steel,
2. Surface degradation (scaling, cracking, spalling, or rutting) due to moisture absorption and freeze-thaw cycles,
3. Loss of composite action,
4. Aging of concrete,
5. Tensile-stress inducement at the deck top,
6. Unequal expansion and contraction coefficients in concrete leading to thermal creep,
7. Stress inducement because of temperature gradients along the stringer depth,
8. Stress inducement at the interface between deck and stringers because of shrinkage and creep, and
9. Out-of-plane (impact) or in-plane (acceleration/deceleration) forces.

Much work has been performed on corrosion of steel reinforcement (4–7). The focus of this paper is on factors other than corrosion that affect deck deterioration. Results from the analysis of a typical composite bridge (Figure 1), including the effect of the most important deteriorating factors covered here, are compared with AASHTO results.

Loss of Composite Action Between Deck and Stringers

Mechanism of Deterioration

Composite concentration has been used extensively in highway bridge design because each material (concrete, steel) is employed to its best advantage (8). When the concrete is cast over steel stringers, shear studs are embedded into the concrete and can be considered to be in full contact with the surrounding concrete. Microcracks develop in the concrete surrounding the shear connectors. Microcracks may be caused by shrinkage or early creep of concrete or to corrosion of studs. Because the shear stud can undergo larger deformations resulting from progressive increases in cracking, the studs begin to crush the surrounding concrete and reduce its strength. Therefore, cyclic loads lead to initial crushing of concrete and possibly to a stud failure in fatigue.
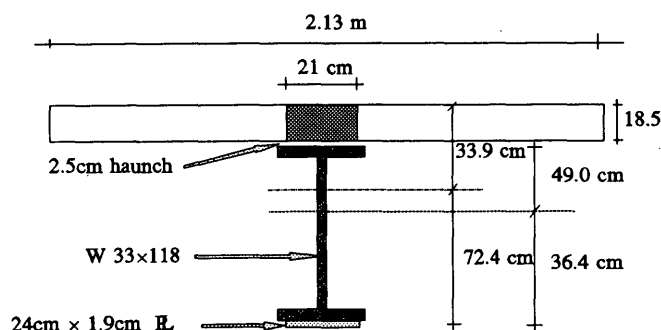
Constructed Facilities Center, College of Engineering, West Virginia University, Morgantown 26506-6101.

FIGURE 1 Design example of a composite concrete deck–steel stringer bridge (b_{ef} = 2.1 m, L = 17.4 m) (1 MPa = 145 psi).

The design of composite concrete and steel bridge superstructures using AASHTO specifications is based on the assumption of full composite action between deck and stringers. However, the slope of the curve of load versus slip decreases with time (9). The presence of slip violates the assumption of full composite action and reduces the bending stiffness. This stiffness reduction leads to additional deflection and induced stresses in the structure.

Status of Current Practice

Design of stud shear connectors in AASHTO or American Institute of Steel Construction (AISC) (10) specifications in composite structures is based on the principle that shear connectors have to withstand the ultimate load on the bridge (ultimate strength design) and resist the numerous applications of serviceability loads (9).

AASHTO specifications provide shear connector design by suggesting the check for ultimate strength (Article 10.38.5.1.2) and fatigue strength (Article 10.38.5.1.1) of the connectors. Oehlers (9) states that the fact that no interaction between monotonic strength of the connectors and fatigue loads is considered in the design can be explained by the absence of a design mechanism to allow the stud to experience fatigue damage. The shear connectors are also designed assuming full composite action between steel and concrete at service loads after a number of fatigue cycles. However, a considerable drop was reported in ultimate load of concrete decks with steel stringers after fatigue loading (11,12). The ultimate strength drop is between 51 and 73 percent of their expected static strengths. Oehlers (9) showed that the residual strength of the studs after a number of cycles also depends on the initial strength of the connectors. The semiempirical equations proposed by Oehlers are based on his experimental work; it is a great design tool.

Cracking or crushing of concrete around the studs and fatigue of the studs lead to a partial composite action that is not accounted for in the AASHTO specifications. Partial composite action in concrete and steel beams has been discussed by a number of authors (8,13) and has also been included in the AISC (10) design code (Article 1.11.4, 1988), but these code provisions lead to the use of fewer shear connectors in the ultimate strength design without consideration of the loss of stiffness of the structure from the loss of composite action. It has been observed that partial interaction of concrete deck

and steel stringers increases deflection with higher concrete strength, lower steel strength, lower modulus of connector, lower ratio of steel area to concrete area, and low span-to-depth ratio (14). Knowles (13) introduced a simple methodology to account for partial composite action by establishing equilibrium equations of forces and moments acting on the partially composite section.

Zaremba (15) also investigated the partial composite action of composite members. Using a nonlinear load-slip relationship for shear connectors and equilibrium equations based on the strain distribution of a partial composite member, he developed a system of two differential equations and a computer-aided solution. He was able to evaluate the loss in stiffness at various load stages.

The fact that interfacial slip in composite structures can cause redistribution of strains and stresses under service or ultimate loads led Al-Amery and Roberts (16) to include the nonlinear material and shear connector behavior in the analysis of partially composite members. Their illustrative example presented the ability of the method to obtain reasonably accurate results for the load range, including failure.

All the findings described reveal that a percentage of composite action between the bridge deck and stringers decreases because of the decrease in contact of shear studs with the surrounding concrete. The stiffness degradation may not be severe for static service loads, but it can be detrimental when fatigue loading is involved. Sotiropoulos and GangaRao (17) have studied the effect of stiffness degradation associated with the loss of composite action for a typical composite bridge 7.3 m (24 ft) wide and 17.4 m (57 ft) long (Figure 1). Using Oehlers' (9) design equations, the interfacial slip between deck and stringers was calculated and the composite deck was designed including partial composite action. Results showed a 25 percent decrease in bending stiffness and 8 and 180 percent in stresses at the bottom and top of the steel stringer, respectively. Stress values for the particular design example are summarized in Table 1.

Thermal Stresses Due to Temperature Variation

Mechanism of Deterioration

Temperature rise or drop during a day or throughout a year induces, in many cases, longitudinal and transverse stresses that are often overlooked during the design of bridge superstructures. Malfunctioning expansion-contraction joints or a nonuniform temperature gradient through the deck depth lead to the development of stresses that can reach high levels. Because of concrete's poor heat conductivity and the increased depth of concrete decks, temperature differentials between upper and lower surfaces (or inner and outer walls in a box-girder section) are observed more often than in steel structures (18).

Most of the temperature-related problems in bridge superstructures have been observed in continuous spans (19). In precast, segmental concrete decks, absence of continuous reinforcement at the bottom of beams (at the intermediate pier location) may cause horizontal movement of each span because of the thermally induced curvature, leading to exertion of horizontal forces on the bearings and possible damage (20).

TABLE 1 Changes in Stresses Due to Effect of Deterioration

	σ_c^{top} (MPa)	σ_c^{bot} (MPa)	σ_s^{top} (MPa)	σ_s^{bot} (MPa)
AASHTO	-3.8	1.63	-20.86	116.41
Loss of Comp. Action	2.0	0.90	-37.46	9.05
Thermal stresses	-0.55	0.32	4.45	-3.72
Creep & Shrinkage	3.48	-0.09	-8.76	65.85
Transverse tensile stress	3.94	-	-	-

1 MPa = 145 psi

σ_c^{top} =   stress at top of concrete deck

σ_c^{bot} =   stress at bottom of concrete deck

σ_s^{top} =   stress at top of steel stringer

σ_s^{bot} =   stress at bottom of steel stringer

- indicates that data are not applicable

Radolli and Green (*18*) stated that temperature differences of 40°F (20°C) can give rise to thermal stresses equal in magnitude to maximum live-load stresses at the bottom fiber of the midspan section and up to three times larger than the live-load stresses at the top fiber. The combination of thermal stresses with dead- or live-load stresses or fatigue can create additional cracking in the concrete deck. It must be noted that cracking causes stress relief, and the reduction of the moment of inertia can lead to a reduction of thermal moments (*21*).

Status of Current Practice

As mentioned before, AASHTO specifications (*2*) do not consider temperature variations through girder depth. They only specify a rise or drop of mean temperature of the bridge superstructure in moderate or cold climates. A nonlinear temperature gradient has, however, been proposed in the draft copy of the load resistance factor design (LRFD) specifications by AASHTO (*22*); these design specifications are pending acceptance by the designers. The particular gradient can be used for concrete or steel superstructures, but no provision was made for composite bridges.

Evaluation of temperature distribution and thermally induced stresses has been a topic of interest for a number of years. A number of different temperature profiles along the deck depth have been proposed. Linear and nonlinear temperature gradients for a composite bridge have been proposed and are presented in Figure 1. The bilinear temperature distribution of the American Society of Civil Engineers (ASCE) (*23*) is selected to illustrate the example (*17*).

A deck subjected to nonlinear temperature distribution through depth experiences three effects: (a) uniform expansion or contraction (covered by AASHTO), (b) a curvature

(hogging) that does not create any stresses in a simply supported case, and (c) Eigen stresses that are developed to compensate for the Navier-Bernoulli assumption of plane sections remaining plane, that is, linear strain distribution through depth. For continuous spans, additional stresses are accounted for in the calculations to compensate for the continuity of the span (continuity stresses). A formulation of one-dimensional heat transfer was used in most of the theoretical investigations to calculate thermal stresses for given temperature variation. The most popular and well-documented methods available in the literature are reported by Priestley (*24*) and Zuk (*25,26*). Both methods are simple static or equilibrium equations, and the former is used mainly for all concrete decks, whereas the latter is used in composite structures. Soliman and Kennedy (*27*) simplified Zuk's method and applied it in an illustrative example for a composite steel and concrete beam. Following the same procedure, but assuming ASCE's temperature distribution (Figure 2), the thermal stresses for the particular design example of the 7.3-m × 17.4-m (24-ft × 57-ft) composite bridge were presented by Sotiropoulos and GangaRao (*17*). The illustrative example
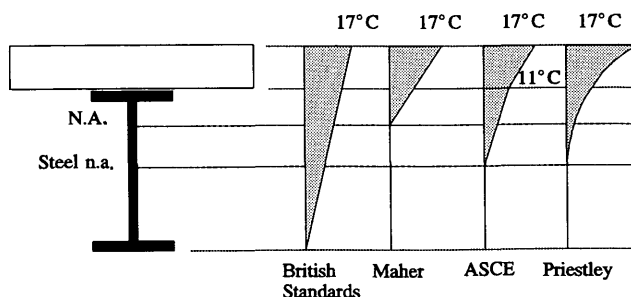

FIGURE 2 Proposed temperature gradients.

revealed that thermal stresses developed in the particular section under ASCE's proposed temperature distribution reached the level of 60 percent of the live-load stresses at the top of the steel beam in the example.

Calculations of thermal stresses developed under a nonlinear temperature gradient through the depth are well documented in the literature, and good correlation with experimental results verified their accuracy (21). Assuming a temperature gradient proposed by ASCE (23), the developed thermal stresses along a deck depth are calculated for simply supported or continuous spans and all concrete or composite decks. Temperature variation across the deck width is not considered in any of the methods mentioned; this variation can have significant effects on box-girder bridges.

Thermal Creep Due to Difference in Thermal Expansion and Contraction Coefficients of Concrete and Steel

Mechanism of Deterioration

Concrete, unlike steel, experiences unequal expansion and contraction when subjected to a temperature rise or drop of the same amount (ΔT). The phenomenon of unequal thermal expansion and contraction coefficients has been observed by a number of researchers, but in most cases no provisions are made during the design of concrete decks. Incompatibility of thermal coefficients between steel and concrete plays a major role in the performance of a deck, including deck growth problems.

The unequal thermal expansion and contraction coefficients in concrete have been recognized as contributing factors in deck deterioration (28). As has been reported by a number of researchers (29–31), thermal coefficients of concrete are different at different temperature ranges (above and below the freezing point of water) and even at the same temperature ranges (30). Variations in expansion and contraction coefficients of concrete and thermal coefficients between concrete and steel lead to inducement of residual thermal stresses and strain incompatibility. These factors in turn lead to deck cracking and "deck growth."

Explanation of the expansion and contraction incompatibility of concrete is based on the composite nature of the material. The thermal coefficient of concrete depends on the quantity of the aggregate in the mix and the coefficient of the aggregate itself (32). Decrease of moisture and increase in age decrease the thermal coefficient (29). Thermal expansion or contraction is the result of the normal expansion and contraction of anhydrous materials and the hygrothermal expansion and contraction associated with the movement of internal moisture from capillaries or from gel pores (31). It has also been suggested (32) that if the thermal coefficients of aggregate and cement differ greatly, a large temperature change may introduce differential movement and a break in the bond between the aggregate and the surrounding paste. Therefore, if this differential movement occurs, cooling of concrete will not lead to recovery of the initial dimensions. The result will be a mismatch in expansion and contraction coefficients causing development of residual stresses.

Status of Current Practice

Although the mismatch of expansion and contraction coefficients of concrete has been observed, little has been done to correlate this effect with concrete deterioration. Limited experimental work has been conducted on specimens from actual bridge decks by GangaRao et al. (28), who studied, among other parameters, the magnitude of thermal creep and residual stress buildup in several concrete and concrete and steel specimens cast in laboratory conditions or cut from actual bridge decks under temperature and freeze-thaw cycles. Results verified the difference between thermal expansion and contraction coefficients that also varied in value at different temperature ranges (the contraction coefficient is always smaller than the expansion coefficient). The difference in expansion and contraction coefficients increased as the temperature range increased. Residual tensile strains were observed in both concrete and steel bars. The fact that their values differed in the same direction verified strain incompatibility between steel and concrete. The thermal strain buildup after 40 to 50 thermal cycles and after subtracting the "shrinkage compensation" was in the range of 400 microstrains (400×10^{-6} in./in.). It has also to be noted that plain concrete behaved differently from reinforced concrete. A good understanding of the behavior of concrete under freeze-thaw cycles awaits additional experimental data.

Shrinkage and Creep Effects in Steel and Concrete Composite Decks

Mechanism of Deterioration

As concrete is integrally connected with steel in composite structures, creep and shrinkage stresses have to be transferred from concrete to steel. The development of these stresses in concrete, resulting from the restraint set by the steel beam, reduces the efficiency of concrete in resisting loads (33). If the shrinkage stresses after reduction of the creep effect are greater than the allowable tensile stresses, cracks form in a concrete deck. As creep relief decreases with age, the tendency to crack becomes greater (32). The shrinkage and creep of concrete and steel structures result in an increase of deflection (34). Stresses induced by differential shrinkage may be as high as 50 percent of the dead load stresses in shorter bridges (35).

The magnitude of the shrinkage and creep stresses in a composite structure depends on the parameters that directly or indirectly affect the shrinkage and creep of the concrete itself. The typical parameters affecting shrinkage and creep are drying rate, size and grading of aggregate, water-to-cement ratio, relative humidity, externally applied stress level, strength of concrete, and so forth (32).

Status of Current Practice

Ghali and Favré (36) have researched the creep and shrinkage (time-dependent parameters) problems in all concrete structures. Their work provides theoretical calculations for shrinkage and creep stresses and deflections for composite steel and

concrete structures. Bradford (34) has also presented a simplified method to calculate deflections resulting from creep and shrinkage of composite structures. The usual method of calculating the shrinkage and creep forces is the so-called "composite section technique," in which the differential shrinkage and creep forces are resisted by the composite section (35). An illustrative example and brief explanation of these proposed methods have been presented by Sotiropoulos and GangaRao (17).

AASHTO specifications do not neglect shrinkage and creep effects in concrete decks. The information given in the specifications is rather conservative for creep and not very explanatory for shrinkage. In particular, AASHTO specifications (Article 9.13.3.3, 1989) state that differential shrinkage of cast-in-place concrete over precast beams may influence the cracking load and the beam deflection profile. When these factors are particularly significant, the effect of differential shrinkage should be added to the effect of loads. In Article 10.38.1.4 (2), a multiplier of 3 is specified on calculated stresses of composite structures to account for creep. It has been noted that creep and shrinkage cannot be fully separated, because they take place simultaneously (35).

Creep and shrinkage stresses are large. The magnitude of tensile stresses developed at the top of the concrete deck for the design example mentioned before was in the area of 3.45 MPa (500 psi) (17). Combining this stress with the instantaneous stress resulting from dead load may lead to excessive tensile stresses and possibly to cracking. AASHTO's approach may not provide good results, especially for composite structures, because the differential shrinkage effect was not included in that calculation.

The methodology of the "composite section" can be considered adequate to address the differential creep and shrinkage between different concrete members in the same structure or composite concrete and steel decks. Cracked concrete sections as well as continuous spans can be studied by adding appropriate continuity stresses (36). All methodologies use the assumption of full composite action (no interfacial slip) between concrete deck and steel stringers, despite the tendency of the deck to lose some composite action with increasing number of load cycles. Therefore, the method of Ghali and Favré needs to be modified to include partial composite action. For simplification, incorporation of partial composite action in the calculations of shrinkage and creep stresses can be accomplished by using an "effective deck thickness," that is, the thickness of the deck that will result in the same effective bending stiffness of the composite beam after reduction resulting from partial composite action (37). The additional in-plane shear forces transmitted to the steel stringer through the connectors caused by shrinkage and creep, or accelerating or braking forces, need to be accounted for in the design of the connectors.

In-Plane and Out-of-Plane Forces on Decks

Mechanism of Deterioration

The in-plane forces from accelerating or braking vehicles can lead to deterioration of the deck surface (concrete spalling, rutting). Local, friction-type loading on decks leads to an increase in stress on top of the deck. Such stress intensity may lead to breaking of the bond between the concrete's constituents or between the concrete and its reinforcement, causing spalling and delamination. Braking or accelerating forces also affect the composite action of composite structures because the in-plane forces are transmitted from the concrete deck to the steel stringers through the shear connectors. Existence of such loads can lead to additional local shear loading of the studs and subsequent loss of composite action with steel in the same manner as described earlier. Braking or accelerating forces cause redistribution of axle loads and can lead to an increase in impact force that may exceed the factors adopted by design codes (38).

Out-of-plane impact loads from the pounding of passing vehicles because of the rough riding surface of the concrete deck or even "launching" of trucks onto the deck because of unleveled approaches often cause deterioration of concrete decks. In addition to the induced vibrations in a local and global sense, high-intensity repetitive loading forms a punching type of load that can be detrimental close to the stringer locations. This out-of-plane fatigue load leads to deterioration of the integrity of concrete and causes spalling and rutting. Also, depending upon the bridge and vehicle characteristics, it may lead to excessive vibrations of the bridge as a whole and excessive stresses and deformations.

Status of Current Practice

Limited experimental or theoretical work has been published on the effect of local in-plane loads on bridge decks. The problem of impact or longitudinal forces on bridge decks has been dealt with in design codes or by individual researchers as a problem of vibration of the bridge superstructure by specifying equivalent static loads (2) or proposing rigorous analyses to predict the actual behavior of a bridge under these loading conditions.

AASHTO specifications define equivalent static loads to represent the longitudinal and impact forces exerted by the vehicular traffic. The design value for the force resulting from braking is taken as 5 percent of the live load in all lanes carrying traffic headed in the same direction (Article 3.9). The center of gravity of this force is assumed to be located 6 ft above the floor slab. Impact forces are considered through an impact allowance factor given by Article 3.8.2.

According to the Committee on Loads and Forces on Bridges (23), AASHTO specifications (2) requirements for minimum longitudinal forces are far less than the longitudinal load required by many other codes.

Modeling of braking forces and the consequent response on bridge decks was attempted by Gupta and Traill-Nash (38). They showed that the impact factor was 0.25 for a symmetric loading case and 0.33 for an eccentric case when AASHTO specified 0.27 for the particular span length. Differences were also reported by O'Connor and Chan (39) between the AASHTO specified impact factor and measured values from tests on composite steel and concrete bridges. O'Connor and Chan presented a method to evaluate the impact factor based on deflection or even strain readings. GangaRao (40) also presented a deterministic procedure, based on the orthotropic plate theory, to compute frequencies, deformations, and

stresses. Analytical results for impact factor correlated well with measured data from a number of highway bridges in West Virginia. Harsh and Darwin (41) stated that traffic-induced vibrations did not appear to be detrimental to bond strength and compressive strength in bridge deck repairs if the concrete had low slump. The majority of recent studies have contradicted the current AASHTO impact factor (40). Maximum values of impact factor in the range of 0.80 were observed in a study of continuous bridge superstructures by Csagoly et al. (42).

As Schilling (43) noted, the impact factors used in fatigue design of bridges are different from those for nonfatigue design because they have to be based on average and not extreme loading conditions and have to account for the dynamic effects on the stress range rather than the peak stress. Analysis of the response of model bridges under four- and five-axle trucks presented an impact factor of 0.25. According to Schilling, the AASHTO formula can be used for fatigue calculations for simple-span and continuous-span bridges.

All the theories presented and research have revealed a number of differences between impact factors and longitudinal forces and AASHTO specifications. The differences are expected because of the dynamic nature of impact and braking forces. It is impossible for a design code to include all parameters that can affect the dynamic response of the deck.

The comparatively low design value for longitudinal force resulting from braking can be verified by a series of wheel-load tests on bridge decks. So far, wheel-load testing has been used for fatigue testing of decks. Such a test will be able to simulate the impact (pounding) nature of traffic loads and the horizontal braking or accelerating forces in the plane of the deck. Such a test can also be used to monitor the durability and wear resistance of the concrete deck surface against rutting, delamination, and spalling.

Tensile Stress Inducement on the Deck Top

Mechanism of Deterioration

Depending on the location of the concentrated loads that a typical vehicle exerts on the deck and relative transverse deck stiffness and longitudinal beam stiffness, eccentric loads on bridge decks may induce net tensile stresses on the concrete top. If the reinforcement is not adequate to withstand the induced tensile stresses, the concrete will crack. This phenomenon can be repeated and in time lead to fatigue failure of the deck.

Status of Current Practice

Current AASHTO specifications (2) lead to the bridge deck design for maximum moment when the design truck has one of its two 142-kN (32-kip) axles over the transverse center line of the bridge (HS20-44 design truck). Similar shear design of the deck uses the location of the truck as close to the extreme stringer as possible. No reference is made in the specifications to the possibility of stress reversals across the width of a deck under eccentric loads.

Using a simplified methodology of a beam on elastic springs developed by Kallomalos (44), an approximation can be made of load distribution factors across the deck width. Establishing the force interactions between deck and stringers, a moment diagram of the deck can be obtained resulting from the load by one axle of the design AASHTO truck and the area of the deck in which stress reversals exist can be located. Theoretical results on a timber deck 7.3 m × 12.2 m (24 ft × 40 ft) with a thickness of 23.5 cm (9.25 in.) presented a tensile stress at the top of the timber deck of the order of 3.45 MPa (500 psi) for an eccentric position of the design truck. The beam-on-elastic-springs model was analyzed by finite elements (17) and by representing the concrete deck of the design example (Figure 1) by a strip 1.52 m (60 in.) wide and the stringers by elastic springs. The resulting maximum tensile stress at the top of the deck for an eccentric position of the AASHTO truck load was 3.94 MPa (571 psi). The magnitude of the tensile forces in this design example may not seem adequate to cause concrete failure, but these tensile forces in conjunction with fatigue cycling can lead to fatigue failure of the deck.

Finite element analysis, including composite and noncomposite action, of concrete bridge decks on steel stringers (45) determined that for a bridge 8.5 m × 18.3 m (28 ft × 60 ft) with an 18-cm (7-in.) concrete slab, tensile stresses in the range of 1.4 MPa (200 psi) developed at the top of the deck away from the truck position. The designed deck has almost the same dimensions as the one that is adopted in the example (17). Noncomposite action between stringers and deck presented a more dispersed distribution of tensile stresses in the center half of the span, whereas when full composite action was assumed, tensile stresses developed along lines coincident to the unloaded stringer positions.

Eccentric fatigue tests of concrete slabs on steel girders need to be performed to monitor the induced tensile stresses and the possible crack formation at the concrete top as well. It is necessary to examine whether the conventional orthotropic reinforcement ratios recommended by AASHTO for deck slabs can provide adequate strength because of this particular extreme loading condition. Batchelor (46) found that deck slabs with such reinforcement presented large reserves of strength against fatigue failure. Csagoly and Lybas (47) also stated that 0.3 percent isotropic reinforcement is adequate for serviceability fatigue and ultimate capacity. Before any of these recommendations are adopted, additional tests should be performed on decks to determine their service life.

RESEARCH NEEDS

As stated in the preceding section, deficiencies exist in the current AASHTO specifications covering the design of highway bridge decks to withstand or tolerate deterioration. Simple numerical calculations presented the effects of various factors on the performance of the deck and the entire bridge superstructure (17).

As the evidence of the growing need to improve deck life becomes paramount, a rank ordering of research needs in this area of bridge design is important; such a listing is suggested here.

1. Loss of composite action constitutes the most urgent aspect that needs to be considered in design computations because it directly affects the stiffness of composite structures and no provisions are made in the specifications about the loss of composite action with time. Considerable progress has been made in predicting the loss of composite action, but additional research is needed to unify all the proposed methods to predict the decrease of bending stiffness with time.

2. Thermal effects on bridge superstructures can be significant under extreme temperature conditions, but more emphasis needs to be placed on understanding the variations of thermal coefficients of concrete leading to thermal creep. As far as thermal stress evaluations due to nonlinear temperature gradients through the depth of the deck are concerned, transportation officials need to include this aspect as an important item for the new AASHTO specifications because design methodologies have a way of gaining general acceptance.

3. Creep and shrinkage effects on composite decks urgently need attention because of the magnitude of the developed stresses. Knowledge and experience gained from the study of creep and shrinkage of plain reinforced concrete are expanded to understand and calculate the resulting stresses on concrete decks and steel beams of composite decks. The significance of this factor is based on the fact that even though creep and shrinkage originate in the concrete deck, their action affects both the deck and stringers.

4. The AASHTO specifications for transverse reinforcement of concrete decks should be revised on the basis of more accurate transverse load distribution formulas. Inducement of tensile stresses at the concrete top (under eccentric loads) should be studied from the point of view of serviceability because tensile stresses may cause cracking or fatigue to the deck.

5. The effects of out-of-plane and in-plane loads on concrete decks should be studied as the main factors of material disintegration in a local and global sense.

A summary of the results of the preliminary analysis (*17*) of a typical 7.3-m × 17.4-m (24-ft × 57-ft) concrete and steel bridge with a deck of 18.5 cm (7.25 in.) is presented (Table 1) to illustrate the need to modify current AASHTO specifications.

CONCLUSIONS

This study presents the major factors affecting bridge deck deterioration. Special emphasis is placed on items not fully covered in the current AASHTO design specifications. A description of the deteriorating mechanisms of each factor is given, with a list of advancements in theory or experiment toward a better understanding of each phenomenon, as reported in the literature. Specific additional research is recommended. This work presents areas in the design of highway bridges that need to be revised by AASHTO. The results from the design example presented are preliminary. Similar calculations for superstructures with different dimensions need to be studied. The paper emphasizes the need to account for the deterioration of bridge superstructures during design.

REFERENCES

1. K. F. Dunker and B. G. Rabbat. Highway Bridge Type and Performance Patterns. *Journal of Performance of Constructed Facilities*, ASCE, Vol. 4, No. 3, 1990, pp. 161–173.
2. *Standard Specifications for Highway Bridges*, 14th ed. AASHTO, Washington, D.C., 1989.
3. R. K. Banks. Bridge Decks: Their Problems and Solutions. *Public Works*, Vol. 117, No. 12, 1986, pp. 26–28.
4. J. T. N. Atkinson and H. VanDroffelaar. *Corrosion and Its Control: An Introduction to the Subject.* National Association of Corrosion Engineers, Houston, Tex., 1982.
5. C. H. Hare et al. *NCHRP, Synthesis of Highway Practice 136: Protective Coatings for Bridge Steel.* TRB, National Research Council, Washington, D.C., Dec. 1987.
6. G. J. Malasheskie et al. *Bridge Deck Protective Systems.* Final Report RP85-17. Pennsylvania Department of Transportation, Harrisburg, July 1988.
7. D. Stark. *Evaluation of the Performance of Galvanized Reinforcement in Concrete Bridge Decks.* Final Report. Portland Cement Association, Skokie, Ill., May 1982.
8. J. P. Cook. *Composite Construction Methods.* John Wiley & Sons, New York, 1977.
9. D. J. Oehlers. Deterioration in Strength of Stud Connectors in Composite Bridge Beams. *Journal of Structural Engineering*, ASCE, Vol. 116, No. 12, 1990, pp. 641–653.
10. *Manual of Steel Construction*, 8th ed. American Institute of Steel Construction, Inc., Chicago, Ill., 1988.
11. C. G. Coughlan. *The Stiffness of Stud Shear Connections in Composite Beams Subjected to Static and Fatigue Loading.* M.S.E. thesis. National University of Ireland at Cork, 1984.
12. D. J. Oehlers and L. Foley. The Fatigue Strength of Stud Shear Connections in Composite Beams. *Proceedings of the Institute of Civil Engineers*, Vol. 79, No. 2, 1985, pp. 349–364.
13. P. R. Knowles. *Composite Steel and Concrete Construction.* John Wiley & Sons, London, 1973.
14. R. P. Johnson and I. M. May. Partial-Interaction Design of Composite Beams. *Structural Engineer*, Vol. 53, No. 8, Aug. 1975, pp. 305–311.
15. C. J. Zaremba. Strength of Steel Frames Using Partial Composite Girders. *Journal of Structural Engineering*, ASCE, Vol. 114, No. 8, 1988, pp. 1741–1760.
16. R. I. M. Al-Amery and T. M. Roberts. Nonlinear Finite Difference Analysis of Composite Beams with Partial Interaction. *Computers & Structures*, Vol. 35, No. 1, 1990, pp. 81–87.
17. S. N. Sotiropoulos and H. V. S. GangaRao. *Design Anomalies in Highway Bridge Decks.* Interim Report. Constructed Facilities Center, West Virginia University, Morgantown, 1992.
18. M. Radolli and R. Green. Thermal Stresses in Concrete Bridge Superstructures Under Summer Conditions. In *Transportation Research Record 547*, TRB, National Research Council, Washington, D.C., 1975, p. 23.
19. R. A. Imbsen, D. E. Vandershaf, R. A. Schamber, and R. V. Nutt. Thermal Effects in Concrete Bridge Superstructures. In *NCHRP Report 276*, TRB, National Research Council, Washington, D.C., 1985, p. 99.
20. M. Elbadry and A. Ghali. Thermal Stresses and Cracking of Concrete Bridges. *ACI Journal*, No. 83-90, Nov./Dec. 1986, pp. 1001–1009.
21. S. J. Thurston, M. J. N. Priestley, and N. Cooke. Influence of Cracking on Thermal Response of Reinforced Concrete Bridges. *Concrete International*, Vol. 6, No. 8, 1984, pp. 36–43.
22. Modjeski and Masters. *Development of Comprehensive Bridge Specifications and Commentary.* 3rd Draft LRFD Specifications and Commentary. Prepared for National Cooperative Highway

Research Program, TRB, National Research Council, Washington, D.C., April 1992.

23. American Society of Civil Engineers, Committee on Loads and Forces on Bridges of the Committee on Bridges of the Structural Division. Recommended Design Loads for Bridges. *Journal of the Structural Division*, ASCE, Vol. 107, No. ST7, 1981, pp. 1161–1213.

24. N. M. J. Priestley. Design of Concrete Bridges for Temperature Gradients. *ACI Journal*, No. 75-23, May 1978, pp. 209–217.

25. W. Zuk. Thermal and Shrinkage Stresses in Composite Beams. *ACI Journal*, Vol. 58, 1961.

26. W. Zuk. Simplified Design Check of Thermal Stresses in Composite Highway Bridges. In *Highway Research Record 103*, HRB, National Research Council, Washington, D.C., 1965, pp. 10–13.

27. M. Soliman and J. B. Kennedy. Simplified Method for Estimating Thermal Stresses in Composite Bridges. In *Transportation Research Record 1072*, TRB, National Research Council, Washington, D.C., 1986, p. 23.

28. H. V. S. GangaRao, P. R. Raju, and H. K. Thippeswamy. *Thermal Studies on Concrete Cubes, Cylinders, Decks and Filled Grid Steel*, Research Report FHWA-WV-86. West Virginia University, Morgantown, April 1992.

29. C. Berwanger and F. A. Sarker. *Effect of Temperature and Age on Thermal Expansion and Modulus of Elasticity of Concrete*. ACI Publication, SP-39. Oct. 1973, pp. 1–22.

30. G. E. Monfore and A. E. Lentz. Physical Properties of Concrete at Very Low Temperatures. *Journal of Portland Cement Association*, May 1962, pp. 33–39.

31. J. A. Rhodes. Thermal Properties. In *Significance of Tests and Properties of Concrete and Concrete-Making Materials*, American Society of Testing and Materials, STP 169B, Committee C-9 on Concrete and Concrete Aggregates, Philadelphia, 1978.

32. A. M. Neville. *Properties of Concrete*. Wiley & Sons, New York, 1973.

33. S. G. Arzoumanidis, R. G. Burg, and J. Shmid. Creep and Shrinkage in Composite Cable-Stayed Bridges. In *Transportation Research Record 1290*, TRB, National Research Council, Washington, D.C., 1991, pp. 20–27.

34. M. A. Bradford. Deflections of Composite Steel-Concrete Beams Subject to Creep and Shrinkage. *ACI Structural Journal*, No. 99-S63, Sept.–Oct. 1991, pp. 610–614.

35. D. R. Schelling. Minimization of Composite Dead Load Effects.

Journal of the Structural Division, ASCE, Vol. 108, No. 11, 1982, pp. 2591–2608.

36. A. Ghali and R. Favré. *Concrete Structures: Stresses & Deformations*. Chapman and Hall, Ltd., New York, 1986.

37. S. N. Sotiropoulos. *Static Response of Bridge Superstructures Made of Fiber Reinforced Plastic*. M.S. thesis. West Virginia University, Morgantown, 1991.

38. R. K. Gupta and R. W. Traill-Nash. Vehicle Braking on Highway Bridges. *Journal of Engineering Mechanics*, ASCE, Vol. 106, No. 4, Aug. 1980, pp. 641–658.

39. C. O'Connor and T. H. T. Chan. Dynamic Wheel Loads from Bridge Strains. *Journal of Structural Engineering*, Vol. 114, No. 8, 1988, pp. 1703–1723.

40. H. V. S. GangaRao. Impact Factors for Highway Bridges. *Vehicle, Tire, Pavement Interface*. ASTM STP 1164 (J. J. Henry and J. C. Wambold, eds.), American Society of Testing and Materials, Philadelphia, Pa., 1992, pp. 155–166.

41. S. Harsh and D. Darwin. Traffic-Induced Vibrations and Bridge Deck Repairs. *Concrete International*, Vol. 8, No. 5, 1986, pp. 36–42.

42. P. F. Csagoly, T. I. Cambell, and A. C. Agarawal. *Bridge Vibrational Study*, Research Report 181. Ontario Ministry of Transportation and Communication, Canada, 1972.

43. C. G. Schilling. Impact Factors for Fatigue Design. *Journal of Structural Engineering*, Vol. 108, No. 9, 1982, pp. 2034–2044.

44. D. A. Kallomalos. *Behavior of Timber Deck-Steel Stringer Bridges Subjected to Gravity Loads*. M.S. thesis. West Virginia University, Morgantown, 1989.

45. R. Lopez-Anido. *Analysis and Evaluation of Top Deck Transverse Tensile Stresses in Concrete Slab-Steel Beam Bridges*. Constructed Facilities Center, West Virginia University, Morgantown, Feb. 1992.

46. B. deV. Batchelor. An Investigation of the Fatigue Strength of Deck Slabs of Composite Steel/Concrete Bridges. In *Transportation Research Record 644*, TRB, National Research Council, Washington, D.C., 1978, pp. 153–161.

47. P. F. Csagoly and J. M. Lybas. Advanced Design Method for Concrete Bridge Deck Slabs. *Concrete International*, Vol. 11, No. 5, 1989, pp. 53–63.

Freeze-Thaw Studies on Concrete Structural Elements

Hota V. S. GangaRao, Hemanth K. Thippeswamy, and
Penmatsa R. Raju

The effect of freeze-thaw cycles on plain concrete decks and concrete-filled steel grid decks is presented. The test program stimulates field temperature conditions. An attempt has been made to correlate the freeze-thaw effect to the longitudinal growth behavior of concrete-filled steel grid decking systems. To study the longitudinal growth, emphasis has been placed on the determination of expansion and contraction coefficients of concrete for different temperature ranges. Residual tensile strain buildup, a result of the differential expansion and contraction coefficient of concrete, is found to be a function of freeze-thaw cycles. Thermal incompatibility between concrete and steel and the consequent growth in concrete-filled steel grid decks are dealt with from the viewpoint of thermal creep.

Concrete is an important construction material that has many advantages and few limitations. One of the major concerns is the response and durability of concrete under environmental conditions such as thermal cycling. In most of the applications, concrete is used along with steel, resulting in composite members of reinforced or prestressed concrete components. In such components, concrete and steel are forced to deform together under temperature fluctuations. However, the difference in thermal properties of concrete and steel results in thermal strain incompatibility and eventually leads to residual stress buildup (*1*). The residual stress buildup is tensile in nature and becomes cumulative with the number of freezing and thawing cycles. The strains due to freezing in the case of saturated cement paste specimens were reported (*2*) to be as high as 1600 microstrains, and about 500 microstrains of permanent elongation after reaching the original temperature was also reported. Pigeon et al. determined the freeze-thaw durability of concrete and found a strain buildup of 2,000 to 5,000 microstrains over 100 cycles for varying constituents in concrete (*3*). Attiogbe et al. determined the freeze-thaw durability of concrete containing superplasticizers and reported a strain buildup on the order of 1,300 microstrains over 300 cycles (*4*). The difference between thermal coefficients of expansion and contraction, which is one of the causes for residual stress buildup, has been reported by many researchers (*5–7*). The variation in coefficients is more pronounced above and below the freezing point of water. The moisture content in the pores of concrete freezes and forms ice below 0°C (32°F). The materials in concrete contract but ice in pores expands below 0°C (32°F), resulting in a decreased coefficient of expansion of concrete. The coefficient of expansion and contraction above and below the freezing point

of water, for a concrete with a 0.49 water-to-cement ratio that has been dry-cured for 28 days, has been reported to be 4.26 $\times 10^{-6}$ and 2.83 $\times 10^{-6}$, respectively (*5*).

The limitations of this phenomenon are cracking and growth of concrete, which are generally associated with regions that experience a number of freeze and thaw cycles during winter seasons. Cracks permit water to enter into concrete. The moisture ingress leads to enlargement of the cracks due to freezing, which in turn permits additional water to seep and cause concrete deterioration.

Longitudinal growth, which poses a very serious maintenance problem, is found extensively in concrete-filled steel grid decks (*8–10*). For instance, an 11-span highway bridge 217 m (710 ft) long, built in 1948 at Massillon, Ohio, that had a concrete-filled steel grid decking system was closed to traffic in December 1964 because of growth in the bridge deck (*8*). The deck growth caused the sidewalks to crack and buckle and the expansion joints to close. The deck growth resulted in failure of welds between the deck and supporting stringers and dislocation of the deck from its abutment. Sturrett (*11*) reported a growth in concrete-filled decks on the order of 102 mm (4 in) for 31 m (100 ft) of length in the field. He also reported that the maximum force in one cross bar of the concrete-filled steel grid deck can be as high as 58 kN (13 kips). Additional literature (*9*) reveals that more than half of the totally bare (without concrete overlay) concrete-filled steel grid decks and more than a quarter of concrete-filled steel grid decks with concrete overlay showed a deck growth problem in Ohio alone.

The probable reasons attributed to the deck growth were corrosion of steel and use of expansive aggregates (*8*). Some researchers (*9,10*) also put forth remedial measures for the concrete-filled deck growth problem. However, the design details accounting for the effect of thermal fluctuations, thermal movements, freeze and thaw cycles, thermal incompatibilities, and separation of concrete from steel, which can be attributed to differential expansion between concrete and steel, were not given much importance. Yanev (*12*) and Callahan et al. (*13*) have pointed out the importance of such parameters in their work.

The objective of this paper is to present (a) expansion and contraction phenomena of concrete at different temperature ranges; (b) expansion and contraction coefficients, and residual stress buildup within concrete due to freeze-thaw cycling, for plain concrete slabs and concrete-filled steel grid decks; (c) thermal incompatibility between concrete and steel in concrete-filled steel grid decks leading to their growth; and

Constructed Facilities Center, West Virginia University, Morgantown, W. Va. 26505.

(d) concrete strength (tensile and compressive) variations before and after freeze-thaw cycles.

SCOPE

Accelerated tests were conducted in a laboratory environment on plain concrete slabs and concrete-filled steel grid decks, simulating field conditions to study the deck growth phenomenon. The test program was designed on the basis of simulating field temperature and freeze-thaw effects only. Test specimens were monitored for dry and wet conditions, and humidity conditions were maintained at the ambient levels only. The length and width of the deck specimens were scaled to suit the apparatus size; however, the specimen thickness was nearly identical to the field conditions. The temperature in the core of the concrete slab and concrete-filled grid decks was monitored with the help of embedded thermocouples. Strain data were obtained using strain gauges.

The test specimens consisted of plain concrete slabs and concrete-filled steel grid decks. Table 1 summarizes the specimen sizes and main bar and cross bar spacing and orientation in addition to other information such as temperature range, duration of each cycle, and number of cycles for each specimen tested for freeze-thaw effect. Figure 1 shows the main bar and cross bar sizes used in the concrete-filled steel grid deck specimens. Eight specimens were studied. Series I consisted of a concrete-filled steel grid deck and an open steel grid deck. The concrete-filled steel grid deck was cast in the laboratory. The specimens of Series I were subjected to 18 cycles in the temperature procession of 21 to −32 to 21°C (70 to −25 to 70°F). Series II and III comprised two concrete-filled steel grid decks and a plain concrete slab. All the specimens in Series II and III were cast in the laboratory. The

temperature procession for specimens in Series II and III was 21 to 2 to −17 to 2 to 21°C (70 to 35 to 0 to 35 to 70°F). Series II and III specimens were subjected to 70 and 155 cycles, respectively. Series III specimens were subjected to both dry and wet cycles. The duration of each cycle for all the specimens in Series I through III was 24 hr. The mix proportions of specimens within the series was kept constant.

EQUIPMENT AND MEASURING DEVICES

The equipment and measuring devices used for the testing program were Tenny Environmental Equipment (chamber), Omega Thermocouple Thermometer, Datran II Multichannel Strain Indicator, thermocouples, and strain gauges.

The Tenny Environmental Equipment was designed to create and control the temperature and relative humidity within the specified operating ranges. Simulated environments were controlled automatically by manual selection switches. The clear working space available inside the chamber was 1.2 × 1.2 × 1.2 m (48 × 48 × 48 in.). The chamber had a full opening door, viewing window, and electrical and thermocouple feed throughs. The temperature variations were achieved using a cam device. The Omega Thermocouple Thermometer, which was used to monitor the temperature in the core of the specimens, was a digital panel meter and served as a readout for J-, K-, T-, or E-type thermocouple sensors. The J-type thermocouple was used throughout the experimental program. The Datran II strain indicator, with a scanner control section and 80 channels used to measure strains in concrete and steel, was a precision DC millivolt-per-volt instrument that had a high degree of operational versatility and reliability. The types of strain gauges used were EA-06-250BG-120 for steel and EA-06-20CBW-120 for concrete. The strain gauges

TABLE 1   Type, Size, and Freeze-Thaw Parameters of Specimens

SPECIMEN TYPE	SERIES #	SPECIMEN SIZE (mm)	MAIN BAR DIRECTION	TEMPERATURE RANGE (^{0}C)	NO. OF CYCLES
1. FILLED DECK	I	254x914x127	LONG	21 To -32 To 21	18
2. OPEN STEEL GRID		254x914x127	LONG	21 to -32 To 21	18
1. FILLED DECK	II	305x914x108	LONG	21 To 2 To -17 To 2 To 21	70
2. FILLED DECK		406x1219x108	SHORT	21 To 2 To -17 To 2 To 21	70
3. PLAIN CONC. DECK		305x914x108	-	21 To 2 To -17 To 2 To 21	70
1. FILLED DECK	III	305x914x108	LONG	21 To 2 To -17 To 2 To 21	155**
2. FILLED DECK		610x610x108	LONG	21 To 2 To -17 To 2 To 21	155**
3. PLAIN CONC. DECK		305x914x108	-	21 To 2 To -17 To 2 To 21	155**

Note: 1 in = 25.4 mm ; $(^0F - 32)/1.8 = {}^0C$
**Wet type of cycles are conducted beyond 105 cycles
Main bar spacing is 203 mm in all the specimens
Cross bar spacing is 102 mm in all the specimens
Duration of each cycle is 24 hours in all the specimens
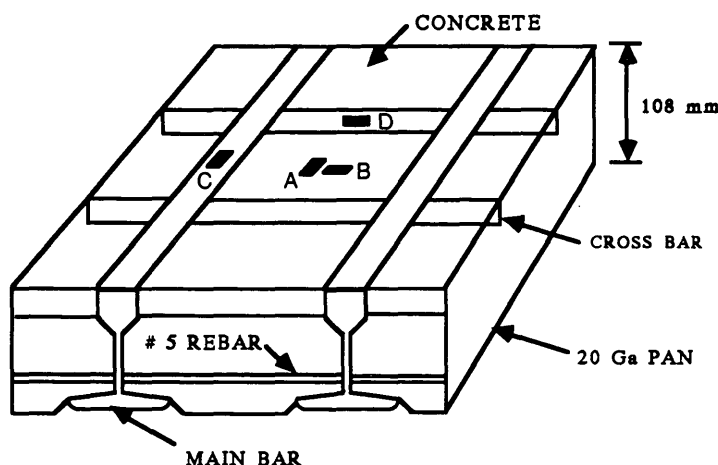
MAIN BAR SIZE AND SPACING: 108mm I SECTION OF 5# @ 203 mm C/C
CROSS BAR SIZE AND SPACING: 38mmx6mm @ 203 mm C/C

A : STRAIN GAGE ON MAIN BAR STEEL (MB)

B : STRAIN GAGE ON CROSS BAR STEEL (CB)

C : STRAIN GAGE ON CONCRETE IN MAIN BAR DIRECTION (MBD)

D : STRAIN GAGE ON CONCRETE IN CROSS BAR DIRECTION (CBD)

FIGURE 1   Strain gauge location and nomenclature in concrete-filled steel grid decks.

were self-temperature-compensating, hence the readings were free from temperature-induced strain. A three-wire lead system was used to eliminate the length effect of lead wires. A 330-DFV type of conductor cable (lead wire) was used.

STRAIN GAUGE POSITIONS AND PLACING OF SPECIMENS

Strain gauges were placed on the main bar steel (MB in figures and tables), on the cross bar steel (CB in figures and tables), and on the concrete, one in the main bar direction (MBD in figures and tables) and one in the cross bar direction (CBD in figures and tables) as shown in Figure 1. This strain gauge pattern was used at the center cells and at the end cells. Since the end cells were free to expand (no restraint from adjacent cells), the strain gauge readings were obviously greater in the end cells than in the center cells and did not represent the actual expansion or contraction values. Therefore, only the readings given by the strain gauges fixed in the center cells were used for the synthesis of experimental data. In the plain concrete slab specimens, strain gauges were fixed in the long and short directions at the center of the specimen. All the specimens of Series I and III were placed flat resting on rollers and supported on wooden blocks. The specimens of Series II were made to rest on their edges in the longer direction by placing them on two wooden blocks at the ends. The arrangement ensured minimum restraint to expansion and contraction in the specimens. Care was taken not to disturb the original position of the specimens until the required number of freeze-thaw cycles was completed.

The experimental procedure mainly involved the measurement of strains during the progress of each cycle. The strain readings were read at regular intervals. The cam, designed according to the required temperature range and duration of each cycle, provided the simulated field conditions. The thermocouple readings, indicating the temperature inside the deck specimens, were read at regular intervals. The temperature readings from the thermocouple and cam indicator were found to be nearly identical at any given time.

EXPERIMENTAL DATA

The experimental data in terms of strain readings were used to

1. Establish the residual strain buildup per cycle and cumulative residual strains in the plain concrete slabs in both long and short directions, main and cross bar steel, and concrete in the main and cross bar directions (for concrete-filled decks). The residual strain was calculated as an increase or decrease in the strain reading from the previous reading at a given time.

2. Compute the coefficients of thermal expansion and contraction in concrete in all the specimens. This was computed by taking the average increase or decrease in strains per degree increase or decrease in the temperature for a given range of temperature.

3. Compute the forces developed because of residual strains in steel and concrete for concrete-filled steel grid decks. The residual strain buildup over a number of cycles was computed.

Forces were then calculated using these residual strains by a simple stress-strain relationship. More details can be found elsewhere (1).

To determine tensile and compressive strengths of concrete, split tension and axial compression tests were conducted on concrete cylinders before and after freeze-thaw cycles. The data from these tests were used to determine the change in the strengths.

RESULTS

Figure 2 indicates the residual strain buildup in concrete and steel for Series I concrete-filled steel grid decks. The initial discrepancy in the strain readings as seen in Figure 2 can be attributed to the initial adjustment that the specimen undergoes for shrinking cracks when subjected to freeze-thaw cycles. Figure 2 indicates that the open steel grid deck is unaffected by the freeze-thaw cycles. However, it can be seen from Figure 2 that there is residual strain buildup in steel for concrete-filled steel grid decks. Figure 3 is a plot showing residual strains versus number of cycles for a Series II plain concrete deck. Figures 4 and 5 show the residual strain plots versus number of freeze-thaw cycles for two concrete-filled steel grid decks of Series II. Because the strain gauge malfunctioned on concrete in the main bar direction of the Series II decks and on cross bar and main bar steel in Series III decks, readings were not available beyond 32 and 105 cycles, respectively, as seen in Figures 4 and 6. From Figure 5, it can be seen that strains in the main bar have stabilized, whereas strains in the cross bar follow an increasing trend. Figures 6 through 8 show the residual strain plots versus number of freeze-thaw cycles for Series III plain concrete deck and two Series III concrete-filled steel grid deck specimens. The residual strain plots up to 105 cycles are due to dry cycles, and the residual strain plots from 106 cycles up to 155 cycles are due to wet cycles. A trend similar to that in Series II specimens can be seen in Series III specimens with regard to the residual strain buildup

in the main and cross bars. Figures 6 through 8 also indicate the effect of moisture on the residual strain buildup.

Tables 2 and 3 give the in-plane force calculations due to residual strain buildup in concrete and steel for concrete-filled steel grid decks of Series I, II, and III. The average coefficients of expansion and contraction for concrete in the concrete-filled steel grid decks and plain concrete deck of Series I and II are shown in Table 4. Similar results for plain concrete slabs of Series II and III are also shown in Table 4.

OBSERVATIONS AND DEDUCTIONS

The following salient features are brought out after synthesizing the experimental data and also from visual examination of the filled deck specimens that were tested in the Major Units Laboratory at West Virginia University:

● Microcracks were observed that were due to concrete shrinkage along the main bar as well as the cross bar directions of concrete-filled decks. The cracks were less severe along the cross bars because of the continuity of concrete beneath the cross bars.
● The initial strain buildup from thermal cycling was large up to a strain level required to overcome shrinkage strains in concrete-filled decks. This was referred to as "shrinkage compensation."
● The initial residual strain buildup in concrete due to thermal creep for 30 to 40 cycles was equivalent to 800 to 1,000 microstrains. This initial concrete strain buildup was attributed to the concrete shrinkage compensation (which was checked by monitoring plastic as well as drying shrinkage after actual pouring of concrete into the steel grid). The thermal strain buildup over the initial 800 to 1,000 microstrains caused by shrinkage strains was found to be 300 to 400 microstrains. Such a magnitude of buildup has also been observed by other researchers (2-4).
● Thermal strains in concrete and steel (cross bar) were found to be tensile and increasing with the number of freeze-thaw cycles.

FIGURE 2   Residual strains versus number of cycles: Series I, Specimens 1 and 2 (254 × 914 × 127 mm).
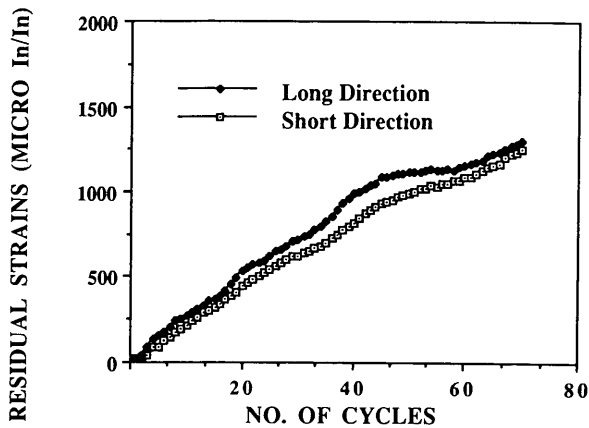
FIGURE 3 Residual strains versus number of cycles: Series II, Specimen 3 (305 × 914 × 108 mm).

• Main bar strains tend to stabilize after about 25 freeze-thaw cycles. The concrete and cross bar strains did not stabilize at the same number of cycles, but continued to increase. The earlier stabilization in the main bar was attributed by the authors to relatively higher stiffness and lower thermal creep in that direction.

• Residual strains in terms of their magnitude in steel and concrete were not same in the same direction (e.g., Figures 4 and 5). This difference led to strain incompatibility between steel and concrete in the filled grid deck and needs to be properly accounted for in the design.

• Concrete was found to be more susceptible than steel in terms of residual strain buildup because of its heterogeneity and anisotropy.

• In laboratory experiments, concrete-filled steel grid decks have been found to develop residual stresses under freeze-thaw cycles. However, such a buildup is not found in open steel grid decks (Figure 2).
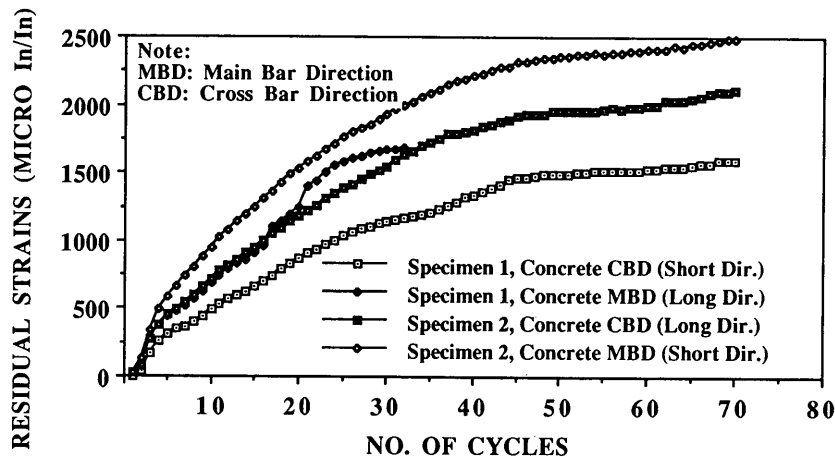
FIGURE 4 Residual strains versus number of cycles: Series II, Specimen 1 (305 × 914 × 108 mm) and Specimen 2 (406 × 1219 × 108 mm).
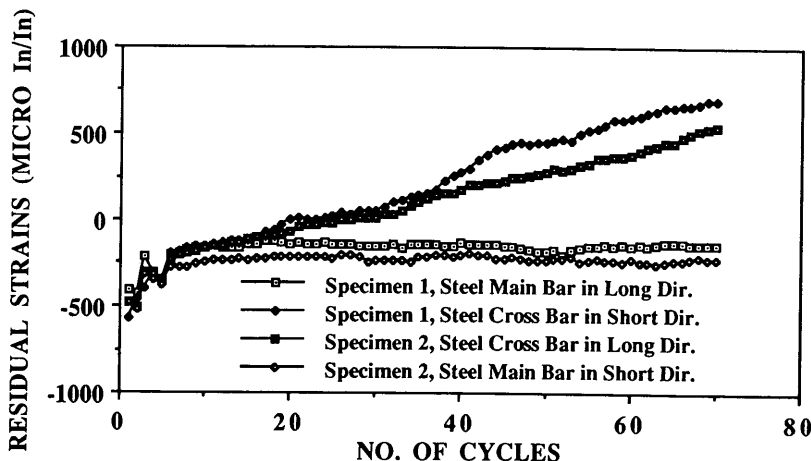
FIGURE 5 Residual strains versus number of cycles: Series II, Specimen 1 (305 × 914 × 108 mm) and Specimen 2 (406 × 1219 × 108 mm).
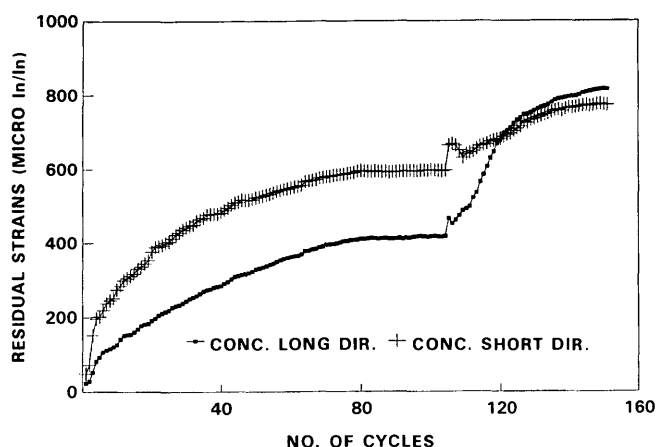
FIGURE 6 Residual strains versus number of cycles: Series III, Specimen 1 (305 × 914 × 108 mm) and Specimen 2 (610 × 610 × 108 mm).
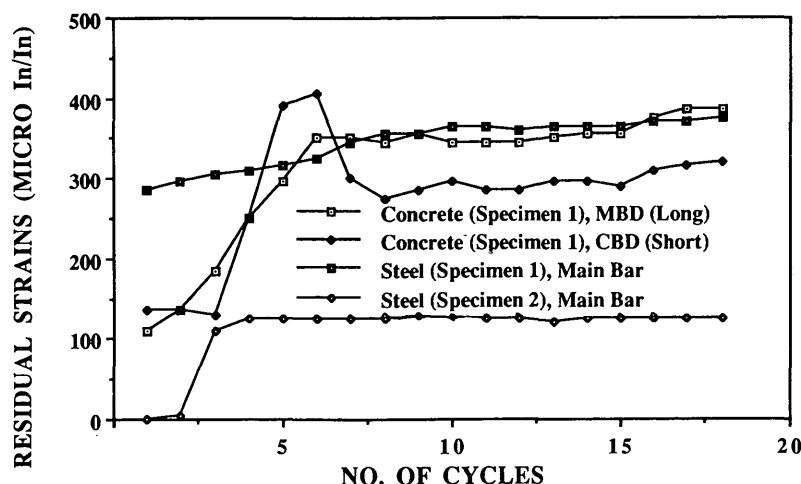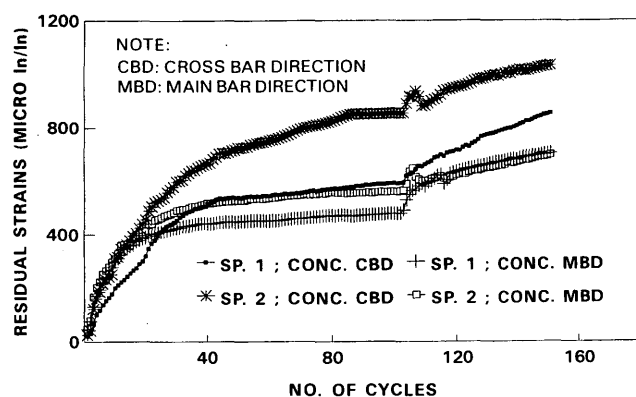

FIGURE 7 Residual strains versus number of cycles: Series III, Specimen 3 (305 × 914 × 108 mm).
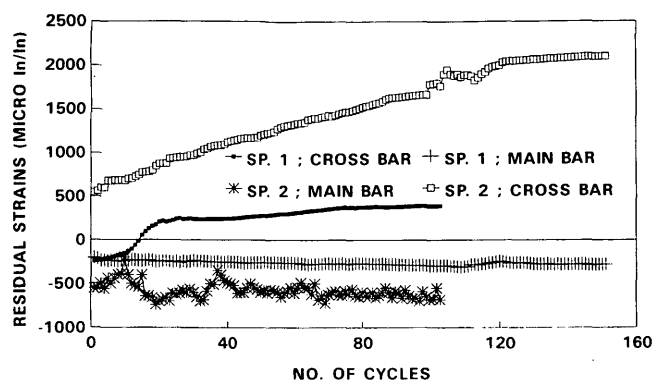
FIGURE 8 Residual strains versus number of cycles: Series III, Specimen 1 (305 × 914 × 108 mm) and Specimen 2 (610 × 610 × 108 mm).

● From Table 4, the coefficients of expansion and contraction of concrete in the filled deck specimens are 2.91×10^{-6} and 2.08×10^{-6} [Series II, Specimen 1, Gauge B, -17 to 2°C (0 to 35°F) temperature rise, and 2 to -17°C (35 to 0°F) temperature fall]. The expansion and contraction coefficients of concrete in the filled decks are lower than the values of the coefficients of expansion and contraction of concrete (3.95×10^{-6} and 3.47×10^{-6}, Series III, Specimen 3, Gauge B) in the plain concrete decks. Such low values in the filled decks have resulted from the presence of steel in filled decks.

● From Tables 2 and 3, the forces developed in concrete and steel due to residual strain buildup were found to be different, which revealed strain incompatibility.

● The tensile strength of concrete was reduced by the effect of freeze-thaw cycles. The maximum decrease in tensile strength was about 30 percent. A very small increase in the compressive strength was observed. Pigeon and Lachance (14) also reported a small increase in the compressive strengths of specimens that were subjected to freeze-thaw cycles.

TABLE 2 Force Due to Residual Strains in Steel Main Bar and Concrete (Main Bar Direction)

SERIES #	SPECIMEN #	RESIDUAL STRAINS (10-6)			FORCE (N)			TOTAL FORCE (N)	
		MB	PAN	CONC. (MBD)	MB	PAN	CONC. (MBD)	STEEL	CONC. (MBD)
I	1	30	-	40	6.6	-	21.4	6.6	21.4
II	1	78	78	46	15.3	3.0	19.7	18.3	19.7
	2	58	58	76	11.4	2.2	32.5	13.6	32.5
III	1	15	15	10	2.9	0.6	4.3	3.5	4.3
	2	34	34	22	6.7	1.4	9.4	8.1	9.4

Note: 1 lbf = 4.45 N; -: No bottom pan
The residual strains in the pan are assumed to be equal to the residual strains in the main bar

TABLE 3   Force Due to Residual Strains in Steel Cross Bar and Concrete (Cross Bar Direction)

SERIES #	SP. #	RESIDUAL STRAINS (10⁻⁶)				FORCE (N)				TOTAL FORCE (N)	
		CB	PAN	REBAR	CONC. (CBD)	CB	PAN	REBAR	CONC. (CBD)	STEEL	CONC. (CBD)
I	1	50	50	50	25	2.5	1.0	2.1	6.7	5.6	6.7
II	1	146	146	146	121	3.4	0.5	6.0	32.3	9.9	32.3
	2	165	165	165	197	3.9	3.2	6.8	42.1	13.1	42.1
III	1	68	68	68	40	1.6	1.3	2.8	8.5	5.7	8.5
	2	228	228	228	88	5.3	4.4	9.4	18.8	19.1	18.8

Note :   1 lbf = 4.45 N
The residual strains in the pan and the rebar are assumed to be equal to the residual strains in the cross bar

• The high strains observed in concrete are not unusual. There are reports (2) that the strains due to freezing in saturated cement paste specimens can be as high as 1,600 microstrains; on thawing to original temperature, about 500 microstrains of permanent elongation has been observed. However, this is encountered where moisture in the specimen is involved in the freeze-thaw cycles.

• From Figures 6 through 8, the residual strain buildup due to water can be noted. A sudden increase in residual strains with the addition of water is noted. Thus, the effect of moisture is severe on residual strain buildup.

CONCLUSIONS

On the basis of our limited experimental results and theoretical analysis, the preliminary conclusions follow.

The thermal coefficients of concrete varied for different temperature ranges. The thermal coefficients of expansion and contraction within the concrete itself were different. Residual tensile strain buildup was observed in concrete and cross bar steel of concrete-filled steel grid decks. However, a significant residual strain buildup was not noted in the main bar steel owing to its relatively higher stiffness. Residual ten-

TABLE 4   Coefficient of Expansion and Contraction as Determined on Concrete in Concrete-Filled Steel Grid Decks and Plain Concrete Decks

SERIES/ SPECIMEN #	INCREASING TEMP. RANGE	COEFF. OF EXPANSION (10⁻⁶)		DECREASING TEMP. RANGE	COEFF. OF CONTRACTION (10⁻⁶)	
		GAGE A	GAGE B		GAGE A	GAGE B
I - 1	-32 TO 21	2.10	1.91	21 TO -32	1.64	1.84
II - 1	-17 TO 2	1.99	2.91	2 TO -17	1.11	2.08
	2 TO 21	1.98	2.39	21 TO 2	1.47	2.74
II - 2	-17 TO 2	1.87	2.62	2 TO -17	1.67	2.12
	2 TO 21	2.18	2.94	21 TO 2	2.19	2.52
II - 3	-17 TO 2	5.10	4.54	2 TO -17	3.81	3.81
	2 TO 21	4.35	4.01	21 TO 2	3.13	2.98
III - 3	-17 TO 2	4.65	3.95	2 TO -17	3.14	3.47
	2 TO 21	4.08	3.73	21 TO 2	3.97	3.33

Note :   All temperatures in °C
$(°F - 32)/1.8 = °C$

sile strains in steel and concrete of a filled grid deck were different in the same direction, which revealed strain incompatibility. The behavior under thermal loads of concrete in combination with steel was different from the behavior of concrete alone in terms of the magnitudes of the expansion and contraction coefficients. Freeze-thaw cyclic effect led to decreased tensile strength of about 30 percent and very little increased compressive strength properties of concrete.

In the present work, the effects of different moisture conditions and humidity levels were considered in a limited manner. To establish proper understanding of freeze-thaw effects in concrete, extensive amounts of experimental data generation and interpretation must be accomplished from the viewpoint of microscopic material behavior. Emphasis was given to thermal expansion and contraction coefficients of concrete. However, other thermal properties such as thermal conductivity, thermal diffusivity, and specific heat, must be investigated. In the present work, there was no special control placed on the concrete mix parameters such as water-cement ratio, mix proportions, type of aggregates, curing techniques, and age. Hence, these must be accounted for in future research. Detailed investigations must be carried out to establish the effect of freeze-thaw cycles on concrete strength properties and strain incompatibility aspects between steel and concrete. Besides filled decking systems, other systems, such as reinforced concrete decks, should be investigated. Finally, the real challenge for future research is to develop concrete admixtures that can minimize, if not eliminate, the freeze-thaw effects on concrete while properly accounting for the behavior of admixtures in the concrete mix.

ACKNOWLEDGMENTS

REFERENCES

1. H. V. S. GangaRao, P. R. Raju, and H. K. Thippeswamy. *Concrete-Filled Steel Grid Decks: Thermal Studies on Plain Concrete and Filled Steel Grid Decks*, Vol. II. Final Report to the West Virginia Department of Highways; Constructed Facilities Center, West Virginia University, Morgantown, Dec. 1992.
2. P. K. Mehta. *Concrete Structure, Properties, and Materials*. Prentice-Hall, Inc., Englewood Cliffs, N.J., 1986.
3. M. Pigeon, J. Prevost, and J. Simard. Freeze-Thaw Durability Versus Freezing Rate. *ACI Journal*, Sept.–Oct. 1985, pp. 684–692.
4. E. K. Attiogbe, C. K. Nami, and F. T. Gay. Air Void System Parameters and Freeze-Thaw Durability of Concrete Containing Superplasticizers. *Concrete International*, July 1992, pp. 57–61.
5. C. Berwanger and A. F. Sarkar. Effect of Temperature and Age on Thermal Expansion and Modulus of Elasticity of Concrete. *ACI SP-39*, Oct. 1973, pp. 1–22.
6. A. J. Rhodes. Thermal Properties. In *ASTM STP-169B: Significance of Tests and Properties of Concrete and Concrete-Making Materials*, ASTM, Philadelphia, Pa., 1978.
7. E. G. Monfore and E. A. Lentz. Physical Properties of Concrete at Very Low Temperatures. *Journal of Portland Cement Association Research and Development Laboratories*, May 1962, pp. 33–39.
8. Growth Destroys a Bridge Deck. *Engineering News Record*, 1965, pp. 163–165.
9. T. H. Timmer. A Study of the Concrete Filled Steel Grid Bridge Decks in Ohio. *Proc., Bridge Maintenance and Rehabilitation Conference*, Morgantown, W. Va., Aug. 1980, pp. 423–475.
10. H. V. S. GangaRao. Performance Studies of Grid Decks for Office Floors. In *Proc., International Conference on Rehabilitation of Buildings and Bridges Including Investigations*, Washington, D.C., Oct. 1982, pp. 136–143.
11. A. J. Sturrett. Bridge Facts Challenged. *American City and County*, April 1977.
12. S. B. Yanev. Bridge Surface Performance. In *ASTM STP-1164: Vehicle, Tire, Pavement Interface*, ASTM, Philadelphia, Pa., 1992.
13. J. P. Callahan, C. P. Siess, and C. E. Kesler. *NCHRP Report 101: Effect of Stress on Freeze-Thaw Durability of Concrete Bridge Decks*. HRB, National Research Council, Washington, D.C., 1970.
14. M. Pigeon and M. Lachance. Critical Air Void Factors for Concrete Submitted to Slow Freeze-Thaw Cycles. *ACI Journal*, July–Aug. 1981, pp. 282–291.

Testing of Bridge Expansion Joints by Large-Scale Testing Apparatus

S. S. Kuo, Kirk Eastman, and D. Michael Waddell

A full-scale accelerated testing facility designed and constructed by the University of Central Florida was used to simultaneously test five separate bridge rehabilitation joint systems under the effects of wear, abrasion, and impact loading. During a 5-week test period, the program established a simulated life expectancy for each joint system as a result of its performance under full-scale live loading. This method of testing proved to be a timely, feasible alternative to live bridge applications and monitoring procedures. Test results indicated several areas of deficiency common to many of the joint components and systems. The results also promoted further development of some of these products to enhance their performance.

During the past several years engineers have become increasingly aware of the importance of bridge joints and joint materials in the design and maintenance of bridge structures. A bridge joint must provide to the various superstructure elements the same level of protection from exposure that would otherwise be provided by the deck, in addition to accommodating all movement transmitted by the superstructure to the joint. The joint materials must be durable enough to withstand the wear and impact of heavy traffic loads and must be resistant to roadway oils and chemicals, debris, ultraviolet rays, and other harmful influences. Yet the joint also must remain flexible and resilient throughout its life to accommodate numerous cycles of temperature extremes.

Histories and documentation indicate that most bridges have a life expectancy in excess of 50 years. However, most bridge joints experience problems within the first 5 to 10 years of life, and many joints experience some failure within the first 6 months to 1 year after installation. Failure of a joint system or individual component can occur in many ways and in varying degrees. For joint nosing materials and headers, failure can occur from a debonding of the nosing and substrate, a delamination of separate material layers, severe wearing or grooving of the material, cracking or spalling of the nosing, or a collapse of the material resulting from improper mixing and placement. Steel armor retainers can experience failure resulting from fatiguing of their anchorage systems under impact loading. Bridge joint seals can become debonded, ripped or torn, disfigured from excessive wear or deformation, or damaged by environmental influences.

Engineers and manufacturers continue to develop new joint configurations and materials in an attempt to improve upon this poor record of serviceability. However, testing methods are limited and most promising new joint products must be placed in live bridge installations to be tested. Although this method of testing is the most reliable and realistic, several years of monitoring may be required to prove a joint product acceptable. A literature search has not revealed any previous methods of full-scale testing or modeling to predict the life expectancy of expansion joints, yet full-scale accelerated testing can prove a timely and economical method of continuously monitoring the performance of bridge joints.

The Department of Civil and Environmental Engineering at the University of Central Florida (UCF) recently developed and constructed a facility for full-scale accelerated testing. The facility comprises a test track 15.2 m in diameter, a variable weight-loading apparatus, and a power source. The circular test track is a reinforced concrete slab 1.2 m wide by 38.1 cm thick supported on an earth embankment. Within the track are two 2-span bridge decks 3.7 m long by 1.8 m wide with a 20.8-cm reinforced concrete slab and transverse center joint. The loading system consists of three support beams 7.6 m long, W36 $\times$ 150 spoked from a center pivot at 120-degree intervals. Each support beam is attached to a hydraulically driven dual-wheel truck-axle assembly. A water tank 3.7 m in diameter by 2.4 m high is centrally mounted on top of the support beams and is used to generate additional weight to the loading system. The total weight of the loading apparatus and water can vary between 133 kN (30,000 lb) and 333.6 kN (75,000 lb), and is evenly distributed to the three dual-wheel assemblies. The entire loading device is powered by a 220-hp diesel engine with a hydraulic transmission and is capable of speeds up to 48 km/hr. A center support assembly, used to hold the entire system in place, is designed to restrain the testing apparatus from horizontal movement while allowing free rotation and vertical movement and a small amount of tilt. The support allows for a total load transfer to the dual-wheel assemblies and is hollow to accommodate the hydraulic transmission lines. Figure 1 shows the complete testing facility. The facility can accelerate the testing of bridge joint products under heavy wear and impact.

It should be noted that there are limitations to this method of testing. The test-track facility is not configured to examine the effects of ultraviolet radiation. Hence this form of testing cannot be included in test programs. Also, because of the scale of the test bridges and relatively short duration of testing for this program, the effects from thermal movement cannot be accurately measured. The 48-km/hr top speed of the loading apparatus is also considerably lower than the speed of actual traffic. To partially compensate for this fact, a heavier-than-normal wheel load is used.

In spring 1992, engineers from the Florida Department of Transportation (FDOT) District 5 and Howard Needles Tam-

S. S. Kuo and K. Eastman, Department of Civil and Environmental Engineering, University of Central Florida, Orlando 32816-0450; D. M. Waddell, Howard Needles Tammen & Bergendoff, 5900 Lake Elknor Drive, Suite 600, Orlando, Fla. 32809.
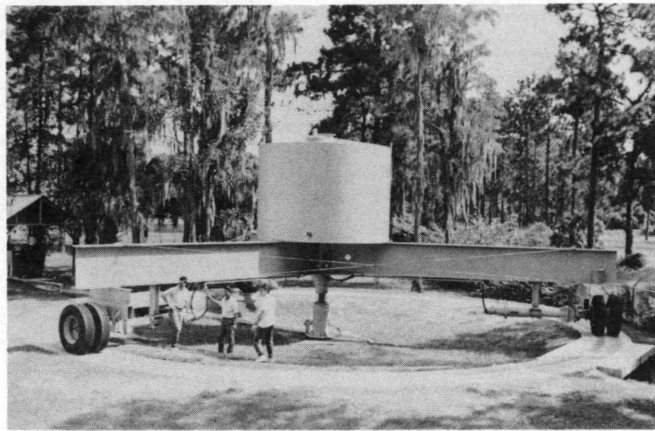
FIGURE 1 University of Central Florida test track.

men & Berdendoff (HNTB) needed to select replacement joints for several bridge joint locations along the heavily traveled corridor of Interstate 4 through Orlando, Florida. A product investigation revealed several new bridge joint products using current technology, but little in-place performance history to aid in selection. It was decided to set up a testing program at the UCF test track to establish a minimum 5-year simulated life expectancy of wear capabilities for various expansion joint types through accelerated testing procedures. Five separate manufacturers of bridge joints agreed to install one of their bridge joint products for testing. Each was asked to install a nominal 6.4-cm joint. Those bridge joint products will be identified here as bridge joints A through E.

LIFE EXPECTANCY SIMULATION ANALYSIS

The test program was developed to monitor continuously the performance of each expansion joint system placed on the large-scale test track under the application of repetitive dual-wheel loading. The sum of the repetitions successfully completed was used to equate the tested joint materials to a simulated life expectancy (SLE) of normal highway use. The SLE has been tailored to site-specific applications through the use of actual traffic volumes and joint opening requirements from the Interstate 4 project mentioned.

The first step of the simulation analysis was to determine the actual volume of yearly heavy truck traffic to equate to the tests. The I-4 joint rehabilitation project is to be constructed in 1993 with a joint life of 5 years determined as a minimum requirement. Therefore, a median year (1995) volume of average daily traffic (ADT) of 75,000 vehicles for three lanes of westbound travel was obtained from the 1989 I-4 Corridor Study for use in this project. The average proportion of trucks through this corridor was determined to be 6 percent, with a conservative assumption that half of these, or 3 percent, would be heavy trucks concentrated mainly in the center lane. Thus the annual volume of heavy truck traffic was determined using the following equation:

$$AHT = ADT \times \%HT \times MLF \times days/year$$

where

AHT = annual heavy truck traffic,
ADT = average daily traffic,
$\%HT$ = percent heavy trucks, and
MLF = multilane factor.

Hence, for this test program, the annual volume of heavy trucks was calculated as

$$75,000 \times 0.03 \times 0.9 \times 365 = 739,125$$

where 0.9 is the multilane loading reduction factor as set forth by AASHTO for three travel lanes in one direction.

For this project, a 66.7-kN wheel load was used for the accelerated testing. This wheel loading is considered to be much heavier than normal applied wheel loads. Therefore, it is necessary to convert this heavier wheel load to an equivalent standard wheel load. For the seven Florida legal load trucks used by FDOT, the maximum single-axle load present on a majority of the trucks is 98 kN. An equivalent wheel-load factor generally defines the damage per pass caused to a specific pavement system by the vehicle in question relative to the damage per pass of an arbitrarily selected standard vehicle moving on the same pavement system. One of the most widely used forms of load equivalency factors is that presented in the *AASHTO Guide for Design of Pavement Structures*. On the basis of AASHTO conversion tables from the 1986 manual, the differential equivalency factor between the 133.4-kN single-axle load used for testing and a standard 98-kN single-axle load is 5.51 for the concrete slabs 20.3 cm thick. The test track, unlike actual field conditions, applies the wheel loading over the same path for every repetition. An assumed probability-of-occurrence factor of 3 has been used for analysis purposes. In other words, every third wheel load is assumed to cover the same path along the bridge joint. The following equation was used to equate the test track results to a simulated life expectancy of one year:

$$N \times DEF \times POF = AHT$$

where

N = number of test track load repetitions per year,
DEF = differential equivalency factor,
POF = probability of occurrence factor, and
AHT = annual volume of heavy truck traffic.

Given DEF, POF, and AHT, solving for N provides a total of 44,715 repetitions required annually. A simulated life expectancy of 5 years thus would require a minimum of 223,600 repetitions of test-track loading for this project. In an effort to allow conservatively for any margin of error in the analysis procedures, a minimum of 250,000 repetitions was used for this testing program.

Although the simulated life expectancy can be equated to site-specific conditions for traffic volumes and joint opening requirements, it is restrictive because as a result of the scale of the testing apparatus and the short duration of the tests, it does not take into account aging or weathering considerations. These factors are not considered as important in the life of a bridge joint as the wear, impacts, and abrasion in-

cluded in this test program, but they can have a significant effect in certain climates. This test was performed in central Florida temperatures of $+27°C$, which, coupled with high temperatures generated from the testing apparatus, showed significant effects on certain products. Other factors, such as freeze-thaw and road salts, can have equally significant effects on some bridge joint materials in northern climates. This testing program could not feasibly test for all external factors affecting the life expectancy of a bridge joint; therefore it targeted the factors considered most important.

TESTING PROCEDURES

The entire program for testing expansion joints was carried out in 5 weeks, including down time for joint and tire repair, with the testing apparatus in operation 8 to 10 hr per day. Approximately 260,450 load repetitions with 66.7 kN of dual wheel load were applied. The program included testing for normal wear, abrasion, and impact. A constant operating speed of 24 km/hr was maintained throughout the testing program. The tire pressure on the radial 12R22.5 tubeless truck tires was maintained at 758 kPa. With this tire pressure, the footprint of the tire was measured at approximately 21.6 by 27.9 cm.

The normal wear test was conducted during the first week. The loading apparatus was run for approximately 25 hr clockwise and another 25 hr counterclockwise. A total of 73,124 repetitions was achieved during this phase of the test.

The second week included the abrasion test. Each joint was covered lightly with a mix of coarse sand, small aggregates, fragments of broken glass, and miscellaneous metal parts (small bolts, screws, etc). As in the previous test, this phase was divided into 25 hr of clockwise rotation followed by 25 hr of counterclockwise rotation. During the clockwise rotation phase, a small bolt punctured one of the tires on the apparatus. All bolts and screws were removed for the remainder of the test. A total of 70,664 repetitions was applied during this test.

The last phase of the project included 2 weeks of impact testing. The concrete bridge slabs were jacked up approximately 1 cm to create a difference in elevation between the expansion joint headers. Because of the geometry of the circular test track, certain joints with elevation differentials would be affected by clockwise rotation, whereas others would be affected by the counterclockwise direction (see Figure 2). The testing apparatus was run counterclockwise for 50 hr. It was intended to accumulate 50 hr of clockwise rotation as well; however, after 28 hr of rotation, one of the dual-wheel assemblies on the apparatus failed and the test was stopped. A total of 116,864 repetitions was achieved during this phase of testing. Although the testing ended prematurely, a total of over 260,000 repetitions was achieved. The numbers exceeded the original proposal of 250,000 repetitions.

BRIDGE JOINT CONFIGURATIONS

A graphic representation of each bridge joint system tested in this program is shown in Figures 3–7 in which the dashed line on each joint system represents the original joint profile.
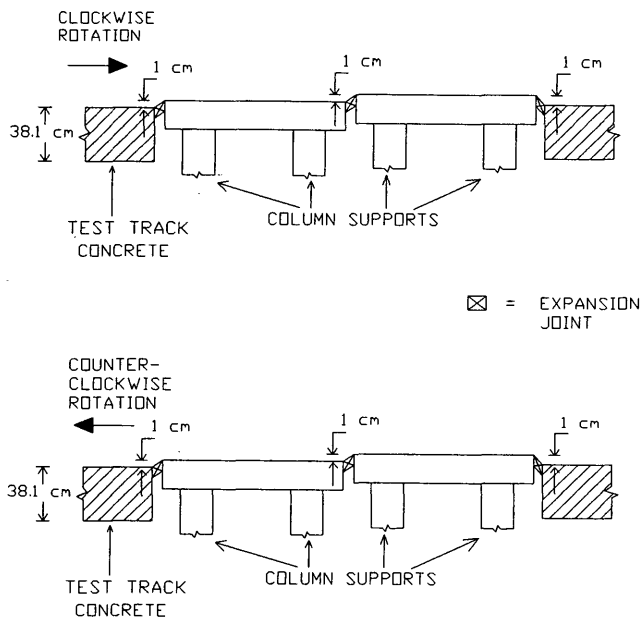
FIGURE 2 Impact test diagram.

The irregular profile under the dashed line shows the damage or wear from the test.

Bridge Joint A

The configuration of Bridge Joint A consisted of two steel armor angle retainers with a sinusoidal anchoring system of No. 4 rebar. Each steel angle retainer was anchored into a nosing of elastomeric concrete approximately 15.2 cm wide by 6.4 cm deep. A primer was used to enhance the bond between the nosing material and the concrete bridge slab, as well as between the nosing material and the steel angle. The square bridge seal, a dense foam material with longitudinal grooving on each vertical face, was bonded to the steel angle retainers with an epoxy. The foam seal allowed for elongation of approximately 20 percent, and the elastomeric concrete yielded an average compressed strength of 8867 kPa.

Bridge Joint B

Bridge Joint B consisted of two-cell neoprene bridge seal seated between a nosing of soft polymeric concrete approximately 7.6 cm wide by 2.5 cm deep on each side. The neoprene seal had small protruding fins running longitudinally down each side and was bonded to the polymeric concrete nosing with an epoxy adhesive. The seal was pressurized against the polymeric nosing until the adhesive curing was complete and allowed for an ultimate movement range of ± 50 percent. The polymer concrete was a pourable self-leveling material that required no primer and had an initial set time of approximately 1 hr.
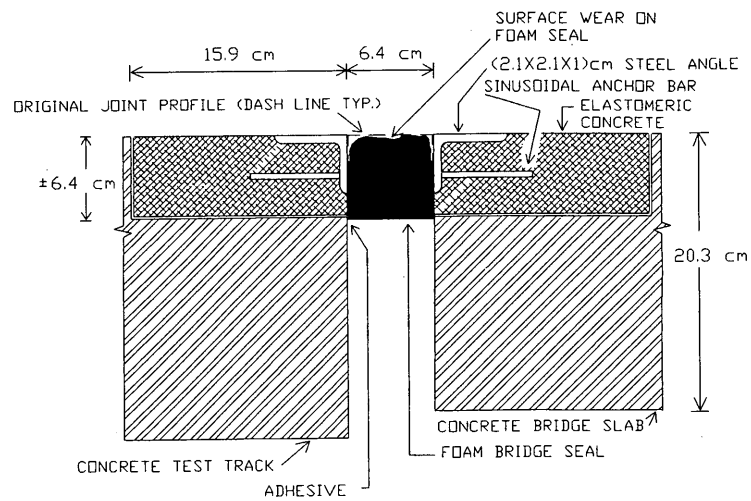
FIGURE 3   Bridge expansion joint system: Joint A.
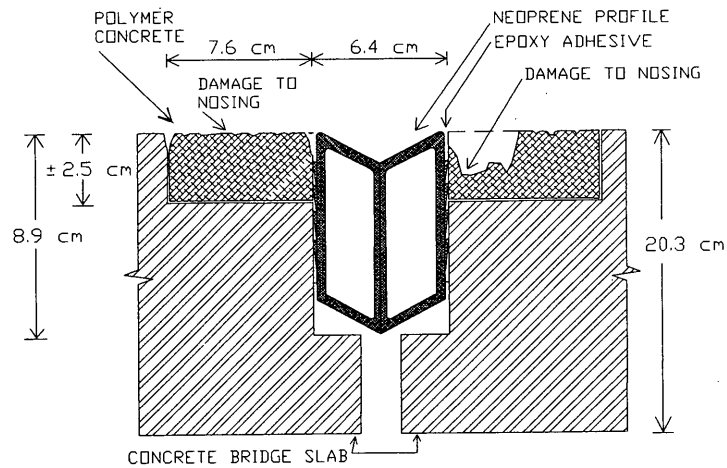
FIGURE 4   Bridge expansion joint system: Joint B.
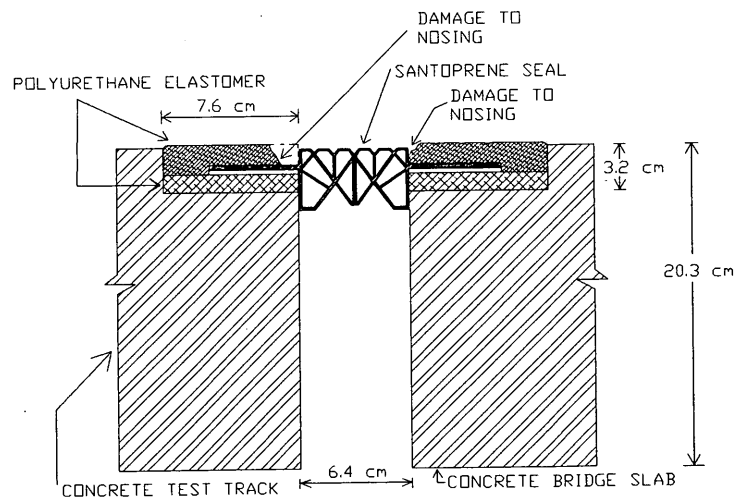
FIGURE 5   Bridge expansion joint system: Joint C.
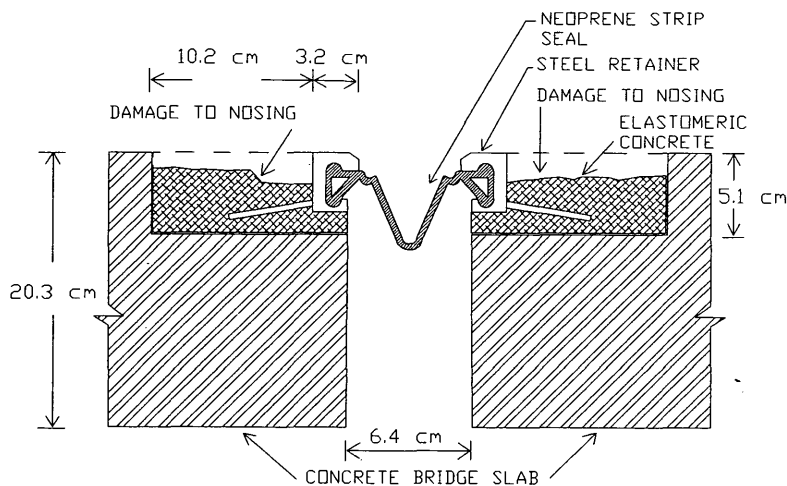
FIGURE 6   Bridge expansion joint system: Joint D.

Bridge Joint C

Bridge Joint C consisted of a winged, multicell Santoprene compression seal with the wings imbedded in a header of polyurethane elastomer concrete approximately 7.6 cm wide and 3.2 cm deep. An elastomer bond coat was used between the seal wings and the various layers of the elastomer concrete header. The Santoprene seal allowed for elongation in excess of 300 percent and the wings used slotted holes for additional bonding and load transfer. The elastomer concrete nosing had an initial cure of approximately 4 to 6 hr.

Bridge Joint D

Bridge Joint D consisted of two steel retainer bars anchored on each side with an angled bar 1 cm in diameter in a soft elastomeric concrete nosing, approximately 12.7 cm wide by 5.1 cm deep. A V-shaped neoprene strip seal was seated in the retainer bar and bonded with an epoxy. The strip seal

was designed to accommodate horizontal movement up to 10.2 cm. The elastomeric concrete nosing material took approximately 2 hr to cure and yielded a compressive strength of 15 169 kPa after 7 days.

Bridge Joint E

Bridge Joint E consisted of two elastomeric concrete nosings, each approximately 5.1 cm wide by 2.5 cm deep, separated by a compressed form-backer rod and a sealant of poured elastomer. A polymer conditioner was required for proper bond between the elastomeric concrete nosing and the concrete test track, as well as between the elastomeric concrete nosing and the poured elastomer seal. The seal, poured to a depth of approximately 0.6 cm over the center of the backer rod, required heat lamps for proper cure. The joint material required approximately 4 hr for initial cure. It was designed to accommodate an elongation of approximately 25 percent.
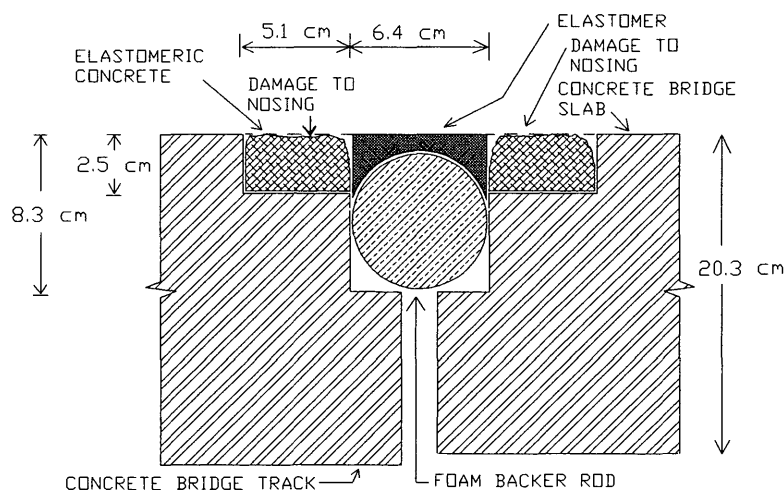
FIGURE 7   Bridge expansion joint system: Joint E.

TEST RESULTS

Bridge Joint A

After 600 repetitions of wear testing, the foam seal of this joint developed slight markings and collected small pieces of burnt rubber from the tires. After approximately 35,000 repetitions, the markings developed into slight scratches that continued to form throughout the normal wear test. Some slight separation between the foam seal and the armor angle occurred with depths of approximately 0.3 cm. At the conclusion of all testing, the foam seal exhibited some grooving and separation along the steel angle bond line to a depth of approximately 0.6 cm. The elastomeric concrete exhibited only slight signs of wear throughout the entire testing, exposing some small aggregate. The steel angle retainers exhibited no problems.

The joint performed satisfactorily throughout the test program. The minimum SLE for this joint is

$$\frac{260,450}{44,715} = 5.8 \text{ years}$$

Bridge Joint B

The polymer concrete nosing of Joint B showed signs of wear during the early stages of the normal wear test. The wear increased with the development of large, deep cracks and incipient spalling throughout the header material after approximately 44,000 repetitions of normal wear testing. The abrasion test brought spalling of the header material and separation of the bond between the polymer concrete and the concrete test track, with resulting gaps approximately 0.3 cm to 0.6 cm wide. Small gaps also appeared in the bond between the neoprene seal and polymer concrete nosing. During the impact testing large bits of polymer concrete broke off at the nosing. A liquid polyuria material was applied to the damaged areas of the polymer nosing in an attempt to repair the damage and reseal the bonds. The repair material seemed to perform fairly well throughout the remainder of the impact testing (approximately 90,000 repetitions). However, by the end of all testing, numerous cracks had developed in the repair material.

The SLE for this joint, as a result of early nosing failure, is

$$\frac{40,000}{44,715} = 0.9 \text{ years}$$

The SLE for the nosing material repaired with the polyuria patch is

$$\frac{90,000}{44,715} = 2.0 \text{ years}$$

Bridge Joint C

The elastomer concrete nosing displayed only slight wear during the normal wear test, with a slight collection of debris noted in the grooves of the seal. The abrasion test brought continued minimal wearing of the elastomeric nosing, with a small crack observed at the end of this phase (approximately 144,000 repetitions). The Santoprene seal collected a large amount of debris in the top grooves, but it did not appear to be damaged. The early portion of the impact testing revealed signs of spalling in the edge of the elastomeric nosing. A small piece (approximately 1.9 cm long) broke away at the seal-nosing bond line after approximately 243,000 repetitions. On further impact, larger chunks of the nosing material broke off; the largest of these was approximately 15.2 cm long. Other signs of incipient spalling also were noted on both sides of the joint. The Santoprene seal resulted in slight wear, with a 5.1-cm tear in the seal wing at the bond line between the wing and the seal body.

The initial signs of nosing material failure yield an SLE of

$$\frac{144,000}{44,715} = 3.2 \text{ years}$$

The occurrence of more severe deterioration of the nosing material and winged seal gives a cumulative SLE of

$$\frac{243,000}{44,715} = 5.4 \text{ years}$$

Bridge Joint D

The soft elastomeric concrete header material in Joint D exhibited moderate wear during early stages of the normal wear test. There was a 0.3-cm groove by the end of that testing, after approximately 74,000 repetitions. The nosing material continued to wear down during the abrasion test to a depth of approximately 1.3 cm below the riding surface. The elastomeric concrete material was repaired at the end of the abrasion test because of concern that the tires might be damaged on the sharp edge of the retainer bar. The impact testing resumed and the header material quickly spalled to its earlier state. It was then removed and replaced for the remainder of the testing (approximately 116,000 repetitions) with a more heat-resistant elastomeric concrete that appeared to hold up well. The retainer bar assembly and neoprene seal showed little or no sign of wear during the testing program.

The classification of extreme nosing material wear as an early stage of failure gives an SLE of

$$\frac{74,000}{44,715} = 1.7 \text{ years}$$

The new higher heat-resistant nosing material performed satisfactorily for the period that it was in place for testing, yielding a minimum SLE of

$$\frac{116,000}{44,715} = 2.6 \text{ years}$$

Bridge Joint E

After approximately 6,000 repetitions, Joint E failed in bond between the elastomeric concrete and the elastomer seal. It

was determined that the joint material was improperly installed and the joint was removed and replaced. The normal wear test proceeded with slight signs of wear and separation of the bond between the elastomeric concrete and the elastomer seal after approximately 112,000 repetitions. During the abrasion test, this bond separation continued to grow to approximately 0.3 cm in depth, and the elastomeric concrete nosing began to wear down. Signs of spalling appeared on the surface of the nosing material. During the impact test, a complete separation between the elastomeric concrete and the elastomer seal occurred in the areas of tire contact. Slight spalling and increased wear also were noted in the elastomer concrete nosing.

The SLE for this joint, as a result of early debonding and wear, is

$$\frac{112,000}{44,715} = 2.5 \text{ years}$$

CONCLUSIONS

Time and cost are major obstacles in the testing of new system technology for bridge joints under the effects of full-scale loading. To date, most full-scale testing has occurred only through the installation of new products on actual Interstate bridges. Although these applications certainly provide the most realistic results, monitoring programs can require years to gather enough load-cycle information to prove or disprove a joint product. In addition, routine inspection of the joint applications can be impractical or virtually impossible because of heavy traffic volumes. Costs for such tests can prove excessive because of material quantity and maintenance-of-traffic requirements, and can continue to increase if the products being tested fail prematurely and require replacement.

The full-scale accelerated testing apparatus in operation at the University of Central Florida has proven to be a timely, cost-effective means of testing bridge joint systems. The joint applications require placement of only a few linear feet of material and can be observed and inspected daily. The field observations of various component deficiencies experienced during this testing program are consistent with actual deficiencies and problems encountered in live applications. Specifically, live field applications of Bridge Joints B and C were inspected during the testing program. Both joint products were located on heavily traveled Interstate routes in central Florida with similar conditions to those in the test simulation. In each case, the bridge joints exhibited wear deficiencies identical to those experienced on the test track. Both Bridge Joint B applications—actual and test track—exhibited wearing and spalling of the nosing material and a debonding of the nosing material to the bridge seal. Both Bridge Joint C applications exhibited cracking and spalling of the nosing material over the seal wings under impact loading. In addition,

the simulated life durations calculated during this program are consistent with information collected from field observations and maintenance reports. It can be concluded that test results are relevant and representative of actual conditions.

Several consistencies in the various joint deficiencies also were observed. First, several of the joint applications revealed that the bond line between the seal and the nosing material is a weak link in the joint system. The bonding of soft, pliable materials to rigid epoxy bonding agents appears to be susceptible to the movements encountered under impact and cyclic loading. Second, the softer nosing materials appear to accommodate impact loading acceptably but are less resistant to excessive wear and abrasion than the harder materials. Conversely, although the harder materials are more wear resistant, they appear to be brittle and susceptible to spalling under impact loading. Steel armored headers obviously were the best component for resisting impact load if the anchorage systems were properly seated in the nosing material. Third, all nosing materials required precise mixture and placement techniques to ensure their intended performance. There seemed little room for error with any of these materials, as witnessed by the fact that Bridge Joint B debonding problems resulted from improper surface preparation and Bridge Joint E had to be removed and replaced early in the testing program because of improper placement.

Finally, it should be noted that the full-scale accelerated testing afforded the bridge joint manufacturers the opportunity to identify weaknesses in their products and to make improvements to their systems. As a result, the physical characteristics of Bridge Joint C have been modified and the chemical properties of Bridge Joint D nosing material were adjusted as discussed.

It can be concluded that full-scale accelerated testing for bridge joint systems is a timely, feasible method of obtaining realistic results. The determination of proper individual component characteristics to be included in a given bridge joint system must be based on site-specific criteria such as location, joint movement requirements, and characteristics of local traffic.

Recommendations for future testing include these observations: Temperature sensors should be installed on the bridge slabs to measure temperature variations during operation. Strain gauges may be placed on the joint nosing to measure strains or stresses. Measurement can be undertaken with a system of computerized data acquisition already at the UCF test track facility.

ACKNOWLEDGMENT

Publication of this paper sponsored by Committee on General Structures.

Rational Weather Model for Highway Structures

J. LEROY HULSEY AND DONALD T. POWELL

Empirical time-dependent equations for ambient air temperature, solar radiation, and wind speed are presented for summer and winter air temperature extremes at two sites for hourly solar radiation-surface meteorological observations (SOLMET): Columbia, Missouri, and Fairbanks, Alaska. The time-dependent equations, in recurrence periods from 1 to 100 years, give engineers a rational basis for selecting a climatic exposure for a desired design period. These time-dependent models may be incorporated into finite element or finite difference heat-flow programs to calculate temperature variations through members of highway structures. Examples demonstrate how a weather exposure may be selected at a geographic location. Mean recurrence of bridge · temperature is presented for composite, box girder and T-beam bridges. The Fairbanks, Alaska, models of weather exposure were used previously to study thermal stresses and movements for a 50-year design event in a jointless composite-girder bridge located in the Arctic.

Ambient air temperature, solar radiation, cloud cover, wind, and precipitation are predominant atmospheric components of weather that cause heat flow in highway structures (1-6). These atmospheric phenomena cause temperatures in outdoor structures to vary nonlinearly with time; temperature changes induce thermal movements and stresses. The magnitude of thermal movements and thermal stresses are affected by temperature profiles, superstructure geometry, material properties, and restraints imposed by connections and substructure stiffness.

The design of structures that are safe and maintenance-free may require two types of weather models to account for thermal effects: one to account for weather extremes with a return period and the other to characterize daily chaos over time so that material damage accumulation may be examined. The importance of these complex time-dependent weather-structure interaction phenomena in relation to other loads is not well understood (7-10).

Because of the complex nature of an environmental exposure, there has been some reluctance to determine recurrence for thermal loading. In 1984, Church and Clark (7) presented probable combinations of highway and temperature difference loads. Recurrences in temperature differences were based on a guess of observed bridge gradients by Emerson (11) for the British Isles and later modified. Potgieter and Gamble (4) studied prestressed bridges for extremes at 26 climatic sites established by the National Oceanic and Atmospheric Administration for hourly solar radiation-surface meteorological observations (SOLMET). Later Kuppa and

Roeder (6) used 11 climatic SOLMET data sites to study extremes in thermal movements for three bridge types. Neither study compared exposures to a return period. Hulsey (2) and later Hulsey and Powell (5) showed that recurrence periods may be determined for annual temperature extremes. In 1989, Ho (10) suggested a random technique for 50-year extremes of thermal highway loading on highway bridges in which attention was given to a statistical approach.

A weather model is presented in this paper to provide a mechanism for assessing environmental factors on response and performance of highway structures. The model approximates maximum summer or minimum winter air temperature days with return periods of 1 to 100 years at two sites: a cold climate in Fairbanks, Alaska, and a hot climate near Columbia, Missouri. Daily maximums, averages, and minimums also are presented for air temperature and solar radiation at each site. This type of model may be used to compare structural temperature profiles from different climates. No attempt is made to include precipitation, wind fluctuations, or spring and fall conditions or to characterize diurnal irregularities. These considerations are under study and will be presented later.

BACKGROUND

Bridge engineers use two design approaches to account for thermal effects: expansion devices and jointless decks. The conventional design approach assumes that bridge deck expansion devices and expansion bearings allow bridges to expand or contract without restraint. Yet it is common to find improperly tilted and frozen bearings, inoperative expansion devices, and distressed appurtenances; these examples show that free movement does not exist (12). Some states design bridges with jointless decks supported by bearings or flexible bents, or both (6,12-14). In either case, Emanuel and Taylor (15) showed that bridge length does not influence stress inducement.

The methodology for calculating movements and stresses involves three steps: (a) characterizing climatic exposure; (b) determining structural temperatures with respect to construction conditions; and (c) using the internal strains caused by temperature to calculate deformations and strains and stresses (2,4,9,14,16-19).

Most research to date has focused on Step b, identifying temperature profiles for different bridges of various exposures, or Steps b and c, assessing stresses and movements for different bridge types. Bridge temperatures in the literature

J. L. Hulsey, Department of Civil Engineering, University of Alaska Fairbanks 99775. D. T. Powell, Boeing Commercial Airplane Group, P.O. Box 3707, Seattle, Wash. 98214.

are usually based on field-measured structure temperatures (*16,17,20–22*), calculations using exposures measured for a limited time (*19*), or laboratory studies (*15,18,23–25*). Some studies have used climatic data to approximate extremes (*2–6,14*). Others have approximated temperature profiles with polynomials (*8,9,21,26*), but no provisions were made for differences in climate or return periods.

In summary, weather-induced thermal stresses can be large and should be considered in design, little understanding exists of the interaction between weather and induced movements and stresses, and AASHTO gives limited guidelines to account for movements, with no guidelines for thermal stresses and no provision for regional climates and design periods. Prediction of induced thermal stresses and movements necessitates a rational method for determining both extreme weather conditions affecting structures in a given geographic region and anticipating climatic conditions over the life of the facility.

SITE CLIMATIC DATA

Tapes were examined of hourly surface observations for Fairbanks, Alaska (1952–1976) and Columbia, Missouri (1946–1965), combined with annual summaries to 1987 (*27*). Fairbanks is at a latitude of N64°49′ and Columbia is N38°45′.

Irregularities aside, weather follows two trends: annual and diurnal. Annual trends account for seasonal change from winter to summer and diurnal trends account for warming during the day and cooling at night. Daily trends may be altered by clouds, precipitation, and circulating cool or warm air masses to the region (*2,3*).

Annual Trends and Extreme Events

Heat transfer occurs through a highway structure by conduction, convection, solar radiation, and thermal long-wave radiation. Climatic boundary conditions such as air temperatures influence both long-wave radiation and convection, wind contributes to convective cooling, and solar flux provides heat to pavements and bridge decks (Figure 1). Precipitation can modify these influences. If contributions of precipitation and variations in wind velocity are ignored, daily accumulated heat transfer energy on the boundaries is a function of ambient air temperature (T_d), solar radiation (Q_d), wind (v), for day (d), or

$$q(t) = f[T_d(t); Q_d(t); v; \ldots] \qquad t = d \text{ (annual)} \qquad (1)$$

Empirical annual expressions for each of the contributions of Equation 1 were determined for Fairbanks, Alaska, and Columbia, Missouri, and are presented herein for consideration.

Ambient Air Temperature

It is valid to assume that annual trends in ambient air temperature will follow a periodic cycle (2) of the form

$$T_d = A_d \sin\left[\frac{2\pi(d - \gamma)}{365}\right] + B_d \qquad 0 \le d \le 365 \qquad (2)$$

where

T_d = daily temperature,

A_d = annual temperature fluctuation about yearly average,

a) Environmental Exposure, Pavements and Bridges

b) Two-Dimensional Heat Flow
(Pavement Structure)

c) Two-Dimensional Heat Flow
(Bridge Structure)
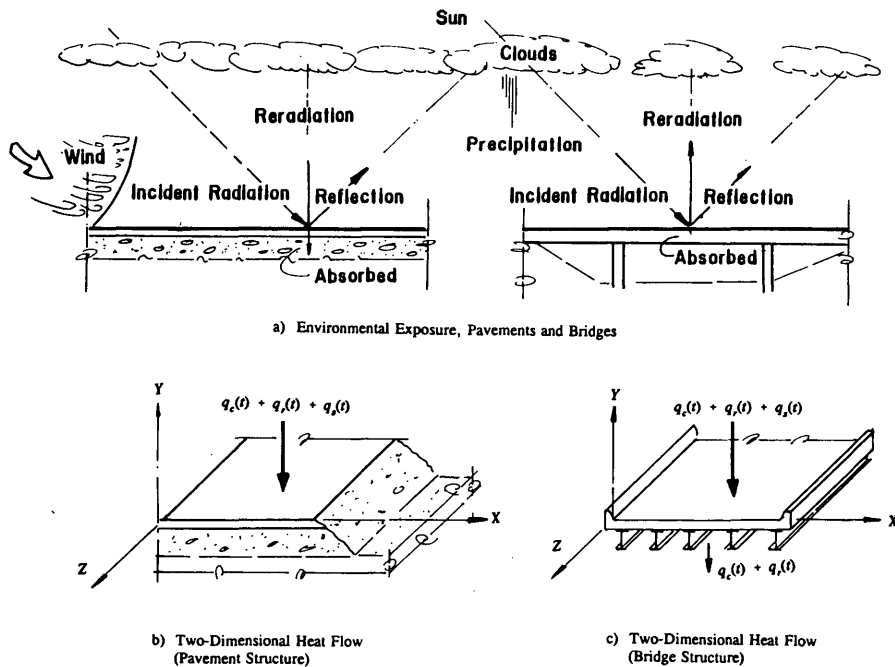
FIGURE 1 Pavements and bridges subjected to climatic conditions.

B_d = average yearly temperature,
γ = lag in days, and
d = day of the year.

Figure 2 presents record maximum, minimum, and average daily ambient air temperatures for the 25-year period 1952–1976 at Fairbanks, Alaska, and Figure 3 represents the 20-year period 1946–1965 at Columbia, Missouri. Applying the Equation 2 curve fit using a regression analysis (28) for record maximum, minimum, and average daily ambient temperatures resulted in curves A, C, and B, respectively. Curves D and E are high and low temperatures valid for concrete placement. Table 1 provides Equation 2 coefficients for T_{min}, T_{avg}, and T_{max} without regard for recurrence.

Although both ambient air temperature and solar radiation influence bridge temperature profiles significantly, air temperature has a dominant effect (2,16,17). For present purposes, the weather model corresponds to ambient air temperature extremes.

Hourly tape temperature data and annual summaries identify yearly record minimum and maximum temperatures for the period 1930 to 1987 for Fairbanks, Alaska, and the period 1921 to 1987 for Columbia, Missouri. These annual maximum and minimum temperatures were separated into data sets and ranked in ascending order for each site. An estimate of recurrence is given elsewhere (29) as

$$t_p = \frac{N + 1}{m} \tag{3}$$

where

t_p = recurrence in years,
m = rank, and
N = number of years in data set.

The probability P that an annual temperature will be equaled or exceeded in a given year is

$$t_p = \frac{1}{P} \tag{4}$$

In 1941, Gumbel (29) reported that recurrence may be estimated statistically if probability is expressed in the form

$$P = 1 - e^{-e^{-b}} \tag{5}$$

where P is the probability of occurrence that an event will be equal to or greater than an extreme event, and e is the base of Napierian logarithms. For this study, b is given by

$$b = \frac{1}{0.7797\sigma} (T - \overline{T} + 0.45\sigma) \tag{6}$$

in which T is a temperature extreme with a probability P, $\overline{T}$ is the arithmetic average of annual temperature extremes in the data set, and σ is the standard deviation computed from

$$\sigma = \left[\frac{\Sigma (T - \overline{T})^2}{N - 1} \right]^{1/2} \tag{7}$$
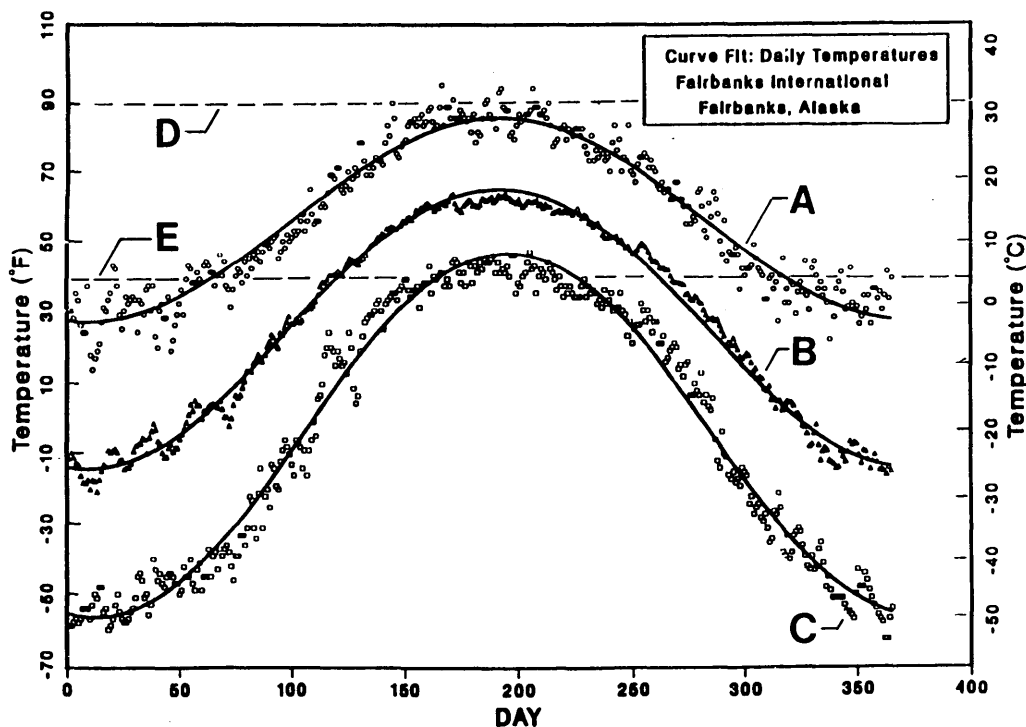
FIGURE 2   Curve fits for observed daily air temperature for the 25-year period 1952–1976, Fairbanks.
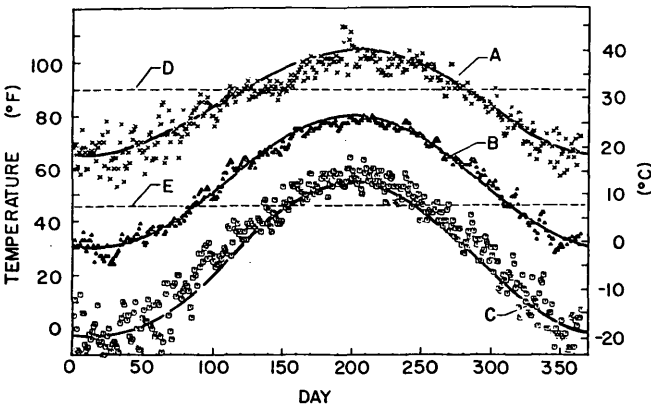
FIGURE 3 Curve fits for observed daily air temperature for the 20-year period 1946–1965, Columbia.

Return periods for yearly maximums and minimums of air temperature are shown in Figures 4 and 5, respectively, for the two sites. Assuming that the annual variation (A_d) and day lag (γ) of Table 1 are valid for maximum and minimum temperature return periods, B_d will vary with recurrence (Table 2). A ratio (ξ_y) is used to measure air temperature at some return period to the 100-year event. Each summer, maximum air temperatures are expected to reach ~82 percent of the 100-year event in Fairbanks and about 79 percent of a 100-year event in Columbia. The 100-year event in Fairbanks is 36.67°C (98°F) and in Columbia, 45.56°C (114°F). Each winter, minimum air temperatures are 43.8 percent of the 100-year event in Fairbanks and −36.3 percent in Columbia. The 100-year event in Fairbanks is −58.3°C (−73°F) and in Columbia, −32.78°C (−27°F).

Record temperatures between 1952 and 1976 for Fairbanks were 34.4°C (94°F), a 30-year event, and −52.2°C (−62°F),

TABLE 1 Ambient Air Temperature, Annual Trends

Site: Annual Temperatures	A_d °F	A_d °C	B_d °F	B_d °C	γ (days)	High Temperatures, T_{max} °F	°C	days	recur(yrs)	Low Temperatures, T_{min} °F	°C	days	recur(yrs)
Fairbanks, Alaska:													
Maximum, $T_{d\,(max)}$	29	16.1	56	13.3	100	85	29.4	191-192	1.5	27	-2.8	8-9	--
Average, $T_{d\,(avg)}$	39	21.7	26	-3.3	100	65	18.3	191-192	--	-13	-25.0	8-9	--
Minimum, $T_{d\,(min)}$	51	28.3	-4.5	-20.3	104	46.5	8.0	195-196	--	-55.5	-48.6	12-13	5
Columbia, Missouri:													
Maximum, $T_{d\,(max)}$	20	11.1	85	29.4	110	105	40.6	201-202	10	65	18.3	18-19	--
Average, $T_{d\,(avg)}$	25	13.9	55	12.8	110	80	26.7	201-202	--	30	-1.1	18-19	--
Minimum, $T_{d\,(min)}$	30	16.7	25	-3.9	110	55	12.8	201-202	--	-5	-20.6	18-19	2

FIGURE 4 Recurrence for maximum daily air temperatures.

FIGURE 5 Recurrence for minimum daily air temperatures.

TABLE 2 Recurrence Coefficients for Ambient Air Temperature Extremes

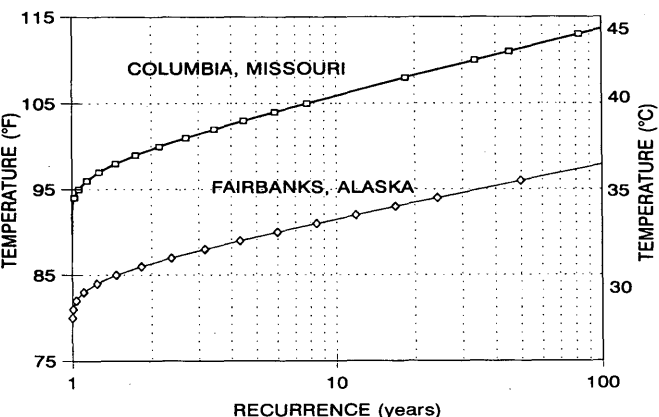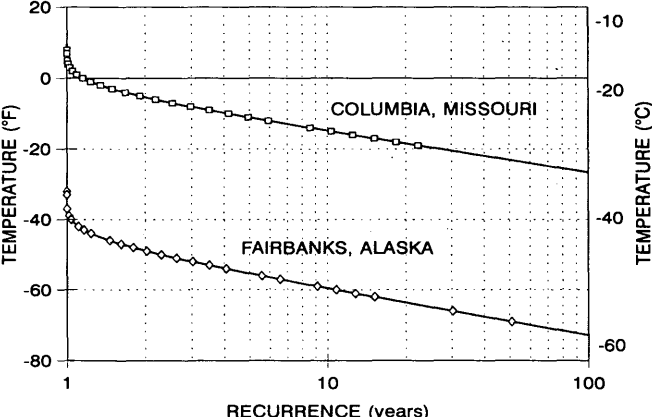| Recurrence Period (Years)	Maximum Temperature, Hot Days							Minimum Temperatures, Cold Days						
	Daily Maximums					Diurnal Variations		Daily Minimums					Diurnal Variations	
	T_{max} °C (°F)	ξ_y	A_d (°F)	B_d (°F)	γ (day)	A_h (°F)	ψ (hour)	T_{min} °C (°F)	ξ_y	A_d (°F)	B_d (°F)	γ (day)	A_h (°F)	ψ (hour)
Fairbanks:														
1	26.7(80)	0.816	29	51	100	15	12	-35.3(-32)	0.438	51	19	104	5	-6
2	30.0(86)	0.878	29	57	100	15	12	-45.0(-49)	0.671	51	-1	104	5	-6
5	31.7(89)	0.908	29	60	100	15	12	-48.3(-55)	0.753	51	-4	104	5	-6
10	32.8(91)	0.928	29	62	100	15	12	-51.1(-60)	0.822	51	-9	104	5	-6
20	33.9(93)	0.949	29	64	100	15	12	-53.3(-64)	0.877	51	-13	104	5	-6
50	35.6(96)	0.980	29	67	100	15	12	-56.1(-69)	0.945	51	-18	104	5	-6
100	36.7(98)	1.000	29	69	100	15	12	-58.3(-73)	1.000	51	-22	104	5	-6
Columbia:														
1	32.2(90)	0.790	20	70	110	15	9	-12.2(10)	-0.363	30	40	110	11	9
2	37.8(100)	0.877	20	79	110	15	9	-20.6(-5)	0.201	30	25	110	11	9
5	39.4(103)	0.910	20	83	110	15	9	-23.9(-11)	0.415	30	19	110	11	9
10	41.1(106)	0.932	20	86	110	15	9	-26.1(-15)	0.557	30	15	110	11	9
20	42.2(108)	0.953	20	88	110	15	9	-27.8(-18)	0.692	30	12	110	11	9
50	43.9(111)	0.980	20	91	110	15	9	-30.6(-23)	0.868	30	7	110	11	9
100	45.6(114)	1.000	20	94	110	15	9	-32.8(-27)	1.000	30	3	110	11	9

Note: $\phi = -1$ for maximum; $\xi_y = \dfrac{T_{(d-yr)}}{T_{(d-100yrs)}}$ Note: $\phi = 1$ for minimum conditions; $\xi_y = \dfrac{T_{(d-yr)}}{T_{(d-100yrs)}}$

a 15-year event. In Columbia, record temperatures were 45°C (113°F), an 80-year event, and −28.3°C (−19°F), a 22-year event.

Solar Radiation

The maximum, average, and minimum daily solar radiation (direct and diffuse) incident on a horizontal surface was examined at each site. In addition, daily solar radiation corresponding to maximum and minimum air temperature days was evaluated. Variations in solar radiation from year to year on a given day indicate fluctuations in factors such as industrial pollution, air turbidity, ozone, and cloud cover. A regression analysis (30) in the form of a general Fourier series expansion was selected to fit daily solar; the fit is of the form

$$Q_d = a_0 + \sum_{n=1}^{N} a_n \sin (n\lambda) + \sum_{n=1}^{N} b_n \cos (n\lambda)$$

$$\lambda = 2\pi \frac{(d - \Omega)}{365} \qquad (8)$$

where

Q_d = amount of daily solar radiation incident upon a horizontal surface;
a_0 = average daily solar radiation;
a_n and b_n = the amplitudes of the series;
Ω = lag in days; and
d = day of the year.

Satisfactory convergence was attained with two terms ($N = 2$) for Fairbanks and one term ($N = 1$, $b_1 = 0$) for Columbia. Figures 6 and 7 and Equation 8 coefficients of Table 3 show Fourier series fit for maximum, minimum, and average daily trends in solar radiation throughout the year for Fairbanks and Columbia, respectively. Solar radiation corresponding to maximum $(Q_{d-max})_{yr}$ and minimum $(Q_{d-min})_{yr}$ temperature days is assumed appropriate for recurrences (Table 3).

Wind

In Fairbanks from 1952 to 1976, the dominant range of maximum wind speed varied between 0 and 8.9 m/sec (0 and 20 mph) with a daily average maximum of 2.2 m/sec (5 mph). Wind speeds corresponding to maximum and minimum temperature days were predominately less than 2.2 m/sec (5 mph). In Columbia the average wind speed was 4.0 m/sec (8.9 mph) and 4.7 m/sec (10.6 mph) for maximum and minimum temperature days, respectively.

Diurnal Trends and Extremes

For simplicity, wind speed was generally low and therefore considered constant. Precipitation was not included. Therefore, heat transfer energy at any time t during the day is assumed to be a function of ambient air temperature, $[T_h(t)]$, solar radiation $[I_h(t)]$, wind $[v(t)]$, and other factors expressed by

$$q(t) = f[T_h(t); I_h(t); v \ldots] \qquad t = \text{(diurnal)} \qquad (9)$$

The trends show that summer extreme temperatures occur on days 191 and 192 in Fairbanks, Alaska, and days 201 and 202 in Columbia, Missouri. Similarly, winter extremes occur on days 12 to 14 and 8 and 9 for Fairbanks and Columbia, respectively. Diurnal equations for ambient air temperature,
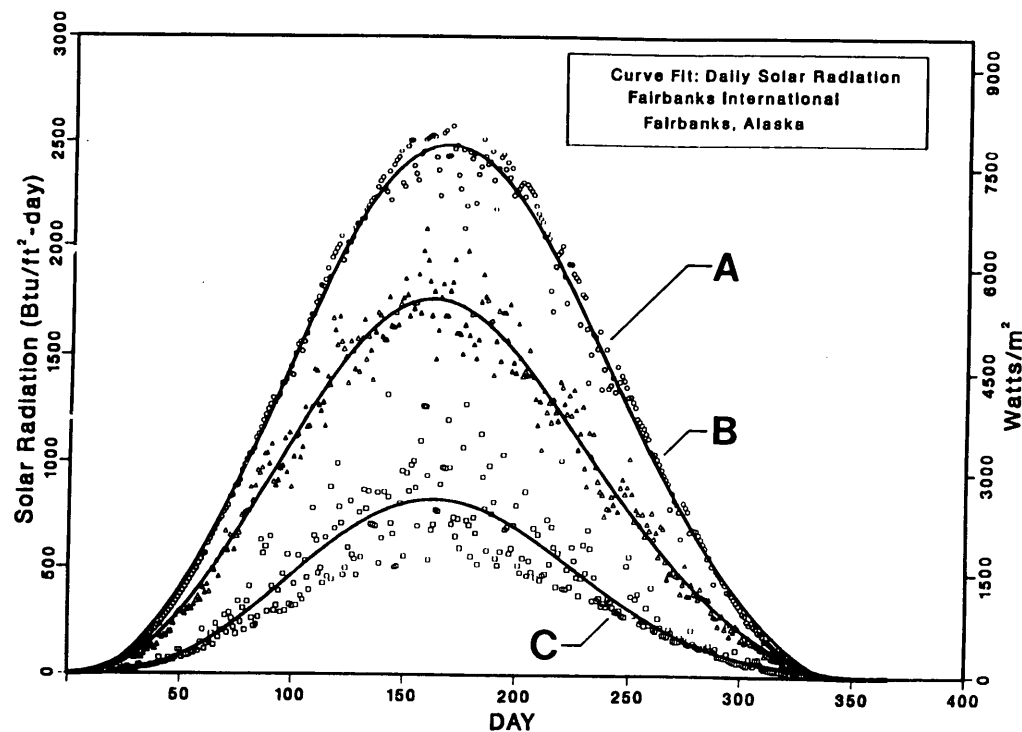
FIGURE 6 Curve fit of daily accumulated solar radiation incident on a horizontal surface, Fairbanks.

corresponding solar radiation, and wind speed for these summer and winter temperature days are presented here.

Air Temperature

Trends in diurnal ambient air temperature are of the form (2,5)

$$T_h(t) = A_h \sin 2\pi \frac{(h - \Psi)}{24}$$

$$+ A_d \sin \frac{2\pi(d - \gamma + h/24)}{365} + B_h$$

$$B_h = B_d + \phi A_h \qquad (10)$$

FIGURE 7 Curve fit of daily accumulated solar radiation incident on a horizontal surface, Columbia.

where

T_h = air temperature,
h = hours,
Ψ = hourly lag,
A_h = half the daily temperature range,
B_h = average of daily temperature, and
ϕ = -1 for summer (maximum), 0 for average, and 1 for winter (minimum).

The daily range in temperatures observed at each site is shown in Figure 8. In Fairbanks, ~75 percent of the days had temperature ranges between 5.56°C (10°F) and 13.89°C (25°F). About 82 percent of the days in Columbia had temperature ranges between 8.33°C (15°F) and 16.67°C (30°F). A random sample of the temperature extremes was used to obtain the daily ranges for the summer and winter recurrence equations (Table 2).

Solar Radiation

The intensity of solar radiation received on a horizontal surface at any time t measured from sunrise may be expressed as (2,3,31)

$$I_h(t) = 0 \qquad (h_{sr} > h > h_{ss}) \qquad (11a)$$

$$I_h(t) = \frac{2Q_d}{d_h} \sin^2 \frac{\pi(h - h_{sr})}{d_h} \qquad (h_{sr} \le h \le h_{ss}) \qquad (11b)$$

where

Q_d = daily integral of solar radiation given of Equation 8,

TABLE 3 Coefficient for Daily Solar Radiation

Site: Conditions	Coefficients, W-h/m^2 (Btu/ft^2)					Ω (days)	Valid Range (days)
	a_0	a_1	b_1	b_1	b_2		
Fairbanks, Alaska:							
Maximum, $Q_{d\,(max)}$	3482 (1105)	3976 (1262)	142 (45)	63 (20)	-353 (-112)	80	$13 \le d \le 338$
Average, $Q_{d\,(avg)}$	2395 (760)	2782 (883)	214 (68)	246 (78)	-290 (-92)	80	$14 \le d \le 9$
Minimum, $Q_{d\,(min)}$	1040 (330)	1273 (440)	110 (35)	94 (30)	-253 (-74)	80	$18 \le d \le 353$
Max temp days, $(Q_{d\text{-}max})_{yr}$	2962 (940)	3845 (1157)	123 (39)	-9 (-3)	-627 (-199)	80	$19 \le d \le 344$
Min temp days, $(Q_{d\text{-}min})_{yr}$	2675 (849)	2899 (920)	79 (25)	139 (44)	-38 (-12)	80	$11 \le d \le 332$
Columbia, Missouri:							
Maximum, $Q_{d\,(max)}$	6648 (2110)	3056 (970)	0	0	0	82	$0 \le d \le 365$
Average, $Q_{d\,(avg)}$	4439 (1409)	2442 (775)	0	0	0	82	$0 \le d \le 365$
Minimum, $Q_{d\,(min)}$	1207 (383)	1084 (344)	0	0	0	99	$0 \le d \le 365$
Max temp days, $(Q_{d\text{-}max})_{yr}$	5155 (1636)	2978 (945)	0	0	0	82	$0 \le d \le 365$
Min temp days, $(Q_{d\text{-}min})_{yr}$	5318 (1688)	2580 (819)	0	0	0	82	$0 \le d \le 365$

h_{sr} and h_{ss} = hour at sunrise and sunset,
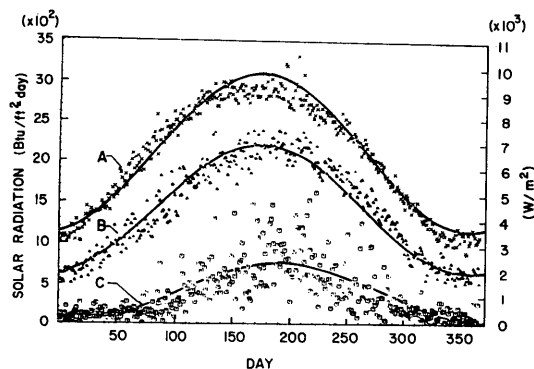d_h = length of day (sunrise to sunset),
h = hour measured from sunrise, and
t = time in hours measured from midnight.

The length of day may be approximated by (*32*)

$$d_h = \frac{2}{15} \text{ arc cos} \,[-\tan\phi \, \tan\delta] \tag{12}$$

where ϕ is the geographic latitude in degrees (north positive). The declination of the sun, δ, may be approximated (*33*) by

$$\delta = (0.006918 - 0.399912 \cos\Gamma$$

$$+ \; 0.070257 \sin\Gamma - 0.006758 \cos2\Gamma$$

$$+ \; 0.000907 \sin2\Gamma - 0.002697 \cos3\Gamma$$

$$+ \; 0.00148 \sin3\Gamma) \left(\frac{180}{\pi}\right)$$

$$\Gamma = \frac{2\pi(d - 1)}{365} \tag{13}$$
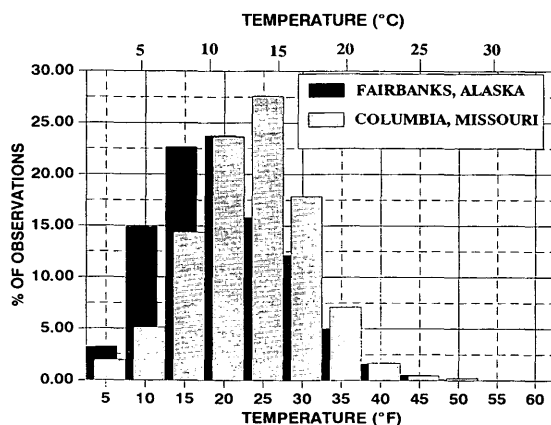
FIGURE 8 Histogram of temperature differentials, Fairbanks and Columbia.

where Γ is day angle and d is day of the year. The latitude, ϕ, is N64°49' in Fairbanks and N38°45' in Columbia. Estimations for the declination of the sun and day length at Fairbanks International Airport compared well with ephemeris values.

STRUCTURAL TEMPERATURE CALCULATIONS

Assuming that a highway structure is isotropic with constant thermal properties over length (Figure 1) temperatures will vary with time through the cross section away from the ends in accordance with the familiar heat flow equation:

$$k\left(\frac{\partial^2 T}{\partial x^2} + \frac{\partial^2 T}{\partial y^2}\right) + \overline{Q}(t) = c\rho\,\frac{\partial T}{\partial t} \tag{14}$$

in which

T = temperature in the structure at x, y, and time t;

$\overline{Q}(t)$ = heat generated per unit volume (e.g., heat of hydration or freeze-thaw);

$\partial^2 T/\partial x^2$, $\partial^2 T/\partial y^2$ = temperature gradients;

$\partial T/\partial t$ = change in temperature; and

k, c, ρ = conductivity, specific heat, and density, respectively.

Table 4 gives thermal properties. Either finite element or finite difference techniques may be used to solve Equation 14 accurately (*2,4,23*).

Mean air temperature $[T_m(d)]$ may be used for initial temperatures, provided analysis is started at least one day earlier, so (*2,4*)

$$T(x, y, 0) = T_m(d) \tag{15a}$$

At any exterior surface exposed to weather, energy is transferred by the Fourier expression of

$$k\,\frac{\partial T}{\partial x}\,l_x + k\,\frac{\partial T}{\partial y}\,l_y + q(b, t) = 0 \tag{15b}$$

TABLE 4 Material Thermal Properties

Items	Values	References
1. Material Properties:		
Density, ρ	k_g/m^3; (lb/ft^3)	2,4,40,41,42,43
air	1.3 (.081)	
Asphalt	2100 - 2580 (130 - 160)	
Concrete	2243 - 2723 (140 - 170)	
Steel	7834 - 7850 (489 - 490)	
Specific heat, c	$J/k_g-°C$; $(Btu/lb-°F)$	2,4,40,41,42,43
air	922 - 1000 (0.22 - 0.24)	
Asphalt	838 - 1673 (0.20 - 0.40)	
Concrete	922 - 1170 (0.22 - 0.28)	
Steel	464 (0.111)	
Conductivity, k	$W/m-°C$; $(Btu/ft^2-hr-°F)$	2,4,40,41,42,43
air	0.023 - 0.028 (.040 - 0.05)	
Asphalt	0.69 - 0.9 (1.21 - 1.58)	
Concrete	1.4 - 3.7 (0.8 - 2.1)	
Steel	45 - 54 (26 - 31)	
Diffusivity, $\alpha = c\rho/k$	m^2/s; (ft^2/hr)	2,4,40,41,42,43
asphalt	0.2e-06 - 0.5e-06 (0.024 - 0.06)	
concrete	0.5e-06 - 1.5e-06 (0.06 - 0.2)	
steel	4.3e-06 (0.570)	
2. Boundaries Coefficients:		
Film Coefficient, h_c	$W/m^2-°C$; $(Btu/ft^2-°F)$	4,22,35,36.37
Fairbanks wind (0 - 2.2 m/s)	5.68 - 22.2 (1.0 - 3.9)	
Columbia wind (0 - 4.7 m/s)	5.68 - 33.3 (1.0 - 5.87)	
Absorptivity, α		2,4,40,41,42,43,44
asphalt pavements, decks	0.90	
concrete pavements, decks	0.50 - 0.80	
steel decks(rusted)	0.65 - 0.80	
steel decks (new paint)	0.12 - 0.15	
layer of ice	0.3	
layer of snow, frost	0.13	
Emissivity, ϵ		2,4,40,41,42,43,44
asphalt pavts, decks	0.92	
concrete pavts, decks	0.88	
steel decks (rusted)	0.80	
steel decks (new paint)	090 - 0.95	
layer of ice	0.96	
layer of snow, frost	0.91	

where

$\partial T/\partial x$ and $\partial T/\partial y$ = change in temperature in x and y directions,

l_x, l_y = direction cosines at boundary,

$q(b, t)$ = heat flow from exposure, and

b = x,y coordinates along pavement or deck.

At a pavement surface, bridge deck, parapet, or any exterior face exposed to the sun, $q(b,t)$ has contributions of solar flux, $q_s(t)$, convection, $q_c(b,t)$; and thermal radiation, $q_r(b,t)$. At the underside of a bridge, $q(b,t)$ consists of convection and thermal radiation (Figure 1).

The heat transfer components of Equation 15b may be determined from the weather model for air temperature, solar radiation, and wind. Heat gain due to the sun's rays received on a deck or pavement may be expressed daily or hourly by

$$q_s(t) = \alpha I_s(t) \qquad \begin{cases} I_s(t) = Q_d \text{ (Equation 8, annual)} \\ I_s(t) = I_h \text{ (Equation 11, diurnal)} \end{cases} \qquad (16)$$

in which α is an absorption coefficient (Table 4) and $I_s(t)$ is the sum of direct and diffuse solar radiation incident upon a horizontal surface. By separating direct and diffuse, any angle of tilt can be accounted for with respect to the horizontal plane (34).

Heat transfer by convection is given by Newton's law of cooling, or

$$q_c(b, t) = h_c[T(b, t) - T_a(t)] \qquad (17)$$

where

h_c = film coefficient depending on surface texture, slope, and wind speed [h_c is defined in the literature (22,35–37)];

$T(b, t)$ = temperature of body boundary, and

$T_a(t)$ = air temperature given by Equation 2 (annual) or Equation 10 (daily).

Heat transfer between the structure and the surrounding atmosphere resulting from long-wave radiation produces a

boundary that is nonlinear and time-dependent. It can be modeled by

$$q_r(b, t) = \sigma\varepsilon[\Theta(b, t)^4 - \Theta_a(t)^4] \quad (18)$$

where

σ = Stephen-Boltzman constant = 5.677 × 10^{-8} W/(m² − °K⁴) or 18.891 × 10^{-8} Btu/ (hr − ft² − °K⁴),

ε = emissivity coefficient that relates radiation of a gray surface to an ideal black body ($0 \le \varepsilon \le 1$), and

$\Theta(b, t), \Theta_a(t)$ = boundary and air temperature in degrees absolute, respectively.

Values are presented in Table 4.

BRIDGE EXPOSURE

AASHTO (38) states that "provisions shall be made for stresses or movements resulting from variations in temperature. The rise and fall in temperature shall be fixed for the locality in which the structure is to be constructed and shall be computed from an assumed temperature at the time of erection." The AASHTO provisions give a range of mean bridge temperatures for steel bridges of 83.3°C (150°F) for cold climates and 66.7°C (120°F) for moderate climates. A rise of 17°C (30°F) and fall of 22°C (40°F) of mean bridge temperatures is given for concrete bridges for moderate climates and a rise of 19°C (35°F) and fall of 25°C (45°F) in cold climates.

Mean Bridge Temperatures and Movements

A 1991 National Science Foundation report by Kuppa and Roeder (6) provides insight into movements in relation to exposure. Movements were calculated and compared with AASHTO using mean temperatures for three types of bridges at 11 SOLMET climatic sites. Columbia, Missouri, was one of the sites Kuppa and Roeder studied. Linear equations for maximum and minimum mean bridge temperature were expressed as a function of maximum, minimum, and air temperature in the form

$$\Theta = a + bT \quad (19)$$

where

Θ = mean bridge temperature,

a and b = constants, and

T = maximum or minimum air temperature. The equations are based on 50 years of temperature extremes and clear sky solar radiation. Assuming that these linear relationships are valid for return periods, T is replaced by return period temperatures giving summer and winter exposure.

Summer Exposure

Using Table 2, maximum mean bridge temperatures in degrees centrigrade are

$$(\Theta_{max})_{yr} = -3.88 + 1.015\,(T_{max})_{yr} \quad \text{composite} \quad (20a)$$

$$(\Theta_{max})_{yr} = -2.19 + 0.979\,(T_{max})_{yr} \quad \text{box girder} \quad (20b)$$

$$(\Theta_{max})_{yr} = -6.74 + 0.9526\,(T_{max})_{yr} \quad \text{T-beam} \quad (20c)$$

Winter Exposure

Using Table 2, minimum mean bridge temperatures in degrees centrigrade are

$$(\Theta_{min})_{yr} = -6.74 + 1.096\,(T_{min})_{yr} \quad \text{composite} \quad (21a)$$

$$(\Theta_{min})_{yr} = -12.88 + 1.186\,(T_{min})_{yr} \quad \text{Box, T-beam} \quad (21b)$$

The proposed modifications to Kuppa and Roeder's equations (6) suggest that 50-year maximum mean bridge temperatures for a composite bridge would be 39.94°C (103.9°F) and 48.4°C (119.2°F) for Fairbanks and Columbia, respectively. The 50-year minimums would be −54.8°C (−66.66°F) for Fairbanks and −26.7°C (−16.1°F) for Columbia. These are temperature ranges of 94.4°C (170°F) for Fairbanks and 75°C (135°F) for Columbia. Kuppa and Roeder suggested 65.4°C (117.7°F) as the mean bridge temperature range for Columbia, but no recurrence was given. The value suggested by AASHTO is 83.3°C (150°F) for a cold climate.

Fairbanks Bridge Temperatures and Stresses

Bridge temperature variations, stresses, and movements in a composite bridge subjected to Fairbanks weather extremes were studied for the effects of varying thermal strain coefficients (39). Exposures consisted of three 50-year extreme temperature days in summer and three 50-year extreme temperatures days in winter (5,39). The summer maximum concrete deck temperature was 47.2°C (117°F); the maximum temperature differential was 18.9°C (34°F). The winter maximum deck temperature was −16.1°C (3°F). The minimum was −56.1°C (−69°F). The maximum temperature differential for the winter exposure was +1.72°C (3.09°F).

EXAMPLES

Air temperature, solar radiation, and a constant wind velocity are the factors considered. A more refined model should allow for variations in precipitation and wind velocity and the daily range of temperatures. The proposed weather model is based on the idea that maximum temperature gradients occur for exposures involving air temperature extremes.

Consider a 10-year design period in Fairbanks, Alaska. The maximum daily ambient air temperature (Day 191) is obtained

by substituting coefficients of Table 2 into Equation 2 to give

$$(T_{d\max})_{10\ yr} = 62 + 29 \sin\left[\frac{2\pi(d - 100)}{365}\right] \quad °F$$

$$= 16.67 + 16.11 \sin\left[\frac{2\pi(d - 100)}{365}\right] \quad °C$$

Substituting coefficients of Table 2 into Equation 10 gives the 10-year maximum hourly temperature equation

$$(T_{h-\max})_{10yr} = 15 \sin\frac{2\pi(h - 12)}{24}$$

$$+ 29 \sin\frac{2\pi(d - 100 + h/24)}{365} + 47 \quad °F$$

$$= 8.33 \sin\frac{2\pi(h - 12)}{24}$$

$$+ 16.11 \sin\frac{2\pi(d - 100 + h/24)}{365} + 8.33 \quad °C$$

The corresponding solar radiation for all ambient air temperature recurrence intervals is given using Equations 11a and 11b

$$I_h(t) = 0 \qquad (h_{sr} > h > h_{ss})$$

$$I_h(t) = \frac{2(Q_{d-\max})_{yr}}{20.13} \sin^2\left[\frac{\pi(h - h_{sr})}{20.13}\right] \qquad (h_{sr} \leq h \leq h_{ss})$$

where $(Q_{d-\max})_{yr}$ is found by substituting the coefficients of Table 3 into Equation 8, to give

$$(Q_{d-\max})_{yr} = 2962 + 3845 \sin(\Gamma) - 9 \cos(\Gamma)$$

$$+ 123 \sin(2\Gamma) - 627 \cos(2\Gamma) \quad W - hr/m^2$$

The equations for minimum periods are obtained by the same procedure.

SUMMARY AND CONCLUSIONS

The discussion provides a rational method for studying the effects of weather extremes on bridges and pavements. The weather exposure models can be incorporated easily into finite element or finite difference programs, or both, to calculate temperature distributions within these structures. A study of a bridge subjected to Fairbanks, Alaska, weather extremes illustrated clearly that the AASHTO provision for thermal loading is inadequate and should be updated to incorporate provisions for design life and thermal gradients.

The method proposed does not account for a random event at any time of year. This type of approach should be developed to provide a rational approach for examining fatigue considerations.

ACKNOWLEDGMENTS

Thanks are due to the University of Washington Regional Transportation Center, Transportation Northwest, for pro-

REFERENCES

1. M. Emerson. *Extreme Values of Bridge Temperatures for Design Requirements.* TRRL Report LR765. U.K. Transport and Road Research Laboratory, Crowthorne, Berkshire, England, 1977.
2. J. L. Hulsey. *Environmental Effects on Composite-Girder Bridge Structures.* Ph.D. thesis. University of Missouri-Rolla, 1976.
3. J. H. Emanuel and J. L. Hulsey. "Temperature Distributions in Composite Bridges. *Journal of Structural Engineering,* ASCE, Vol. 104, No. 1, Proc. Paper 13474, Jan. 1978, pp. 65–78.
4. I. C. Potgieter and W. L. Gamble. *Response of Highway Bridges to Nonlinear Temperature Distributions.* Department of Transportation, University of Illinois, Urbana, 1983.
5. J. L. Hulsey and D. T. Powell. *The No Expansion Joint Bridge for Northern Regions.* Final Report TNW 90-08. Transportation Northwest (TRANSNOW), University of Washington, Sept. 1990.
6. S. M. Kuppa and C. W. Roeder. *Thermal Movements in Bridges.* National Science Foundation Final Report. University of Washington, Jan. 1991.
7. J. G. Church and L. A. Clark. Combination of Highway Loads and Temperature Difference Loading on Bridges. *Structural Engineer,* Part A, Vol. 62A, No. 6, June 1984, pp. 177–181.
8. P. G. Buckland. Recommended Design Loads for Bridges. *Journal of Structural Engineering.* ASCE, Vol. 107, No. 7, Dec. 1981, pp. 1161–1213.
9. R. A. Imbsen, D. E. Vandershaf, and C. F. Stewart. *NCHRP Report 276: Thermal Effects in Concrete Bridge Superstructures.* TRB, National Research Council, Washington, D.C., 1985.
10. D. Ho and C. Liu. Extreme Thermal Loadings in Highway Bridges. *Journal of Structural Engineering,* ASCE, Vol. 115, No. 7, July 1989, pp. 1681–1696.
11. M. Emerson. *Bridge Temperatures.* Supplementary Report 442. U.K. Transport and Road Research Laboratory, Crowthorne, Berkshire, England, 1978.
12. J. H. Emanuel, J. L. Best, J. L. Hulsey, J. H. Senne, and L. E. Thompson. *An Investigation of Design Criteria for Stresses Induced by Semi-Integral End Bents: Phase 1—Feasibility Study.* Missouri Cooperative Highway Research Program Final Report 72-9. University of Missouri-Rolla, 1973.
13. R. A. Imbsen and D. E. Vandershaf. Thermal Effects in Concrete Bridge Superstructures. In *Transportation Research Record 950,* TRB, National Research Council, Washington, D.C., 1984, Vol. 2, pp. 110–113.
14. J. L. Hulsey and J. H. Emanuel. Environmental Stresses in Flexibly Supported Bridges. In *Transportation Research Record 664.* TRB, National Research Council, Washington, D.C., 1978, pp. 262–270.
15. J. H. Emanuel and C. M. Taylor. Length-Thermal Stress Relations for Composite Bridges. *Journal of Structural Engineering,* ASCE, Vol. 111, No. 4, 1985, pp. 788–804.
16. W. Zuk. Thermal and Shrinkage Stresses in Composite Beams. *Journal of the American Concrete Institute,* Vol. 58, No. 3, Sept. 1961, pp. 327–340.
17. W. Zuk. Thermal Behavior of Composite Bridges—Insulated and Uninsulated. In *Highway Research Record 76.* HRB, National Research Council, Washington, D.C., 1965, pp. 231–253.
18. C. Berwanger. Transient Thermal Behavior of Composite Bridges. *Journal of the Structural Division,* ASCE, Vol. 109, No. 10, Proc. paper 18314, Oct. 1983, pp. 2325–2339.
19. H. C. Fu, S. F. Ng, and M. S. Cheung. Thermal Behavior of Composite Bridges. *Journal of Structural Engineering,* ASCE, Vol. 116, No. 12, Dec. 1989, pp. 3302–3323.
20. M. Emerson. *Extreme Values of Bridge Temperatures for Design Requirements.* TRRL Report LR765. U.K. Transport and Road Research Laboratory, Crowthorne, Berkshire, England, 1977.
21. M. J. N. Priestley. Design of Concrete Bridges for Temperature

Gradients. *Journal of the American Concrete Institute*, Vol. 75, No. 5, May 1978, pp. 209–217.

22. M. J. N. Priestley and I. G. Buckle. *Ambient Thermal Response of Concrete Bridges*. Road Research Unit Bulletin 42. National Roads Research Board, New Zealand State Highways, Wellington, 1979.

23. A. G. Lanigan. *The Temperature Response of Concrete Box Girder Bridges*. Ph.D. thesis. University of Auckland, Auckland, New Zealand, 1973.

24. J. H. Emanuel and D. J. Wisch. Thermal Response of Continuous Two-Span Bridge Structures. In *Transportation Research Record 711*, TRB, National Research Council, Washington, D.C., 1979, pp. 40–46.

25. J. H. Emanuel and D. B. Lewis. Abutment-Thermal Interaction of Composite Bridge. *Journal of the Structural Division*, ASCE, Vol. 107, No. 11, Nov. 1981, pp. 2111–2126.

26. J. B. Kennedy and M. H. Soliman. Temperature Distribution in Composite Bridges. *Journal of Structural Engineering*, ASCE, Vol. 113, No. 3, March 1987, pp. 475–482.

27. *Hourly Solar Radiation-Surface Meteorological Observations*. SOLMET, Vol. 2, Final Report, TD-9724. National Oceanic and Atmospheric Administration, National Climatic Center, Environmental Data and Information Service, Asheville, N.C., 1980.

28. S. S. Kuo. *Numerical Methods and Computers*. Addison-Wesley Publishing Company, Reading, Mass., 1965, pp. 219–238.

29. E. J. Gumbel. The Return of Flood Flows. *The Annals of Mathematical Statistics*, Vol. 12, 1941, pp. 163–190.

30. M. L. James, G. M. Smith, and J. L. Wolford. *Applied Numerical Methods for Digital Computations*, 2nd ed. Harper and Row, New York, 1977, pp. 283–313.

31. R. W. Gloyne. The Diurnal Variation of Global Radiation on a Horizontal Surface with Special Reference to Aberdeen. *Meteorological Magazine*, No. 101, 1972, pp. 41–51.

32. M. Iqbal. *An Introduction to Solar Radiation*. Academic Press, Canada, 1983, pp. 1–28.

33. J. W. Spencer. Fourier Series Representation of the Position of the Sun. *Search*, Vol. 2, No. 5, May 1971, p. 172.

34. J. A. Duffie and W. A. Beckman. *Solar Engineering of Thermal Processes*. John Wiley & Sons, Inc., 1980.

35. E. S. Barber. Calculation of Maximum Pavement Temperatures from Weather Reports. *Bulletin 168*. HRB, National Research Council, Washington, D.C., 1957, pp. 1–8.

36. A. H. Bryant, I. G. Buckle, and A. G. Laningan. Prediction of Temperatures in Box Girder Bridges. *Proc., Australian Road Research Board Conference, 7th Adelaide*, Vol. 7, Part 7, 1974, pp. 296–308.

37. S. J. Thurston. *Thermal Stresses in Concrete Structures*. Research Report 78-21. Department of Civil Engineering, University of Canterbury, Christchurch, New Zealand, Nov. 1978.

38. *Standard Specifications for Highway Bridges*. AASHTO, 1983, 1990.

39. D. T. Powell. *The No Expansion Joint Bridge for Northern Regions*. M.S. thesis. University of Alaska-Fairbanks, 1990.

40. W. H. Dilger, A. Ghali, M. Chan, and M. S. Cheung. Temperature Stresses in Composite Box Girder Bridges. *Journal of Structural Engineering*, ASCE, Vol. 109, No. 6, 1983, pp. 1460–1478.

41. M. M. Elbadry and A. Ghali. Temperature Variations in Concrete Bridges. *Journal of Structural Engineering*, ASCE, Vol. 109, No. 10, Oct. 1983, pp. 2355–2374.

42. M. Emerson. *The Calculation of the Distribution of Temperature in Bridges*. TRRL Report LR561. U.K. Transport and Road Research Laboratory, Crowthorne, Berkshire, England, 1973.

43. M. J. S. Hirst. Thermal Loading of Concrete Bridges. *Canadian Journal of Civil Engineering*, Vol. 11, 1984, pp. 423–429.

44. A. M. Zarem and D. D. Erway. *Introduction to the Utilization of Solar Energy*. University of California Engineering and Sciences Extension Series, McGraw-Hill Book Co., New York, 1963.

Experimental Performance and Modeling Study of a 30-Year-Old Bridge with Steel Bearings

J. B. Mander, J. H. Kim, and S. S. Chen

The strength and deformation characteristics of 30-year-old steel bridge bearings, both fixed and expansion, are presented on the basis of field and laboratory experiments. The interaction between the deck and the substructure is analyzed. Field experiments were performed on a two-span, slab-on-girder bridge at Niagara Falls, New York, where the bridge deck was cyclically loaded over the central pier by alternating the placement of a hydraulic jack, forcing the spans apart in transverse and longitudinal directions. For the transverse tests, a ratio of about 1.5 of high lateral force to tributary weight was observed without bearing failure. Overall deformation was due mostly to diaphragm action between the deck and bearings, with only minimal movement in the bearings themselves. For longitudinal loading the expansion bearings did not slide on the bronze-steel sliding surface as expected, but the sole plate slid at a friction coefficient of about 0.6. An analytical study of the longitudinal test is presented in an attempt to account for the effects of girder depth and to identify the abutment stiffness from the results of the field experiments. The conclusion is that such bearings should behave satisfactorily in the event of a moderate earthquake such as may be expected in the eastern and central United States.

For existing bridges throughout the United States, abutment bearings and girder seats are often considered the most vulnerable elements in earthquakes. In high-risk seismic zones (such as in California), current practice may require retrofitting with isolation bearings and the provision of shear keys or cable restrainers to limit seat width demand. In zones of low to medium seismicity, such as the eastern and central United States, sophisticated retrofits may not be warranted. The existing bearings may possess sufficient intrinsic strength, displacement capability, or both, to survive a moderate level of ground shaking; thus, replacement may not be required. However, the performance of steel bearings, particularly those in most older bridges built during the highway construction boom period of the 1950s, is not well understood. Their behavior under a variety of loading conditions requires investigation.

To assess the strength and deformation characteristics of bearings in nonseismically designed bridges, an experimental field study has been carried out on a 30-year-old concrete slab on a steel-girder two-span bridge. The results are compared with companion laboratory experiments on bearings and can be used to study the deck-to-substructure interaction when the bridge is subjected to strong longitudinal and transverse ground shaking. It is also of interest to glean relevant information pertaining to the performance of bridge bearings under

Department of Civil Engineering, State University of New York at Buffalo, Buffalo 14260.

thermal expansion in the longitudinal direction, which is how they were designed to perform. A survey of the literature reveals little, if any, research on the performance of steel bridge bearings under generalized loadings. Limited work has been done on the longitudinal resistance of steel expansion bearings under monotonic loading (1).

The results are described of experimental field studies on a 30-year-old bridge at Niagara Falls, New York, with two spans of composite concrete slabs on steel girders. This bridge, shown in Figure 1, was formerly part of an on-off ramp system for the Robert Moses Parkway. Because of adjacent realignment of the parkway, the bridge was no longer needed and was demolished. A number of associated experiments were conducted before the bridge was destroyed. These included tests of ambient (traffic) vibration and transverse free vibration (snap-back). This study is concerned principally with the response of the bridge deck to large in-plane quasi-static loads to determine the in situ response of the bearings. This loading was applied in both longitudinal and transverse directions. The in situ response of the bridge as a whole is compared with the longitudinal and transverse loading behavior of companion bridge bearings tested in the laboratory. For the longitudinal field test, an analytical study was performed by considering the pre- and post-sliding behavior of the bearings. This analysis is used to assess the stiffness of the abutments. Results from an eigenfrequency analysis are then compared with the observed ambient (traffic) and free vibration (snap-back) frequencies.

IN SITU FIELD EXPERIMENTS

Bridge Configuration

The 30-year-old bridge shown in Figure 1 was in sound condition with the exception of the concrete deck around the expansion joints and girder corrosion at span ends. The bridge had a curved, two-lane roadway with a 220-m centerline radius. The northern and southern spans of the bridge were skewed by 7°35' and 3°18' respectively. The deck and pier cap of the bridge had a superelevation of 1:24 from west to east. At both the abutments and the central pier the steel girders were seated on a series of fixed and expansion bearings of the low type shown in Figure 2. The 20-mm gap for each of the three expansion joints was partially clogged with debris.
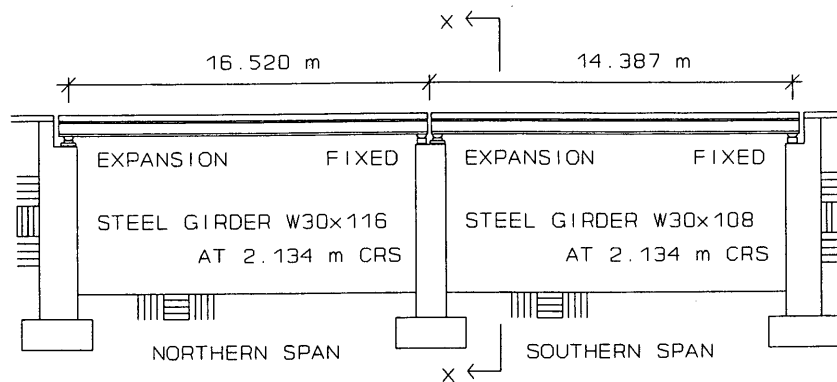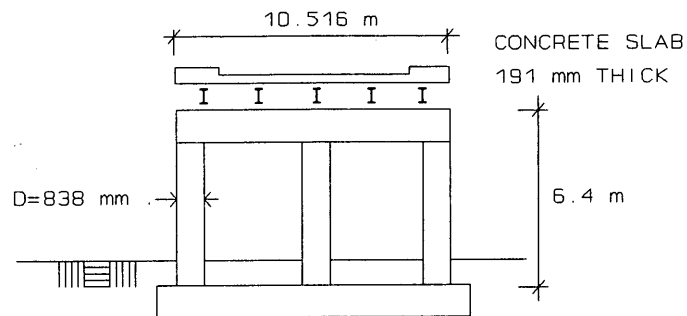
FIGURE 1   Niagara Parkway bridge: (*a*) longitudinal elevation; (*b*) section *X–X*.
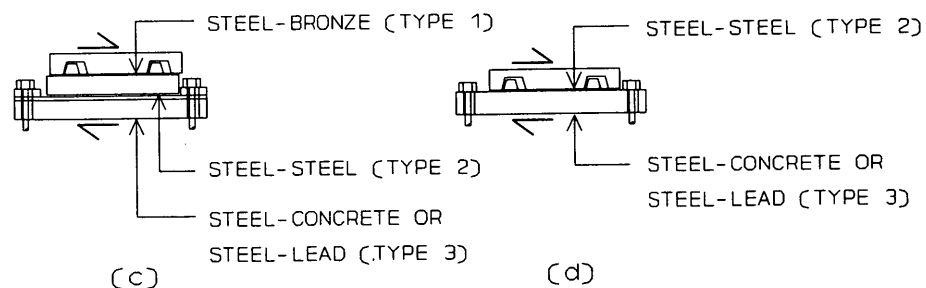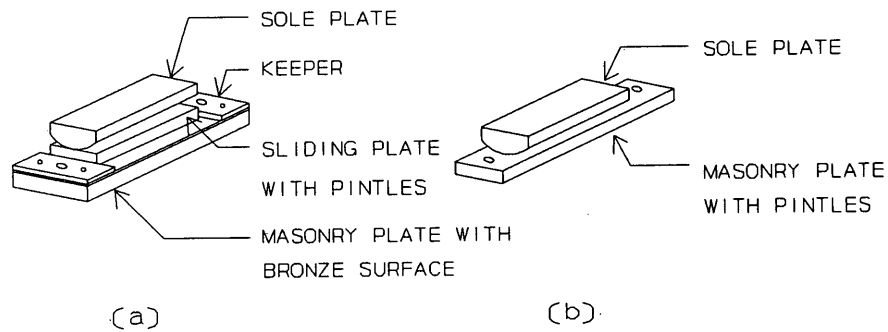
FIGURE 2   Low-type steel bearings: (*a*) expansion sliding bearing; (*b*) fixed pintle-rocker bearing; (*c*) frictional interfaces of bearing *a*; (*d*) frictional interfaces of bearing *b*.

Experimental Setup, Instrumentation, and Testing Procedure

Horizontal quasi-static loads in the longitudinal and transverse directions were applied to the bridge deck by a hydraulic jack with 900-kN capacity. To apply these large forces, pockets 250 mm × 750 mm were cut into the concrete deck to accommodate a hydraulic jack and a cylindrical load cell. The configuration of the jacking pockets over the pier for the transverse and longitudinal loadings is shown in Figures 3 and 4, respectively. An electrical pump controlled the hydraulic pressure in the jack. This enabled force to be applied gradually to the bridge through the concrete deck via the load cell in the jacking pocket with its capacity of 1.3 MN. The stroke

rate of the hydraulic jack was about 45 mm/min, with a maximum stroke of 150 mm.

The bridge was loaded cyclically in the transverse direction by alternating the placement of the hydraulic jack and the load cell as shown in Figure 3. In the longitudinal direction, the bridge was loaded over the central pier by forcing the spans apart toward each abutment.

Displacements were measured using a combination of sonic transducers and linear potentiometers. Data were logged into a 24-channel portable PC-based data acquisition system. The measured components of the bridge displacements are denoted by the arrows shown in Figures 3 and 4.

LABORATORY EXPERIMENTS TO DETERMINE STEEL-BEARING PERFORMANCE

For comparative purposes, the results of the field test are compared with the results of laboratory experiments on similar fixed and expansion steel bearings. The bearing specimens were retrieved from a bridge on Jewett-Holmwood Road in Erie County, New York, with bearings similar to those on the Niagara Parkway structure. These bearings were also 30 years old and had been operated in a salt-laden winter environment like that of the Niagara Parkway bridge. Both the expansion and fixed bearing types were tested under a variety of longitudinal and transverse horizontal loads with different vertical loads to emulate the effect of varying span lengths on bearing performance. In all cases, several reversed cycles of quasi-dynamic lateral load were applied with increasing displacement amplitudes until failure occurred. Further results, together with a description of the experimental test facility, are discussed elsewhere (2).

With the exception of two monotonic tests, all experiments were performed in displacement control. The control waveforms were sinusoidal in both monotonic and cyclic tests. In general, the nominal velocity of the waveforms was varied between 1.6 and 16 mm/sec. Depending on the displacement amplitude, cycling frequencies ranged from 0.01 to 2 Hz.

Each kind of bearing was tested under nominal vertical loads of 180, 270, and 360 kN representative of 18-, 24-, and 30-m spans, respectively. Test results for four specimens are presented here as a representative sample of the responses for the low type of bearing that was also present in the field tests on the Niagara Parkway bridge. For simple Coulomb-type frictional sliding surfaces, the results are expressed as a coefficient of friction; for nonsliding surfaces, the resistance is expressed as a horizontal-to-vertical-force ratio referred to as the base shear coefficient.

Three types of sliding interfaces are encountered in the discussion that follows. These interfaces are shown diagrammatically in Figure 2, and the corresponding coefficients of friction for laboratory and field experiments are summarized in Table 1.

Type 1: Steel-Bronze Interface

At the steel-bronze interface, sliding occurs between the steel sliding plate and a phosphor bronze surface riveted to the masonry plate. This type of interface exists in the low expan-
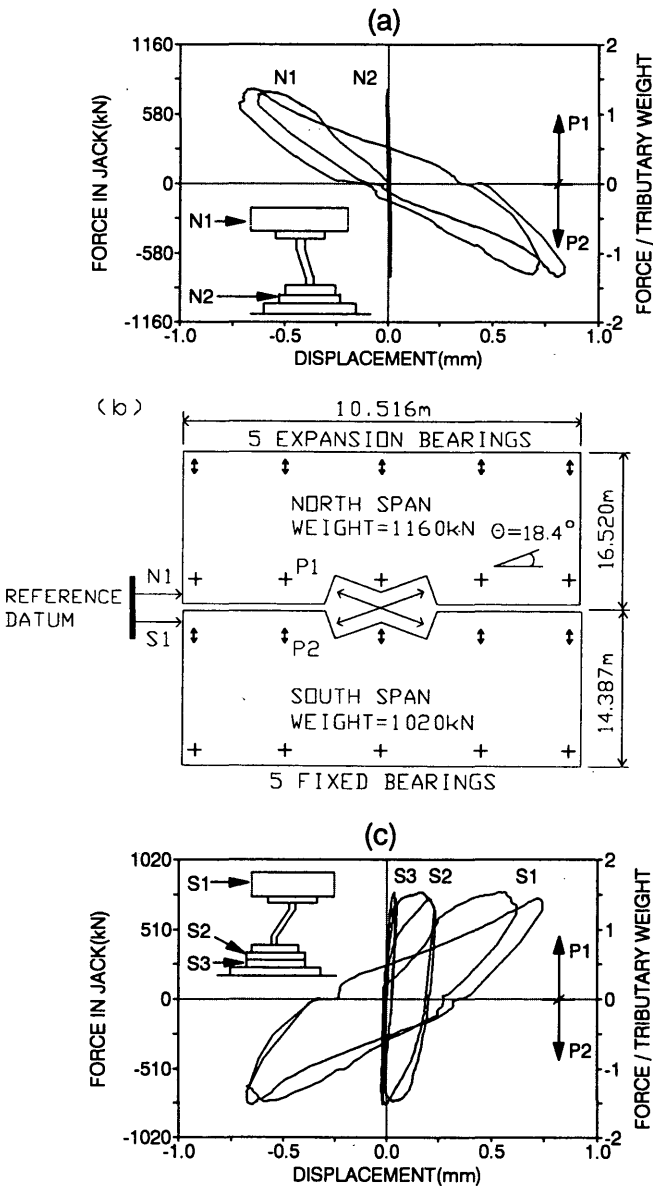
FIGURE 3 Transverse test results on the Niagara Parkway bridge: (*a*) north fixed bearing over the pier; (*b*) plan view of the bridge; (*c*) south expansion bearing over the pier.
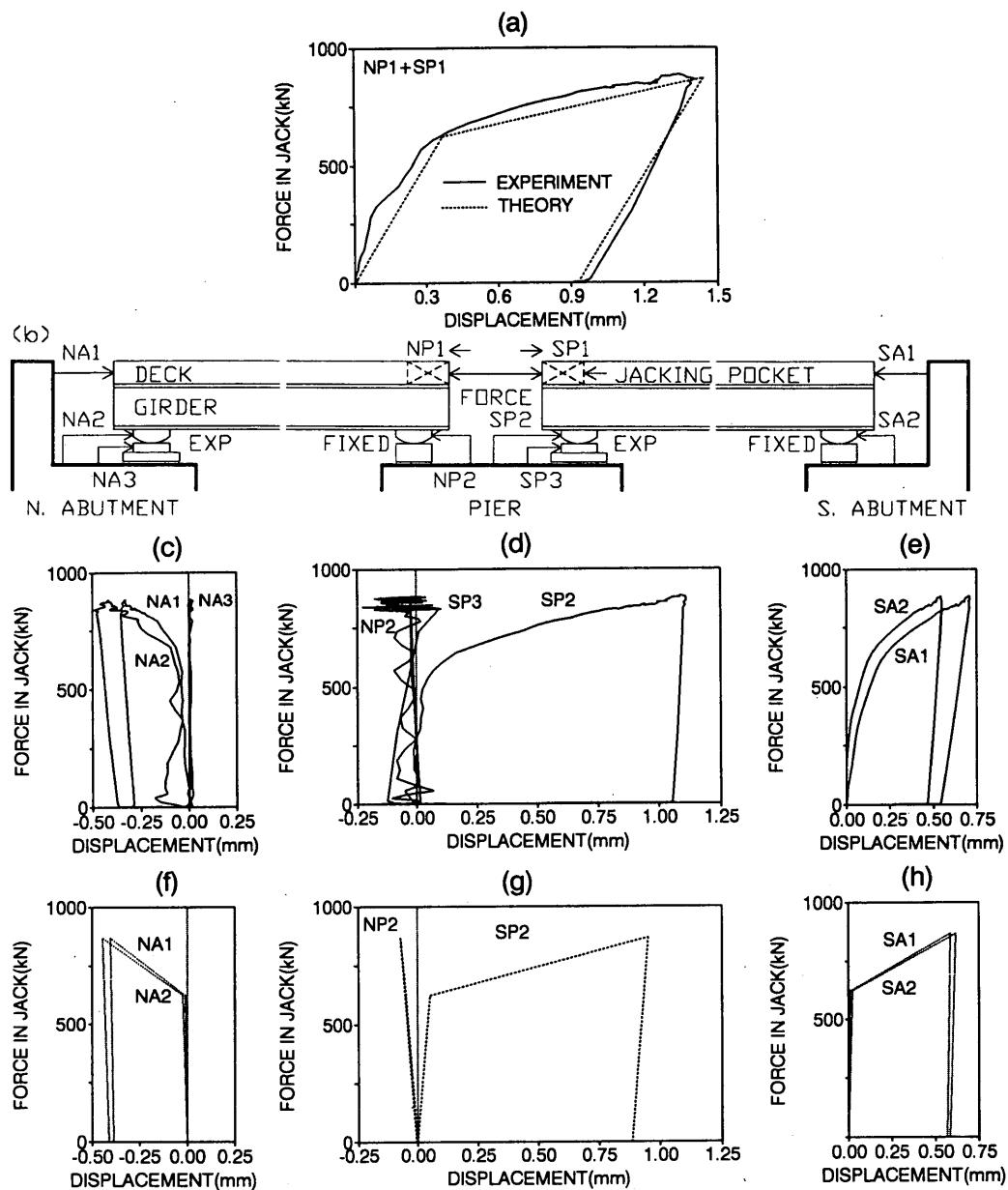
FIGURE 4 Longitudinal field test results for (*a*) deck movement, (*b*) instrumentation, (*c*) north abutment bearings, (*d*) pier bearings, and (*e*) south abutment bearings; theoretical responses for (*f*) north abutment bearings, (*g*) pier bearings, and (*h*) south abutment bearings.

TABLE 1   Coefficients of Friction for Low-Type Bearing Interfaces

	Coefficient of Friction			
	Transverse		Longitudinal	
	Laboratory	Field	Laboratory	Field
Expansion Sliding Bearing:				
Steel - Bronze	0.50	NS[a]	0.20	NS[a]
Steel - Lead	0.65	NA[c]	NS[b]	NA[c]
Steel - Steel	0.80	1.4	NS[b]	0.59
Fixed Pintle-Rocker Bearing:				
Steel - Lead	0.38	NA[c]	0.22	NA[c]
Steel - Steel	0.45	NS[b]	0.60	0.59

[a]Interfaces were bonded due to corrosion adhesion.
[b]Sliding did not occur.
[c]Lead did not present in Niagara Parkway Bridge.

sion sliding bearing only. In the transverse direction, sliding is limited to ±3.2 mm by keeper plates strongly riveted to the masonry plate. In the longitudinal direction sliding is limited to the half seat width dimension, which in this case is ±100 mm. Beyond this limit, seating instability begins.

Type 2: Steel-Steel Interface

At the steel-steel interface, sliding occurs between the sole plate and the sliding plate in the case of the expansion bearings and the masonry plate in the case of the fixed bearings. Sliding in both the longitudinal and transverse directions is limited to ±1.6 mm by the hole clearance around the pintles.

Type 3: Steel-Concrete or Steel-Lead Interface

The steel-concrete and steel-lead interfaces exist between the masonry plate and the concrete mounting pedestal. Sliding in either the longitudinal or transverse direction for both the fixed and expansion bearings is limited to ±4.8 mm by the masonry plate hole clearance around the anchor bolts.

It should be noted that for the Niagara Parkway bridge the bearings were mounted directly onto the concrete abutment or pier pedestals. For the Jewett-Holmwood Road bridge lead shims were placed beneath the masonry plate for leveling and seating purposes. These constructions were also duplicated in the laboratory tests.

TRANSVERSE LOADING BEHAVIOR

Laboratory Test Results on Individual Bearings

Figure 5(a) presents the results for a typical low expansion sliding bearing in the transverse direction that was observed to slide progressively at the steel-bronze, steel-lead, and steel-steel interfaces. The slip at each of these interfaces was limited by impact with the keeper plates, anchor bolts, and pintles, respectively. The result indicated respective frictional coefficients of 0.50, 0.65, and 0.80. With concurrent pintle and keeper impact, the resistance to further displacement increased rapidly and led to yielding of the pintles with base shear coefficients in excess of 3.0.

Figure 5(b) presents the behavior of a typical low fixed pintle-rocker bearing under transverse loading. These bearings were observed to slide progressively at the steel-lead and steel-steel interfaces. The results in Figure 5(b) show that the masonry plate slid first on the lead shim (Type 3) with an average friction coefficient of 0.38 until the masonry plate impinged on the anchor bolts. Then the sole plate slid on the masonry plate (Type 2) with an average friction coefficient of 0.45 until the sole plate impinged on the pintles. Once both the anchor bolt and pintle clearances were exhausted, the resistance to further sliding increased rapidly.

Experimental Results from the Field Test

The results of the field test in the transverse direction are presented in Figure 3. It should be emphasized that in the

FIGURE 5 Laboratory test results in the transverse direction: (*a*) low expansion sliding bearing (vertical force, 272 kN); (*b*) low fixed pintle-rocker bearing (vertical force, 182 kN).

transverse direction not all bearings were able to slide, with the exception of some play resulting from clearances mentioned. Even though individual bearings may permit some sliding within the clearances described, it is improbable that all five bearings at a given support line will be uniformly aligned to permit this magnitude of displacement. It is likely that at least one or more of these gaps have been closed and are already in contact with a bolt, a pintle, or a keeper plate. It is thus not surprising to find that the resistance to transverse movement was much higher than the highest breakaway friction values observed previously for similar bearings in the laboratory tests.

The experimental field test results revealed that there was minimal movement between the concrete contacting surface on the pier and the masonry plates for both the fixed and expansion bearings. This movement was much less than displacements *N2* in Figure 3(*a*) and *S3* in Figure 3(*c*), respectively. For the expansion bearings, one of the components of movement was steel-steel sliding limited by pintle yielding that commenced at a radio of lateral load to normal force of 1.4. This displacement is the difference between *S2* and *S3* in Figure 3(*c*).

It is evident from this experiment that the majority of the transverse movement in the two decks resulted from transverse diaphragm-girder distortion. The transverse diaphragms were located at the span ends and one-third points. Each diaphragm was rigidly bolted to a web stiffener by eight bolts 22 mm in diameter. The net displacement can be obtained by subtracting the sole plate displacement from the deck displacement, that is, $N1 - N2$ in Figure 3(a) and $S1 - S2$ in Figure 3(c) for the north and south spans, respectively. These results suggest an elastoplastic bilinear-type behavior attributed to slippage in the diaphragm-web stiffener semirigid bolted connections.

Implications from Experimentally Observed Behavior

In the event of an earthquake, it is normal for spectral accelerations to be less than about 1.2 g regardless of the seismic risk zone and return period. The observed high ratio of lateral to vertical load strength, which is in excess of 1.4 in the transverse direction for this bridge, implies that under transverse ground motions large inertia forces could be transmitted to the substructure by this class of bearing system through elastic response of the superstructure. The substructure, therefore, would be subjected to the full effect of the inertia loading from the bridge deck. If the pier does not possess sufficient strength, pier yielding would result in the subsequent inelastic response of the bridge system.

LONGITUDINAL LOADING BEHAVIOR

Laboratory Test Results for Individual Bearings

Figure 6(a) presents the results for a typical low expansion sliding bearing in the longitudinal direction. These bearings were observed to slide at the bronze-steel interface. It was observed during the test that this interface was being polished and that dirt and corrosion debris were being plowed by the sliding plate. For the example bearing shown, an initial breakaway friction coefficient of 0.25 and reversal coefficient of 0.21 were indicated for the first cycle of this previously tested specimen. The average friction coefficient for subsequent cycles was lower at 0.20. At large displacements near 100 mm, the sliding plates were observed to rock on the edge of the masonry plates, indicating potential instability.

Figure 6(b) presents the results for a typical low fixed steel bearing test in the longitudinal direction. Behavior was similar to the transverse test on a fixed bearing. For the example shown in Figure 6(b), the data indicate that the lead interface slid first, with an average friction coefficient of 0.22, until the masonry plate impinged on one or both anchor bolts. This was followed by sliding at the steel-steel interface, with an average friction coefficient of 0.60, until the sole plate impinged on one or both of pintles. Once both the anchor bolt and pintle clearances were exhausted, the resistance to further displacement increased rapidly. One specimen was taken monotonically to failure by severe plastic deformation of the pintles in shear and the pintle sockets in the bearing. This deformation was accompanied by loss of articulation of the sole plate and masonry plate at the maximum measured resis-
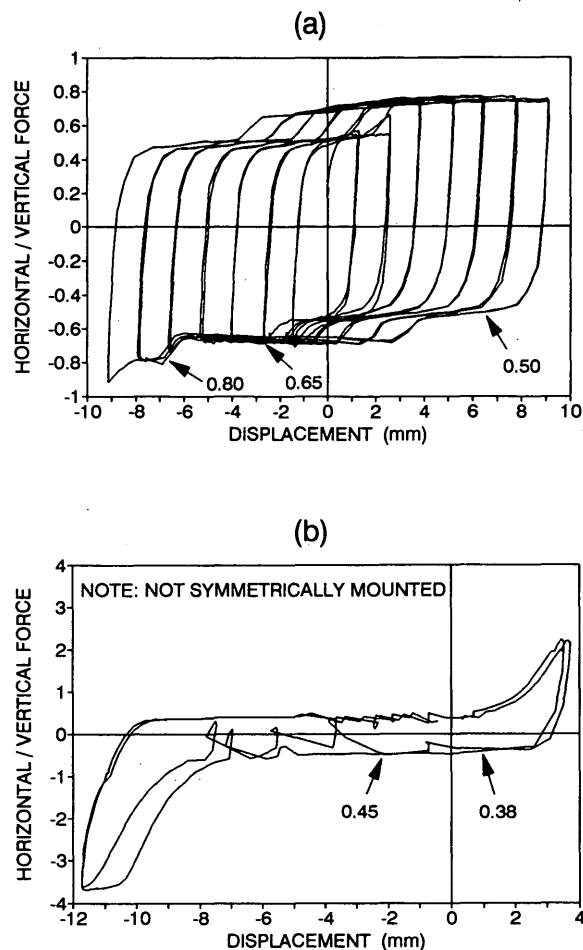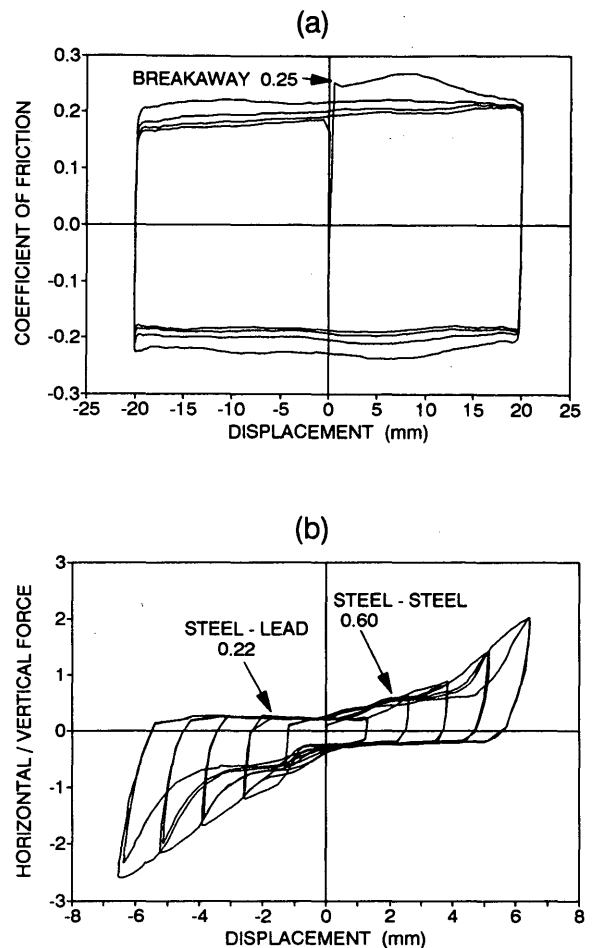

FIGURE 6 Laboratory test results in the longitudinal direction: (a) low expansion sliding bearing (vertical force, 245 kN); (b) low fixed pintle-rocker bearing (vertical force, 182 kN).

tance of 675 kN for the normal load of 182 kN. The result was a very high base shear coefficient of 3.7.

Experimental Results of the Field Test

Figure 4 presents the results of the field test in the longitudinal direction. The transverse direction bearing clearances previously mentioned also permit similar limitations to movements in the longitudinal direction. Movements also may be limited because of the 4°17′ misalignment resulting from the curved and skewed nature of the bridge geometry. Adhesion resulting from a significant amount of corrosion also limits displacements. It is evident from the results [displacements $NA3$ and $SP3$ in Figures 4(c) and (d), respectively] that virtually no sliding movement between the bronze-steel interfaces took place (Type 1 sliding). However, the results show that some Type 2 sliding was accommodated by the pintle clearances [displacements $NA2$, $SP2$, and $SA2$ in Figures 4(c), (d), and (e)]. The overall trend shown in the results indicates a form of bilinear response with an apparent yield point at a jacking force of 620 kN. The subsequent post-breakaway stiffness represents the stiffness of the central supporting pier and some

abutment resistance. These effects are discussed and analyzed more fully.

Implications from Experimentally Observed Behavior

In the longitudinal direction, the observed lateral-load-to-strength ratio is about 0.6, which implies that energy due to inertia forces could be dissipated by dry (Coulomb) friction in the expansion bearings. The inertial driving forces from deck to pier would thus be limited through the sliding bearings. The magnitude of the sliding displacements will depend on whether the pier response is elastic or inelastic because of a low pier strength. The sliding displacement magnitude needs to be quantified for various earthquake motions, bridge geometrics, and pier strength in future research.

ANALYTICAL MODELING OF LONGITUDINAL PERFORMANCE

From the bilinear response observed in the longitudinal field test, it is evident that the complex interplay of forces is due to superstructure-bearing interaction as well as interaction of the substructure (pier and abutment) and the soil. In an attempt to understand these interactions better, a structural model of the bridge was used to investigate the behavior analytically.

From the test results, it is immediately obvious that a conventional one-dimensional beam-column element cannot be used to model the composite concrete deck on steel girders.

With the bearing reactions some 860 mm below the applied jacking force (at deck level), it is apparent that this eccentricity leads to girder moments that significantly affect the displacement response. Hence the bridge superstructure was modeled as a two-dimensional (2-D) beam-column member as shown in Figure 7(b).

Two approaches using the stiffness method of analysis were employed to obtain solutions. In the first approach a fundamental matrix structural analysis was used in which a stiffness matrix for a 2-D beam-column was derived, and in the second, existing frame analysis computer programs were used to model the 2-D beam-column effects with an analogous portal frame. These two methods are described below.

Matrix Structural Analysis

Figure 7(a) shows the structural modeling of the Niagara Parkway bridge in the longitudinal direction. Member and component stiffnesses are represented by K_p for the pier, K_{an} and K_{as} for the northern and southern abutments, and K_{bn}, K_{bs}, K_{bpn}, and K_{bps} for the bearing stiffnesses of the northern and southern abutments and north and south bearings over the central pier, respectively. The superstructure of the composite concrete deck on steel girder is represented by a single 2-D beam-column member for each span. The reference datum shown in Figure 7(a) denotes the location where the field experimental measurements were taken. This represents where either the linear potentiometers or the sonic transducers were mounted. All displacements are computed as relative movements with respect to the corresponding measurement data.
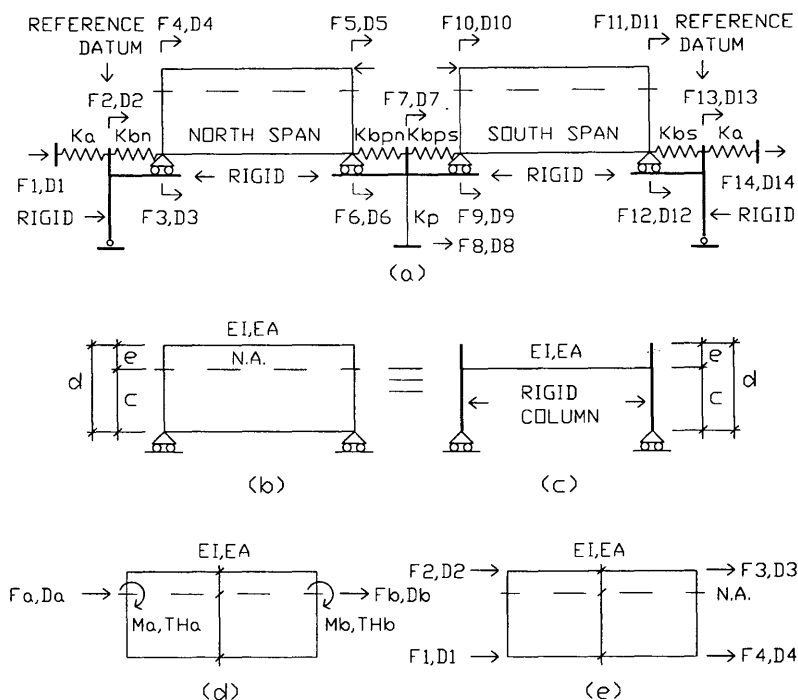
FIGURE 7 Model for analysis: (a) bridge in longitudinal direction; (b) 2-D beam-column; (c) portal frame analogy; (d) coordinate for 2-D beam-column; (e) transformed coordinate.

The stiffness matrix for a 2-D beam-column member that represents each span can be obtained by transforming for the coordinate set d to e shown in Figure 7, as discussed elsewhere (3). The stiffness matrix of Figure $7(d)$ for an ordinary beam-column member is given by

$$[S]_{(d)} = \frac{E}{L} \begin{bmatrix} A & -A & 0 & 0 \\ -A & A & 0 & 0 \\ 0 & 0 & 4I & 2I \\ 0 & 0 & 2I & 4I \end{bmatrix} \quad (1)$$

where E is the modulus of elasticity for concrete, and A, I, and L are respectively the transformed section area, transformed moment of inertia, and span length of a 2-D beam-column. The subscript denotes a corresponding coordinate. The following transformation equations provide the stiffness matrix of coordinate e:

$$\{F\}_{(e)} = [H]^T \{F\}_{(d)} \quad (2)$$

$$[S]_{(e)} = [H]^T [S]_{(d)} [H] \quad (3)$$

where $\{F\}$ is a force vector and $[H]$ is a transformation matrix. Carrying out the transformation from d to e demonstrates that the transformed 2-D stiffness matrix that relates end displacements and forces is given by

$[S]_{(e)}$

$$= \frac{E}{d^2 L} \begin{bmatrix} 4I + Ae^2 & -4I + Ace & -2I - Ace & 2I - Ae^2 \\ -4I + Ace & 4I + sAc^2 & 2I - Ac^2 & -2I - Ace \\ -2I - Ace & 2I - Ac^2 & 4I + Ac^2 & -4I + Ace \\ 2I - Ae^2 & -2I - Ace & -4I + Ace & 4I + Ae^2 \end{bmatrix}$$

$$(4)$$

where

c = location of neutral axis from base,

e = eccentricity of applied jack force from neutral axis, and

d = sum of c and e (distance of applied jack force from base of a 2-D beam-column).

The global stiffness matrix for the entire bridge model then can be expressed in the well-known form $\{F\} = [K]\{D\}$ and partitioned into known and unknown variables as follows

$$\begin{Bmatrix} F_K \\ F_U \end{Bmatrix} = \begin{bmatrix} K_{11} & | & K_{12} \\ \hline K_{21} & | & K_{22} \end{bmatrix} \begin{Bmatrix} D_U \\ D_K \end{Bmatrix} \quad (5)$$

in which $[K]$ is the global stiffness matrix and $\{F\}$ and $\{D\}$ are force and displacement vectors with subscripts K and U respectively denoting known and unknown quantities. Because $\{D_K\} = \{0\}$ from the boundary conditions of the model, the solution of the matrix equation can be obtained from

$$\{D_U\} = [K_{11}]^{-1} \{F_K\} \quad (6)$$

$$\{F_U\} = [K_{21}] \{D_U\} \quad (7)$$

Deck Modeling Using Portal Frame Analogy

A portal frame analogy can be used as an alternative to the approach described in Equations 4–7. This portal approach modifies standard beam theory to account for depth of fix of the superstructure. Figure $7(c)$ presents a portal frame that has the same global displacement attributes as the 2-D beam-column shown in Figure $7(b)$. Both beams have the same flexural and axial stiffnesses of EI and EA. To model the effects of 2-D beam depth, the portal frame analogy uses rigid (or very stiff) end columns with an overall length equivalent to the beam depth $(c + e)$. The analogous beam is located at the neutral axis of the real beam, given by the dimension c from the base.

The utility of the portal frame analogy becomes evident in the modeling of a large bridge structure. Conventional frame analysis computer programs can use this approach without resorting to modeling the 2-D action of the deck with multiple solid or plate finite elements or both types. The entire bridge structure can be modeled with conventional beam-column elements requiring only prescriptions of EI, EA, and L. One-dimensional spring elements also can be modeled this way by using a low I; alternatively, truss members can be employed as used in this study.

Application to Niagara Parkway Bridge

The foregoing analysis was applied to study the performance of the Niagara Parkway bridge, principally to assess the abutment stiffness. In this analysis real material and sectional properties were used for all of the clearly identifiable elements.

Because of the small strains mobilized in the tests, the stiffness properties for the Niagara Parkway bridge were based on an initial tangent modulus of elasticity for concrete of E_{ci}, where $E_{ci} = 5000 f'_c$ in which f'_c is the compressive strength of concrete in megapascals (4). Compressive tests of core specimens retrieved from the pier of the bridge gave $f'_c = 48$ MPa; thus $E_{ci} = 35$ GPa. Thus the transformed cross-section areas for the northern and southern spans are 3.84 and 3.71 m², and the transformed moments of inertia are 0.395 and 0.322 m⁴, respectively.

Table 2 presents the stiffness calculated (a) for the pier assuming an uncracked transformed section and (b) for the pre- and post-sliding bearing on the basis of results from the laboratory and field tests. It is worth noting that true Coulomb sliding of the steel-bronze interface would exhibit an elasto-perfectly-plastic type of response. The sliding invoked in the field tests, however, was at the steel-steel interface. It is apparent from the laboratory and field tests that for this case the post-sliding stiffness was about 1 to 3 percent of the pre-sliding stiffness [Figures $6(b)$ and $4(c)$ and (d)].

From the longitudinal field test results it is evident that there are two behavioral states; (a) pre-sliding at loads below about 620 kN and (b) post-sliding at loads above 620 kN. The second stage commences at an equivalent coefficient of friction of about 0.59 in the bearings. This corresponds well with the laboratory test results of similar steel-steel interfaces as shown in Figure $5(a)$ and (b) and Figure $6(b)$.

From the foregoing discussion it is evident that stiffnesses for the structural model can be determined from first prin-

TABLE 2 Values Used in the Stiffness Analysis of the Niagara Parkway Bridge

	Component Stiffness (kN/mm)	
	Pre - Sliding	Post - Sliding
Pier, K_p	42.9	42.9
Abutment, K_a	1930	1930
Bearings:		
Northern Abutment Expansion, K_{bn}	8580	85.8
Southern Abutment Fixed, K_{bs}	8580	85.8
Pier Fixed, K_{bpn}	8580	8580
Pier Expansion, K_{bps}	8580	215

ciples (deck), separate component tests (bearings), or rational assumptions (pier). Only abutment stiffnesses remain unknown.

Various values were assumed for the abutment stiffnesses, and the forces in the model for the applied load were computed. The total post-sliding displacements and forces were found by superposition on the pre-sliding results found at a jack force of 620 kN.

The value of abutment stiffness found to match the observed displacements well was 1930 kN/mm. The results from this analysis are plotted for comparison with the experimental observation in Figure 4(*f*), (*g*) and (*h*). The analyses by the matrix method and the computer-based portal frame analogy gave close agreement, with differences not detectable within plotting accuracy. The stiffness corresponds favorably with a value of 115 kN/(mm·m) recommended by the California Department of Transportation (Caltrans) for bridge abutment analysis and design (5). It is worth noting, however, that the displacements were small and engagement of the abutment with the backfill is probably minimal.

A check on the validity of this result was made by comparing the eigenfrequencies of the structural model using a lumped mass matrix with masses located at nodal points and midspan of the girders. The analytical and experimentally observed frequencies are presented in Table 3. To obtain the appropriate analytical first-mode frequency, the full mass of each abutment (295 tonnes) was used in the eigenfrequency analysis.

2. The low steel expansion sliding bearings in the longitudinal direction may result in residual steel-bronze sliding friction coefficients as low as 0.2. This relatively low resistance to motion could potentially lead to displacement demands in earthquakes with bearing instability at 100 mm displacement. This could subsequently lead to unseating of the girders. The theoretical longitudinal seismic displacement demand needs further quantification. However, the laboratory experiments showed that resistance to longitudinal motion is governed primarily by the degree of corrosion present in the bearings. The in situ field tests also demonstrated that because of misalignments and corrosion adhesion in the bearings, breakaway of the steel-bronze interfaces may not occur for normal magnitudes of seismic loading. Thus seat widths may not be of concern, because high breakaway forces are necessary to induce movement to overcome the adhesion resulting from corrosion.

3. Rigorous structural analysis is needed that accounts for the two-dimensional effects of beams, because it is able to capture the pre- and post-sliding response if abutment stiffnesses can be determined. The present study revealed that an abutment stiffness of 180 kN/(mm·m) compares favorably with the design value of 115 kN/(mm·m)[200 kips/(in.·ft)] recommended by Caltrans.

4. Further theoretical study is needed on the diaphragm action to evaluate the strength and displacement demand of the pier in the transverse direction.

CONCLUSIONS

The following conclusions can be drawn from the experimental observations and analytical study presented:

1. The low steel bearings possess a series of multiple sliding surfaces that will progressively engage as the displacements increase until all the clearances are exhausted. At this point, yielding of the anchor bolts or pintles inhibits further sliding. Pintle yielding may provide base shear resistance well in excess of earthquake loading demand.

TABLE 3 Comparison of Natural Frequencies

	Modal Frequencies (Hz)	
	First Mode	Second Mode
Analytical	10.1	14.7
Experimental Ambient (Traffic)	8 -12[a]	13 - 17[a]
Experimental Free Vibration (Snap-Back)	10.1	19.9

[a]Range dependent on mass of vehicle crossing the bridge.

REFERENCES

1. A. Mazroi, L. R.-L. Wang, and T. H. Murray. Effective Coefficient of Friction of Steel Bridge Bearings. In *Transportation Research Record 903*, TRB, National Research Council, Washington, D.C., 1983, pp. 79–86.
2. J. B. Mander, S. S. Chen, J. H. Kim, and G. J. Premus. The Performance of 30-Year-Old Steel Bridge Bearings. *Proc., 8th US-Japan Bridge Engineering Workshop*, Chicago, Il., May 11–12, 1992.
3. A. Ghali and A. M. Neville. *Structural Analysis: Unified Classical and Matrix Approach*, 3rd ed., Chapman and Hall, New York, 1989.
4. J. B. Mander, M. J. N. Priestley, and R. Park. Theoretical Stress-Strain Model for Confined Concrete. *Journal of Structural Engineering*, ASCE, Vol. 114, No. 8, Aug. 1988, pp. 1804–1826.
5. G. M. Calvi and M. J. N. Priestley, eds. Seismic Design and Retrofitting of Reinforced Concrete Bridges. *Proc., International Workshop*, Bormio, Italy, April 2–5, 1991.

Bearings in Structural Systems: Action and Reaction

BARRIE ATKINSON

Specifications for modern high-load multirotational bridge bearings tend to create the impression that they can be used interchangeably on any structure. In general, bearings are specified and approved for use on the basis of three traditional parameters: maximum vertical load, maximum service rotation, and in the case of expansion bearings, maximum expected expansion and contraction. Although it is usually possible to design a pot bearing, a spherical bearing, or an unconfined elastomer pad (or disc) bearing to fit a given set of such parameters, it is important to understand that each of the three reacts differently within a structural system. Clues to differing reactions can be found by looking at how the three types of bearings carry load and absorb rotation. An examination of these behavior patterns relates them to typical structural systems and points out areas of incompatibility, which in extreme cases result in malfunction of the bearing. One such case is presented involving the leaking of elastomer from pot bearings at the end of a continuous span. A theory for the leakage mechanism is postulated. Increased awareness of the interaction of bearings and structural systems is indicated and research into certain aspects is suggested.

Modern high-load, multirotational bridge bearings fall into three categories: pot bearings, spherical bearings, and unconfined pad (or disc) bearings. State specifications, bid items, and project details seldom differentiate among the types and thus give the impression that they are interchangeable—and in some cases they are specified as being interchangeable.

Typically, project plans detail bearings on the basis of three parameters: bearing capacity, or maximum vertical load; maximum rotation; and in the case of expansion bearings, maximum expansion and contraction. Because bearings in all three categories use similar polytetrafluoroethylene/stainless steel slide systems for expansion and contraction, only loading and rotation data will be discussed here to draw attention to the widely different characteristics of the three types of bearings.

Given these limited data on maximum load and rotation plus a few dimensional requirements, it is possible to design a bearing from any of the categories to fit the requirements. However, it is important to understand that each of the three may react quite differently within a structural system. Further, any of the three may not react in one structural system as it does in another.

Clues to these differing reactions can be found by considering how the three types of bearing carry load and absorb rotation.

Cosmec, Inc., P.O. 390, Walpole, Mass. 02081.

LOAD AND ROTATION CHARACTERISTICS

The pot bearing (Figure 1) transfers load from a circular plate (piston) onto a round rubber pad confined within a mating recess in a steel plate (pot). There is virtually no vertical deflection. When the bearing is loaded, rotation input causes the rubber within the pot to flow from beneath the downward-tilting side of the piston toward the upward-tilting side.

The spherical bearing (Figure 2) transfers load from a circular concave plate directly onto a mating convex plate; the actual curved interfaces are stainless steel and ptfe. Rotation input results in sliding at this interface.

Unconfined elastomer pad (or disc) bearings (Figure 3) transfer load through the pad onto a steel base plate. When the bearing is loaded, the pad compresses. Compression must be kept within acceptable limits, generally by steel laminates or by increased hardness of the elastomer. Rotation input further compresses one edge and relieves the opposite edge.

The pot bearing is basically a closed hydraulic system; under pressure, the rubber reacts like a fluid. When lightly loaded, however, this hydraulic system breaks down. The rubber strength dominates and rotation input may result in lift-off or separation at the piston-elastomer interface. Seal rings may be momentarily unloaded and a leakage mechanism may be started.

In the spherical system, effective rotation is available at any load (within the bearing's capacity) down to zero, but it is vital that this type of bearing not be subjected to a coincident horizontal force. Low vertical load together with high horizontal load could cause a critical dislocation of the concave and convex parts. This instability has been documented by Gilstad (1).

In the unconfined pad (or disc) system, there is an inherent conflict between the need to limit compression and the requirements for rotation. Design specifications limit strain at the compressed edge of a pad under rotation and dictate no lift-off at the relieved edge. This coupled with a maximum acceptable vertical compression clearly restricts rotation (Figure 4). Unconfined elastomers under load are subject to further deflection beyond the initial amount; this is due to creep of as much as 40 percent.

Consider the manner in which these bearing systems react to rotational input. Figure 5 shows a comparison of eccentricity and rotation characteristics for the principal types of structural bearing from a paper by Kauschke and Baigent (2). Curves B, C, and D relate to the bearings discussed here. Of these three, the pot bearing offers the lowest reaction to ro-
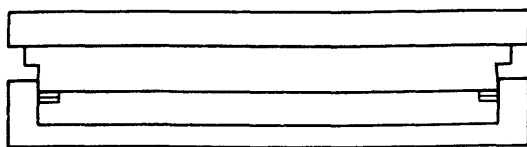
FIGURE 1 Diagram of pot bearing.
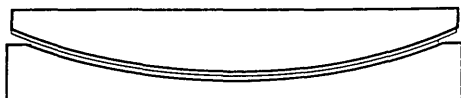
FIGURE 2 Diagram of spherical bearing.
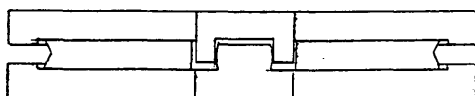
FIGURE 3 Diagram of unconfined elastomer pad (disc) bearing.
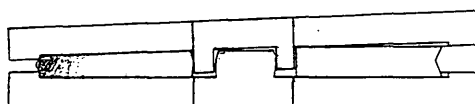
FIGURE 4 Diagram of unconfined pad bearing in rotated state.
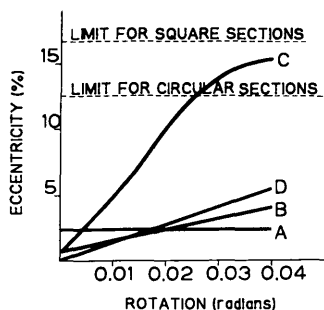
FIGURE 5 Comparison of eccentricity and rotation characteristics for the principal types of structural bearings.

tation up to about 0.02 rad, beyond which the spherical bearing, with its constant rate resistance, gives the least eccentricity. The unconfined pad or disc unit has eccentricity several orders greater than the other two for all practicable rotation requirements.

Consider also the geometry. The pot bearing and unconfined pad bearing allow rotation about the approximate center of their upper elastomeric surfaces; the spherical bearing rotates about the center of the sphere. Obviously the orientation of the up curve or down curve will affect such structural details as the expansion joints, but it will also affect the amount of horizontal travel imposed on an expansion bearing by rotation (Figure 6). Wear characteristics of ptfe on such bearings might warrant closer attention.

In general, pot bearings are best suited to high vertical loads, medium and high horizontal loads, and 0.02 to 0.03 rad rotation. Their strong feature is their low load eccentricity under rotation, and their weak feature is their limited ability to accept rotation at low vertical loads. Spherical bearings are best suited to high vertical loads, low and medium horizontal loads, and rotation above 0.02 rad. Their strong feature is their ability to accept high rotations at constant eccentricity under rotation, and their weak feature is their limited ability to sustain horizontal force at low vertical loads. Unconfined pad bearings are best suited to medium vertical loads, low and medium horizontal loads, and rotations up to 0.02 rad. Their strong feature is simplicity, and their weak features include amount and variability of compression deflection and a high resistance to rotation, which results in high edge loading on ptfe when used. All types can be adapted to accept uplift loads.

RELATION OF BEARINGS TO STRUCTURES

Relating the reactions of the three types of bearings to various structural designs indicates that some structures are better suited to one bearing design than to another.
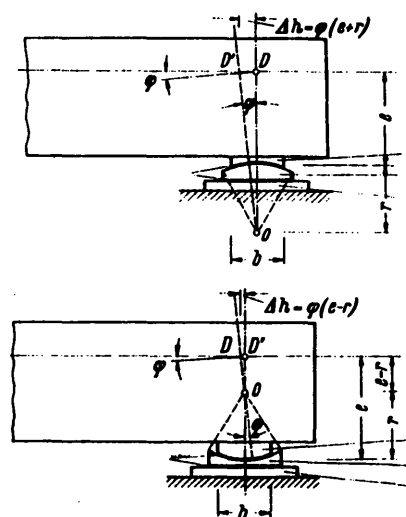
FIGURE 6 Comparison of the geometry of up-curved and down-curved spherical bearings.

The bridge in Figure 7 is well suited to pot bearings. It imposes a high permanent load and moderate rotation and requires the minimum of eccentricity to reduce bending moments in the tall piers. Spherical bearings, which require supplemental lateral restraint (the structure is vulnerable to hurricanes), would be less satisfactory. Unconfined pad bearings would be unsatisfactory because of the high bending moments induced in the tall piers and possibly because of the compression differential between the two bearings on any pier.

The bridge in Figure 8 makes excellent use of spherical bearings. The high rotation requirement and low load during initial construction make pot bearings less satisfactory for this structure. Unconfined pad bearings must be made thicker to accommodate higher rotation and this results in even more compression deflection. There also exists, under these loading conditions, the probability of lift-off and concomitant high edge loading of ptfe.

Unconfined pad bearings would be satisfactory in the type of structure shown in Figure 9. Although the other two types of bearings would be serviceable here, their particular attributes would not be of significant advantage.

The compatibility of structural action and bearing reaction is so important that without it, bearing malfunction may result. It is possible, for example, that this incompatibility exists in the structure shown in Figure 10. This overpass has a two-span composite plate girder–concrete deck superstructure, fully continuous over the pier. Contract bearing notes indicate that pot, spherical, or unconfined disc bearings should be used. It may be, however, that because of the competitive bid system, the pots used were not the appropriate bearing for the structure.

Figure 11 shows a pot bearing with some elastomer leakage. This bearing, one of the abutment bearings on the structure, was made by a second manufacturer to replace one of the original lot that was leaking. It can safely be assumed that the replacement bearing was fabricated with particular care and diligently inspected and load-tested, yet it is leaking also. The reason for the leakage is postulated as follows: This superstructure is sufficiently stiff to transfer live loading of one span into uplift at the opposite abutment. Such uplift loading may result in widely fluctuating pressures within a pot bearing.
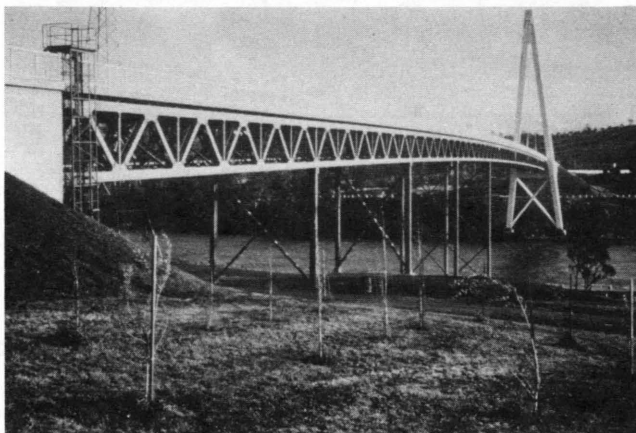
FIGURE 8   Typical structure suited to spherical bearings.

FIGURE 9   Typical structure suited to unconfined pad bearings.

FIGURE 7   Typical structure suited to pot bearings.

FIGURE 10   Structure in which pot bearing leakage was found.
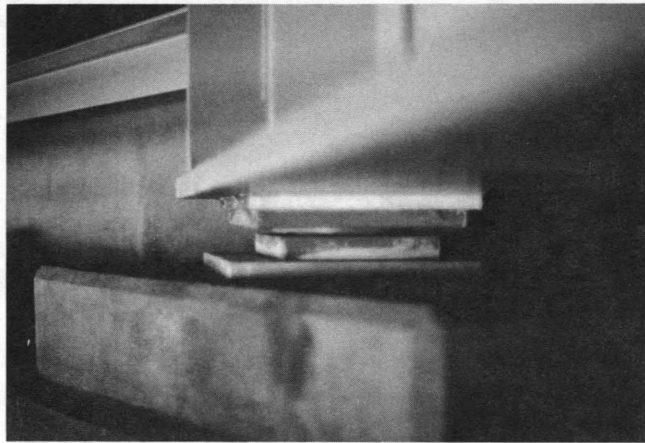
FIGURE 11   Abutment bearing on structure in Figure 10.

FIGURE 12   Typical modern spherical bearing.

This "bounce-loading" would be of high frequency and, because of hysteresis in the elastomer, its reaction would be out of phase with the springier brass sealing rings. Thus, during each fluctuating load cycle, there could be an instant when the seal rings are not loaded against the pot wall, yet the elastomer is still loaded. At this moment, a small amount of elastomer would escape upward and be pinched between the seal ring and pot wall. Once there is elastomer in this area, pressure within the system would tend to equalize the loading on the inside and outside edges of the seal ring, reduce the ring's effectiveness, and allow more elastomer to be pumped out during succeeding cycles. This leakage mechanism is consistent with the finely shredded appearance of the escaping elastomer.

There is also consistency between the design of this structure and that of the other few structures experiencing similar leakage. However, research into this theory is clearly needed.

CONCLUSION

This paper is not a damage report. The example presented is intended to emphasize to structural engineers the importance of awareness of the way different bearing designs react under given circumstances.

In his paper on bridge deck joints, Burke (3) stated, "Poor performance and failures cannot be used as a general condemnation of the devices themselves. The success or failure of a design is directly related to the expertise of those responsible for its creation, development and application." High-load multirotational bearings have achieved a refined state of development (Figure 12). Their creation is governed by a process of approval, specification, and inspection that, although onerous, goes a long way toward assuring the owners of good quality products. Problems will continue to arise, however, until due attention is given to the application.

The bearing industry and structural engineers must work together to ensure full understanding of the way these devices react in any particular structure.

REFERENCES

1. D. E. Gilstad. Bridge Bearings and Stability. *Journal of Structural Engineering*, Vol. 116, No. 5, May 1990.
2. W. Kauschke and M. Baigent. Improvements in the Long Term. Durability of Bearings in Bridges. Presented at the 2nd World Congress of Joint Sealing and Bearing Systems, San Antonio, Texas, Sept. 1986.
3. Martin P. Burke, Jr. Flawed Assumptions—Why Bridge Deck Joints Fail. *Civil Engineering*, Vol. 61, No. 11, Nov. 1991.

Fatigue Design of Welded Aluminum Structures

Craig C. Menzemer and John W. Fisher

Welded structures subjected to repeated loads often exhibit stable crack growth or fatigue. Fatigue cracking has not been limited to a single class of material or application. Reasons for these failures are numerous but in general may be linked to some shortcoming in the design process. Despite the long history associated with welded aluminum structures, comprehensive fatigue design specifications did not appear in a U.S. code until 1986. Experimental results used in the development of this specification are based primarily on fatigue tests of small specimens. Limitations on the application of such data to large structures have been documented for steel. This specification is further constrained by the lack of provisions governing variable amplitude loadings. A study was undertaken in 1988 to examine some of the issues associated with the design of welded aluminum structures. Experimentation included material characterization aimed at the development of predictive models, residual stress measurements, fatigue testing of axial specimens and beams, and detailed examination of fracture surfaces. Results pertinent to the development of the next generation fatigue design provisions are examined.

Welded structures subjected to repeated loads often exhibit subcritical crack growth or fatigue. Given the proper root conditions, crack growth normally occurs along the weld toe adjacent to the fusion line or through the weld throat. Details that fail from internal flaws, such as porosity, usually possess higher fatigue strengths as there is no geometric condition worse than the discontinuity itself (1). Joints with failure initiating from the weld toes require lower design stresses because the detail geometry results in large stress concentrations. Detail categories are essentially a geometric ranking of the severity of the stress concentration condition of the various joint types.

Field experience has shown that fatigue cracking is not limited to specific types of applications or to individual classes of materials. Reasons for the failures often may be attributed to inadequacies in the design process. Examples include an inadequate data and knowledge base for design provisions, cursory treatment of member interaction and joint behavior, improper detail classification, and poor definition of controlling load cases (2,3). This is by no means an all-inclusive list, but it does point to some of the deficiencies in current specifications.

Welded aluminum structures have been designed and built for more than 40 years. Examples include bridges, sign and luminary structures, railings, automotive and truck frames and components, cryogenic storage tanks, and so forth (4). Despite the application history, fatigue design provisions did

C. C. Menzemer, Alcoa Technical Center, 100 Technical Drive, Alcoa Center, Pa. 15069. J. W. Fisher, ATLSS Research Center, 117 ATLSS Drive, Building H, Lehigh University, Bethlehem, Pa. 18015.

not appear in a governing U.S. aluminum specification until 1986 (5). Most of the experimental results incorporated into the code are based on small specimen tests (6–8). Fatigue tests of any welded member or component should be consistent with the geometric, mechanical, and service conditions of the intended application. Any general fatigue design provisions then should reflect the lower-bound behavior of the various classes of joints. Limitations on small-scale specimens have been well documented for the case of steel structures (9,10). As the volume or size of the test specimen increases, the fatigue resistance decreases. Such behavior may be attributed in part to residual stresses and in part to the distribution of initial discontinuities. Simply stated, the larger the test specimen, the greater the constraint to expansion and contraction during welding. As a result, residual stresses in full-scale test samples are greater than those in smaller specimens. A decrease in fatigue strength normally accompanies an increase in the residual stresses.

All welded joints contain defects (11–13). Typical discontinuities include porosity, undercut, lack of fusion, large-grain structures, nonmetallic inclusions, and solidification cracks. The origin of fatigue cracks may be traced to such discontinuities. In fact, much of the fatigue resistance is consumed in the early stages of subcritical crack growth, when the defect develops into a macrocrack. As the size of the test sample increases, the probability of finding larger, more dominant flaws increases. A larger initial discontinuity will lead to a shorter fatigue life. Characterization of such discontinuity distributions allows fracture mechanics to be used to "predict" the lives of welded members and components.

COMPARISON OF ALUMINUM FATIGUE DESIGN CODES

Recent comparisons of worldwide provisions for fatigue design for aluminum structures revealed significant discrepancies in philosophy and strength values (14,15). Among the codes considered were the Italian or UNI 8634 (1985) specification, a draft of the British BS 8118 document (1985), the Canadian Standards Association code or the Alcan specification (1983), the 1986 version of the Aluminum Association (AA) code, and the European ECCS (1991) design provisions. Philosophical differences among these documents allow the classification of specifications into two broad groups. The Italian UNI 8634, the Canadian Standards Association, and to a limited degree the ECCS specification consider the fatigue strength to be a function of the loading, or R, ratio. R-ratio is the minimum stress in a load cycle divided by the maximum

stress in the cycle. Both the AA and the British BS 8118 design provisions assume an R-ratio independence.

Inherent in the assumption of R-ratio independence is the influence of tensile residual stresses. Much of the fatigue life of a welded structure is spent in the formation and growth of small cracks. As a result of the tensile residual stress fields, a relatively large portion of the structure's life is spent under high mean stress levels. Even under reversed loading, the material near the initial discontinuity will be subject to a fully effective stress cycle. This is the primary justification for use of stress range as the variable that describes the fatigue resistance of welded details. Full-scale details in steel have had measurements confirming residual stresses as high as the parent material yield point (16). Although the presence of large tensile residual stresses has been confirmed for aluminum as well, some localized softening may prevent the stresses from approaching the base metal yield point (17). This, combined with tests of small-scale specimens, has given rise to the R-ratio effect. It is interesting to note that the most comprehensive specification, the ECCS document, considers fatigue strength a function of stress range. However, for cases in which the residual stresses are known, a fatigue-enhancement factor may be applied to the strength when the applied R-ratio is less than -0.25. Given the complexity of quantifying residual stresses under laboratory conditions, it seems unlikely that designers will be able to take advantage of the enhancement factor.

Variable amplitude fatigue damage is accounted for through the use of Miner's rule, with the exception of the 1986 version of the AA specification. This code gives no guidance to design or assessment of details subjected to a variable stress history. S-N curves for the British BS8118, ECCS, and newly proposed Canadian Standard employ a dual slope. Beyond the constant amplitude fatigue limit, the curves are given a second slope that implies that damage accumulates at a different rate for relatively low applied stresses. The particular value of the second slope varies between specifications, but the shapes of the S-N curves reflect the multifaceted crack-propagation behavior of aluminum.

PROJECT SCOPE AND OBJECTIVES

Early in 1988 a cooperative project was developed between the ATLSS Engineering Research Center at Lehigh University and Alcoa Laboratories. Objectives of this study included the extension of the full-scale fatigue data base for aluminum structures, examination of the behavior differences between small axial test specimens and full-scale beams, investigation of life prediction techniques, and recommendation of design rules. In support of these goals, tensile, smooth S-N fatigue, strain control fatigue, fatigue crack growth, and fracture toughness tests were conducted. Component testing included axial fatigue of plate specimens with cover plates (Figure 1)
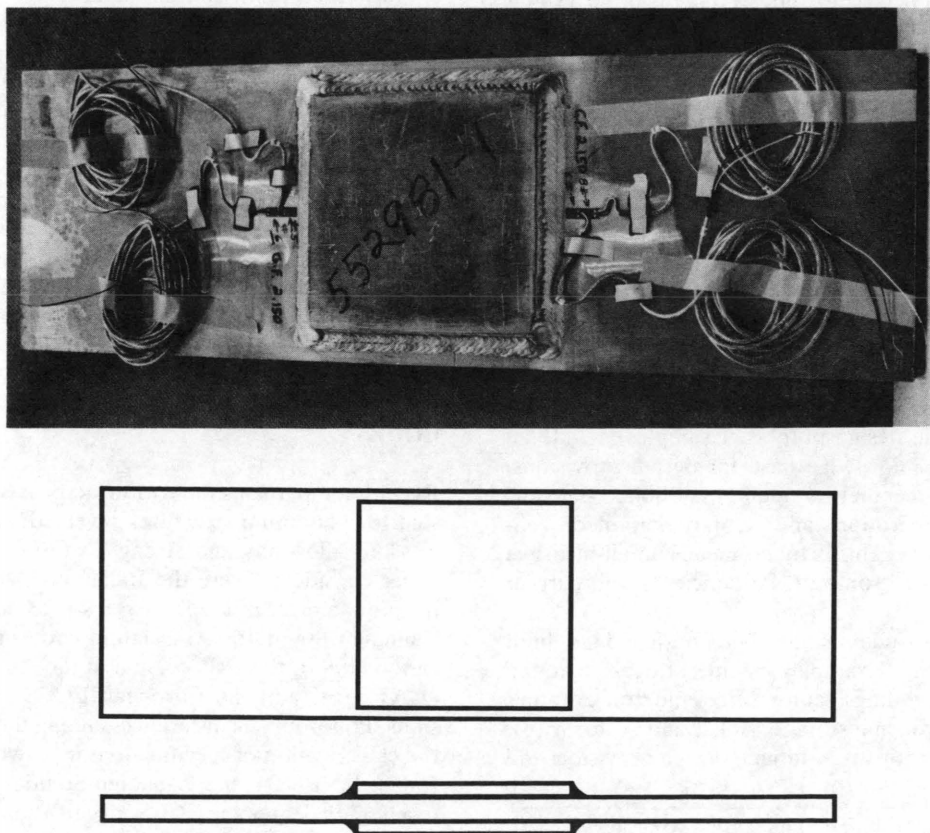
FIGURE 1 Axial cover-plate specimen: *top*, photograph; *bottom*, schematic.

and unloaded fillet-welded attachments (Figure 2). Axial cover-plate details were fabricated one at a time, while the cruciform specimens were fabricated from large welded panels that were subsequently saw-cut. Beam details tested were cover plates, stiffeners, butt-weld splices, and web-to-flange fillet welds as shown in Figure 3. Scanning electron microscopy (SEM) examinations of fracture surfaces were used to establish failure locations, defect sizes, orientations, and mechanistic differences in crack propagation under controlled environmental conditions.

Fatigue life prediction traditionally has used both fracture mechanics and strain control methodologies. Both techniques were explored for the constant amplitude behavior of the cover plate and stiffener beam details. Predicted S-N curves were compared to the experimental results as a means of assessing their applicability to full-scale welded aluminum details. Variable amplitude behavior was examined through extension of the fracture mechanics model. Several stress spectrums were chosen to yield applicable stress range values and included constant, linear, and Rayleigh distributions.

As the amount of work conducted in this study is beyond the present scope, emphasis will be placed on results that directly address design issues. The specifics of the residual stress measurements have been discussed elsewhere, so only the conclusions will be reviewed (*18*). Toughness of weldable aluminum alloys has been an issue that has, on occasion,
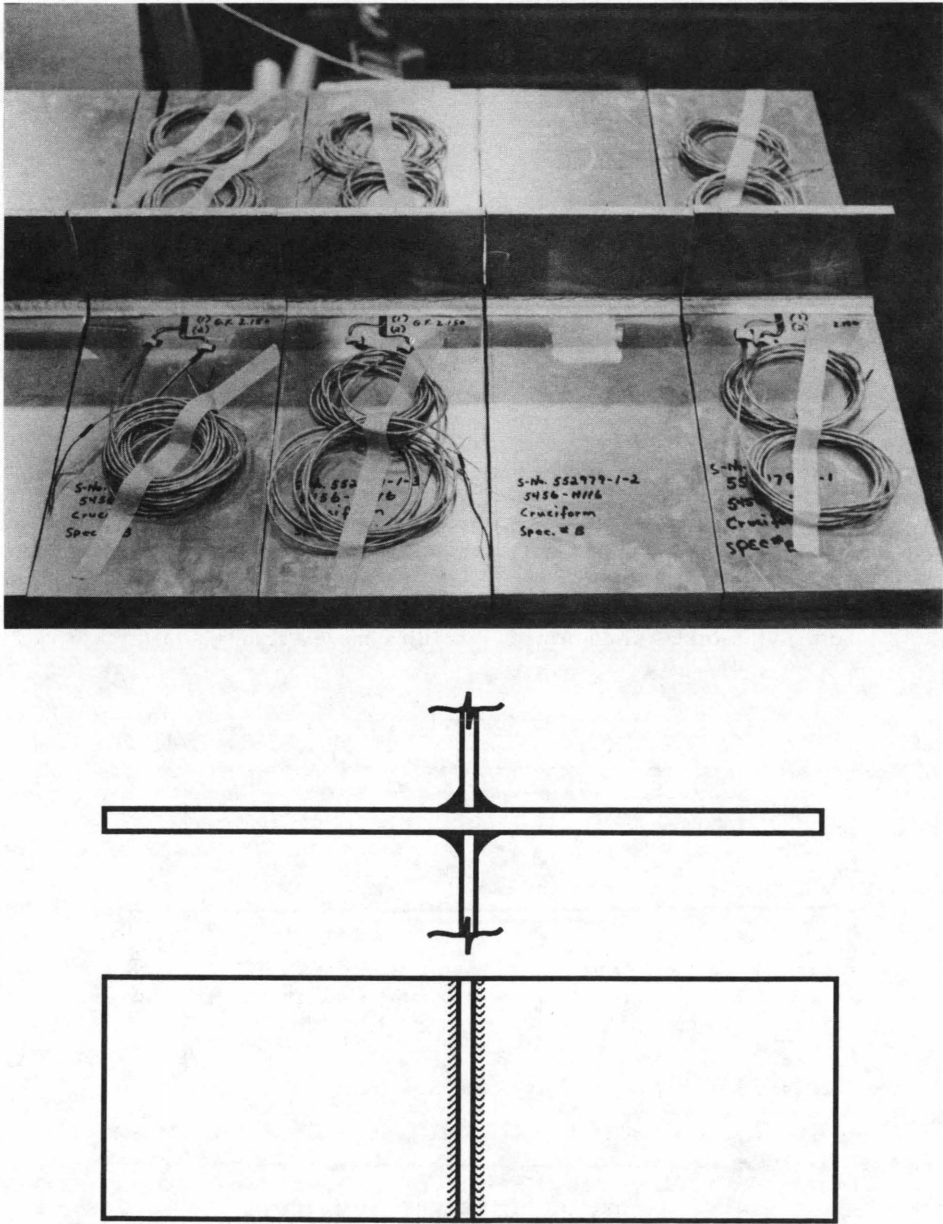
FIGURE 2 Cruciform joint: *top*, **photograph of cruciform joints cut from plate;** *bottom*, **schematic of cruciform joint test specimens.**
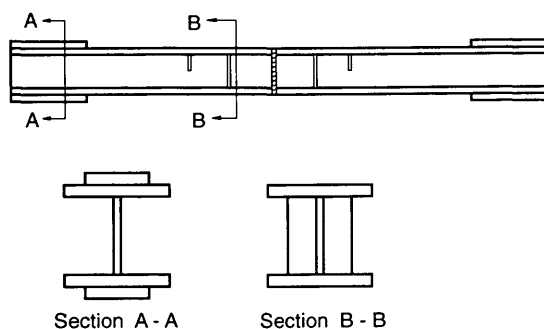
FIGURE 3   Elevation of full-scale beam sample, showing details of two sections.

restricted applications. *R*-curve tests of 5456-H116 and A36 steel will be discussed. Component fatigue tests and the impact on current design specifications will be examined. A brief discussion of the variable amplitude modeling and its impact on the code will follow.

RESIDUAL STRESS MEASUREMENTS

The existence of residual stresses in welded components significantly influences the fatigue behavior of the components. During the course of this study, residual stresses were measured on as-fabricated beams and axial fatigue specimens. In addition, measurements were taken on samples that had been tested but that contained no evidence of fatigue damage. In all cases, the hole-drilling technique was used (*19*).

Residual stress measurements demonstrated that significant differences exist between full-scale and small axial specimens. Maximum residual stresses for the cruciform panel and cover-plated beam details typically reached 80 degrees of the parent metal yield strength. The axial test samples, on the other hand, typically had residual stresses of 40 to 50 percent of the parent metal strengths. Figure 4 illustrates as-fabricated

residual stresses for a cruciform panel and axial specimens cut from the panel. Such differences may be attributed to constraint developed around the detail during welding. Measurement comparisons on as-fabricated and tested details showed no appreciable change of the surface residual stresses as a result of elastic cyclic loading. As much of the fatigue resistance is consumed in the growth of small defects, it is reasonable to conclude that the residual stresses have a major impact on the behavior of welded aluminum structures. In addition, residual stresses of this magnitude are consistent with fatigue failures observed on the compression side of the beams.

FRACTURE TOUGHNESS

Material toughness is often a secondary consideration in the minimization of cracking. Of primary importance is the design and selection of fatigue-resistant details and quality assurance in the shop during fabrication. Over the past three decades, a number of localized failures have developed in welded structures as a result of fatigue crack growth. In a few cases, subcritical crack growth eventually led to failure of the structure by rapid fracture. Most of these failures could not have been prevented by increased material toughness alone (*20*). However, some such failures have had catastrophic consequences; as a result, emphasis has been placed on forgiving materials and measurement of the appropriate properties.

Toughness of many of the structural aluminum alloys cannot be characterized by any of the currently available standardized test methods (*21*). Given the difficulties in crack tip characterization when the plastic zone is large, a comparison of the fracture behavior of 5456-H116 and A36 steel was undertaken nevertheless. As none of simple screening tests are considered applicable to both aluminum and steel, compact tension samples and *R*-curve testing seemed most suitable. A schematic of a compact tension specimen is shown with some test results in Figure 5. Loads are applied through
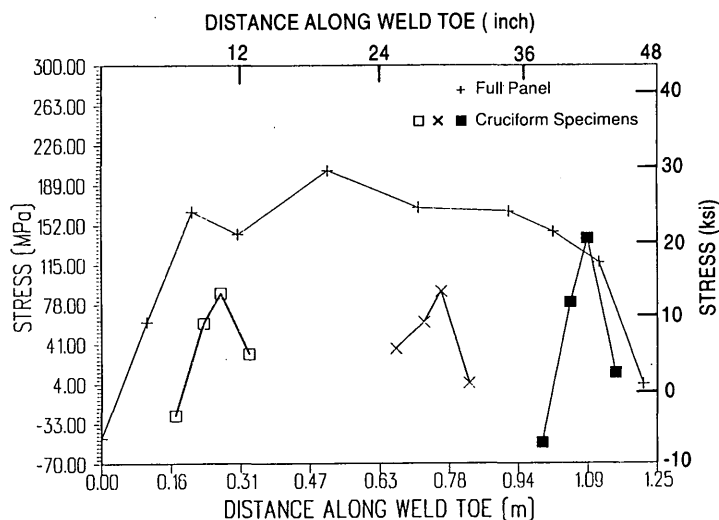
FIGURE 4   Residual stress profile for cruciform panels and fabrication axial specimens.
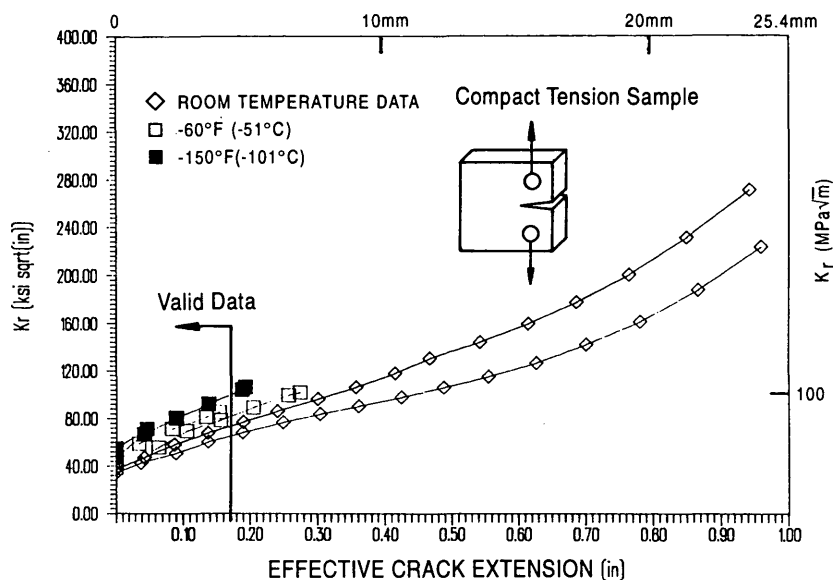
FIGURE 5 Curves for A36 steel specimens tested at +75°F and −150°F.

pins placed in the holes. Because the ductility of both materials would result in prohibitively large specimen dimensions not representative of practical applications, specimens were chosen to be 1.0 in. thick. Tests were conducted at room temperature, −60°F, −150°F, and −200°F. The −60°F toughness requirements are typical of many structural specifications (22).

An *R*-curve is a plot of a material's resistance as a function of effective crack extension. Material resistance may be defined by the stress intensity factor, K_r. From a practical standpoint, K_r is a measure of the magnitude of the stress field around the crack tip. Effective crack extension comprises the physical crack length and the plastic zone correction. Around the tip of a crack is a region where the material is plastically deformed. The presence of such a region makes the crack behave as if it were slightly larger than the physical crack size

itself. Crack extension implies that the increment of crack growth is plotted as the ordinate of the *R* curve.

Figure 5 summarizes the test results for the A36 steel samples over the range of temperatures considered. Room temperature data indicate the development of large toughness values throughout the range of crack growth. Behavior at −60°F and at −150°F is markedly different. Both of these data sets show a reduction in the material's resistance to crack extension. What is more striking is the reduction in amount of stable crack extension before failure. Comparison of fracture surfaces also showed a decrease in shear lip development and specimen thinning as the test temperature was lowered. Smaller amounts of plastic deformation indicate a drop in toughness.

Figure 6 summarizes the aluminum test results for the range of temperatures considered. Room temperature response shows
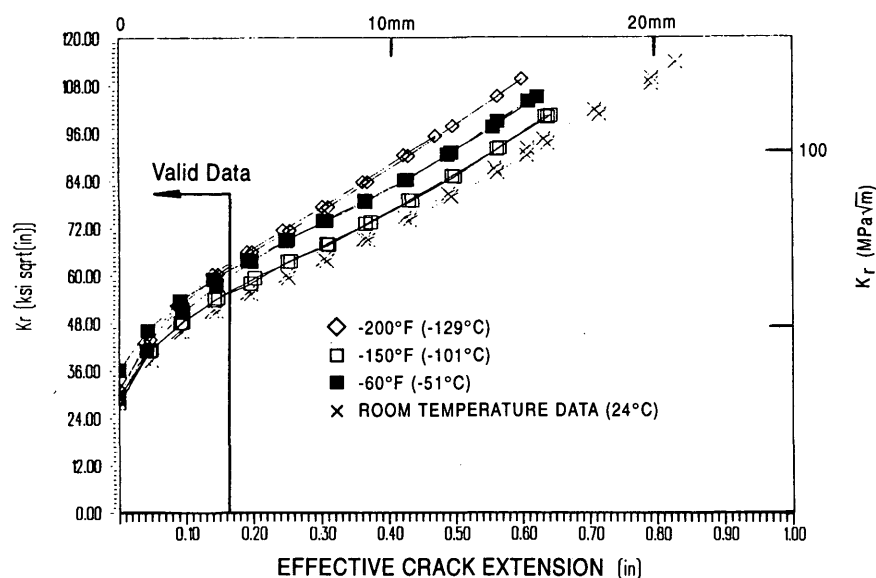
FIGURE 6 Aluminum specimen *R*-curves for the range of temperatures.

a rising *R*-curve throughout the range of stable crack extension. Behavior at the lower temperatures is not significantly different. Although the amount of stable crack extension is somewhat smaller, the difference is less than that observed for the A36 steel. Maximum toughness values increase with a decrease in temperature. Further, all specimens tested showed evidence of plastic deformation, even at the lowest temperature considered.

Both sets of curves show a slight reversal in curvature near the center of the plots. This is indicative of specimens too small to obtain valid, linear elastic test results. Implicit in the calculation of K_r is the assumption of small-scale yielding. Materials with significant ductility are difficult to characterize with any of the currently available techniques. As such, the vertical lines in Figures 5 and 6 indicate the range of valid data. Further, the elevation of toughness with decreasing temperature is consistent with the increase in yield point at lower temperatures. As the temperature is decreased, an equivalent crack opening displacement will require an increase in the load. This will correspond to an increase in the stress intensity factor.

A comparison between aluminum and steel *R*-curves by like temperature conditions reveals several interesting trends. At room temperature, the A36 exhibits larger resistance values over the entire range of stable crack extension. At the lower temperatures, the aluminum samples developed toughness equal to or greater than the A36. Also, the 5456-H116 specimens show a wider range of stable crack extension before failure.

A36 steel has been successfully used in welded structures for many years. Given the difference in modulus values and crack propagation rates, a similar aluminum structure will have dimensions somewhat larger and be designed for lower allowable stresses. As a result, a direct comparison of toughness should be made on resistance values normalized to reflect this difference. Figure 7 compares room temperature R curves

that have been normalized with an effective driving force. Category C constant amplitude fatigue limits of 10 and 4 ksi were used as the applied stress ranges for the steel and aluminum samples respectively. Crack lengths were taken to be those measured in the tests. In the context of allowable fatigue design provisions, the 5456-H116 alloy shows larger resistances to crack extension. The same trend is apparent at lower temperatures as well.

Fatigue tests on full-scale welded beams further demonstrated the ability of 5456-H116 to resist and arrest unstable crack extension under realistic loading conditions. In no case was there rapid fracture that completely severed a beam.

COMPONENT FATIGUE TESTS

Twelve beams were tested in four-point bending. This allowed evaluation of 48 cover-plate details, 96 stiffeners, and 24 butt splices. Tests were conducted using closed-loop servohydraulics with digital control. To accompany the beams, 32 axial tests on cover plates and cruciform joints were completed. All plate thicknesses and weld dimensions were the same on the axial and beam samples to minimize any "thickness" effect. Fatigue cracks on the beams were allowed to grow through the plate thickness; then the damage was repaired by splicing, drilling stop holes, or both. Tests were resumed until failure occurred at another location.

Figure 8 compares the performance of the axial cruciforms and beam stiffener samples. Also shown is the mean regression line for each. As is easily seen, there is a significant difference in the mean resistance of the two sample types. The difference appears to increase with the number of applied cycles. Figure 9 compares the results of the beam tests with the current AA Category C design curve. It should be noted that the specification provides fatigue strengths in tabular form although the continuous curve is shown here. Category
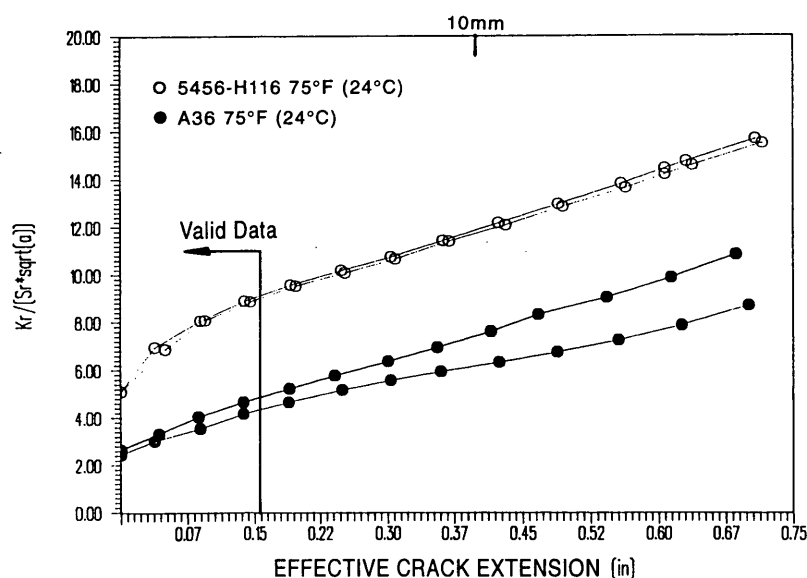
FIGURE 7 **Room-temperature comparison of normalized *R*-curves using Category C.**
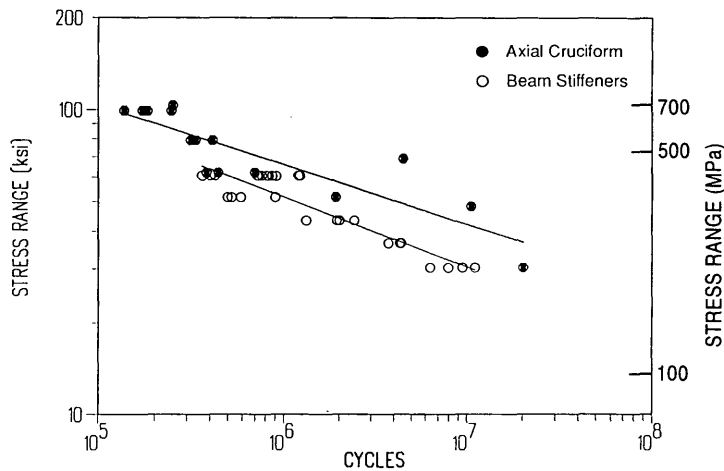
FIGURE 8 Comparison of stiffener details and axial joints with mean regression lines.

C is slightly unconservative as compared with the test results. Several of the points plot on or below the design curve.

The axial cover plate and beam detail test results were compared. Regression analysis used to develop the 95 percent confidence limits for 97.5 percent probability of survival showed a significant difference in the lower-bound fatigue resistance. As expected, the limit for the beam samples is lower than for the axial samples. Figure 10 compares the beam cover-plate data with Category E of the 1986 AA specification. The design category appears to be somewhat conservative. The band of the data appears to be rotated upward as compared with the design curve. Increasing the design strengths may be warranted but will require review of other full-scale data above 2×10^6 cycles.

VARIABLE AMPLITUDE BEHAVIOR MODEL

A fracture mechanics model was developed for the constant amplitude case and verified through comparison with the beam

data. This model was then extended to the case of variable amplitude loadings. Specifics of the model have been discussed elsewhere, and only a review pertinent to assessment and design is presented here.

Stress intensity factors were developed from well-known handbook solutions (23). Crack-growth information for a 5XXX series alloy was taken from a compendium of curves and was based on the K_{max}, ΔK decreasing test procedure (24). Such information is thought to be representative of crack growth in welded structures as closure is diminished. Several shapes of loading spectrums were considered including constant, linear, and Rayleigh distributions. Either the spectrums were shifted or smaller stress cycles were truncated to obtain different characteristic stress range levels. Overloads were applied at different frequencies. An overload is a stress cycle that exceeded the constant amplitude limit. Emphasis was on examining cover-plate details.

Several methods were used to define an equivalent characteristic stress for the distributions. These included a fourth-order transformation of Miner's rule and an equivalent con-
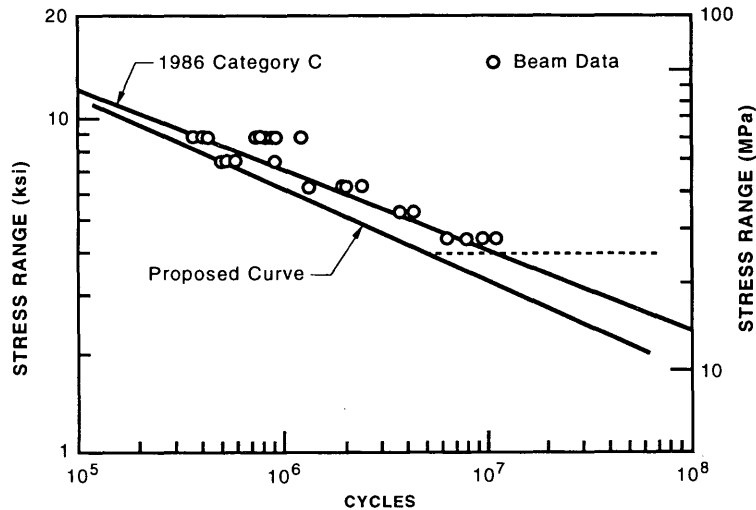
FIGURE 9 Comparison of stiffener test data with current specification Category C and proposed design curve.
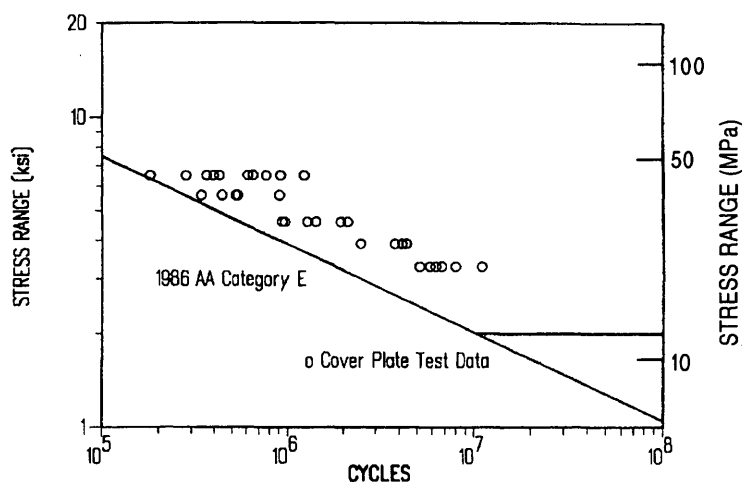
FIGURE 10 Cover-plate data compared with 1986 version AA Code Category E.

stant amplitude stress range that resulted in the same amount of damage. Miner's rule may be given by

$$\sum \left(\frac{n}{N} \right) = 1 \tag{1}$$

where n is the number of cycles applied at a specific stress range and N is the number of cycles to failure at that stress range. Assuming a straight-line S-N relationship, Miner's rule may be transformed to

$$S_{rc} = \left(\sum \alpha_i S_{ri}^b \right)^{1/b} \tag{2}$$

where

α_i = frequency of occurrence of ith stress range,
S_{ri} = ith stress range in spectrum,

b = slope of S-N curve, and
S_{rc} = characteristic stress range for distribution.

For Miner's rule, both nominal stress ranges and effective stress ranges were calculated. Nominal values include all the stress cycles in the spectrum, whereas effective stress ranges include only those cycles contributing to crack growth. General trends in the behavior were the same, regardless of the stress range definition employed.

Figure 11 illustrates the predicted response of the cover plate to a linear stress spectrum shift with overload frequencies varying from 0 to 0.1 percent. Crack growth occurred even though the nominal stress range is below the constant amplitude fatigue limit. The outermost point had a characteristic stress range of 1.7 ksi and a maximum stress in the spectrum only slightly above the fatigue limit of 3 ksi. Overloads of 1.0 ksi plus the maximum stress in the spectrum were considered as well. As the frequency of this overload in-
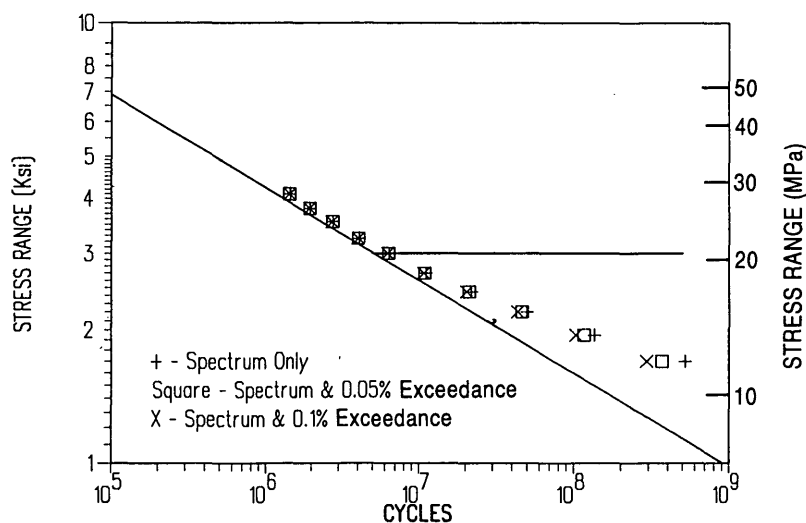
FIGURE 11 Influence of overload on the fatigue resistance of cover plates—linear spectrum.

creases, the S-N curve is pulled downward or the resistance is decreased. This is most pronounced for lives greater than 10^7 cycles. As the number of cycles in the spectrum exceeding the constant amplitude fatigue limit increases, there is little if any influence of the overload.

Figure 12 illustrates cover-plate response to a linear spectrum shift with no overloads but with all three definitions of the characteristic stress. Each curve shows the same general shape, and the difference between the stress ranges at any given life is less than 0.6 ksi. This difference is largest at the lowest stresses considered but becomes significantly smaller as the number of cycles exceeding the fatigue limit increases. In addition, it seems unlikely that stresses can be calculated or measured within a 0.6 ksi spread; so many of the arguments as to which stress definition is correct are of theoretical importance only. This is to be expected, because most cycles in the spectrum contribute to growth when the characteristic stress approaches the fatigue limit. It is interesting to note that the equivalent constant amplitude stress range falls between the bounds as defined by Miner's rule.

SUMMARY

Residual stress measurements confirmed the existence of large tensile residual stresses in full-scale welded aluminum components. Peak stresses were on the order of 80 percent of the parent metal yield strength, but the axial specimens showed maximum values closer to 40 or 50 percent. Measurements on tested, but undamaged, specimens showed that shakedown was minimal and that the residual stresses are present for a significant portion of the fatigue life. For general-purpose design specifications, stress range is the appropriate strength variable and any enhancement at full reversal should not be taken advantage of.

Fracture toughness tests on 5456-H116 illustrated the ability of the material to deform plastically in the presence of a notch at temperatures down to $-200°F$. Comparisons with A36 steel revealed that in the context of allowable fatigue design provisions, the aluminum alloy gave a higher degree of damage tolerance and toughness. Fatigue tests on the beams confirmed the ability of the material to arrest cracks before complete member separation. A36 has been used successfully in welded structures for many years, so a properly designed aluminum structure should give adequate performance.

Component fatigue tests showed that in general, the details on the beams defined the lower bound on fatigue resistance compared to the flat-plate specimens. Current aluminum specifications are slightly overconservative for Category C joints; some adjustment in the Category C allowable design stresses is warranted. Cover-plate beam details did not follow current design provisions. Further long-life data review is warranted before Category E design constraints are relaxed.

An extension of the fracture mechanics model demonstrated that crack growth could occur when the characteristic stress was below the fatigue limit. Furthermore, it seems likely that variable amplitude behavior may be assessed using constant amplitude design data and a fourth-order representation Miner's rule. Comparisons of different characteristic stress definitions showed that the differences were small and were largely of academic interest.

Overloads had the greatest influence on the variable amplitude response when the number of cycles exceeding the fatigue limit was small. As the frequency and magnitude of the overload increased, the high cycle portion of the S-N curve was pulled downward. The result was a reduction in fatigue resistance. When exceedance levels became large, the overload appeared to have no influence on the cover plate behavior. A lack of variable amplitude data makes further recommendations difficult. Additional data are needed for comparison to the models and for further development of design guidelines.
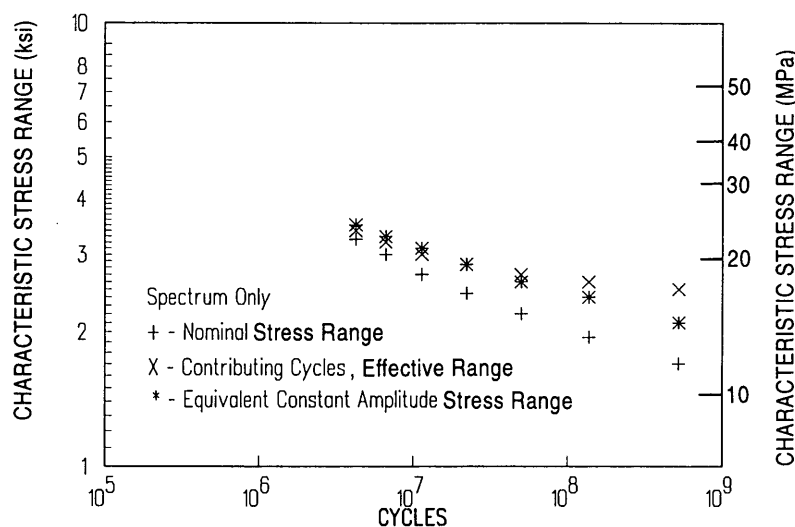
FIGURE 12 Comparison of effective stress range defined by Miner's rule or by crack-growth model.

REFERENCES

1. J. W. Fisher. *Bridge Fatigue-Guide—Design and Details*. American Institute of Steel Construction, Chicago, Ill., 1977.
2. J. W. Fisher and C. Demers. *A Survey of Localized Cracking in Steel Bridges 1981–1988*. ATLSS Report 89-01. Lehigh University, Bethlehem, Pa., 1989.
3. J. W. Fisher and C. Menzemer. *Case Studies and Repair of Fatigue Damaged Structures, Structures Subjected to Repeated Loading*. Stability and Strength Series, No. 9, Elsevier, New York, N.Y., 1990, Chapter 7.
4. *Welding Alcoa Aluminum*. Aluminum Company of America, Pittsburgh, Pa., 1972.
5. *Specifications for Aluminum Structures*. Aluminum Association, Washington, D.C., 1986.
6. W. W. Sanders. *Fatigue Behavior of Aluminum Weldments*. Bulletin 171. Welding Research Council, New York, N.Y., April 1972.
7. W. W. Sanders and R. H. Day. *Fatigue Behavior of Aluminum Alloy Weldments*. Bulletin 286, Welding Research Council, New York, N.Y., Aug. 1983.
8. W. W. Sanders and J. W. Fisher. *Recommended Specifications for Fatigue Design of Aluminum Structures*. Submitted to the Aluminum Association, Washington, D.C., 1985.
9. P. B. Keating and J. W. Fisher. *NCHRP Report 286: Evaluation of Fatigue Tests and Design Criteria on Welded Details*. TRB, National Research Council, Washington, D.C., 1986.
10. D. Kosteas. Fatigue Design—Background, Assumptions, and Practical Concepts. *Proc., 8th International Light Metals Congress*, Vienna, Austria, 1987.
11. R. Jaccard. Fatigue Life Prediction of Aluminum Structures Based on S-N Curve Simulation. *Proc., 2nd International Conference on Aluminum Weldments*, Munich, Germany, 1982.
12. *Structural Welding Code*. American Welding Society, Miami, Fla., 1983.
13. J. Barsom and S. T. Rolfe. *Fracture and Fatigue Control in Structures, Applications of Fracture Mechanics*, 2nd ed. Prentice Hall, Englewood Cliffs, N.J., 1987.
14. A. Mandra, F. M. Mazzolani, and E. Mele. Fatigue of Aluminum Alloy Joints—Comparison of Codification. *Proc., 5th International Aluminum Conference*, Munich, Germany, 1992.
15. I. J. J. Van Straalen, F. Soetens, and O. D. Dijkstra. *Inventory and Comparison of Fatigue Design Codes for Aluminum Alloy Structures*. Report B-89-714. TNO Institute for Building Materials and Structures, Apeldoorn, The Netherlands, 1990.
16. R. Roberts et al. *Determination of Tolerable Flaw Sizes in Full-Scale Welded Bridge Details*. Report FHWA-RD-77-170. FHWA, U.S. Department of Transportation, 1977.
17. S. J. Maddox. Fatigue Design of Welded Aluminum Alloy Structures. *Proc., 2nd International Conference on Aluminum Weldments*, Munich, Germany, 1982.
18. C. Menzemer and J. W. Fisher. Fatigue Behavior of Welded Aluminum Structures. *Proc., 5th International Aluminum Conference*, Munich, Germany, 1992.
19. *Measurement of Residual Stresses by the Hole Drilling Strain Gage Method*. Technical Note 503-3. Measurements Group, Raleigh, N.C., 1988.
20. J. Barsom et al. Fracture Control Considerations for Steel Bridges. *Workshop Proceedings*. FHWA, U.S. Department of Transportation, Atlanta, Ga., 1977.
21. *The Aluminum Association Position on Fracture Toughness Requirements and Quality Control Testing*. Report T-5. Aluminum Association, Washington, D.C., 1971.
22. *Standard Specifications for Highway Bridges*, 13th ed. AASHTO, Washington, D.C., 1983.
23. H. Tada, P. Paris, and G. Irwin. *The Stress Analysis of Cracks Handbook*. Del Research Corp., Hellertown, Pa., 1973.
24. R. Jaccard. *Fatigue Crack Propagation in Aluminum*. Document XIII-1377-90. International Institute of Welding, London, England, 1990.

Economical Steel Box Girder Bridges

KEN D. PRICE

Composite steel box girder bridges have become an effective alternative to more conventional plate girder bridges and concrete girder bridges in North America in the past 25 years. At present a number of innovations taking place in Ontario and elsewhere have the potential of further enhancing the design, durability, constructibility and, by extension, the economics of steel box girder bridges. These innovations include reduction in the number of boxes, posttensioning of the concrete deck, and construction technology. These developments are by no means the end of opportunities to further enhance steel box girder technology. Combinations of steel boxes and concrete boxes, posttensioned decks, single box girder bridges, multiweb and multicell boxes are all design and construction options that have potential. For the evolution of steel box girder bridges to continue, researchers, code writers, and designers must continue to cooperate with owners and agencies to take advantage of current advances in modeling and analysis software, instrumentation and testing technology, and the current trend among designers and researchers to do more full-scale modeling, analysis, and testing of total bridge structures.

Steel box girder bridges have become an accepted method of constructing highway bridges. Significant design and construction advances have occurred in the past 25 years.

THE PAST

In 1965 the "Criteria for Design of Steel-Concrete Composite Box Girder Bridges" were incorporated into the AASHTO bridge specifications. These criteria were based on folded plate analysis methods and scale model testing completed at that time. Richard Fountain presented this background research to the Canadian Society for Civil Engineering in 1968. This research has provided the basis for current code provisions in the AASHTO specifications, Ontario Highway Bridge Design Code (OHBDC), and elsewhere for the past two or more decades.

At the conclusion of his paper, Fountain made the following comment: "By using the least number of boxes practical to support a cross section, it should be possible to obtain designs requiring the least amount of steel. Such designs will also require the least number of boxes to be fabricated and erected" (1). This statement is fundamental to the design principles presented in this paper.

THE PRESENT

There have been a few bridge projects recently for which the designers have reduced the number of boxes to support a

Delcan Corp., 133 Wynford Drive, North York, Ontario, M3C 1K1, Canada.

given cross section. The result has been a corresponding increase in the number of design lanes per box. Some owners and agencies have encouraged this trend through the technical review and approvals process and through inclusion of provisions in current codes that allow designers to move outside the limitations of the original criteria published in 1965, providing they can demonstrate an appropriate methodology for analysis and design. Significant economic advantage can be achieved by reducing the number of boxes required to support a given cross section.

Bridges are complex structures. For this reason, designers have sometimes attempted to reduce their analytical models to simple or continuous beams to reduce the analytical effort. Design codes have reflected this approach. Typically a complex bridge deck is idealized as a beam or an orthotropic plate to assist designers by providing simplified methods of live load distribution. This has resulted in bridges that are difficult to calibrate to the actual design because many important characteristics of the superstructure are ignored in the analytical method. This situation is beginning to change.

Modeling bridges in three dimensions using elements designed to simulate the behavior of actual bridge components is particularly important for steel box girder bridges. Designers are gradually moving in this direction as desktop hardware and software with modeling capability becomes available in the design office. The result will be bridges with a more uniform strength reserve, that are more economical as a result. Researchers can begin to correlate structural responses based on testing to actual designs.

THE FUTURE

The history of box girder bridges in North America is relatively short. Many innovative and cost-effective steel box girder bridges have been constructed in the past 25 years. Future design innovations may include posttensioning of concrete decks, precast decks, multimaterial designs that integrate concrete and steel box girders, multicell/multiuse, and single box bridges. Construction innovations may include more incremental launching and lateral sliding.

Current codes in North America generally provide designers with a simplified method of live load distribution for bridges. This approach is rational for a large percentage of the smaller and less complex structures. However, it may be counterproductive in some respects by limiting designers to approximate solutions and simplified methods of analysis when a more direct method of analysis and design could result in a better understanding of bridge behavior and in significant economies. This is particularly true of larger and more complex structures.

Limiting criteria in current codes restrict the designer to a maximum number of design lanes per box. These criteria are defined by the original research and development on which the current provisions are based and have been used effectively for many years. These limiting criteria should be reviewed carefully to explore box girder configurations outside the limitations of the current code provisions. Further research and development in this area have the potential for increasing the cost-effectiveness of steel box girder bridges in the future.

DESIGN FOR ECONOMY

Fewer Boxes

Steel box girder bridges are inherently more efficient than conventional plate girders and reduce the amount of steel required for bending and shear by virtue of their torsional stiffness and enhanced live load distribution. A significant incidental benefit is the reduced transverse bending in the deck due to better load sharing between boxes and corresponding reductions in differential deflections.

Figure 1 demonstrates schematically how the torsional stiffness of a closed box girder section contributes to better live load distribution in a bridge superstructure.

Several current codes contain the following live load distribution provisions for composite steel box girder bridges. The provisions are in accordance with the 1989 AASHTO bridge specifications, Clause 10.39.2.1, and the 1983 Ontario Highway Bridge Design Code (OHBDC), Clause 3.7.1.4.2(b).

$$W_L = 0.1 + 1.7\,R + \frac{0.85}{N_w} \qquad 0.5 < R < 1.5 \qquad (1)$$
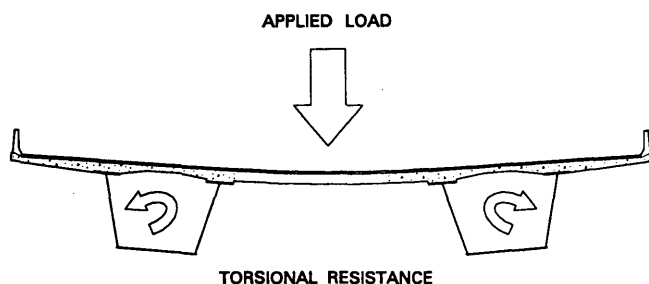
FIGURE 1   Live load distribution.

where

W_L = fraction of wheel load;

$R = \dfrac{N_w}{\text{number of box girders}}$;

N_w = number of design lanes;

N_w = $W_c/12$, reduced to nearest whole number; and

W_c = roadway width between curbs (ft).

As can be observed in Table 1, Ontario designers have typically designed bridges for one design lane per box. This is not accidental, given the limiting criteria for R.

On several recent projects listed in Table 1, there have been significant increases in the ratio of design lanes per box.

Figure 2 demonstrates how the total live load carried by a given cross section decreases as the number of boxes is reduced. In the process, the amount of steel in the bridge has been reduced. This is a result of the inherent torsional behavior that makes steel boxes more efficient for live load distribution, but, more significantly, it is a result of reducing the number of webs. Webs are typically underused in box girder bridges. Minimum thicknesses are required for fabrication and handling. Much of the web in a bridge cross section

TABLE 1 Bridge Design in Ontario

	SPAN (m/ft)	NUMBER OF LANES[a]	NUMBER OF GIRDERS	R
Communication Rd	58/190	2	2	1
Burnstown	76/249	2	2	1
Lacroix	46/151	4	4	1
Whirlpool	50/164	3	3	1
Brimley	51/167	3	3	1
Trenton	74/243	2	2	1
Burlington Bay Skyway	64/210	5	3	1.67
Hunt Club	100/328	3	1	3
Hwy 407	80/262	7	2	3.5
Humber 1	81/266	3+	2	1.5
Humber 2	81/266	5	2	2.5

[a] Design Lanes as defined by AASHTO (1989) and OHBDC (1983)

WL (PER BOX) = 2.01 x 4 BOXES (R = 1)

TOTAL = 8.04 WHEEL LOADS

WL (PER BOX) = 2.57 x 3 BOXES (R = 1.33)

TOTAL = 7.71 WHEEL LOADS

WL (PER BOX) = 3.71 x 2 BOXES (R = 2) *

TOTAL = 7.42 WHEEL LOADS

* EXCEEDS CURRENT AASHTO LIMITATIONS
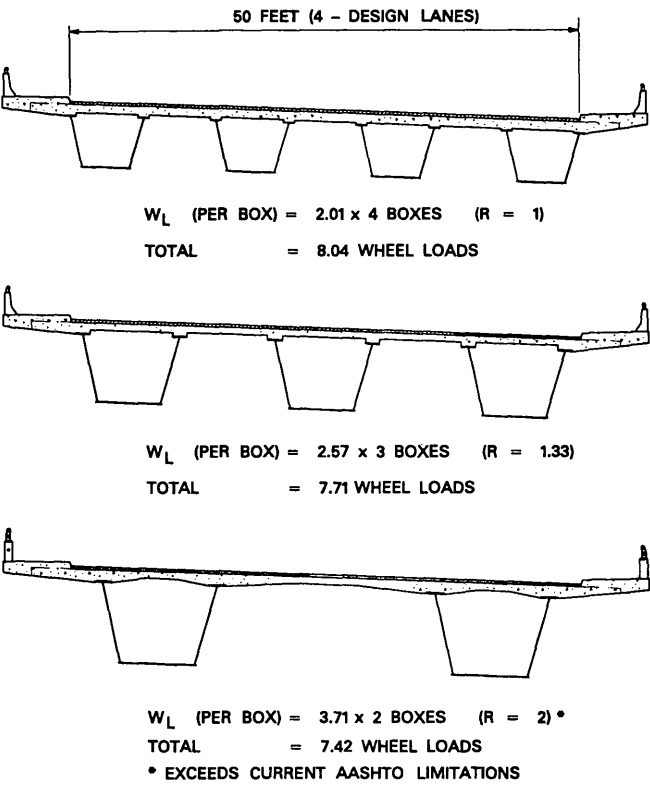
FIGURE 2   Total live load.

'is required to provide a reasonable separation between the top and bottom flanges and occurs in areas of relatively low shear.

Redundancy and Fatigue

Redundancy becomes an issue in multispine bridges where the number of spines is reduced. Several factors alleviate this concern for box girder bridges:

● As the number of girders is decreased, the ratio of dead load to live load increases. This in turn reduces the stress ranges for fatigue and the potential for fatigue problems.
● Boxes consist of individual plate elements. It can be argued that as such, even single box girder bridges have multiple load paths and significant redistribution potential.
● Fatigue cracks in the web will typically commence in regions of high stress and move toward regions of lower stress. This has the effect of slowing rather than accelerating the propagation of these cracks.
● Sometimes the designer will choose to carry longitudinal bottom flange stiffeners continuously through positive moment regions for stability and strength, particularly during construction. This provides additional load paths should fatigue cracks develop in the flanges.
● The same arguments can be applied to longitudinal web stiffeners.
● Quality control continues to improve in fabricating plants. Fully automated welding, NDT methods, and girder building machines are increasing the quality of the finished product.

Unit Weight of Steel

Figure 3 represents the relationship between the unit weight of steel in a bridge relative to its longest span. These curves represent a data base of several hundred steel bridges constructed in Ontario between 1980 and 1990. Several observations can be made from this figure:

● Single-span bridges become inefficient compared to multispan bridges in the range of 40 m (130 ft).
● The unit weight of steel for multispan continuous bridges is linearly proportional to the span.
● The unit weight of steel is consistently reduced where the number of boxes is reduced ($R > 1.5$) on the basis of these data.

Figure 4 illustrates an actual bridge for which an alternative preliminary design was completed using two boxes instead of four. This bridge is a five-span structure with main spans of 72 m (236 ft) and an overall length of 319 m (1,047 ft). The alternative design reduced the total weight of steel in the structure by 500 tonnes (550 tons), or about 20 percent of the total.

Longer Transverse Deck Spans

Reducing the number of boxes increases the transverse deck spans. This could be considered a disadvantage. Several solutions to this apparent disadvantage could be considered by the designer:

● Increasing the deck thickness,
● Vaulting the deck soffit,
● Considering arching action, or
● Transverse posttensioning.

Increasing the deck thickness, within limits, can have certain benefits: increased stiffness, reduced cracking, increased mass, and better dynamics are examples. The cost of material and forming probably begin to offset these benefits for average deck thicknesses of more than 250 to 300 mm (10 to 12 in.).
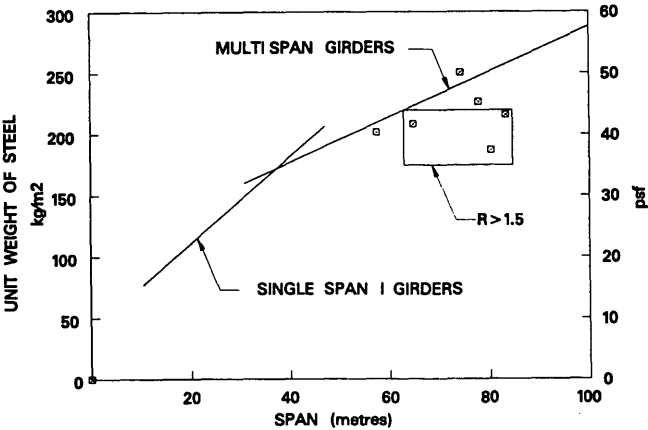
FIGURE 3   Unit weight of steel.
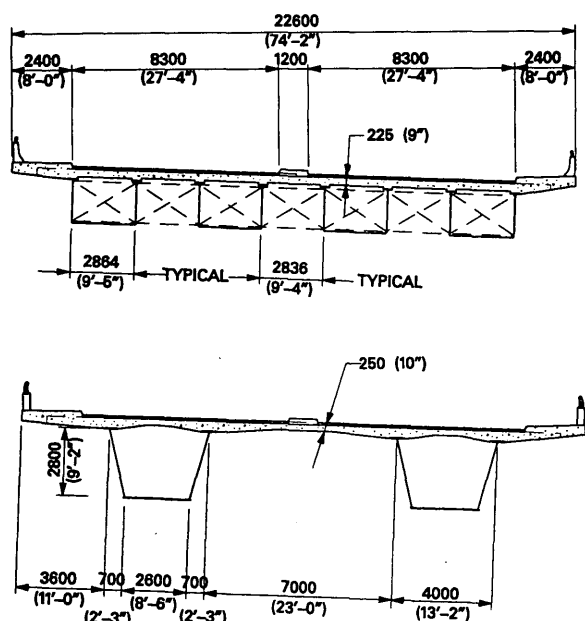
FIGURE 4 Longer deck spans: *top*, conventional cross section; *bottom*, alternative cross sections.

Vaulting the deck results in a thicker deck, which requires more concrete. Some benefits are associated with this practice, including enhanced durability and damping of dynamic effects.

Deck arching becomes more effective in resisting live loads when the deck thickness is increased. Deck arching has been adopted by some agencies (such as Ontario) when certain geometric criteria are met; it reduces significantly the amount of reinforcing steel needed.

Current code provisions have relatively stringent requirements for the maximum tensile stress in concrete decks. The result can be a significant amount of reinforcing steel for longer spans. Transverse posttensioning is a cost-effective way of controlling the maximum design tensile stress, providing the required strength and reducing the amount of normal reinforcement at the same time.

As the deck span increases between adjacent girders, the designers must consider the distribution of both live load and dead load effects for the following components and configuration of the design:

● Framing,
● Transverse deck bending,
● Girder torsion, and
● Bearing configuration.

The relative stiffness and interaction of these elements is fundamental to the behavior of a steel box girder bridge. If the designer wishes to consider single bearings, for example, the torsional effectiveness of the girders for live load distribution may be significantly reduced as the torsional fixity provided by double bearings is eliminated. This has the effect of redistributing torsional effects into the cross frames and the deck.

Deck Posttensioning

As a result of reducing the number of boxes, the transverse deck span can exceed the practical limits for normally reinforced concrete and transverse posttensioning becomes necessary. The transition to posttensioning appears to be necessary in the range of 5 to 6 m (16–20 ft).

The following parameters were used on a recent bridge using transverse posttensioning in Ontario: the clear span between boxes was 9.86 m (32 ft 4 in.); the deck thickness varied from 260 to 460 mm (10.24 to 20 in.). The transverse posttensioning consisted of four 15-mm (⅝ in.) strands at 700-mm (30-in.) centers.

The cross section of this bridge is illustrated in Figure 5. Figure 6 is a schematic representation of the posttensioning layout, staging, profiles, and type. This deck was posttensioned using a combination of strand and threadbar to accommodate geometric and staging constraints.

Table 2 gives some of the key data used for this posttensioning design. The amount of reinforcing steel compares favorably to Ontario deck designs, which average 30 to 40 kg/m² (6 to 8 lb/ft²) based on the empirical deck design provisions of the OHBDC, and transverse deck spans that vary from 2 to 4 m (6 to 12 ft). Posttensioning the deck can have significant
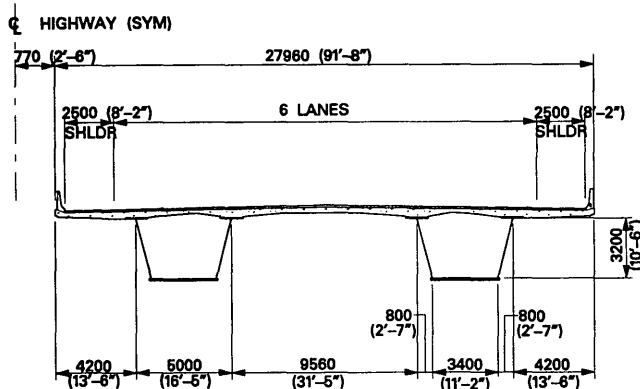
FIGURE 5 Posttensioned deck, Highway 407.
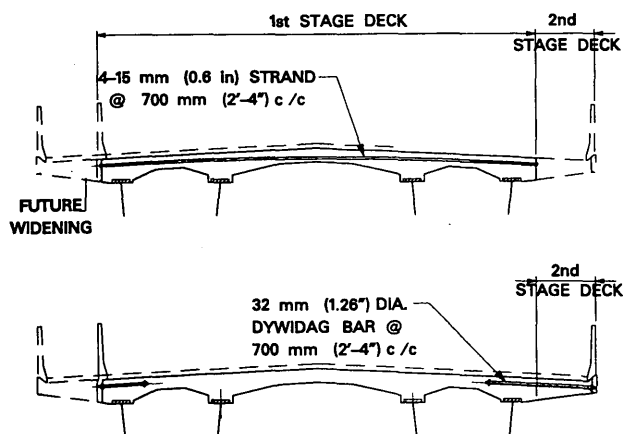
FIGURE 6 Posttensioning profiles: *top*, strand; *bottom*, threadbar.

TABLE 2 Key Data Used for Posttensioning Design

Datum	Value
Class of concrete	40 MPa (5800 psi)
Ultimate tensile strength of transverse strand	1860 MPA (270 ksi)
Ultimate tensile strength of transverse threadbar	1030 MPa (150 ksi)
Average transverse prestress in concrete deck	1.49 to 3.18 MPa (216 to 462 psi)
Maximum design tensile stress at SLS II[a]	1.52 MPa (220 psi)
Maximum design compression stress at SLS II[a]	15.98 MPa (2,320 psi)
Total weight of posttensioning steel	9.2 kg/m² (1.88 psf)
Total weight of reinforcing steel	46.0 kg/m² (9.42 psf)

[a]SLS II refers to Serviceability Limit State II as defined by the 1983 OHBDC. This limit state limits deformations and cracking.

advantages relative to the amount of reinforcing required for longer transverse spans.

These decks responses, and in particular the maximum design tensile stress, conform to the ASSHTO criteria of 1.57 MPa (228 psi) for severe exposure conditions. The amount of transverse reinforcing steel required for this design consisted of 20M bars at 225 mm (No. 6 bars at 8.5 in.) top and bottom.

In some cases, depending on the relative transverse spans, cross-frame stiffness and box girder proportions, transverse posttensioning effects can result in a significant redistribution of bearing reactions and axial forces in crossframes. The designer must account for these effects in the analysis and design.

Bracing, Framing, and Diaphragms

Several different elements of the framing and bracing systems are effective in distributing live and dead loads through the structure:

- Cross frames between boxes,
- Diaphragms inside and outside the boxes,
- Upper lateral bracing inside the boxes, and
- Distortion bracing within the boxes.

It is imperative that the designer take full account of the proposed bracing configurations and the relative stiffness of each for the distribution of both dead and live loads within the structure. In many cases dead load governs the design—particularly for larger spans, bigger boxes, and wide cross sections. Staged placement of the deck concrete can produce very different responses within the steel girder and bracing systems than the responses predicted by simultaneous placement of the deck. This factor becomes important as the spans increase over 60 m (200 ft) in conjunction with transverse eccentricity of the dead load relative to the shear center of the boxes.

One bracing option and associated details are shown schematically in Figure 7. This continuous transverse framing system is carried into each box and occurs at quarter points.

Nonprismatic Girders

Intermediate- and long-span bridge girders with the same approximate shape as the bending moment diagram use material
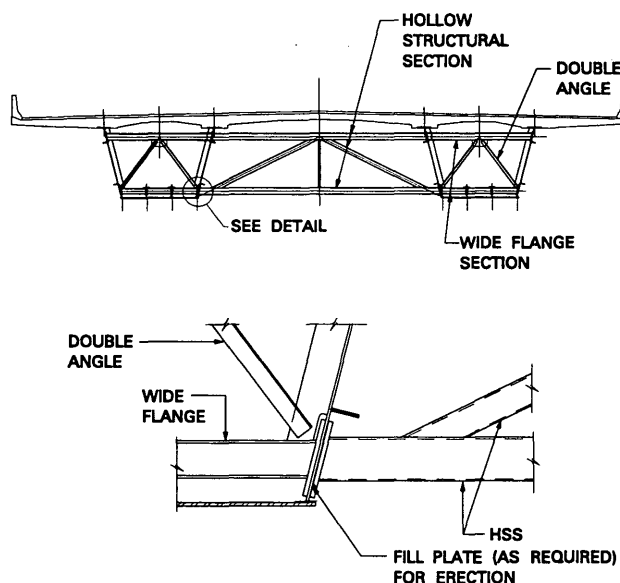
FIGURE 7 Crossframe (*top*) and detail (*bottom*).

most efficiently. In most cases it is possible to reduce, and in some cases even eliminate, changes in flange-plate thickness. This has the benefit of reducing fabrication costs associated with shop splices.

In addition to the above, haunched girders typically are reduced in depth in regions where there is reduced shear with associated material savings in the web.

Fountain originally predicted that a span-to-depth ratio (*L/d*) for box girders in the range of 25 would result in the most economical design. He also noted that box girders would conform to current AASHTO provisions for live load deflection with a span-to-depth ratio as high as 40. Typically in Ontario, noncomposite span-to-depth ratios are in the order of 30 to 32 and composite ratios are in the order of 28. Deeper girders have been used when incremental launching is proposed, to control cantilever deflections when necessary.

A nonprismatic girder can be proportioned in such a way as to require a single thickness of bottom flange throughout the entire bridge. This minimizes the need for bottom flange shop splices at thickness changes. For example, a three-span bridge with spans of 32 × 46 × 32 m (105 × 151 × 105 ft) was designed recently with a continuous 16-mm (⅝-in.) bottom flange plate throughout the entire bridge. The span-to-

depth ratio at the piers was 27 and at midspan, 42. This resulted in a very economical steel box.

Use of a nonprismatic girder usually results in material savings when the design is properly executed. With the use of modern digitally controlled cutting machines there is little, if any, cost penalty in fabricating webs with variable depths. Webs are frequently cut to a profile for curvature or camber in any event.

Trapezoidal Section

The typical trapezoidal section used in many box girder bridges has the benefit of allowing the designer to provide the same amount of material required in the bottom flange for bending in a thicker plate. This increases the stability of the wider bottom flanges and reduces the need for longitudinal stiffening.

Typically the neutral axis goes up in a trapezoidal section and makes the bottom flange more efficient. This does not necessarily mitigate against the efficiency of the top flange because most of the load in the top flange is dead load due to composite action of the deck for live loads.

In addition, the trapezoidal shape is inherently more stable for fabrication and erection and reduces the fatigue problems arising from secondary vibrations.

Software

There is good news for the designers of larger and more complex steel box girder bridges. Software exists that enables the designer to model, analyze, and design for the specific responses of a complex box girder bridge of any configuration. If the designer had to list modeling, analysis, and design tools in order of importance, accurate bridge modeling would probably be the most important tool. The value of a software package that provides the designer with the tools for building a realistic yet practical model of his bridge for analysis cannot be overestimated.

DESIGN FOR CONSTRUCTION

Erection Methods

Designers should work closely with contractors for construction design. Specialist contracting experience exists that, if properly considered during design, can be effectively incorporated into the contract documents without eliminating effective competition, and can reduce construction costs.

Conventional Techniques

More and more structures are being constructed in urban areas where access is increasingly difficult because of built-up conditions and adjacent infrastructure. These conditions make the erection of steel girders more attractive where field sections can be placed quickly at night with limited impact on the traveling public. By contrast, falsework construction for concrete bridges can be expensive, time-consuming, and in many cases disruptive.

Reducing the number of boxes will generally result in fewer field sections. Fewer field sections means fewer field splices.

Offsetting this advantage is the fact that the field sections will generally increase in weight. Field sections should be sized as a function of local fabricator and contractor capability. Fabricators and contractors normally prefer to fabricate sections that are a maximum of 45 tonnes (50 tons) but are capable of increasingly large sections, in some cases up to 105 tonnes (115 tons) or more.

Incremental Launching

Reducing the number of boxes is a direct advantage for steel bridges that must be incrementally launched.

In some cases, new infrastructure projects for "green field" locations are subject to increasingly onerous environmental restrictions. In other cases, existing transportation functions or site topography impose significant limiting criteria for conventional construction techniques. Mobilization of large cranes and delivery of field sections to environmentally sensitive or functionally difficult locations are specifically prohibited by owners and other agencies. Steel boxes are ideally suited for incrementally launching given their relatively light weight and inherent torsional stability (particularly on curved bridges), their reduced self-weight relative to concrete, and the fact that they can be fabricated off-site and off the critical path for construction.

One of the advantages to incremental launching of steel box girder bridges is that in most cases they can be launched over longer spans without the expensive intermediate piers and bents required for incrementally launched concrete bridges. In addition, steel boxes require very limited additional design effort or material to be added to the girder section for launching. Incrementally launched concrete structures must be designed specifically for the launching conditions because of the dead weight associated with concrete cantilevers. Concrete structures likewise are very sensitive to dimensional tolerances and elastic/inelastic deformations. Steel structures are forgiving and can experience large elastic deformations without distress. During launching, steel box girders are typically braced at the top flange, resulting in a quasiclosed section that is torsionally relatively flexible. This arrangement provides torsional as well as flexural flexibility during launching that assists in redistribution of launching reactions between webs.

Sliding: A Case Study

Steel bridges provide the opportunity for innovative construction techniques. The opportunities sometimes increase as the number of boxes is reduced.

The city of Trenton in Ontario, Canada, requested consultants to submit a technical proposal for replacing an existing swing bridge. The bridge spanned a busy recreational waterway on a major highway feeding the central business district of a popular tourist town. The owner specified several constraints:

• The new bridge was to be a fixed-span high-level crossing to replace the existing swing span, which was becoming more and more expensive to operate and maintain.
• The new bridge was to be located in the same position as the existing structure to avoid any property acquisition on the main street through town.

• The new bridge was to be constructed without any impact on existing traffic operations through the central business district.

• The new bridge was to be constructed without any impact on existing recreational boat traffic.

The solution consisted of a high-level fixed three-span box girder bridge constructed in a temporary location adjacent to the existing bridge. Construction was scheduled so the new bridge could be built around the seasonal operation of the existing swing span and then at off-peak hours be slid into its final position in the location of the existing bridge. The final bridge was 184 m (518 ft) long, carried two lanes of traffic and two sidewalks, and weighed 3000 tonnes (3,300 tons). It was slid into its final location in 3 hr 20 min.

Steel box girder technology provided the solution to construction over a busy waterway without interruption to recreational traffic and resulted in a structure light enough to be relocated easily in a short time.

DESIGN FOR REHABILITATION

How Long Do Bridges Live?

Several factors should increase the durability, lifespan, and feasibility of rehabilitation of steel girder bridges with a reduced number of boxes and longer posttensioned transverse deck spans. These include

• Increased thickness of deck,

• Controlled cracking resulting from posttensioning,

• Increased capacity to carry live load under partial deck demolition, and

• Staged deck replacement.

Recent statistics published by the Organization for Economic Cooperation and Development (2) on the average lifespan of bridges in Europe indicate that bridges are usually replaced for functional reasons before they reach their structural life expectancy. Life expectancies for a sample population of steel and concrete bridges using an a posteriori estimation of bridge life were reported as follows:

Bridge Material	Estimated Life (years)
Steel	63
Reinforced concrete	59
Prestressed concrete	33

This study indicates that steel bridges can be expected to last at least as long as concrete bridges. The bridge designer should be sensitive to measures that make the bridge more durable in the first place and that facilitate future rehabilitation.

What Components Die First?

Recent analysis of National Bridge Inventory (NBI) data in the United States (3) has indicated that the most common source of deficiencies in prestressed bridges is the concrete deck. This is no doubt true of steel bridges as well.

One of the significant advantages of a slab-on-girder type of structure is the fact that the deck can be replaced relatively simply compared to a concrete box girder bridge. Replace-

ment can often be accomplished incrementally under live traffic conditions.

Other components of the superstructure can easily be replaced or repaired on steel girder bridges to extend their service life and increasing load-carrying capacity where required.

What To Do?

On the evidence that deck components are often the most common cause of deficiencies, two options could be considered: (a) design decks to last longer in the first instance, and (b) design decks as throwaway components to be replaced when they have reached the end of their service life.

Slightly thicker concrete decks associated with longer transverse spans that are transversely posttensioned should last longer than thin decks using conventional reinforced concrete.

Steel structures that can be designed in the manner described can be very attractive in the long term when total life-cycle costs are considered, especially if they are capable of significantly reducing negative impacts on existing traffic functions at the same time.

CONCLUSIONS

Reduce the number of boxes wherever possible in steel box girder bridges. This design principle will result in more efficient box girder bridges for both design and construction.

• The amount of steel can be reduced. This results in reducing fabricating cost, which is typically labor-intensive.

• Posttensioned decks are a cost-effective solution to longer transverse deck spans. Conventional posttensioning in the transverse direction can be introduced to enhance the strength and durability of longer transverse deck spans.

• Construction technology such as incremental launching is cost-effective in many structures. A reduced number of boxes lends itself well to this technique. Launching is a proven solution where site constraints mitigate against conventional erection techniques. Owners and designers should address the feasibility of incremental launching on a site-specific basis to satisfy specific environmental or infrastructure constraints.

Reducing the number of boxes in a bridge cross section will, in some cases, result in increased analytical effort. This could well be an advantage, as the increased understanding of steel box girder structures will result in more economical structures and further design developments that will further advance the state of the art for steel box girder bridges. This benefit should more than offset the additional design effort.

REFERENCES

1. *Proc., Canadian Structural Engineering Conference*, University of Toronto, Canadian Institute of Steel Construction, Toronto, Ontario, 1968.
2. OECD Scientific Expert Group. *Bridge Management*. OECD, 1992, Table IV 3, p. 60.
3. Performance of Prestressed Concrete Highway Bridges in the United States—The First 40 Years. *PCI Journal*, May–June 1992, pp. 48–62.

Vibration and Impact in Multigirder Steel Bridges

Ton-Lo Wang, Dongzhou Huang, and Mohsen Shahawy

Vibration and impact due to multiple vehicles moving across rough bridge decks are studied in seven steel multigirder bridges with different span lengths. The bridges are modeled as grillage beam systems. The vehicle is simulated as a nonlinear vehicle model with 12 degrees of freedom according to the HS20-44 truck design loading specified by AASHTO. Four classes of road surface roughness generated from power spectral density function for the approach roadways and bridge decks are used in the analysis. The results indicate that the impact of exterior girders of short-span bridges are highly sensitive to lateral loading position, vehicle weight, road roughness, and so forth. Maximum impact factors of girders were obtained for two trucks (side by side) through changing their transverse positions, with different speeds and road surface roughness. Results are useful for the bridge design and the further study of impact formula proposed by AASHTO.

The impact on highway bridges of vehicles passing across the spans is a significant problem of interest to bridge engineers. A considerable amount of literature exists on this subject. The literature most relevant to this study concerns code provisions, experimental impact values, and the models for vehicles and bridges used in analytical studies.

The 1989 AASHTO specifications (1) are the basis for the design of highway bridges in many countries. They specify

$$I = \frac{50}{(L + 125)} \tag{1}$$

where I is an impact factor not greater than 0.3, and L is the loaded length in feet. The 1983 Ontario Bridge Design Code (2) has introduced more conservative values of I.

In the past two decades, many experimental studies reported that high impact occurred in some highway bridges (3–7). Many papers on the theoretical study of the dynamic loading of girder bridges have been published during the past three decades (8–11). The theoretical and experimental investigations indicate that the impact of a bridge depends on many factors: (a) the type of bridge and its natural frequencies of vibration, (b) vehicle characteristics, (c) speed of the vehicle, (d) the profile of approach roadway and of bridge deck, (e) the damping characteristics of bridge and vehicle, (f) weight of the vehicle, and so forth.

However, most of these previous studies used a planar beam model or orthotropic model to simulate bridge structure and a single car to simulate vehicle loading. A recent investigation

T.-L. Wang, D. Z. Huang, Department of Civil and Environmental Engineering, Florida International University, Miami, Fla. 33199. M. Shahawy, Structures Research and Testing Center, Florida Department of Transportation, Tallahassee, Fla. 32310.

by Wang and Huang (12,13) has shown that the impact of bridges was greatly influenced by the wheel-load distribution, and the impact of each girder is not same. Nevertheless, a thorough investigation on this subject needs to be conducted.

The present objective is to analyze systematically the vibration and impact of multigirder steel bridges with seven span lengths from 35 to 140 ft (10.67 to 42.67 m), under the passage of design vehicle loading. The results obtained are useful for further theoretical and field study of bridge impact as well as for modification of highway bridge design specifications.

MATHEMATICAL MODEL FOR VEHICLE

The mathematical model for HS20-44 truck loading is illustrated in Figure 1. The nonlinear vehicle model consists of five rigid masses representing the tractor, semitrailer, steer wheel/axle set, tractor wheel/axle set, and trailer wheel/axle set, respectively. In the model, the tractor and semitrailer were each assigned 3 degrees of freedom (df), corresponding to the vertical displacement (y), rotation about the transverse axis (pitch, or θ), and rotation about the longitudinal axis (roll, or ϕ). Each wheel/axle set is provided with two df in the vertical and roll directions. The total degrees of freedom are 12. The tractor and semitrailer were interconnected at the pivot point (the so-called fifth wheel point; see Figure 1). Both distances between the steer axle and the tractor axle as well as the tractor axle and the trailer axle are taken as 14 ft (4.27 m). The equations of motion of the system were derived by using Lagrange's formulation. Details of derivation and data are discussed by Wang and Huang (13).

ROAD SURFACE ROUGHNESS

The power spectral density (PSD) functions for highway surface roughness have been developed by Dodds and Robson (14) and modified by Wang and Huang (13). They are shown as

$$S(\bar{\phi}) = A_r \left(\frac{\bar{\phi}}{\bar{\phi}_0}\right)^{-2} \tag{2}$$

where

$S(\bar{\phi})$ = PSD (m²/cycle/m)
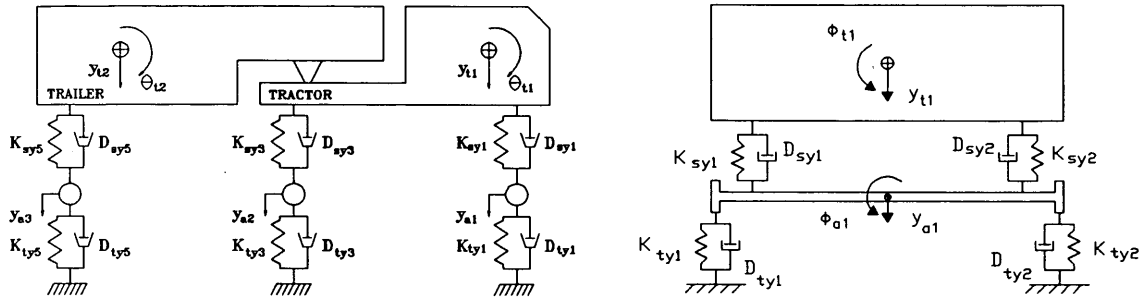$\bar{\phi}$, = wave number (cycle/m),

FIGURE 1 HS20-44 vehicle model: *left*, side view; *right*, front view.

A_r = roughness coefficient (m³/cycle)
$\bar{\phi}_0$ = discontinuity frequency = $1/(2\pi)$ (cycle/m).

The detail of the procedure has been discussed by Wang and Huang (*13*). In this study, the values of 5×10^{-6}, 20×10^{-6}, 80×10^{-6}, and 256×10^{-6} m³/cycle were used according to International Organization for Standardization (ISO) specifications (*15*) as the roughness coefficient A_r for the classes of very good, good, average, and poor roads, respectively. The sample length was taken as 256 m (839.9 ft), and 2,048 (2^{11}) data points were generated for this distance. The average vertical highway surface profiles from five simulations are shown in Figure 2.

BRIDGE MODEL AND EQUATIONS OF MOTION

To study the general impact behavior of steel multigirder bridges, seven highway steel bridges were designed according to 1989 AASHTO specifications (*1*) and the 1982 Standard Plans for Highway Bridges of the U.S. Department of Transportation (*16*). The span lengths range from 35 to 140 ft (10.67 to 42.67 m). These bridges are designed for the HS20-44 loading. Figure 3 (*top*) shows the typical bridge cross section. All seven bridges consist of five identical girders that are simply supported. The plan of the bridge with a span of 100 ft is given in Figure 3 (*bottom*); the other bridges have similar arrangements. The number of diaphragms for bridges with span lengths of 35, 45, 55, 75, 100, 120, and 140 ft (1 ft = 0.305 m) are 1, 1, 2, 2, 3, 4, and 5, respectively. The primary bridge data are given in Table 1.

The multigirder bridges are treated as grillage beam systems (Figure 4). Dynamic response of the bridge was analyzed with finite element method. The bridge was divided into grillage elements (Figure 5). The node parameters are

$$\{\delta\}^e = \begin{Bmatrix} \delta_i \\ \delta_j \end{Bmatrix} \tag{3}$$

where

$\{\delta_i\} = [w_{zi}\ \theta_{xi}\ \theta_{yi}]^T$ = displacement vector of left joint,
$\{\delta_j\} = [w_{zj}\ \theta_{xj}\ \theta_{yj}]^T$ = displacement vector of right joint,
w = vertical displacement in z-direction, and
θ_x, θ_y = rotational displacements about x- and y-axes, respectively.

The equations of motion of the bridge are

$$[M_B]\{\ddot{\delta}\} + [D_B]\{\dot{\delta}\} + [K_B]\{\delta\} = \{F_{BT}\} \tag{4}$$

where

$[M_B]$ = global mass matrix;
$[K_B]$ = global stiffness matrix;
$[D_B]$ = global damping matrix;
$\{\delta\}, \{\dot{\delta}\}, \{\ddot{\delta}\}$ = global nodal displacement, velocity, acceleration vectors; and
$\{F_{BT}\}$ = global nodal loading vector, resulting from interaction between bridge and vehicle.

INTERACTION EQUATIONS AND NUMERICAL METHODS

The interaction force of the *i*th axle between the bridge and vehicle is given as

$$F^i_{BT} = K_{tyi}U_{tyi} + D_{tyi}\dot{U}_{tyi} \tag{5}$$

where

K_{tyi} = tire stiffness of *i*th axle,
D_{tyi} = tire damping coefficient of *i*th axle, and
U_{tyi} = relative displacement between *i*th axle and bridge
= $y_{si} - (-u_{sri}) - (-w_{bi})$, where y_{ai} = vertical displacement of *i*th axle,
u_{sri} = road surface roughness under *i*th axle (positive upward), and
w_{bi} = bridge vertical displacement under *i*th axle (positive upward); w_{bi} can be evaluated by nodal displacements $\{\delta\}^e$ of element and displacement interpolation function of element (*12*); a dot superscript denotes differential with respect to time.

The equations of motion of the vehicle are nonlinear, while those of the bridge are considered linear. According to the different characteristics of the equations of motion, the fourth-order Runge-Kutta integration scheme (*17*) was used to solve the equations of motion of the vehicle, while the solutions of those of the bridge were determined by the mode-superposition procedure based on the subspace iteration method. The main procedure for dynamic analysis of the bridges is discussed elsewhere (*12*).
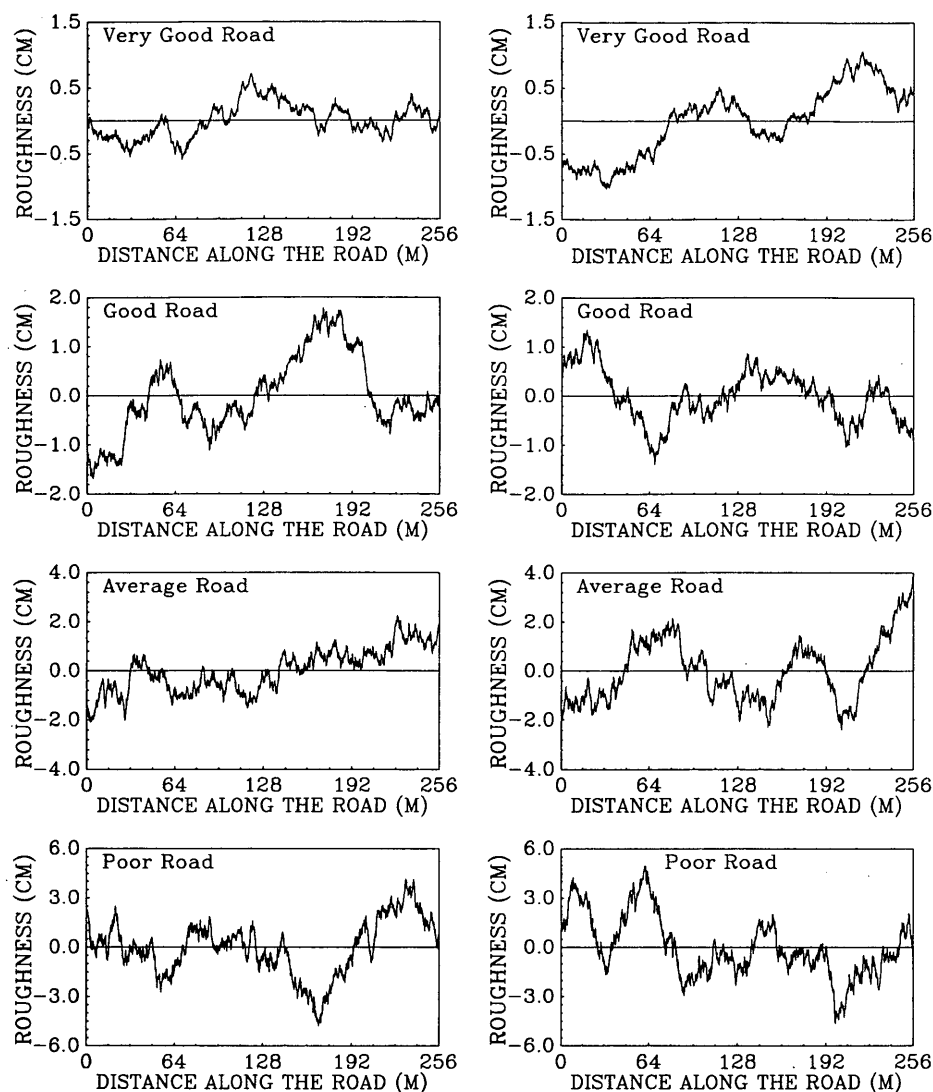
FIGURE 2 Vertical highway surface profiles: *left*, right line; *right*, left line.

VIBRATION AND IMPACT CHARACTERISTICS

It is assumed that the bridges have damping characteristics that can be modeled as viscous. One percent of critical damping is adopted for the first and second modes according to the experiment results. The mode-damping coefficients were determined by using an approach described by Clough and Penzien (*18*). To obtain the initial displacements and velocities of vehicle degrees of freedom when the vehicle entered the bridge, the vehicle was started in motion at a distance of 140 ft (42.67 m, i.e., a five-car length) away from the left end of the bridge and continued moving until the entire vehicle cleared the right end of the bridge. The same class of road surface was assumed for both the approach roadways and bridge decks.

Table 2 presents the first six frequencies of each bridge. From the table, it is apparent that the first two frequencies of each bridge—corresponding with bending and torsion modes, respectively—are nearly the same.

To learn the space impact characteristics of multigirder bridges, two loading cases, symmetric and asymmetric loadings of a single truck [Figure 6 (*top*) Loading 1 and Loading 2], are considered. Under the conditions of vehicle speed of 45 mph (72.41 km/hr) and good road surface, the lateral wheel-load distribution factors and impact factors of three bridges with span lengths of 35, 55, and 100 ft (10.67, 16.75, and 30.48 m), respectively, are computed and shown in Figure 7. The wheel-load distribution factor acquired for the study is defined as

$$\eta = F_{MQi}/F_{MQt} \tag{6}$$

where

$F_{MQt} = F_{MQ}/n$

F_{MQ} = sum of bending moment or shear of all girders at one section,

n = number of wheel-loads in transverse direction, and
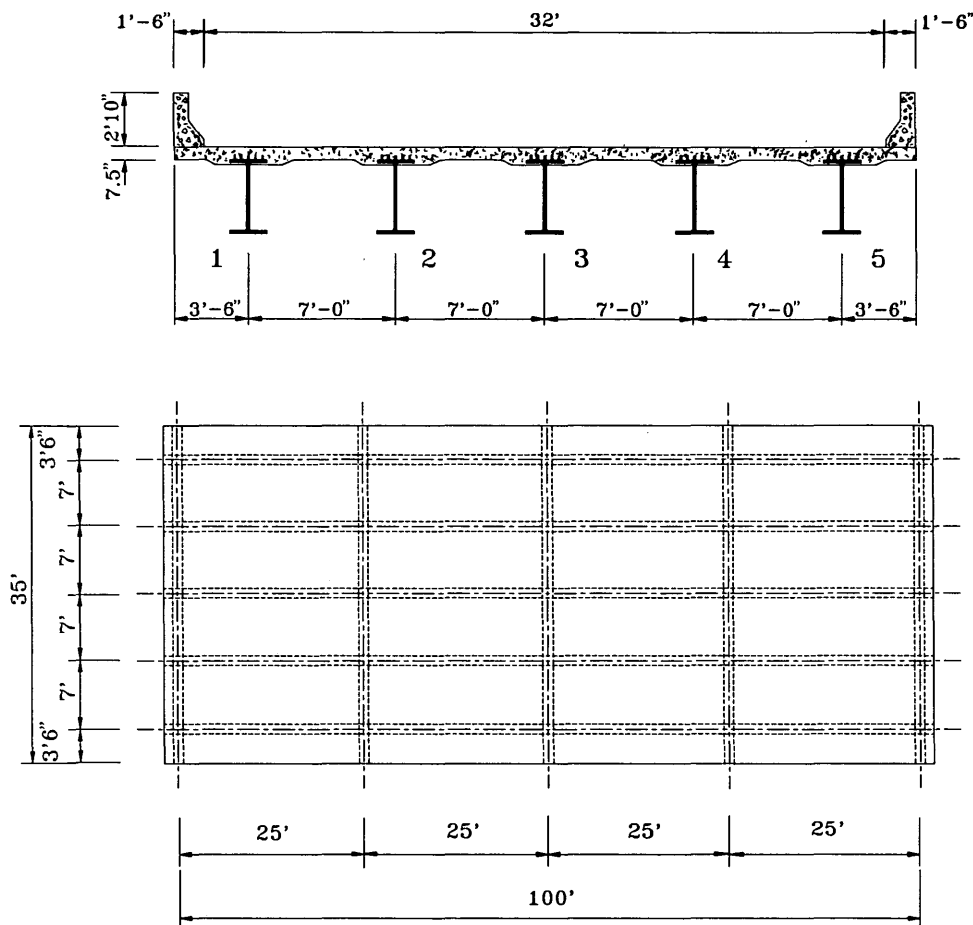
FIGURE 3 Typical analytical bridge: *top*, typical cross section; *bottom*, typical plan.

TABLE 1 Properties and Masses of Bridges

Span length ft	Girder				Intermediate diaphragm			Diaphragm at ends		
	I* x 10⁴ (in⁴)	J*_d* x 10³ (in⁴)	Mass (kips/in)		I* x 10⁴ (in⁴)	J*_d* x 10³ (in⁴)	Mass (kips/in)	I* x 10⁴ (in⁴)	J*_d* x 10³ (in⁴)	Mass (kips/in)
			Exterior girder	Interior girder						
35	1.209	1.792	0.0927	0.0661	0.211	0.498	0.0027	0.211	0.498	0.0027
45	1.659	1.792	0.0941	0.0676	0.225	0.640	0.0027	0.225	0.640	0.0027
55	2.352	1.799	0.0967	0.0701	0.355	0.783	0.0027	0.228	0.782	0.0035
75	3.734	1.830	0.1052	0.0787	0.367	1.066	0.0027	0.256	1.065	0.0035
100	8.002	1.797	0.0991	0.0725	0.981	1.420	0.0057	1.852	1.420	0.0031
120	10.688	1.801	0.1037	0.0776	1.222	1.705	0.0064	2.802	1.704	0.0038
140	15.475	1.805	0.1078	0.0812	1.765	1.989	0.0064	3.965	1.988	0.0038

* Inertia moment.
** Torsional inertia moment.
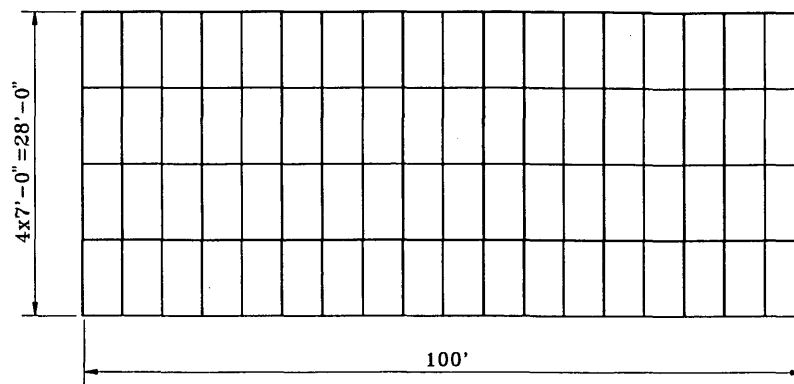
FIGURE 4 Idealization of multigirder bridges.
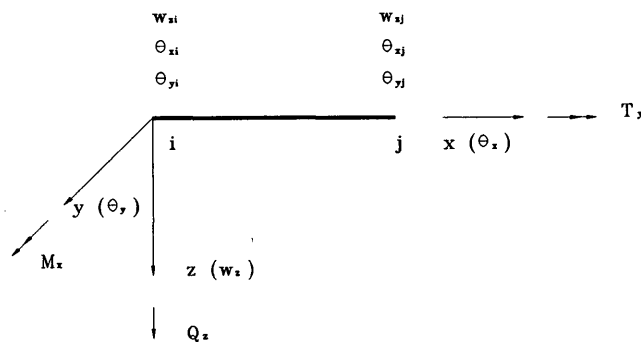
FIGURE 5 Grillage elements.

F_{MQi} = maximum bending moment or shear of one girder at the section.

The impact factor is defined as

$$I_{mp}(\%) = [R_d/R_s - 1] \times 100\% \tag{7}$$

in which R_d and R_s are the absolute maximum response for dynamic and static studies, respectively.

Figure 7 (left) presents the static load distribution factors and impact factors of each girder for the three bridges subjected to lateral symmetrical loading of a single truck. It is

interesting to observe from Figure 7 (left) that lateral static and dynamic load distributions are quite different, especially for short-span bridges. The larger the static lateral load distribution factor is, the smaller the impact factor will be. The impact factors of exterior girders are much larger than those of interior girders. Therefore, taking an average impact factor of all girders as that of each girder in the theoretical and field study is not reasonable. However, the difference of impact factors between exterior and interior girders will decrease with the increase of span length.

Figure 7 (right) shows the results for the case of asymmetrical loading of a single truck. The same relation between static wheel-load distribution factor and impact factor will be observed from Figure 7 (right). However, because of the effect of torsion, the impact factors of Girders 1 to 3 have nearly the same value.

Figure 8 gives the variation of the impact factors of moment at midspan for exterior and center girders of three bridges with varying vehicle weight. The results in Figure 8 were based on the conditions of a single truck loading symmetrically [Figure 6 (top), Loading 1], 45-mph (72.41-km/hr) vehicle speed, and good road surface. Figure 8 shows the impact factor increases as the weight decreases. However, the relation between impact and vehicle weight is related to different span lengths, girders, and cross sections. The shorter the span length is, the more rapidly the impact factor will increase with less-

TABLE 2 Frequencies of Seven Bridges

No. of frequency	Span length (ft)						
	35	45	55	75	100	120	140
1	11.657	8.231	6.467	4.185	3.502	2.791	2.410
2	11.754	8.368	6.588	4.327	3.526	2.814	2.411
3	16.882	13.247	12.967	10.131	13.368	10.647	9.152
4	31.096	26.877	24.970	16.256	13.617	11.186	9.694
5	44.844	31.713	25.282	16.533	13.961	13.956	15.488
6	44.854	31.729	29.996	20.054	18.767	17.796	17.654
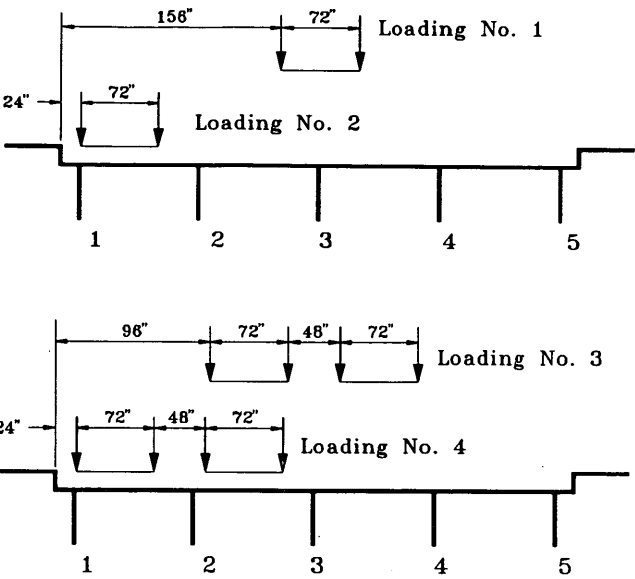
FIGURE 6 Truck-loading model: *top*, one-truck loading; *bottom*, two-truck loading.

ening vehicle weight; the impact factors of exterior girders increase much faster than those of center girders.

Figure 9 illustrates the variation of the maximum impact factor with varying span length for two typical sections of midspan and span fourth point. Figure 9 (*left*) represents the response of exterior girders, while that of center girders is given in Figure 9 (*right*). The maximum impact factors were obtained on the basis of the transverse position that can produce the maximum static response in the girders concerned (see Figure 6) and vehicle speeds ranging from 15 to 75 mph (24.14 to 120.68 km/hr).

Figure 9 provides important information concerning the relationship among maximum impact factor, span length, and others. For all seven bridges, the maximum impact factors of exterior girders are apparently larger than those of center girders. Generally, the impact factors of moment of exterior girders for bridges with span length in excess of 60 ft (18.29 m) are distinctly smaller than those evaluated according to Equation 1, provided that bridges have a deck of good road surface roughness. Higher impact factors will occur in the bridges with short spans, for which the AASHTO specifications may underestimate the impact of exterior girders. Nevertheless, the impact factors of center girders of the seven bridges with good road surface are all smaller than those predicted by Equation 1. It seems that Equation 1 will overestimate the impact of center girders for the bridges whose span lengths are in excess of 55 ft (16.76 m). The variation of the impact factors of moment at span fourth point with span lengths is different from that at midspan. For the bridges with short span lengths and very good roughness, the impact factors at span fourth point are generally less than those at midspan. For the opposite situation, most impact factors at span fourth point are greater than those at midspan. Figure 9 also shows that the impact of bridges increases considerably with increasing road roughness.

CONCLUSIONS

1. The impact of each girder of steel multigirder bridges is closely related to the lateral loading position of vehicles. Lateral static and dynamic distributions of the bridges are quite different, especially for short-span bridges. The larger the static lateral distribution factor is, the smaller the impact factor will be. It appears more reasonable to study the maximum
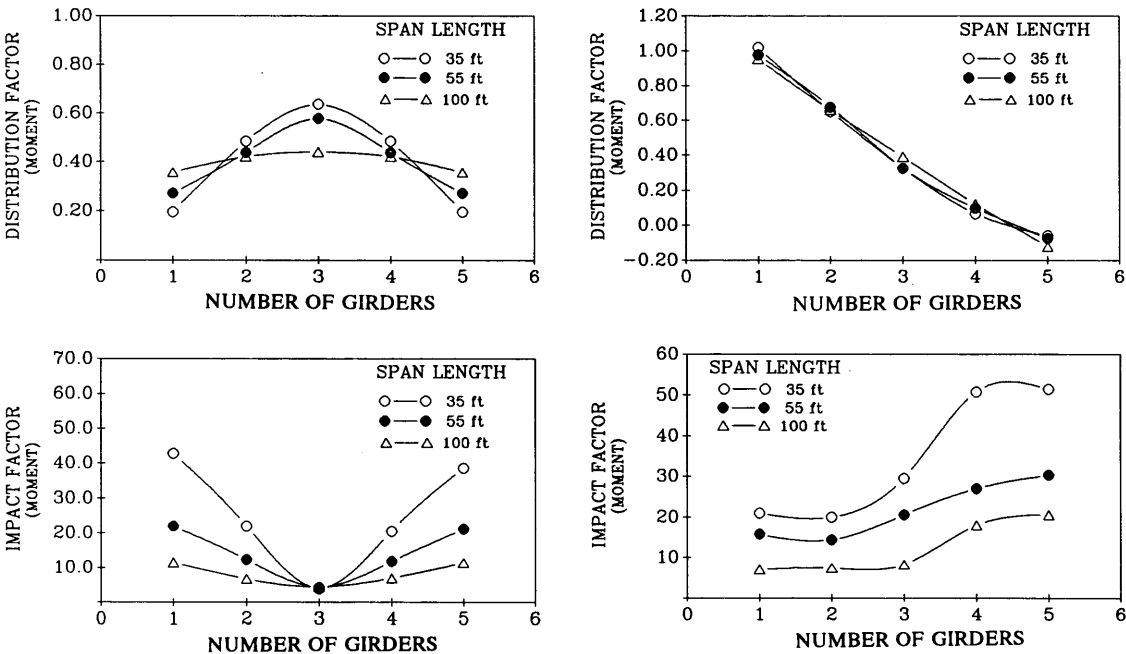
FIGURE 7 Static and dynamic distribution: *left*, symmetric loading; *right*, asymmetric loading.
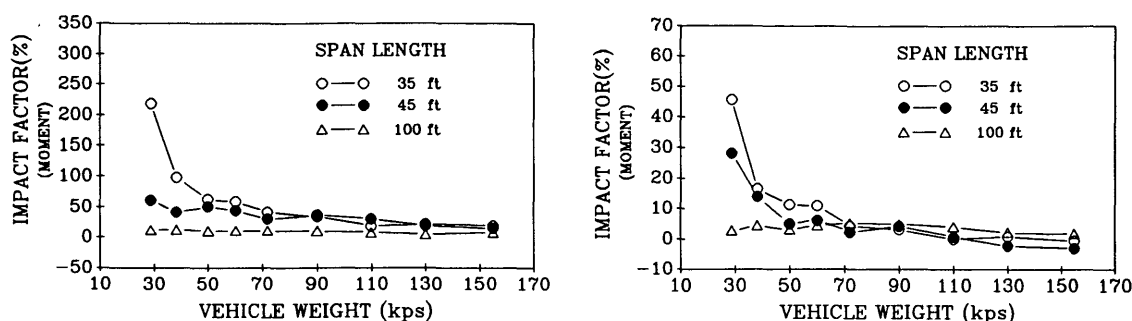
FIGURE 8 Effect of vehicle weight: *left*, exterior girders; *right*, center girders.
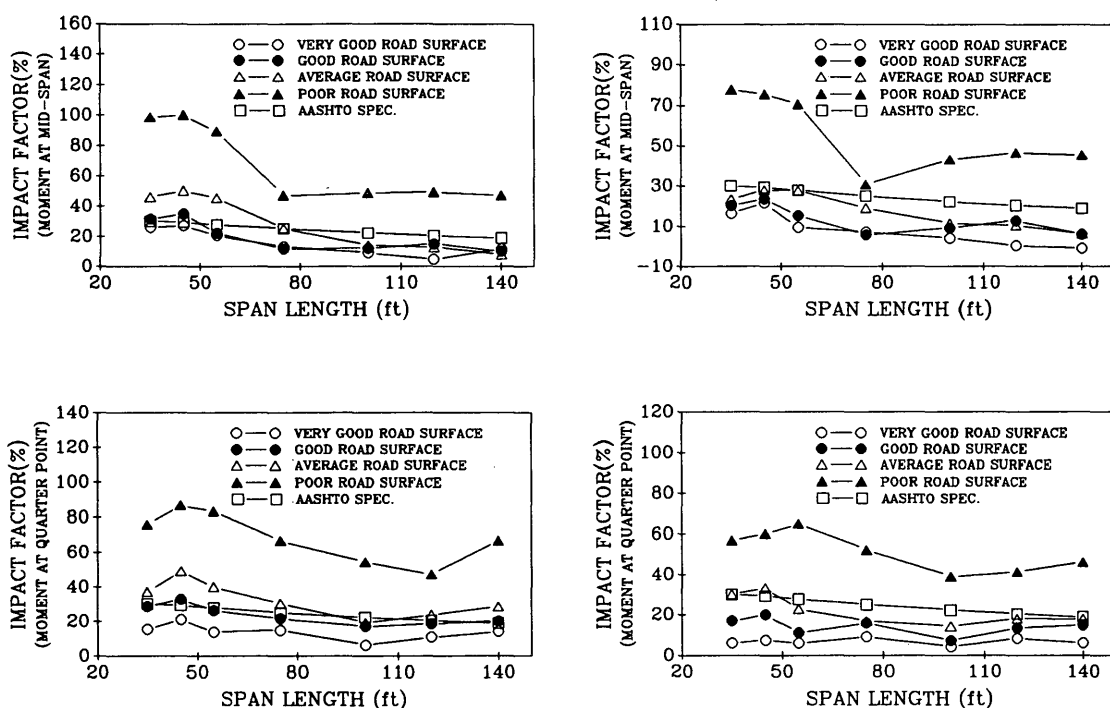
FIGURE 9 Variation of maximum-impact factors with span lengths: *left*, exterior girders; *right*, center girders.

impact of each girder than to adopt the average value of all girders in field investigations, particularly for short-span bridges.

2. Impact factors of bridges decrease with increasing vehicle weight. However, the relation between the impact and the weight of vehicle is correlated with different span lengths, girders, and sections. The shorter the span length is, the more rapidly the impact factor will increase with lessening vehicle weight. The impact factors of exterior girders increase faster than those of interior girders.

3. The maximum impact factors of interior girders for all seven bridges are significantly smaller than those of exterior girders and less than the results calculated by AASHTO specifications, provided that the bridges have good road surface. It appears that Equation 1 will overestimate the maximum factors of moment for bridges with span lengths longer than 55 ft (16.76 m), especially for midspan.

4. Generally, the maximum impact factors of moment of exterior girders with span lengths longer than 75 ft (22.86 m)

are distinctly lower than those predicted by AASHTO specifications, provided that bridges have good road surface. For bridges with short spans, it appears that Equation 1 may underestimate impact value. This situation should be noted in practice.

REFERENCES

1. *Standard Specifications for Highway Bridges*, 14th ed. AASHTO, Washington, D.C., 1989.
2. *Ontario Highway Bridge Design Code*. Ministry of Transportation and Communications, Ontario, Canada, (1983).
3. D. R. Leonard, J. W. Grainger, and R. Eyre. *Loads and Vibrations Caused by Eight Commercial Vehicles with Gross Weights Exceeding 32 Tons*. Laboratory Report LR52. Transport and Road Research Laboratory, Crowthorne, England, 1974.
4. J. Page. *Dynamic Wheel Load Measurements on Motorway Bridges*. Laboratory Report LR 722. Transport and Road Research Laboratory, Crowthorne, England, 1976.

5. R. Shepard and R. J. Aves. Impact Factors of Simple Concrete Bridges. *Proc., Institution of Civil Engineering*, Part 2, Vol. 55, 1973, pp. 191–210.

6. R. Green. *Dynamic Response of Bridge Superstructures—Ontario Observations*. Supplementary Report 275. Transport and Road Research Laboratory, Crowthorne, England, 1977, pp. 40–48.

7. C. O'Connor and R. W. Pritchard. Impact Studies on Small Composite Girder Bridge. *Journal of Structural Engineering*, ASCE, Vol. 116, No. 7, 1985.

8. T. Huang. *Dynamic Response of Three-Span Continuous Highway Bridges*. Ph.D. dissertation. University of Illinois, Urbana, 1960.

9. R. K. Gupta and R. W. Trail-Nash. Vehicle Braking on Highway Bridges. *Journal of the Engineering Mechanics Division*, ASCE, Vol. 106, No. EM4, 1980, 641–658.

10. C. Oran. *Analysis of the Static and Dynamic Response of Single-Span Multigirder Highway Bridges*. Ph.D. dissertation. University of Illinois, Urbana, 1961.

11. E. S. Hwang and A. S. Nowak. Simulation of Dynamic Load for Bridges. *Journal of Structural Engineering*, ASCE, Vol. 117, No. 5, pp. 1413–1434.

12. T. L. Wang and D. Z. Huang. Cable-Stayed Bridge Vibration Due to Road Surface Roughness. *Journal of Structural Engineering*, ASCE, Vol. 118, No. 5, 1992, pp. 1354–1374.

13. T. L. Wang and D. Z. Huang. *Computer Modeling Analysis in Bridge Evaluation*. Interim Research Report FL/DOT/RMC/0542-3394. Florida Department of Transportation, Tallahassee, 1992.

14. C. J. Dodds. and J. D. Robson. The Description of Road Surface Roughness. *Journal of Sound and Vibration*, Vol. 31, No. 2, 1973, pp. 175–183.

15. C. J. Dodds. *BSI Proposals for Generalized Terrain Dynamic Inputs to Vehicles*. ISO/TC/108/WG9, Document 5. International Organization for Standardization, 1972.

16. *Standard Plans for Highway Bridge Superstructures*. FHWA, U.S. Department of Transportation, 1982.

17. T. L. Wang. Ramp/Bridge Interface in Railway Prestressed Concrete Bridges. *Journal of Structural Engineering*, ASCE, Vol. 116, No. 6, 1990, pp. 1648–1659.

18. R. W. Clough and J. Penzien. *Dynamics of Structures*. McGraw-Hill Book Co., New York, N.Y., 1975.

Service, Fatigue, and Ultimate Load Evaluation of a Continuous Prestressed Flat-Slab Bridge System

Ronald A. Cook, Fernando E. Fagundo, Adrian D. Rozen, and Haskel Mayer

A new type of short-span bridge system for traversing wetlands and shallow waters (i.e., a trestle-type bridge) has been developed and implemented over the Albemarle Sound south of Edenton, North Carolina. The new system incorporates precast flat-slab sections that are posttensioned for continuity. The new system has the potential to replace traditional trestle-type bridges constructed using simple-span prestressed beams with a cast-in-place deck. A continuous two-span, half-scale model of this precast, posttensioned, flat-slab bridge system was built and tested under various load conditions. The bridge was evaluated analytically and experimentally for the transfer load case (deal load plus prestress), the maximum negative moment service load case, the maximum positive moment service load case, fatigue load, cracking load, and ultimate load. The model bridge performed as predicted for all load cases. Comparisons between analytical and physical models showed good correlation for all types of tests. At service load levels the bridge exhibited an elastic response with no evidence of cracking. The results of the fatigue load tests showed no degradation of stiffness. The ultimate load and deflections of the new bridge system were readily predicted by standard behavioral models for prestressed concrete. With the cost savings, short erection time, and multispan continuity of this system, it should be considered a viable alternative to the standard girder systems available for trestle-type bridges.

The selection of a bridge system for any application is linked to the site's physical constraints, such as clearances, accessibility, sensitivity of environment, location, and availability of local materials and labor. Even with these constraints a number of options remain to the designer, with the final selection usually directed by cost and aesthetics.

Much work has been done in the area of standard prestressed girders with cast-in-place bridge decks. These systems are currently being used with a high degree of efficiency. To realize further savings, new systems must be explored.

One new system consisting of a precast segmental flat-slab bridge, posttensioned for continuity, has the potential to replace most low, short-span bridges such as those that traverse wetlands and relatively shallow waters. This system has been used successfully over the Albemarle Sound south of Edenton, North Carolina (see Figure 1). A 50 percent to 60 percent cost savings could be obtained with this system for certain applications. The bid price for the superstructure of the existing bridge system was only $23/ft² (*1*).

R. A. Cook and F. E. Fagundo, Department of Civil Engineering, University of Florida, Gainesville, Fla. 32611. A. D. Rozen, Kimley-Horn & Associates, Inc., West Palm Beach, Fla. 33407. H. Mayer, E. N. Bechamps & Associates, Inc., Miami, Fla. 33126.

The cost savings is realized through an efficiently designed cross section and decreased labor costs through assembly-line production of individual segments. Another advantage of this system is an integrally cast pile cap in the bent segment. This allows for the segment to be placed directly on piles without the need for a bent to be formed and cast in the field. As with any standardized system, the savings are proportional to the repetition of the application.

OBJECTIVES

An experimental and analytical research program was undertaken to evaluate the behavior of the new bridge system.

The objectives of the research program were to

1. Develop and construct a physical scale model of the bridge system;
2. Test the model bridge system for service, fatigue, and ultimate loads;
3. Develop analytical models to predict the performance of the system; and
4. Verify the analytical results by comparing them with those obtained from experimental data to develop a degree of confidence in the new system.

EXISTING STRUCTURE

As mentioned, the original structure used as the basis for this study is a bridge over the Albemarle Sound in northeastern North Carolina on State Highway 32. The concept and design for the bridge were developed by the Figg Engineering Group. This posttensioned flat-slab concrete bridge system consists of precast segments that range from 4.57 to 6.10 m (15 to 20 ft) in length with a cross section 34 ft 3 in. 10.44 m wide and a center slap thickness of 413 mm (16¼ in.). The crown slope is 2 percent and the edge slab thickness is 203 mm (8 in.). The segments were transversely prestressed with both pretensioned and postensioned steel in the casting yard. The bridge was designed for three lanes of AASHTO (*2*) loading. The segments were placed on temporary steel erection girders that spanned pile groups (three piles per group). Concrete then was placed in 1-ft closure joints between each segment and in voids shaped like truncated pyramids directly over each
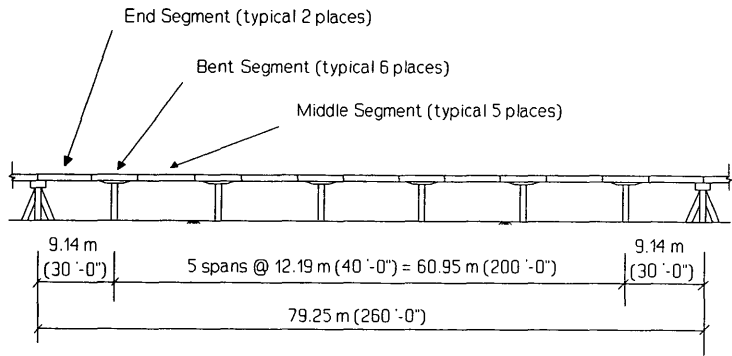
FIGURE 1 Existing bridge.

pile to create the section 79.25 m (260 ft) long shown in Figure 1. The section was posttensioned longitudinally, after which the temporary erection girders were removed. All posttensioning tendons were grouted. The total length of the original project was approximately 5.6 km (3.5 mi).

TEST SPECIMEN

When a new structural system is developed, it is important that the analytical models used to predict the behavior of the system be reliable. One method of ensuring the validity and reliability of the analytical models is by the physical testing of a scale model of the system. The results of the analytical models can then be compared with test results. The structural model chosen for this study is shown in Figures 2 and 3. The test specimen chosen represents a two-span, three-segment, half-scale model of the existing structure.

The model was constructed using two end segments and one bent segment from the existing structure (see Figure 1). Although the distance between the centerlines of the pile groups at the end spans was 9.14 m (30 ft), the actual span length was 8.79 m (28 ft 10 in.) because of end-bearing details. The span length of the model was exactly half that of the end spans of the existing structure as indicated in Figure 3. The actual length of the end segments in the model was slightly less than half the length of the full-scale end segment. The discrepancy results from a protective concrete cover that was provided over the tendon anchors in the existing structure.

All requirements for similitude between the model and existing system were met (*3*). To correctly model dead load, dead load compensating blocks were distributed evenly over the surface of the model bridge before posttensioning.
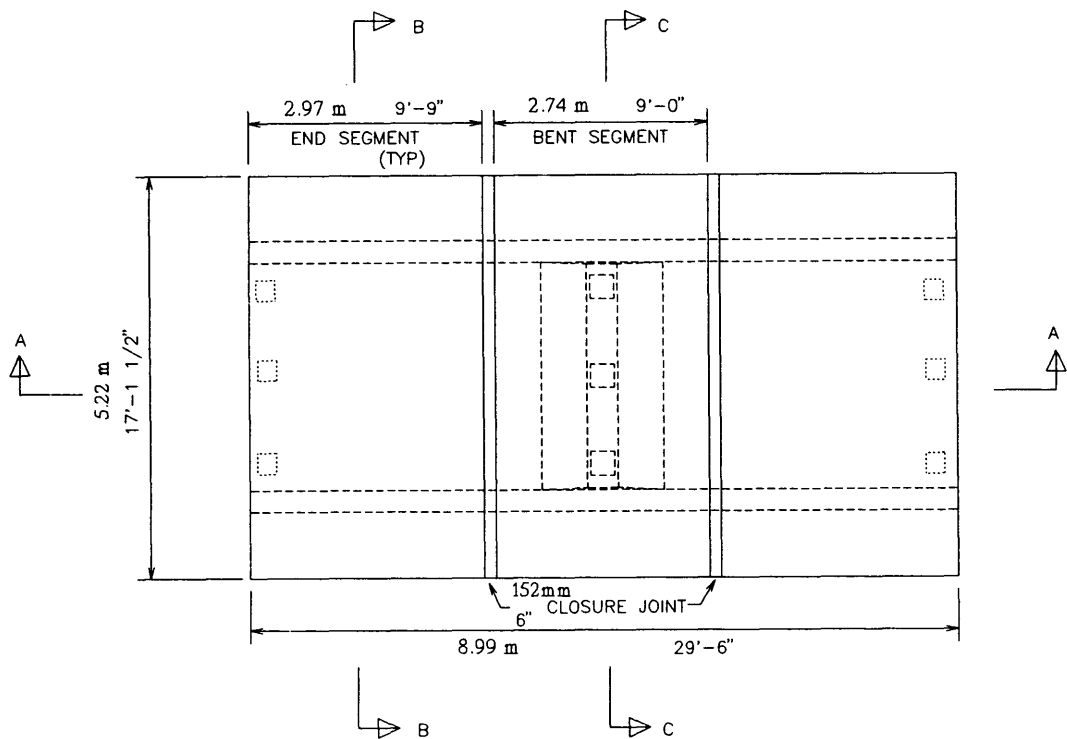
FIGURE 2 Model bridge: plan view.
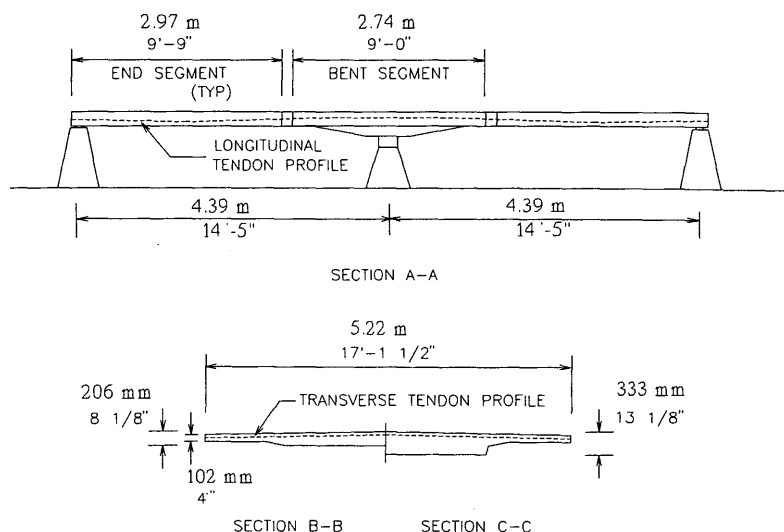
FIGURE 3 Model bridge: sections.

The model bridge was constructed using the same type of erection procedure as used for the existing structure. The bridge segments were cast on the floor of the laboratory. After curing, the segments were placed on temporary shoring located between the two end supports and center pier support shown in Figure 3. Closure pours were then made between the segments and in the three voids over the piers at the center support. The bridge was then posttensioned and the tendons were grouted, after which the temporary supports were removed.

All nonprestressed and prestressed reinforcement in the existing bridge system was duplicated in the model bridge with appropriate similitude requirements. The prestressing forces and losses were determined on the basis of the dimensions of the model bridge. Details of nonprestressed and prestressed reinforcement are provided by G. M Sabnis et al. (3). In the model, all prestressing strands were 13 mm (0.5 in.)

in diameter, seven-wire, low-relaxation Grade 1860 MPa (270 ksi).

The concrete had a 28-day compressive strength of 37.9 MPa (5,500 psi). Displacements were measured with 20 linear variable differential transformers (LVDTs). Strains were measured with internal and surface strain gauges.

TEST SETUP

Three loading systems were used during the testing program. As shown in Figure 4, the service load tests (both static and fatigue) were performed using a test apparatus that reproduced the effects of three lanes of the AASHTO (2) HS20-44 truck load. Loading configurations were used that produced maximum positive and negative moments in the two-span continuous bridge. These loading configurations repre-
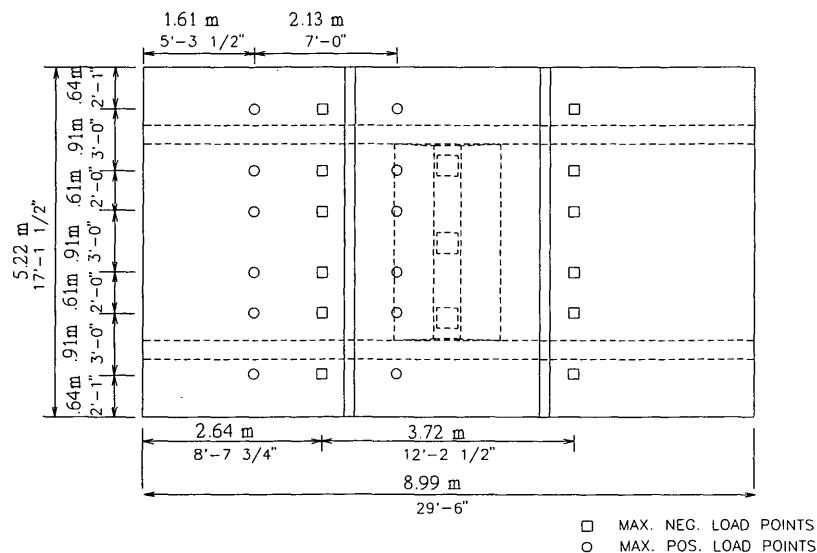
FIGURE 4 Load points for service load tests (static and fatigue).

sent the controlling design conditions for the existing bridge. Note that the loading arrangement shown in Figure 4 indicates only four wheel loads per truck. The effects of the front wheels of the standard AASHTO HS20-44 truck were neglected because their contribution to the overall maximum moment was insignificant. As shown in Figure 4, in the maximum positive moment test configuration all axle loads were placed in one span, whereas in the maximum negative moment test configuration the axle loads straddled the center support. To be sure of having equal loads on all wheels, the test rig was designed to be fully determinate by using a series of stacked beams and one central hydraulic ram.

A single line of concentrated loads was used for fatigue-load testing after cracking and for the ultimate load test. The loading arrangement used for these test series is shown in Figure 5. Analysis based on conventional prestressed, reinforced concrete beam theory indicated that the positive moment load case (i.e., all the load on one span) would control both the minimum cracking load and the ultimate load.

Because different loading configurations were used for the positive moment load case, it was necessary to establish the load equivalence between the configurations. For the three lanes of truck loading used in the service-level load tests (Figure 4), the maximum load applied to the system was 250 kN (56.2 kips). This load was based on three trucks, each with four wheel loads of 71 kN (16 kip). The AASHTO (2) multiplication factor of 1.30 for impact and 0.90 for three lanes of loading as well as the model scale factor of one-fourth for load were included in the calculation of this load. For the single line load configuration used for the ultimate load tests, the equivalent load was determined to be 147 kN (33.0 kips). The equivalence of this load was determined analytically by influence lines and verified experimentally by both strain and deflection measurements. This means that a total load of 147 kN (33.0 kips) applied as shown in Figure 5 produced the same maximum strain and deflection as a total load of 250 kN (56.2 kips) applied in the positive moment load configu-

ration shown in Figure 4. Therefore, a 1.70 multiplication factor should be used to determine the equivalent Figure 4 load for a load applied in the Figure 5 test setup.

SERVICE LOAD TESTS

Experimental results obtained from the transfer (dead load plus prestress) load case, the maximum positive moment service load case, and the maximum negative moment service load case are discussed and compared to analytical results. Analytical results were obtained from a finite element analysis (FEA) of the prestressed bridge system performed with commercially available software (4).

Unless noted, all experimental results represent only the load case under consideration (i.e., transfer plus dead load, live load positive moment, and live load negative moment). For example, the deflections shown for the positive moment load case are the deflections that occurred during that load case only, not the total deflections that occurred since construction of the model. For the figures in this paper, positive deflection is defined as up.

Test Results for Transfer (Dead Load plus Prestress)

Figure 6 shows the deflection profile measured along the longitudinal centerline axis of the bridge. In Figure 6, the experimental data in general show the same shape as the analytical data. One span exhibited higher experimental deflections and the other span exhibited lower deflections compared to the analytical solution. As more of the longitudinal stressing occurred from the end with the higher deflections, this appears to be reasonable. The loss of prestress because of tendon friction and wobble would cause the deflections for the span farthest from the stressing operation to have lower deflections.
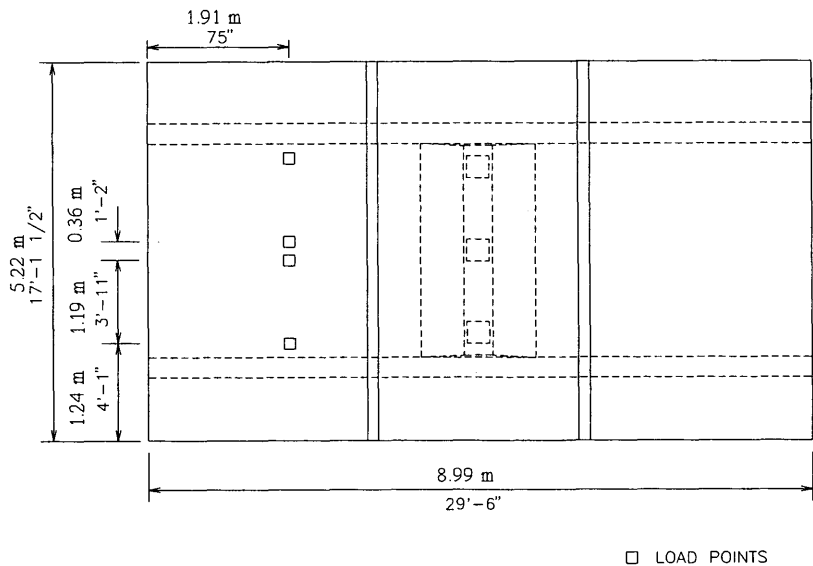
FIGURE 5 Load points for cracking, fatigue load after cracking, and ultimate load tests.
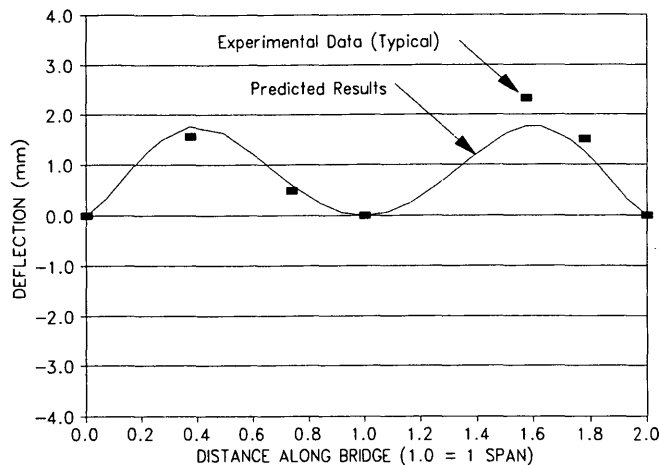
FIGURE 6   Longitudinal deflection for transfer (dead load and prestress).

Results for Maximum Positive Moment Service Load Test

Figure 7 presents the longitudinal deflection curve at the centerline of the bridge for the positive moment load case. The shape of the longitudinal profile appears to indicate that the structure was not performing as expected. Although the basic form of the deformations is close to that predicted, the magnitude of the measured deflections is smaller than those obtained from the analysis. In the analysis, the center support was modeled as a frictionless hinge whereas the end supports were modeled as rollers. The test indicates that some stiffness was in fact associated with the center pile support constructed in the laboratory that allowed less rotation than expected; this stiffness accounts for the differences in deflections. The pile support constructed in the laboratory incorporated a built-in hinge 229 mm (9 in.) below the bottom of the bridge deck (5).

Test results for load-strain and load-deflection relationships at all locations indicated linear response. Stress distributions
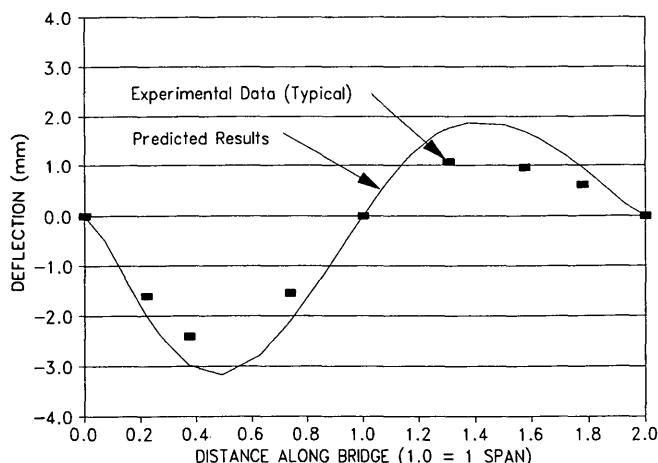
through the slab thickness (determined from strain measurements at the top, interior, and bottom of the slab) indicated linear distribution in close agreement with analytical results.

Results for Maximum Negative Moment Service Load Test

The longitudinal deflection profile in Figure 8 shows very good correlation between experimental and predicted results. The right span's deflections were slightly less than those predicted. This is attributed to that span having a greater prestress force, which would tend to reduce deflections due to live load. Load-strain and load-deflection relationships at all locations indicated a linear elastic response.

Discussion of Service Load Test Results

The experimental results closely matched those predicted by the analysis for all individual load cases. As previously noted, the major differences occurred in the cases of transfer and maximum positive moment load. For the case of maximum negative moment load, the experimental and analytical results matched almost exactly.

In the transfer load case, the measured deflections were slightly higher than predicted in one span and lower than predicted in the other. This difference can be attributed to the posttensioning sequence used in construction of the bridge.

In the maximum positive moment load case, the measured deflections were slightly less than expected in both spans. This result can be attributed to the rotational stiffness of the center pier support, which was not accounted for in the analysis. The rotational stiffness of this support reduced the moment transfer between spans. The result was smaller experimental deflections than predicted by the analysis.

In summary, the model bridge performed very well and remained in the elastic range of behavior. The test results were close to the analytical predictions for each load case. The service load tests are discussed further elsewhere (5).

FIGURE 7   Longitudinal deflection for maximum positive moment service load test.
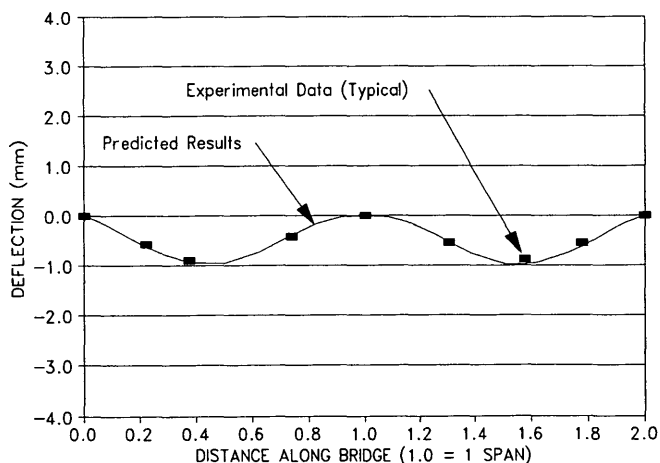
FIGURE 8   Longitudinal deflection for maximum negative moment service load test.

FATIGUE LOAD TESTS

Two types of fatigue load tests were performed. The first type of fatigue load test was performed for the maximum service level fatigue loading expected on the bridge. This maximum was considered to be two lanes of AASHTO HS20-44 truck loading. This condition assumes that two trucks are located at the worst possible position at the same time. This type of fatigue test was conducted for a total of 3 million cycles, which was considered to be far in excess of the number of cycles that the actual bridge would experience for this load condition. The loading was applied as shown in Figure 4. The total load for this type of test was determined to be 185 kN (41.6 kips) based on eight wheel loads of 71 kN (16 kips), an impact factor of 1.3, and a model scale factor of one-fourth for load.

The second type of fatigue load test was conducted after the bridge was cracked. The loading configuration shown in Figure 5 was used for this test. The maximum fatigue load for this type of test was 150 percent of the design service load of three lanes of AASHTO HS20-44 truck loading. Two million cycles of fatigue load were performed for this type of test.

To determine if any degradation in stiffness had occurred, a static load test equivalent to the maximum service level design load of three AASHTO HS20-44 trucks was performed about every 100,000 cycles. For each of these static tests, the relative stiffness of the system was evaluated by dividing the applied load by the displacement measured at different locations in the spans.

Results for Fatigue Load Tests

Two load configurations were used for the service level fatigue load tests. The first 2 million cycles of load were applied with the test setup in the maximum negative moment test configuration (see Figure 4). Another 1 million cycles of loading were performed with the test setup in the test configuration of maximum positive moment (see Figure 4). Figure 9 shows the actual load history for these tests as a percent of the two-lane AASHTO HS20-44 truck loading. No degradation in

stiffness or variation from linear behavior was observed during these tests.

After the service-level fatigue load tests were performed, the loading configuration was changed to the single line loading indicated in Figure 5. The bridge was then loaded monotonically until cracking occurred at a load of 418 kN (94 kips). As observed, this load was equivalent to 710 kN (160 kips) applied in the positive moment test configuration in Figure 4 (1.70 multiplication factor for converting Figure 5 loads to Figure 4 loads). After the bridge was cracked, another 2 million cycles of load was applied in the test configuration in Figure 5. The maximum load applied for this test was 220 kN (49.5 kips) and the minimum load was 89 kN (20 kips). The maximum load was equivalent to 150 percent of the three-lane service load, 200 percent of the two-lane service load, 28 percent of the predicted ultimate load, and 26 percent of the measured ultimate load. No degradation of stiffness or variation in linear behavior was observed over the course of this test.

Discussion of Fatigue Load Test Results

No degradation of stiffness or structural integrity was noted during any of the fatigue load tests. The system response remained linear elastic throughout the fatigue load testing program. This is not surprising as the load applied in these tests was below the cracking load of the prestressed bridge system. As with most prestressed, posttensioned systems with grouted tendons, reasonable fatigue loading does not affect the integrity of the system. To obtain early fatigue failure, the bridge would need to be subjected to fatigue loads above cracking. In the case of this particular system, this would amount to a loading above 50 percent of the ultimate load or 270 percent of the three-lane design service load. Because these load levels will never be experienced in the actual bridge, it is reasonable to assume that fatigue loading is not a problem for the new bridge system. Further discussions of the fatigue load tests are presented elsewhere (6,7).

ULTIMATE LOAD TEST

The predicted behavior from service load to ultimate load was determined from conventional prestressed, reinforced concrete beam theory (8). The analysis indicated that the critical load condition was controlled by flexure due to positive moment. Punching shear at the center piers, negative moment over the piers, and negative moment in the unloaded span also were investigated as possible critical load conditions. These factors were found not to produce the minimum cracking or failure load on the bridge system.

For cracking and ultimate load analysis, the entire cross section of the three-lane bridge was considered a longitudinally spanning beam continuous over three supports. The moment-curvature diagrams for both the loaded and unloaded spans were developed to predict the results. Because the cross section and reinforcement in both spans were identical, one moment-curvature diagram was developed. The live load produces positive curvature in the loaded span, whereas in the unloaded span the live load produces negative curvature. The
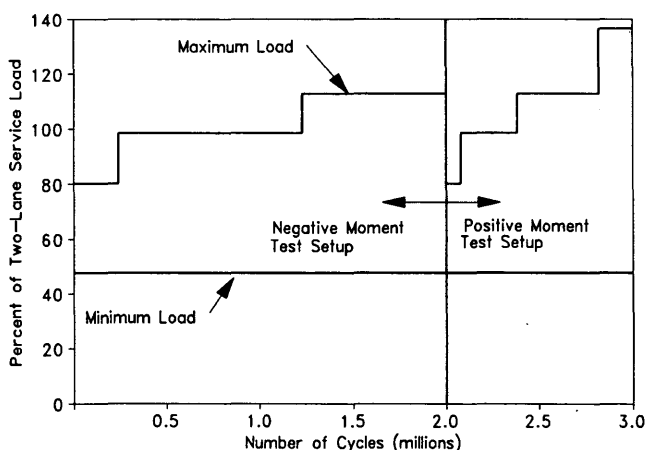
FIGURE 9 Load history for service level fatigue tests.

moment-curvature diagrams for both spans are shown in Figure 10. Before the addition of any live load, the moment in both spans resulting from dead load and secondary moments was determined to be 55.6 kN-m (41 kip-ft). According to Figure 10, this indicates an initial negative curvature in both spans that is verified by Figure 6.

The values on the moment-curvature diagram in Figure 10 were used to predict the cracking load of 342 kN (77 kips) and ultimate load of 787 kN (177 kips) of the bridge system. The moment-curvature diagram in Figure 10 was also used to predict the load-strain and load-deflection behavior of the system.

Results for Ultimate Load Test

Figure 11 shows the measured longitudinal displacements for various stages of the ultimate load test. Displacements were linear up to the cracking load of 418 kN (94 kips). After initial cracking in the loaded span, the deflection under the load increased significantly. The unloaded span also cracked at the construction joint between segments before ultimate load and began to experience large upward deflections. The observed crack in the construction joint was minimal and confined to the interface between the cast-in-place closure joint and the end segment. The formation of this crack should not be considered to be detrimental to the performance of the bridge system because it occurred at a load substantially higher than the design service load.

Figure 12 shows the predicted and measured strains on the top surface of the concrete at the bridge centerline directly under the load for the ultimate load test. The predicted and measured strains are in close agreement. Figure 13 shows the measured load-deflection relationship at the bridge centerline directly under the load compared to the calculated load-deflection relationship for the ultimate load test. Figure 13 indicates that the predicted results are in close agreement with test results.

The actual ultimate load for the bridge system was 832 kN (187 kips). The controlling failure mode was by flexural failure

FIGURE 11   Longitudinal deflection for ultimate load test.
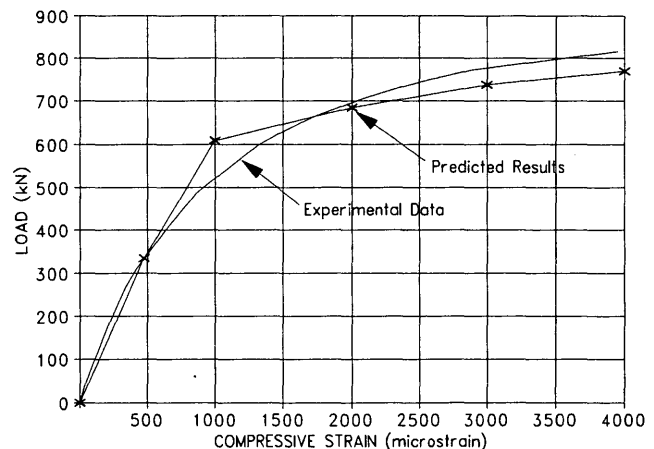
FIGURE 12   Maximum top surface compressive strains for ultimate load test.

FIGURE 10   Moment-curvature diagram for loaded and unloaded spans.
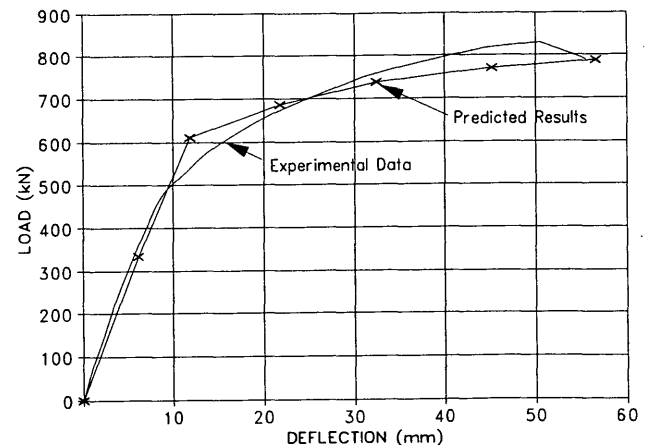
FIGURE 13   Load-deflection diagram for ultimate load test.

resulting from crushing of the concrete at the top surface of the bridge deck directly under the load. The flexural compression failure occurred over about half the width of the bridge at this location.

Discussion of Ultimate Load Test Results

Both Figures 12 and 13 show that the predicted results are in close agreement with test results. This fact indicates that the behavior of the bridge system from service load to cracking load and from cracking load to ultimate load is readily predictable by the theory of conventional prestressed, reinforced concrete beam. The ratio of experimental to predicted cracking load was 1.22, and the ratio of experimental to predicted ultimate load was 1.06.

In both experimental and predicted results, the cracking load was about 2.5 times the design service load, and the ultimate load was about 5.5 times the design service load. Further discussion of the ultimate load test is presented elsewhere (7).

SUMMARY

A half-scale model of a flat-slab bridge system that was continuous, precast, and posttensioned was built and tested for service load, fatigue load, and ultimate load. Individual load cases studied included transfer (dead load plus prestress), maximum negative service load moment, maximum positive service load moment, fatigue load before and after cracking, and ultimate load. Analytical models were developed and the results were compared to experimental results.

For the tests of service load, the model bridge remained in the linear elastic response range throughout its loading history. No cracking developed and the data indicated that the bridge remained in compression for all load cases. Test results compared well with results predicted by analysis.

No degradation of stiffness or loss of structural integrity was noted in 5 million cycles of fatigue loading. The behavior of the bridge system remained linear after the fatigue load tests.
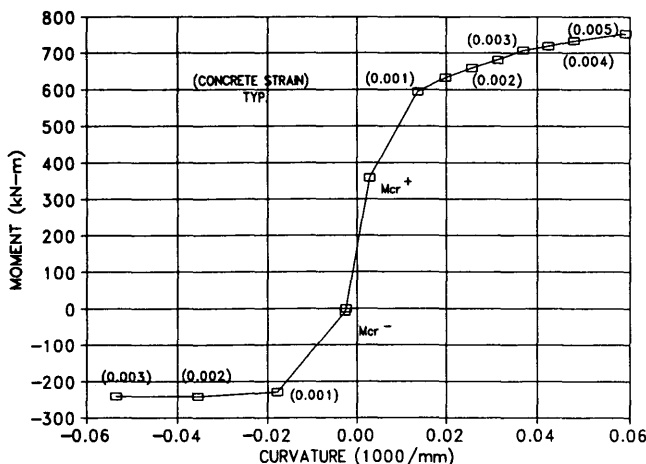
The results of the ultimate load test indicate that the behavior of the bridge system can be determined from conventional prestressed, reinforced concrete beam theory. Both the cracking strength and ultimate strength of the system were well in excess of minimum AASHTO requirements.

CONCLUSIONS

The multispan bridge system appears to be an excellent alternative to the standard simple-span prestressed girder sys-

tem for short-span applications that traverse wetlands and shallow water. The behavior of the new system is readily predicted by standard analytical and behavioral models.

With the apparent cost savings, short erection time, and multispan continuity of this system, it should certainly be considered as an alternative to the simple-span prestressed girder system with a cast-in-place deck for this application.

REFERENCES

1. H. Carr and M. May. A Sound Investment: Trestle at $23 per Sq. Ft. *Engineering News Record*, Vol. 221, No. 8, Aug. 25, 1988, pp. 30–31.
2. *Standard Specifications for Highway Bridges: Interim Specifications—Bridges—1990*, 14th ed. AASHTO, Washington, D.C., 1990.
3. G. M. Sabnis, H. G. Harris, R. N. White, and M. S. Mirza. *Structural Modeling and Experimental Techniques*. Prentice-Hall, Inc., Englewood Cliffs, N.J., 1983.
4. E. L. Wilson and A. Habibullah. *SAP90: A Series of Computer Programs for the Static and Dynamic Finite Element Analysis of Structures*. Computers & Structures, Inc., Berkeley, Calif., 1989.
5. R. A. Cook, F. E. Fagundo, B. A. Munson, B. M. Schafer, and D. E. Richardson. *Analytical and Experimental Evaluation of a Precast, Post-Tensioned, Segmental Flat Slab Bridge System for Service Loads*. Structures and Materials Research Report No. 91-2, University of Florida, Gainesville.
6. H. Mayer. *Analytical and Experimental Evaluation of a Precast, Post-Tensioned, Segmental Flat Slab Bridge System for Service Level Fatigue Loading*. Master's thesis. Department of Civil Engineering, University of Florida, Gainesville, Aug. 1992.
7. A. D. Rozen. *Evaluation of a Post-Tensioned Flat Slab Bridge System for Fatigue and Ultimate Load*. Master's thesis. Department of Civil Engineering, University of Florida, Gainesville, Aug. 1992.
8. T. Y. Lin and N. H. Burns. *Design of Prestressed Concrete Structures, 3rd ed.* John Wiley & Sons, New York, N.Y., 1981.

Effect of Alternative Truck Configurations and Weights on the Fatigue Life of Bridges

Mohammad A. Khaleel and Rafik Y. Itani

The life of a bridge is principally influenced by repetitive loading resulting from vehicular traffic. The service data on the fatigue life of concrete, reinforcing bars, and prestressing steel show considerable scatter in their service life. This is due to both the stochastic nature of the imposed loading and the variability in their strengths as determined by the quality control in their manufacture. The fatigue life of partially prestressed concrete girder bridges, subjected to a spectrum of traffic imposed by the Poisson arrival of various categories is investigated. Each category examined has a different expected frequency of arrivals per unit time and a different distribution of gross weight. The allocation of the live load to the girders in skew and normal bridges is determined using the finite element method. The girders of the bridge are each assumed to be part of a series system consisting of four components: prestressing strands, reinforcing bars, cast-in-place concrete slab, and precast girder. The nine-axle B-train double trucks were found to be most damaging, whereas two-axle single trucks were least damaging. The incremental damage caused by each truck depends on the truck configuration, gross weight, axle-load distribution, and lateral load distribution. The median life of ordinary reinforcing bars is the lowest among the girder components.

Concrete structures, when subjected to fluctuation in strain during duty cycles, will eventually accumulate sufficient damage within the constituent materials of their components to limit their useful service life. These repetitive loadings can reduce bonding properties at the interface between steel and concrete and lead to cracks of substantial width, thereby allowing extensive deflections under service loads. The degree of damage is a function of many factors. Principally, these factors are the number and magnitude of the stresses during load cycles; the variability of loads; the configuration of the loads and their allocation to the structural components inducing the corresponding strains; and the degree of microscopic cracking with resultant change in constituent material properties.

A primary example of such structures of importance in civil engineering is the partially prestressed concrete (PPC) girder bridges that are subjected to repeated heavy loadings from truck traffic. The effect of loading on the bridge components is modified somewhat through different truck designs now necessary because of extreme truck weight allowed. If, as a result of these continual load fluctuations, significant cracking

M. A. Khaleel, Automation and Measurements Department, Battelle Pacific Northwest Laboratories, Richland, Wash. 99352. R. Y. Itani, Department of Civil and Environmental Engineering, Washington State University, Pullman, Wash. 99164.

occurs in the concrete and material losses occur with the alteration of the material properties entailed, the structure may eventually fail in fatigue.

Nearly 45 percent of the nation's 600,000 bridges have been classified by FHWA as severely damaged and deteriorated because of heavy vehicles, natural environmental hazards, or lack of maintenance. Many studies using various experimental techniques, have been conducted to investigate the fatigue properties of prestressed concrete girders. In some instances, the reliability of the results of the tests was questioned by members of the prestressed concrete industry who claimed that inappropriate test techniques were used or that the experimenters were ignorant of material properties (1).

All available data on the fatigue life or cumulative damage of structural materials show considerable scatter and lack of deterministic predictability. This is due both to the variability of material properties among specimens and to uncertainties in predicting the deterioration of the structural material under cyclic loading. Moreover, simplified deterministic methods of analysis do not allow for uncertainties in calculating actual loads that will be applied to the structure. Most studies on the safe-life for concrete structures not only have ignored the considerable scatter induced by material variability and the randomness in anticipated loads but also have bypassed the necessity of censoring (i.e., aborted tests or run-outs in the specimens) the fatigue-test data.

Adopting Turner trucks may contribute significantly to fatigue damage of PPC bridges because cracks are more likely to develop in the bridge girders. Crack formation will accelerate fatigue damage and shorten the lives of these bridges. The present objective is to develop a model of fatigue reliability for PPC bridges using a theory of stochastic cumulative damage to evaluate the bridges in the nation's highway system.

LOAD MODELS

Truck weight is considered to be well defined by the inverse Gaussian distribution (2). In this study, the trucks are grouped into six categories on the basis of the number of their axles. Table 1 shows the categories of trucks and the average and standard deviations of their gross weight in each class. Because of the lack of statistical data on such trucks, the coefficient of variation of a Turner truck weight is assumed to be .30. Hwang and Nowak (3) found that the mean value of dynamic load factors and coefficient of variation for pre-

TABLE 1 Truck Categories and Their Statistical Parameters

Class	A.W.[a] (KN)	S.D.[b] (KN)	Axle Spacing (m)								Axle Weight Distribution		
2-Axle Single	70.	26.6	5.1	-[c]	-	-	-	-	-	-	33.6	66.4	-
3-Axle Single	124.	30.0	5.1	1.3	-	-	-	-	-	-	30.1	69.5	-
4-Axle Semi-Trailer	144.	53.9	3.6	7.7	1.1	-	-	-	-	-	17.9	38.3	43.8
5-Axle Semi-Trailer	226.	78.7	3.6	1.3	8.7	1.2	-	-	-	-	13.9	48.1	38.0
5-Axle Split	240.	78.3	3.7	1.3	7.7	2.8	-	-	-	-	11.9	47.5	40.5
Nine-Axle B-Train Double	494.	148.	3.0	1.3	7.3	1.3	1.3	1.3	7.2	1.3	9.91	11.3	11.3[d]

[a] Average gross weight of a truck.
[b] Standard deviation of truck weight.
[c] Not applicable.
[d] All other 6-remaining axles have the same weight.

stressed concrete girder bridges are span-dependent. The dynamic load factor (I) is assumed to be log-normal; its coefficients of variation are equal to .53 and .62 for bridge spans of 80 and 100 ft, respectively. The mean value of I is constant and equal to 0.12.

ALLOCATION OF LOAD

Khaleel and Itani (4) investigated the live load distribution for slab-girder bridges. They proposed an analysis procedure expressed in the form of an algorithm. The maximum bending moment is given by

$$M = M_0 \frac{b}{D} KI \qquad (1)$$

where

b/D = lateral load distribution factor,
K = skew reduction factor,
I = impact allowance, and
M_0 = maximum static moment (half the truck load applied to a single isolated girder).

The maximum static moment for a k-axle truck (or semitrailer or tractor) is expressed by

$$M_0 = \frac{W}{8a} a^2 + a A_k(s, \delta) + B_k(s, \delta) \qquad (2)$$

where

a = span of bridge,
W = gross weight of truck,
s = vector of axle spacings,
δ = vector of ratios of axle weight to gross weight, and
$A_k(.) > B_k(.)$ = functions of s and δ.

The lateral distribution and skew reduction factor are assumed to be normally distributed. Khaleel (5) used the finite element method to derive expressions for b/D and K for both single-span and continuous-skew girder bridges. Expressions of D-values for exterior and interior girders are presented in Figures 1 and 2.

Live and dead loads are allocated to girders on the basis of the model described in Equations 1 and 2. Al-Zaid et al.
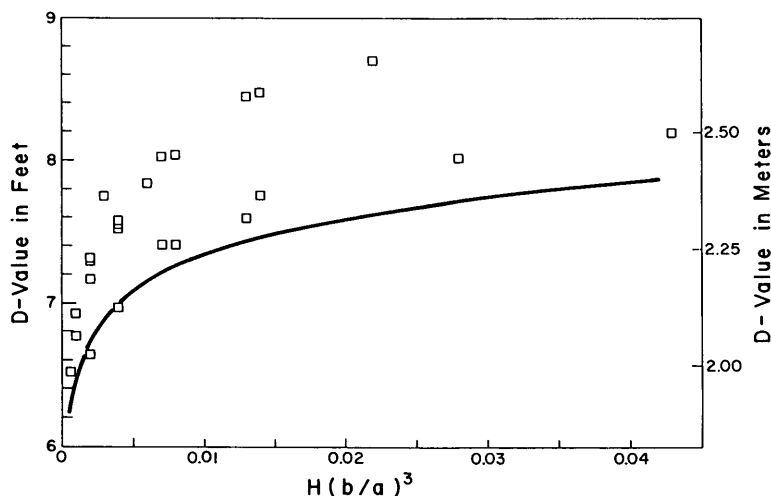
FIGURE 1 D-values for exterior girders in a normal bridge.
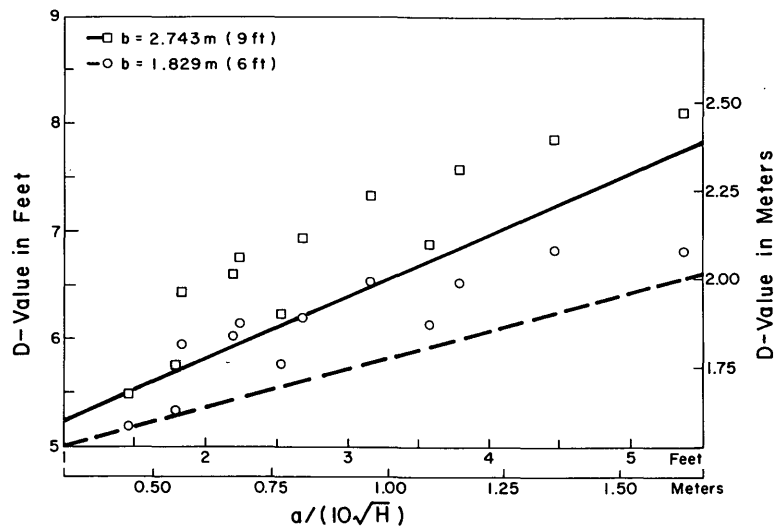
FIGURE 2 D-values for interior girders in a normal bridge.

(6) developed a general time-step analysis procedure that considers the effects of time- and cycle-dependent creep, concrete shrinkage and relaxation of prestressing steel. This model calculates stress in cracked or uncracked composite sections; it is used here to compute maximum and minimum stresses in bridge components, with maximum stress resulting from total load and minimum stress from dead load only. These stresses are then used to compute median life (β) and shape parameter (α) for cumulative-damage distribution for bridge life under stochastic loading.

Cumulative Damage Distribution

Khaleel (2) derived composite fatigue life that has the following formula:

$$\bar{\beta} = \frac{1}{\sum_{i=1}^{k} \frac{\lambda_i}{\hat{\beta}_i}} \qquad (3)$$

where

$\bar{\beta}$ = units of average daily truck traffic (ADTT),
k = number of traffic categories,
$\hat{\beta}_i$ = bridge fatigue life resulting from arrival of all trucks in category i, and
λ_i = expected number of truck per day for ith category.

For each passing truck, β_{ij} is calculated on the basis of engineering data presented by Khaleel (2) and the shape and scale parameters from the B-S distribution fitted to all stress ranges. Then $\hat{\beta}_i$ is calculated as

$$\hat{\beta}_i = \frac{1}{\sum_{j=1}^{N_i(t)} \frac{1}{\beta_{ij}}} \qquad (4)$$

Equation 3 is the Miner's rule in central tendency (i.e., median). It has been empirically shown to hold better than any

other fatigue-life rule. The harmonic mean, Miner's rule, is rigorously derived as the actual value of the median life under the assumptions specified.

Moreover, Khaleel (2) calculated the corresponding shape parameter for the distribution of the fatigue life for the structure under the mixture of loads imposed, which is given by

$$(\bar{\alpha})^2 = \bar{\beta} \sum_{i=1}^{k} \frac{\lambda_i}{\hat{\beta}_i} \left[\hat{\alpha}_i + \frac{1}{\hat{\beta}_i} \right] \qquad (5)$$

Thus, a distribution has been found to which the median life (i.e., composite fatigue life) can be calculated under a mixture of traffic using Miner's rule and the coefficient of variation determined so that it is possible to calculate "the fraction of life used," that is, the probability of failure after any fraction of the characteristic life has been spent. But, as is known empirically, this probability depends upon factors other than the median life. The formula in Equation 3 recognizes this influence through the corresponding cumulative-damage distribution and the associated $\bar{\alpha}$.

Traffic Influence Model

Consider a structure that sustains random loads in service but in which each load is allocated to all its multiple components. The strain (or stress) for each component, for a given geometry of the structure and a fixed type of load, is a complex but deterministic function found by using finite element analysis. Unfortunately the magnitudes, intensity, and allocation of total load to each component are random. Moreover, it is assumed the load order is random, the sequences of a given type form an identically independent distributed sequence, and the frequency of loads of each category is a stationary stochastic process.

The total cumulative damage sustained by the structure up to time $t > 0$ is the damage from all categories of load fluctuations (2) and is given by

$$Y_t = \sum_{i=1}^{k} \sum_{j=1}^{N_i(t)} Y_{i,j} \qquad (6)$$

where

$Y_{i,1}, Y_{i,2}, \ldots$ = incremental damages to structure from successive loads of type $i = 1, 2, \ldots, k$;

k = number of truck categories; and

$N_i(t)$ = frequency of loading under each category assumed to be a Poisson process.

The probability of survival of the structure (2) is given by

$$Pr[T \geq t] \cong 1 - \Phi\left[\frac{1}{\alpha}\, \xi\left(\frac{t}{\beta}\right)\right] \qquad (7)$$

where $\xi(x) = x^{1/2} - 1/x^{1/2}$ and Φ is cumulative normal distribution function.

VERIFICATION OF MODEL

The method for calculating the number of cycles to fatigue failure is verified by comparison of experimental and predicted data. Holmen (7) studied the effect of various load histories on the fatigue behavior of plain concrete. Experimental results from two- and multistage constant amplitude loadings (7) are compared against theoretical results. In two-stage loading, the test specimen was exposed to a constant stress amplitude of a given level until a fixed number of cycles was completed. Then, in the second stage, the level was changed and maintained until failure. The calculated number of cycles to failure are compared with the experimental ones as shown in Tables 2, 3, and 4. For the multistage constant-amplitude loading, the predicted and experimental numbers of cycles to failure are 1,338,907 and 1,502,931, respectively. The maximum stress in the multistage case ranged from 0.12 to 0.88 of the concrete compressive strength, f'_c. The results for Al-

ternatives A and B of the two-stage loading show good agreement between the experimental and theoretical results. The maximum stress levels in the two-stage loading are very high; this fact explains the differences in the predicted and experimental results. The experimental and theoretical results show that the presence of small amplitudes in a loading histogram seems to reduce the sequence effects. Bridges are generally subjected to small amplitudes of stresses; therefore, it is reasonable to ignore the load-order effect.

RESULTS

A simply supported bridge with a span of 80 ft is considered. The reinforced concrete slab is supported by 10 AASHTO Type IV precast and pretensioned girders spaced at 8 ft as shown in Figure 3. The girders were designed according to the AASHTO specifications (8). The traffic is grouped into six categories on the basis of number of truck axles. Moses and Ghosn (9) conducted a study using weigh-in-motion technology to obtain reliable information on bridge traffic. A FORTRAN program was written to implement the traffic model. This program is available from the lead author of this paper.

Effect of Truck Configuration

For purposes of investigating the effect of truck configuration on bridge fatigue life, the ADTT is assumed to consist entirely of one category of trucks of varying gross weights. Figure 4 shows the composite fatigue life of two of the girder components (i.e., prestressing steel and reinforcing steel) versus the truck category (two-axle single, three-axle single, four-axle semitrailer, five-axle semitrailer, five-axle split, and nine-

TABLE 2 Multistage Constant Amplitude Loading: Experimental and Theoretical Results

$\dfrac{\sigma_{max}}{f'_c}$	Applied Cycles	β_{ij}	$\dfrac{\lambda_i}{\beta_{ij}}$
.88	380	656	.579
.82	1,069	3458	.309
.75	3,470	2,4071	.144
.68	9,882	167,556	.059
.61	24,917	1,166,326	.021
.54	54,588	8,118,579	.006
.47	105,561	5.65×10^7	1.86×10^{-3}
.40	177,354	3.93×10^8	4.51×10^{-4}
.33	256,555	2.74×10^9	9.37×10^{-5}
.26	314,583	1.91×10^{10}	1.65×10^{-6}
.19	315,864	1.33×10^{11}	2.38×10^{-6}
.12	238,708	9.24×10^{11}	2.58×10^{-7}
N_F [a]	1,502,931	$-$[b]	1,338,907

[a] N_F is the total number of cycles to fatigue failure.
[b] Not applicable.

TABLE 3 Predicted and Experimental Number of Cycles to Failure Based on Two-Stage Constant Amplitude Loading: Alternative A

Specimen Number	Number of Cycles			
	Experimental		Predicted	
	.75 $f_c'^a$	.90 $f_c'^b$	.75 $f_c'^a$	.90 $f_c'^b$
1	4980	136	8824	239
2	4110	520	2680	335
3	6710	344	5735	287
4	6760	195	8515	243
5	2260	187	3804	317
–	4136[c]	276[c]	4926[c]	236[c]

[a] Maximum applied stress (the first stage) was maintained until a fixed number of cycles were completed.
[b] Maximum applied stress (the second stage) was maintained until failure.
[c] Average number of cycles of the five specimens at a certain maximum stress level.

axle B-train are Categories 1 to 6, respectively). The nine-axle B-train double trucks were the most damaging, whereas the two-axle single trucks were least damaging. The four-axle semitrailer trucks are less damaging than three-axle single trucks, even though their average weight is higher than that of three-axle single trucks. The incremental damage caused by each passing truck depends on its gross weight, configuration, axle load distribution, and lateral load distribution on the bridge.

Effect of Concrete Strength

The compressive strength of concrete was varied to study its influence on the fatigue life of the structural components subjected to the spectrum of loads. The effect of increasing f_c' from 30 to 40 MPa yields a slight increase in the fatigue life of prestressing and nonprestressing steel. The fatigue lives of

cast-in-place slab and precast girder were increased 233 and 355 percent, respectively. The results are shown in Figure 5.

Effect of Change from Nominal Values

Figure 6 shows that the effect of uniform reduction of the nominal area of reinforcing steel on the fatigue life of prestressing steel is negligible. Reducing the area of prestressing steel by 20 percent, however, results in 62 and 79 percent reductions in the fatigue life of prestressing and reinforcing steel, respectively.

Effect of Partial Prestressing Ratio

Several girders were designed with the same moment capacity but with different partial prestressing ratios (PPRs) to inves-

TABLE 4 Predicted and Experimental Number of Cycles to Failure Based on Two-Stage Constant Amplitude Loading: Alternative B

Specimen Number	Number of Cycles			
	Experimental		Predicted	
	.90 $f_c'^a$	.75 $f_c'^b$	.90 $f_c'^a$	.75 $f_c'^b$
1	108	22140	90	18348
2	74	10940	62	9145
3	40	710	294	5288
4	45	4340	151	14448
5	80	4110	209	10681
–	69[c]	8448[c]	161[c]	11582[c]

[a] Maximum applied stress (the first stage) was maintained until a fixed number of cycles were completed.
[b] Maximum applied stress (the second stage) was maintained until failure.
[c] Average number of cycles of the five specimens at a certain maximum stress level.
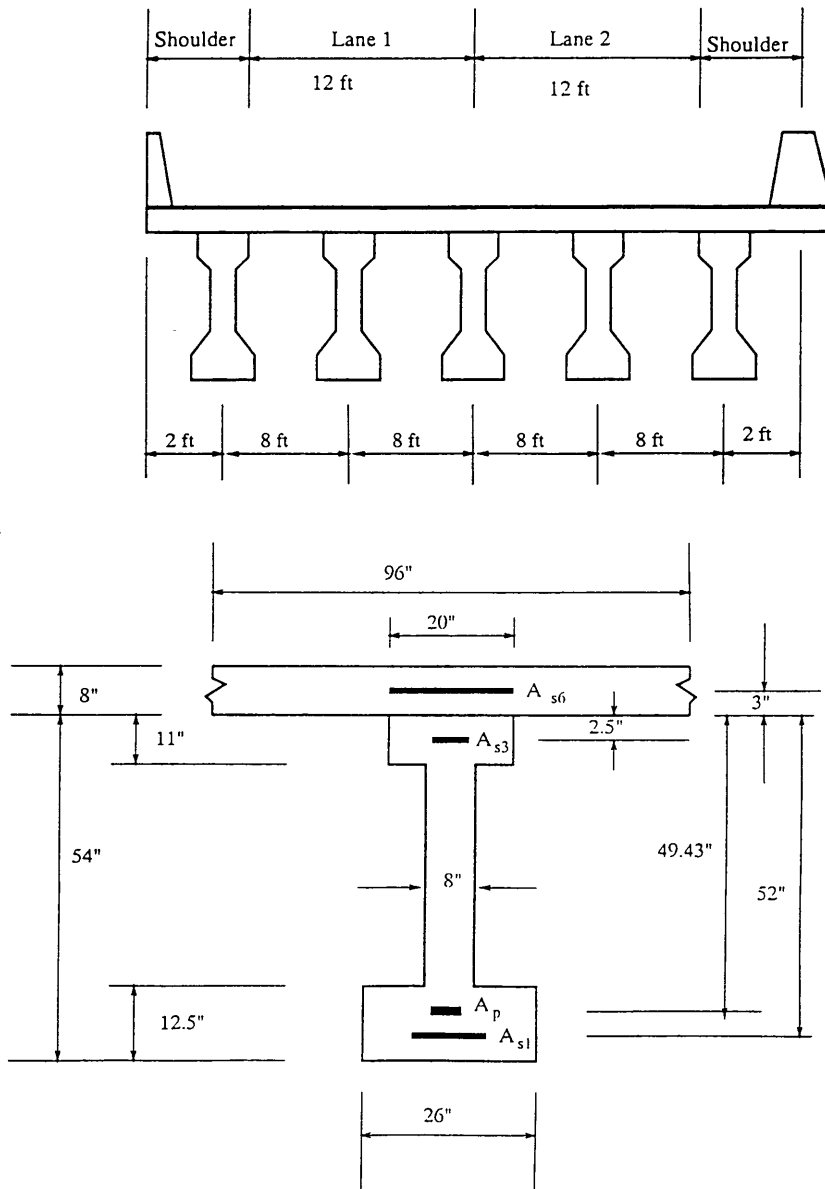
FIGURE 3 Cross section of a typical slab-and-girder bridge.
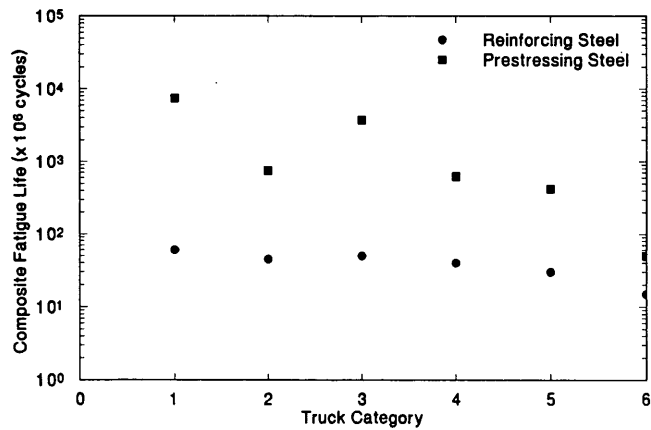
FIGURE 4 Effect of truck configuration on fatigue life.
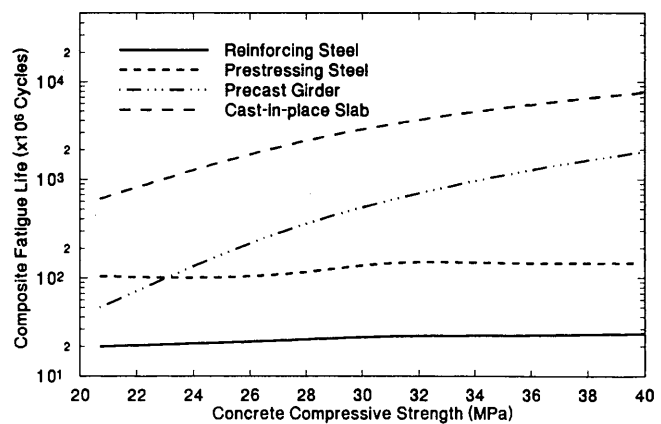
FIGURE 5 Effect of concrete strength on fatigue life.
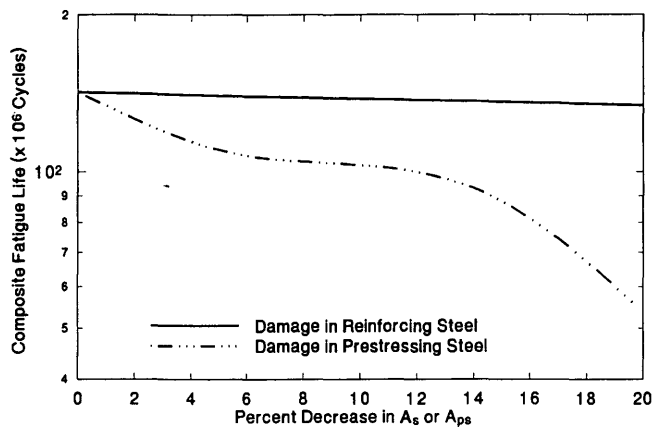
FIGURE 6 Effect of damage in reinforcement on fatigue life of prestressing steel.

tigate the effect of PPR on fatigue life. Figure 7 shows that a girder with a high PPR has a higher fatigue life than one with a low PPR.

SUMMARY AND CONCLUSIONS

An efficient method is presented for calculating the number of loadings a bridge member can withstand before a detectable fatigue crack develops. This method recognizes that the probability of survival depends on factors other than the median
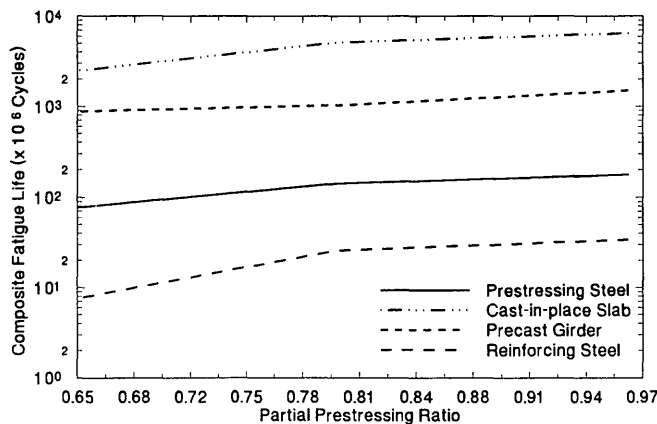
FIGURE 7 Effect of PPR on fatigue life.

life through the corresponding cumulative damage distribution and the associated $\bar{\alpha}$. The following major conclusions are drawn from the study:

● The nine-axle B-train double (i.e., one of the Turner) trucks were found to be most damaging, whereas two-axle single trucks were least damaging. The incremental damage caused by each truck depends on truck configuration, gross weight, axle-load distribution, and lateral load distribution factor.

● The median life of ordinary reinforcing bars is the lowest among the girder components. Cast-in-place slab, on the other hand, has the highest median life.

● Reducing the nominal cross-sectional area of prestressing steel reduces the fatigue life of all components significantly, whereas reducing the area of reinforcing steel has virtually no effect on the fatigue life of the structure.

● Girders designed with low PPR have a much shorter median fatigue life than those designed with high PPR.

REFERENCES

1. B. G. Rabbat, P. H. Karr, H. G. Russel, and N. G. Bruce Jr. *Fatigue Tests of Full-Size Prestressed Girders.* Research Report 113. Portland Cement Association, Skokie, Ill., 1978.
2. M. A. Khaleel. *Reliability-Based Analysis, Sensitivity and Design of Partially Prestressed Concrete Systems.* Ph.D. thesis. Washington State University, Pullman, 1992.
3. E.-S. Hwang and A. S. Nowak. Simulation of Dynamic Load for Bridges. *Journal of the Structural Division,* ASCE, Vol. 117, No. 5, 1991, pp. 1413–1434.
4. M. A. Khaleel and R. Y. Itani. Live-Load Moments for Continuous Skew Bridges. *Journal of the Structural Division,* ASCE, Vol. 116, No. 9, 1990, pp. 2361–2372.
5. M. A. Khaleel. *Development of Design Criteria for Continuous Skew Slab-and-Girder Bridges.* M.S. thesis. Washington State University, Pullman, 1988.
6. R. Z. Al-Zaid, A. E. Naaman, and A. S. Nowak. Partially Prestressed Composite Beams Under Sustained and Cyclic Loads. *Journal of the Structural Division,* ASCE, Vol. 114, No. 2, 1988, pp. 269–291.
7. J. O. Holmen. *Fatigue of Concrete by Constant and Variable Amplitude Loading.* Bulletin 79-1, NTH, Division of Concrete Structures, Trondheim, Norway, 1979.
8. *Standard Specification for Highway Bridges.* AASHTO, Washington, D.C., 1989.
9. F. Moses and M. Ghosn. *Instrumentation for Weighing Trucks-in-Motion for Highway Bridge Loads.* Report FHWA/OH-83/001. Case Western Reserve University, Cleveland, Ohio, 1983.

Natural Frequencies of Concrete Bridges in the Pacific Northwest

Ralph A. Dusseau and Hassan N. Dubaisi

Analyses of field ambient vibration were performed on 50 concrete bridge spans along Interstate highways I-5 and I-405 in Washington State. These 50 spans included 21 pretensioned concrete beam (PCB) spans, 19 reinforced concrete box-girder (CBOX) spans, and 10 reinforced concrete slab (CS) spans. Eight measurement transducers were used to record ambient bridge vibrations at three locations on each span: midspan, one-quarter point, and one support. These records of bridge motion versus time were each subjected to a fast Fourier transformation, and plots of amplitude versus frequency were generated for each record. The plots of amplitude versus frequency were used to determine the fundamental vertical and lateral frequencies for the bridge spans measured. These fundamental frequencies were used with the bridge design parameters to derive empirical formulas that will be used to estimate the fundamental vertical and lateral frequencies of other PCB, CBOX, and CS bridge spans along I-5, I-205, and I-405 in the Pacific Northwest.

The research reported here was part of a 3-year project sponsored by the U.S. Geological Survey (USGS) as part of the National Earthquake Hazards Reduction Program. This study is referred to as the "I-5 Bridge Project." Two major objectives of the research are

1. To develop a computer data base, called the I-5 Bridge Database, containing design information for all 1,000 highway, railway, and pedestrian bridges on and over Interstate highways I-5, I-205, and I-405 (collectively referred to as "the I-5 corridor") in western Washington and northwestern Oregon.
2. To perform field ambient vibration analyses on a representative sample of highway bridge spans in Washington and to derive empirical formulas for estimating the fundamental vertical and lateral frequencies of other bridges in the I-5 Bridge Database.

The present focus is on the second objective, which includes the results generated by the field ambient vibration analyses and the empirical formulas derived from these results.

The importance of structure frequency in seismic analysis is well established. In the wake of the September 19, 1985, Mexico City earthquakes (*1*), which demonstrated a strong correlation among earthquake frequency, structure frequency, and structure damage, structure frequency has become an even more important issue in earthquake engineering. The maximum ground acceleration in the Mexico City area during the earthquakes was about 0.5*g*, with a dominant frequency of 0.5 cycles per second (cps) and a secondary

frequency near 1.0 cps. The majority of the buildings damaged in these shocks (61 percent) were 6- to 15-stories tall with fundamental frequencies of approximately 0.6 to 1.4 cps. This strong correlation between ground motion frequency, structure frequency, and structure damage has provided an important new indication of the criticality of structure frequency in the determination of structure seismic damage.

With the goal of determining natural structure frequencies, field ambient vibration analyses have been conducted on a variety of structures, including multistory buildings (*2,3*), steel truss bridges (*4*), and suspension bridges (*5* to *9*). Thus the state of the art of field ambient vibration analysis is well established and the procedures are well known (*10*).

The goal in performing field ambient vibration analyses as part of the I-5 Bridge Project was to determine the natural frequencies for a representative sample of bridge spans along the I-5 corridor in Washington and to extrapolate these results to other bridges in the I-5 Bridge Database. To this end, field ambient vibration measurements and laboratory data analyses were performed on 52 spans from 20 typical highway bridges.

BRIDGE SPANS ANALYZED

The 52 bridge spans analyzed were chosen to reflect as closely as possible the actual distribution of bridge span type and length for the highway bridges along the I-5 corridor in Washington. These 52 spans were distributed as follows among four types of concrete bridges:

- 21 (40 percent) pretensioned concrete beam (PCB) spans,
- 19 (37 percent) reinforced concrete box-girder (CBOX) spans,
- 10 (19 percent) reinforced concrete slab (CS) spans, and
- 2 (4 percent) reinforced concrete T-beam spans.

Although other bridge types, such as prestressed concrete box-girders, steel beams and girders, steel trusses, timber trestles, steel and concrete arches, and steel box-girders, exist along the I-5 corridor in Washington, none represent more than 3 percent of the total number of bridge spans along the I-5 corridor.

The results presented here are for the 21 PCB spans, 19 CBOX spans, and 10 CS spans. These three span types represent approximately 90 percent of the bridge spans along the I-5 corridor in Washington. These 50 spans are part of 19 different bridges along the I-5 corridor. The bridge type; Washington State Department of Transportation (WSDOT) bridge number; bridge name; number of spans per bridge;

Department of Civil and Environmental Engineering, Wayne State University, Detroit, Mich. 48202.

top and bottom slab thickness (where applicable); number of beams, box-girders, or slabs; and number of columns or walls per intermediate support for each of these 19 bridges are presented in Table 1.

For safety reasons, most of the bridges measured in the field were undercrossings with wide sidewalks. The traffic along the I-5 corridor was deemed too heavy to permit safe measurements on most highway overcrossings or ramps, and wide sidewalks were necessary to facilitate safe access to each bridge without disruption of vehicular traffic. At each bridge site, the measurement transducers, equipment, and cables were placed on only one of the two sidewalks to avoid having cables stretched across the roadway.

FIELD MEASUREMENTS

The bridge motion measured in the field was generated by ambient loads that consisted primarily of traffic and wind loads. For each bridge span analyzed, field ambient vibration

measurements were taken using eight signal transducers—six SS-1 seismometers and two FBA-11 accelerometers. The signal output from these eight transducers was amplified and then recorded on tape recorder. The two transducer configurations used covered half each bridge span, from midspan to one of the two supports. The configuration that was initially used and applied to all 21 PCB spans was as follows:

1. Seismometer—midspan location and vertical orientation,
2. Seismometer—midspan location and lateral orientation,
3. Seismometer—midspan location and longitudinal orientation,
4. Seismometer—quarter-point location and vertical orientation,
5. Seismometer—quarter-point location and lateral orientation,
6. Seismometer—support location and vertical orientation,
7. Accelerometer—midspan location and vertical orientation, and

TABLE 1   General Information for Concrete Bridges Analyzed

Bridge Type	WSDOT Bridge Number	Bridge Name (OC = Overcrossing, UC = Undercrossing, RR = Railroad)	Number of Spans per Bridge	Slab Thicknesses, mm		Number of Beams, Box-Girders or Slabs	Number of Columns or Walls per Support
				Top	Bot.		
Pretensioned Concrete Beam (PCB) Bridges	5/457	PORT OF TACOMA UC	4	146	NA	9	5
	5/602	236TH STREET SW UC	4	146	NA	6	3
	5/605	220TH STREET SW UC	4	178	NA	15	7
	5/615	164TH STREET SW UC	4	178	NA	12	6
	5/630	41ST STREET UC	4	165	NA	7	3
	5/656	MARSHALL ROAD UC	2	165	NA	8	2
	405/42	MAIN STREET UC	3	146	NA	9	3
	405/42.5	NE 4TH STREET UC	2	191	NA	13	6
Reinforced Concrete Box-Girder (CBOX) Bridges	5/418	BRIDGEPORT WAY UC	4	165	165	7	4
	5/419	CARLYLE ROAD UC	4	165	152	4	1
	5/596	NE 185TH STREET UC	4	165	152	7	4
	405/17	BENSON ROAD UC	4	165	152	5	1
	405/50 N	NE 72ND PLACE UC	4	191	178	4	1
	405/50 S	NE 72ND PLACE UC	4	191	178	4	1
	405/57 S	NE 124TH STREET UC	4	191	178	4	1
Reinforced Concrete Slab (CS) Bridges	5/415 A	GRAVELLY LAKE RR OC	1	305	NA	1	1
	5/417	CLOVER CREEK BRIDGE	3	330	NA	1	1
	5/425	S 84TH STREET UC	2	864	NA	1	1
	5/428	S 56TH STREET UC	4	584	NA	2	6

8. Accelerometer—quarter-point location and vertical orientation.

Because the vertical direction was initially assumed to be the most flexible for each bridge span, three seismometers were oriented in that direction with one at midspan, one at a quarter point, and one at a support. In order to cover the full range of potential vertical bridge frequencies, the two accelerometers were also oriented vertically, with one at midspan and one at the quarter point. Two seismometers were oriented laterally, with one at midspan and one at the quarter point. The longitudinal direction was assumed to be the least flexible, and only one seismometer (located at midspan) was oriented longitudinally.

On the basis of the results for the PCB spans, the seismometers were considered sufficient for recording all vertical frequencies, but additional information on bridge responses at the supports was desired. Therefore for the CBOX and CS spans, the two accelerometers were moved to the support with one oriented longitudinally and one laterally.

LABORATORY DATA ANALYSES

In the laboratory analyses of the data recorded in the field, the signal output from each transducer was played back through a spectrum analyzer, and a fast Fourier transformation was performed. The final results for each transducer were plots of signal amplitude (velocity for the seismometers and acceleration for the accelerometers) versus frequency, from which the natural frequencies of the bridge span at the given location and in the given direction could be read directly. These analyses also included comparisons of phase and coherence between pairs of transducer signals. The comparisons aid in deducing the mode shape associated with each frequency.

SAMPLE OUTPUT

As samples of the analysis results that were derived for each bridge span, Figure 1 shows the amplitude versus frequency
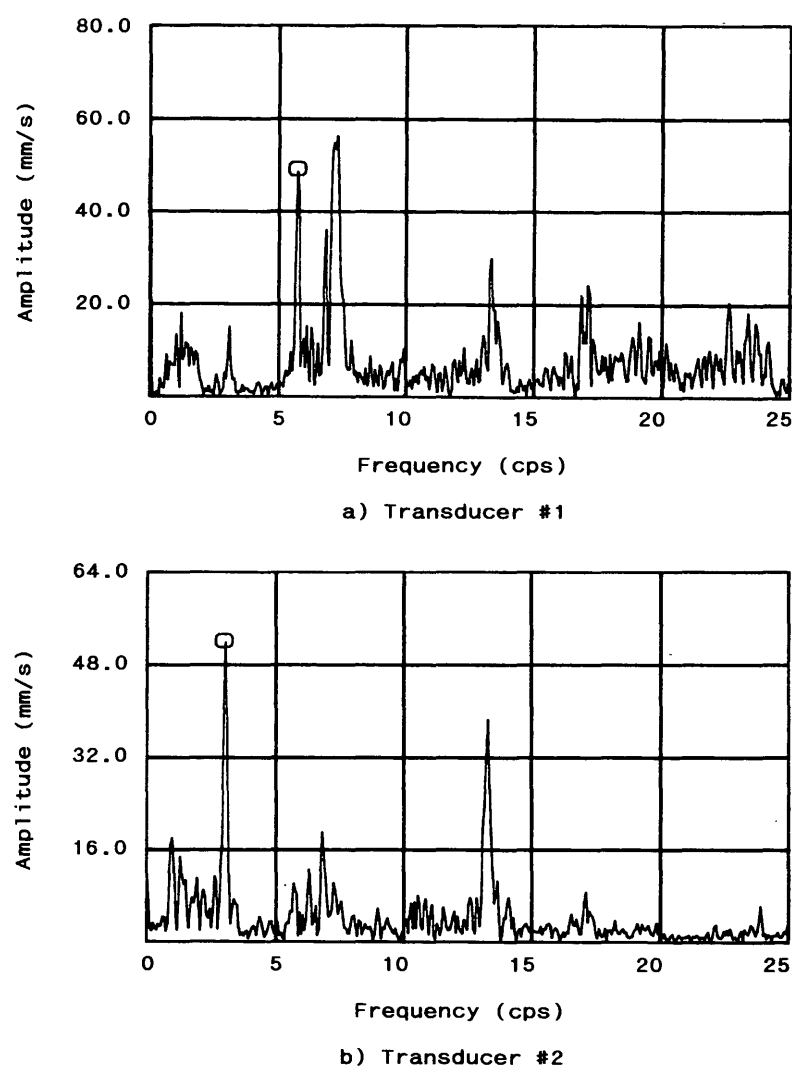
FIGURE 1   Sample output for Span 3 of WSDOT Bridge 405/17:
(*a*) Transducer 1, (*b*) Transducer 2.

results for Transducers 1 and 2 as recorded on Span 3 of WSDOT Bridge 405/17. The results shown in Figure 1(a) for Transducer 1, which represent vertical motion at midspan, indicate that for this span the fundamental frequency in the vertical direction is 5.8 cps. Previous experience suggests the associated mode shape is probably a half sine wave vertical motion of the bridge span.

The results for Transducer 2, which are plotted in Figure 1(b) and which represent lateral motion at midspan, show that the fundamental lateral frequency for WSDOT Bridge 405/17 is 3.1 cps. The corresponding mode shape is most likely a half sine wave lateral motion of the entire bridge deck. This conclusion is supported by the fact that this frequency is also the fundamental lateral frequency for Spans 1 and 2 of this bridge as measured in the field.

FUNDAMENTAL VERTICAL FREQUENCIES

Because each bridge support is essentially rigid with respect to vertical versus lateral motion, the results of field ambient vibration analysis generally indicated that each bridge span has its own unique fundamental vertical frequency, whereas each bridge has a fundamental lateral frequency that is the same for all bridge spans. For each PCB span, the WSDOT bridge number, span number, span length, beam depth, and fundamental vertical frequency derived by field measurement are presented in Table 2. The WSDOT bridge number, span number, span length, box-girder depth, and fundamental vertical frequency derived by field measurement for each CBOX span are presented in Table 3. The WSDOT bridge number, span number, span length, slab thickness, and fundamental

TABLE 2 Vertical Results for PCB Bridge Spans

WSDOT Bridge Number	Span No.	Span Length, meters	Beam Depth, meters	Span End Continuity	$\dfrac{D^{0.5}}{Ls^{1.7}}$, $m^{-1.2}$	Fundamental Vertical Frequencies, cycles/second			Percent Difference Between Empirical and Measured Values
						Theoretical Formula	Field-Measured	Empirical Formula	
5/457	1	12.47	0.81	none	0.01234	10.2	14.1	15.6	+ 10.6
5/630	4	12.95	1.27	none	0.01449	15.2	16.0	18.3	+ 14.4
405/42	3	15.85	1.47	one	0.01106	18.9	14.5	14.0	− 3.4
5/457	4	16.72	0.86	none	0.00772	6.4	11.1	9.8	− 11.7
5/615	1	16.92	1.47	none	0.00989	10.9	12.9	12.5	− 3.1
5/605	1	17.06	1.47	none	0.00976	10.8	12.9	12.4	− 3.9
5/602	4	18.29	1.35	none	0.00831	8.1	10.2	10.5	+ 2.9
5/615	4	20.42	1.47	none	0.00719	7.5	8.9	9.1	+ 2.2
405/42.5	1	20.84	1.27	one	0.00645	9.7	8.9	8.2	− 7.9
405/42.5	2	20.84	1.27	one	0.00645	9.7	8.7	8.2	− 5.7
5/630	3	22.40	1.27	none	0.00571	5.2	6.8	7.2	+ 5.9
5/602	1	22.71	1.35	none	0.00575	5.3	7.1	7.3	+ 2.8
5/605	4	23.77	1.47	none	0.00555	5.6	7.4	7.0	− 5.4
5/602	2	28.04	1.35	none	0.00402	3.4	4.6	5.1	+ 10.9
405/42	1	28.50	1.47	one	0.00408	5.9	4.9	5.2	+ 6.1
5/615	2	30.48	1.47	none	0.00364	3.3	4.2	4.6	+ 9.5
5/457	2	30.78	1.47	none	0.00358	3.2	4.1	4.5	+ 9.8
5/605	2	31.08	1.47	none	0.00352	3.2	4.6	4.5	− 2.2
5/656	1	33.07	1.47	one	0.00317	4.3	3.9	4.0	+ 2.6
5/656	2	33.07	1.47	one	0.00317	4.3	3.9	4.0	+ 2.6
405/42	2	34.90	1.47	both	0.00289	5.7	4.6	3.7	− 19.6

TABLE 3   Vertical Results for Reinforced CBOX Bridge Spans

WSDOT Bridge Number	Span No.	Span Length, meters	Girder Depth, meters	Span End Continuity	$\dfrac{D^{0.5}}{Ls^{1.8}}$, $m^{-1.3}$	Fundamental Vertical Frequencies, cycles/second			Percent Difference Between Empirical and Measured Values
						Theoretical Formula	Field-Measured	Empirical Formula	
5/596	4	13.72	1.21	one	0.00987	21.5	16.2	17.4	+ 7.4
5/596	1	16.46	1.21	one	0.00711	14.9	13.0	12.5	- 3.8
5/418	1	18.07	1.12	one	0.00578	11.4	11.5	10.2	- 11.3
5/418	4	18.07	1.12	one	0.00578	11.4	12.8	10.2	- 20.3
405/17	1	18.43	1.16	one	0.00568	11.0	7.2	10.0	+ 38.9
5/419	4	20.73	1.17	one	0.00462	8.5	8.9	8.1	- 9.0
5/596	2	22.96	1.21	both	0.00391	11.1	6.2	6.9	+ 11.3
5/596	3	22.96	1.21	both	0.00391	11.1	6.2	6.9	+ 11.3
405/57 S	4	23.77	2.36	one	0.00512	12.7	10.5	9.0	- 14.3
405/17	2	23.77	1.16	both	0.00359	9.6	5.8	6.3	+ 8.6
405/17	3	23.77	1.16	both	0.00359	9.6	5.8	6.3	+ 8.6
5/418	2	26.67	1.12	both	0.00287	7.6	5.5	5.1	- 7.3
5/418	3	26.67	1.12	both	0.00287	7.6	5.6	5.1	- 8.9
5/419	3	27.58	1.17	both	0.00276	7.0	5.1	4.9	- 3.9
405/50 N	3	29.81	1.65	both	0.00285	8.4	3.9	5.0	+ 28.2
405/50 S	3	31.30	1.65	both	0.00261	7.6	4.1	4.6	+ 12.2
405/50 N	4	33.83	1.65	one	0.00227	4.5	3.8	4.0	+ 5.3
405/50 S	4	34.14	1.65	one	0.00223	4.4	4.1	3.9	- 4.9
405/57 S	3	43.59	2.36	both	0.00172	5.5	3.4	3.0	- 11.8

vertical frequency derived by field measurement for each CS span are presented in Table 4.

Rough theoretical estimates of the fundamental vertical frequencies for each span are also presented in Tables 2–4. These rough estimates were based on consistent-mass systems that assumed the ends of each span to be either simply supported, fixed at one end only, or fixed at both ends. The resulting theoretical formulas for fundamental vertical frequency are functions of the main member depth (beam depth, box-girder depth, or slab thickness) divided by the square of the span length. The end conditions for each bridge span are also noted in Tables 2–4. Because of the prestressing effects, the gross moments of inertia of the bridge deck were used to derive the theoretical fundamental vertical frequencies for the PCB spans, whereas half the gross moments of inertia of the bridge deck were used to calculate the theoretical fundamental vertical frequencies for the CBOX and CS spans.

In deriving empirical formulas to estimate the fundamental vertical frequencies of other PCB, CBOX, and CS spans along the I-5 corridor, it was assumed that because the vertical stiffness and total mass of a given bridge span are functions

of the span length and depth, the fundamental vertical frequency of the span will also be a function of the span length and depth (similar to the theoretical formulas discussed here). Thus the following general form for these empirical formulas was assumed:

$$fv = \frac{Kv \cdot D^m}{Ls^n} \tag{1}$$

where

fv = estimated fundamental vertical frequency,
Ls = span length, and
D = beam depth, box-girder depth, or slab thickness.

The constant Kv and the coefficients m and n were derived for each bridge type by minimizing the standard deviation of the field-measured data points versus the empirical results. More precisely, for each bridge type and each trial empirical formula, the quantity $Fv \cdot Ls^n/D^m$ was calculated for each span, where Fv is the fundamental vertical frequency based on field ambient vibration measurement. The mean value and stan-

TABLE 4 Vertical Results for Reinforced CS Bridge Spans

WSDOT Bridge Number	Span No.	Span Length, meters	Slab Thickness, meters	Span End Continuity	$\dfrac{D^{0.4}}{Ls^{1.5}}$, $m^{-1.1}$	Fundamental Vertical Frequencies, cycles/second			Percent Difference Between Empirical and Measured Values
						Theoretical Formula	Field-Measured	Empirical Formula	
5/417	1	6.37	0.33	one	0.03992	25.3	19.0	24.5	+ 28.9
5/417	3	6.37	0.33	one	0.03992	25.2	18.6	24.5	+ 31.7
5/415 A	1	8.17	0.30	none	0.02646	12.0	20.1	16.3	− 18.9
5/417	2	8.23	0.33	both	0.02718	22.0	18.4	16.7	− 9.2
5/428	1	13.72	0.58	one	0.01582	8.5	13.5	9.7	− 28.1
5/428	4	13.72	0.58	one	0.01582	8.5	13.5	9.7	− 28.1
5/428	2	17.37	0.58	both	0.01111	7.7	5.6	6.8	+ 21.4
5/428	3	17.37	0.58	both	0.01111	7.7	5.6	6.8	+ 21.4
5/425	1	21.45	0.86	one	0.00948	4.9	5.1	5.8	+ 13.7
5/425	2	21.45	0.86	one	0.00948	4.9	4.9	5.8	+ 18.4

dard deviation for the quantities $Fv \cdot Ls^n/D^m$ were then calculated for each bridge type and each trial empirical formula. The empirical formulas that yielded the lowest standard deviation for each bridge type are presented next.

PCB Spans

The empirical formula derived for the PCB spans is as follows:

$$fv = \frac{1230 \cdot D^{0.5}}{Ls^{1.7}} \tag{2}$$

The quantity $D^{0.5}/Ls^{1.7}$ for each PCB span, the fundamental vertical frequency derived by Equation 2 for each span, and the percent difference between the latter and the fundamental vertical frequency derived by field measurement are presented in Table 2. A plot of the fundamental vertical frequency for each span as derived by field measurement versus $D^{0.5}/Ls^{1.7}$ is presented in Figure 2. Figure 2 also contains a straight-line plot of Equation 2 for comparison.

The empirically derived fundamental vertical frequencies for the PCB spans, as presented in Table 2, are close to the field-measured values, with the results for 9 of 21 spans within 4 percent, 14 of 21 spans within 8 percent, 19 of 21 spans within 12 percent, and all 21 spans within 20 percent. Only one of the empirically derived fundamental vertical frequencies is more than 15 percent different from the corresponding field-measured value.

Reinforced CBOX Spans

For the CBOX spans, the empirical formula derived is as follows:

$$fv = \frac{1760 \cdot D^{0.5}}{Ls^{1.8}} \tag{3}$$

The quantity $D^{0.5}/Ls^{1.8}$ for each CBOX span, the fundamental vertical frequency derived by Equation 3 for each span, and the percent difference between the latter and the fundamental vertical frequency derived by field measurement are presented in Table 3. Figure 3 shows a plot of the fundamental vertical frequency for each span as derived by field measurement versus $D^{0.5}/Ls^{1.8}$. A plot of Equation 3 is also shown in Figure 3 for comparison.

The empirically derived fundamental vertical frequencies presented in Table 3 for the CBOX spans are moderately close to the field-measured values. The results for 4 of 19 spans are within 6 percent, 10 of 19 spans are within 9 percent, 16 of 19 spans are within 15 percent, and all 19 spans are within 39 percent. Only one of the empirically derived fundamental vertical frequencies is more than 29 percent different from the corresponding field-measured value.

Reinforced CS Spans

The empirical formula derived for the CS spans is as follows:

$$fv = \frac{615 \cdot D^{0.4}}{Ls^{1.5}} \tag{4}$$

The quantity $D^{0.4}/Ls^{1.5}$ for each CS span, the fundamental vertical frequency derived by Equation 4 for each span, and the percent difference between the latter and the fundamental vertical frequency derived by field measurement are presented in Table 4. A plot of the fundamental vertical frequency
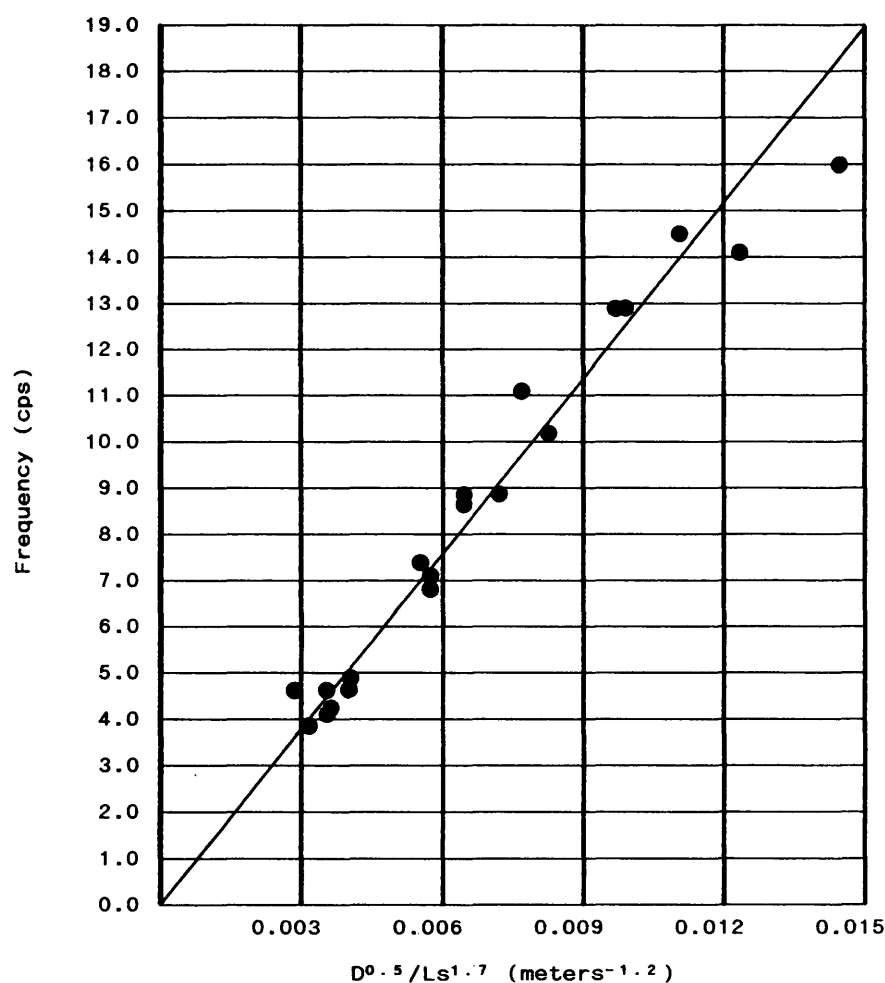
FIGURE 2 Vertical frequency plot for PCB bridge spans.

for each span as derived by field measurement versus $D^{0.4}/Ls^{1.5}$ is shown in Figure 4. For comparison, a plot of Equation 4 is also presented in Figure 4.

For the CS spans, the empirically derived fundamental vertical frequencies presented in Table 4 are moderately close to the field-measured values with the results for 2 of 10 spans within 14 percent, 6 of 10 spans within 22 percent, and all 10 spans within 32 percent. Only one of the empirically derived fundamental vertical frequencies is more than 29 percent different from the corresponding field-measured value.

FUNDAMENTAL LATERAL FREQUENCIES

Tables 5–7 present the WSDOT bridge number, bridge length, deck width, maximum support height, and fundamental lateral frequency derived by field ambient vibration measurement for each PCB, CBOX, and CS bridge, respectively.

To estimate the fundamental lateral frequencies of other concrete bridges along the I-5 corridor, it was assumed that because the lateral stiffness and total mass of a given bridge are functions of the bridge length, deck width, and maximum support height, the fundamental lateral frequency of the bridge

will also be a function of these three parameters. Thus the following general form for these empirical formulas was assumed:

$$fl = \frac{Kl \cdot W^m}{Lb^n \cdot H^p} \tag{5}$$

where

fl = estimated fundamental lateral frequency,
Lb = overall bridge length,
W = deck width, and
H = maximum support height.

The constant Kl and the coefficients m, n, and p were derived for each bridge type using a procedure similar to the one described previously for the vertical direction. For each bridge type and trial empirical formula, the quantity $Fl \cdot Lb^n \cdot H^p/W^m$ was calculated for each bridge, where Fl is the fundamental lateral frequency derived by field ambient vibration analysis. The mean value and standard deviation for the quantities $Fl \cdot Lb^n \cdot H^p/W^m$ were then calculated for each bridge type and each trial empirical formula. The empirical formulas that yielded the lowest standard deviation for each bridge type follow.
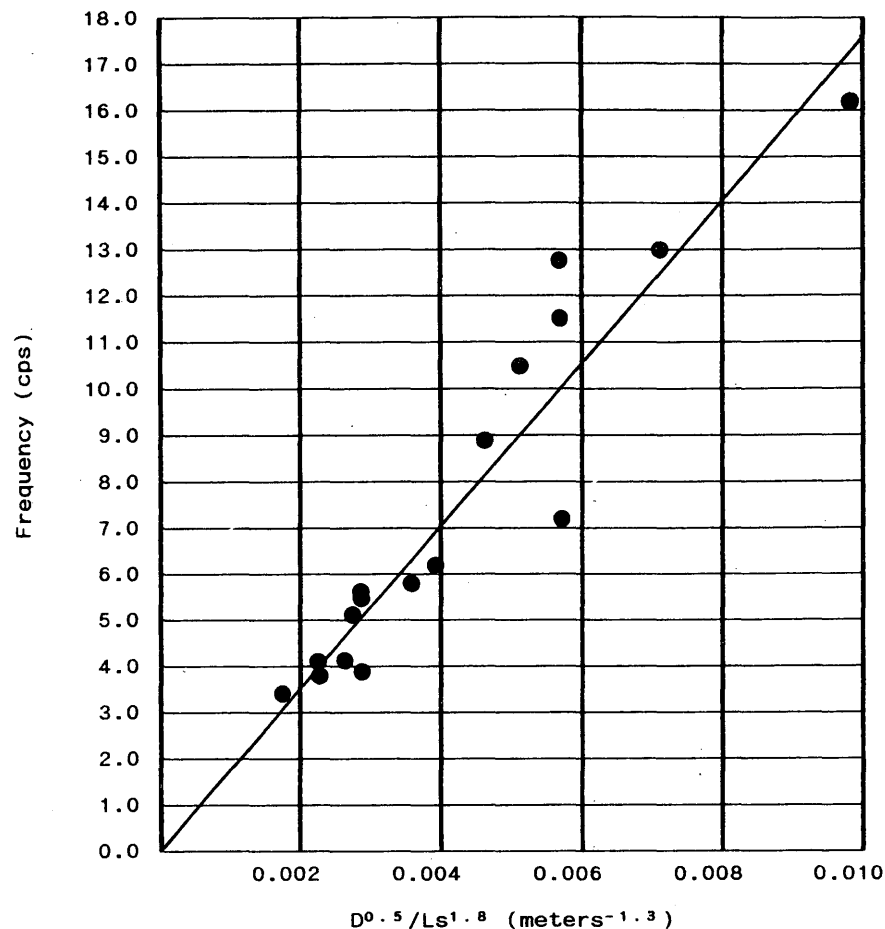
FIGURE 3 Vertical frequency plot for reinforced CBOX bridge spans.

PCB Bridges

For the PCB bridges, the empirical formula derived is as follows:

$$fl = \frac{836 \cdot W^{0.5}}{Lb \cdot H} \qquad (6)$$

The quantity $W^{0.5}/Lb \cdot H$ for each PCB bridge, the fundamental lateral frequency derived by Equation 6 for each bridge, and the percent difference between the latter and the fundamental lateral frequency derived by field measurement are presented in Table 5. Figure 5 shows a plot of the fundamental lateral frequency for each bridge as derived by field measurement versus $W^{0.5}/Lb \cdot H$. A plot of Equation 6 also is presented in Figure 5 for comparison.

The empirically derived fundamental lateral frequencies for the PCB bridges, as presented in Table 5, are close to the field-measured values with the results for five of eight bridges within 5 percent and all eight bridges within 14 percent. Only one of the empirically derived fundamental lateral frequencies is more than 9 percent different from the corresponding field-measured value.

Reinforced CBOX Bridges

The empirical formula derived for the CBOX bridges is as follows:

$$fl = \frac{9.17 \cdot W^{0.6}}{Lb^{0.4} \cdot H^{0.3}} \qquad (7)$$

Table 6 presents the quantity $W^{0.6}/Lb^{0.4} \cdot H^{0.3}$ for each CBOX bridge, the fundamental lateral frequency derived by Equation 7 for each bridge, and the percent difference between the latter and the fundamental lateral frequency derived by field measurement. A plot of the fundamental lateral frequency for each bridge as derived by field measurement versus $W^{0.6}/Lb^{0.4} \cdot H^{0.3}$ is shown in Figure 6. For comparison purposes, a plot of Equation 7 is also presented in Figure 6.

As listed in Table 6 for the CBOX bridges, the empirically derived fundamental lateral frequencies are close to the field-measured values, with the results for all seven bridges within 10 percent. Only one of the empirically derived fundamental lateral frequencies is more than 5 percent different from the corresponding field-measured value.
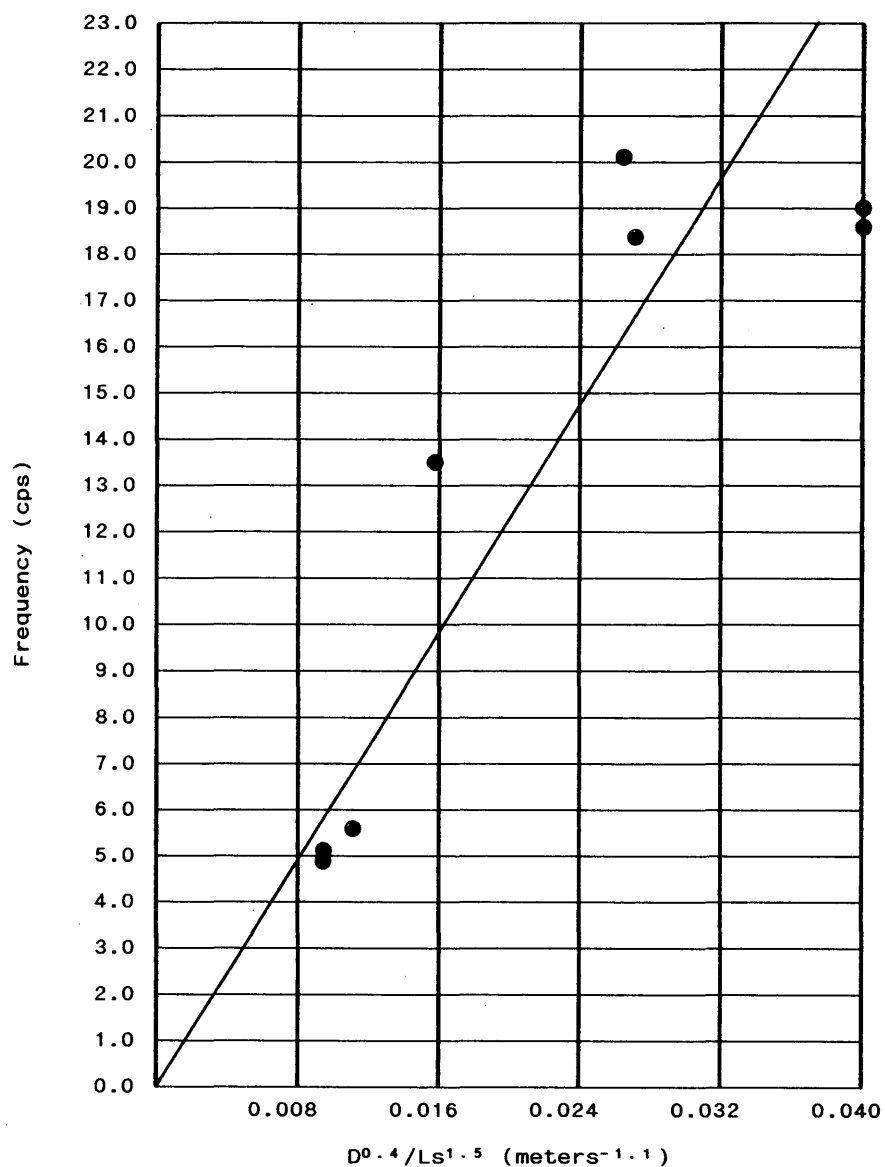
FIGURE 4 Vertical frequency plot for reinforced CS bridge spans.

TABLE 5 Lateral Results for PCB Bridges

WSDOT Bridge Number	Bridge Length, meters	Deck Width, meters	Maximum Support Height, meters	$\dfrac{W^{0.5}}{Lb \cdot H}$, $m^{-1.5}$	Fundamental Lateral Frequencies, cycles/second		Percent Difference Between Empirical and Measured Values
					Field–Measured	Empirical Formula	
405/42.5	41.68	27.95	8.38	0.01514	13.0	12.7	– 2.3
5/656	66.14	14.20	9.88	0.00577	4.6	4.8	+ 4.3
5/630	79.25	15.09	11.06	0.00443	3.4	3.7	+ 8.8
405/42	79.25	17.37	10.52	0.00500	4.6	4.2	– 8.7
5/457	90.75	15.91	10.97	0.00401	3.0	3.4	+ 13.3
5/602	97.08	10.88	11.49	0.00296	2.6	2.5	– 3.8
5/615	98.30	20.36	11.28	0.00407	3.4	3.4	+ 0.0
5/605	102.99	26.09	14.54	0.00341	3.0	2.9	– 3.3

TABLE 6 Lateral Results for Reinforced CBOX Bridges

WSDOT Bridge Number	Bridge Length, meters	Deck Width, meters	Maximum Support Height, meters	$\dfrac{W^{0.6}}{Lb^{0.4} \cdot H^{0.3}}$, $m^{-0.1}$	Fundamental Lateral Frequencies, cycles/second		Percent Difference Between Empirical and Measured Values
					Field-Measured	Empirical Formula	
5/596	76.10	18.07	10.61	0.494	4.6	4.5	− 2.2
405/17	84.41	11.67	11.92	0.352	3.1	3.2	+ 3.2
5/418	89.48	19.51	13.17	0.455	4.4	4.2	− 4.5
5/419	96.62	10.36	8.90	0.339	3.1	3.1	+ 0.0
405/50 N	127.29	9.02	12.56	0.252	2.4	2.3	− 4.2
405/50 S	130.88	9.02	12.16	0.252	2.4	2.3	− 4.2
405/57 S	134.72	10.12	13.87	0.256	2.1	2.3	+ 9.5

Reinforced CS Bridges

For the CS bridges, the empirical formula derived is as follows:

$$fl = \frac{17.4 \cdot W^{0.4}}{Lb^{0.5}} \tag{8}$$

The quantity $W^{0.4}/Lb^{0.5}$ for each CS bridge, the fundamental lateral frequency derived by Equation 8 for each bridge, and the percent difference between the latter and the fundamental lateral frequency derived by field measurement are presented in Table 7. Figure 7 shows a plot of the fundamental lateral frequency for each bridge as derived by field measurement versus $W^{0.4}/Lb^{0.5}$. Figure 7 also contains a plot of Equation 8 for comparison.

For the CS bridges, the empirically derived fundamental lateral frequencies presented in Table 7 are close to the field-measured values, with the results for all four bridges within 6 percent. Only one of the empirically derived fundamental lateral frequencies is more than 5 percent different from the corresponding field-measured value.

CONCLUSIONS

For vertical motion, the best fit between the empirical formulas and the field-measured results was obtained for the PCB spans. For lateral motion, however, the CBOX and CS bridges yielded somewhat better fits between the empirical formulas and the field-measured results. All the CBOX and CS bridges have continuous spans, with expansion joints (if any) located at the abutments. Only two of the eight PCB bridges have continuous spans, however. Thus, in general, the PCB spans act independently with respect to vertical motion. Therefore the influence of adjacent spans is much lower for the PCB bridge spans under vertical motion, and the empirical formula, which is based on span length, is closer to the field-measured results. With respect to lateral motion, however, the CBOX and CS spans are continuous. Therefore the CBOX or CS spans for a given bridge act as a single unit with respect to lateral motion, and the empirical formulas, which are based on overall bridge length, are somewhat closer to the field-measured results.

For all three bridge types the empirically derived fundamental frequencies were closer to the field-measured values

TABLE 7 Lateral Results for Reinforced CS Bridges

WSDOT Bridge Number	Bridge Length, meters	Deck Width, meters	Maximum Support Height, meters	$\dfrac{W^{0.4}}{Lb^{0.5}}$, $m^{-0.1}$	Fundamental Lateral Frequencies, cycles/second		Percent Difference Between Empirical and Measured Values
					Field-Measured	Empirical Formula	
5/415 A	8.17	21.06	9.42	1.184	19.6	20.6	+ 5.1
5/417	20.97	53.19	2.13	1.070	18.6	18.6	+ 0.0
5/425	42.90	19.51	7.41	0.501	8.8	8.7	− 1.1
5/428	62.18	27.68	7.83	0.479	8.7	8.3	− 4.6
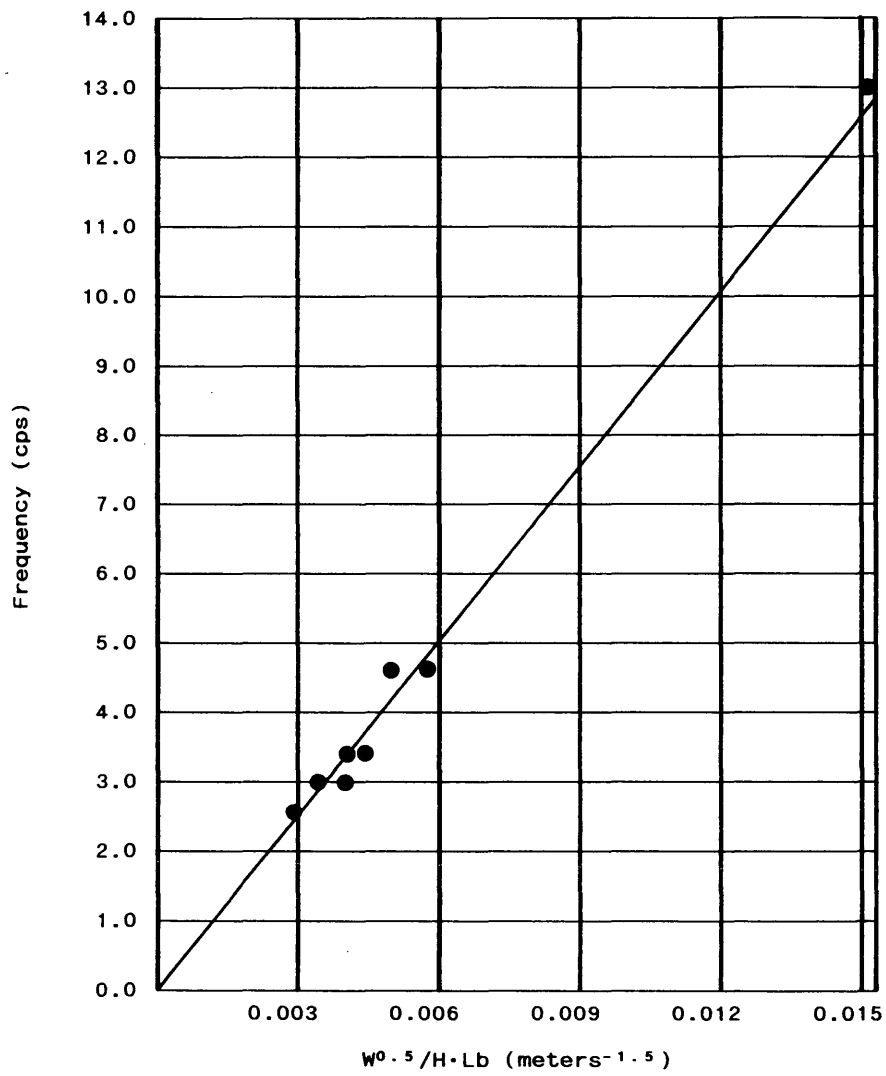
FIGURE 5   Lateral frequency plot for PCB bridges.
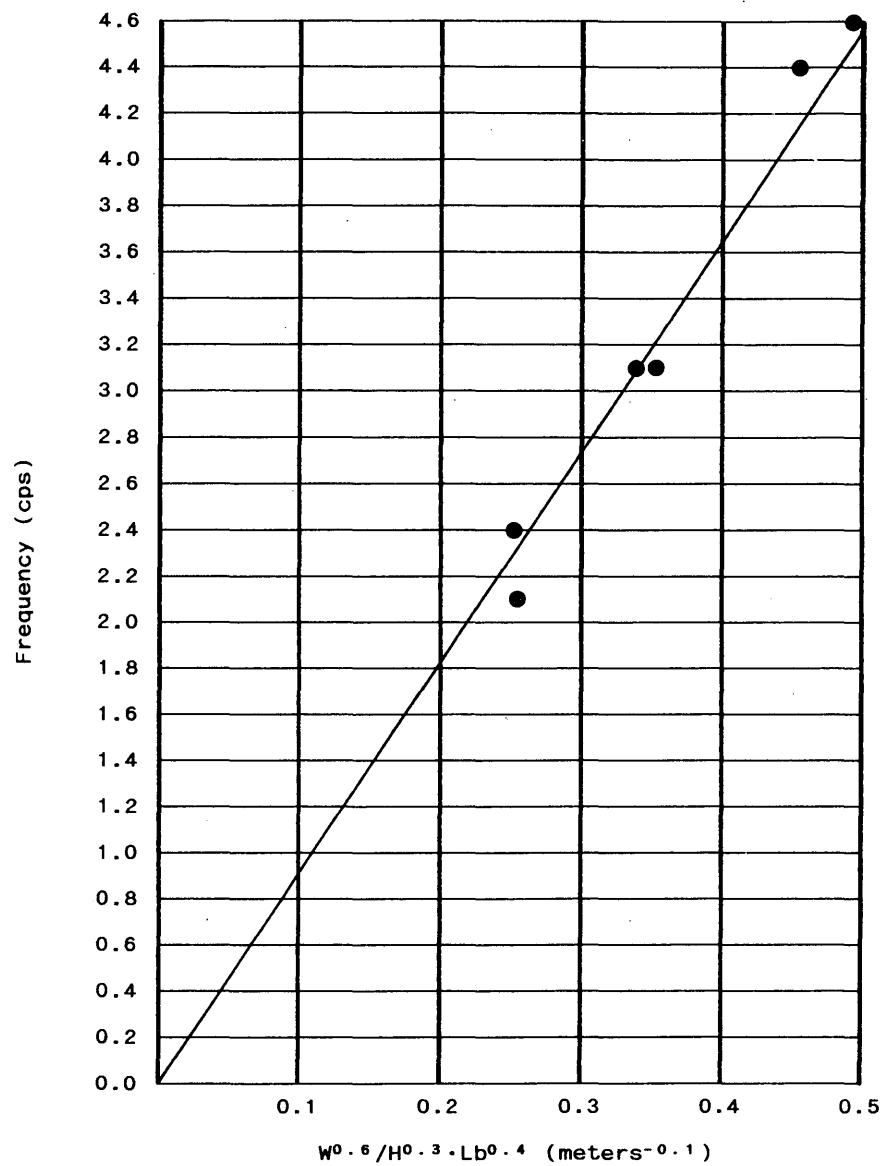
FIGURE 6 Lateral frequency plot for reinforced CBOX bridges.
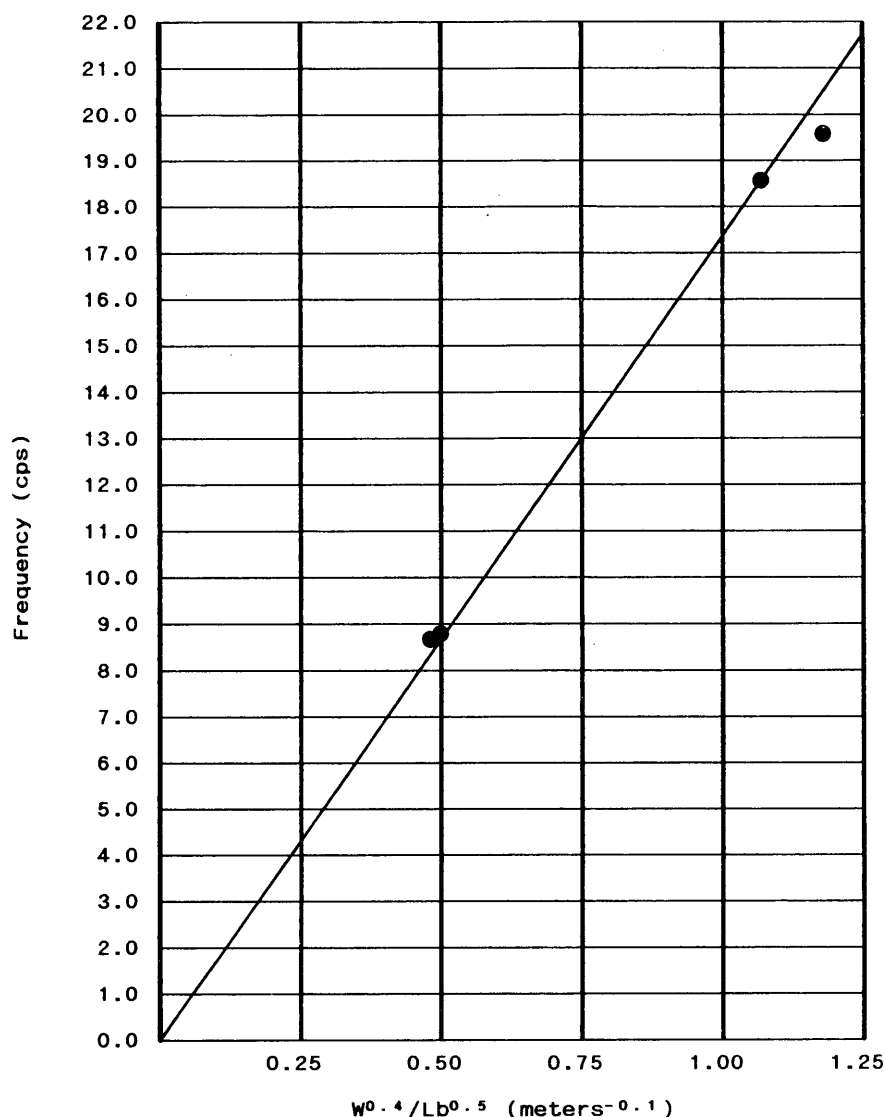
FIGURE 7 Lateral frequency plot for reinforced CS bridges.

for the lateral direction than the vertical direction. For each bridge type, however, the empirical formula for the vertical direction was based on more than twice as many data points as the empirical formula for the lateral direction. Therefore for each type of bridge the moderate-to-good fit of the empirical formula for vertical motion, which is based on more data points and hence has greater reliability, would seem to balance the good-to-very-good fit of the empirical formula for lateral motion, which is based on fewer data points and hence has less reliability. All six empirical formulas presented here will be used in the future to estimate the fundamental vertical and lateral frequencies of other PCB, CBOX, and CS bridges along the I-5 corridor in the Pacific Northwest.

ACKNOWLEDGMENTS

REFERENCES

1. *Research Agenda: Learning from the 19 September 1985 Mexico Earthquake.* Consejo Nacional de Ciencia y Technologia, Mexico, and the Committee on Earthquake Engineering, Commission on Engineering and Technical Systems, National Research Council, Washington, D.C., Jan. 1986.
2. D. E. Hudson. Dynamic Tests of Full-Scale Structures. *Journal of the Engineering Mechanics Division*, ASCE, Vol. 103, Dec. 1977, pp. 1141–1157.
3. J. G. Diehl. Roof-Top Ambient Vibration Measurements. *Proc., 3rd U.S. National Conference on Earthquake Engineering*, Charleston, S.C., Aug. 1986, pp. 1575–1585.
4. G. C. Pardoen, A. J. Carr, and P. J. Moss. Bridge Modal Iden-

tification Problems. *Proc., 2nd Annual ASCE Engineering Mechanics Specialty Conference on the Dynamic Response of Structures*, Atlanta, Ga., Jan. 1981, pp. 29–45.

5. A. M. Abdel-Ghaffar and G. W. Housner. Ambient Vibration Tests of Suspension Bridge. *Journal of the Engineering Mechanics Division*, ASCE, Vol. 108, Oct. 1982, pp. 2295–2312.

6. A. M. Abdel-Ghaffar and R. H. Scanlon. Ambient Vibration Studies of the Golden Gate Bridge: Suspended Structure. *Journal of the Engineering Mechanics Division*, ASCE, Vol. 111, April 1985, pp. 463–482.

7. P. G. Buckland, R. Hooley, B. D. Morgenstern, J. H. Rainer, and A. M. van Selst. Suspension Bridge Vibrations: Computed and Measured. *Journal of the Structural Division*, ASCE, Vol. 105, May 1979, pp. 859–874.

8. V. R. McLamore, G. C. Hart, and I. R. Stubbs. Ambient Vibration of Two Suspension Bridges. *Journal of the Structural Division*, ASCE, Vol. 97, Oct. 1971, pp. 2567–2582.

9. A. H. Mason and D. S. Carder. Vibration Frequencies of the Chesapeake Bay Bridge. *Journal of the Structural Division*, ASCE, Vol. 93, April 1967, pp. 237–245.

10. J. G. Diehl. *Ambient Vibration Survey: Application, Theory and Analytical Techniques*. Application Note 3, Kinemetrics, Inc., Pasadena, Calif., Undated.

Tests of Concrete Bridge Columns with Interlocking Spiral Reinforcement

Grant C. Buckingham, David I. McLean, and C. Ernest Nelson

The behavior of concrete bridge columns incorporating interlocking spirals under flexural, shear, and torsional loadings was investigated experimentally. Tests were performed on approximately 1/5-scale column specimens subjected to increasing levels of cycled inelastic displacements under constant axial load. Rectangular and oval cross sections with either two interlocking spirals or conventional ties were investigated. Variables studied included the performance of interlocking spirals compared to ties, the amount of spiral overlap, and the size of longitudinal bars required in the overlap region to maintain spiral interlock. Column performance was evaluated in terms of lateral load capacity, strength degradation, energy dissipation, and failure mechanisms. Columns with interlocking spirals performed as well or better than columns with ties, despite approximately 50 percent more transverse reinforcement being provided in the tied columns. Test results indicated improved performance when the center-to-center spacing of interlocking spirals was not greater than 0.6 times the spiral diameter. At least four longitudinal bars of approximately the same size as the main longitudinal reinforcement are required in the overlap region to maintain spiral interlock. When adequate longitudinal bars and spiral overlap were provided, the spirals remained interlocked even when loaded to large displacements thus preserving load transfer between the spirals.

Transverse reinforcement in bridge columns normally consists of spiral reinforcement in columns with circular cross sections and tied reinforcement in columns with square or rectangular cross sections. The circular shape of spiral reinforcement is inherently efficient in providing confinement to the concrete core and restraint of longitudinal bar buckling. In contrast, rectangular columns require cross ties or overlapping ties in addition to the perimeter tie to provide adequate confinement and restraint of bar buckling. As a result, tied columns are often more difficult to construct and require larger amounts of transverse reinforcement than columns with spiral reinforcement.

To incorporate the benefits of spiral reinforcement into noncircular columns, the California Department of Transportation (Caltrans) has begun to use interlocking spirals. Although special construction techniques are required for columns with interlocking spirals, the volume of transverse reinforcement is normally less than that for columns with ties. The seismic performance of columns with interlocking spirals may also be superior to that for tied columns. However, the

performance of columns with interlocking spirals has not been fully established.

The Caltrans specifications contain provisions for the design of columns with interlocking spirals (1). However, most of the design provisions are apparently based on specifications for single spiral columns with circular cross sections, which may not be adequate for interlocking spiral columns. Furthermore, several important design elements are not addressed in the specifications. Additional information on the behavior of columns with interlocking spirals is needed in order to determine specific design requirements.

The objective of this study was to investigate experimentally the behavior of columns incorporating interlocking spiral reinforcement under shear, flexural, and torsional loading. The effects of several design variables on the behavior of columns with interlocking spirals were investigated, including transverse reinforcement requirements, size of longitudinal bars in the interlock zone, flexural detailing of interlocking spirals in rectangular columns, and performance of columns with interlocking spirals compared with columns with ties. Recommendations are made for the design of bridge columns incorporating interlocking spirals as the transverse reinforcement.

PREVIOUS RESEARCH AND CURRENT PRACTICE

Tests of Columns with Interlocking Spirals

The work done by Tanaka and Park is the only information now available on the experimental behavior of interlocking spiral columns (2). Tanaka and Park tested three interlocking spiral columns and one tied column under cyclic lateral load and constant axial load. The column specimens were designed to fail in flexure, and each column was detailed for plastic hinging at the base of the column in accordance with the New Zealand Concrete Design Code. Results of the tests showed similar levels of satisfactory performance for the tied column and the interlocking spiral columns, even though the tied column contained approximately 200 percent more transverse reinforcement by volume than the similar interlocking spiral column.

To ensure force transfer between interlocking spirals, Tanaka and Park proposed that at least four longitudinal bars be placed within the interlock region and that the spacing between centers of adjacent spirals be limited to $1.2r_1$, where r_1 is the radius of the spiral reinforcement. The spacing criterion corresponds to a minimum spiral overlap of 25 percent, where the overlap percentage is defined as the depth of the

G. C. Buckingham, U.S. Army Corps of Engineers, Walla Walla, Wash. 99362. D. I. McLean, Department of Civil and Environmental Engineering, Washington State University, Pullman, Wash. 99164. C. E. Nelson, Bridge and Structures Branch, Washington State Department of Transportation, Transportation Building KF-01, Olympia, Wash. 98504.

interlock region divided by the total depth of the transverse reinforcement.

Caltrans Specifications for Interlocking Spirals

Columns with interlocking spirals are widely used in California, but only limited guidance is given for the design of such columns in the Caltrans specifications (*1*). The specifications set the maximum allowable center-to-center spacing of adjacent spirals at "0.75 times the diameter of the cage," or a minimum spiral overlap of 14.3 percent. Caltrans also requires that at least four longitudinal bars be placed in the interlock region. No requirement is given in the specifications for the minimum cross-sectional area of these interlock bars. Special detailing requirements for interlocking spiral columns with rectangular cross sections have been addressed in the Caltrans bridge design manual (*3*). Longitudinal bars are placed in the four corners of the column and outside both points of spiral intersection to minimize strength losses due to spalling in these areas. The unconfined longitudinal bars are tied into the interlocking spiral core of the column using dead-ended anchors.

EXPERIMENTAL TESTING PROGRAM

Test Specimens and Parameters

Experimental tests were conducted on column specimens with both tied and interlocking spiral transverse reinforcement. The main tests were performed on eight approximately 1/5-scale column specimens subjected to cycled inelastic lateral displacements under constant axial load. The selection of specimen details and test parameters was based on areas of design uncertainty and on results obtained from preliminary tests conducted on approximately 1/25-scale specimens.

Parameters investigated in the experimental testing program included the following:

• Variation in spiral overlap percentage,
• Use of small-diameter (nominal) longitudinal reinforcement in the interlock zone,
• Comparison of column performance with ties and interlocking spirals,
  • Variations in flexural detailing, and
  • Column cross-sectional shape.

Cross sections and reinforcement layout for the specimens investigated in the 1/5-scale study are shown in Figure 1. Details of the 1/5-scale testing program are summarized in Table 1. Additional information on the testing program can be found elsewhere (*4*).

The concrete used for all 1/5-scale specimens was typical of concrete used for bridge column construction. The concrete consisted of Type I/II portland cement, river-gravel coarse aggregate with a maximum size of $\frac{3}{4}$ in., sand, water reducer, and an air-entraining agent. The average compressive strength at the time of testing was approximately 4600 psi. (Conversion factors for this paper are as follows: 1 in. = 25.4 mm, 1 kip = 4.448 kN, 1 in.-kip = 113 N-m, and 1 psi = 0.006895 MPa.)

All reinforcement in the 1/5-scale specimens was Grade 60. The ties and spirals were constructed of No. 2 deformed rebar. The column longitudinal steel consisted of No. 4 rebar in the flexural specimens and No. 5 rebar in the shear and torsion specimens, except for Column 4, which had No. 2 rebar in the interlock zone.

Test Setup and Procedures

The test setup for the 1/5-scale shear and flexure specimens is shown in Figure 2. The footing of the test specimen was anchored to a laboratory strong floor. Lateral load was applied using a 55-kip actuator operated under displacement control. Axial load was applied to the top of the column using a 200-kip jack. An axial load of approximately $0.09 f'_c A_g$ was applied to all specimens except that used in the torsion test, which had no axial load (f'_c is the compressive cylinder strength of the concrete, and A_g is the gross area of the column section). The axial loading system resulted in a variation of the axial load during testing of approximately ±6 percent. The contribution to total applied moment resulting from displacement of the axial loading system was determined to be negligible.

The determination of the column tip horizontal displacement at first yield (Δ_y) and the loading sequence was similar to the procedures used by Priestley and Park (*5*). To demonstrate the ductility and hysteretic behavior of the test specimens, the specimens were subjected to a simulated seismic loading pattern consisting of increasing multiples of Δ_y. The loading pattern for the flexure specimens consisted of two cycles at displacement ductility levels (i.e., multiple values of Δ_y) of $\mu = \pm1$, ±2, ±4, ±6, and ±8, with the exception of Column 2, which was taken to a maximum displacement level of $\mu \approx \pm7$ because of actuator stroke limitations; μ is the structure displacement ductility factor, or Δ/Δ_y, where Δ is the column tip horizontal displacement. The loading pattern for the shear test specimens was halted at a displacement ductility level $\mu = \pm4$ because of failure of the specimen and possible instability of the axial load application system.

The specimen for the 1/5-scale combined shear and torsion test was attached to the laboratory strong floor in the same manner as those for the shear and flexure tests. However, the specimen was offset approximately 6 in. in the direction perpendicular to loading to better facilitate the eccentric loading system. Load was applied to the column with the same 55-kip hydraulic actuator described earlier. A loading collar with a steel W-section welded horizontally to one side provided the eccentric connection necessary to produce the desired combined loading effect. The loading sequence used to test Column 8 consisted of two cycles at displacements of ±0.5, ±1.0, ±1.5, ±2.0, ±2.5, ±3.0, and ±3.5 in. Deflections and loads recorded from the actuator were transformed to equivalent rotations and torques using trigonometric relationships.

Strain gauges were used to monitor the strains in the flexural and transverse reinforcement. Linear variable displacement transformers and load cells measured column displace-
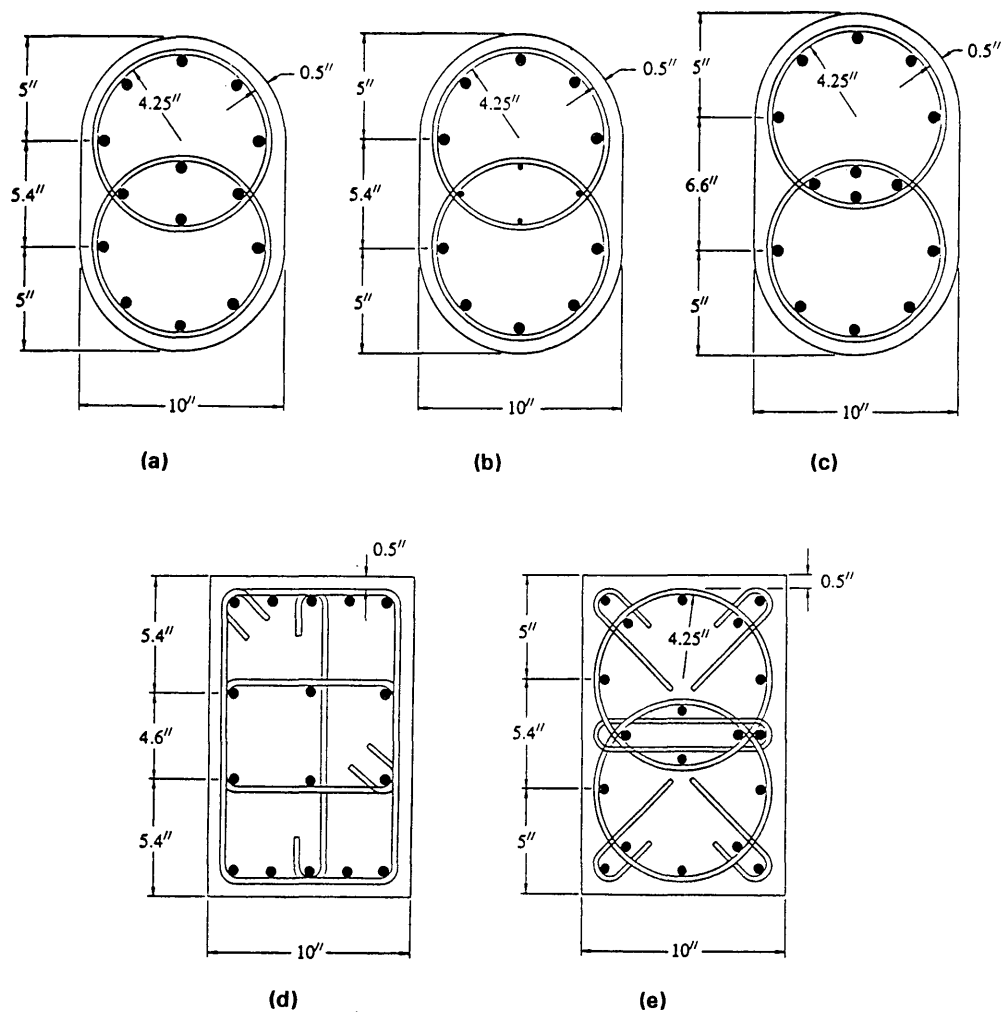
FIGURE 1 Column cross sections and reinforcement layout: *a*, Columns 1, 5, and 8; *b*, Column 4; *c*, Column 3; *d*, Columns 6 and 7; and *e*, Column 2.

TABLE 1 Parameters for 1/5-Scale Specimens

Specimen Number	Type of Loading	Transverse Reinforcement	Spiral/Tie Spacing (in.)	Spiral Overlap (%)	Nominal Interlock Steel	Column Cross-section
1	Shear	Spirals	5.0	25	No	Oval
2	Flexural	Spirals	1.25	25	No	Rectangular
3	Shear	Spirals	5.0	15	No	Oval
4	Shear	Spirals	5.0	25	Yes	Oval
5	Flexural	Spirals	2.5	25	No	Oval
6	Flexural	Ties	2.5	NA	NA	Rectangular
7	Shear	Ties	5.0	NA	NA	Rectangular
8	Torsion	Spirals	5.0	25	No	Oval
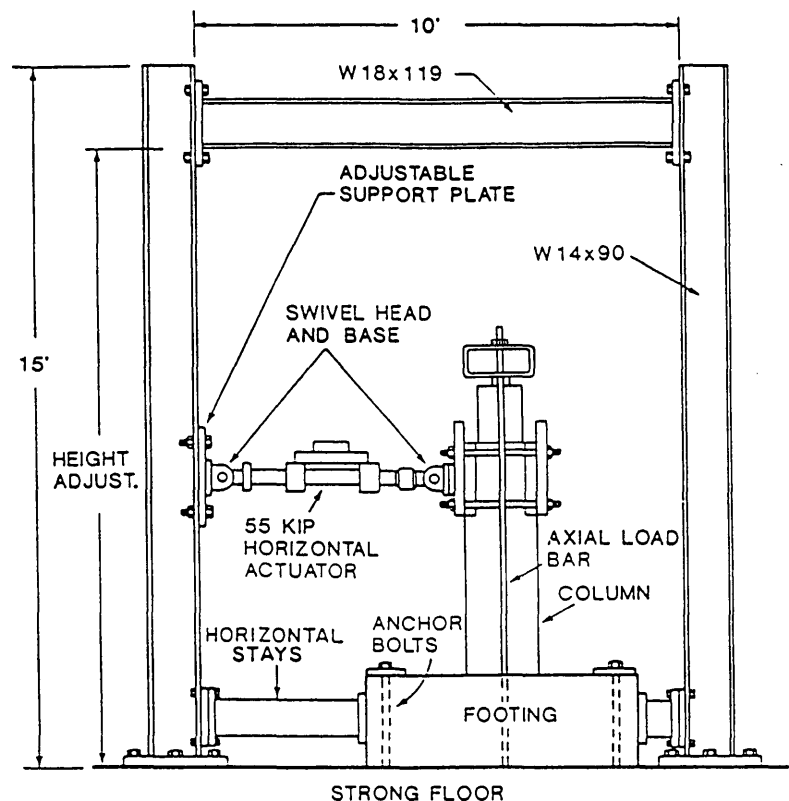
FIGURE 2 Test setup.

ments and applied loads. All data were recorded intermittently during testing.

TEST RESULTS AND DISCUSSION

Shear Tests

General Behavior

Column 1 was an interlocking spiral column with the minimum overlap percentage of 25 recommended by Tanaka and Park (2) and full-size longitudinal bars in the interlock zone. Test results from this specimen were used as a guideline for comparison with the other shear tests. Initial cracking occurred at a lateral load of approximately 20 kips. An x-crack pattern typical of shear deficient reinforced concrete columns under cycled inelastic displacements formed at $\mu = \pm 1$, and crack widths increased at $\mu = \pm 2$. Cracking in the specimen eventually led to spalling of the cover concrete and internal fragmentation of the core at $\mu = \pm 4$. The load-displacement curve for Column 1 is shown in Figure 3. The load-carrying capacity of the specimen remains virtually constant at $\mu = \pm 1$ and displays a small decrease at $\mu = \pm 2$. However, severe degradations in lateral load capacity corresponding to the physical damage mentioned earlier are apparent at $\mu = \pm 4$.

Column 4 was designed in the same manner as Column 1 with the exception of the smaller longitudinal bars (No. 2 rebar) in the interlock zone. The initial cracking load for Column 4 was approximately 22 kips. The x-crack pattern displayed in Column 1 was also apparent in this specimen for

displacement levels of $\mu \le \pm 2$. However, the crack widths in Column 4 were larger than those in Column 1 at $\mu = \pm 2$. Spalling of the cover concrete started early in the $\mu = \pm 4$ cycle and was followed by core fragmentation and straightening of the spiral reinforcement. The two nominal interlock bars on the transverse faces of the column displayed significant amounts of deformation due to tensile forces acting on the spiral reinforcement arising from shear on the column. A posttest photograph of one of the nominal interlock bars is shown in Figure 4. The load-deflection curve for Column 4, shown in Figure 5, reflects the physical behavior described previously. Moderate degradation occurs for $\mu \le \pm 2$, followed by severe degradation at $\mu = \pm 4$ due to core fragmentation and longitudinal reinforcement damage.

Column 3 was constructed with an overlap percentage of 15 to examine the minimum overlap of 14.3 percent recommended by Caltrans (1). All of the longitudinal bars in the interlock zone were the same size as the bars used in the rest of the specimen. The initial cracking load and crack pattern exhibited in this specimen were similar to those described for Columns 1 and 4. However, crack widths in Column 3 at $\mu = \pm 2$, shown in Figure 6, were significantly larger than those encountered in the previous two tests at the same level of displacement. Spalling of cover concrete in this specimen commenced in the latter stages of the $\mu = \pm 2$ cycle and continued into the final two cycles at $\mu = \pm 4$. Rupture of the spiral reinforcement, shown in Figure 7, occurred on the first cycle to $\mu = +4$ at approximately 93 percent of full cycle displacement. The load-deflection plot for Column 3 is shown in Figure 8. Decreases in the load-carrying capacity of the column are detectable at every level of displacement ductility past the
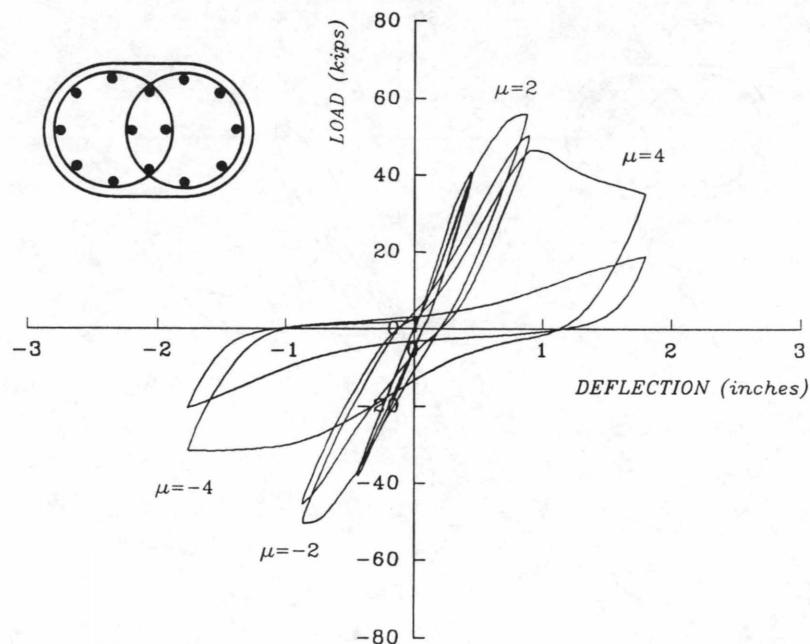
FIGURE 3 Load-displacement curves for shear test, Column 1; $\Delta_y = 0.45$ in.

first cycle to $\mu = +2$. The fracture point of the spiral rein-forcement is indicated by the drop in lateral load on the first cycle to $\mu = +4$.

Rectangular ties and cross ties were used as transverse re-inforcement in Column 7 to compare the performance of a conventionally reinforced column with one using the inter-locking spiral detail (Column 1). A modified testing procedure was used for Column 7 because of limitations encountered in

the capacity of the testing equipment. The first two cycles at $\mu = \pm 1$ were accomplished without any alterations to the testing procedure or equipment. However, the load required to attain a displacement corresponding to $\mu = \pm 2$ was beyond the range of the 55-kip hydraulic actuator. After two failed attempts to reach $\mu = +2$ with normal testing procedures, the specimen was relieved of all axial load and cycled manually to produce strength deterioration until the desired displace-

FIGURE 4 Nominal interlock bar in Column 4.
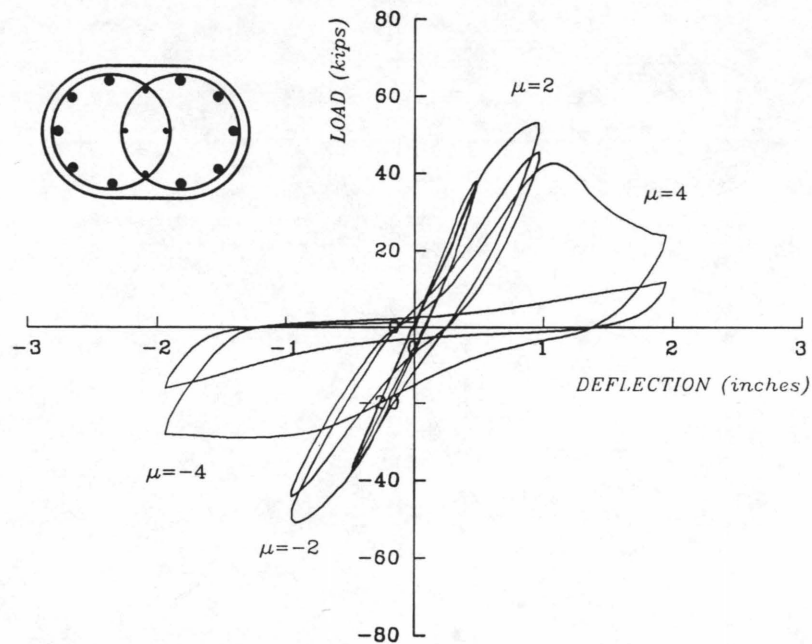
FIGURE 5 Load-displacement curves for shear test, Column 4; $\Delta_y = 0.495$ in.
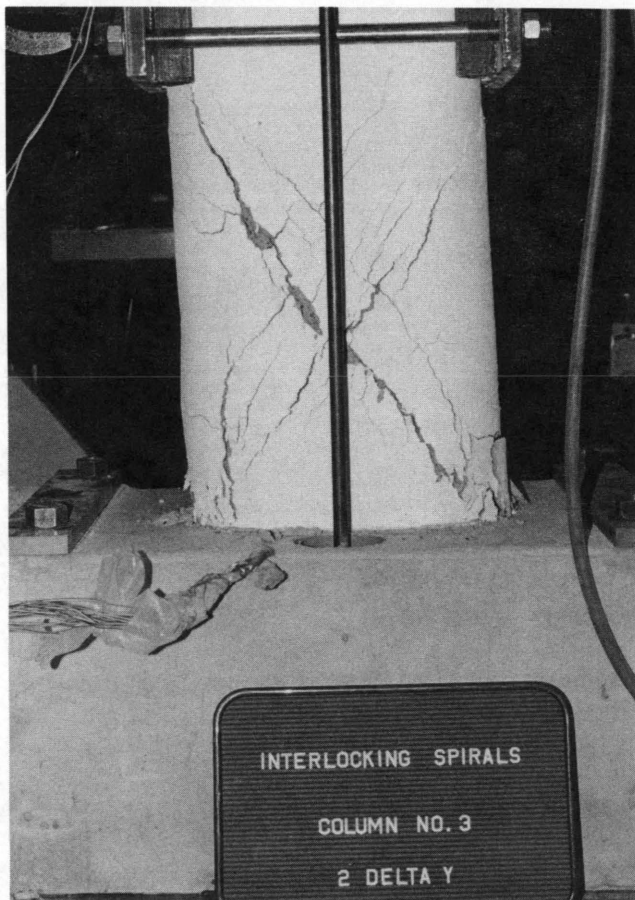
FIGURE 6 Crack patterns in Column 3 at $\mu = \pm 2$.

ment was obtained. For the cycle to $\mu = \pm 4$, axial load was returned to the specimen and normal procedures for controlling the lateral load and displacement were resumed. Degradation of Column 7 occurred rapidly in the final two cycles at $\mu = \pm 4$. The core concrete was reduced to rubble at this stage because of the loss of confinement and possibly also because of the increased number of load cycles imposed on the specimen. A posttest photograph of one of the rectangular ties in Column 7 is shown in Figure 9. The bend angle on the end return has rotated from an original position of 135 degrees to approximately 90 degrees, resulting in a reduction in the confining capability of the tie. Similar damage to the end returns on the internal ties and cross ties also occurred. The load-deflection plot for Column 7 is shown in Figure 10. Although influenced by the increased number of cycles used at $\mu = \pm 2$, the graph reveals rapid deterioration of the load-carrying capacity of the specimen at $\mu = \pm 4$, as described earlier. The two sharp drops in load at deflections of approximately 2.0 and 2.5 in. on the first cycle to $\mu = \pm 4$ correspond to sudden unraveling of rectangular tie end returns.

Comparison of Hysteresis Curves

Comparison of the load-deflection hysteresis curves for the four shear specimens indicates that the reductions in load-carrying capacity for Columns 3 and 4 were greater than the reduction for Column 1 at similar levels of displacement ductility. The hysteresis curves for Column 7 indicate a degradation in load-carrying capacity that is comparable to that in Columns 3 and 4 and is greater than that in Column 1. How-

FIGURE 7   Spiral reinforcement rupture in Column 3.

ever, it is important to note that the testing procedure used for Column 7 was different from that used in the rest of the tests.

Comparison of Calculated and Experimental Strengths

A summary of the experimental and theoretical ultimate shear strengths for the 1/5-scale shear test specimens is given in

Table 2. The theoretical shear strengths for the interlocking spiral columns were calculated assuming that the spiral reinforcement was fully effective, and hence the shear contribution of the interlocking spirals was equivalent to that for two spirals. The ratios of experimental to theoretical shear strength for the interlocking spiral columns (Columns 1, 3, and 4) are all within 3 percent of one another. This difference is negligible considering the inconsistent nature of shear failure in reinforced concrete members. The normalized shear

FIGURE 8   Load-displacement curves for shear test, Column 3; Δ_y = 0.52 in.

FIGURE 9   Rectangular tie and returns in Column 7.

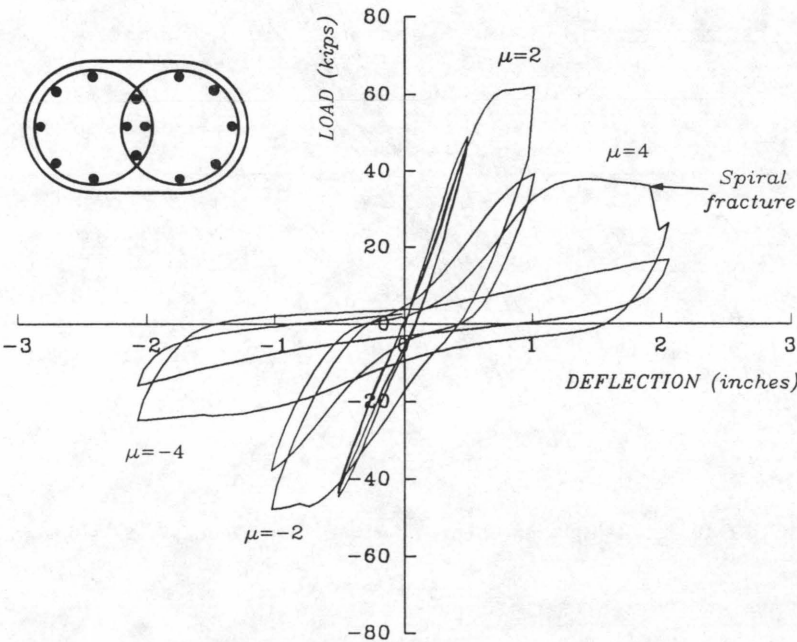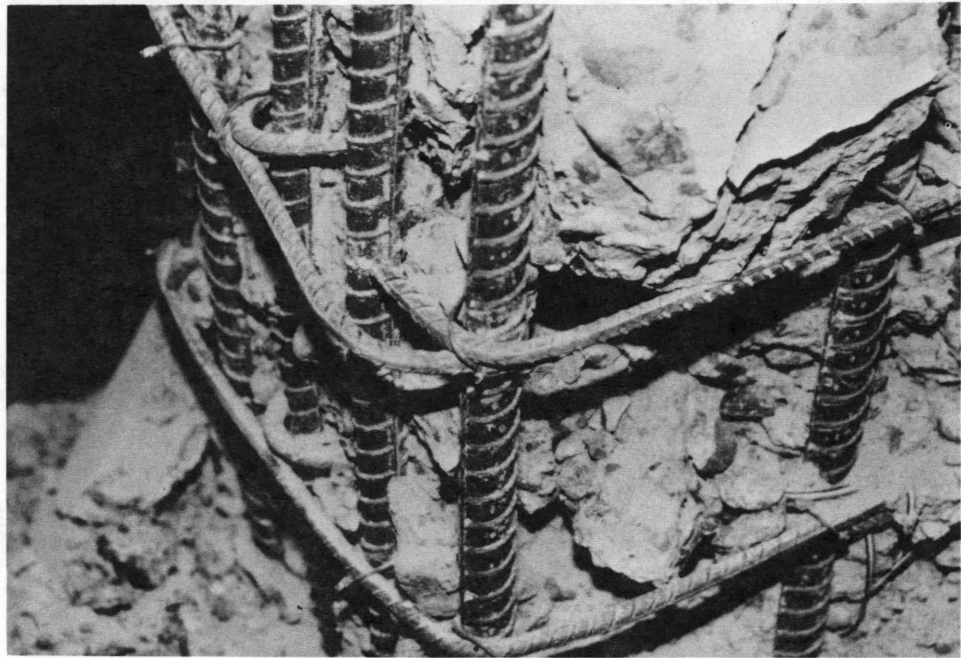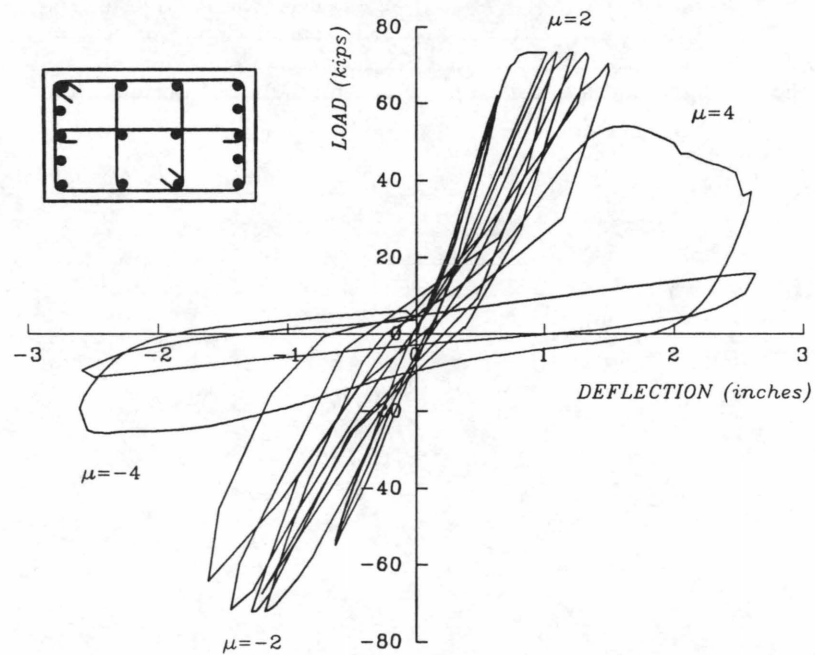**FIGURE 10   Load-displacement curves for shear test, Column 7; $\Delta_y = 0.66$ in.**

TABLE 2 Summary of 1/5-Scale Shear Test Results

Specimen Number	V_{test} (kips)	V_n (kips)	$\dfrac{V_{test}}{V_n}$
1	55.5	41.2	1.347
3	61.9	44.5	1.391
4	53.1	38.5	1.379
7	73.4	53.8	1.364

V_{test} = experimental shear strength
V_n = theoretical shear strength

strength for Column 7 also falls within the range of scatter established by the other shear specimens. The calculated shear strength for Column 7 was determined assuming that all portions of the outer ties, inner ties, and cross ties parallel to the direction of load contributed to shear resistance.

Flexure Tests

General Behavior

The interlocking spiral detail used in Column 5 consisted of a spiral overlap percentage of 25 in an oval-shaped cross section. Flexure cracks initially appeared in Column 5 at a lateral load of approximately 15 kips. At $\mu = \pm 1$, shear and flexure-shear cracks formed along the entire height of the specimen at intervals of 3 to 4 in. Although these cracks persisted throughout the duration of the test, the primary mode of failure in the specimen remained flexural in nature. Crushing of the concrete on the extreme load-bearing faces of the spec-

imen just above the top of the footing occurred at $\mu = \pm 4$ and eventually led to spalling in these areas at $\mu = \pm 6$. On the final cycle to $\mu = +6$, a longitudinal bar buckled outward between two sections of spiral reinforcement. Further cycling of the specimen resulted in fracture of this bar at $\mu = -8$ due to fatigue stress. The load-displacement curve for Column 5 is shown in Figure 11. Except for the sharp drop in lateral load at the point of longitudinal bar fracture, the load-carrying capacity of the specimen remains nearly constant throughout the test.

Column 6 represented a conventionally designed reinforced concrete column with rectangular ties and cross ties used as transverse reinforcement. The initial cracking load for Column 6 was approximately 13 kips. Crack patterns and crack development for this specimen were similar to those in Column 5 for $\mu \leq \pm 2$. Spalling of the cover concrete on both of the extreme compression faces began at $\mu = \pm 4$ because of minor buckling of the longitudinal reinforcement. The lack of confinement from the rectangular ties and cross ties led to severe buckling of the longitudinal reinforcement and unraveling of tie and cross-tie end returns at $\mu = \pm 6$, as shown in Figure 12. Continued cycling through $\mu = \pm 8$ resulted in the fracture of 5 of the 10 longitudinal reinforcing bars concentrated on each of the short faces of the column. The load-deflection plot for Column 6 is shown in Figure 13. The load-carrying capacity of the specimen remains stable for $\mu \leq \pm 6$, then drops significantly at $\mu = \pm 8$ because of fracture of the longitudinal reinforcement.

Column 2 was constructed to investigate a reinforcing detail used for interlocking spiral columns enclosed in rectangular concrete cross sections. The cracking pattern in Column 2 for $\mu \leq \pm 2$ was similar to that described for Column 5. Deterioration of the cover concrete began at $\mu = \pm 4$, along with moderate buckling of the four unconfined corner longitudinal bars. Cycles to $\mu = \pm 6$ and $\mu \approx \pm 7$ led to the fracture of
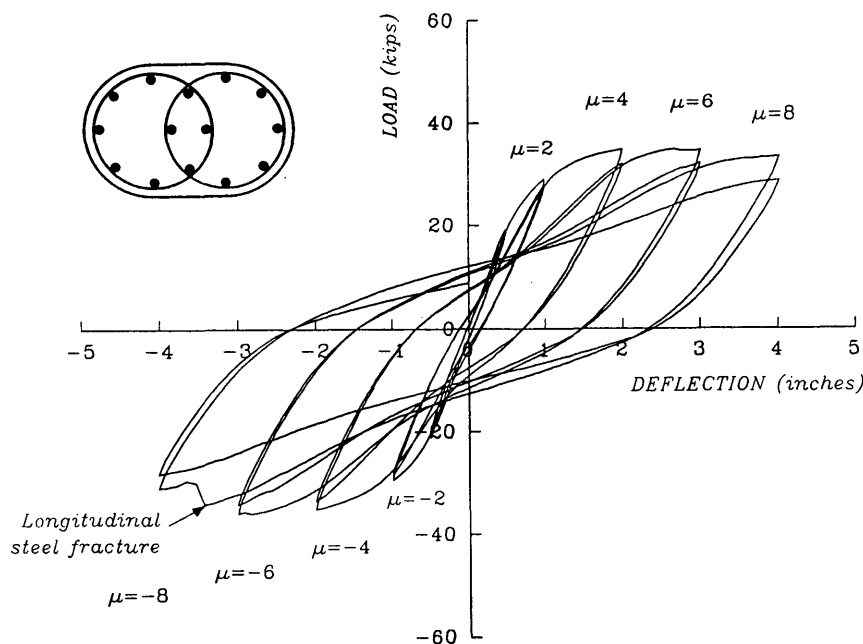

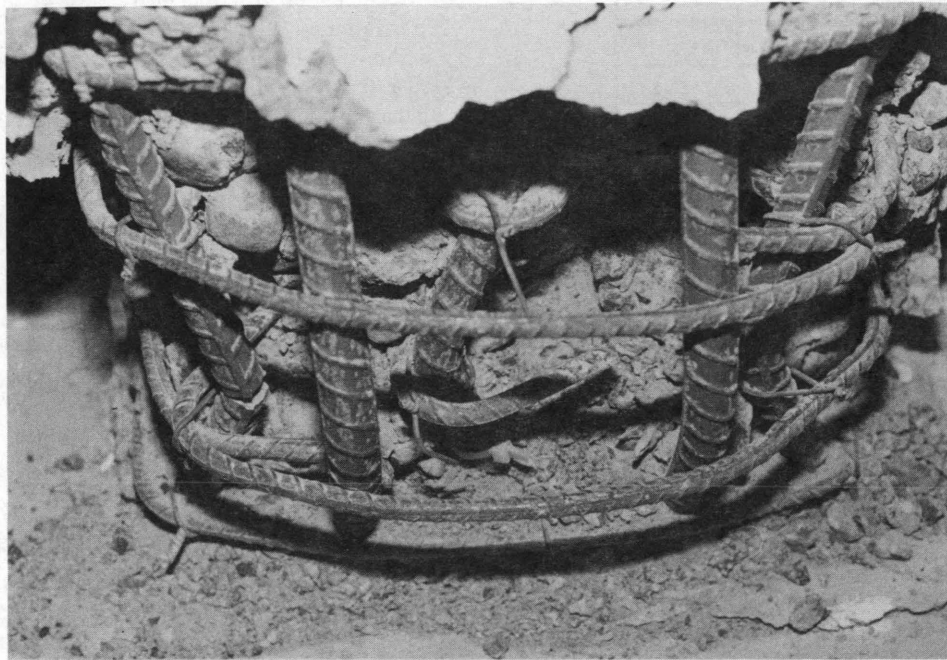**FIGURE 11** Load-displacement curves for flexural test, Column 5; $\Delta_y = 0.51$ in.

FIGURE 12   Buckling of longitudinal reinforcement in Column 6.
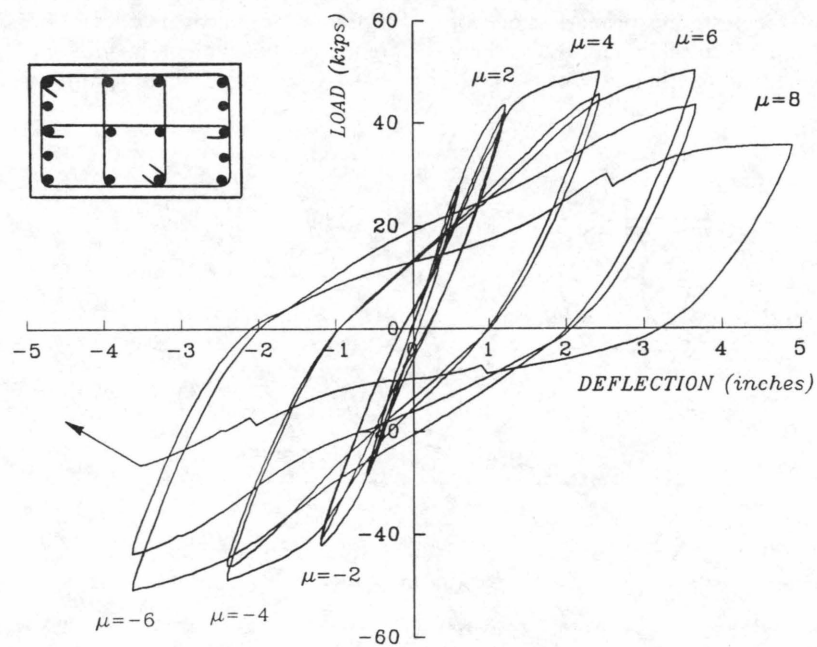

FIGURE 13   Load-displacement curves for flexural test, Column 6; $\Delta_y =$ 0.62 in.

all four unconfined corner bars, moderate buckling of the confined longitudinal bar on the extreme bending face, and necking of the spiral reinforcement. The load-deflection plot for Column 2 is shown in Figure 14. The load-carrying capacity of the specimen shows little degradation through $\mu = \pm 4$, then drops sharply during loading to $\mu = \pm 6$ and $\mu \approx \pm 7$ because of longitudinal bar fracture.

Comparison of Hysteresis Curves

Comparison of the load-deflection hysteresis curves for the three flexure specimens indicates that Column 5 maintained a higher percentage of peak load than Columns 6 and 2 at similar levels of displacement ductility. The degradation in load-carrying capacity for Column 2 from $\mu = +4$ to $\mu \approx +7$ is primarily the result of unconfined longitudinal bar fracture.

Comparison of Calculated and Experimental Strengths

A summary of the calculated (using strain compatibility) and experimental ultimate strengths for the 1/5-scale flexure specimens is shown in Table 3. Ratios of experimental and theoretical flexural strength for Columns 2, 5, and 6 display a maximum difference of less than 4 percent.

Combined Shear and Torsion Test

General Behavior

Column 8 was an exact replica of Column 1, with an overlap percentage of 25 and an oval-shaped cross section. The pur-

pose of this test was to investigate the ultimate state behavior of an interlocking spiral column under combined shear and torsional load. Initial cracking in Column 8 occurred at a torsional load of approximately 110 in.-kips. A spiral cracking pattern was exhibited in the specimen and was typical of cracking in reinforced concrete members under combined shear and torsional load. Cracking became more severe at $\Delta = \pm 1.0$ in. (approximately ± 2.88-degree rotation) and was followed by spalling of the cover concrete at $\Delta = \pm 1.5$ in. (approximately ± 4.3-degree rotation). Additional cycles resulted in straightening of the spiral reinforcement around the longitudinal bars and some internal cracking of the concrete core.

The torque-twist curve for Column 8 is shown in Figure 15. The data displayed in the graph include corrections for rotations in the loading collar and actuator and translations parallel and perpendicular to the plane of the reaction frame. The most prominent characteristic depicted in this graph is the difference in specimen degradation at positive and negative values of rotation. A possible explanation for this phenomenon is the fact that spiral reinforcement tends to tighten around the concrete core when twisted in one direction and separate from the core when twisted in the opposite direction.

Interaction Curve for Shear and Torsion

A graph displaying the results from Column 8 with respect to shear and torsion interaction is shown in Figure 16, in which T_{test} is theoretical torsional strength and T_n is experimental torsional strength. The procedure used for calculating the shear strength of Column 8 was the same as that used for the shear test specimens. The torsional strength for Column 8 was calculated using the procedures in ACI 318-89 for rectangular
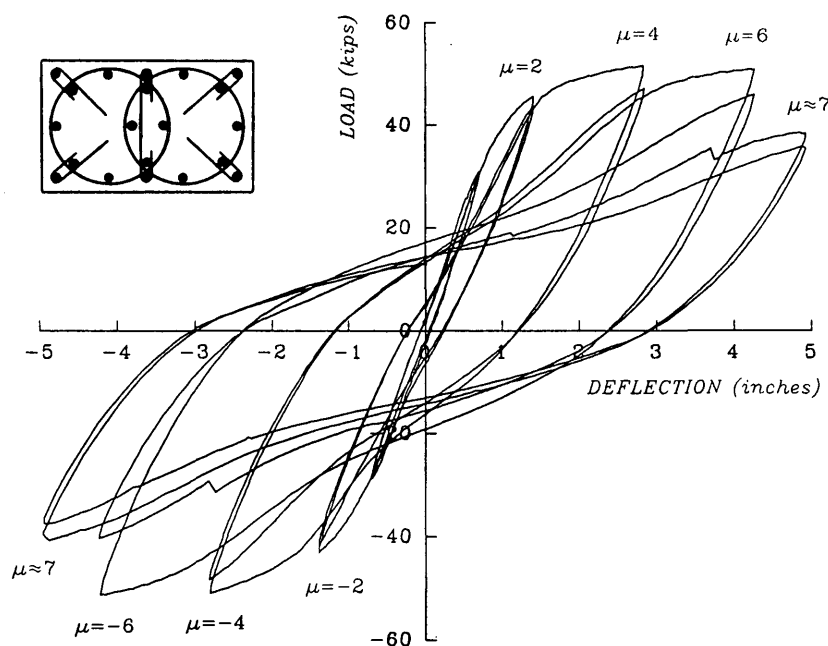
FIGURE 14   Load-displacement curves for flexural test, Column 2; $\Delta_y = 0.72$ in.

TABLE 3 Summary of 1/5-Scale Flexural Test Results

Specimen Number	M_{test} (in.-kips)	M_n (in.-kips)	$\dfrac{M_{test}}{M_n}$
2	2,477	1,913	1.295
5	1,723	1,291	1.335
6	2,438	1,824	1.337

M_{test} = experimental flexural strength
M_n = theoretical flexural strength

beams. With respect to the shear and torsional strengths, it can be seen in the graph that most of the load applied to Column 8 was torsional in nature. The overstrength displayed for Column 8 is approximately 48 percent. The procedures for calculating the torsional strength of the oval column with interlocking spirals, although apparently conservative, are likely to be inexact. Further research is needed on the behavior of interlocking spiral columns subjected to torsional loading.

CONCLUSIONS AND RECOMMENDATIONS

Conclusions

On the basis of the results of this experimental investigation, the following conclusions are made:

1. Specimens constructed with interlocking spirals for transverse reinforcement performed as well as or better than spec-

imens with ties under both shear and flexural loading, even though the specimens reinforced with ties contained 50 percent more transverse reinforcement than the specimens with interlocking spirals. The superior performance of the interlocking spiral detail would be particularly beneficial in earthquake regions.

2. When loaded to failure in shear, the specimen incorporating a spiral overlap of 25 percent (center-to-center spacing of spirals equal to 0.6 times the spiral diameter) demonstrated less strength degradation than the similar specimen incorporating a spiral overlap of 15 percent (center-to-center spacing of spirals equal to 0.75 times the spiral diameter). Failure in the specimen with the 15 percent overlap was caused by rupture of the spiral reinforcement, whereas failure in the specimen with the 25 percent overlap was a result of gradual deterioration of the concrete core of the column.

3. The use of small-diameter (nominal) longitudinal bars in the interlock region resulted in higher degradation when compared with the similar specimen with the same size of longitudinal bars in the interlock region as that used for the main column reinforcement. The reduced performance of the specimen using nominal interlock bars was due to separation of the spiral cages resulting from severe deformation of the interlock bars.

4. The shear and flexural capacities of columns with interlocking spirals can be reasonably estimated using current procedures for the design of reinforced concrete structures. The torsional capacity of columns with interlocking spirals can be conservatively predicted using an approach adapted from current design equations for the torsional capacity of rectangular beams.
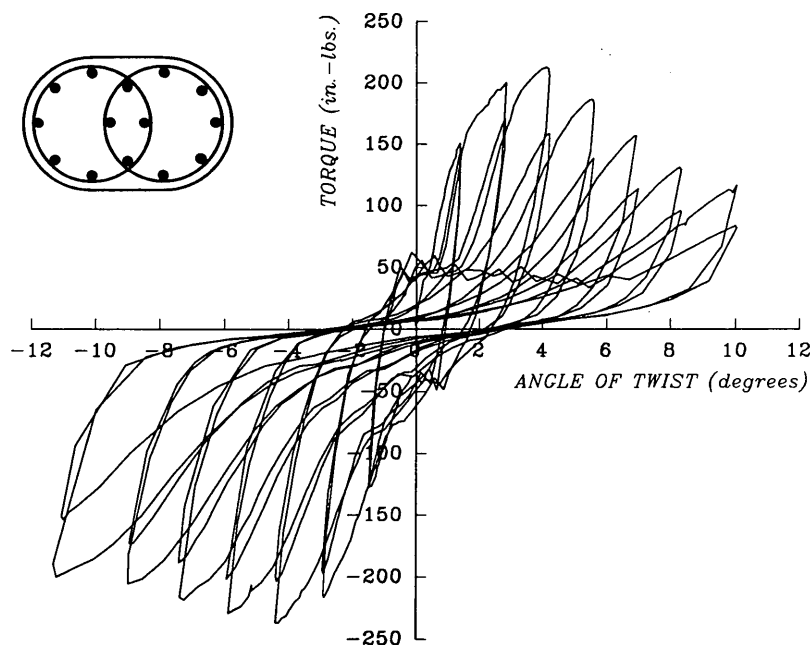
FIGURE 15 Torque-twist curve for Column 8.
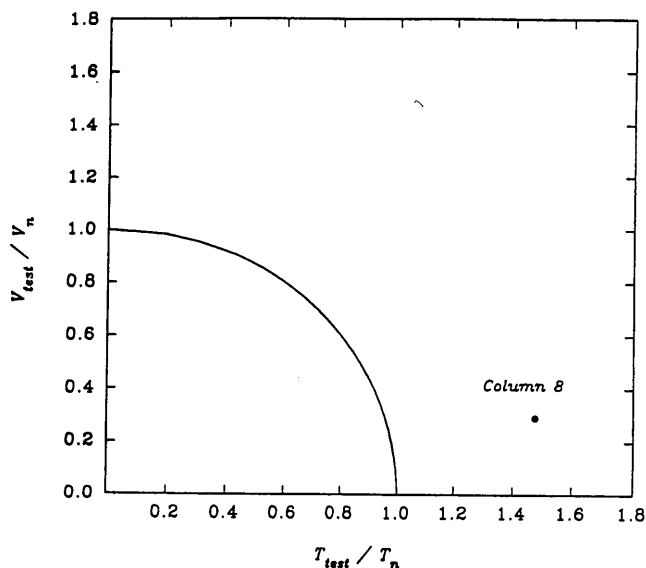
FIGURE 16 Shear-torsion interaction curve for Column 8.

Recommendations

The following recommendations are based on the results of this study and a survey of literature:

1. The center-to-center spacing of adjacent spirals in columns with interlocking spirals should not exceed 0.6 times the diameter of the spiral cage.

2. At least four longitudinal bars of approximately the same size as the main longitudinal reinforcement should be incorporated into the interlock region to prevent the individual spiral cages from separating.

3. Further research is recommended on the torsional behavior of columns with interlocking spirals, particularly in regard to rotation-direction bias resulting in unwinding of the spirals. It is also recommended that the behavior of columns with more than two interlocking spirals be investigated.

REFERENCES

1. *Standard Specifications for Highway Bridges Relating to Seismic Design* (13th ed.). AASHTO, Washington, D.C., 1983. Revisions by the Office of Structures Design, California Department of Transportation, Sacramento, Nov. 1989.
2. H. Tanaka and R. Park. *Effect of Lateral Confining Reinforcement on the Ductile Behavior of Reinforced Concrete Columns.* Report 90-2. Department of Civil Engineering, University of Canterbury, New Zealand, June 1990.
3. *Standard Specifications for Highway Bridges Relating to Seismic Design* (12th ed.). AASHTO, Washington, D.C., 1977. Revisions by the Office of Structures Design, California Department of Transportation, Sacramento, Nov. 1979.
4. G. C. Buckingham. *Seismic Performance of Bridge Columns with Interlocking Spiral Reinforcement.* M.S. thesis. Washington State University, Pullman, 1992.
5. M. J. N. Priestley and R. Park. Strength and Ductility of Concrete Bridge Columns Under Seismic Loading. *ACI Structural Journal*, Vol. 84, No. 1, Jan.–Feb. 1987, pp. 61–76.

Behavior of Prestressed AASHTO Girders Under Static Loading

J. Harold Deatherage, Chong Key Chew, and Edwin G. Burdette

Recently FHWA restricted the use of certain sizes of seven-wire prestressing strand in the fabrication of highway bridge beams. The research reported is the result of the prestressing industry's interest in evaluating the effects of development length and transfer length on the behavior of AASHTO Type I beams. Additionally, variations in transfer and development length were investigated for different diameters of reinforcing and different wire manufacturers. Twenty-two full-scale AASHTO Type I beams were static-tested to failure; the results of these tests are reported. Factors that affect both transfer and development length are evaluated and discussed. The computed and measured moment capacities are compared, and reasons for variations are evaluated. Three distinct failure modes were observed, depending on the location of the load in relation to the development length of the prestressing strand. The relationship between failure modes and the ultimate moment capacity is evaluated.

Recently FHWA limited the use of certain sizes and spacings of seven-wire prestressing strand in AASHTO bridge girders. This restriction was primarily based on the results of the experimental research in which both transfer and development lengths significantly larger than those predicted by the American Concrete Institute (ACI) and AASHTO equations were obtained (1). Since the FHWA mandate severely restricted the ability of many AASHTO prestress producers to satisfy the needs of the construction programs of several state departments of transportation, the Precast/Prestressed Concrete Institute in conjunction with the Regional Transportation Center program funded the University of Tennessee to perform additional research to confirm or refute these results (1). The results of the University of Tennessee research were reported in 1991 (2).

The purpose of the research at Tennessee was twofold:

1. To determine whether or not the existing AASHTO design criteria for transfer lengths and development lengths in prestressed beams were satisfactory or should be modified to reflect changes in technology and methodology of production since the code criteria were established.
2. To identify the factors affecting both transfer and development lengths and to quantify their effects.

Consideration of these factors is the subject of this paper. Twenty-two full-scale beams were tested to failure to evaluate their performance when loaded at or near the expected development length of the strand. Since the loads were applied at a position closer to the reaction than to the centerline of the beam, each beam allowed for two static tests; therefore,

Transportation Center, University of Tennessee, 357 South Stadium Hall, Knoxville, Tenn. 37996.

44 static tests were performed, and results were obtained on 43 of the tests.

DESCRIPTION OF TEST PROGRAM

Each of the 22 beams was 31 ft long with a cross section conforming to the AASHTO Type I configuration and having varying strand configurations depending on the diameter of the strand. Figure 1 describes the shear and confinement reinforcing used for each beam, and Figure 2 shows the various strand configurations used. Prestress reinforcement manufactured by four manufacturers was evaluated. A three-part designation is used to identify an end of a beam, as illustrated by 5S-1-EXT. The first part refers to the diameter of the strands used in a beam for which

- 5 = $\frac{1}{2}$-in. regular strand, nominal diameter of 0.500 in.
- 5S = $\frac{1}{2}$-in. special strand, nominal diameter of 0.5224 in.
- 916 = $\frac{9}{16}$-in. strand, nominal diameter of 0.5625 in.
- 6 = $\frac{6}{10}$-in. strand, nominal diameter of 0.600 in.
- 5E = $\frac{1}{2}$-in. epoxy-coated strand.

For the beams from the strand-diameter groups or with the epoxy-coated strands, the second part of the designation refers to one of the beams prestressed with the strands, and the third part refers to a specific end of this beam. INT or EXT refers to the interior or exterior end of a beam, because two beams were stressed with strands between the same two abutments. For the beams from the strand manufacturer's group, the second part of the designation refers to the name of the manufacturer, and the third part refers to an end of the beam. A summary of the beam properties is given in Table 1.

TRANSFER LENGTH TESTS

Transfer lengths of the strands were measured at prestress transfer on 26 Type I AASHTO girders. These results were initially reported by Smith (3). Table 2 gives the average transfer bond strengths for all milled surface strands. Confinement reinforcement was placed over a distance of about 40 in. from each end of the beams, a distance that is longer than almost all the measured transfer lengths. In some exploratory tests with spiral smooth-wire confinement reinforcement around each strand, Kaar et al. found a decrease of 15 percent in transfer length as compared with those without the reinforcement (4). Accordingly, transfer bond strengths for the beam tests should be higher than for strands with no
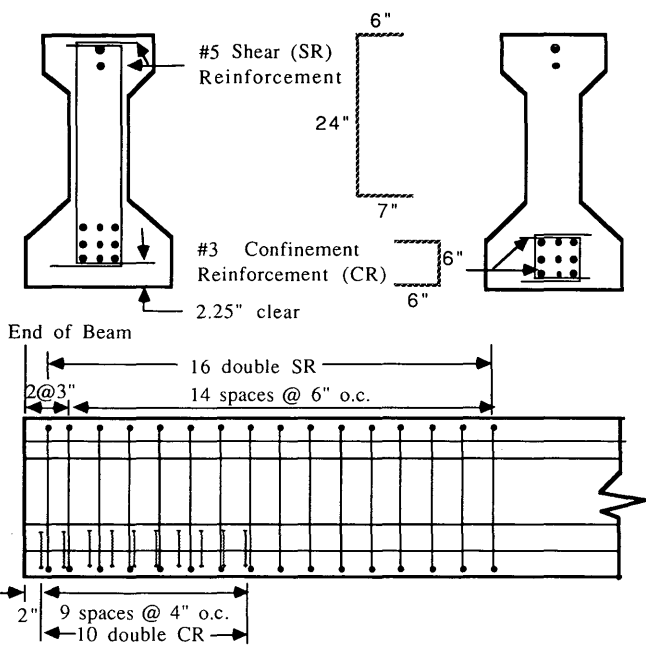
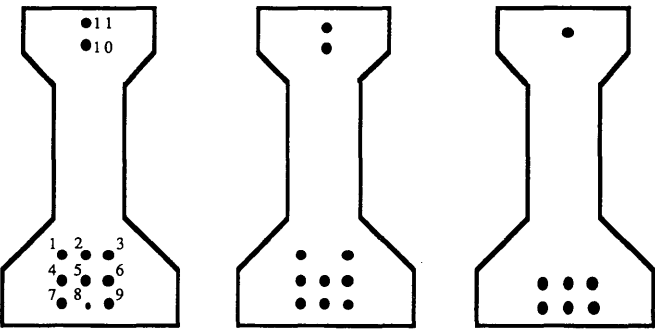FIGURE 1 Shear and confinement reinforcement in each end of beam.

FIGURE 2 Strand configurations: *left*, Pattern A; *middle*, Pattern B; *right*, Pattern C.

TABLE 1 Measured Transfer Bond Strength for Beams

Milled Surface Strand Diameter (in.)	Bond Strength (kips/inch)	Number of Tests
1/2" Regular	0.889	4
1/2" Special	0.982	4
9/16"	1.050	4
6/10"	1.700	8

TABLE 2 Average Measured Transfer Lengths of Beams

Strand	Average Transfer Length (d_b)		
	Milled	Weathered 1-day	Weathered 3-day
1/2" Regular	64.5	46.5	39.0 (8)
1/2" Special	62.2	--	59.3 (4)
9/16"	62.2	--	48.9 (4)
6/10"	40.6	--	--

confining reinforcing. However, other factors such as the multiple strands in beams may have a negative influence on the bond strength. Multiple strands in beams were flame-cut one at a time, and strands cut earlier might have been affected by the transfer force of strands cut later. This effect could degrade the transfer bond strength in beams, perhaps more so for beams with more strands. From Table 2, the decrease in the measured bond strengths for ½-in. regular and $\frac{6}{10}$-in. strands were about 25 and 10 percent, respectively. Greater reduction in bond strengths of beams with the ½-in. regular strands may be due to the greater number of strands in the beams.

Effects of Strand Diameter

The perimeter of seven-wire prestressing strand is approximately equal to $4/3\pi d_b$. Adhesion force, which is directly proportional to the amount of adhered surface, is therefore directly proportional to strand diameter. Friction may be affected by strand diameter because of the difference in normal force from different wire sizes. Because the grooves between the outer wires of a strand get larger with increasing strand diameter, mechanical bond strength would increase with strand diameter. Table 3 illustrates that the average transfer lengths for the ½-in. special, ½-in. regular, and $\frac{9}{16}$-in. strands of milled surface condition are approximately proportional to the strand diameter, but this relationship is not true for the $\frac{6}{10}$-in. strands. The shorter transfer length for $\frac{6}{10}$-in. strands may be attributed to the increase in mechanical bond. The numbers in parentheses are the number of tests.

Effects of Strand Surface Condition

The wires of all stress-relieved and low-relaxation strands have residual surface oil from the wire drawing process. The residuals prevent good adhesion and lower the coefficient of friction at shear interface, thereby decreasing friction bonds. Weathered strands have their residual surface oil washed away and have roughened rusted surfaces with higher coefficients of friction, which are also better for concrete adhesion. From Table 3, the average improvement in the transfer length for 1-day weathering of ½-in. regular strands was about 27.9 percent, and that for 3-day weathering for the same strand appears to be about 40 percent. The average improvement for all the 3-day weathered strands was about 22 percent. This reduction in transfer length may be due to an increase in friction for the slightly roughened surface.

DEVELOPMENT LENGTH TESTS

Development length of strand in a pretensioned member consists partly of transfer length and an additional bonded length called flexural bond length. Development length, unlike transfer length, cannot be measured directly: it can be measured only with an indirect approach in which the behavior and strength of beams loaded at different locations from the ends of beams are studied to determine whether the ultimate stress of the strands could be developed at the load points. This procedure

TABLE 3   Summary of *fcu/f'c* and Steel Stress Calculations

Specimen Designation	Concrete Strength f'c,(ksi)	Horizontal Reaction H, Kips	Measured Moment Mn, (k-ft)	Mode of Failure	With Strain Compatibility Steel Stress fs,(ksi)	Depth to N.A. kd (in.)	Calculated fcu/f'c	Force Equilibrium Adjusted fcu/f'c	Calculated kd (in.)	fsc (ksi)
5-1-EXT	5.48	12.7	645	B-F	277	6.20	1.05	1.20	5.13	270
5-1-INT	5.48	10.6	564	B-S	273	11.18	0.69	1.20	4.49	232
5-2-EXT	6.75	11.6	612	B-S	276	8.28	0.70	1.20	3.90	248
5-2-INT	6.75	12.3	639	B-F	277	6.57	0.81	1.20	4.04	260
5-3-EXT	6.86	12.9	675	F	278	4.44	1.13	1.20	4.17	277
5-3-INT	6.86	12.7	679	B-F	279	4.23	1.19	1.20	4.19	279
5-4-EXT	7.60	12.8	676	F	278	4.37	1.03	1.20	3.77	274
5-4-INT	7.60	12.5	665	B-F	278	4.99	0.91	1.20	3.72	269
5-SWAI-EAST	5.55	12.2	641	F	277	6.81	0.96	1.20	4.96	265
5-SWAI-WEST	5.55	12.2	660	F-B	277	5.58	1.12	1.20	5.12	275
5-UWR-EAST	5.99	12.7	679	B-F	278	4.57	1.26	1.20	4.81	280
5-UWR-WEST	5.99	20.7	707	B-F	279	4.01	1.47	1.20	5.00	286
5-FWC-EAST	5.34	11.9	641	B-F	277	6.81	1.00	1.20	5.19	267
5-FWC-WEST	5.34	12.4	660	F	277	5.65	1.15	1.20	5.37	276
5-ASW-EAST	5.40	11.9	633	F	277	7.27	0.95	1.20	5.06	263
5-ASW-WEST	5.40	11.8	638	F	277	6.93	0.98	1.20	5.11	265
5S-1-EXT	6.62	10.7	569	B-S	256	15.83	0.51	0.90	5.19	196
5S-1-INT	6.62	13.6	724	F-B	268	8.08	0.85	0.90	7.26	263
5S-2-EXT	-	-	-	-	-	-	-	-	-	-
5S-2-INT	-	-	-	F-B	-	-	-	0.90	5.95	223
5S-3-EXT	5.97	12.2	640	F	268	8.84	0.80	0.90	7.01	257
5S-3-INT	5.97	11.1	587	B-S	263	11.66	0.65	0.90	6.14	231
5S-4-EXT	6.18	10.7	574	B-S	262	12.32	0.60	0.90	5.67	223
5S-4-INT	6.18	12.3	666	B-F	269	7.19	0.89	0.90	7.03	268
916-1-EXT	5.53	14.0	688	B-F	261	10.63	0.85	0.90	9.56	254
916-1-INT	5.53	13.5	703	B-F	262	9.85	0.90	0.90	9.95	263
916-2-EXT	5.92	13.2	666	B-F	260	11.71	0.74	0.90	7.85	237
916-2-INT	5.92	13.1	682	B-F	261	10.86	0.78	0.90	8.19	245
916-3-EXT	6.12	13.1	663	B-F	274	2.85	1.76	2.20	2.31	271
916-3-INT	6.12	13.7	675	F	277	2.45	2.10	2.20	2.34	276
916-4-EXT	6.24	13.6	669	B-F	275	2.66	1.88	2.20	2.28	272
916-4-INT	6.24	14.0	684	F	278	2.20	2.33	2.20	2.34	281
6-1-EXT	5.13	13.9	658	F	264	7.22	0.98	1.00	6.91	262
6-1-INT	5.13	27.4	682	F	263	7.44	1.00	1.00	7.37	263
6-2-EXT	5.29	12.6	660	B-F	264	6.89	0.98	1.00	6.57	262
6-2-INT	5.29	12.3	657	B-F	264	7.06	0.96	1.00	6.51	261
6-3-EXT	7.46	13.3	701	B-F	268	4.72	0.94	1.00	4.42	266
6-3-INT	7.46	13.6	704	F	268	4.59	0.97	1.00	4.44	268
6-4-EXT	7.98	13.3	695	F	267	5.00	0.83	1.00	4.08	262
6-4-INT	7.98	13.6	711	F	269	4.29	0.97	1.00	4.16	269
5E-1-EXT	5.78	12.2	684	F	279	3.88	1.55	1.20	5.11	288
5E-1-INT	5.78	12.3	665	F	278	4.93	1.21	1.20	4.96	278
5E-2-EXT	6.57	10.9	620	B-S-F	277	7.65	0.75	1.20	4.04	253
5E-2-INT	6.57	11.5	652	F	277	5.63	0.94	1.20	4.22	268

was followed for different strand diameters, surface conditions, concrete strengths, and pretension levels. Different spacings of strands from different manufacturers were used. Blended in the results are other variables such as concrete strength, reinforcement ratio, and strand pretension level, all of which have some influence on both the behavior and the strength of the beam section.

The development length for a beam is interrelated with the beam behavior. The steel stress that a strand can develop at a beam section is affected by variables such as concrete strength, steel pretension level, reinforcement percentage, concrete confinement, and beam geometry. The corresponding force in the strand must also be adequately transmitted along the development length into the concrete. Transmission of the force over the available development length is dependent on the bond behavior and the beam behavior. For example, the deformational characteristics of the strand at the beam section when the steel force is transmitted over the development length affect the steel stress that can be developed at the section. Using the following procedure to obtain the steel stress developed, the effects on the steel stress of the variables that affect beam strength are minimized.

Theoretical Steel Stress at Ultimate Flexural Compression Failure

The ultimate moment strength of each beam was measured during the development length tests. Because of confinement vertically and laterally by the steel bearing plate at the load point of the top fibers of the concrete in compression and the sharp stress gradient beneath the single load point, a considerably higher concrete strength was apparently attainable at the critical load-point section. The moment strength calculated according to the ACI allowable rectangular stress block and strain-compatibility method was therefore somewhat lower than the actual moment strength for these beams. The steel stress is overestimated greatly if it is calculated from the measured moment strength using the ACI method. This overestimation leads to an error in the steel stress assumed to have been developed, which is then used in the derivation of the bond strength for the development length. Though the ACI method for the calculation of flexural strength is adequate for general design purposes, particularly for a flexural member without lateral confinement for the concrete in compression, it is not sufficiently accurate for the needs of the present research.

A fundamental approach somewhat similar to the analysis method found in the publication by Warwaruk et al. (5) is devised here to solve this problem. In their research, the compressive concrete in the beams loaded at mid-span appeared to have twice the effective strength of the concrete in beams with two-point loadings. Typically, a condition of strain and stress at failure is assumed for a beam as in Figure 3. The steel strain at ultimate is calculated by adding the steel strain at effective prestress (ε_{se}), the elastic shortening (ε_{ce}), and the additional steel strain beyond flexural cracking of the section (ε_{sa}). Assumptions for the present analysis include the following:

1. Plane sections remain plane under flexure;
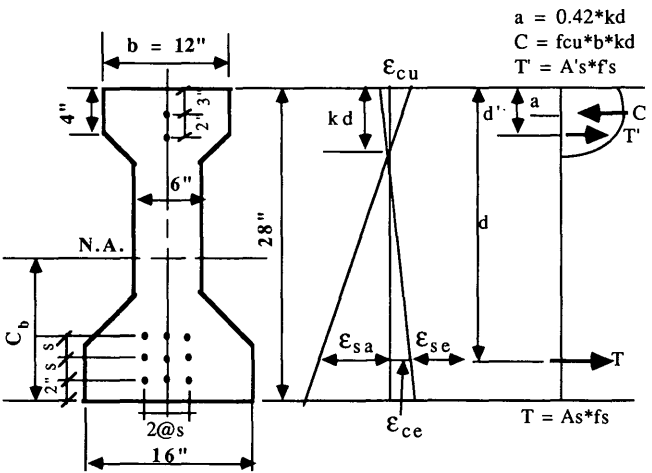2. Strain compatibility factor is known and is a constant 1.0;

FIGURE 3 Conditions of strain and stress for AASHTO Type I beam, cross section; area = 276 in.^{2}, I = 22,750 in.^{4}, C_b = 12.59 in., s = strand spacing (in.).

3. Failure of concrete occurs when concrete strain in the extreme fibers reaches a useful limit of 0.005 (i.e., ε_{cu} = 0.005.4);
4. The location of the resultant compressive force of the concrete is at a distance from the extreme compressive fibers equal to 0.42 of the depth of the neutral axis (i.e., a = 0.42 * kd);
5. Concrete does not carry tension.
6. The stress-strain relationship for the reinforcement is known.
7. A horizontal inward reaction, H, is equal to a friction coefficient of 0.4 times the smaller of the two support reaction forces.

It is realized that the fourth assumption is likely to vary very slightly with concrete strength or when kd is greater than the flange thickness of 4 in. However, the calculated flexural strength is quite insensitive to such small variation. For example, for an actual value of a = 0.35kd in comparison to the assumed a = 0.42kd, only an error of 0.35 in. in moment arm results for a typical kd value of 5 in. This translates into an error in the flexural strength of less than 1.5 percent.

It is necessary to determine the effective concrete strength, fcu, of the concrete subjected to the effect of confinement for the beams in this test program. A computer program was written that iteratively calculates the fcu for each of the beams from the measured ultimate moment in accordance with the strain compatibility condition for the steel strand and the assumptions stated previously.

The ratio of the effective concrete strength to the 6 × 12-in. concrete cylinder strength, $fcu/f'c$, is calculated. The results of the calculation are summarized in Table 4 under the heading "With Strain Compatibility." The value of $fcu/f'c$ is plotted against the depth to the neutral axis, kd, in Figure 4. From this figure, the ratio of $fcu/f'c$ is much larger at smaller values of kd and rapidly reduces to a more-stable lower value of approximately 0.85 as kd increases. The data points with the smaller values of kd correspond to the beams with the smaller reinforcement ratios. The larger $fcu/f'c$ with smaller kd values is consistent with the knowledge that the effect of

TABLE 4 Measured Moment and Mode of Failure

Specimen Designation	fc (psi)	Steel Reinforcement Ratio, (%)	Mode of Failure	Moment (kip-ft) Measured Mcr	Mb	Mu	ACI Mn	Mcr / Mu	Mb / Mn	Mu / Mn
5-1-EXT	5476	0.421	B-F	396	611	645	572	0.61	1.07	1.13
5-1-INT	5476	0.421	B-S	469	550	564	572	0.83	0.96	0.99
5-2-EXT	6746	0.421	B-S	444	612	612	596	0.73	1.03	1.03
5-2-INT	6746	0.421	B-F	415	623	639	596	0.65	1.05	1.07
5-3-EXT	6858	0.421	F	388	-	675	598	0.57	-	1.13
5-3-INT	6858	0.421	B-F	408	645	679	598	0.60	1.08	1.14
5-4-EXT	7600	0.421	F	410	-	676	607	0.61	-	1.11
5-4-INT	7600	0.421	B-F	453	644	664	607	0.68	1.06	1.09
5-SWAI-EAST	5553	0.417	F	430	-	641	579	0.67	-	1.11
5-SWAI-WEST	5553	0.417	F-B	485	660	660	579	0.73	1.14	1.14
5-UWR-EAST	5989	0.417	B-F	463	630	679	593	0.68	1.06	1.15
5-UWR-WEST(S)	5989	0.417	B-F	459	611	707	593	0.65	1.03	1.19
5-FWC-EAST	5341	0.417	B-F	419	624	640	572	0.65	1.09	1.12
5-FWC-WEST	5341	0.417	F	448	-	660	572	0.68	-	1.15
5-ASW-EAST	5400	0.417	F	429	-	633	574	0.68	-	1.10
5-ASW-WEST	5400	0.417	F	463	-	638	574	0.73	-	1.11
5S-1-EXT	6624	0.522	B-S	466	565	569	669	0.82	0.84	0.85
5S-1-INT(LC)	6624	0.522	F-B	449	719	724	669	0.62	1.07	1.08
5S-2-EXT	-	0.522	-	-	-	-	672	-	-	-
5S-2-INT(S)	6800	0.522	F-B	408	692	692	672	0.59	1.03	1.03
5S-3-EXT	5967	0.459	F-B	471	-	640	602	0.74	-	1.06
5S-3-INT	5967	0.459	B-S	457	587	587	602	0.78	0.98	0.98
5S-4-EXT	6181	0.459	B-S	442	530	574	606	0.77	0.87	0.95
5S-4-INT	6181	0.459	B-F	472	601	666	606	0.71	0.99	1.10
916-1-EXT	5533	0.528	B-F	488	682	688	641	0.71	1.06	1.07
916-1-INT	5533	0.528	B-F	476	633	703	641	0.68	0.99	1.10
916-2-EXT	5921	0.528	B-F	455	642	665	661	0.68	0.97	1.01
916-2-INT	5921	0.528	B-F	465	677	682	661	0.68	1.02	1.03
916-3-EXT	6119	0.384	B-F	419	628	663	557	0.63	1.13	1.19
916-3-INT	6119	0.384	F	390	-	675	557	0.58	-	1.21
916-4-EXT	6237	0.384	B-F	390	601	669	559	0.58	1.08	1.20
916-4-INT(LC)	6237	0.384	F	429	-	688	559	0.62	-	1.23
6-1-EXT	5126	0.434	F	412	-	658	595	0.63	-	1.11
6-1-INT(S)	5126	0.434	F	335	-	682	595	0.49	-	1.15
6-2-EXT	5285	0.434	B-F	398	660	660	600	0.60	1.10	1.10
6-2-INT	5285	0.434	B-F	462	609	657	600	0.70	1.02	1.10
6-3-EXT	7463	0.434	B-F	424	696	701	637	0.60	1.09	1.10
6-3-INT	7463	0.434	F	426	-	704	637	0.61	-	1.11
6-4-EXT	7984	0.434	F	406	-	695	642	0.58	-	1.08
6-4-INT	7984	0.434	F	428	-	711	642	0.60	-	1.11
5E-1-EXT	5783	0.421	F	436	-	683	579	0.64	-	1.18
5E-1-INT	5783	0.421	F	449	-	665	579	0.68	-	1.15
5E-2-EXT	6573	0.421	B-S-F	382	565	620	593	0.62	0.95	1.05
5E-2-INT	6573	0.421	F	417	-	652	593	0.64	-	1.10

NOTES: B - Bond Failure (Strands Slip), S - Shear Failure,
F - Flexural Compression Failure, (S) - Short Portion of Broken Beam

confinement is more significant right beneath the bearing plate and within a shallower kd. The figure also shows that for the beams with bond failure, the data points for which are plotted as BF, the $fcu/f'c$ ratio is generally smaller than for the beams without bond failure (F). This is, however, an inherent result of the assumption for the analysis that strain compatibility holds and of the fact that the beams with bond failure generally have slightly lower moment strengths. For the beams with bond failures, deviation from the strain compatibility condition leads to a kd value greater than it would have been with no bond failure. This greater kd value consequently enters into the calculation of the resulting lower fcu value. Thus, only the beams that develop the full flexural strengths without any end slippages were used in establishing the fcu needed for the calculation of the steel stresses developed in the beams with bond failure.

For the beams with bond failure, the steel stresses can be calculated from the measured moment strengths with a chosen

approximate fcu value for each beam group in reference to the $fcu/f'c$ calculated earlier with strain compatibility for beams without bond failure. Because the bottom strands in the beams with bond failure slip, the assumption of perfect strain compatibility condition is not valid. Except for the strain compatibility condition for the bottom steel, the assumptions for the flexural strength analysis stated previously are used. The top steel does not slip; its stress can therefore be calculated from strain compatibility with the previously set $\varepsilon_{cu} = 0.005$ and a kd value. The concrete force, C, and position, $a = 0.42kd$, from which the moment, Mn, can be calculated, are only dependent on the kd value. There is a unique kd value that gives the Mn that is equal to the measured moment. A computer program was written to iteratively seek for this kd value. The steel stress was then calculated for this kd from the equilibrium of horizontal forces. The calculated steel stresses and the corresponding adjusted fcu values are presented in Table 4 under the heading "Force Equilibrium." The steel
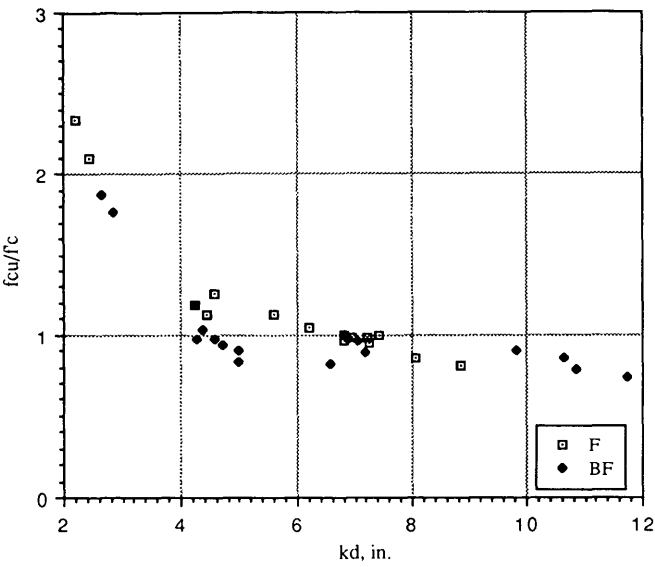
FIGURE 4 *fcu/f'c* versus *kd* for all beams with flexural failure.

Ld : Development Length

Type I: Web-Shear Crack

For Beam 5-1-INT :

V = R = 74 kips

Transfer Bond, Ut = 0.95 kips/in.

Approx. Ld = 6+4 = 10"

T' = Ut * Ld = 9.5 kips/strand

or, = 8 * 9.5 = 76 kips

V = 74 kips is approx. equal to T'

Type II: Flexural-Shear Crack

Development Length = Load Location - Ineffective bond length

FIGURE 5 Interaction of shear crack with development length.

stress in the beams that failed by shear is not predictable with the flexural analysis. These beams are shaded in Table 4.

For beams with lower reinforcement ratios, slight slippage of some strands will only redistribute the stresses among the strands and do not immediately result in a lower flexural strength. Thus, a steel stress higher than that at first slippage may be achieved for an underreinforced beam. However, steel in underreinforced beams is generally stressed more than steel in highly reinforced beams. Although bond failure is more likely for an underreinforced beam, the flexural strength of the beam may not be affected by the bond failure. On the other hand, flexural strength of overreinforced beams is controlled by the available area of compressive concrete. The overreinforced beams, therefore, cannot tolerate slippage that reduces the compressive concrete area. These relationships are studied for a better understanding of the effects of strand slippage on beam behavior.

The different modes of failure observed in the destructive tests were examined in detail, particularly the interaction between the flexural compression failure or shear failure with a bond failure. As illustrated in Figure 5, a sudden shear failure at the initiation of diagonal shear cracking (Type I failure) may occur without an adequate development length from the end of a beam to the shear crack that starts at the interior face of support. The measured shear load, *V*, that beam 5-1-INT could sustain after the diagonal cracking was much reduced—only 74 kips. The effects of the diagonal shear cracks on the bond development seem to be adequately analyzed using the Truss analogy method. The total tensile force (*T'*) that can be developed at the shear crack that initiates from the face of support is calculated from the transfer bond strength for the number of bottom strands. For a 45-degree angle of the shear crack, the shear force *V* at the cracked section that failed because of insufficient development length would be close to *T'*. Also illustrated in the figure is a flexural-shear failure (Type II failure) with crack that propagates from a flexural crack some distance closer to the end of beam. The cracking from Type I and Type II failures in essence move
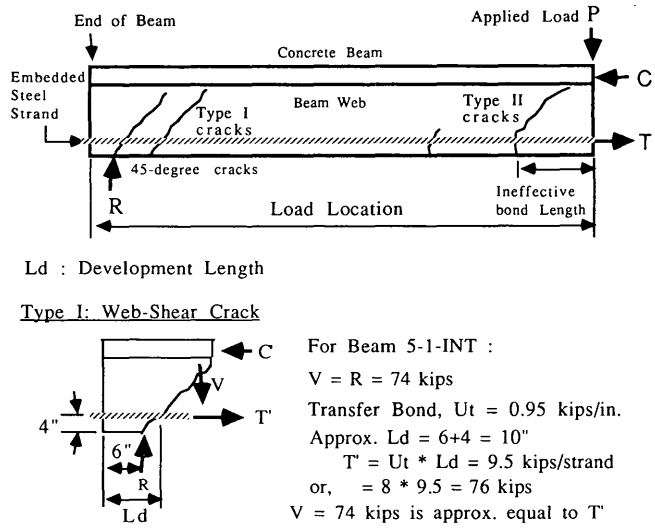
the critical section for the evaluation of development length to the cracks.

Effects of Bond Failure on Beam Behavior

The effects of bond failure on the behavior of all the bridge beams tested are examined in detail and discussed with illustrations. As has also been observed by previous investigators, many of the beams tested could develop additional beam strength even after end slips of some strands were detected. Bond failure of the strands apparently did not cause a significant loss in the steel stress of the strands, and the additional flexural strength gained was probably contributed by the other strands that did not slip. The plastic nature of the bond behavior permits the strands to keep slipping with virtually no loss of bond resistance. This is an extremely important characteristic of the strand performance in contrast to the plain wires. Slippage of the strands that have exhausted their "usable" bond strength is beneficial because it permits the other strands—those that are not yet slipping and have some reserve bond strength—to continue to participate in carrying the extra load. Ideally, for a beam that has less than the full development length, maximum flexural strength is developed only when all usable bond strength in all the strands has been exhausted. However, the inability of slipping strands to carry any additional tension reduces the stiffness of the beam. For a beam approaching its ultimate strength with the steel stressed past the yield point and the extreme fiber of compressive concrete stressed into the inelastic range, this loss of stiffness certainly would result in a flexural compression failure.

Research with pullout bond tests has suggested that the bond resistance, although with significant variability, generally drops slightly when the last of the adhesive bond is broken at the initiation of strand end slip, and that higher bond resistance is attainable at greater slip when mechanical bond takes

effect (6). Therefore, bond length has an effect on the drop in load at the loaded end when end slip at the free end occurs. Stocker and Sozen observed from their test results that the mechanical bond may become effective immediately after slip or only after a relatively large slip of about 0.01 in. (7). The large slip cannot be accommodated at a flexural section without excessively reducing the compressive concrete area and causing a failure. When only a small proportion of the strands suffer "slight" slips, there may be just a minor drop in load with the stiffness provided by the other strands. Creep of the concrete surrounding a strand that experiences the high intensity of bond stress has been observed in pullout tests to gradually relieve bond resistance and permit slight slippage of the strand to occur until it becomes stabilized. This slight slippage probably occurred for the strands in the UTK beams. The load-versus-deflection plots in Figures 6 and 7 show that a slight drop in load occurred while the end slips of a small number of the strands were detected. The load capacity of the beams did not reduce with increasing applied deflection until flexural compression failure occurred. However, when most of the strands in a beam slip nearly at the same time, the load drops off significantly, to not regain strength and finally fail in a flexural compression failure at increasing deflection; Figure 8 shows the load-versus-deflection plot of Test 6-2-INT, which has five out of six strands slipping when load drops.

Increases in the steel stresses of strands that did not slip were measured by strain gauges, which confirmed that higher bond resistance was possible after slippage of some strands in the beam. As presented in Table 4, not all strands had slipped when the beam finally failed in flexural compression and lost most of its strength. Further increase in steel stress was also observed beyond flexural compression failure of some beams.

Some slight slippage of the strands during static testing did not significantly reduce a beam's flexural strength, but it did make the beam more susceptible to shear failure, especially when loaded at short shear span. Bond failure relieves the compressive strain in the lower beam web to permit greater participation of the concrete to carry tensile stresses until
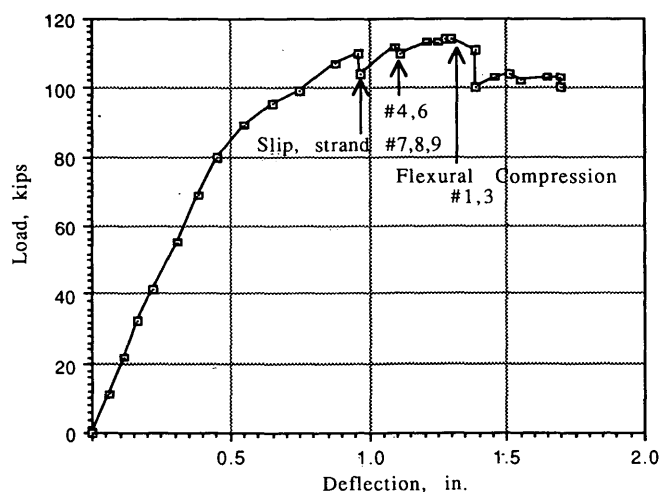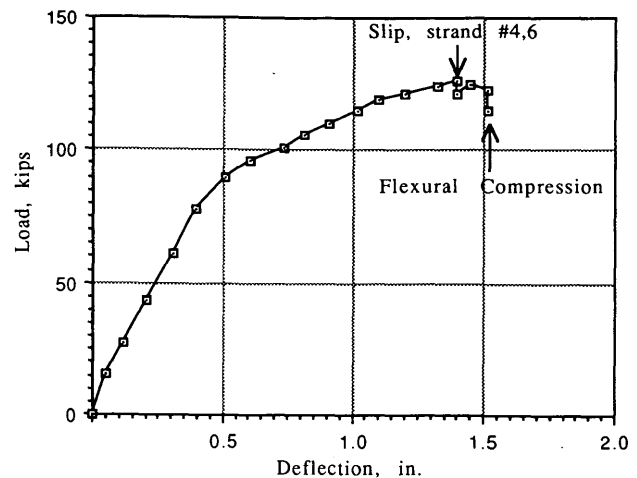

FIGURE 7 Load versus deflection for Beam 6-2-EXT.

cracking of the concrete occurs. Shear cracks further reduce the available development length and precipitate a shear failure with a significantly reduced beam strength. Flexural compression failure of beams having web-shear cracks is often not reached.

Load Capacity and Mode of Failure

In accordance with the ACI equivalent concrete stress block and the strain compatibility condition with an ultimate compressive strain of 0.003 for the concrete extreme fiber, the theoretical moment strength is computed for each beam section and listed in Table 5 as Mn. The computed Mn values are compared with the measured Mu and Mb of the corresponding beams. As seen in the table, all beams without a bond failure had Mu exceeding Mn. The ratios of measured to computed ultimate moments of the beams, Mu/Mn, appear to be somewhat related to the reinforcement ratios—the lower the reinforcement ratio, the higher the Mu/Mn. The higher Mu/Mn ratios for the beams with lower reinforcement ratios
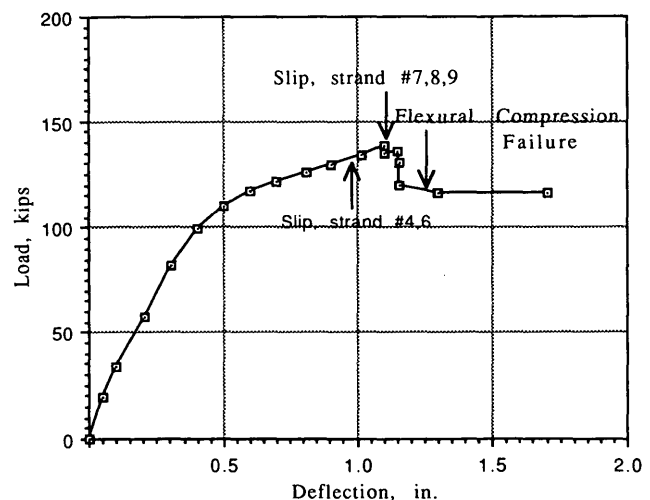

FIGURE 6 Load versus deflection for Beam 916-2-EXT.

FIGURE 8 Load versus deflection for Beam 6-2-INT.

TABLE 5 Minimum and Full Development Lengths

Strand (Mill Condition)	Minimum Development Length (in.)	Full Development Length (in.)
1/2" Regular	77.4	above 92
1/2" Special	81	above 83
9/16"	87	above 106
6/10"	74.4	86

are due to the effects of greater confinement of the compressive concrete in these beams.

All the tests with bond failure also developed *Mu* exceeding the *Mn*. Bond failure of these beams occurred also at a moment above the *Mn*, except for four tests that developed the moments of slightly less than the *Mn* when bond failures occurred (i.e., tests 5S-4-INT, 916-1-INT, 916-2-EXT, and 5E-2-EXT). All the beams with bond failure were near to flexural compression failures when bond failures occurred, and the strengths of these beams did not seem to be affected significantly by the bond failures.

Only four tests did not ultimately develop the calculated *Mn*. In each of these tests, the beam experienced a shear failure soon after strand end slips were detected. One other test (5-2-EXT) reached an *Mu* slightly greater than *Mn* when shear cracking occurred simultaneously with a bond failure; it failed in shear immediately thereafter. Flexural compression failure of these five beams was not reached. The beams with shear failure apparently had load capacities after shear cracking that were below the load at bond failure. These beams are previously explained to have failed due to insufficient development length (or anchorage) at the shear cracks. According to the truss analogy for the Type I failure as illustrated in Figure 5, the load capacities of these beams after shear cracking are calculated and presented in Table 5.

The "minimum measured development lengths" of the strands to develop the computed ultimate moment, *Mn*, of the beams are 77.4, 81, 87, and 74.4 in., respectively, for $\frac{1}{2}$-in. regular, $\frac{1}{2}$-in. special, $\frac{9}{16}$-in., and $\frac{6}{10}$-in. strands of milled condition and pretension of 202.5 ksi. These minimum development lengths correspond to approximately 155 times the diameter of the strands ($155d_b$) for all the strands except the $\frac{6}{10}$-in. strand. Contrary to expectation, the $\frac{6}{10}$-in. strand requires only about 125 d_b or less than what is required for the $\frac{1}{2}$-in. regular strand. However, significantly longer development lengths are required to totally prevent any slippage of the strands at the ultimate flexural moments of the beams; in Table 5 these lengths are tabulated as the full development length. Strands exposed to weathering of up to 3 days in comparison with milled surface condition strands have better bonding characteristics and thus reduced development lengths.

The epoxy-coated $\frac{1}{2}$-in. strands performed significantly better than all the uncoated strands with a full development length of less than 51 in. Reduction of strand spacing from 2 to 1.75 in. for $\frac{1}{2}$-in. strands did not appear to cause any adverse effects on the development length. In the eight tests with the smaller spacing, there was no evidence of splitting between the strands.

CONCLUSIONS

Information is presented herein regarding the bond strength of seven-wire strand in AASHTO-PCI beams and the effect of strand diameter and of weathering on bond strength and, in turn, on transfer length. Exposure to weathering has a significant effect on transfer length, as illustrated in Table 3.

An analysis is presented of the behavior of the beams tested in the research project on which this paper is based, and the effects of bond failure on this behavior are discussed. It was found that although bond failure and the resulting strand slip does not typically lead to a moment capacity less than that calculated by the ACI code, strand slippage did make the beam more susceptible to shear failure. Some of the most interesting information to emerge from the tests relates to the variation of average stress in the compressive stress block, *kd*, as illustrated in Figure 4. For beams with relatively low areas of reinforcement, *kd* is relatively small and the average concrete stress significantly larger than that assumed in conventional strength analysis.

REFERENCES

1. T. Cousins, D. Johnston, and P. Zia. Bond of Epoxy-Coated Prestressing Strand. Department of Civil Engineering, North Carolina State University, Raleigh, 1986.
2. J. H. Deatherage and E. G. Burdette. *Development Length and Lateral Spacing Requirements of Prestressing Strand for Prestressed Concrete Bridge Products*. Final Report. Precast/Prestressed Concrete Institute; University of Tennessee, Knoxville, 1991.
3. B. R. Smith. *An Investigation of the Variables Affecting the Transfer Length of Prestressed Concrete Members*. M.S. thesis. University of Tennessee, Knoxville, Dec. 1989.
4. P. H. Kaar, R. W. LaFraugh, and M. A. Mass. Influence of Concrete Strength on Strand Transfer Length. *Journal of Prestressed Concrete Institute*, Vol. 8, No. 5, 1963, pp. 47–67.
5. J. Warwaruk, M. A. Sozen, and C. P. Siess. *Strength and Behavior in Flexure of Prestressed Concrete Beams*. Bulletin 464. Engineering Experiment Station, University of Illinois, Urbana, 1962.
6. K. L. Griffin. *An Investigation of the Variables Affecting Pullout of Seven-Wire Prestressing Strand*. M.S. thesis. University of Tennessee, Knoxville, May 1989.
7. M. F. Stocker and M. A. Sozen. *Bond Characteristics of Prestressing Strand*. Bulletin 503. Engineering Experiment Station, University of Illinois, Urbana, 1970.

Fatigue Load Spectra for a Steel Girder Bridge

Andrzej S. Nowak, Hani Nassif, and Karl H. Frank

The objective is to present an approach for the evaluation of fatigue performance. The proposed method is a combination analytical and experimental approach. The steps include identification of critical components and details, determination of the load distribution factors and stress range, instrumentation of the bridge, measurement of strains under a control vehicle to calibrate the equipment and determine the load distribution factors, measurement of strain under normal traffic, verification of load distribution factors, verification of load range, and evaluation of fatigue performance. Critical components and details are identified on the basis of analysis and past experience. The analysis provides theoretical values of load distribution factors and stress ranges. Measurement results provide a basis for verification of the analytical values. The number of load cycles is determined from the stress record under normal traffic. For a given number of load cycles, the effective stress range is calculated and compared with the critical level. Then the remaining fatigue life is estimated as a percent of the remaining number of cycles to failure. This serves as a basis for the evaluation of fatigue performance. The proposed approach is applied to an existing steel girder bridge. The superstructure consists of four plate girders and transverse floor beams. The bridge is instrumented, and the results of measurements are presented and discussed. For the considered components and details, the measured stress range and estimated number of load cycles are not critical. Some minor cracking may be expected, but in general the bridge may be considered as adequate with regard to fatigue.

Knowledge of fatigue load spectra is important in evaluating the performance of existing steel bridges. Live load effects may be different for different components and details. In many cases analytical methods do not allow for an accurate estimation of load, in particular load distribution factor and actual stress range. Therefore there is a need for field measurements to verify the analytical results.

Estimation of fatigue life of an existing bridge involves evaluation of fatigue resistance (capacity) and load spectra. Fatigue resistance depends on material properties, type of detail, degree of corrosion, and other deterioration. Load analysis requires knowledge of load history (accumulated damage), current load spectra, and prediction of future loads. The objective of this paper is to present an approach to evaluation of the fatigue load for an existing steel girder bridge.

The load is modeled on the basis of weigh-in-motion (WIM) measurements, truck count, and statistical analysis. The resulting load spectrum (number of cycles and effective stress range) is compared with fatigue strength. This comparison

A. S. Nowak and H. Nassif, Department of Civil and Environmental Engineering, 2370 CG Brown Building, University of Michigan, Ann Arbor, Mich. 48109. K. H. Frank, Department of Civil Engineering, University of Texas, Austin, Tex. 78712.

serves as a basis for evaluation of the adequacy of the considered component or detail.

The approach is demonstrated on the evaluation of fatigue performance for the Woodrow Wilson Memorial Bridge (1). The structure carries Interstate I-95 over the Potomac River between Maryland and Virginia. When the bridge was opened to traffic in 1962, the average daily traffic (ADT) was estimated to be 75,000. The current ADT is 165,000, and it is estimated that it will increase in the future to 235,000. There are three lanes of traffic in each direction. The bridge has a moveable portion, which is not considered in this study.

EVALUATION PROCEDURE

The procedure for evaluating fatigue performance includes analysis and field measurements. A list of the major steps follows.

1. Review the available drawings. Identify the fatigue-prone components and details on the basis of experience. Special attention should be paid to distortion-induced fatigue (transverse components and connections, varying stiffness of girders).
2. Perform analysis to determine the load spectra for main girders (load distribution factors) and fatigue-prone components and details.
3. Instrument the bridge and take WIM measurements. Measure the actual load distribution to girders (girder distribution factors). Measure stress and stress range under a normal flow of traffic.
4. Verify the accuracy of analytical girder distribution factors by comparison with measured distribution factors.
5. Verify the calculated stress ranges by comparison with measured values.
6. Establish the cumulative distribution functions for stress range (for the critical components and details).
7. Estimate the fatigue resistance of the critical components and details.
8. Evaluate the fatigue performance of critical components and details by comparison of load and resistance.
9. Estimate the remaining fatigue life.

The evaluation of fatigue load (Steps 3–6) is the primary consideration here. The instrumentation and measurements are described for the bridge. The formula for the remaining fatigue life, in terms of number of load cycles to failure, is also provided.

INSTRUMENTATION

The tests were performed on the western approach spans, shown in Figure 1. The bridge, considered the Woodrow Wilson Memorial Bridge, is a multispan continuous structure with typical spans equal to 19 m (62 ft). The superstructure consists of four steel plate girders spaced at 7.8 m (25 ft 8 in.), as shown in Figure 2. Main girders have identical webs; however flanges are larger in interior girders. Therefore exterior girders have a lower stiffness than interior girders. Transverse floor beams are spaced at 6.3 m (20 ft 8 in.). The calculations showed high fatigue stress levels in exterior girders. To verify the analytical results, strain gauges were installed at these locations. Evaluation of plans and site inspection revealed other fatigue-prone details. Several years ago cracks were observed in the connections of transverse floor beams with main girders. Another fatigue-prone detail was intersection of longitudinal to transverse stiffener. Typical connection and stiffeners of floor beam to girder are shown in Figure 3.

The bridge was instrumented using strain gauges and strain gauge transducers. In particular, strains were measured at the critical connections between floor beams and exterior girders. Main girders were instrumented to verify girder distribution factors. The location of strain gauges is shown in Figure 4. A test truck was used to determine bridge response to a known load and to compare the measured response to that obtained by analysis. The test truck was a three-axle vehicle with a total weight of 275 kN (62.5 kips).

The waveform of the measured stresses agreed with the predictions, an indication that the bridge was responding as predicted in the analysis. However the measured stresses were always considerably less than the calculated stresses, because of the distribution of the truck load to the adjacent girders in the actual bridge.

Examples of typical plots of the floor beam gauge outputs are shown in Figure 5. The recorded stress ranges resulting from the test truck are presented in Tables 1 and 2, for the truck in the right and center lanes, respectively. On average the response for the truck in the center lane was 50 percent larger than the response for the truck in the right lane.

The floor beam gauges produced some unexpected results. The stresses measured at the end of the floor beams, near the exterior girder, indicate that the top flange of the floor beam is subjected to compression and that the bottom flange is subjected to tension during passage of the test truck over the floor beam. It was expected that the stresses would have the opposite sign. If the floor beam behaves as a fixed-end beam, loaded in the center, with no rotation and displacement at its ends, the stress would have been tension at top and compression on the bottom at the connection to the exterior girder. The measured compression stress at the top and tension stress at the bottom of the floor beam at its exterior
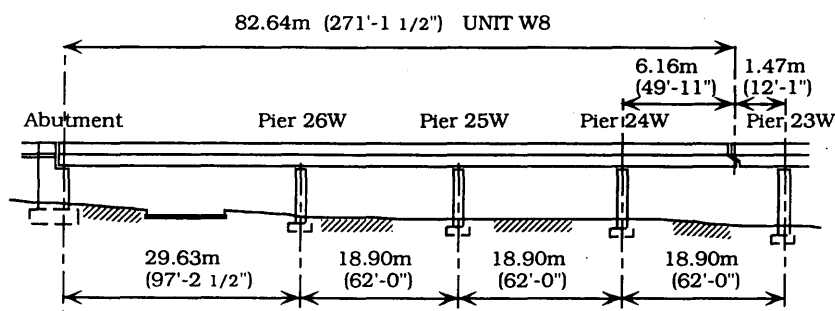

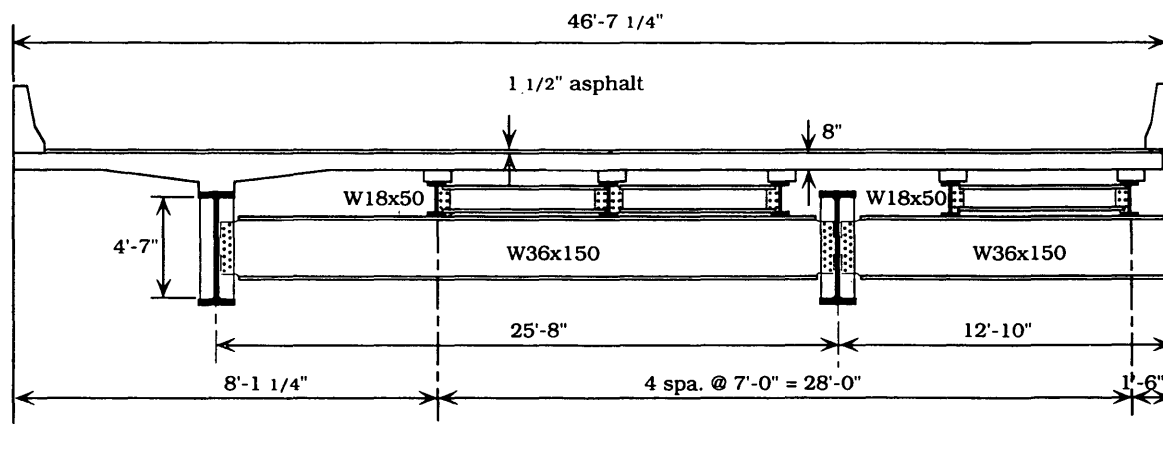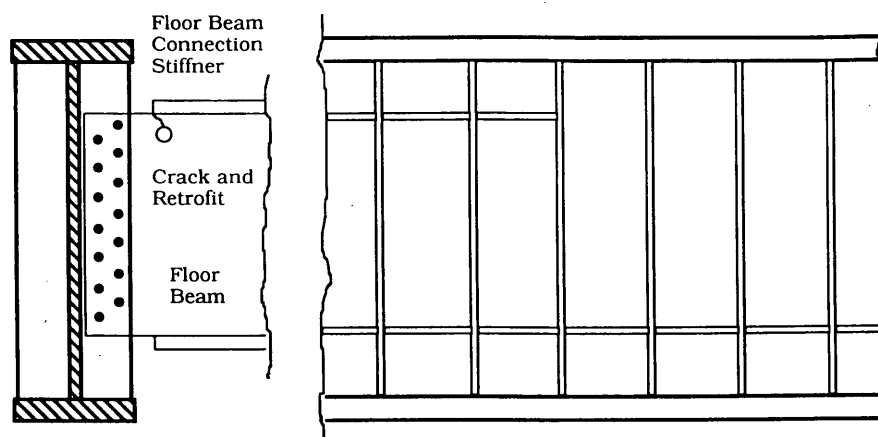**FIGURE 1** Elevation of considered portion of bridge.

FIGURE 2 Cross section of bridge.

FIGURE 3 Girder-to-floor beam connection and stiffener intersection.
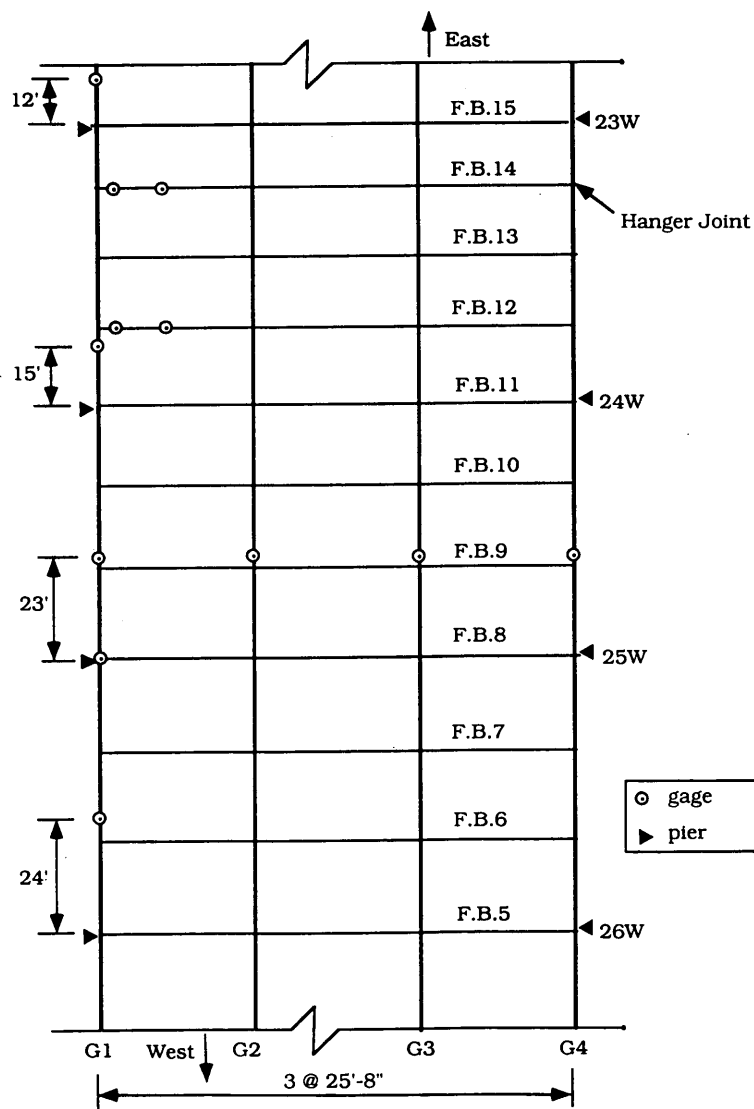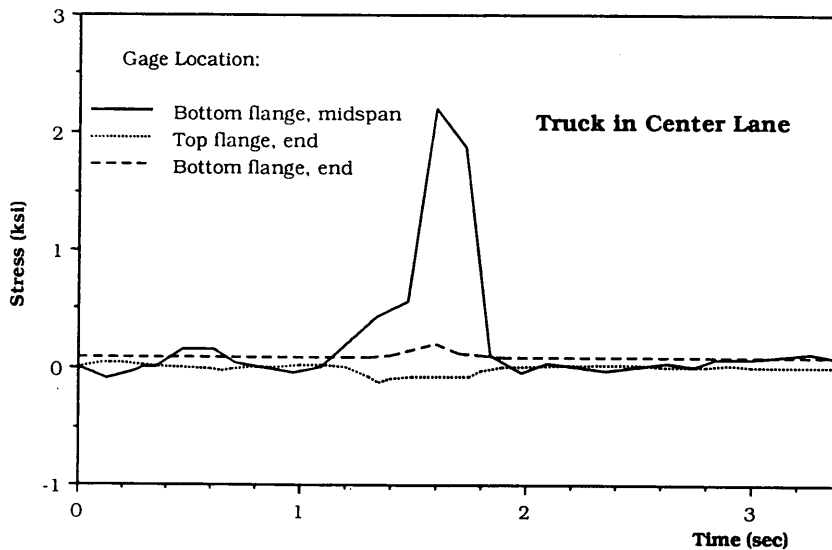

FIGURE 4 Location of strain gauges.
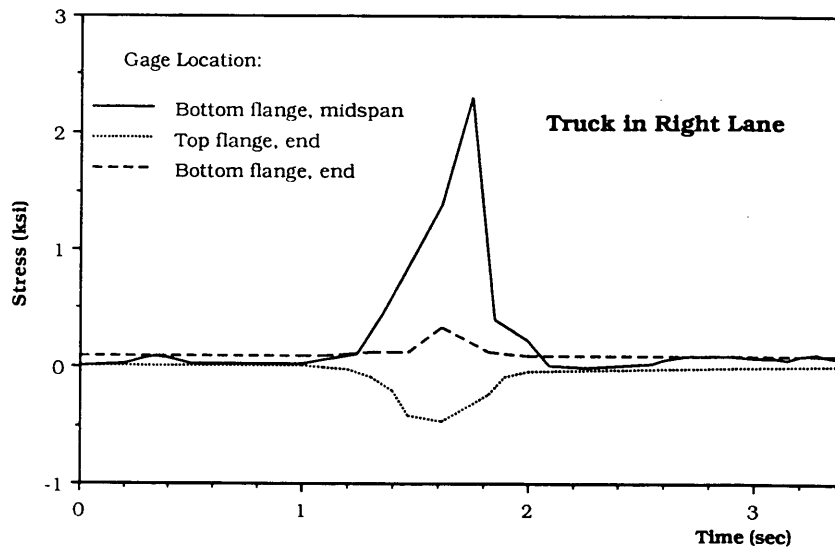
FIGURE 5 Typical stress range versus time for floor beam.

TABLE 1 Stress Ranges for Test Truck in Right Lane

Gage location Number of girder	Distance from support	Top/bottom	Stress Range (ksi) Measured	Calculated	Measured/ Calculated
First week:					
G1	24'	bottom	2.43	9.24	.263
G1	12'	bottom	3.49	9.98	.350
G1	0'	top	0.51	4.93	.104
G1	15'	bottom	1.16	6.87	.169
Second week:					
G2	5'	bottom	1.01	6.18	.163
G1	9.5'	bottom	4.00	9.61	.416

1' = 305 mm; 1 ksi = 6.89 MPa

TABLE 2 Stress Ranges for Test Truck in Center Lane

Gage location Number of girder	Distance from support	Top/bottom	Stress Range (ksi) Measured	Calculated	Measured/ Calculated
First week:					
G1	24'	bottom	1.15	9.24	.124
G1	12'	bottom	1.59	9.98	.159
G1	0'	top	0.25	4.93	.051
G1	15'	bottom	0.44	6.87	.064
Second week:					
G2	5'	bottom	1.70	6.18	.275
G1	9.5'	bottom	1.76	9.61	.183

1' = 305 mm; 1 ksi = 6.89 MPa

support indicate that it is responding as a beam fixed against rotation but undergoing a relative displacement between its supports, the exterior, and the first interior girders. The primary stresses at the end of the floor beams are generated by the differential deflection of the girders and not by the fixed-end moments caused by the rotational restraint provided by the girders. The floor beams are acting like a cantilever from the interior girders supporting the more flexible exterior girders.

To determine the lateral distribution of truck load, gauges were placed at the bottom flanges at the midspans of the main girders. The resulting stress ranges are shown in Figure 6. Each curve corresponds to a passage of the test truck. The highest stress ranges were observed in exterior girders for the controlled truck traveling in the right lanes, close to the exterior girders. The lateral distribution of the moment caused by the truck weight is shown in Figure 7. In Figure 7, a mo-
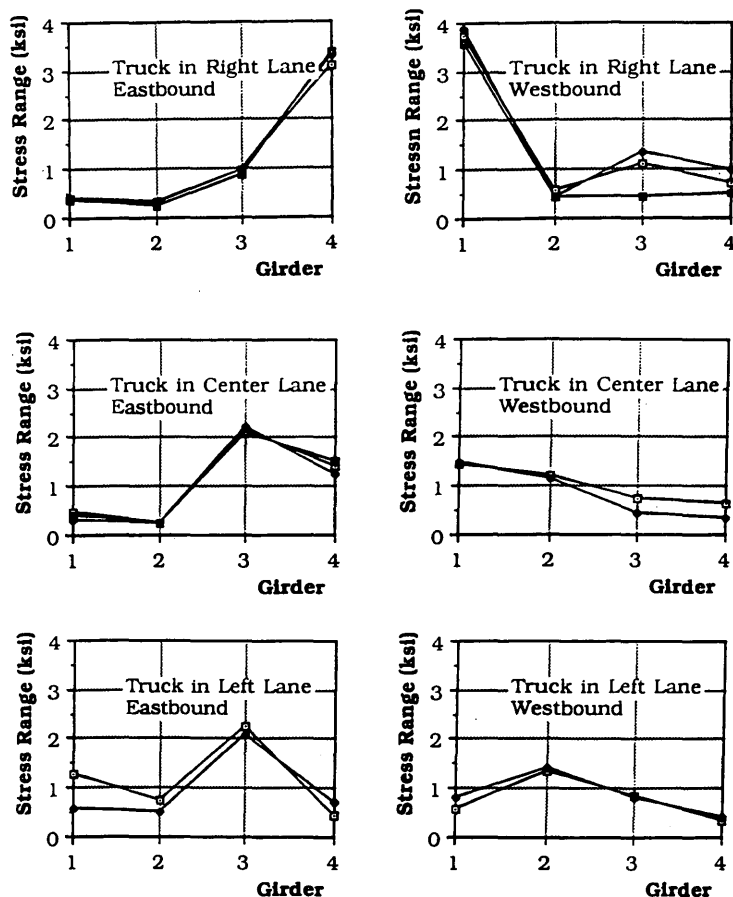

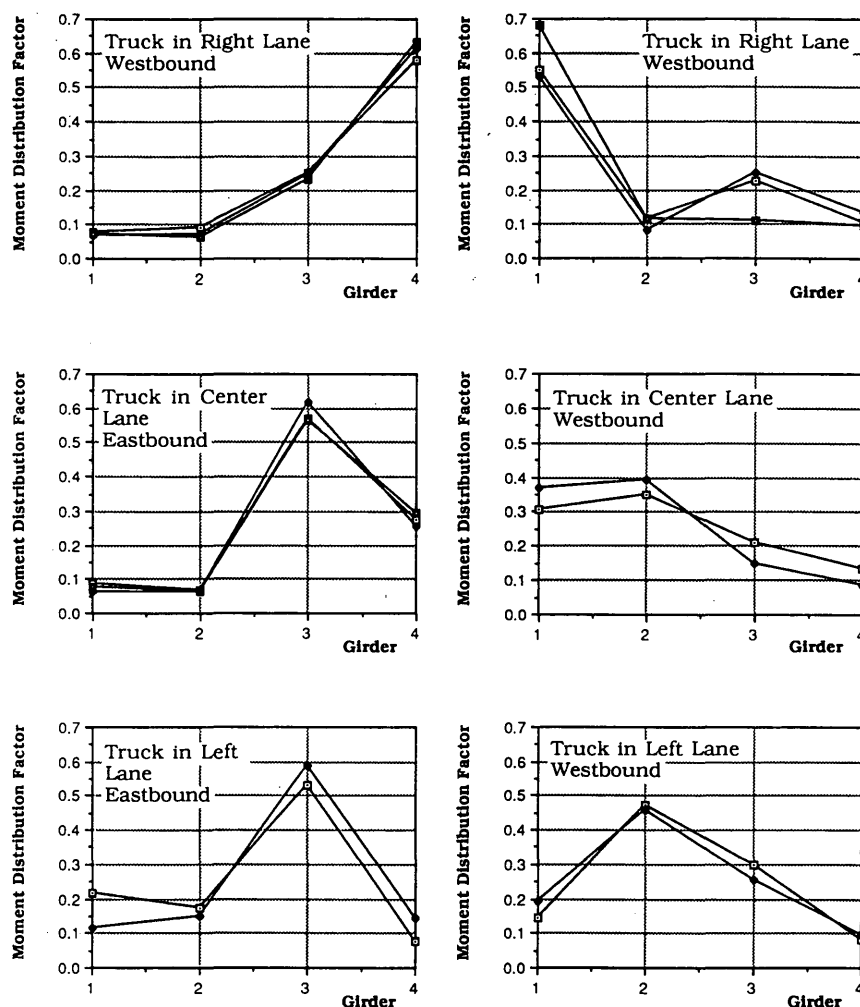**FIGURE 6 Measured stress in girders for various truck positions.**

FIGURE 7 Moment distribution to girders.

ment distribution factor denotes the fraction of the total moment resisted by a girder.

TRUCK SURVEY

To verify the estimates of truck numbers, the Maryland Department of Transportation (DOT) carried out a traffic survey. The traffic flow was recorded for 24 hr with a video camera. The filmed traffic was analyzed to count trucks in each lane and direction. Multiple presence cases (more than one truck per span) were also counted. A total of 11,334 trucks was counted, with 5,174 in the eastbound direction. Less than 10 percent of trucks used the left lane (closest to the median). Approximately every 20th to 25th truck is on the bridge simultaneously with another truck moving side by side in the adjacent lane (within the same span and traveling in the same direction).

The number of trucks also was obtained from the strain/stress data in field tests. The measurements were carried out continuously for 2 weeks. The equipment counts the stress cycles at each location using a rainflow counting scheme. The rainflow counting method counts each individual stress cycle

measured. The fatigue life estimate is based on Miner's rule, which includes all the measured stress cycles. The number of stress ranges at various levels is stored for each day counted.

In the fatigue analysis, the average daily truck traffic (ADTT) values are based on the results of truck surveys, field tests, and Maryland DOT estimates. They vary from 7,000 in 1962 (opening of the bridge) to 12,000 in 1991 to an estimated 16,000 in 2010.

NORMAL TRAFFIC TESTS

The girder gauges and floor beam gauges were installed to measure the stresses caused by normal traffic on the bridge. Results are plotted in a histogram of the stress range at each location as well as an effective stress range calculation. A typical histogram of the stress range is shown in Figure 8. The effective stress range, S_{ref}, is the stress range of constant amplitude that would produce the same fatigue damage as the variable amplitude stresses recorded on the bridge. It can be determined from the linear damage assumption (2,3) as

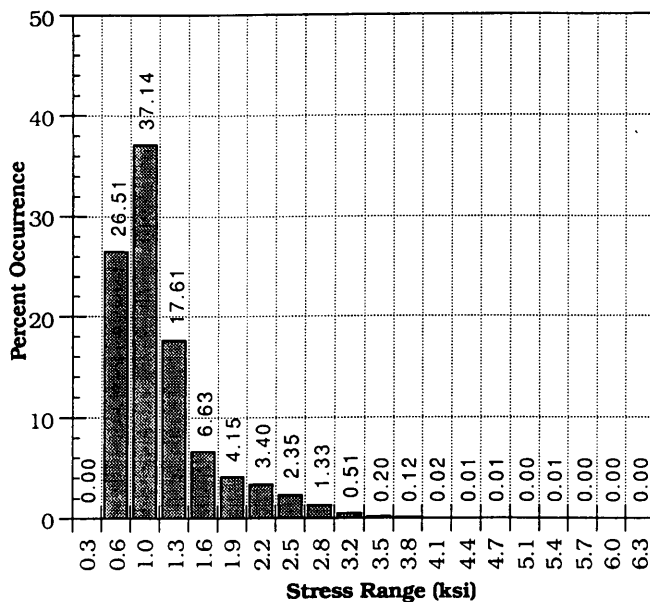$$S_{ref} = \sqrt[3]{\Sigma(S_i^3 \, \gamma_i)} \tag{1}$$

FIGURE 8   Typical histogram of stress range.

where

$$\gamma_i = n_i/n \tag{2}$$

where n_i is the number of cycles recorded at stress level S_i and n is the total number of stress cycles recorded.

The effective stress range and the number of cycles counted were used to evaluate the expected fatigue performance of the bridge. The largest traffic volume was observed on Wednesday; therefore Wednesday traffic was used as a reference. The results of measurements and calculations are presented in Table 3. Girders are denoted by G1 (exterior girder) and G2 (interior girder). Floor beams are denoted by FB. Strain gauges were attached to bottom or top flange of girders and floor beams. Location of a strain gauge is described by the distance from the support (pier). The number of cycles recorded on each Wednesday and the effective stress range of each gauge are given. The sixth column presents the number of cycles measured at the gauge divided by the es-

timated ADTT of 12,000 both ways from the truck traffic prediction. The number of cycles at each gauge is different because of the counting threshold imposed. In the first test week stress ranges below 3.5 MPa (0.5 ksi) were ignored. In the second week the level was reduced to 1.75 MPa (0.25 ksi). It was observed that about half the westbound trucks produced a measured stress cycle. The readings for floor beams indicate that each truck had two axles that produced a stress cycle.

FATIGUE LOAD ANALYSIS

The fatigue life of a welded detail, expressed in terms of the number of load cycles (N) may be represented as

$$N = A/S_{ref}^3 \tag{3}$$

where A is a constant depending on the welded detail and S_{ref} is the effective stress range. The value of A may be calculated from the values of stress range and life (number of load cycles) in the AASHTO specification (1989) for each category of welded detail. The fraction of the fatigue life consumed for the given number of cycles, n, and effective stress range, S_{ref}, is denoted by D and may be calculated as

$$D = n\,S_{ref}^3/A \tag{4}$$

Using the estimated past, present, and future ADTT, the percent of the fatigue life of the girders and floor beams were estimated. The estimated life is calculated for AASHTO Category C, D, E, and E' details. The stiffener intersection fatigue category was also evaluated. Fatigue life was estimated for the weld at the end of a longitudinal stiffener close to a transverse stiffener weld. This is a severe fatigue detail producing lives below a Category E' (denoted by > E'). The fraction of fatigue life consumed, D, is plotted versus year in Figures 9, 10, and 11, for a girder, floor beam, and stiffener intersection, respectively. For girders and floor beams, the value of D is determined for detail categories C, D, E, E' and >E'. For a stiffener intersection, only category >E' is considered. The analysis based on experimental results indicates that only the stiffener intersection detail has a potential

TABLE 3   Effective Stress Range and Number of Cycles

Gage location: No.	Distance	Top/ bottom	Stress Cycles Wednesday	S_{ref} (ksi)	Cycles/ 12,000
First week:					
G1	24'	bottom	6,679	1.12	0.56
G1	12'	bottom	5,746	1.39	0.48
G1	0'	top	33	0.70	0.00
G1	15'	bottom	450	0.77	0.04
FB	midspan	bottom	7,062	1.28	0.59
FB	midspan	bottom	7,103	1.29	0.59
Second week:					
G2	5'	bottom	5,906	1.07	0.49
G1	9.5'	bottom	6,560	1.49	0.55
FB	midspan	bottom	11,794	1.01	0.98
FB	midspan	bottom	12,387	1.03	1.03

1' = 305 mm; 1 ksi = 6.89 MPa
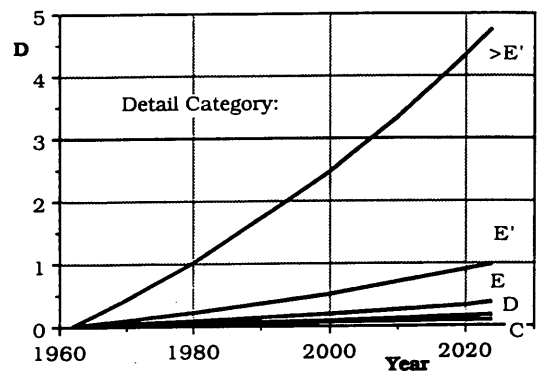

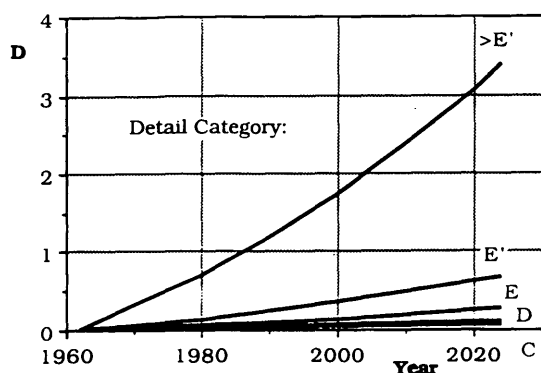**FIGURE 9   Fatigue damage estimate for girder.**

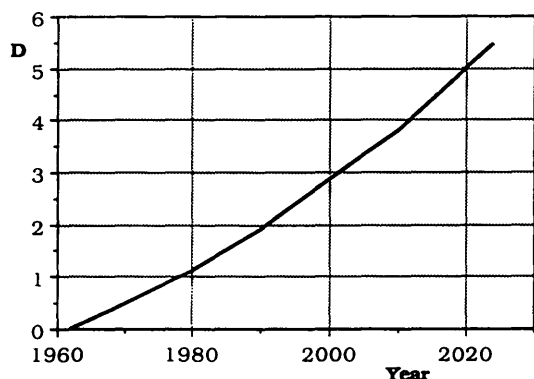**FIGURE 10   Fatigue damage estimate for floor beam.**

FIGURE 11   Fatigue damage estimate for stiffener intersection.

for fatigue cracking during the next 30 years of service. The girders have only Category C and D details. The floor beams have welded stiffeners, which are Category C details. The analysis indicates that no cracking is expected at these welded details on either the girders or floor beams.

CONCLUSIONS

A procedure is presented for evaluation of fatigue performance of an existing steel girder bridge. The study is focused on the development of fatigue load spectra. The structure is instrumented and truck loads are recorded. A control truck is used to verify load distribution factors. Stress history was measured under normal traffic conditions. The fatigue performance is evaluated by comparison of load (number of cycles and effective stress range) and fatigue strength.

The proposed procedure is demonstrated on a fatigue performance evaluation of an actual bridge. Based on this study, it was found that the main girder flanges should not exhibit fatigue cracking at the flange butt welds and stiffener welds during the next 30 years of service. Cracking in the webs of

the girder and in the floor beams caused by the restraint of the connection between the floor beam and the girder may occur. It may also occur in the girder webs at the stiffener intersections. These web cracks are slow-growing cracks that may be detected and repaired easily. This should be considered a maintenance problem and not a safety tissue.

Based on the available information, measurements, and analysis, it is found that the bridge evaluated is capable of continued service for an unlimited period of time. The measured fatigue load spectra are within the stress ranges for unlimited periods. However further fatigue cracks may be expected in fatigue-prone details at the end of the floor beams and possibly at the longitudinal-to-transverse stiffener intersections. In the future more refined analysis and field studies are needed to determine the extent of the possible cracking and development of required retrofits. Inspection of these suspect areas should be undertaken regularly.

Previously observed cracks in transverse beams are caused by the differences in girder stiffness between exterior and interior girders. Therefore further cracking may be expected. However these are slow-growing cracks, their potential location is known, they are accessible for inspection from the walkways, and therefore they do not pose a serious problem.

AASHTO specifications provide the requirements and provisions for analytical evaluation of fatigue performance for bridge components. The tests demonstrated that experimental results can provide additional information about the actual load distribution and fatigue load spectra for components and details. This can improve the accuracy of fatigue life predictions.

REFERENCES

1. K. H. Frank and A. S. Nowak. *Report on Evaluation of Remaining Life in Structural Steel Portion of Approach Spans of Woodrow Wilson Bridge Carrying I-95 over the Potomac River.* FHWA, U.S. Department of Transportation, Baltimore, Md., May 1991.
2. K. H. Frank. Using Measured Stress Histories to Evaluate the Remaining Fatigue Life of Bridges. In *Bridge Rehabilitation* (Konig and Nowak, eds.), Ernst & Sohn, Berlin, Germany, 1992.
3. F. J. Zwerneman and K. H. Frank. Fatigue Damage Under Variable Amplitude Loads. *Journal of Structural Engineering*, Vol. 114, No. 1, 1988, pp. 76–83.

Static Live Load Tests on a Cable-Stayed Bridge

J. Leroy Hulsey and David K. Delaney

A 91.4-m (300-ft) fracture critical cable-stayed bridge near Skagway, Alaska, carries conventional traffic and 712-kN (160,000-lb) ore trucks. The bridge has a laminated timber deck supported by transverse floor beams spanning two stiffened ASTM A588 steel box girders. Two inclined cables stay each girder near mid-length to a single tower. The abutments and tower are rock-anchored to the canyon walls. The bridge was instrumented and field tested with statically positioned trucks to help determine boundary conditions provided by rock anchor supports and assess behavior for non-AASHTO ore trucks. Two types of trucks were used to load the bridge: (a) a 176.84-kN (39.74-kip) snooper truck, and (b) four different ore trucks with weights from 699.1 to 701.1 kN (155.1 to 157.6 kips). A fracture critical inspection was also conducted and cracks were found. Strain, girder deflection, a temperature profile of the girder, wind velocity, solar radiation, and ambient air temperature were monitored. Experimental deflections and strains compared with a traditional two-dimensional (2-D) analysis are presented. Maximum strains for ore truck static load tests were: 224 microstrain (276 calculated) in the box girder and 134 microstrain (193 calculated) in the tower support. Ore truck loads did not vary significantly and like loading produced excellent repeatability. For this structure, a 2-D analysis provided satisfactory results for symmetric loads; conservative answers on the loaded side for asymmetric loads. A three-dimensional analysis is suggested for modifications. Rock anchors acted as fixed supports.

Consider an unusual 91.44-m (300-ft) cable-stayed highway bridge near Skagway, Alaska. The bridge carries about forty 712-kN (160,000-lb) ore trucks a day in addition to normal traffic and is exposed to harsh climatic conditions. The backstays, tower, and abutments are anchored to the canyon walls with prestressed rock anchors. Recently, modifications were made to provide for an increase in ore truck load limits and volume of traffic (Arvid Grant and Associates, unpublished data). This paper is based on the bridge condition before 1991–1992 design modifications.

GENERAL INFORMATION

The Captain William Moore Creek bridge is a two-lane bridge located between Skagway, Alaska, and Carcross, Canada. A 5.08-cm (2-in.) asphalt wearing surface is attached to a timber deck with wire mesh. The deck consists of 17.78-cm (7-in.) laminated timber planks supported by transverse floor beams spaced at 3.66 m (12 ft) on center. Floor beams connected

J. L. Hulsey, Transportation Research Center, University of Alaska Fairbanks, 263 Duckering Building, Fairbanks, Alaska 99775. D. K. Delaney, Centennial Engineering, Inc., 15000 West 64th Avenue, Arvada, Colo. 80004.

by shear plates (no-moment transfer connection) span two stiffened ASTM A588 steel box-shaped girders (Figures 1 and 2). Each girder is supported at the ends by columns and a bearing assembly at the pylon and is stayed about mid-span by cable pairs in a double plane arrangement. The pylon bearing assembly has a curved steel plate adjacent to and slightly below a 2.54-cm (1-in.) neoprene pad. The bridge length of 91.44 m (300 ft) is divided into four span lengths of 9.14, 36.16, 38.17, and 6.10 m (30, 123, 127, and 20 ft) [Figure 1 (*top*)].

The two main box-shaped longitudinal girders are 80 cm (2 ft 6⅝ in.) wide and 154.9 cm (5 ft 1 in.) deep and fabricated from 18.28-m (60-ft) ASTM A588 steel plates welded and spliced at the ends with bolts [Figure 1 (*bottom*)]. Ventilation ports were not installed. Each girder is stayed by two inclined cables 7.62 cm (3 in.) in diameter made of galvanized structural strands that extend through the girders and are anchored to the underside of the bottom flange. The stays are supported above the deck by an inclined H-shaped tower. The tower is supported by the canyon wall and extends up to and supports the girders and then continues approximately 32.31 m (106 ft) with a tapered box-shaped cross section. The ASTM A588 steel tower is inclined forward over the canyon wall at about 15 degrees to vertical. The backstays terminate at tripod supports attached to the canyon by prestressed rock anchors.

The bridge was designed in 1974 (constructed in 1975) for AASHTO HS20-44 highway loads. During winter 1986–1987, cover plates were welded to the main girders to strengthen the bridge to accommodate ore truck traffic between a mine at Whitehorse, Canada, and a barge port in Skagway. Final inspection was completed in February 1987. Between 1986 and 1990, in addition to other traffic, up to 40 ore trucks a day made round trips across the bridge. On each trip to Skagway, a loaded truck weighs about 712 kN (160,000 lb); on the return trip, an empty truck weighs 244.7 kN (55,000 lb).

Sometime during the latter part of 1987, a request was made to increase ore truck load limits to 756.5 kN (170,000 lb) and the trips to 50 per day. Subsequently, the Alaska Department of Transportation and Public Facilities (AKDOT&PF) performed a two-dimensional (2-D) analysis for the existing loading. Calculated stresses were significantly affected by boundary condition assumptions, which led to the question: Do prestressed rock anchor supports act as pinned, fixed, or other? This influenced decision making. Other questions were these: Is a 2-D model sufficient? What type of elements should be used? How are non-AASHTO loads distributed to the girders? Answers were not available by mathematical means.

In 1988 the bridge was instrumented and static-tested with a control load (snooper truck) and four ore trucks. Strains
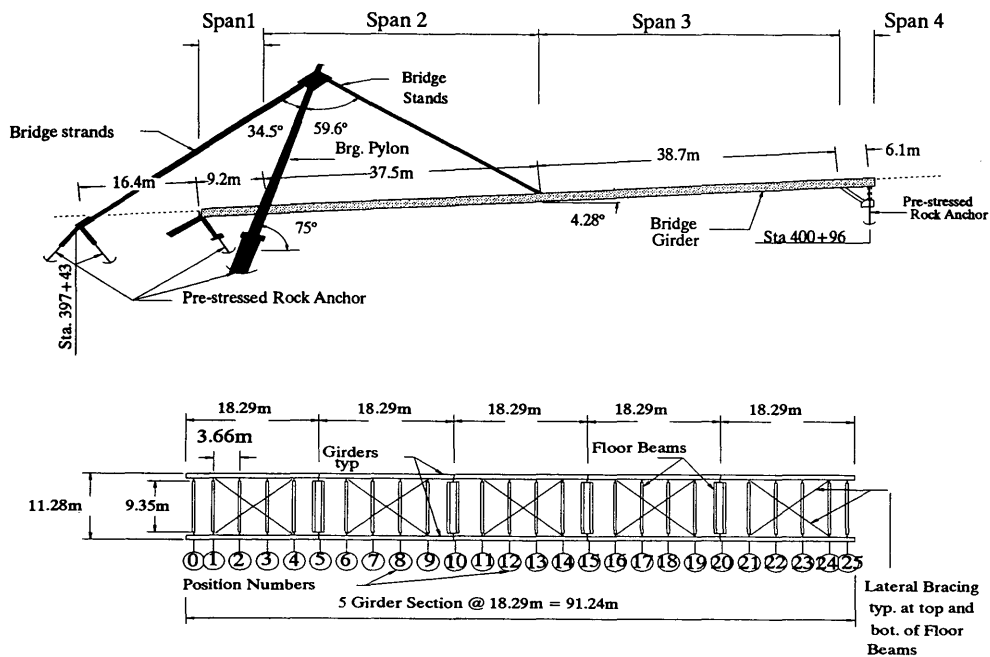
FIGURE 1 Captain William Moore Creek bridge geometry: *top*, bridge geometry elevation; *bottom*, bridge frame plan view.

and girder deflections were recorded to assist in obtaining answers to the preceding questions.

During 1991 and 1992 cracks were found during fracture critical inspections of the bridge (Arvid Grant Associates and Mayes Testing, unpublished data). A three-dimensional (3-D) sophisticated analysis was performed in 1990, dynamic tests in 1991 and 1992, and structural modifications in 1991 and 1992; these results will be presented later.

It is the purpose of this paper to give static test results for a control vehicle and ore truck loading, show an experimental comparison with a 2-D analysis, and present the general condition of the structure. The validity of using a 2-D model is

FIGURE 2 Bridge section geometry: *top*, bridge section; *bottom*, pylon bearing pad.

discussed. Degree of fixity for rock anchor supports and sensitivity of the girder pylon bearing assembly are discussed.

STATIC TESTS

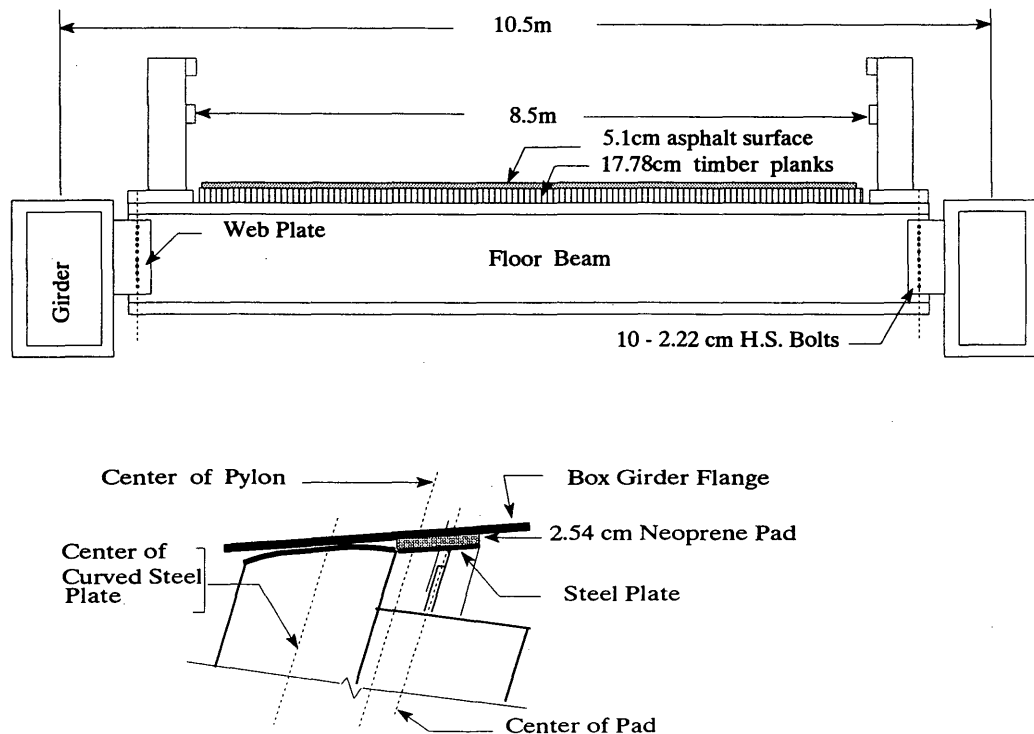The literature reveals that laboratory models of cable-stayed bridges have been used to study erection stresses, construction sequencing, cable anchorage stresses, and nonlinear effects and to develop techniques for analysis and design of these types of structures (1–3).

In the full-scale testing category, the 366-m Tjorn Bridge in Sweden was subjected to dynamic tests 1 week before being opened to traffic (4). Acceleration measurements were taken for three types of tests: dynamic load, free decay, and forced vibration. Except for tests on this structure (5–7), there is no evidence of field static tests on cable-stayed bridges in the literature.

Planning and Preparation

Before an instrumentation strategy was formulated, an analysis was conducted and influence lines were prepared for the

box girders. This information was used to locate strain gauges and position trucks for field testing. Instruments selected were 25 full-bridge, 350-ohm weldable strain gauges; a 25.4-cm (10-in.) clamp-on extensiometer; transit and level; velocity seismoprobe; eight 3000-ohm thermistors; one Type-T thermocouple; an annometer; and a pryanometer. Because of a limited budget, rosettes were not used.

Field Test Procedure

Each test was designed to provide results for a known truck load at a given static position on the bridge. This was accomplished by referencing for each test (a) the type of truck, (b) its position across the deck, (c) the location of the front axle along the girder, and (d) the direction of movement (Figure 3). The terms left and right are used to reference truck position across the roadway when facing upstation.

For each test, the front wheels of a truck were positioned in a lane or centerline over paint marks on the deck. Data were collected with a data acquisition system and stored on a floppy disk; the system was located in a van parked off the bridge (Figure 3) (5–7).
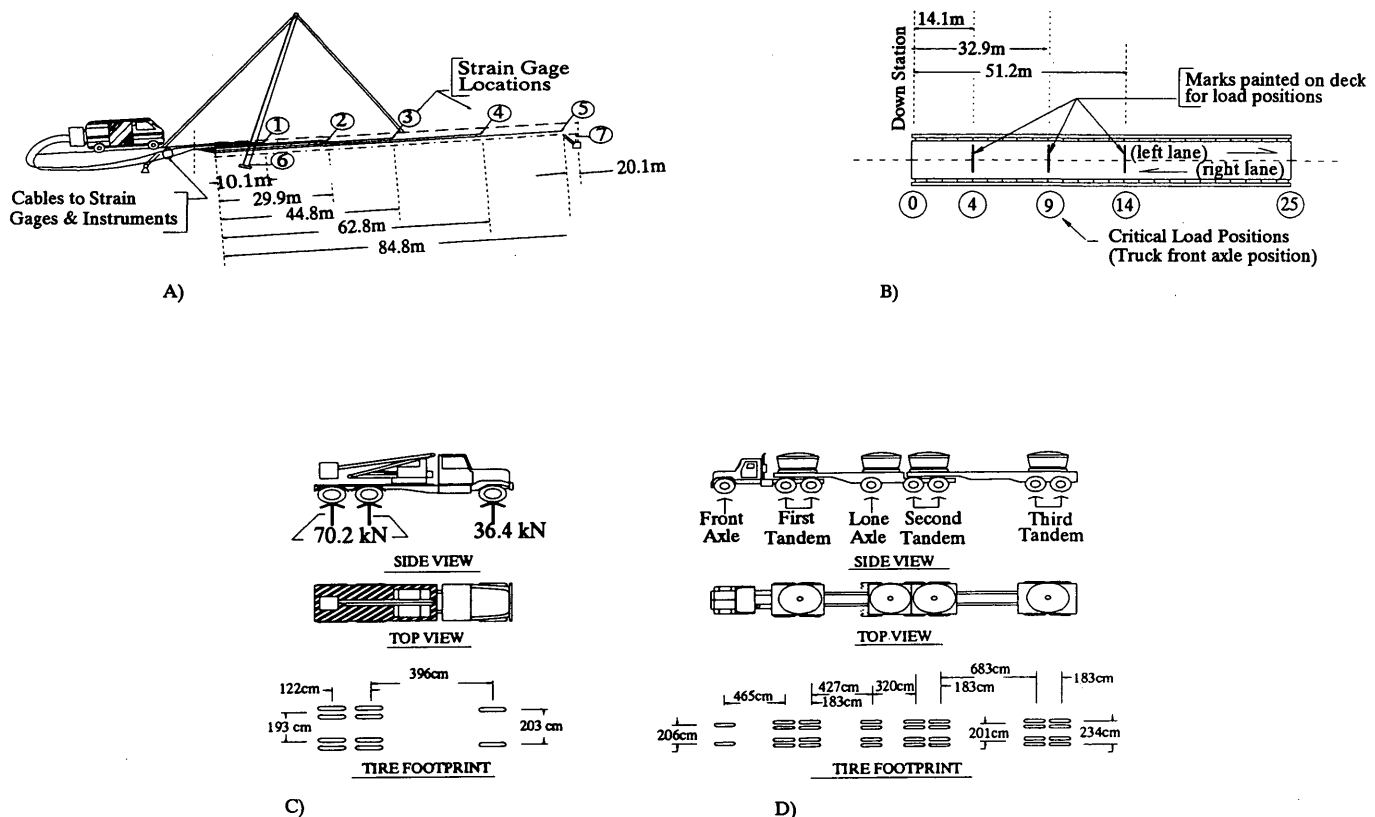

FIGURE 3 Arrangements for testing: a, instrument monitoring equipment; b, bridge frame and load position; c, snooper truck; d, B-train (ore truck).

A typical static test series involved initializing instrumentation, positioning the truck, and checking for vibration dampening with a velocity probe; then time and voltages for each strain gauge, linear variable differential transformer, thermistor, anemometer, and pyranometer were recorded. Vibrations of the structure occurred from normal movements, potholes in the asphalt, and wind.

Field Tests

Two types of trucks were used for static load tests over a 2-day period (Figure 3). The first was a snooper (control vehicle) approximating AASHTO H20-44 with a front-axle weight of 36.4 kN (8.18 kips) and two axles of 70.22 kN (15.78 kips) each. On the first day, five series of tests for a total of 106 load positions were conducted with the snooper truck: 53 with the truck in the left lane, 28 in the right lane, and 25 on the centerline (Table 1). Girder elevations were measured for nine of the 106 load positions. Because of procedural errors (electronic spikes from a hand-held radio), data for the first 25 tests were contaminated and rejected.

On the second day, data were recorded for three load positions for four B-trains (Table 1). Each B-train carried ore in four pots mounted on the lowboy trailers (Figure 3d). Truck weights varied from 690.06 to 701.12 kN (155.07 to 157.556 kips). Axle weights for B-trains were obtained from weight tickets. Twelve static B-train tests were conducted: six in the left lane, three on the bridge centerline, and three in the right lane. Girder elevations were measured for 6 of the 12 tests.

TEST RESULTS (EXPERIMENTAL AND ANALYTICAL)

Cable stiffness is dependent on cable tension, angle, weight, and end restraints (8; D. K. Delaney, unpublished data, 1990). Therefore, several techniques have been suggested for analysis of cable-stayed bridges, such as iterative 2-D methods

(9,10), 3-D methods (11–13), and elastic-plastic schemes (14). Others have used models to predict nonlinear behavior (1,3,15). It is one of the objectives of this paper to determine whether a 2-D linear elastic finite element model with beam and axial elements can be used with enough accuracy to calculate strains and deflections.

Finite Element Models

A two-dimensional frame analysis computer program with 6 degrees of freedom (d.o.f.) beam elements, 2 d.o.f. axial elements, linear/axial rotational springs with provisions for eccentric connections, linear flexibility matrix, and nonlinear axial springs were selected. Nodal point loads, concentrated element loads, varying distributed element loads, element temperatures, element strains, and load case combinations are available in the program library.

The program was modified to create a table of computed forces and a table of displacements for the elements and nodes that correspond with measured values. A postprocessor was written in FORTRAN 77 to transform computed forces into strains, sort the information, and create tables comparing computed strains and deflections with experimental results.

Parametric Studies

The analytical study was used to determine the degree of fixity provided by rock anchor supports and the adequacy of a 2-D analysis. In an attempt to seek answers, parametric studies were initiated to investigate boundary condition sensitivity, influence of constant section element approximations of the tapered pylon, and interaction between the curved steel bearing plate and neoprene pad at the pylon bearing assembly. These parameters were studied by comparing analytical with experimental results for load positions when the B-train was on the bridge centerline.

TABLE 1 Truck Test Series

Test	Truck Weights (kN)	Front Axle Positions	Truck Locations	Movement	Measured Deflection Locations
Snooper Truck Test Series:					
SLDOS01	106.86	0-24	Center of left lane	downstation	none
SLDOS02	106.86	0-24	Center of left lane	downstation	none
SLDOS03	106.86	24-0	Center of right lane	upstation	none
SCDOS04	106.86	0-24	Center of bridge	downstation	14,9,4
SCDOS05	106.86	4,9,14	Center of right lane	upstation	4,9,14
		14,9,4	Center of left lane	downstation	14,9,4
B-Train Test Series:					
SLDOB06	690.06	4,9,14	Left lane wheel path	downstation	none
SLDOB08	700.03	4,9,14	Left lane wheel path	downstation	14,9,4
SCDOB10	701.12	4,9,14	Center of bridge	downstation	14,9,4
SRDOB11	699.06	4,9,14	Center of right lane	downstation	none

NOTE: "Left" and "right" refer to view upstation.

Load Distribution

It was assumed that axle weights are distributed equally to each wheel line of the tested vehicles. Each floor beam is connected to a girder with a web plate and a single line of H.S. bolts 2.22 cm ($\frac{7}{8}$ in.) in diameter [Figure 2 (*top*)]. First, it was assumed that the web plate transfers only shear forces (i.e., simple beam theory). The validity of this approximation was tested against both rigid and eccentric shear connector assumptions with girder torsional stiffness included. Analytical comparisons illustrated that simple beam distribution more accurately approximated behavior. Interaction of deck flexibility was not considered.

Pylon and Cables

The upper tapered section of the pylon was approximated with three constant section 6 d.o.f. beam elements. Analysis showed that three equal length elements with section properties for the average section over the length of the element provided satisfactory results. A preliminary investigation of cable tension indicated that sufficient accuracy could be obtained by using linear axial elements (8).

Pylon Bearing Assembly

The box girders are supported at the pylon by a curved steel plate and neoprene pad bearing assembly that is mounted on a shelf [Figure 2 (*bottom*)]. The steel plate was coated with teflon and used to launch the girder and is slightly lower than the neoprene pad. Thus, it was initially assumed that the pad supported the girder. A comparison between analytical and experimental pylon base strains showed that moments were transferred from the girders through both bearings to the pylons; the results further showed that the structure is extremely sensitive to the load path through this bearing assembly. The bearing assembly was approximated by Elements 70, 11, and 68 (Figure 4). Element 70 is a rigid link, Element 11 approximates the plate (large area, zero moment of inertia), and Element 68 approximates the pad (modulus of neoprene, 25 percent pad area since neoprene modulus varies with compressive stress, and zero moment of inertia).

Support Boundary Conditions

Pylons are supported by piles and anchored with prestressed rock anchors (Figure 1). The upstation end bent column is
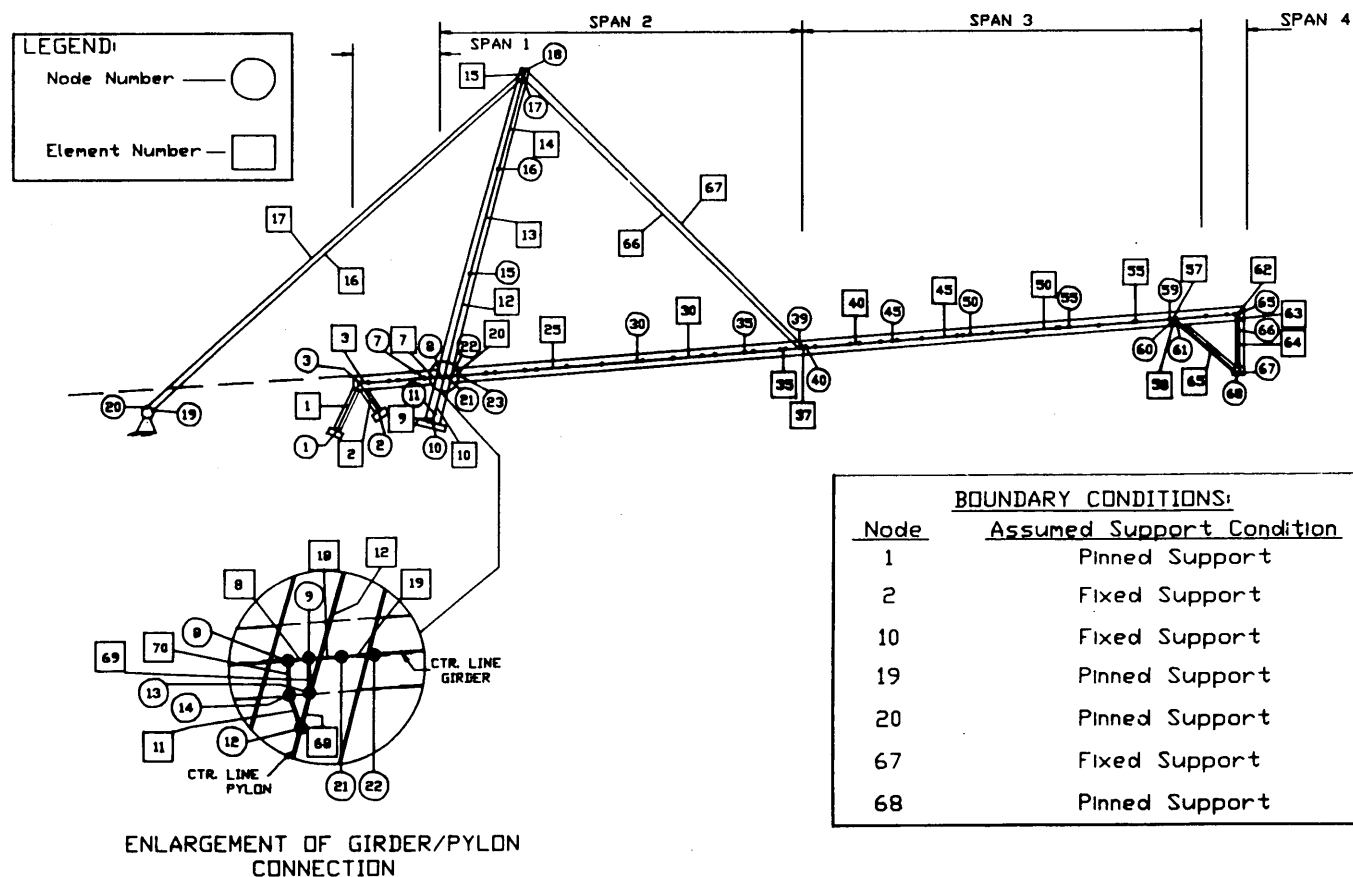

FIGURE 4   Final finite element model.

anchored with prestressed rock anchors, and the base of the strut is not. At the downstation end bent, one is anchored with a prestressed rock anchor and the other is not. Different boundary conditions assumptions were examined by analysis and compared with experimental data. The studies showed that rock anchors act fixed, other supports pinned, and behavior is sensitive to boundary condition assumptions.

Final Model

Except for 2 d.o.f. axial elements used to approximate cables, all members were approximated with 6 d.o.f. beam elements. Nodes were placed at changes in section, floor beam-to-girder connections, locations of strain gauges, pylon intersection, forestay cable connections, and column and strut connections. The final model had 68 nodes, 64 beam type elements, and 4 axial elements (Figure 4).

Strains

Strains at the extreme inside face of the girders, exterior face of the pylon bases (above the stiffeners), and the exterior face of the upstation left column were monitored during testing (Figure 3a). In this paper, results of 9 snooper truck tests and 12 ore truck tests are presented for a truck at positions 4, 9, and 14 for left lane, bridge centerline, and right lane (Table 1). For comparative purposes, the snooper truck weighed 176.85 kN (39.74 kips) and the four ore trucks weighed 690.06, 699.06, 700.34, and 700.3 kN (155.07, 157.093, 157.379, and 157.379 kips).

Figures 5 and 6 show a comparison between measured and calculated girder strains for three truck positions when a 700.3-kN (157.379-kip) B-train is parked in the left lane. The results show that calculated strains overpredict strains for the left girder and underpredict the right girder. Figure 7 shows that except for a change of section near the strut (84.8m), calcu-
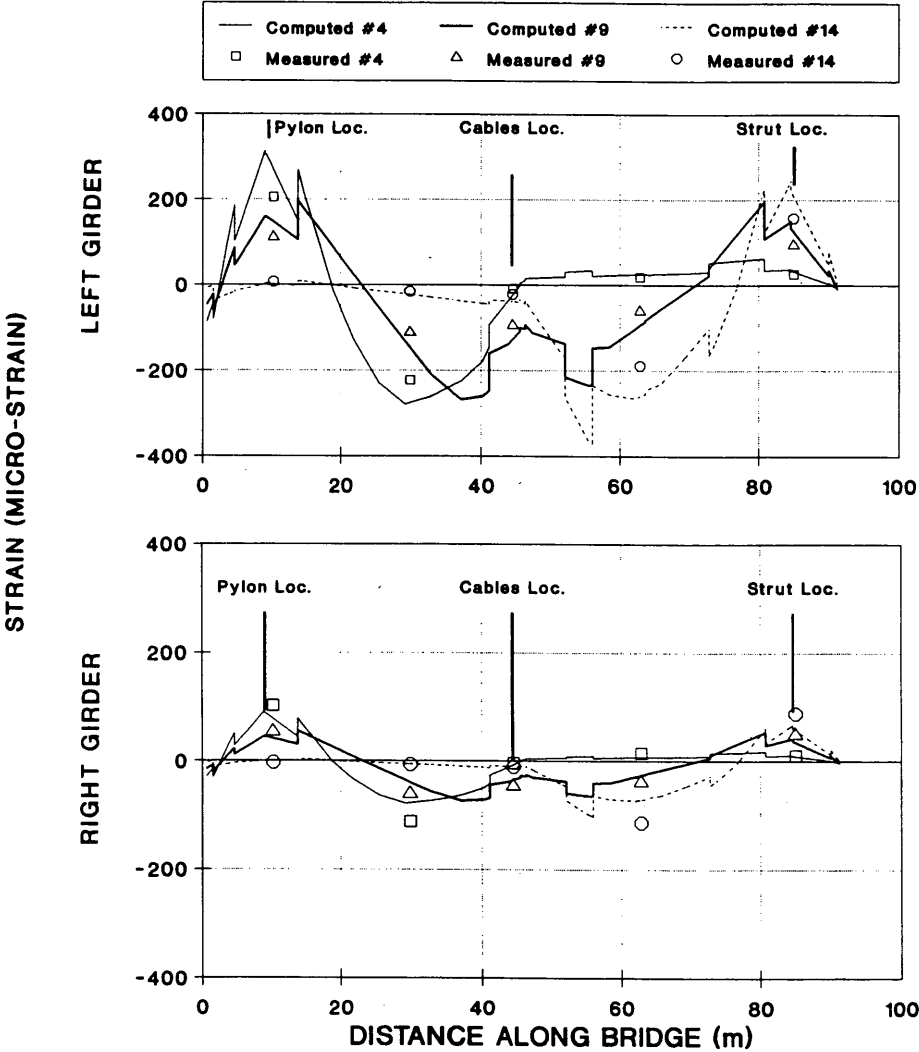

FIGURE 5   Top of girder strains, 700.3-kN (157.379-kip) B-train in left lane.
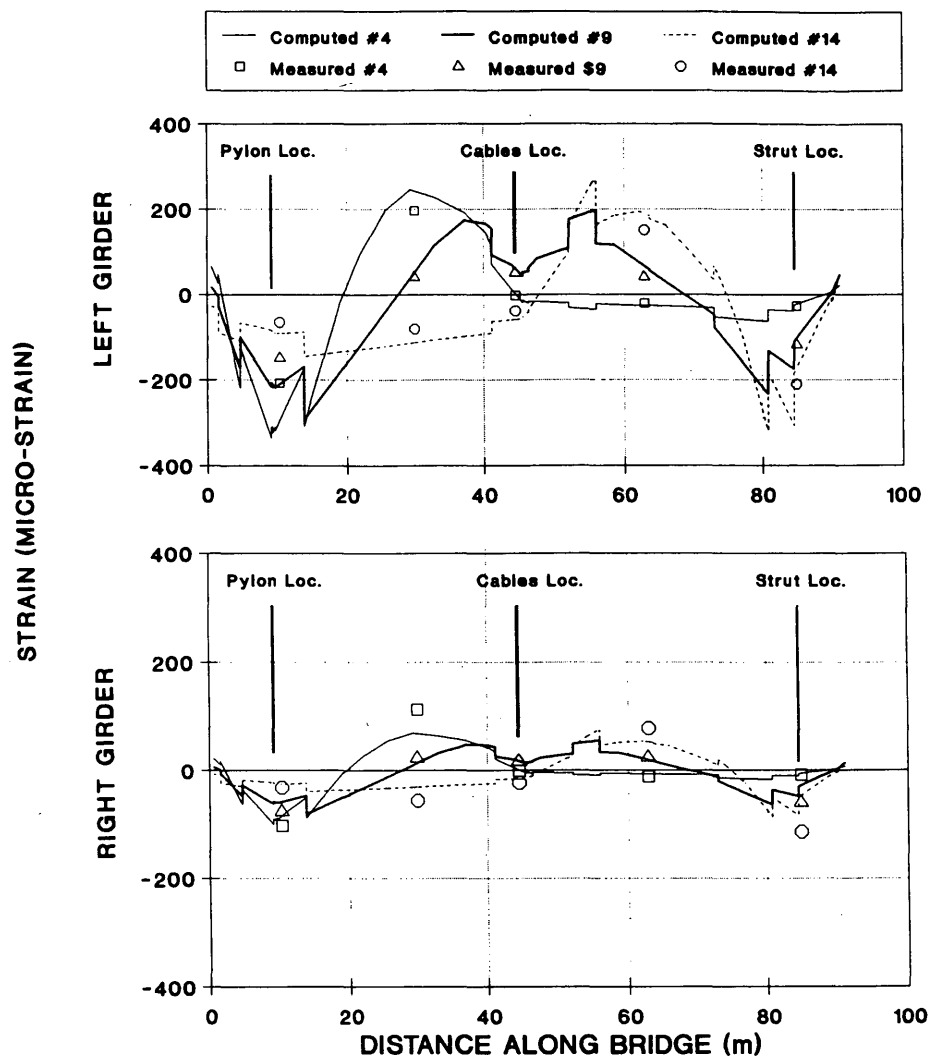
FIGURE 6   Bottom of girder strains, 700.3-kN (157.379-kip) B-train in left lane.

lated and experimental strains compare well when a 701.1-kN (157.556-kip) B-train is parked at three positions on the bridge centerline. Figure 8 shows that the calculated top of girder strains overpredict experimental strains on the loaded side and underpredict on the unloaded side when a 699.1-kN (157.093-kip) B-train is parked in the right lane. Similar results were found for the bottom of the girder.

Table 2 presents a comparison between measured and calculated girder strains for the three B-train static tests. The results show that the maximum measured girder strain is 224 microstrain and the corresponding calculated value is 276 microstrain.

Table 3 gives maximum measured strains in girders, pylon, and upstation columns for the three B-trains. Except for a condition when the truck was on the bridge centerline, calculated maximum strains typically overpredicted the maximum experimental strains.

For comparison, a summary of 9 snooper truck tests and 12 ore trucks at the three load positions is presented in Table 4.

Girder Deflections

Fog and wind precluded accurate deflection data for most of the snooper truck tests. However, the maximum measured snooper truck girder deflection for load positions 4, 9, and 14 was 1.96 cm (0.77 in.). The maximum girder deflection for the B-train tests occurred in position 9, with a truck in the left lane giving 7.0 cm (2.76 in.) measured and 8.6 cm (3.4 in.) calculated. The maximum girder deflection for a B-train on the bridge centerline was 5.49 cm (2.16 in.) measured and 5.54 cm (2.18 in.) calculated. Figures 9 and 10 present calculated and experimental deflections for B-train loads. The deflections show that the analysis overpredicts the loaded side
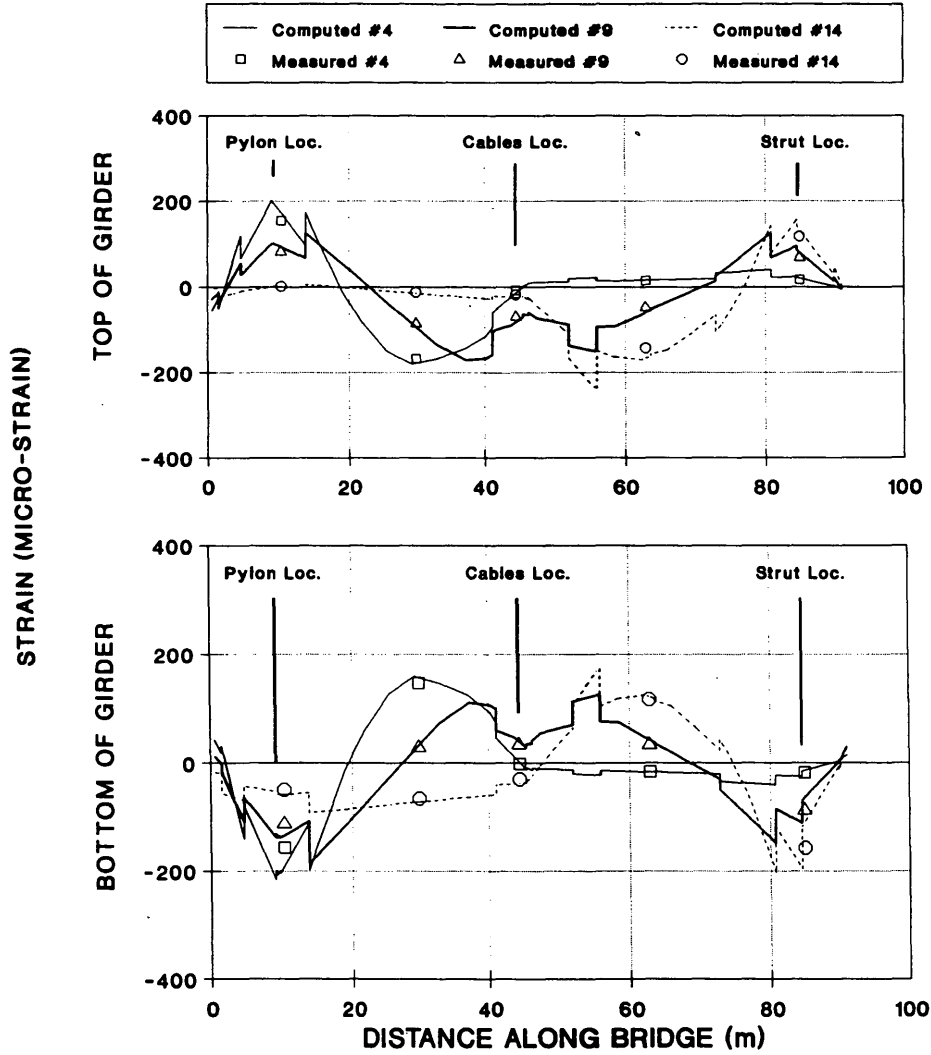
FIGURE 7   Girder strains for 701.1-kN (157.556-kip) B-train on centerline.

for asymmetric loading and gives accurate results for symmetric loading.

FRACTURE CRITICAL INSPECTION

An inspection of the cable-stay assemblies was conducted in September 1990 (Arvid Grant and Associates, unpublished data) using ultrasonic, magnetic particle, and X-ray nondestructive testing. Cables, zinc-poured cable anchorage sockets, and cable anchorage connections were inspected. Cables, spanner nuts, and connectors were in good condition. An X-ray of the anchorage sockets revealed cracks in the zinc and voids between the zinc, cable wires, and steel socket.

In June and July 1991, visual and magnetic particle inspections were performed on the upper pylon and strand connection plate welds, box girder cover plates, box girder internal longitudinal stiffeners, and floor beam connections (Mayes Testing Engineers, unpublished data). Fifty percent of the cover plate ends (14) showed signs of cracks (Figure 11). Most of the cracks were in the ASTM A588 girder flanges

adjacent to the fillet weld toe, in or near the zone affected by the weld heat. Approximately 80 weld terminations were examined inside a box at the longitudinal stiffeners, with no cracks found. Cracks were visually evident at the top of the floor beam webs at the termination of the web flange weld in 31 of 60 locations and 1 bottom location. The largest cracks in the beam webs exceeded 2.54 cm (1 in.). The floor beam webs were not coped. Other items found included three deep gouges in the flange of one box girder and improper welding techniques.

In June 1992, fracture critical inspections were again conducted to assess crack growth. Ten of 18 previously cracked locations showed some crack growth.

SUMMARY AND CONCLUSIONS

Experimental results indicated that wheel loads on the loaded ore trucks did not vary significantly and, like loading produced excellent repeatability. Comparisons between analytical and
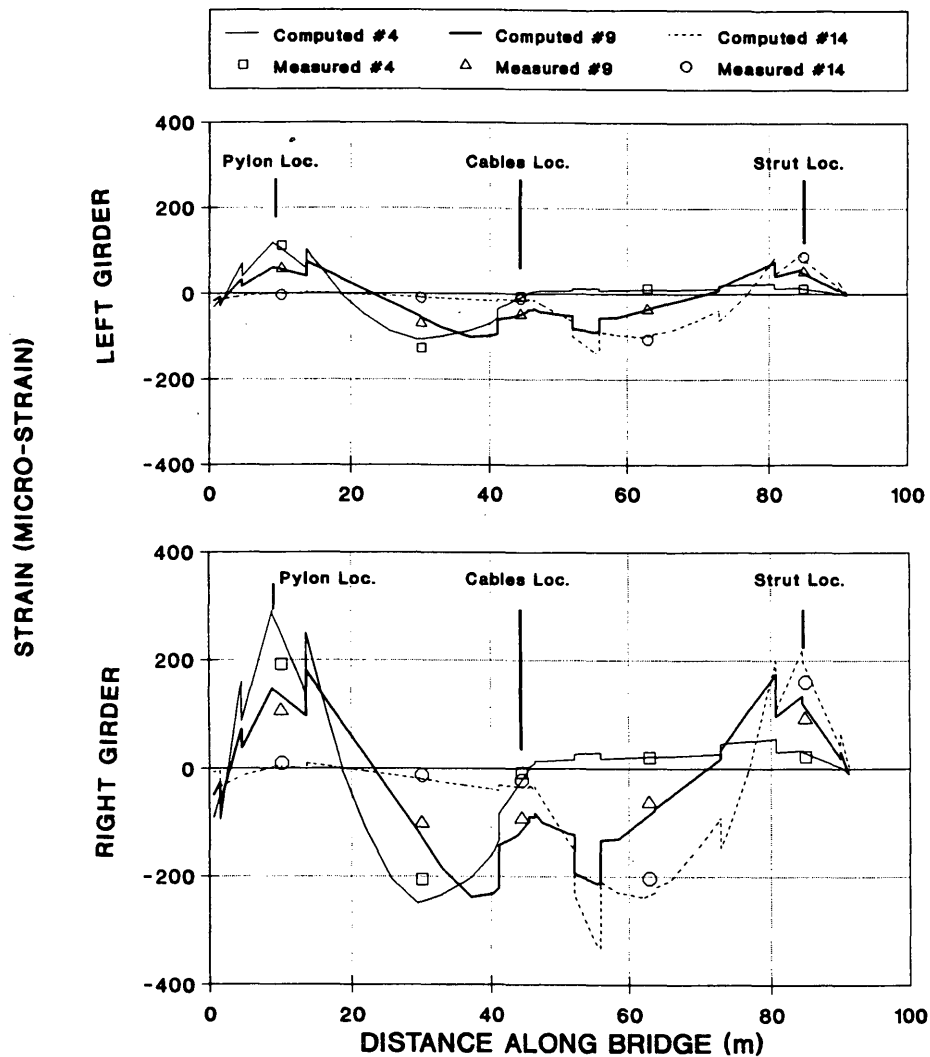
FIGURE 8 Top of girder strains, 699.1-kN (157.093-kip) B-train in right lane.

experimental results showed that

• Behavior is sensitive to interaction between the curved steel plate and neoprene bearing pad at the girder pylon interface (i.e., results were influenced by deformation of the neoprene);
• Boundary condition assumptions significantly influenced load distribution; and
• Supports with prestressed rock anchors act fixed and other supports act pinned.

A 2-D linear elastic model was satisfactory for symmetrically applied loads. For asymmetrical loads, the 2-D model overpredicts the load side and underpredicts the unloaded side of the structure. A 2-D model (conventional frame programs) will give conservative answers for this geometric configuration as long as special attention is given to the support conditions.

Floor beams were connected to the box girders with shear connections. At this connection, the web-to-flange of the floor

beam was not properly coped and visible cracks existed at the top of the web in more than 50 percent of the floor beams. In 1987 cover plates were added to the flanges of the ASTM A588 box girders to accommodate 712 kN ore truck loads. In 1991 and 1992 about 50 percent (14 locations) of the flanges in this fracture critical structure showed evidence of cracks at the weld terminations at the end of the cover plates. Generally, the cracks varied between 0.16 to 3.12 cm and were approximately 0.16 cm deep.

Calculated maximum stresses using a 2-D model were conservative. However, because of cracks and a need to strengthen the structure for heavier loads and more traffic, this structure should be tuned for asymmetric loads by a 3-D model with provisions for geometric nonlinear stiffness of existing or additional cables. It is important that the material condition of fracture critical structures be considered when modifications are made. Visible cracks are difficult to identify in ASTM A588 steel, and nondestructive testing should be used at critical locations.

TABLE 2 Strain Extremes for Symmetric and Asymmetric B-Train Loads

Gauge Loc. (m) a)	Top of Girder (microstrain)								Bottom of Girder (microstrain)							
	Left Girder				Right Girder				Left Girder				Right Girder			
	Max. Tens.		Max. Comp.		Max. Tens.		Max. Comp.		Max. Tens.		Max. Comp.		Max. Tens.		Max. Comp.	
	Exp	Calc	Exp	Calc	Exp	Calc	Exp	Calc	Exp	Calc	Exp	Calc	Exp	Calc	Exp	Calc
Symmetric																
10.1	153	175	---	---	152	178	---	---	---	---	157	191	---	---	158	193
29.9	---	---	169	178	---	---	164	176	146	157	67	72	163	156	74	72
44.5	---	---	69	82	---	---	72	82	34	40	31	38	33	41	31	47
62.8	14	16	144	167	15	16	165	168	116	122	17	17	111	124	15	15
84.8	117	134	---	---	127	135	---	---	---	---	158	111	---	---	171	111
Max diff.b	-22		-23		-26		-12		-11		47		-13		60	
Asymmetric																
10.1	204	272	4	---	191	249	4	---	---	---	208	297	---	---	197	271
29.9	---	---	224	276	---	---	207	216	196	243	81	112	205	219	85	100
44.5	---	---	94	128	---	---	93	115	51	62	38	59	47	56	35	52
62.8	17	25	189	260	20	22	204	234	150	190	22	26	138	173	18	22
84.8	157	210	---	---	160	189	---	---	---	---	211	174	---	---	215	155
Max diff.b	-68		-7		-58		-30		-47		-89		-35		-74	

a) 1 m = 3.2787 ft
b) Maximum strain difference = (Measured - Computed)

TABLE 3 Maximum Strains Produced by B-Trains

Load Condition	Truck wt (kN)	Type of Member	Strain (micro-strain)			
			Tension		Compression	
			Exper.	Calc.	Exper.	Calc
A) MAXIMUM B-TRAIN LOAD CONDITIONS						
Symmetrical	699.1-701.1	Along the girders	163	156	171	111
		Pylon base	40	50	99	124
		Upstation column (left side)	22	15	---	
Asymmetrical	699.1-701.1	Along the girders	205	219	224	276
		Pylon base	54	78	134	193
		Upstation column (left side)	26	23	---	
B) B-TRAIN LOAD LOCATION (LANE POSITION)						
Left lane	700.3	Girder (10.1m,29.9m)	204	272	224	276
		Pylon base (left)	54	78	134	193
		Left column	25	23	---	---
Centerline	701.1	Girder (10.1m,84.8m)	163	156	171	111
		Pylon base (left)	40	50	99	124
		Left column	22	15	---	---
Right lane	699.1	Girder (29.9m,29.9m)	205	219	207	246
		Pylon base (right)	26	42	103	143
		Left column	17	9	---	---

1 kN = 0.2247 kips;   1 m = 3.2787 ft

TABLE 4 Bridge Maximum Measured Strains and Stresses

Item	Location	Experimental		Calculated	
		Strain (microstrain)	Stress[b] (kPa)	Strain (microstrain)	Stress[b] (kPa)
Snooper truck					
Left girder	10.1 m[a]	58	11,589	71	14,186
Right girder	10.1 m[a]	53	10,590	72	14,386
Left column	upstation	8	1,598	2	400
Left pylon	base	39	7,792	49	9,791
Right pylon	base	30	5,994	25	4,995
B-train					
Left girder	29.9 m[a]	224	44,757	276	55,148
Right girder	29.9 m[a]	207	41,361	246	49,153
Left column	upstation	26	5,195	23	4,596
Left pylon	base	134	26,774	193	38,563
Right pylon	base	103	20,580	143	28,573

[a]Distances are along bridge incline from downstation end; 1 m = 3.279 ft.
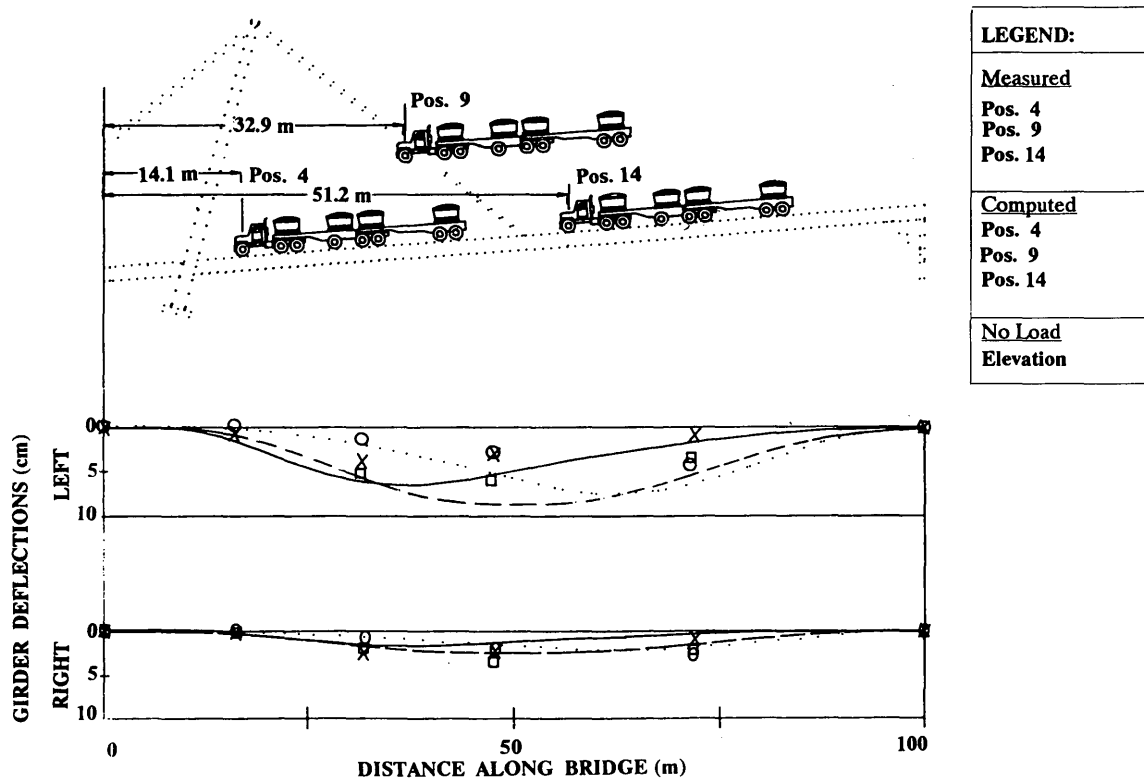[b]Stress is calculated from $\sigma = E\varepsilon$; 1 kPa = 0.1451 psi.

FIGURE 9   Girder deflections, 700.3-kN (157.379-kip) B-train in left lane.
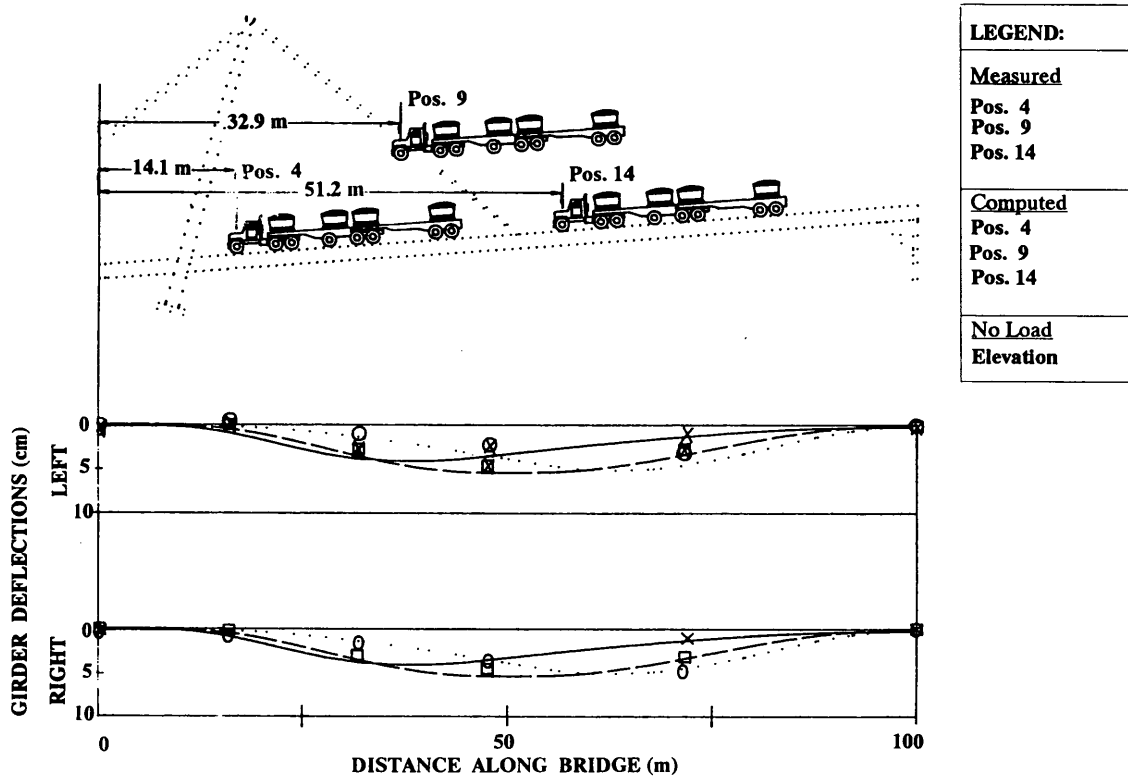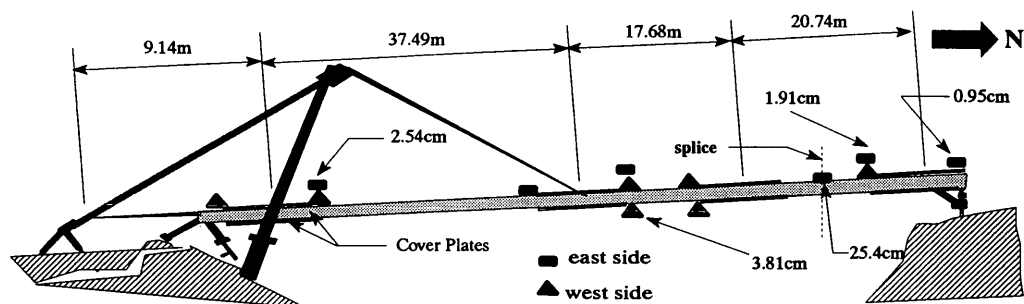
LEGEND:

Measured
Pos. 4
Pos. 9
Pos. 14

Computed
Pos. 4
Pos. 9
Pos. 14

No Load
Elevation

32.9 m

14.1 m Pos. 4

51.2 m

Pos. 9

Pos. 14

GIRDER DEFLECTIONS (cm)

LEFT

0
5
10

RIGHT

0
5
10

DISTANCE ALONG BRIDGE (m)

0   50   100

FIGURE 10   Girder deflections, 699.1-kN (157.093-kip) B-train on centerline.

9.14m   37.49m   17.68m   20.74m

N

1.91cm   0.95cm

2.54cm

splice

Cover Plates

■ east side
▲ west side

3.81cm

25.4cm

Note: All other cracks are 0.32cm to 0.64cm long

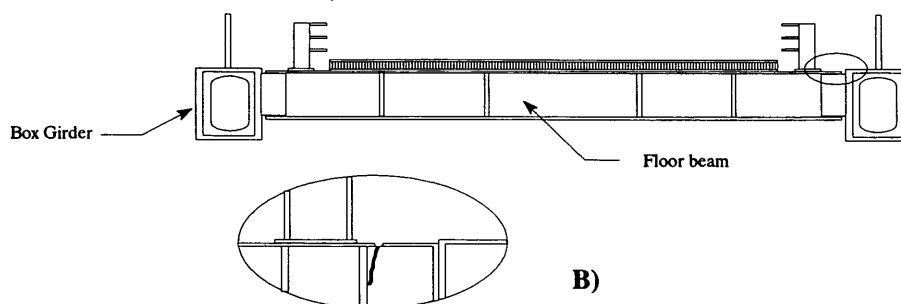**A)**

Box Girder

Floor beam

B)

FIGURE 11   Bridge cracks from fracture critical inspections: *top*, crack length at cover plates; *bottom*, cracks at connection.

ACKNOWLEDGMENTS

REFERENCES

1. T. H. Kayser and J. Binkorst. *Computer Calculations of a Complex Steel Bridge Verified by Model Investigations (Applied at the Steel Bridge Spanning the River Waal Near Ewijk).* Ministry of Transport, Netherlands, Rijkswaterstaat, The Hague, 1975.
2. M. Koizumi, A. Senpaku, H. Araki, Y. Kosugi, R. Yonehara, and S. Kawanobe. *Construction of Mieko-Hishi Bridge.* Technical Report Overseas 45. Nippon Kokan, Dec. 1985, pp. 2–12.
3. M. S. Troitsky and B. E. Lazar. Model Analysis and Design of Cable-Stayed Bridges. *Proc., Institute of Civil Engineers*, Vol. 48, London, England, March 1971, pp. 439–464.
4. S. Ohleson. *Dynamic Properties of the Tjorn Bridge Experimental Program.* Report 81:3. Chalmers University of Technology, Sweden Institute of Transportation, Onsternik, Staal-och Trae-bvbggnad. Nov. 1981.
5. J. L. Hulsey, D. K. Delaney, and R. W. Briggs. *Cable-Stayed Static Tests—An Experimental Study for the Captain William Moore Creek Bridge.* FHWA Final Report AK-RD-90-08. Alaska Department of Transportation, Fairbanks, 1989.
6. J. L. Hulsey and D. K. Delaney. *Cable-Stayed Static Linear Analysis for the Captain William Moore Creek Bridge.* FHWA Final Report AK-RRD-90-08A. Alaska Department of Transportation, Fairbanks, 1989.
7. J. L. Hulsey, D. K. Delaney, R. B. Bunch, and R. W. Briggs. *Proc., Eight Structures Congress*, ASCE, Baltimore, Md., 1990.
8. M. S. Troitsky. *Cable-Stayed Bridges; An Approach to Modern Bridge Design.* Van Nostrand Reinhold Company, New York, N.Y., 1988.
9. B. E. Lazar. Stiffness Analysis of Cable-Stayed Bridges. *Journal of the Structural Division*, ASCE, Vol. 98, No. ST7, 1972, pp. 1605–1612.
10. A. M. C. Tang. Analysis of Cable-Stayed Bridges. *Journal of the Structural Division*, ASCE, Vol. 97, No. ST5, 1971, pp. 1481–1485.
11. M. Como, A. Grimaldi, and F. Maceri. Static Behavior of Long-Span Cable-Stayed Bridges. *International Journal Solids and Structures*, Vol. 21, No. 8, 1985, pp. 831–850.
12. Y. C. Loo and S. Srivanich. A Simplified Analysis of Cable-Stayed Box Bridges. *International Journal of Structures*, Vol. 3, Paper 35, 1983, pp. 93–103.
13. C. Crawford and P. Loris. Brooklyn Bridge Computer Model. *Proc., 3rd Conference on Computing in Civil Engineering*, ASCE, New York, N.Y., 1984, pp. 540–549.
14. H. Naki, T. Kitada, R. Ohminami, and T. Nishimura. Elasto-Plastic and Finite Displacement Analysis of Cable-Stayed Bridges. In *Memoirs of the Faculty of Engineering*, Vol. 26, Osaka City University, Japan, 1985, pp. 251–271.
15. H. Gimsing. Multi-Span Cable-Stayed Girder Bridges. *Journal of the Structural Division*, ASCE, Vol. 102, No. ST10, 1976, pp. 1989–2003.

Structural Identification of a Steel Stringer Bridge

A. Emin Aktan, Chuan Chuntavan, Kuo-Liang Lee, and Tolgay Toksoy

The concept of structural identification may help improve an understanding of the actual load-carrying mechanisms of bridges by integrating experimentation with analysis. A process of comprehensive structural identification incorporating dynamic and static tests for a 3-D finite element modeling of a three-span steel stringer bridge with continuous integral abutment is described. Researchers were able to conceptualize, then instrument and reliably measure, a number of critical local response mechanisms. These mechanisms were then incorporated in the analytical model, with resulting excellent correlation with the experiment. Bridge-rating factors, obtained by idealized models, increased by several times when the identified analytical model was used for rating. Field experimentation in the context of structural identification research greatly enhanced the reliability of the experiments and increased the benefit-to-cost ratio of the research.

A recent National Science Foundation study (*1*) defined three critical emerging research and application areas as "condition assessment technologies," "deterioration science," and "renewal engineering." The consensus is that "condition assessment" is the most important prerequisite for effective preservation (*2*).

The concept of structural identification (*3*) may hold the key for "carrying out meaningful large-scale assessments of the state of health of constructed facilities," which is identified by the National Science Foundation as a major problem in infrastructure preservation (*1*). In the last decade identification has been used as a component of structural control applications or as a tool to characterize buildings, bridges, and towers for conceptualizing their behavior; to test design assumptions; to establish effects of a loading environment; or to detect damage (*4,5*).

Inspired by the potential of the concept of structural identification, the authors have been conducting research in an effort to improve the state of the art for its implementation. Here they discuss steel stringer bridge behavior and demonstrate the potential of structural identification as a rational approach for condition assessment, damage diagnosis, and prediction of remaining capacities and service life.

OBJECTIVES AND SCOPE

The first objective is to identify local and global behavior mechanisms of continuous steel stringer bridges with integral abutments. These included modal tests by impact and vertical

University of Cincinnati Infrastructure Institute, Cincinnati, Ohio 45221-0071.

and lateral forced excitation, which were followed by truck-load tests for measuring global and local responses of the bridge under different static loading patterns by 60 transducers. The results of these experiments helped improve an understanding of some obscure local response mechanisms that significantly influenced bridge behavior at the service limit states.

The second objective is to present and discuss the rating coefficients of the test bridge on the basis of analyses of the experimentally identified 3-D finite element (FE) model. Significant discrepancies were observed when the corresponding rating coefficients were obtained based on analysis of idealized models recommended by the AASHTO *Guide* specifications. These discrepancies are discussed and the reasons for their existence are summarized.

STRUCTURAL IDENTIFICATION OF A STEEL STRINGER BRIDGE

The Westbound Cross-County Highway Bridge (Figure 1) in Cincinnati was selected as a test specimen because it represents a large population of bridges in Ohio. The noncomposite steel stringer bridge has two lanes, three spans (16.76 m, 23.77 m, and 16.76 m), and continuous, integral abutments. It was constructed in 1990 in accordance with the 1983 AASHTO specifications for two-lane HS 20-44 loading. It is skewed by 15 degrees 11 ft 16 in. The superstructure is composed of six 91.4-cm (36-in.) W-flange girders of ASTM A-36 steel, resting on elastomeric pads over the main piers and supporting a reinforced concrete (RC) slab 21.6 cm (8.5 in.) thick. At the abutments, the girders and deck slab are integrated together by a cast-in-place RC head-beam that rests on the abutment with a 2.54-cm (1-in.) preformed expansion joint filler. The abutment further functions as lateral brackets at each end.

3-D Analytical Modeling and Analytical Studies

An a priori 3-D FE model (Figure 2) of the bridge was constructed based on the nominal geometric and material properties presented in Table 1. Every effort was made to conceptualize and analytically simulate the 3-D geometry as well as the boundary, interelement, and span-continuity conditions of the bridge.

PC-based SAP90 (*6*) was selected as the software for structural analyses. The shell elements were used to model the
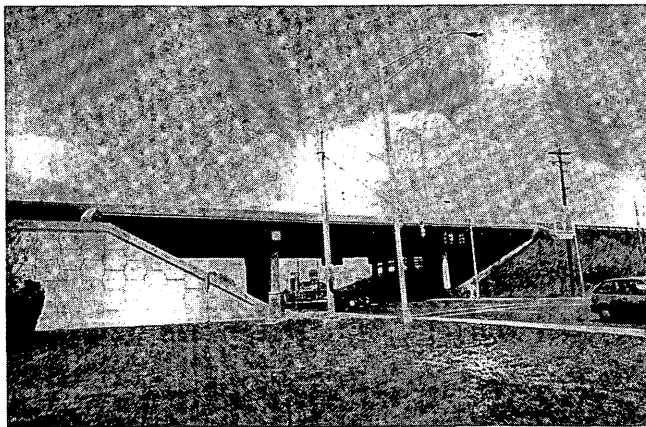
FIGURE 1 Test bridge.

deck; frame elements were used to model the girders, transverse diaphragms, pile caps, piles, and side barriers; and stiff frame elements were used to connect the elements together, preserving the local 3-D geometric attributes while ensuring interelement compatibility.

A sensitivity study of the a priori model was carried out for two reasons: to identify important response mechanisms with the associated model parameters and their possible ranges and to refine the a priori model. This sensitivity study revealed that the level of composite action between the girders and the deck, the manner of simulating the boundary conditions at the abutment, and the girder-pier continuity conditions at the piers were critical mechanisms.

An eigenvalue analysis of the a priori model was carried out to predict frequencies, mode shapes, and modal density. The results served as a guide for discretizing the bridge for
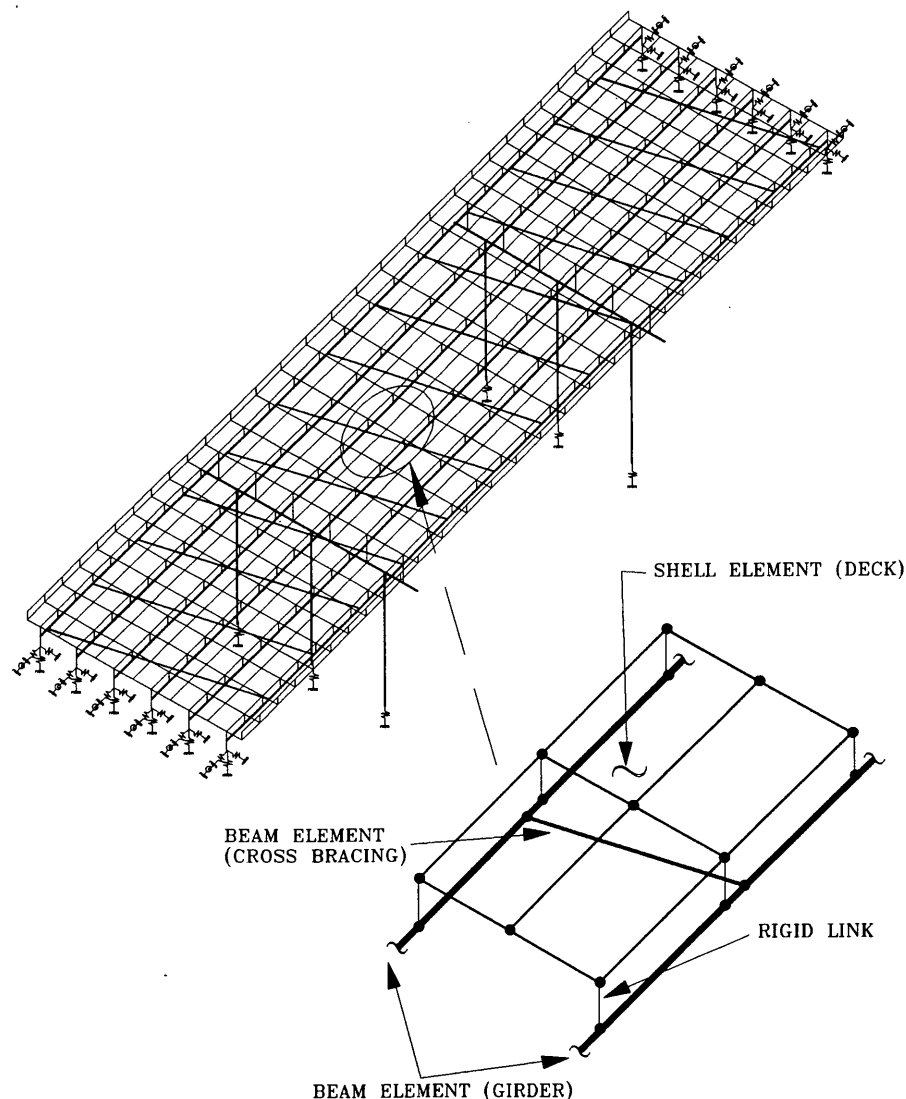

FIGURE 2 A priori finite element model of the test bridge: global attributes.

TABLE 1 Nominal Versus Calibrated Parameters of A Priori Model 1 and Model 2

Parameter	Nominal Value	Model 1 Calibrated Value	Model 2 Calibrated Value
MATERIAL PROPERTIES			
- CONCRETE: Modulus of Elasticity, E (MPa)	28042	Nominal	Nominal
: Shear Modulus, G (MPa)	10784	"	11700
- STEEL : Modulus of Elasticity, E (MPa)	200000	"	"
: Shear Modulus, G (MPa)	76907	"	"
SUPPORTING SPRINGS:			
- ABUTMENTS:			
: X-dir. translational spring (kN/cm)	Fixed	1.75E7	Fixed
: Y-dir. translational spring (kN/cm)	Fixed	1.75E7	Fixed
: Z-dir. translational spring (kN/cm)	Fixed	1.75E5	1.75E5
: Y-dir. rotational spring (kN-cm/rad)	Free	11.3E3	11.3E9
: Y-dir. rotational spring at the end of girder	Fixed	-	11.3E2
- PIER BASES:			
: Z-dir. translational spring (kN/cm)	Fixed	1.75E5	1.75E5
CROSS SECTIONAL PROPERTIES OF ELEMENTS			
- DECK SLAB (SHELL ELEMENT):			
: thickness (cm)	21.59	Nominal	Nominal
: mass density (kg/cu cm)	6.2183E-6	"	"
- STEEL GIRDER (BEAM ELEMENT):			
END SPANS (W36x150)			
: area (sq cm)	285	Nominal	Nominal
: moment of inertias (cm^4)			
(about major and minor axes)	376273 ; 11238	"	"
: torsional inertia (cm^4)	420	"	"
: mass / unit length (kg/cm)	5.7771E-5	"	"
MID SPAN (W36x170)			
: area (sq cm)	323	Nominal	Nominal
: moment of inertias (cm^4)	437043 ; 13319	"	"
: torsional inertia (cm^4)	629	"	"
: mass / unit length (kg/cm)	6.5473E-5	"	"
- BEARING PAD ELEMENT:			
: axial stiffness, AE/L, (kN/cm)	7215	11.68E4	5.83E4
- PILE CAP BEAM ELEMENT:			
: area (sq cm)	11239	Nominal	Nominal
: moment of inertias (cm^4)	14135760; 7828564	"	"
: torsional inertia (cm^4)	16632982	"	"
: mass / unit length (kg/cm)	6.9873E-4	"	"
- PILE COLUMN ELEMENT:			
: area (sq cm)	6568	Nominal	Nominal
: moment of inertias (cm^4)	3431745;3431745	"	"
: torsional inertia (cm^4)	6863490	"	"
: mass / unit length (kg/cm)	4.0836E-4	"	"

1 cm. = 0.3937 in.; 1 MPa. = 6.895 ksi.; 1 kN. = 4.448 kip force; 1 kg/cm = 1.7858 kip/in.

the modal tests, selecting the frequency band of interest, and locating the reference stations for optimum data acquisition during field testing.

Modal Tests

The bridge was subjected to two separate modal tests to measure the dynamic characteristics in both the vertical and horizontal directions: the modal test by vertical impact and the modal test by horizontal forced vibration.

Procedures for reliable vertical impact testing of bridges have been reported by Raghavendrachar and Aktan (7). The study reported here is the first-time application of multireference impact testing to a steel stringer bridge.

The modal test by horizontal forced vibration was conducted to capture the lateral response characteristics of the

bridge. The forced vibration testing was performed in the horizontal direction transverse to the traffic direction. The excitations were produced by a linear inertia-mass exciter that was integrated with multichannel signal-processing software and hardware as described by Somaprasad et al. (8).

Some of the bridge's natural frequencies, damping factors, and mode shapes obtained from the impact and forced-vibration tests are summarized in Figure 3.

Modal Flexibility As Bridge Signature

Many researchers have recognized that the frequencies, damping coefficients, and mode shapes of bridges do not serve as reliable condition indices. The authors have made similar observations. For example, the maximum change in the measured 20 frequencies of a slab bridge, after it yielded under
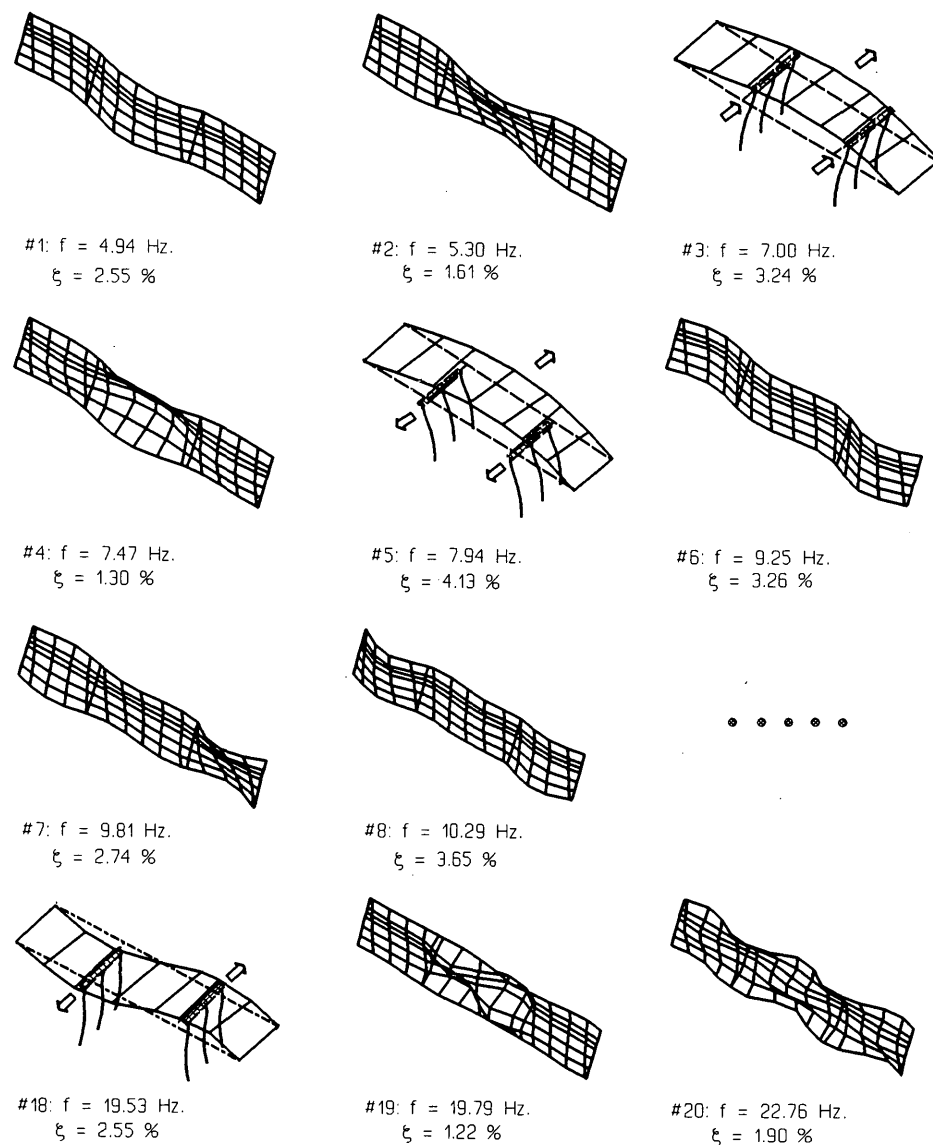
#1: f = 4.94 Hz.
ξ = 2.55 %

#2: f = 5.30 Hz.
ξ = 1.61 %

#3: f = 7.00 Hz.
ξ = 3.24 %

#4: f = 7.47 Hz.
ξ = 1.30 %

#5: f = 7.94 Hz.
ξ = 4.13 %

#6: f = 9.25 Hz.
ξ = 3.26 %

#7: f = 9.81 Hz.
ξ = 2.74 %

#8: f = 10.29 Hz.
ξ = 3.65 %

#18: f = 19.53 Hz.
ξ = 2.55 %

#19: f = 19.79 Hz.
ξ = 1.22 %

#20: f = 22.76 Hz.
ξ = 1.90 %

FIGURE 3 Mode shapes, frequencies, and damping ratios obtained from impact and horizontal forced-vibration tests.

a single-lane loading equivalent to 20 HS 20-44 trucks, was less than 5 percent (*9*). No appreciable changes were discerned in the mode shapes, whereas the changes measured in the damping coefficients were of the same order because of postprocessing errors. Moreover, frequency shifts in some modes on the order of 5 percent may also occur because of changes in bridge characteristics resulting from ambient effects as well as the inherent linearization, experimentation, and postprocessing errors in field modal testing of large bridges (*7*).

The authors therefore caution against using modal characteristics as signature. On the other hand, if a sufficiently large number of frequencies and mass-normalized mode shapes of a bridge may be accurately experimentally measured (generally about 20 modes would be needed), these may be transformed directly into a close measure of the flexibility matrix of the structure, termed "modal flexibility" (*7*). It should be clearly noted that multireference modal testing and postpro-

cessing conducted with extremely stringent standards are required to accurately measure 20 mass-normalized modal vectors. Currently this may be accomplished only in the context of collaborative research between civil and mechanical structural engineers combining facility-specific experience with field modal testing of large constructed facilities.

Relative changes in the local flexibility coefficients of adjacent nodes were shown to correlate strongly to damage in redundant offshore platform towers (*10*). More recently, the authors demonstrated that modal flexibility may serve as a reliable condition index for slab bridges (*7,11*). In this research, the modal flexibility of the test bridge was used for model calibration; this is discussed in the following section.

Analytical Model Calibration

The measured dynamic characteristics, as well as the modal flexibility obtained from a transformation of unit-mass-normal

modal vectors, contain a wealth of information regarding the current state of the bridge. It is important to exploit rationally this ensemble of experimental results to quantify the analytical model parameters.

Because the number of independent parameters in the analytical model typically exceeds the number of experimentally measured characteristics even when a comprehensive modal test is conducted, no unique solution to the parameter identification and model calibration problem exists. On the other hand, a proper conceptualization of the bridge's behavior is possible by incorporating heuristic and rational procedures. The band of uncertainty in the numerical bounds of critical parameters may be considerably narrowed. Thus it may be possible to arrive at a sufficiently complete and reliable analytical model.

Calibration in the Modal Space

Analytical model parameters were adjusted until the correlation between analytical and measured frequencies and mode shapes improved while the sequencing of the measured modes was preserved. The calibrated a priori model is termed Model 1 from here on. Its analytical parameters are presented in Table 1. The frequency correlation between analysis and experiment are presented in Table 2. Improving the correlation

further, particularly without violating the modal sequence, proved difficult. This difficulty indicated that certain fundamental response mechanisms may not have been properly simulated in the analytical model.

Testing "Completeness" of the Analytical Model in the Flexibility Space

Uncertainties prevailed in spite of efforts to generate a complete representation of the bridge. Although it is not possible to identify a unique analytical model for the bridge, it is important to ensure "completeness." The model should correctly and completely incorporate the 3-D geometry, boundary, and continuity conditions and the existing conditions of all the bridge components so that the global and local flexibility distributions and the 3-D displacement kinematics are correctly simulated. This would ensure that all the critical response mechanisms and the load paths are accurately simulated.

One possible test of model completeness is conducted by correlating the analytical flexibility of the model (after calibrating in the modal space) with the experimental "modal flexibility." The 3-D deflection profiles (Figure 4) permit such a correlation because these profiles correspond with loading the measured modal flexibility and the analytical model of

TABLE 2   Comparison of Experimental Frequencies with Analytical Counterparts

MODE NO.	A-PRIORI ANALYTICAL MODEL 1 (Hz)[a]	CALIBRATED ANALYTICAL MODEL 2 (Hz)[a]	EXPERIMENTALLY IDENTIFIED			
			IMPACT TEST		FORCED-VIBRATION	
			FREQ (Hz)	ζ (%)	FREQ (Hz)	ζ (%)
1	5.28	4.901	4.94	2.55	-	-
2	5.93	5.385	5.30	1.61	-	-
3	8.94[b]	7.609[b]	-	-	7.00	3.24
4	9.64	7.298	7.47	1.30	-	-
5	-	-	-	-	7.94	4.13
6	10.34	8.777	9.25	3.26	-	-
7	11.25	9.631	9.81	2.74	9.67[c]	2.45
8	11.30	9.831	10.29	3.65	-	-
9	11.99	10.374	10.58	3.10	10.84[c]	2.86
10	14.98	11.219	11.58	1.54	11.51[c]	3.40
11	15.47	11.429	12.01	1.53	-	-
12	16.03	12.597	13.34	1.05	-	-
13	15.89	14.211	14.56	2.16	-	-
14	16.18	14.268	14.90	2.21	-	-
15	18.24	15.341	15.71	1.47	-	-
16	20.50	15.612	16.49	1.36	16.42[c]	3.28
17	20.41	15.966	17.02	1.08	-	-
18	17.62[b]	16.64[b]	-	-	19.53	2.55
19	22.20	18.505	19.79	1.22	-	-
20	22.96	21.916	22.76	1.90	-	-
21	23.91	22.063	23.59	1.20	-	-

[a]Each frequency listed so that corresponding mode shape matches experimental mode shape for given mode number
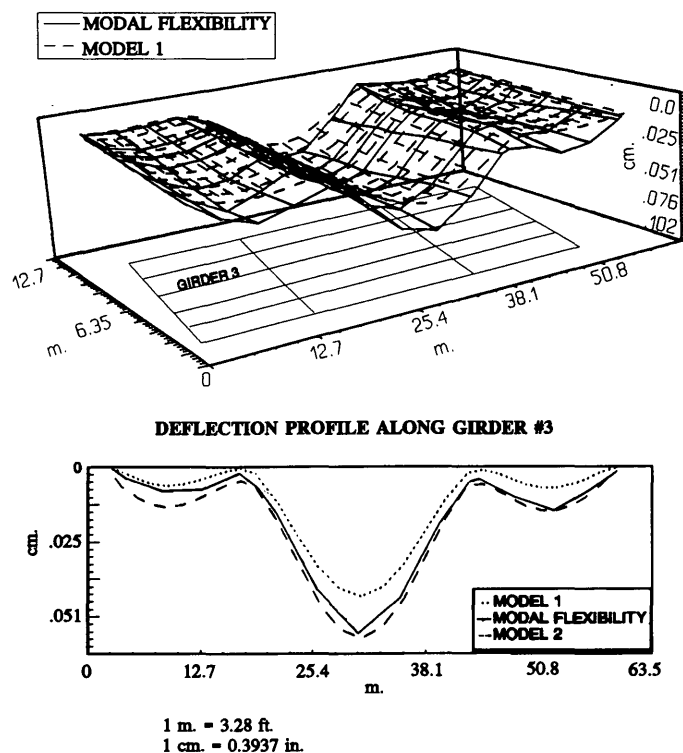[b]Analytical transverse bending mode.
[c]Coupled modes.

DEFLECTION PROFILE ALONG GIRDER #3

1 m. = 3.28 ft.
1 cm. = 0.3937 in.

FIGURE 4 Correlation of bridge deflections under uniform load given by modal flexibility, Models 1 and 2.
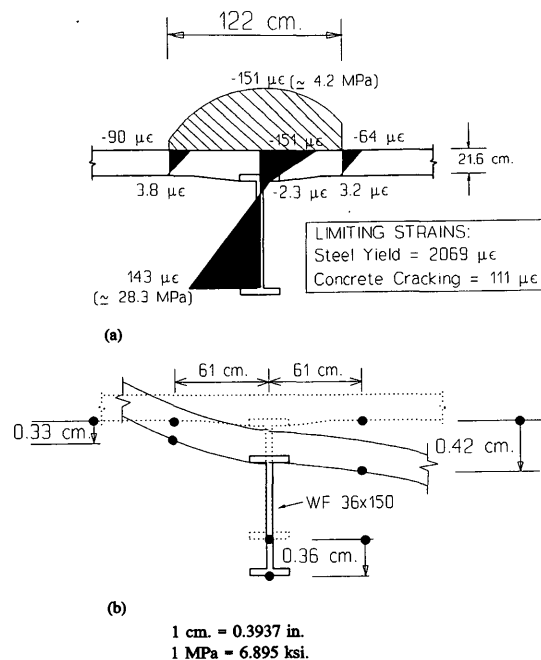

FIGURE 5 Strains and distortion of girder-slab under 4-222 kN (50 kip) trucks (Type 3 equivalent): (a) strain profile at midspan, Girder 3; (b) distortion of Girder 2 and deck at midspan.

the bridge by a uniformly distributed load. Normally deflections from the modal flexibility should be somewhat less because of modal truncation. However, the deflections given by the analytical flexibility are less than the deflections given by the modal flexibility (Figure 4), particularly with discrepancies at the piers and abutments. This indicated a lack of "completeness."

Additional Experiments for Completing the Model

Additional experiments were designed to better observe, conceptualize, instrument, and measure the critical response mechanisms of the bridge that are not adequately represented in the a priori model. The test bridge was loaded statically by positioning four trucks in various configurations. Each truck weighed approximately 222 kN (50 kips) and featured a tandem axle, making it equivalent to a Type 3 AASHTO vehicle. The bridge was extensively instrumented by 60 strain, distortion, and displacement transducers concentrated in one end span. Measured responses included closely spaced deflections along a girder and a lateral brace; the strain profile at a cross section at the midspan of a girder, including the RC deck; and displacements and rotations of a girder at the pier and at the abutment.

Figure 5 shows the strain profile at the middle of the end span when the bridge was loaded by all four trucks positioned back to back and side by side to maximize the positive moment demand of the girder at the instrumented cross section. The measured strains indicate a nearly fully composite action. The

maximum girder flange strain indicates an incremental stress of only 27.58 MPa (4 ksi). Attenuation in the compressive strains in concrete at the top of the deck indicates an effective flange width of about six times the deck thickness. The displacement kinematics of the deck [Figure 5(b)] further confirms the composite action.

Figure 6 indicates the vertical displacement and rotation of a girder at the pier as the end span was loaded by four trucks. Before the truck loading, the girder exhibited a counterclockwise rotation at the pad resulting from dead loads. Because of this rotation, one edge of the pad was observed to lift up while the opposite edge was firmly compressed against the pier-cap. Truck loading induced a rotation in the opposite sense while also resulting in a vertical distortion at the pad. The observed displacement kinematics resulting from the finite size of the pad were properly simulated by modifying the analytical model as shown in Figure 6.

The construction details at the integral abutment are shown in Figure 7. This region was instrumented to measure the torsional rotation of the RC head-beam, vertical displacement of the steel girder relative to the abutment, and flexural rotation of the steel girder relative to the RC head-beam. The latter relative rotation occurred although the steel girder was encased within the RC head-beam. This type of relative rotation occurs as a result of the slippage of a steel element at an interface. The corresponding displacement kinematics were represented by modifying the analytical model to incorporate the girder-RC beam interface rotation, vertical displacement of the steel girder relative to the abutment, and the torsional twist of the RC head-beam relative to the abutment.
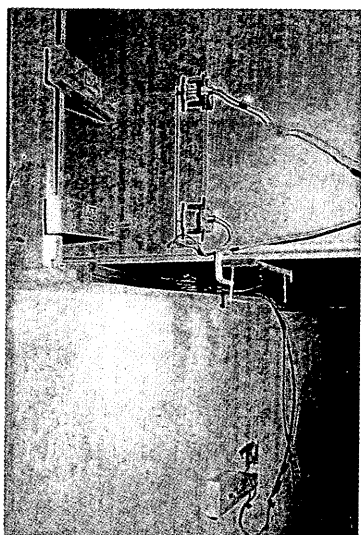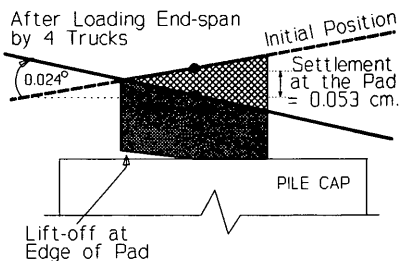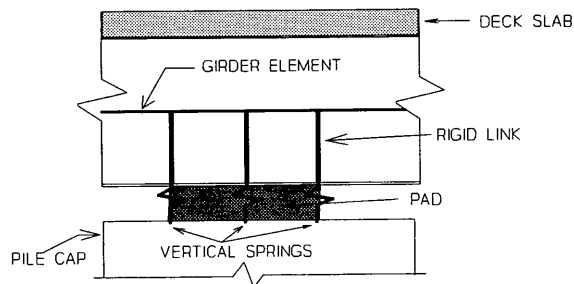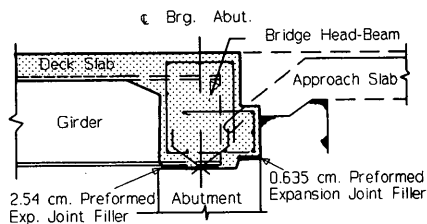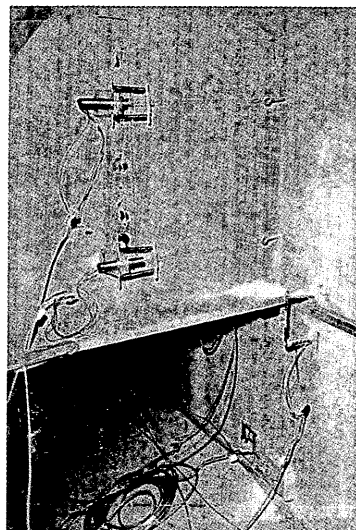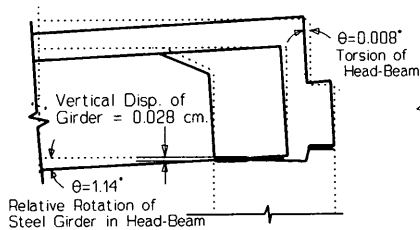
FIGURE 6 Displacement kinematics at the pier under truck loading: (*a*) instruments at pier, (*b*) measured responses, and (*c*) analytical simulation (Model 2).
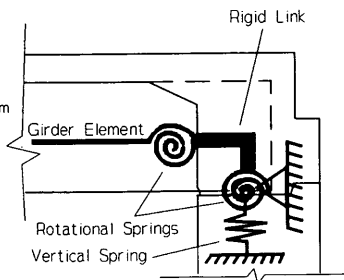

FIGURE 7 Displacement kinematics at the integral abutment.

Calibrating and Verifying the Completed Model

Following the second round of experiments, the analytical model was modified for completeness, and some of the parameters were adjusted to simulate closely the measured local responses. The calibrated parameter values of the completed model are presented in Table 1 in the fourth column, labeled "Model 2." Correlation between the experimental and analytically simulated frequencies may be observed in Table 2 by comparing the third column with the fourth and sixth columns. The agreement between the measured frequencies versus those simulated by Model 2 is less than 2 percent for the lower modes, whereas errors of 5 percent are observed for the higher modes.

Correlation between the simulated and measured bridge characteristics is more definitively confirmed in the flexibility space in Figure 4, which indicates that the 3-D displacement profile under uniform vertical loading of the bridge given by Model 2 is close to the profile given by the modal flexibility.

In fact, modal flexibility yields a slightly stiffer response as expected because of modal truncation.

Further verification of the fidelity of analytical Model 2 is shown in Figure 8, in which the simulated and measured vertical deflections of the bridge along a girder and a lateral brace at the end span under truck loading are compared. The responses labeled "truck" were measured directly when four loaded trucks were positioned on the bridge, as shown in Figure 8. The responses labeled "Model 1" and "Model 2" were simulated by analyzing the respective analytical models subjected to the same truck loads. The responses labeled "modal flexibility" are obtained by multiplying the experimental modal flexibility with the appropriate load vectors corresponding to the measured truck loads.

Whereas Model 1 is about 30 percent stiffer than is indicated by the measured deflections on the bridge, responses simulated by Model 2 show close correlation with their experimentally measured counterparts. This result illustrates the significance of correctly conceptualizing and simulating local
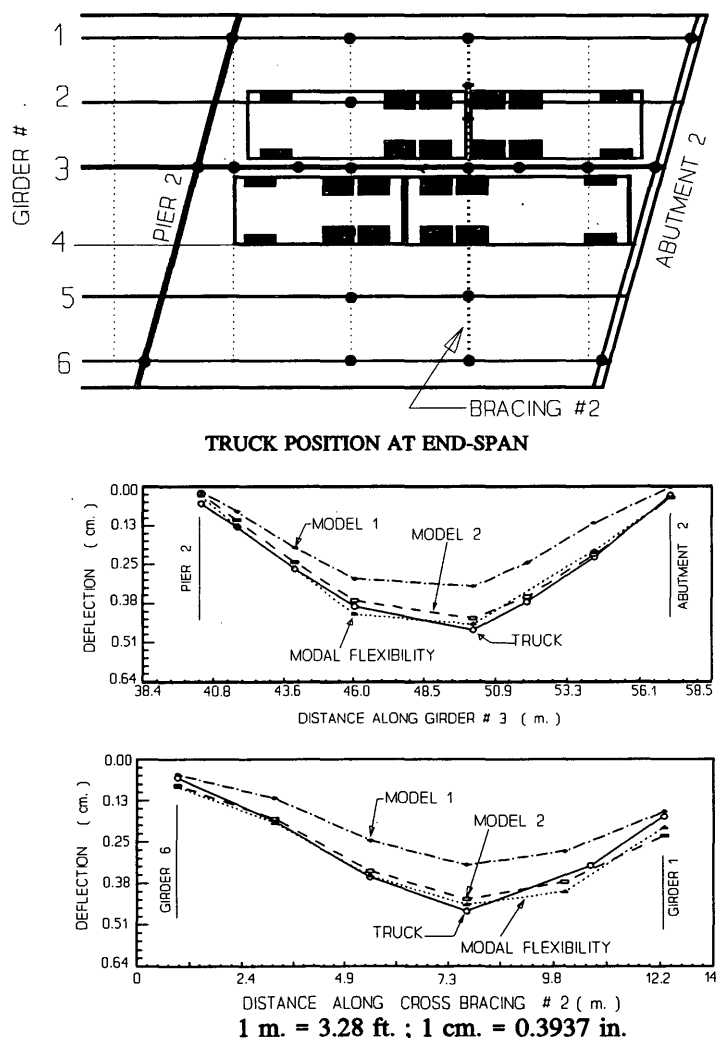

FIGURE 8   Correlation of truck-load deformations with simulations by analytical and modal flexibility.

response mechanisms for good analytical correlation. It is also significant that the deflection profiles given by the modal flexibility agree closely with the profiles measured directly under four loaded trucks clustered on one lane at an end span. The concentration of trucks in the experiment creates a considerably higher stress level under the loaded region than any legal two-lane loading configuration, even after allowing for the impact factors. The truck loading shown was permitted by highway officials during the experiments only because the critical bridge responses were being monitored in real time and the test could be stopped if the strains approached the limiting values shown in Figure 5. It follows, therefore, that this test may also be considered a proof-load test.

APPLICATIONS OF STRUCTURAL IDENTIFICATION

The agreement between the deflection profiles obtained from modal flexibility and those measured under truck loads indicates that modal flexibility, obtained by impacts applied at the dead load stress level of the bridge, may be considered a reliable condition index or signature capable of reflecting bridge conditions even at the upper levels of serviceability. This condition is attributed to the remarkable linearity of the new bridge even under proof-load stress levels. In the case of deteriorated bridges, such an accord between impact and proof-test results should not always be expected. For example, the writers observed considerable nonlinearity even at the service-load stages when a concrete slab bridge, which had extensive delamination at the shoulder regions, was loaded at these areas (*11*).

It is natural that if long-term deterioration is permitted or damage resulting from overloading occurs at the ultimate limit states, the structural condition of the new bridge (and therefore its flexibility) will change. For example, the chemical bond providing composite action between the deck and steel girders may deteriorate in aged or overloaded bridges, and the flexibility may increase significantly. In such cases, the analytical model identified cannot be relied on for estimating the strength capacity available. On the other hand, because the analytical model identified for the test specimen is shown to simulate closely bridge behavior even at the upper levels of the serviceability limit, it should serve reliably for rating the test bridge.

Once a completed analytical model is identified, more practical modal tests with only a sparse measurement grid, or truck load tests with only a few transducers measuring only some critical responses, may be carried out intermittently to update selected critical terms in bridge flexibility. For example, an impact modal test may be conceived for measuring only girder flexibility at midspan. Advances in sensor technologies should make it possible and practical to monitor continuously certain instantaneous and residual deflections of the bridge under truck loads. In this manner it may be possible to diagnose changes in structural condition. If future tests reveal a noticeable increase in flexibility relative to when the bridge was new, the identified 3-D FE model would have to be modified to incorporate mechanisms leading to increase in flexibility before it may be used for further predictions.

Rating the Test Bridge by Using the Identified 3-D FE Model

The test bridge was rated by the identified 3-D FE model. In the following discussion, some of the critical rating factors are compared against corresponding factors obtained by analysis of idealized models recommended by AASHTO (*12,13*). This phase of the study helped to evaluate the realism provided by different analytical modeling and analysis procedures for stringer bridges. Because the 3-D FE model captured the important global and local response characteristics of the bridge in its current state, rating the bridge with this model constituted an "academic" example of integrated field testing and bridge rating.

Issues To Consider in Rating the Bridge

The issues to consider in rating the bridge with the 3-D FE model were these:

1. *The limit-state that should govern rating*. Current practice is to consider yielding of the girder. However the truck-load test revealed that the bridge could maintain perfectly linear response at stress levels considerably exceeding any legal loading. Furthermore, evidence indicates that if the chemical bond in a noncomposite bridge is lost, significant serviceability and maintenance problems come soon after. Therefore it is rational to carry out strength evaluation of the bridge with the analytical model that reflects the linear service limit state. If maintaining the composite action resulting from chemical bond is a desired feature of the bridge, because of the evidence that the loss of composite action may render a bridge unserviceable and difficult to maintain, it should make even more sense to evaluate the bridge capacity for the limit state where this composite action is still available. Because the actual structural behavior is far more complex than the behavior of a simple steel beam, it does not make sense to evaluate the structural capacity based on beam steel yielding.

2. *Establishing critical elements, regions, and various capacities*. Slab and girders may be considered separate or compositely behaving elements on the basis of the measured strain distributions under truck load. Flexural and shear capacities of the girder would depend on cracking, separating, or yielding of the slab.

3. *Establishing the truck positions that would maximize demands at the critical regions*. In the case of a 3-D model incorporating the transverse load distributions between girders as facilitated by the slab and lateral braces, considerable analysis effort is required for locating trucks for rating.

Some of the resulting rating factors for the steel girder obtained from different recommendations and analysis approaches are shown in Figure 9. This figure shows the maximum positive and negative moments at the critical regions of the critical girder. Rating factors are also obtained based on the current Ohio Department of Transportation (DOT) practice, using the software BARS in conjunction with idealized 1-D beam models.

Significant differences are revealed in the rating factors based on the different approaches. Rating factors derived
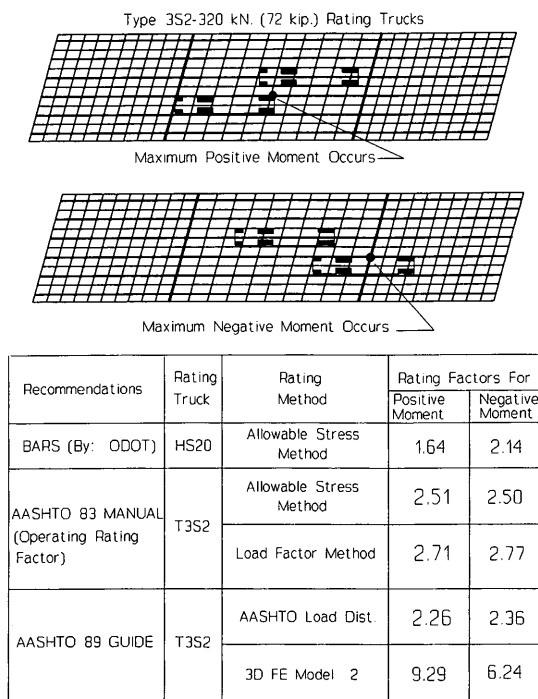
Type 3S2-320 kN. (72 kip.) Rating Trucks

Maximum Positive Moment Occurs

Maximum Negative Moment Occurs

Recommendations	Rating Truck	Rating Method	Rating Factors For	
			Positive Moment	Negative Moment
BARS (By: ODOT)	HS20	Allowable Stress Method	1.64	2.14
AASHTO 83 MANUAL (Operating Rating Factor)	T3S2	Allowable Stress Method	2.51	2.50
		Load Factor Method	2.71	2.77
AASHTO 89 GUIDE	T3S2	AASHTO Load Dist.	2.26	2.36
		3D FE Model 2	9.29	6.24

FIGURE 9   Rating factors for steel girder.

from the analyses of the 3-D FE model are several times larger than the corresponding factors obtained from planar idealizations of the bridge. The discrepancy caused by different approaches to computing demand is revealed when the two rating factors corresponding to the AASHTO *Guide* specifications are compared. Here, the same capacity computations and coefficients were used, and the only difference was in the demands computed from the AASHTO load distribution versus the prediction of the 3-D FE model.

In the case of positive moment the 3-D FE model incorporates composite action, reducing the girder demands. Therefore a rating factor of 9.29, which is more than four times the corresponding factor based on the AASHTO recommended load distribution, is obtained. In the case of negative moment the 3-D FE model yields a rating factor of 6.24, which is 2.6 times the corresponding factor obtained by the AASHTO load distribution. Such differences clearly demonstrate that in rating stringer bridges the uncertainty that may arise because of idealizations in analytical modeling may be of the same order of magnitude as the uncertainty that governs the loading envelopes.

It is also noted that if cracking of the slab is considered as the critical limit state, this may control the rating factor. What is important is that the idealized AASHTO load distribution does not permit correct evaluation of the demands of the concrete slab, whereas the 3-D FE model permits evaluation of all the possible critical components and regions of the bridge.

CONCLUSIONS

The concept of structural identification may hold the key for improving the state of the art in bridge field testing, condition evaluation, rating, health monitoring, and other applications. The authors have developed tools for demonstrating a comprehensive structural identification methodology and applied this to a newly commissioned continuous steel stringer bridge with integral abutments.

Modal flexibility is shown to serve as a conceptual, reliable, and comprehensive experimental signature, perhaps the best collection of numerical indices expressing bridge condition. In this application modal flexibility also served for testing the completeness of the 3-D FE model that is calibrated as a byproduct of the structural identification process.

The 3-D FE model of the bridge was completed by incorporating the observed local deformation kinematics at the critical regions and by calibrating the numerical model parameters so that the measured and simulated modal and flexibility characteristics of the bridge agreed to exacting goodness of fit. It is important that the test stress levels under truck loads considerably exceeded the stress levels that may be expected under legal loads even after allowing for impact and other safety factors. Because the 3-D FE model was shown to simulate the measured behavior under the test truck loading, it was considered a reliable tool for rating the bridge.

The rating factors obtained from analyses of the identified 3-D FE model exceeded those obtained by considering the AASHTO recommended load distributions by several times. This revealed that the uncertainties in rating resulting from failure to represent the load distribution mechanisms of steel stringer bridges correctly may exceed the uncertainties known to prevail in the load envelopes. Significantly, the 3-D FE model revealed the distribution of demands throughout the elements, including the slab and lateral braces, which are typically omitted in the rating process because of analytical limitations. These secondary elements may sometimes govern rating depending on the limit state considered. However unless a 3-D FE model is calibrated through structural identification, the potential for large errors cannot be overlooked. The confidence in the analysis results from a 3-D FE model that has not been verified and calibrated to exacting standards and cannot exceed the confidence in the estimates from the idealized analysis approaches currently used by experienced bridge engineers.

A global conclusion is that structural identification research of the type outlined here is essential for true appreciation of the limitations in current understanding of bridge behavior and in the manner of design, inspection, evaluation, and rating of bridges.

REFERENCES

1. *Civil Infrastructure Systems Research*. Workshop Report. Directorate for Engineering, National Science Foundation, Sept. 1992.
2. J. M. Cooper. Keynote Address. Presented at 9th International Bridge Conference, Pittsburgh, Pa., 1992.
3. S. C. Liu and J. T. P. Yao. Structural Identification Concept. *Journal of the Structural Division*, ASCE, 104, ST12, 1978, pp. 1845–1858.
4. H. G. Natke and J. T. P. Yao, ed. *Proc., Workshop on Structural Safety Evaluation Based on System Identification Approaches*, Lambrect/Pfalz, Germany, 1988.
5. T. D. Hogue, A. E. Aktan, and A. Hoyos. Localized Identification of Constructed Facilities. *Journal of Structural Engineering*, ASCE, Vol. 117, No. 1, 1991, pp. 128–148.
6. A. Habibullah and E. L. Wilson. *SAP 90*. Computers and Structures Inc., Berkeley, Calif., 1989.
7. M. Raghavendrachar and A. E. Aktan. Flexibility by Multireference Impact Testing for Bridge Diagnostics. *Journal of Structural Engineering*, ASCE, Vol. 118, No. 8, Aug. 1992, pp. 2186–2203.
8. H. Somaprasad, T. Toksoy, H. Yoshiyuki, and A. E. Aktan. *Closed-Loop Modal Testing of a 27-Story RC Flat Plate-Core Building*. Technical Report NCEER-91-0016. National Center for Earthquake Engineering Research, Buffalo, N.Y., 1991.
9. A. E. Aktan, C. Chuntavan, T. Toksoy, and K. L. Lee. Bridge Nondestructive Evaluation by Structural Identification: 1. Description of the Methodology and 2. Applications. *Proc., 3rd NSF Workshop on Bridge Engineering Research in Progress*, Department of AMES, University of California at San Diego, Nov. 1992.
10. S. Rubin and R. Coppolino. *Flexibility Monitoring Evaluation Study*. U.S. Department of the Interior, Minerals Management Service, 1983.
11. A. E. Aktan, M. J. Zwick, R. A. Miller, and B. M. Shahrooz. Nondestructive and Destructive Testing of a Decommissioned RC Slab Highway Bridge and Associated Analytical Studies. In *Transportation Research Record 1371*, TRB, National Research Council, Washington, D.C., 1992.
12. *Manual of Maintenance Inspection of Bridges*. AASHTO, Washington, D.C., 1989.
13. *Guide Specifications for Strength Evaluation of Existing Steel and Concrete Bridges*. AASHTO, Washington, D.C., 1989.

Optimization of Seismic Design of Single-Column Circular Reinforced Concrete Bridge Piers

RAVINDRA VERMA AND M. J. NIGEL PRIESTLEY

A design algorithm is developed to incorporate design philosophy for seismic capacity in a computer program for the optimal design of single-column circular reinforced concrete bridge piers for seismic loading. The program designs the circular column as a single degree of freedom system under the combined effect of axial and lateral seismic loads over a broad range of axial load ratio, column height, and design displacement ductility capacity. For a given column height and axial load, results indicate the existence of an optimal column diameter and design displacement ductility level. As the column diameter is reduced, cost savings are effected by reduced volume of concrete but tend to be offset by $P - \Delta$ effects, increased longitudinal reinforcement for flexure, and increased transverse reinforcement for confinement and shear. On the basis of common trends, solutions are provided for the most economical range of axial load ratio and design displacement ductility capacity for a given column height.

Any structural design should include consideration of aspects of optimization. This means developing several technically feasible alternatives, evaluating their efficiency, and then making the best engineering choice. Comparative assessment of design efficiency requires predicting structural response and expected cost of design and construction, and estimating potential damage under design-level earthquake loading. Guidance on selection of structural alternatives and optimization procedure is not provided by design codes, the role of which is the specification of criteria to ensure that performance goals are met. The purpose of this study was to investigate cost-based optimal solutions for single-column circular reinforced concrete bridge bents subjected to transverse seismic loading. This is to be done by encoding a capacity design procedure in a computer program and performing comparative designs over a practical range of column height, column diameter, and design displacement ductility level.

The designer's prime variable will be the column diameter, which is directly related to the costs. A change in the column diameter would influence factors such as column stiffness and hence the natural period and lateral design force. For a given superstructure mass, a natural direction toward optimization thus would appear to be to decrease column diameter, which generally reduces the lateral seismic design forces because the reduction in stiffness normally will shift the natural period to a range of lesser dynamic response. Other effects, however, could become important: increased confinement steel require-

ments, greater longitudinal steel requirements, more prominent $P - \Delta$ effects, and increased shear requirements. Optimization of the design thus involves finding the right balance among these counteracting influences.

SCOPE OF RESEARCH

Although the seismic capacity design approach for ensuring a ductile response of bridges has been prevalent for some time, not much has been done to investigate optimal choices in the seismic design of reinforced concrete columns. It is common practice in Japan to build bridge columns with low axial load ratios and low ductility demand and, hence, large diameter sections. On the other hand, in New Zealand and the United States, columns tend to be designed with higher ductilities and higher axial load ratios, and hence smaller diameter sections. The economics and structural desirability of the alternatives are unclear. To obtain insight into this area, a circular single-column bridge bent under transverse response was investigated. Various aspects of seismic design were considered by analysis for the following range of column axial load ratio, column height, and ductility capacity:

1. Axial load ratio, $A = P/f'_c A_g$, between 0.05 and 0.50, in steps of 0.05, where P is the axial load acting on the column and is equal to 1,200 kips (5338 kN) in this study; f'_c is the concrete compressive strength, which is assumed to be equal to 4 ksi (27.6 MPa) in this study; and A_g is the gross sectional area of the circular column.
2. Column height, L, ranging between 10 ft (3.05 m) and 50 ft (15.25 m), in increments of 10 ft (3.05 m).
3. Design displacement ductility demand, μ, varying between 2 and 10, in increments of 1.

Some of the more detailed aspects of capacity design approach, as applicable to the seismic design of circular bridge columns, have been discussed elsewhere (1); only issues relevant to the optimization computer program OPTCOL are addressed here.

RELATIONSHIP AMONG DUCTILITY, FORCE REDUCTION FACTOR, AND TRANSVERSE REINFORCEMENT

Displacement ductility, related to lateral displacements measured at the center of mass, is the most convenient measure

Department of Applied Mechanics and Engineering Sciences, University of California at San Diego, 9500 Gilman Drive, La Jolla, Calif., 92093-0411.

of gross deformation; it can be related directly to the force reduction factor reducing the design lateral force from the elastic response level. Thus, the displacement ductility ratio is given by

$$\mu_\Delta = \Delta_u/\Delta_y \qquad (1)$$

where Δ_u is the ultimate, or maximum, displacement and Δ_y is the lateral displacement corresponding to the yield point of equivalent elastoplastic response. This concept of displacement ductility is shown in Figure 1 for a single-column cantilever bridge pier idealized as a single degree of freedom system subjected to an axial load and a transverse seismic force. Also shown are the assumed deflected shapes of the column at first yield and at maximum ductility demand.

The following relationship between displacement ductility factor, μ_Δ, and the force reduction factor, R, is used in this study to assess the required levels of inelastic seismic response forces (*1*):

$$R = 1 + \frac{(\mu_\Delta - 1)T}{1.5T_0} \geq \mu_\Delta \qquad (2)$$

where T_0 is the period corresponding to peak spectral response and T is the fundamental period. Equation 2 provides a gradual reduction in R from the equal acceleration principle ($R = 1$, regardless of μ) at $T = 0$, through the equal energy approximation [$R = (2\mu_\Delta - 1)^{1/2}$] at about $T = 0.75T_0$, to the equal displacement approximation ($R = \mu$) for $T \geq 1.5T_0$. For this study, $1.5T_0$ was taken to be equal to 0.7 sec.

Concepts addressing issues related to column curvature ductility, its relationship with displacement ductility and plastic hinge length L_p, and required level of transverse reinforcement for confinement provision are discussed elsewhere (*1*). These concepts have been incorporated in the program OPTCOL.

FLEXURAL DESIGN PRINCIPLES

Based on tests on large-scale bridge columns, it has been noted that the prediction of flexural strength of confined col-
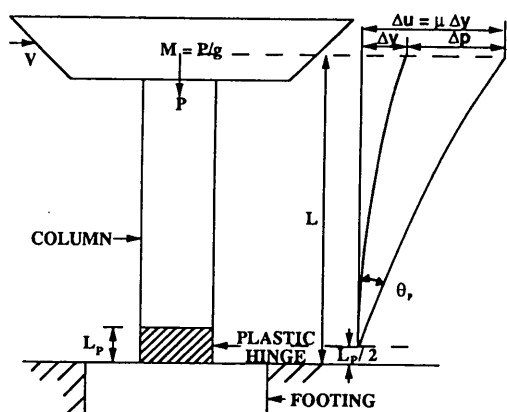

FIGURE 1 Lateral seismic response of a cantilever bridge column.

umns on the basis of the American Concrete Institute (ACI) concrete compressive stress block—which assumes a mean stress of $0.85f_c'$, an ultimate compression strain of 0.003, and the measured material strengths—results in excessively conservative prediction of actual strength. This predicted moment is hereafter termed the "ACI moment." Based on a large number of tests, the average moment enhancement as related to the ACI moment may be expressed empirically (*1*) as

for $P/(f_c'A_g) \leq 0.1$: $M_{max}/M_{i,ACI} = 1.13 \qquad (3a)$

for $P/(f_c'A_g) > 0.1$: $M_{max}/M_{i,ACI} = 1.13$

$$+ 2.35 \{(P/f_c'A_g) - 0.1\}^2 \qquad (3b)$$

To avoid the unnecessary conservatism inherent in the ACI computations, flexural strength calculations should use a stress-strain relationship applicable to confined concrete (*2*) and a higher ultimate compression strain, say 0.005. Alternately, as suggested by Priestley and Park, the dependable flexural strength may be taken as

$$M_u = \phi K M_{i,ACI} \qquad (4)$$

where K is the moment enhancement ratio given by Equation 3 ($K = M_{max}/M_i$), and ϕ is a flexural strength reduction factor, taken as $\phi = 0.9$ for all axial force levels of well-confined columns. This procedure has been included in the program OPTCOL for the enhanced level of column flexural strength.

DESIGN SHEAR FORCE

The current seismic design philosophy is to ensure against shear failure by setting the shear strength of a bridge pier higher than the maximum flexural strength that can be developed. These actual shear forces generated during earthquakes may be as high as three times the code-specified nominal values (*3*), if conventional flexural strength design is adopted. The ideal shear strength, V_i, should be matched to the overstrength shear force, V_D, because use of a reduction factor for shear strength is generally deemed inappropriate when the shear force is established on the basis of principles of capacity design. In this study, the shear strength of a column is based on the ACI approach of considering separate concrete shear-resisting mechanisms, V_c, and steel shear-resisting truss mechanisms, V_s. Thus the actual requirement is

$$V_i = V_c + V_s \geq V_D \qquad (5)$$

Shear carried by concrete and steel can be assessed conservatively in accordance with the provisions of the New Zealand (NZ) Concrete Design Code (*4*), which is followed in the program OPTCOL for the design of column shear reinforcement, both within and outside the plastic hinge regions. It should be noted that recent research shows the shear strength of plastic hinge regions is a function of ductility demand and the NZ shear design equations for both hinging and non-hinging zones are somewhat conservative. Consequently, the amount of transverse reinforcement provided in this study for shear strength will be slightly conservative compared with

more recently developed design criteria (5) currently under evaluation for design.

SEQUENCE OF OPERATIONS FOR OPTIMIZATION

The design approach outlined previously is appropriate for the design of any simple bridge column, given a knowledge of the required flexural strength and ductility. To draw conclusions about the economic consequences of adopting different design alternatives, the following sequence of operations was adopted for a specified column height:

1. Select the design response spectrum. Five elastic spectra were considered in this study.
2. Select an axial load ratio. This defines the circular column diameter.
3. Select the design displacement ductility. This enables the lateral design force to be selected by an iterative procedure requiring sequential estimation of member stiffness, natural period and, hence, the lateral seismic force.
4. Design longitudinal reinforcement for the provision of flexural strength.
5. Design transverse reinforcement for the provision of ductility and shear requirements.
6. Estimate the total costs involved in the design alternatives.

Some of the aspects of this optimization sequence are discussed in the following sections.

Response Spectra

The traditional method for describing ground shaking is a smoothed elastic response spectrum for single degree of freedom systems. Five response spectra, shown in Figure 2, were used to allow assessment of the influence of various spectral characteristics on the overall seismic design of bridge columns. They are the AASHTO Guide-based spectra specifications for an acceleration coefficient equal to 0.4 and for stiff clay or deep cohesionless conditions (6); the California Department of Transportation (Caltrans) A.R.S. Spectra for 150 ft or deeper soil alluvium, with peak ground acceleration equal to 0.5g and 0.7g (7); the Seed/Sun spectra proposed for deep soft soils after the Loma Prieta earthquake; the New Zealand Zone A inelastic design spectra for a peak ground acceleration equal to 0.5g (8); and a constant elastic design spectrum at 0.75g.

Natural Period

Following the choice of a certain axial load ratio (and hence the column diameter, for a known axial load) and a design displacement ductility capacity for a circular column with a specified height, the next step involves calculating the equivalent natural period of vibration of the cantilever column idealized as a single degree of freedom system, as shown in
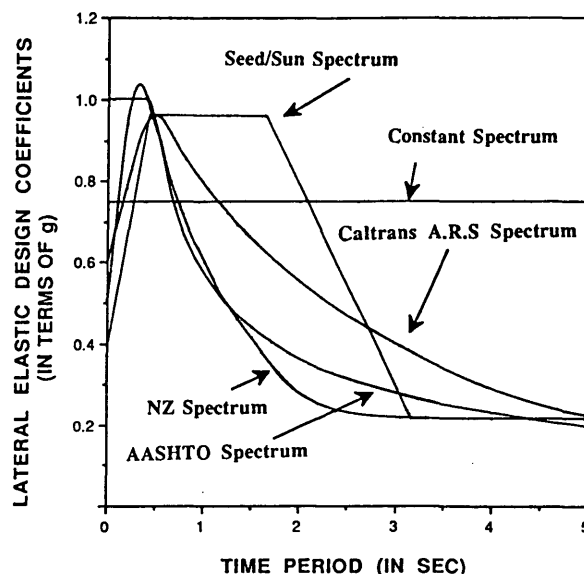

FIGURE 2 Comparison of five response spectra.

Figure 1. This is given by

$$T = 2\pi \sqrt{\frac{m}{k_{eq}}} \tag{6}$$

where

m = mass of the superstructure = P/g,
P = specified axial load on column,
g = acceleration resulting from gravity, and
k_{eq} = equivalent lateral stiffness of the cantilever column including both flexure and shear flexibility terms.

The stiffness should correspond to conditions at first yield and thus is influenced by the axial force level and the reinforcement content (9). Since the latter is not known at the start of the analyses, an iterative approach was used in this study (10). The initial lateral stiffness of the section was calculated by assuming the sectional moment of inertia to be 50 percent of that for the gross circular section and ignoring the influence of longitudinal reinforcement. The effective shear area was assumed to be equal to 0.9Ag, where Ag is the gross sectional area, and the value for the shear modulus G was assumed equal to 0.4E. This was followed by the estimation of the lateral seismic design forces and assessment of the longitudinal steel requirements for the total flexural moment including the $P - \Delta$ moments. An iteration scheme was followed for achieving a desired level of accuracy in the amount of longitudinal steel. For the first iteration in every cycle in the column design and for all other subsequent cycles when the accuracy was not reached, the actual lateral stiffness of the cracked section was computed on the basis of a modified equation for the effective moment of inertia of the circular reinforced concrete column section.

Design Base Moment

Once the actual design lateral seismic force has been evaluated on the basis of a modified natural period of the section, an

estimate of the total overturning moment acting on the column base is made, as shown in Figure 3. The base moment will thus equal

$$M_b = V \cdot L + P \cdot \Delta \tag{7}$$

where

V = lateral seismic design force,
P = axial load,
Δ = peak lateral displacement, and
L = column height.

Designing for the full $P - \Delta$ moments is known to be somewhat conservative, and approaches suggesting reductions of close to 50 percent have been made (9) on the basis of energy considerations. The trend toward more slender columns, mainly in the United States and New Zealand, has led to potentially more significant $P - \Delta$ effects, and thus the justification to include these effects in the calculation of the total bending moment acting on the column.

Figure 3 also compares the bending moment diagram and the deflected shape of the column at an initial ductility level of $\mu = 2$ and for an inelastic state at $\mu = 10$. As is evident from the diagrams, the influence of $P - \Delta$ effects is significant at higher ductility levels for the same column. Also, the deflected shape, and hence the bending moment diagram, are almost linear at high ductility levels, with the majority of rotation being concentrated at the plastic hinge forming at the column base.

To include the $P - \Delta$ effects in the program OPTCOL, an approximate approach was used to determine the column peak lateral displacements. In the elastic case, the equation for simple harmonic motion can be used to determine the peak

yield displacement of the column. If Δ is the total maximum inelastic displacement occurring at the designed displacement ductility level μ, it can be shown (10) that

$$\Delta = |y_{\text{inelastic}}|_{\max} = \mu \, |y|_{\max} = \mu \, \frac{T^2}{4\pi^2} |\ddot{y}|_{\max} \tag{8}$$

where $|\ddot{y}|_{\max}$ is the magnitude of the peak ground acceleration and $w \, (= 2\pi/T)$ is the angular frequency specified in radians per second, $|\ddot{y}|_{\max}$ can be obtained, for a specified natural period of vibration and on the basis of any characteristic design response spectra, as the inelastic design coefficient times the acceleration due to gravity.

Concrete and Steel Cost Evaluation

The total amount of concrete and steel used in the various cases of column design was calculated. This calculation was followed by an estimation of the respective costs on the basis of current rates in California, including the cost of form work, pouring of concrete, and cost of cutting, bending, and placing the steel. The costs were assumed to be equal to \$350/yd³ for concrete and \$0.60/lb for the steel. To assess the effect of varying the ratio of unit prices of concrete and steel, all cases also were analyzed for a concrete price of \$60/yd³, while the steel price was held constant.

Figures 4 and 5 show typical total cost versus axial load ratio plots for a design displacement ductility level of μ equal to 6 for the AASHTO response spectra, the New Zealand Zone A spectra, and the Caltrans A.R.S spectra, respectively. Figure 6 shows total cost versus displacement ductility capacity plots for the AASHTO response spectra for column heights equal to 20 ft (*top*) and 40 ft (*bottom*), respectively.

RESULTS AND CONCLUSIONS

The following conclusions may be drawn from results for the five cases analyzed:

1. For a specified column height and required design displacement ductility level, an increase in the axial load ratio, and hence a decrease in the column diameter, results in cost savings for a limited range of the axial load ratio. Beyond the value of the optimal column diameter, other effects—such as dominant $P - \Delta$ effects, increased confinement requirements for shear and ductility, and greater longitudinal steel for flexure—result in either increased costs or "flattening" of the cost plots, as shown in Figures 4 and 5. The optimal axial load ratio decreases as the column height increases and is usually in the range of $0.10 \le A \le 0.30$ for column height in the range of 50 ft (3.05 m) $\ge L \ge$ 10 ft (15.24 m).

2. For a specified column height and a low value of the axial load ratio, the total cost decreases for increasing the design level of the displacement ductility capacity up to a certain optimal μ, beyond which the costs start increasing, as shown in Figure 6 (*top*). This subsequent increase is due to greater costs for provision of transverse confinement for the higher levels of ductility capacity. The optimal design ductility capacity is typically in the range of $6 \le \mu \le 10$. However, for slender piers with higher levels of axial load ratios, the
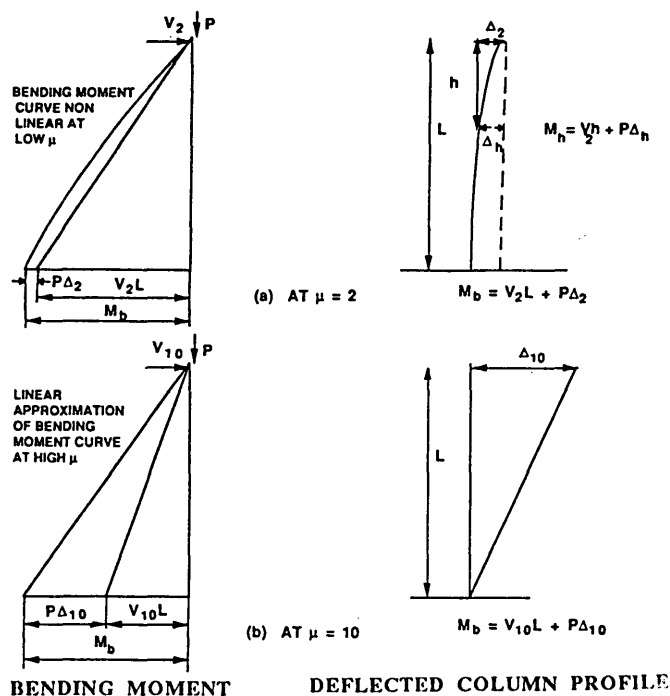

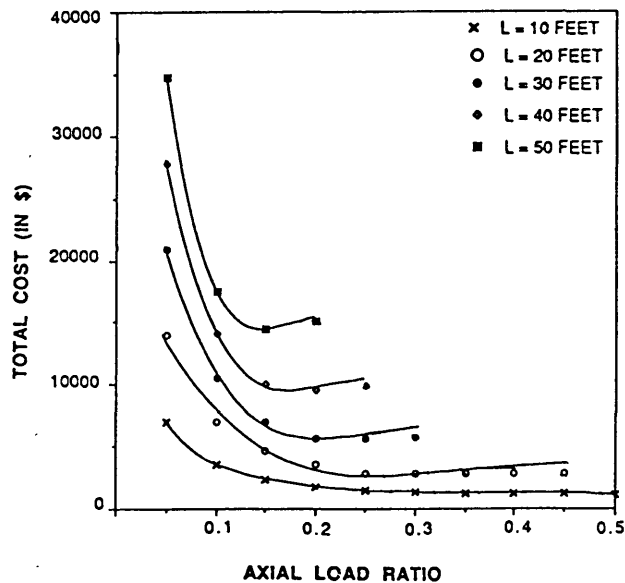FIGURE 3   Design base moments and $P - \Delta$ effects for a cantilever column.
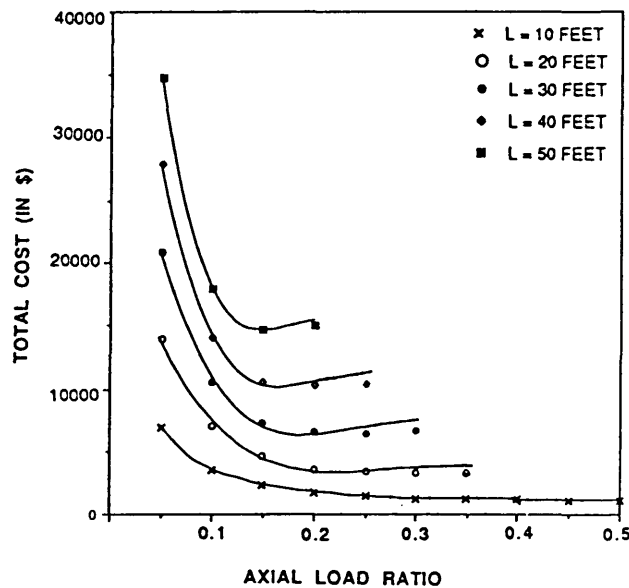
FIGURE 4 Total column cost versus axial load ratio $(P/f_c'Ag)$ for AASHTO spectra (top) and New Zealand spectra (bottom).

FIGURE 5 Total column cost versus axial load ratio $(P/f_c'Ag)$ for Caltrans A.R.S spectra.

costs simply go on decreasing for increased levels of design displacement ductility level, as shown in Figure 6 (bottom). This occurs because for slender piers, for a specified column height and a selected value of the column diameter, the increase in costs caused by increased confinement requirements for greater μ is offset by the decrease in the longitudinal steel requirements owing to the reduced design inelastic seismic forces for higher levels of ductile response.

3. An increase in the maximum allowable longitudinal steel ratio from 6 to 8 percent leads only to more design cases being possible, without any associated savings in the total design cost, as the steel cost is already dominant at that stage. The effect of increasing the design peak ground acceleration is to
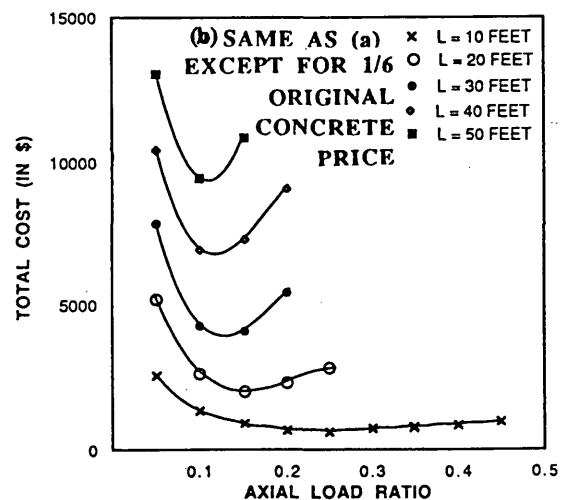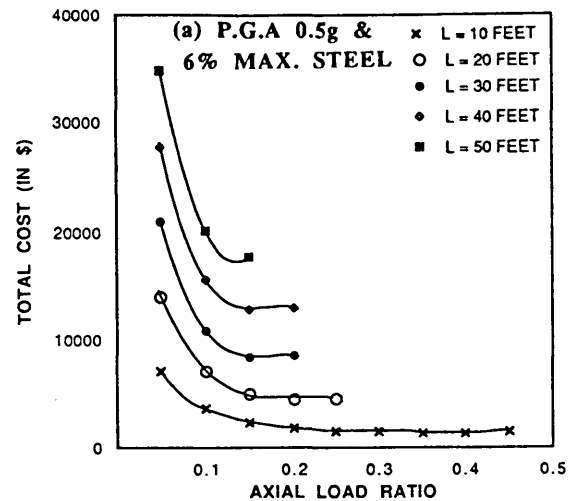
reduce the number of possible design cases as the maximum steel ratio limit of 6 percent is exceeded for higher seismic design moments. This effect also significantly increases the total costs for slender piers for the same reason.

4. To study the effect of altering the ratio of unit concrete to steel price, the concrete price was reduced from $350/yd^3 to almost one-sixth value at $60/yd^3 while the steel cost was held constant. The result: the existence of distinct optimal axial load ratios for given column heights and design displacement ductility levels is observed, in accompaniment with sharply rising cost curves beyond the optimal minima. This is shown in Figure 5(b) for the Caltrans spectra, which, when compared with cost plots at concrete price of $350/yd^3 in Figure 5(a), reflects the sensitivity of the shape of the cost plots to varying cost ratios. However, the influence of lower concrete cost on the optimal axial load ratio is not significant. The tendency, as expected, is to lower somewhat the values of the optimal axial load ratio.
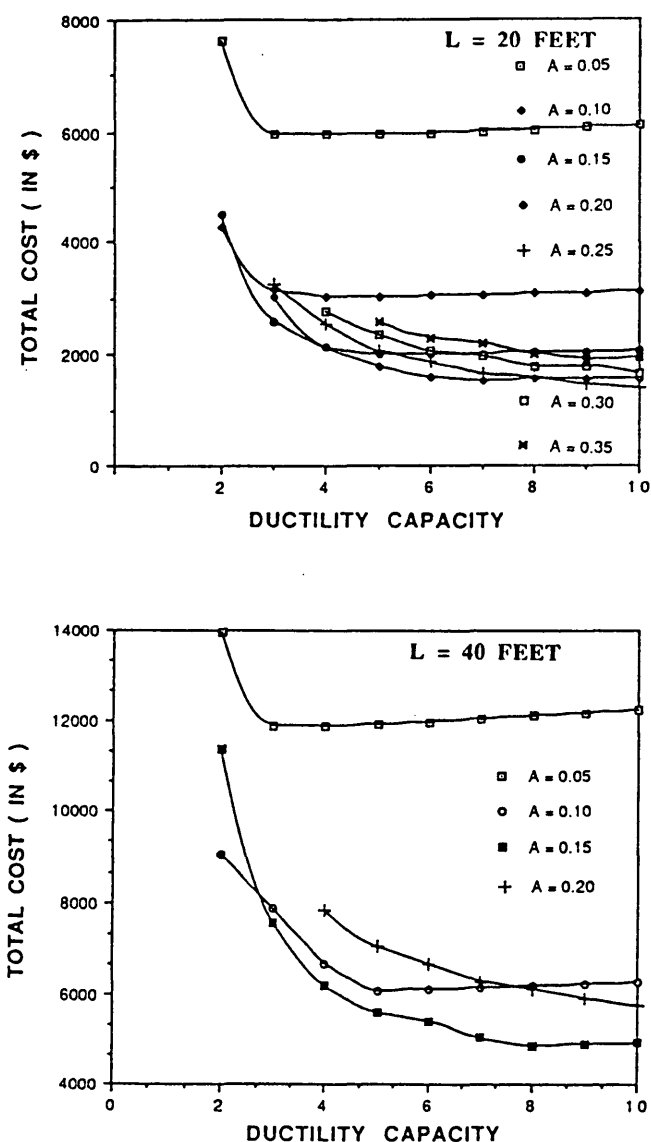
TABLE 1 Optimal Range of Design Axial Load Ratio and Displacement Ductility Capacity

COLUMN HEIGHT (FT.)	OPTIMAL AXIAL LOAD RATIO RANGE	OPTIMAL DUCTILITY CAPACITY RANGE
10	$0.25 \leq A \leq 0.35$	$6 \leq \mu \leq 10$
20	$0.20 \leq A \leq 0.25$	$6 \leq \mu \leq 10$
30	$0.15 \leq A \leq 0.20$	$7 \leq \mu \leq 10$
40	$0.10 \leq A \leq 0.15$	$7 \leq \mu \leq 10$
50	$0.10 \leq A \leq 0.125$	$7 \leq \mu \leq 10$

This will be particularly pronounced in the case of columns with high axial load ratios and high longitudinal reinforcement ratios.

Nevertheless, the results appear to justify, both technically and economically, current practice for seismic design of columns in axial load ratio and ductility level. However, current Caltrans practice (7) of limiting displacement ductility factors for single-column piers to values as low as $\mu = 3$ (dependent on the period) does not appear to be justified based on the results of this study.

RECOMMENDATIONS FOR FUTURE RESEARCH

This study focused on single-column piers in their transverse response to seismic excitation. Extending the study for multiple-column bridge bents, especially with taller piers and under bidirectional seismic attack, should then follow as a logical step. Rectangular column piers also may be included in the study. Comparative study should be made as to the most efficient number of columns at any bent (e.g., comparing the cases for two- and three-column bents with the results for the single-column bent).

Influence of foundation flexibility on the optimization of the seismic design of the bridge bent also should be investigated further and included in the optimization procedure. Its effects will particularly pronounce the $P - \Delta$ moments for slender piers and could alter the existing trends. Also, a change in the column diameter, and hence the stiffness, would affect both the footing and the superstructure design. These aspects also need to be examined.

A more consistent approach should be used to assess the shear strength of the bridge columns during ductile response. Further research needs to be done on aspects related to dynamic shear strength of single- and multiple-column bridge piers, behavior of columns in double curvature, influence of practical levels of reinforcement on shear strength, and effects of axial tension and multidirectional loading on the concrete shear carrying capacity.

FIGURE 6 Total column cost versus design displacement ductility capacity, μ, for AASHTO spectra.

5. From the cost plots for this study, the general trends in the seismic design solutions for single-column reinforced concrete bridge piers are clear. Table 1, based on the results of the optimal seismic design of bridge bents of single-column circular reinforced concrete and using five design response spectra, presents the range of axial load ratio A and the corresponding range of the possible design displacement capacity, μ, for the most economical solutions at a specified column height L, in the range of $L = 10$ ft (3.05 m) to 50 ft (15.24 m).

6. The solutions recommended by this optimization approach are based solely on ultimate seismic displacement consideration. In many cases, gravity load considerations may dominate and make the recommended high ductility factors impractical. The use of high ductility factors also may result in excessive incidence of minor damage, such as spalling of cover concrete, under a moderate earthquake that may be expected to occur several times in the design life of a bridge.

ACKNOWLEDGMENTS

REFERENCES

1. M. J. N. Priestley and R. Park. Strength and Ductility of Concrete Bridge Columns Under Seismic Loading. *ACI Structural Journal*, Vol. 84, No. 1, Jan.–Feb. 1987, pp. 61–76.
2. J. B. Mander, M. J. N. Priestley, and R. Park. Theoretical Stress Strain Model for Confined Concrete. *Journal of Structural Engineering*, ASCE, Vol. 114, No. 8, Aug. 1988, pp. 1804–1825.
3. B. G. Ang, M. J. N. Priestley, and T. Paulay. Seismic Shear Strength of Circular Reinforced Concrete Columns. *ACI Structural Journal*, Vol. 86, No. 1, Jan.–Feb. 1989, pp. 45–59.
4. *The Design of Concrete Structures: NZS 3101:1982*. Standards Association of New Zealand, Wellington, 1982, 127 pp.
5. M. J. N. Priestley, R. Verma, and Y. Xiao. Shear Strength of Reinforced Concrete Bridge Columns. *Journal of Structural Engineering*, ASCE, in preparation.
6. *Guide Specifications for Seismic Design of Highway Bridges*. AASHTO, Washington, D.C., 1983.
7. *Standard Specifications for Highway Bridges Relating to Seismic Design*. California Department of Transportation, Division of Structures, 1990.
8. J. B. Berill, M. J. N. Priestley, and H. E. Chapman. Design Earthquake Loading and Ductility Demand. *Bulletin of the New Zealand National Society for Earthquake Engineering*, Vol. 13, No. 3, Sept. 1980, pp. 232–241.
9. T. Paulay and M. J. N. Priestley. *Seismic Design of Concrete and Masonry Structures*. John Wiley and Sons, New York, 1992, 744 pp.
10. R. Verma and M. J. N. Priestley. *Optimization of Seismic Design of Single Column Circular RC Bridge Piers*. SSRP-90/02 Report. Department of Applied Mechanics and Engineering Sciences, University of California at San Diego, La Jolla, July 1990, 151 pp.

Updated Environmental Limits for Aluminized Steel Type 2 Pipe Application

L. Bednar

The limits of environmental conditions over which aluminized steel Type 2 drainage pipe exhibits good long-term service life have been defined more clearly owing to the results of continuing field inspections. As a result, the strengths of the material compared with galvanized steel and its behavior under severe exposure can now be illustrated with increased clarity.

The advantageous durability of aluminized steel Type 2 pipe demonstrated in field tests and in actual service (1–3) provides an effective means to address the statistically more important limitations in corrosion behavior of galvanized steel in drainage pipe environments. Aluminized steel complements galvanized steel in drainage pipe applications in a fashion that results in expansion of the limits of environmental conditions over which corrugated steel pipe can be effectively used. However, for best results it is important to specify the limits of environmental tolerance for both materials reasonably well. The California Department of Transportation (Caltrans) chart has filled this need for galvanized steel pipe for many years, although it has proven to be unreliable under some environmental conditions. To help ensure that galvanized steel is used within the limits of its capabilities, Armco Research spent considerable time in field studies to develop a more realistic modified Caltrans-type graph to guide galvanized steel application. The results were introduced a few years ago (4,5). Recently, cumulative studies on aluminized steel pipe field performance became sufficiently comprehensive to permit construction of a new graph for reasonable conservative estimation of product durability under a range of conditions, including those approaching and exceeding the limits of environmental tolerance.

BACKGROUND

Initially, aluminized steel application was guided mainly by the results of a series of inspections of 30-year-old riveted pipe installed at numerous culvert sites in 14 states in the United States (1). The ranges of environmental conditions existing among these sites did not establish the limits of environmental tolerance but were sufficiently comprehensive to justify stipulation of general water and soil limits of a pH range of 5–9 and a resistivity above 1500 ohm·cm. Some of the data suggested the resistivity limit could be as low as 1000 ohm·cm under some conditions, but Armco preferred to use a conservative 1500 ohm·cm general limit until the field data

became sufficiently comprehensive to determine the conditions under which a lower resistivity limit would apply. As is the case with any new product, during the years following the introduction of aluminized steel, occasionally the product was exposed under corrosive conditions too severe for expected service life to be realized. Such cases emphasized the need to determine the limits of environmental tolerance.

Sufficient field performance data now exist on newer lock seam and weld seam aluminized steel pipe exposed over a range of conditions in service for a sufficient length of time (up to about 12 years) to begin to estimate better the limits of environmental tolerance. For pipe water environments, these limits have now been estimated with reasonable confidence, and behavioral trends have been determined using simple water alkalinity and hardness measurements in addition to the normal resistivity and pH measurements. Water data are believed to be sufficiently accurate and comprehensive to permit a realistic comparison with galvanized steel pipe, for which there is a good deal of Armco data. This is fortunate because, for the nation as a whole, water chemistry is the primary factor controlling galvanized pipe durability. Generally, therefore, water chemistry is the only environmental factor requiring testing and usually it is the only factor aluminized steel must address.

Armco data for aluminized and galvanized steel performance in soil environments are less comprehensive than the data for water environments, and soil corrosivity is inherently difficult to investigate. Fortunately, soilside corrosion problems for corrugated steel pipe are unlikely (6) except under well-defined conditions found in certain geographical areas. Such areas include those with saline soils found mainly in arid regions (4,5) and those with highly acidic soils found in parts of certain wet regions (7,8). In these areas, adverse soil conditions associated with low resistivity or low pH can control durability, and soil guidelines based on minimum resistivity (water-saturated resistivity) and pH are quite useful.

Although an increasingly strong case can be made for extending the soil minimum resistivity limit of aluminized steel to about 1000 ohm·cm with a reduced pH range (~6.0–8.5) below 1500 ohm·cm, Armco is still uncertain of the actual limit of tolerance and prefers to retain a conservative general nationwide lower limit of 1500 ohm·cm for the present. However, because of the results of a recent field inspection survey in western states, Armco has enough field data from arid climates to recognize a considerably lower soil minimum resistivity limit for regions with arid climates. This special limit applies because waterflow in such climates is generally too infrequent to influence durability considerations, and soils are usually dry enough that the effect of salt content is greatly

Armco Steel Co., Research & Technology, 703 Curtis Street, Middletown, Ohio 45044-3999.

reduced (in situ resistivity controls corrosion). Of course, a condition of infrequent waterflow means that, in general, soil minimum resistivity and pH will be the only criteria governing materials selection in arid climates.

DISCUSSION ON MECHANICS OF THE METHOD

Water Environments

The graph for behavior of aluminized and galvanized steel in waters shown in Figure 1 includes the effect of water alkalinity and hardness as well as pH and resistivity because this effect is important in determining the reaction of both materials to the water. For galvanized steel, alkalinity and hardness are important in determining the tendency toward protective mineral scaling necessary for good long-term service life (4). For both materials, the determination of alkalinity and hardness reveals the proportion of corrosive Cl^- and SO_4^{-2} salts contributing to the resistivity. The total dissolved salt content indicated by the resistivity generally consists mainly of beneficial or nonharmful alkalinity or hardness salts instead of corrosive salts such as SO_4^{-2} and Cl^-, and it is necessary to determine the proportions of the two types of salts to characterize the effect of resistivity on behavior. At any level of hardness and alkalinity, decreasing resistivity corresponds to increasing Cl^- and SO_4^{-2} and decreasing service life. It is also important to determine free carbonic acid (CO_2) (calculated from pH and alkalinity) because free CO_2 is the only form of free acidity present in most pipe waters.

CO_2 has a direct adverse effect on galvanized steel and can enhance the adverse effect of Cl^- and SO_4^{-2} on galvanized and aluminized steel. At any given level of hardness and alkalinity, increasing free CO_2 corresponds to decreasing ser-

vice life to a degree determined by Cl^-, SO_4^{-2}, and resistivity. To express the corrosive influence of free acidity, the free CO_2 concentration is more realistic than the pH alone (4). Figure 1 does not deal with acidity other than CO_2 because water containing other free acidity would necessarily be below pH 4.5. Water below pH 4.5 is likely to contain other free acidity. The result of having pipe water containing such free acidity would be a condition too severe for most common pipe materials (4). Thus, the graph cannot be used for waters with pH values below 4.5, and a negative sum on the graph vertical axis refers only to water relatively low in hardness and alkalinity and relatively high in free CO_2. The graph also cannot be used at pH values above 9.0, where normally beneficial alkalinity becomes partially detrimental because of an adverse effect on the aluminum layer of the bilayer aluminized coating.

The 50-year and 20-year lines in the graph of Figure 1 represent the lower water chemistry limits at which at least 50-year or 20-year service life is realized for each material. Any chemistry falling below these lines will tend to give lower service life because such a low reading indicates higher proportions of Cl^- and SO_4^{-2} or free CO_2, or both, at a given resistivity. Service life is defined as the time in service before pipe maintenance at certain minimum gauges is likely to be needed. The minimum gauges representing the two materials in the graph are different because the data were from two different studies using baseline materials of 2.0-mm (14-gauge) galvanized steel and 1.62-mm (16-gauge) aluminized steel. The limit lines for galvanized steel were developed from earlier field studies (4). The limit lines for aluminized steel were developed from later field studies; the data are presented in Figure 2. Thus Figure 1 is a composite of Figure 2 and the earlier figure for galvanized steel. The aluminized steel data are from random field inspections except for the five problem waters (less than 20-year life), which are from three problem
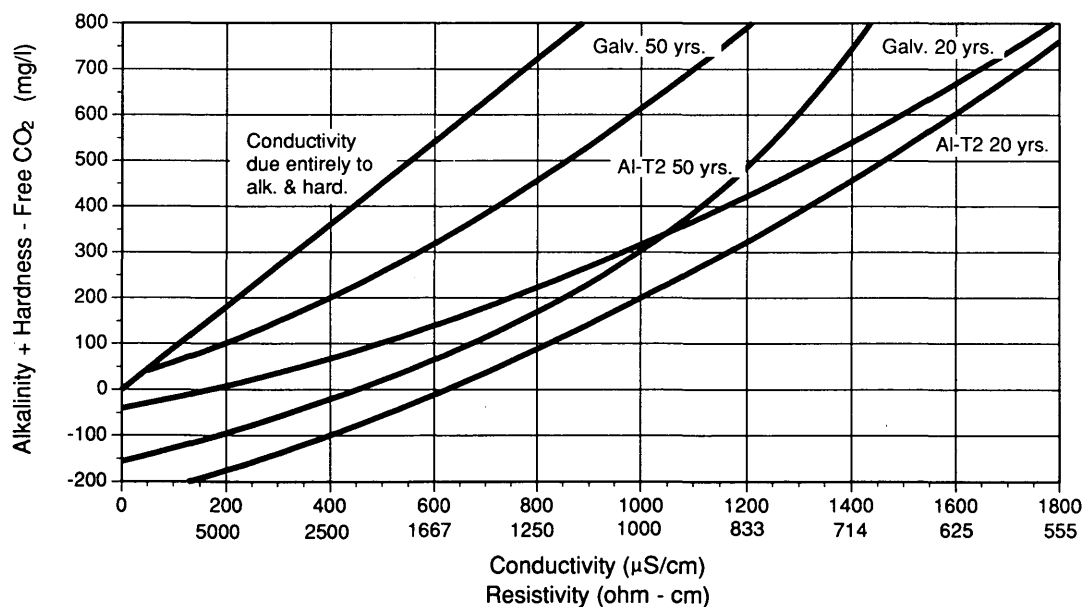

FIGURE 1 Comparative minimum service life for 1.62-mm-thick Type 2 aluminized steel and 2.0-mm-thick galvanized steel as a function of water chemistry ($\mu S/cm$ = umho/cm, mg/l = ppm, 1.62 mm = 16 gauge, 2 mm = 14 gauge).

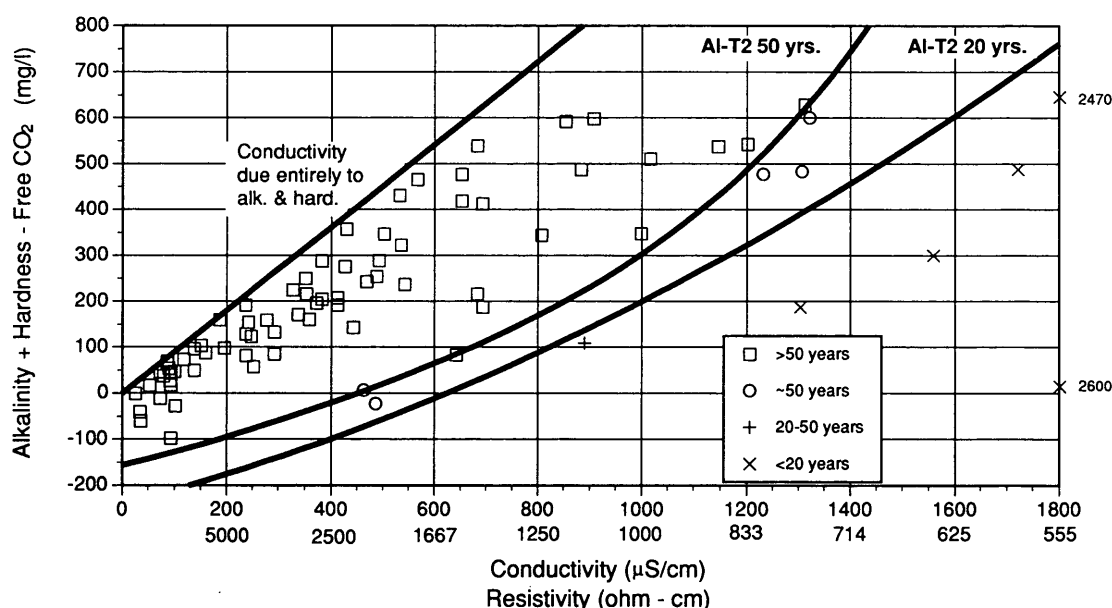**FIGURE 2** Estimated service life of 1.62-mm-thick Type 2 aluminized steel as a function of water chemistry (μS/cm = umho/cm, mg/l = ppm, 1.62 mm = 16 gauge).

sites specifically chosen for study. Two of these sites had multiple waterflow sources (lateral intercept flow as well as main invert flow), thus affording the opportunity to investigate the effect of more than one water at one site. Because the problem sites were not chosen randomly, their number with regard to the total number studied obviously has no statistical significance, but inclusion of data from these sites is helpful in establishing the limits of environmental tolerance.

Figure 1 is intended for groundwater evaluation at sites where the groundwater table is high enough to produce at least some slight dry weather groundwater seepage and flow at the depth of pipe burial. At aluminized sites that are dry during nonrainfall periods, there is normally no need for a water evaluation because the material is generally not substantially affected by rainwater surface runoff. Likewise there is normally no significant effect of surface runoff in the high-water zone above the groundwater level. Surface runoff is usually relatively soft and near-neutral in pH because of dilution or aeration effects, and aluminized steel has optimum resistance to such water (*1*). The higher velocity of surface runoff is no problem because of the enhanced resistance of aluminized steel to erosion corrosion and abrasion by turbulent rapid flow (*1*).

Because groundwater is normally the only pipe effluent of any concern, water testing should be accomplished in dry weather at least 2 days after the last rainfall, when dissolved mineral concentration is maximal. In arid climates, only sites with significantly prolonged flow or standing water resulting from a local high water table are of concern. The degree of accuracy required in water analysis is not high enough to justify use of standardized methods of analysis. For hardness and alkalinity testing, simplistic digital titration kits employing prequantified encapsulated reagents are adequate. Alkalinity and hardness data are commonly expressed in ppm as $CaCO_3$. These data must be converted to ionic concentration form before use in Figure 1 by multiplication of the alkalinity by 1.22 and of the hardness by 0.4.

Soil Environments

The graph for behavior in soil environments is shown in Figure 3. This graph is more simplistic and less specific for three reasons. First, for practical purposes it is limited to the parameters of pH and resistivity. Second, because of the limited data available, the limits of environmental tolerance have not yet been estimated, and it is necessary to use conservative limits adequately supported by the available data. Third, the data limitations prevent a reliable soilside comparison of the two materials. The present form of the soilside graph in Figure 3 serves only to illustrate the soilside conditions necessary to ensure a minimum 50-year service life for aluminized steel at 1.62 mm thickness (16 gauge) according to present knowledge.

One potential problem in detecting low soil pH values that must be recognized is the possibility that in a nonselect heterogeneous backfill there may be a highly acidic phase that directly contacts the pipe but is not detected because of the normal practice of mixing soil for pH measurement. A dark or light gray, blue, or olive-colored clay phase in a native-soil fill may be acidic and should be isolated for a pH measurement. Highly acidic clays of such color are found in certain geographical areas and arise from conditions chemically comparable to those that produce environments of acid mine-water. When extensively distributed in a pipe watershed soil, such clays may give rise to groundwater seepage of temporary high acidity during prolonged dry weather when the volume of groundwater flow is minimal.

One potential problem in resistivity measurements arises because of the influence of chloride deicing salts. These salts induce snow and ice melting that produces a trickle flow of salty moisture that percolates through the soil and may attack the pipe if the salt content is high enough. The advent of spring weather brings rains that leach the soil to remove this temporal salt, and measurement of resistivities afterward gives misleading high values. In sandy or other granular soils, drain-
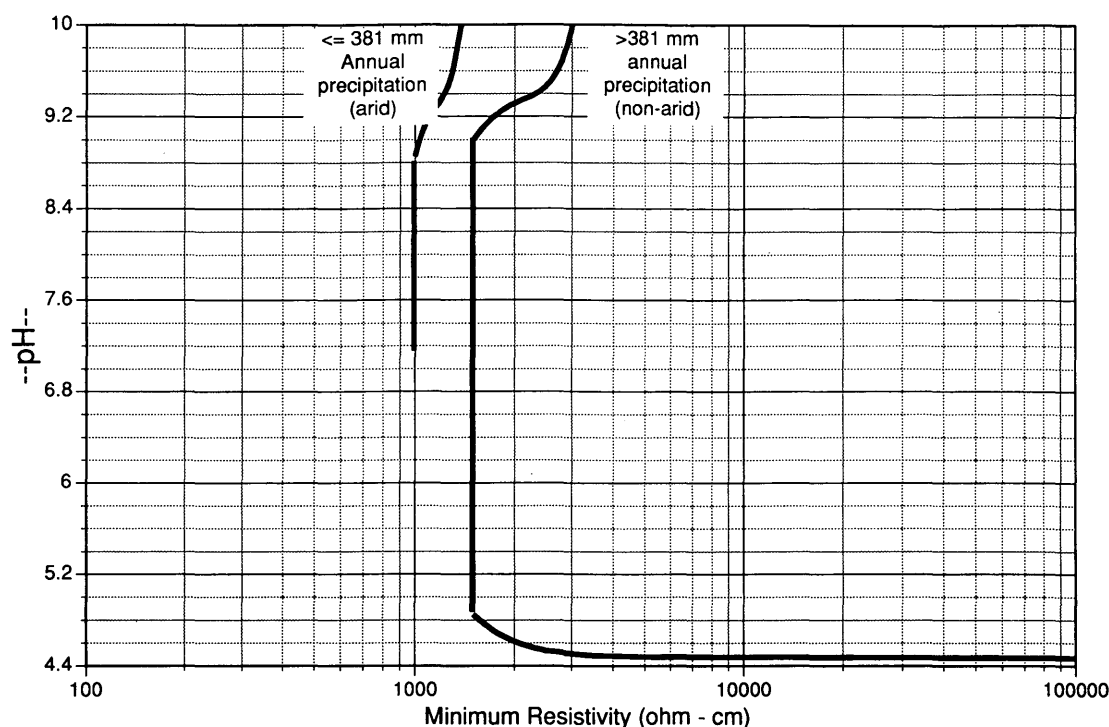
FIGURE 3 pH/resistivity soilside tolerance limits of Type 2 aluminized steel for good long-term durability
approaching 50 years minimum in nonarid and arid regions (1 in. = 25.4 mm).

age and leaching occur quickly after the first rainfall, and even in arid climates, all traces of chloride from deicing salt are removed after the first appreciable rainfall.

Other Comments

The estimation of pipe service life in waters and soils is derived by extrapolation of field performance under a variety of exposure conditions and has been described previously (9). The method is based on the results of inspections of 30-year-old culvert sites in which the progress of coating and substrate attack at 20- and 30-year intervals was studied. Extrapolation of performance from 30 to 50 years involved little uncertainty. Actually, the inspection results showed that the long-term behavior of aluminized steel is predictable early in the exposure period. This is so largely because a passive metal such as aluminum that exhibits normal good passive behavior during the first several years in service continues to do so over the long term, and the existence of any troublesome conditions becomes evident early.

RESULTS AND DISCUSSION

Characteristics of Graph for Water Environments

The most important factor limiting galvanized steel service life for the nation as a whole is softer higher-resistivity water containing significant free CO_2 and having little or no natural protective mineral scaling tendency (10). This condition is common in certain regions of the country, and the use of aluminized steel in such regions effectively addresses the prob-

lem, as shown in Figure 1. According to the figure, a minimum 50-year aluminized steel service life is realized under conditions of higher resistivity and free CO_2 encompassing even those severe enough to limit galvanized service life to somewhat less than 20 years. As a passive metal with passive oxide film protection, aluminum is highly resistant to soft high-resistivity water and to a weak acid like carbonic acid (11). Nonpassive zinc develops minimal film protection of any kind in such water and is subject to acceleration of corrosion by CO_2 in accordance with the free acidity concentration (12).

As resistivity decreases from high levels, the combined adverse effect of increasing Cl^-/SO_4^{-2} and any significant free CO_2 becomes increasingly potent. However, aluminized steel continues to maintain a minimum 50-year service life under conditions of moderately low resistivity, even those severe enough to limit galvanized steel to a service life of less than 20 years. This degree of advantage persists down to a resistivity level on the order of 950 ohm·cm. Thus, aluminized steel may be used effectively to address corrosion problems existing over the range of high to moderately low resistivity. This advantage is the result of the combined influence of superior resistance to free CO_2 and a modestly superior resistance to Cl^-/SO_4^{-2}. As resistivity decreases still further and Cl^- and SO_4^{-2} increase further, pitting corrosion accelerates notably and the advantage of aluminized steel over galvanized steel decreases more and more abruptly. At some point over the 950 to 600 ohm·cm range, pitting becomes severe enough that the advantage becomes minimal. Thus, aluminized cannot be used to address corrosion problems caused by low resistivity. If water resistivity is low enough and water chemistry coordinates on the graph fall far enough below the 50-year service life line, service life can be relatively short.

Characteristics of Graph for Soil Environments

In general, field experience indicates that soilside environments are less severe than waterside environments (*6*), and problems for aluminized or galvanized steel pipe are less likely, except for cases involving certain well-defined avoidable conditions. This is fortunate because soilside studies are inherently more difficult, and Armco soilside performance data are not yet sufficient to permit a reliable estimation of the limits of tolerance for either material. The most useful approach under these circumstances is to use for good long-term durability conservative limits that are supportable by comprehensive data, and to depict known behavioral trends near these limits.

As shown in Figure 2, for good long-term aluminized steel service life (approaching 50 years as a minimum), a 1500 ohm·cm general nationwide lower limit on soilside minimum resistivity and a 5–9 pH range will be retained until soilside data become sufficiently comprehensive to determine the conditions under which lower resistivity can be tolerated. For the present, the only exception sufficiently supportable by available data is a general 1000 ohm·cm minimum resistivity limit for arid climates with 381 mm/year (15 in./year) or less total annual precipitation. Armco's experience suggests the lower general limit in arid climates is as low as 800 ohm·cm and possibly even as low as 600 ohm·cm, but 1000 ohm·cm is better supported by the present data and will be used for the present. For arid climates Armco has no idea of resistivity tolerances at pH values below a level of about 7.2 because the company has never observed lower pH values than this at low resistivity levels in arid climates. Such conditions appear to be rare and may not exist at all. Of course, the special 1000 ohm·cm limit applies in recognition of the benefit of dry soil conditions and does not apply at installations where soil is wetted by groundwater. In arid or nonarid regions, the presence of groundwater seepage resulting from a groundwater table that reaches up to the pipe burial depth necessitates the use of Figure 1 for further guidance.

Figure 3 also shows a mild adverse effect of soil alkalinity at pH values above 9.0 on aluminized behavior. This effect is mild because high alkalinity adversely affects only the aluminum layer of the coating. The Fe and Al alloy (intermetallic) layer of the coating is not attacked by excessive alkalinity, and the substrate performs better as pH increases. Data above pH 9.0 are limited but suggest that a mild adverse effect on total service life can be expected in the 9–10 soil pH range. As the pH approaches 10, long-term performance of the substrate and the Fe and Al alloy coating layer are expected to be quite good, so the long-term effect of loss of the coating aluminum layer will become insignificant in attaining 50-year minimum life.

Figure 3 further shows a pronounced accelerating adverse effect of acidity on performance below pH 4.8, and good long-term service life over the 4.8–4.5 pH range is attainable only at increasingly high resistivity. Although this is a bit conservative, it is nonetheless indicative of the trend of a pronounced adverse effect of acidity that begins at some pH value near the 4.5 level at which free acidity other than CO_2 is likely to be introduced. The effect of acidity throughout the 4.0–4.8 pH range actually varies considerably, being minimal in well-drained oxidizing soils and maximal in poorly drained reduc-

ing soils (similar to the effect on galvanized steel). In water-logged reducing soils, the effect of acidity is sometimes controlled by water-soluble heavy metals, primarily iron, in certain geographical areas. In such soils, pH values may drop below 4.0. Armco studies on materials behavior in water-logged soils are continuing, and behavioral characteristics will be discussed in future reports.

CONCLUSIONS

1. The use of aluminized steel Type 2 to complement galvanized steel by effectively addressing the more important limitations in galvanized corrosion resistance substantially expands the limits of environmental chemistry over which corrugated steel pipe can be used. However, the limits of corrosion resistance capabilities of aluminized as well as galvanized steel must be recognized. Recognizing these limits is readily and easily accomplished by using new updated field-derived application guidelines and by conducting simple groundwater hardness and alkalinity tests in addition to the normal pH and resistivity tests wherever groundwater is a factor.

2. Updated guidelines indicate 50-year minimum service life for aluminized steel over water conditions ranging from high resistivity and high free CO_2 to moderately low resistivity and significant free CO_2. Throughout this range, conditions encompassed include those severe enough to limit galvanized steel life to somewhat less than 20 years. This advantage for aluminized steel persists down to resistivity values on the order of 950 ohm·cm, but the degree of advantage diminishes increasingly abruptly at lower values and becomes minimal at a point somewhere over the 950–600 ohm·cm range. Thus, use of aluminized steel effectively addresses water problems existing over the high to moderately low resistivity range down to at least 950 ohm·cm but does not effectively address problems resulting from very low resistivity. The use of aluminized steel also effectively addresses problems associated with rain-water surface runoff.

3. Updated soil guidelines retain the pH and resistivity basis for evaluating soil corrosivity and retain the 1500 ohm·cm minimum resistivity and 5–9 pH limits for aluminized steel for the nation as a whole. However, in arid climates with 381 mm/year (15 in./year) or less annual precipitation and with generally dry pipe inverts and soils, a general minimum resistivity lower limit of 1000 ohm·cm over the 7.2–9.0 pH range is now recognized. Exceptions to the arid-region soil application guidelines exist at installations where the groundwater table reaches the pipe burial depth. In arid or nonarid regions, any groundwater seepage at the pipe burial depth necessitates the use of Figure 1 for further guidance.

4. Updated guidelines illustrate the effect of excessive soil acidity and alkalinity somewhat more specifically than has been done in the past. It is well known that pipe materials are not expected to give good service life beyond certain critical levels of acidity, and for aluminized steel this critical level can be exceeded somewhere near pH 5.0–4.8. Severe limitations in service life can occur at pH values below 4.5 where various types of free organic or inorganic acidity are likely to appear. Alkalinity at pH values above 9.0 has a rather mild adverse effect on service life because, although strong alkalinity attacks the aluminum layer of the aluminized steel

coating, it does not attack the Fe and Al alloy layer, and it helps protect the steel substrate.

REFERENCES

1. G. E. Morris and L. Bednar. Comprehensive Evaluation of Aluminized Steel Type 2 Pipe Field Performance. In *Transportation Research Record 1001*, TRB, National Research Council, Washington, D.C., 1984.
2. J. C. Potter. Aluminum-Coated Corrugated Steel-Pipe Field Performance. *Journal of Transportation Engineering*, Vol. 116, No. 2, 1990.
3. R. M. Pyskadlo. *Experimental Culvert Test Plates—A 10-Year Summary of Performance*. Client Report 56. New York Department of Transportation, Albany, 1992.
4. L. Bednar. Plain Galvanized Steel Drainage Pipe Durability Estimation with a Modified California Chart. In *Transportation Research Record 1231*, TRB, National Research Council, Washington, D.C., 1989.
5. L. Bednar. Durability of Plain Galvanized Steel Drainage Pipe in South America: Criteria for Selection. In *Transportation Research Record 1231*, TRB, National Research Council, Washington, D.C., 1989.
6. J. B. Bushman et al. *Soil Side Durability of Corrugated Steel Pipe*. NCSPA, Washington, D.C., 1991.
7. P. Bos and J. G. Kuenen. Microbiology of Sulfur-Oxidizing Bacteria. *Proc., Microbial Corrosion Conference*, Metals Society, London, England, 1983.
8. R. L. Starkey and K. M. Wight. *Anaerobic Corrosion of Iron in Soil*. American Gas Association, New York, 1945, pp. 86–88.
9. L. Bednar. *Resistivity and pH Limits for the Use of Aluminized Steel Type 2 Drainage Pipe*. Armco Inc. Internal Report, Jan. 13, 1987.
10. J. F. Ferguson. Corrosion Arising from Low Alkalinity, Low Hardness or High Neutral Salt Content Waters. In *Internal Corrosion of Water Distribution Systems*, AWWA Research Foundation Report, Denver, Colo., 1985.
11. F. L. La Que and H. R. Copson. *Corrosion Resistance of Metals and Alloys*. Reinhold, New York, N.Y., 1963, pp. 195–203.
12. L. Kenworthy and M. D. Smith. Corrosion of Galvanized Coatings and Zinc by Waters Containing Free Carbon Dioxide. *Journal of Institute of Metals*, Vol. 70, 1944, pp. 463.